Proceedings of

NETS-2015

Nuclear and Emerging Technologies for Space

February 23-26, 2015

Sponsored by
ANS Aerospace Nuclear Science and Technology Division
Universities Space Research Association
NASA

TABLE OF CONTENTS

Design of a Flight Demonstration Experiment for Radioisotope Thermophotovoltaic (RTPV) Power System

A. Goel[1], B. Franz[2], K. J. Schillo[3], S. Reddy[2], S. Howe[4]

[1]Stanford University, 584 Capistrano Way, Stanford, CA 94305
[2]University of Southern California, Los Angeles, CA 90089
[3]University of Alabama in Huntsville, 301 Sparkman Dr NW, Huntsville, AL 35805
[4]Center for Space Nuclear Research, 995 University Blvd, Idaho Falls, ID 83401
Telephone:6508044689 Email:ashish09@stanford.edu

Abstract. Radioisotopes have been used as the power source for many unmanned missions throughout the solar system. In most cases, the power system used has been the radioisotope thermoelectric generator (RTG) with plutonium-238 dioxide (PuO_2) serving as the radioisotope of choice. Despite their proven flight heritage, RTGs have low power conversion efficiencies, on the order of 6-8%. By contrast, a radioisotope thermophotovoltaic (RTPV) system can offer efficiencies above 15%. In addition to this, the shortage of plutonium has made americium an attractive alternative. In this paper, we describe the design of an RTPV flight demonstration experiment using americium 241 as the radioactive thermal source.

Due to the regulations associated with launching radioisotopes in space, we choose the Payload Orbital Delivery System from Space Systems Loral to host our experiment on a geostationary satellite. With analysis done using Monte Carlo N-Particle code, we find that while pure AmO2 poses challenges in terms of source preparation and handling, a couple of millimeters of tungsten shielding is enough to reduce the radioactivity levels to almost zero. Static and vibrational loading analysis coupled with the thermal radiation modeling leads to the choice of six, 3mm diameter Incoloy 903 rods for mounting. Based on the analysis of the power conversion efficiency, roughened tantalum emerges as the best option for selective emitter. The overall system efficiency is estimated to be around 6-8% and a sensitivity analysis reveals that this value is highly sensitive to the reflectivity profile of the filters used on the PV cells. Our algorithm also shows that by going to larger sizes or by switching to PuO2, we can achieve efficiencies close to 15%. Finally, we discuss the changes in shielding requirements and temperatures if the system were to use plutonium instead of americium.

Keywords: radioisotope, thermophotovoltaic, americium, plutonium, efficiency

INTRODUCTION

RTGs have been used on many missions in the solar system, such as the Galileo, Ulysses, Cassini, and New Horizons probes. While they have been extremely successful as a power source on these missions, their efficiencies are only on the order of 6-8%. On the other hand, a radioisotope thermophotovoltaic (RTPV) power system is capable of achieving overall efficiency in excess of 15% [1-3]. In addition, RTPVs can be scaled down to small sizes, making them extremely attractive for small satellite missions. RTPVs can hence enable low-cost exploration of the solar system, opening the doors of planetary exploration to universities and other research institutions. While the concept of an RTPV has been around for quite some time, the technology is yet to be flown in space. We propose to carry out a flight demonstration experiment to prove the flight worthiness of RTPV, thereby raising its technology readiness level (TRL) and eventually leading to its deployment as a power source on future planetary exploration missions.

Traditional RTG designs have used PuO2 as the radioisotope heat source. However, there is a shortage of plutonium-

238 (Pu238) that may make future discovery-class NASA missions impossible. One possible solution is to use americium-241 (Am241) instead of plutonium. While americium has a lower power density than plutonium, it is more widely available and easier to procure. We hence chose AmO2 for the design of the RTPV flight demonstration experiment.

MISSION OVERVIEW

In order to deploy a new radioisotope based technology in space, the technology will have to go through reviews by numerous agencies such as the DOD, DOE, NASA and eventually, the office of the President of the United States himself. In addition to this, the UN regulation on the use of radioisotopes in space rules out the possibility of deploying the experiment as a free-flying satellite in a low Earth orbit. We hence propose to the host the experiment on a geostationary satellite using the Payload Orbital Delivery System (PODS) provided by Space Systems Loral [4]. Figure 1 shows the PODS on a typical geostationary satellite. The host satellite provides power and relays the science

FIGURE 1. The Payload Orbital Delivery System (PODS) on a typical geostationary satellite

data from the experiment to the ground station. Since geostationary satellites are disposed of in a graveyard orbit at the end of their lifetime, our primary mode of disposal would not involve reentering through the Earth's atmosphere, thereby allowing us to meet the UN regulations. In order to keep the experiment simple and low-cost and to leverage commercial off-the-shelf parts available in the burgeoning CubeSat industry, we designed our experiment using the 1U CubeSat form factor.

SYSTEM CONFIGURATION

A CAD rendering of the flight demonstration module can be seen in Figure 2. The red radioisotope core is cylindrical in shape with a radius of 4 cm and height of 4 cm. It is held in place by a mechanism which shall be discussed further in the structural analysis section. The core is enclosed in a shell made of copper whose inner surfaces are lined with photovoltaic cells. The Electrical Power System (EPS) and Command and Data Handling (C&DH) boards are mounted above the RTPV along with the batteries. One can also see the small thermocouples and thermistors that have been added for monitoring the temperature of the core and that of the PV cells during the course of the mission. The total mass of the module is 3.5 kg with the core accounting for more than 80% of the mass of the system.

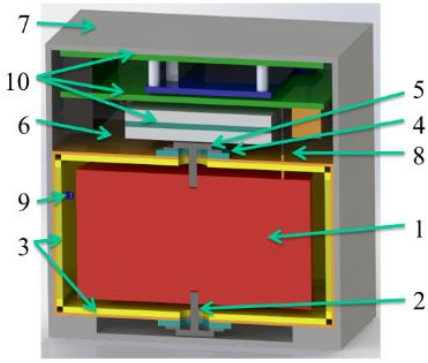

Number	Description
1	Fuel Core
2	Axial Mounting Rod
3	PV Cell Array
4	ZrC Insulator
5	Fastening Nut
6	Cu Shell
7	Al Chassis
8	Thermocouple
9	Thermistor
10	Electronics

FIGURE 2. CAD rendering showing a cross section of the RTPV flight demonstration experiment

RADIATION SHIELDING ANALYSIS

Providing adequate shielding from radiation emitted by radioisotopes is a vital design aspect for the RTPV. In our analysis, four different core materials were investigated: AmO2, an AmO2/tungsten matrix, PuO2, and a PuO2/tungsten matrix. In the case of the tungsten matrix, forty percent of the core's volume consisted of tungsten, and the remaining sixty percent consisted of AmO2 or PuO2. The radioactive material we intend to use on the flight experiment will be in the form of the tungsten cermet. The pure AmO2 and PuO2 cores were analyzed for the sake of comparison.

Simulations of the radiation generated by the cores were conducted using Monte Carlo N-Particle Transport Code (MCNP). For the AmO2 and AmO2/tungsten matrix, the shield consisted of a two millimeter-thick skin of tungsten on the surface of the core. Tungsten was chosen as the shielding material since it serves as a good selective emitter for our wavelength range in addition to having good thermal and structural properties. A comparison between the radiation dose from the two core materials with and without a shield is presented in Table 1.

TABLE 1. Radiation dosage for shielded and unshielded AmO2 cores

Material	Dosage (no shield)	Dosage (2 mm tungsten shield)
AmO_2	235.0 rem/hr	4.53×10^{-4} rem/hr
AmO_2/W Matrix	197.2 rem/hr	2.72×10^{-4} rem/hr

Am241 is primarily an emitter of alpha particles which are very easy to shield against. The radiation dosage is mainly due to 60 keV gamma rays that can be shielded with the help of a high-Z material like tungsten. From the results in Table 1, it can clearly be seen that the radiation generated by both the AmO2 and the AmO2/tungsten matrix is too high for workers to handle directly, while also showing that a two-millimeter shield of tungsten is very effective in reducing radiation levels to an acceptable level. The lower dose rate from the tungsten matrix can be attributed to there being less americium present in the core.
After these results were obtained, a core with plutonium fuel was investigated. Like americium, plutonium is primarily an alpha particle emitter, but gamma rays generated by plutonium are considerably less intensive than those generated by americium. However, in stark contrast to the americium core, a tungsten shield was found to be almost completely ineffective at reducing the radiation from a plutonium core. This is due to the fact that plutonium also generates neutrons from spontaneous fission reactions, which tungsten is very ineffective at shielding from.

Boron carbide and a layer of polyethylene and borated polyethylene were then investigated as shielding materials for the plutonium core. For these simulations, the detector was placed at a distance of five centimeters from the surface of the core, with the shielding placed directly on the core's surface. The reduction in radiation caused by varying the shield thickness is presented in Figure 3. One can see that borated polyethylene is more effective at reducing radiation from the core, albeit not by a very significant amount. Additional simulations found that using 40 millimeters of shielding does significantly reduce the dose rate, but this is beyond the volume constraints of the 1U form factor.

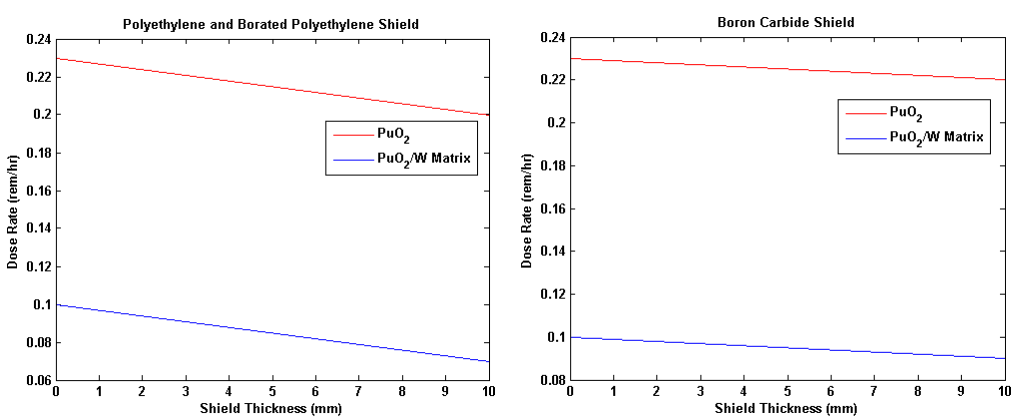

FIGURE 3. (left) Radiation dose rate with polyethylene and borated polyethylene shield; (right) Radiation dose rate with boron carbide shield

For this reason, shrinking the plutonium core was investigated as another method to reduce the radiation. In this case, the core was shrunk as the thickness of the shield was increased, keeping the overall size of the core and shielding combination the same. Simulations were also conducted without any shielding in order to assess how effective the shielding was on radiation reduction. The results of these analyses are presented in Figure 5. One can see that there is almost no difference between the dose rate of a shrinking plutonium core when a shield is present or absent. This is consistent with the very low reduction observed in Figure 3. This indicates that almost all of the reduction in radiation is due to an increasing distance from the surface of the core and a reduction in the amount of plutonium present. Therefore, it may not even be necessary to include radiation shielding for the plutonium core. We also note that by shrinking the core down to 3 cm in radius, we were able to bring down the dose rate below 200 mrem/hr, which is a benchmark set for the GPHS modules in an RTG [5].

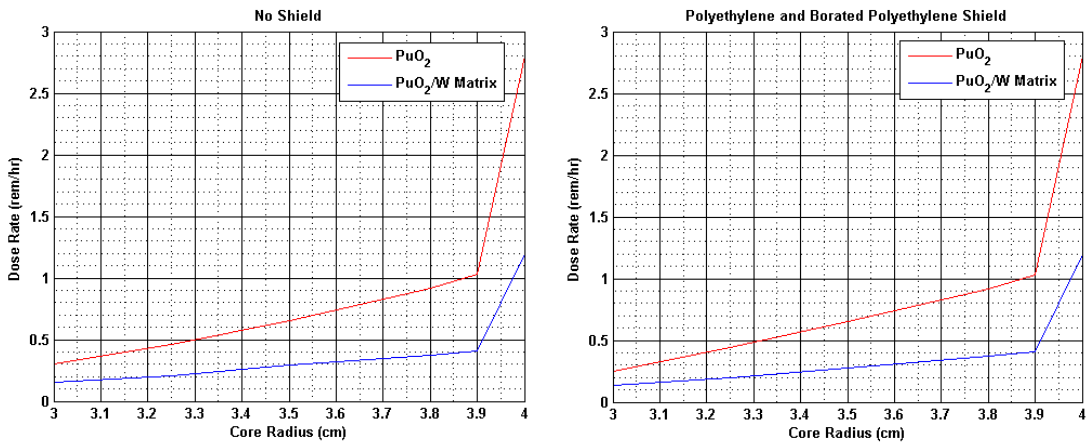

FIGURE 5. Radiation dose rate of shrinking PuO_2 core without (left) and with polyethylene and borated polyethylene shield (right)

STRUCTURAL ANALYSIS

In the case of an RTPV, the goal is to minimize heat loss from the core, so that more thermal photons can contribute to the process of generating electrical power. The mounting mechanism hence has to survive various launch and on-orbit loads, while minimizing heat loss due to conduction. The three types of loading that the system experiences are

1) static g-force loading
2) sinusoidal and random vibration loading
3) thermal loading

Space Systems Loral's PODS interface specifies the following launch loads [4] that the RTPV must withstand

1) Static g-force load of 13 g's on all three axes
2) Sinusoidal vibration load of 13 g's between 5-50 Hz and 5.2 g's between 50-100 Hz
3) Random vibration power spectral density (PSD) envelope of 6 dB/oct between 20-50 Hz, $0.2g^2$/Hz between 50-600 Hz and -4.5 dB/oct between 600-2000 Hz

The structural mount that holds the radioisotope core in place consists of axial mounted rods that pressure fit into slots in the core to suspend the core inside the shell as shown in Figure 6.

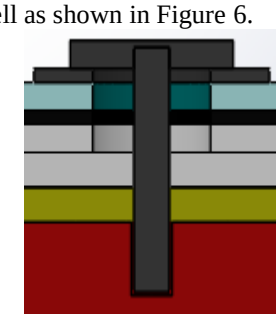

FIGURE 6. Structural mounting system

Another aspect of the structural mounting mechanism that can be seen in Figure 6 is the zirconium carbide washer (denoted in turquoise) that acts as a thermal insulator in order to minimize the conductive heat loss from the core. The bolt-washer-rod-core mechanism also allows for an easy assembly of the system.
The material selection for the bolt, washer and mounting rod was based on the following three properties

1) Coefficient of thermal expansion (CTE)
2) Thermal conductivity
3) Yield strength

The CTE was determined to be one of the driving parameters for material selection due to the thermal expansion and subsequent thermal stress that results when the mounting rods are introduced into the slots in the fuel core. The more the material expands, the higher the resultant thermal stresses due to the mismatch in CTE of the core and the mounting rod material. Thermal conductivity was chosen as a key material parameter to minimize conduction losses since a material with a high thermal conductivity would result in a lower core temperature. The yield strength of the chosen material must be higher than the stresses computed during both static and vibration analyses, at the temperature generated by the core inside the shell. Based on these considerations, materials like tungsten, zirconium carbide etc. were compared at the operating temperature of 1000 K and based on the results of the static analysis, Incoloy 903 was chosen as the material for the bolt, the washer and the mounting rod.

The analysis of static loading shed light on a couple of important characteristics of the structural mounting system chosen to support the core. The first of these is that a mounting rod of diameter less than 3 mm in diameter would not withstand the launch loads regardless of the thermal environment as shown in Figure 7. Note that the stresses for axial loading were found to be considerably lower than the stresses for lateral loading. We hence only present numbers for loading perpendicular to the length of the rod.

The second major insight was the realization of the fact that thermal stress was the dominant form of stress as shown in Figure 7. This caused the first change to the design of the structural mounting system because the thermal stress had to be mitigated. This was accomplished by sizing the slot in the fuel core to be just large enough to allow both the mounting rods and the core to thermally expand into the pressure fit design at the operating temperature. This “gap” can be seen in Figure 6.

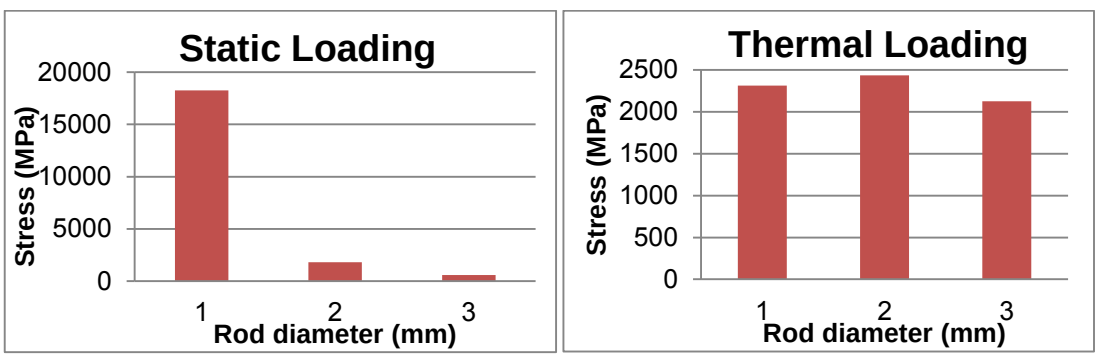

FIGURE 7. (left) Stresses due to static loading during launch; (right) Thermal loading from thermal expansion

The possibility of using an inert gas in the cavity at the time of launch was also considered. The inert gas would reduce the temperature of the core due to convectional heat transfer, thereby mitigating the thermal stresses. This would also provide an added benefit from the fact that the yield strength of the Incoloy 903 rods would be higher at the lower temperature and hence provide a larger safety margin in our design. However, a cold environment at launch would lead to the gap between the core and the mounting rod not getting filled up. From our analysis, we found that this causes a large spike in the static loading stress that the system would experience during launch due to a stress concentration at the small area of contact. Hence this approach was abandoned.

Sinusoidal vibration analysis was carried out to determine the resonance frequency for the structural mounting system. The analysis for 13 g’s of loading between 5 and 50 Hz yielded a resonance at 26 Hz as shown in Figure 8.

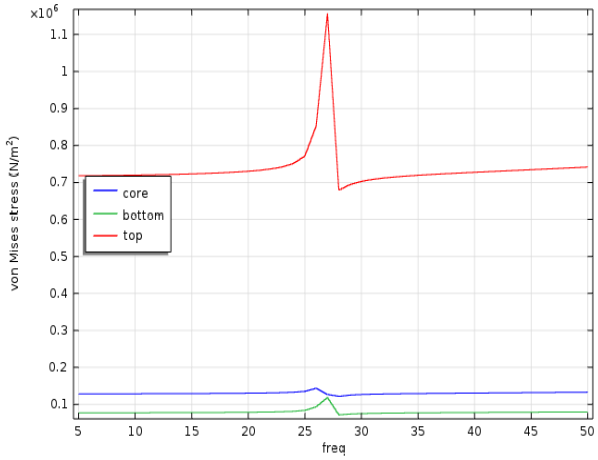

FIGURE 8. Resonance frequency plot for single 3mm mounting rod on both top and bottom faces

These results caused the second major change to the structural mounting system because the resonance occurred within the frequency range provided by Space Systems Loral for the PODS interface. The two options for a solution to this problem were to make the mounting rod larger in diameter and hollow or have multiple smaller rods. A trade study was performed for both options resulting in either a 7mm (OD) - 5mm (ID) single hollow rod or three 2mm rods on each face. The data for both these options is shown in Table 2.

TABLE 2. Hollow rod verses multiple rods comparison

	OD 7mm, ID 5mm	2mm X 3
Max Static Stress (MPa)	101	701
Max Stress @ 5-50 Hz (MPa)	109	741
Max Stress @ 50-100 Hz (MPa)	74.7	39
Resonance (Hz)	121	213

The three rod per face configuration, as seen in Figure 9, was chosen for two reasons. First, the surface area in contact with the core is smaller, leading to lower conductive heat loss. Second, there is a larger safety factor for resonance in the three rod configuration, while still within the threshold of allowable stress for Incoloy 903 at 1000 K.

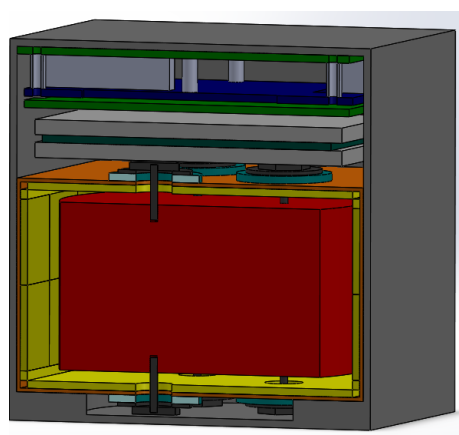

FIGURE 9. Configuration showing three 2mm rods on each face

A sensitivity analysis was performed for thermal expansion, the resultant thermal stress and for resonance in order to determine how much change would occur if the empirical values of the system deviated from the calculated theoretical values. The thermal expansion and resulting thermal stress was calculated to estimate how much added stress the structural mounting mechanism would experience if there was a deviation in the temperature of the core. Figure 10 shows the additional thermal stress as a function of the underestimation in core temperature. Note that in the case of

an overestimation, the gap between the core and mounting rods does not get filled up completely by thermal expansion, leading to large spikes in stress from launch loads. It would hence be advisable to size the mounting rods using the lower end of the temperature range over which the core is expected to operate.

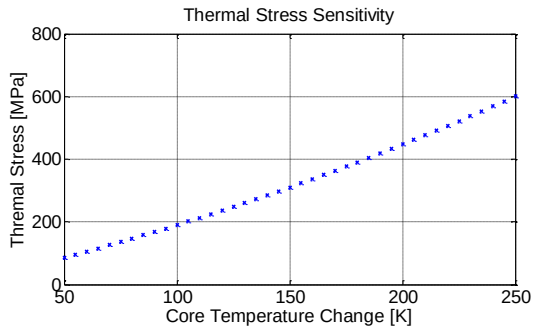

FIGURE 10. Thermal Stress Sensitivity

THERMAL RADIATION ANALYSIS

Having chosen the material and dimensions of the mounting rods, a radiation analysis was carried out to estimate the temperature of the core and the temperatures of the PV cells. The PV cells can operate only up to a temperature of 85^{0}C and their efficiency drops as their temperature increases. It is hence beneficial to operate the PV cells at as low a temperature as possible. In terms of core temperature, the higher the temperature, the higher is the efficiency of the power conversion process. We hence face a difficult engineering challenge of retaining as much heat in the core as possible but quickly rejecting the heat that escapes the cavity so as to keep the PV cell temperature low.

A thermal model comprising radiation and conduction was set up in COMSOL Multiphysics to simulate the thermal performance of the RTPV. It was assumed that since the experiment is mounted on a large geostationary satellite with a huge thermal mass, the temperature of the latter can be assumed to be a constant. The PODS interface requires the experiment module to survive temperatures ranging from -35^{0}C to 60^{0}C. In order to account for the worst case scenario, this temperature was assumed to be 60^{0}C. We also assumed that the chassis is coated with a thermal paint having a high emissivity of 0.9 in order to radiate the excess heat away.

The material of the shell of the RTPV was chosen to be copper because of its high thermal conductivity. This would allow the heat from the PV cells to be dissipated easily to the chassis and hence to the outer surface or the host satellite. The wavelength-dependent emissivities of tungsten and roughened tantalum selective emitters were incorporated into the model and filters were also used on the PV cells to minimize radiation losses [3]. And finally, it was also assumed that sunlight and Earth albedo at 35% are incident on the satellite at all points of time.

As can be seen from the results for the AmO2-tungsten matrix in Figure 11, the core reaches a temperature around 1000 K. The PV cells near the bottom are at a relatively low temperature of 60 ^{0}C on account of being mated with the geostationary satellite and their temperature gradually increases up to 72 ^{0}C as we move up.

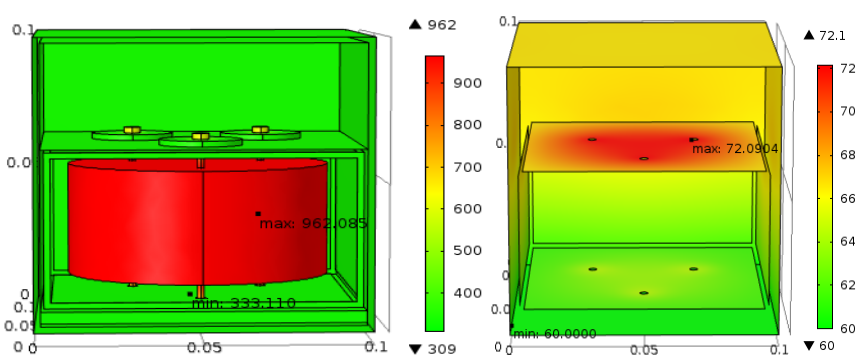

FIGURE 11. Core temperature in K for AmO2; (right) PV cell temperatures in ^{0}C

POWER CONVERSION EFFICIENCY

From Planck's law, for a given emitter temperature, there is an optimum bandgap energy of the PV cell. For reasonable emitter operating temperatures i.e. between 1000 - 2000 K, the bandgap energy must be less than 1 eV. Based on this and other factors like high quantum efficiency and availability, a trade-study was performed to choose the right type of PV cell for our application. From our thermal analysis, the emitter temperatures were found to be between 900 and 1200 K and hence Si, Ge and GaSb had to be ruled out as they all require very high operating temperatures. While InGaAsSb and InPAsSb have low operating temperatures suited for our project, their performance has not been validated yet. Hence, InGaAs PV cells were chosen for our design. These cells are available in the form of Monolithic Integrated Modules (MIM). Each of these MIMs comprises 25-junctions and has dimensions of 2.25*2.25 cm [6-8]. In our design, 8 such MIMs are arranged on each lateral side of the cavity in two rows and the remaining area is covered with reflector material. These MIMs would be arranged in series-parallel combinations to generate power at a standard voltage bus of 28 V. On the top and bottom surfaces, we are yet to ascertain if the manufacturer can provide MIMs in customizes shapes so that they can be mounted around the mounting rods.

Based on the software written by Dr. Donald Chubb from NASA Glenn [9], an algorithm was developed to carry out the radiation balance in the optical cavity, accounting for the emissivities and reflectivities of the surfaces. The algorithm was used to vary the geometry and other parameters to carry out the different analyses described hereunder.

For the choice of the selective emitter, roughened tantalum, polished tantalum, tungsten, rhenium and iridium surfaces due to their very low vapor pressure. Although polished tantalum has a closer response to an ideal emitter, roughened tantalum has higher emissivities in the bandgap region and since a highly efficient filter is used in our design, it compensates for the higher emissivity values beyond the bandgap. Hence roughened tantalum was chosen to be the most suitable emitter for our application. We would however like to note that as can be seen from the results in Figure 14, due to the choice of a highly efficient filter, the choice of the selective emitter is not very critical.

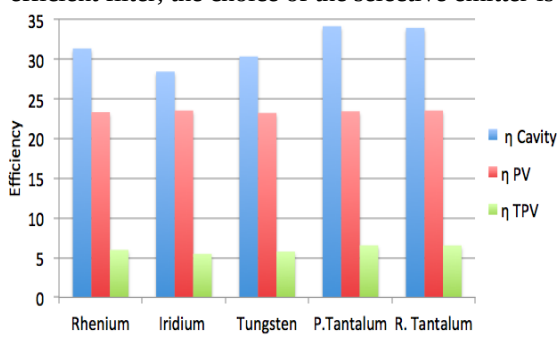

FIGURE 14. Efficiency of the system for different choices of the selective emitter material

Based on the choice of the PV cells, it was found that the emitted radiation spectrum peaks optimally in the bandgap for a core temperature of 1748K. Figure 15 shows how the black body curve is shifted by the roughened tantalum selective emitter for AmO_2 core, PuO_2 core and a core which operates at the optimum temperature of 1748 K.

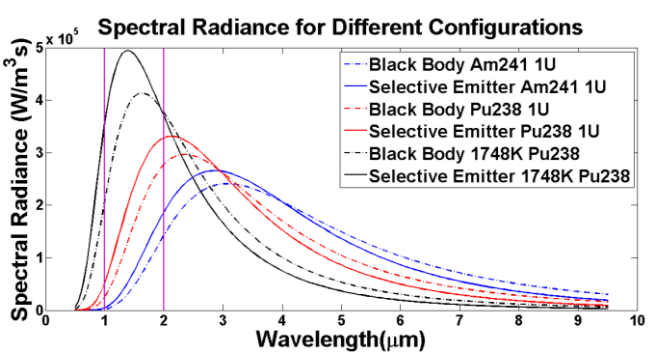

FIGURE 15. Effect of selective emitter

Since we are operating at very low temperatures, a majority of the radiation lies beyond the bandgap (as can be seen

in Figure 15) making the filter and reflector more crucial to our design. We assumed that the system would incorporate both a front surface filter and a back surface reflector (BSR) to ensure a filter response very close to the ideal case. A sensitivity analysis was carried out and it was found that the system is very sensitive to the reflectivity of the filter, as shown in Figure 16.

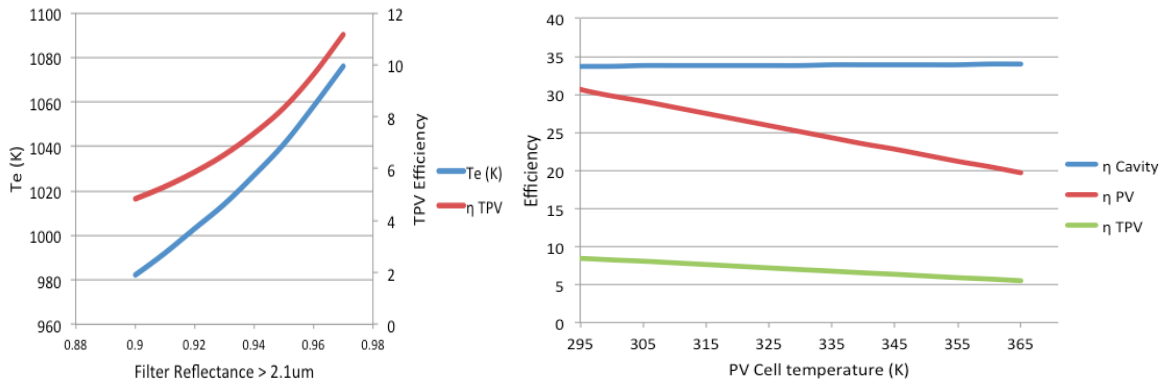

FIGURE 16. (left) Dependence of efficiency and emitter temperature on filter reflectance; (right) Effect of PV array temperature on efficiencies.

The dark saturation current increases rapidly with increasing PV array temperature, leading to a decrease in the PV cell efficiency. Figure 16 also shows the effect of PV array temperature on η_{th}, η_c and η_{PV}. The cavity efficiency experiences very small increase as the PV array temperature increases. This results from more thermal energy being emitted by the PV arrays that is added to the optical cavity. However, the PV efficiency shows a large decrease in going from temperature of 295 K to 350 K. Based on the thermal analysis, the PV cells in our system are expected to operate at around 340 K.

Taking into consideration the possible variation in all the parameters discussed so far, the worst-case and best-case performance of the RTPV with the AmO_2-tungsten power source was estimated. The results for a thermal input power of 126.9 W, a roughened tantalum selective emitter, and 0.6 eV InGaAs MIMs are provided in Table 3.

TABLE 3. RTPV performance with AmO_2-tungsten core

	Minimum	Maximum
Thermal Efficiency	80%	92%
Emitter Temperature	980 K	1090 K
Cavity Efficiency	29%	40%
PV Cell Temperature	333 K	353 K
PV Efficiency	21%	25%
TPV Efficiency	5%	9%
Output Power	6.345 W	11.42 W

As mentioned earlier, the PV cells are arranged to generate power at a voltage of 28 V. However, due the variation in temperatures across the MIMs, the current generated from different MIM units will be different. Hence in the design of our power conversion and distribution system, a maximum power point tracker (MPPT) is used to ensure that the system operates at the optimum current and voltage, ensuring maximum power transfer [10]. The critical unit on the Electrical Power System (EPS) board is the power dissipation system. Since the RTPV unit generates roughly 10 W of electrical power continuously, shunt resistors are connected in parallel with the battery to dissipate the excess power. In the future, one may consider increasing the size of the experiment module to incorporate a payload that would help with the power dissipation.

CONCLUSION

A CubeSat-sized module powered by an RTPV power source has been designed for flight demonstration on a geostationary satellite. Although prior research work on RTPV's have shown that efficiencies above 15% can be

achieved, due to the limitations of size and the choice of the Am241 isotope, the system is expected to have lower efficiencies. While the radiation levels are easily suppressed for an americium-based core, the neutron flux on the PV cells is relatively high for the plutonium-based system. Recent experiments carried out by General Atomics suggests that the performance of the MIMs does not deteriorate significantly under long duration exposure to neutron flux [11].

While the primary mode of disposal at the end of the mission lifetime does not involve re-entry into the Earth's atmosphere, we have to account for possible re-entry due to launch vehicle failure. We cannot afford to have the radioactive material disintegrate in the Earth's atmosphere and hence a skin of tungsten, graphite or some other material will have to be introduced between the selective emitter and the core to maintain the integrity of the core during the re-entry ablation process. While there is some data available for the performance of such materials during hypersonic re-entry [12], we propose that ablation tests be carried out using the arc jet test facility at NASA Ames Research Center. The temperature profile that the system must be subjected to can be borrowed from the testing that was carried out on the GPHS modules to qualify them for space applications [13]. Additional tests such as impact testing and exposure to solid and liquid rocket exhaust will also have to be carried out to space qualify the RTPV.

ACKNOWLEDGMENTS

The authors would like to acknowledge the contribution of all the personnel at the Center for Space Nuclear Research (CSNR) for their support and guidance during the course of this work. The authors would also like to thank the members of the Mission Design Division at NASA Ames for their valuable guidance and support.

REFERENCES

[1] A. Schock, C. Or and V. Kumar, "Design and integration of small RTPV generators with new millennium spacecraft for outer solar system," *Acta Astronaut.*, vol. 41, pp. 801-816, 12, 1997.

[2] J. E. Strauch, A. Klein, C. Murray and P. Charles, "Watt scale thermophotovoltaic power system testing results-consider for ITAR session," in *12th International Energy Conversion Engineering Conference, American Institute of Aeronautics and Astronautics*, 2014.

[3] D. Wolford and D. Chubb, "Theoretical performance of a radioisotope thermophotovoltaic (RTPV) power system," in *7th International Energy Conversion Engineering Conference, American Institute of Aeronautics and Astronautics*, 2009.

[4] B. Sullivan, D. Barnhart, L. Hill, P. Oppenheimer, B. L. Benedict, G. Van Ommering, L. Chappell, J. Ratti, P. Will and A. FAQs, "DARPA Phoenix Payload Orbital Delivery System (PODs):"FedEx to GEO"," in *AIAA Space 2013 Conference and Exposition*, 2013.

[5] G. L. Bennett, J. J. Lombardo, R. J. Hemler, G. Silverman, C. Whitmore, W. R. Amos, E. Johnson, A. Schock, R. W. Zocher and T. K. Keenan, "Mission of daring: The general-purpose heat source radioisotope thermoelectric generator," in *4th International Energy Conversion Engineering Conference and Exhibit*, 2006, .

[6] N. S. Fatemi, D. M. Wilt, P. P. Jenkins, V. G. Weizer, R. W. Hoffman Jr., C. S. Murray, D. Scheiman, D. Brinker and D. Riley, "InGaAs monolithic interconnected modules (MIMs)," in *Photovoltaic Specialists Conference, 1997., Conference Record of the Twenty-Sixth IEEE*, 1997, pp. 799-804.

[7] D. Wilt, R. Wehrer, M. Palmisiano, M. Wanlass and C. Murray, "Monolithic interconnected modules (MIMs) for thermophotovoltaic energy conversion," *Semiconductor Science and Technology*, vol. 18, pp. S209, 2003.

[8] D. M. Wilt, N. S. Fatemi, P. P. Jenkins, R. W. Hoffman Jr., G. A. Landis and R. K. Jain, "Monolithically interconnected InGaAs TPV module development," in *Photovoltaic Specialists Conference, 1996., Conference Record of the Twenty Fifth IEEE*, 1996, pp. 43-48.

[9] D. Chubb, *Fundamentals of Thermophotovoltaic Energy Conversion.* Elsevier, 2007.

[10] R. C. Pilawa-Podgurski, N. A. Pallo, W. R. Chan, D. J. Perreault and I. L. Celanovic, "Low-power maximum power point tracker with digital control for thermophotovoltaic generators," in *Applied Power Electronics Conference and Exposition (APEC), 2010 Twenty-Fifth Annual IEEE*, 2010, pp. 961-967.

[11] J. E. Strauch, A. Klein, C. Murray and M. Du, "Neutron degradation of TPV cells-consider for ITAR session," in 12*th International Energy Conversion Engineering Conference, American Institute of Aeronautics and Astronautics*, 2014.

[12] H. Moody, D. Smith, R. Haddock and S. Dunn, "Tungsten and molybdenum ablation modeling for re-entry applications," *J. Spacecraft Rockets*, vol. 13, pp. 746-753, 1976.

[13] T. G. George and D. Pavone, *General-Purpose Heat Source Safety Verification Test Series: SVT-11 through SVT-13*, 1986.

Post-Irradiation Examination of ^{237}Np Targets for ^{238}Pu Production

Robert N. Morris, Charles A. Baldwin, Randy W. Hobbs, Joshua E. Schmidlin

Oak Ridge National Laboratory, Oak Ridge, Tennessee 37830
865-241-4237, morrisrn@ornl.gov

Abstract[1]. Oak Ridge National Laboratory is recovering the US ^{238}Pu production capability and the first step in the process has been to evaluate the performance of a ^{237}Np target cermet pellet encased in an aluminum clad. The process proceeded in 3 steps; the first step was to irradiate capsules of single pellets composed of NpO_2 and aluminum power to examine their shrinkage and gas release. These pellets were formed by compressing sintered NpO_2 and aluminum powder in a die at high pressure followed by sintering in a vacuum furnace. Three temperatures were chosen for sintering the solution precipitated NpO_2 power used for pellet fabrication. The second step was to irradiate partial targets composed of 8 pellets in a semi-prototypical arrangement at the two best performing sintering temperatures to determine which temperature gave a pellet that performed the best under the actual planned irradiation conditions. The third step was to irradiate ~50 pellets in an actual target configuration at design irradiation conditions to assess pellet shrinkage and gas release, target heat transfer, and dimensional stability. The higher sintering temperature appeared to offer the best performance after one cycle of irradiation by having the least shrinkage, thus keeping the heat transfer gap between the pellets and clad small minimizing the pellet operating temperature. The final result of the testing was a target that can meet the initial production goals, satisfy the reactor safety requirements, and can be fabricated in production quantities. The current focus of the program is to verify that the target can be remotely dissembled, the pellets dissolved, and the ^{238}Pu recovered. Tests are being conducted to examine these concerns and to compare results to code predictions. Once the performance of the full length targets has been quantified, the pellet ^{237}Np loading will be revisited to determine if it can be increased to increase ^{238}Pu production.

Keywords: Post-Irradiation, ^{237}Np target, ^{238}Pu, cermet pellet.

TARGET PELLET AND POST IRRADIATON PATH

A three step process has been chosen for the recovery of the US ^{238}Pu production capability which incorporates a graded approach to provide high confidence to the High Flux Isotope Reactor (HFIR) operator that the probability of developmental target failure is low [1]. The 3 steps are:

1. Irradiation of robust single pellet capsules for initial examination of pellet gas release and pellet dimensional change. These capsules were irradiated for 1 and 2 cycles in the HFIR;
2. Partially loaded targets, containing 8 pellets, in a prototypic target configuration were irradiated for first 1 cycle and then 2 cycles in the HFIR. The targets were punctured for gas release measurements and disassembled for individual pellet dimensional measurements;

[1] *This manuscript has been authored by UT-Battelle, LLC under Contract No. DE-AC05-00OR22725 with the U.S. Department of Energy. The United States Government retains and the publisher, by accepting the article for publication, acknowledges that the United States Government retains a non-exclusive, paid-up, irrevocable, world-wide license to publish or reproduce the published form of this manuscript, or allow others to do so, for United States Government purposes. The Department of Energy will provide public access to these results of federally sponsored research in accordance with the DOE Public Access Plan (http://energy.gov/downloads/doe-public-access-plan).*

3. Fully loaded prototypic targets, containing approximately 50 pellets, were irradiated for first 1 cycle and then 2 cycles in the HFIR. The targets were punctured for gas release measurements and disassembled for individual pellet dimensional measurements.

The pellets were formed by compressing sintered NpO_2 and aluminum powder in a die at high pressure followed by sintering in a vacuum furnace. Three temperatures were chosen for sintering the solution precipitated NpO_2 power used for pellet fabrication. A goal of the irradiation testing was to examine the effects of NpO_2 sintering temperature on pellet in-pile behavior and chemical process solubility. Pellet pressing pressures were as high as practical consistent with reasonable die and punch life. High NpO_2 sintering temperatures offer less shrinkage during irradiation; this results in smaller pellet/cladding gaps and better heat transfer with the resulting low operating temperatures. Low temperatures generally give less gas releases and greater reactor safety margins. However, these high sintering temperatures also make the irradiated pellets more difficult to dissolve and thus complicate the downstream chemical processing required to recover the plutonium.

After loading the targets with the pellets and welding shut, the completed target was hydrostatically compressed to reduce the pellet/clad gap to the minimum practical to give the pellet fabricators as much design/processing leeway as possible.

SINGLE PELLET CAPSULE POST IRRADIATON EXAMINATION

A total 14 single pellet capsules underwent post-irradiation examination (PIE). The capsule design was very robust to contain the fission gases and any pellet debris should problems have arisen. The primary goal was to measure gas release and pellet dimensional change on the first batch of pellet designs to gain general information and to reduce the field of candidates for the partial length targets. The capsule contained the test pellet in an aluminum mount with an upper copper heat sink spring loaded to provide firm contact surface for heat transfer. The design of the single pellet capsule is shown in Figure 1.

After irradiation, the capsules were transferred to the Irradiated Fuels Examination Laboratory (IFEL) for remote examination and disassembly. After an initial visual examination, the capsule was prepared for gas puncture by trimming the capsule wall thickness down so that it could be punctured by a hardened steel punch. After trimming, the capsule was placed into a puncture unit, the unit evacuated, sealed, and then punctured. The released gas was then routed, by a helium sweep gas, into a liquid nitrogen cooled charcoal cold trap where the fission gases were frozen out. After the system had been sweep out by the flowing He, the cold trap was removed from the flow path and gamma counted to determine the ^{85}Kr, ^{131m}Xe, and ^{133}Xe inventories. The puncture unit was also used to measure the capsule plenum volume; an abnormal volume would have been an indication of unexpected behavior. No unusual measurements were noted. Finally, the capsule was opened so that the pellet and internal components could be removed. This sequence of operations is shown in Figure 2. All work was done remotely because of the very high radiation levels.

Gas release varied over a wide range, but was less than 5% (^{85}Kr). After removal, each pellet was measured for length and diameter and the dimensional measurements indicated that the pellets shrunk by 1-6% in volume. The pellets with the higher NpO_2 sintering temperatures shrunk less overall. A metallographic mount was prepared of one of the pellets and it appeared some of the pellet shrinkage was due to the irradiation induced sintering of the NpO_2 particles. The particles appear to be shrinking and drawing away from the aluminum matrix leaving a small gap. It is likely that a small amount of additional matrix sintering is taking part as well, with the net result that early in the irradiation the pellets are increasing in density and thus a reduction in volume is taking place. Later on, much later in the irradiation, one would expect the pellets to begin swelling as fission products accumulate from parasitic fissions. The NpO_2 powder with the higher sintering temperature is denser to begin with and thus suffers less in-pile sintering and volume reduction. A before irradiation and after irradiation micrograph is shown in Figure 3. An evaluation of the irradiation parameters and the observed pellet performance indicated to the program that the maximum acceptable NpO_2 powder sintering temperature and maximum pellet pressing pressures along with the existing fabrication pellet sintering schedule would provide best target pellet.

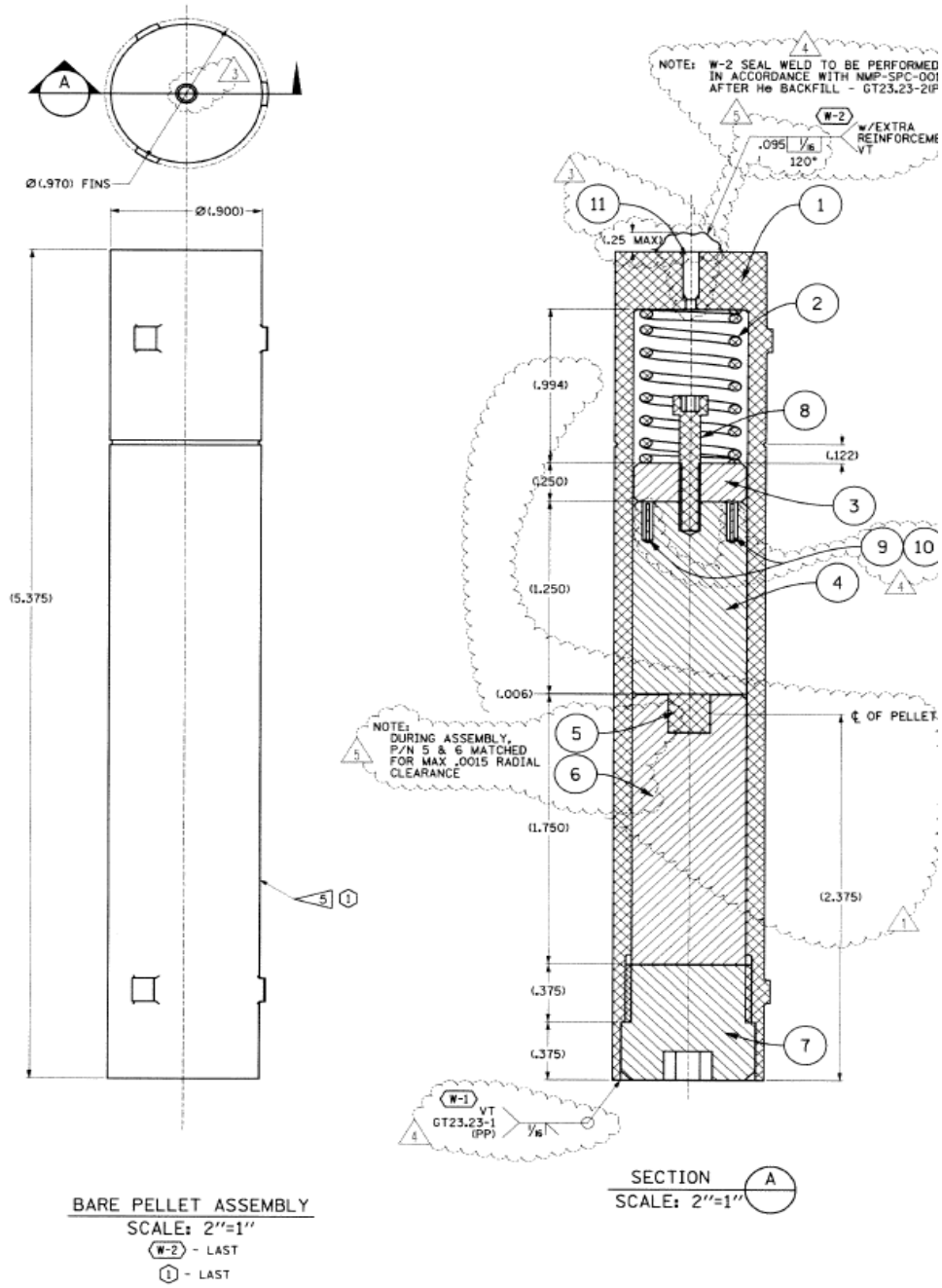

FIGURE 1. Robust single pellet capsule for initial testing. Item 5 is the pellet, 6 is the aluminum mount, and 4 is the copper heat sink.

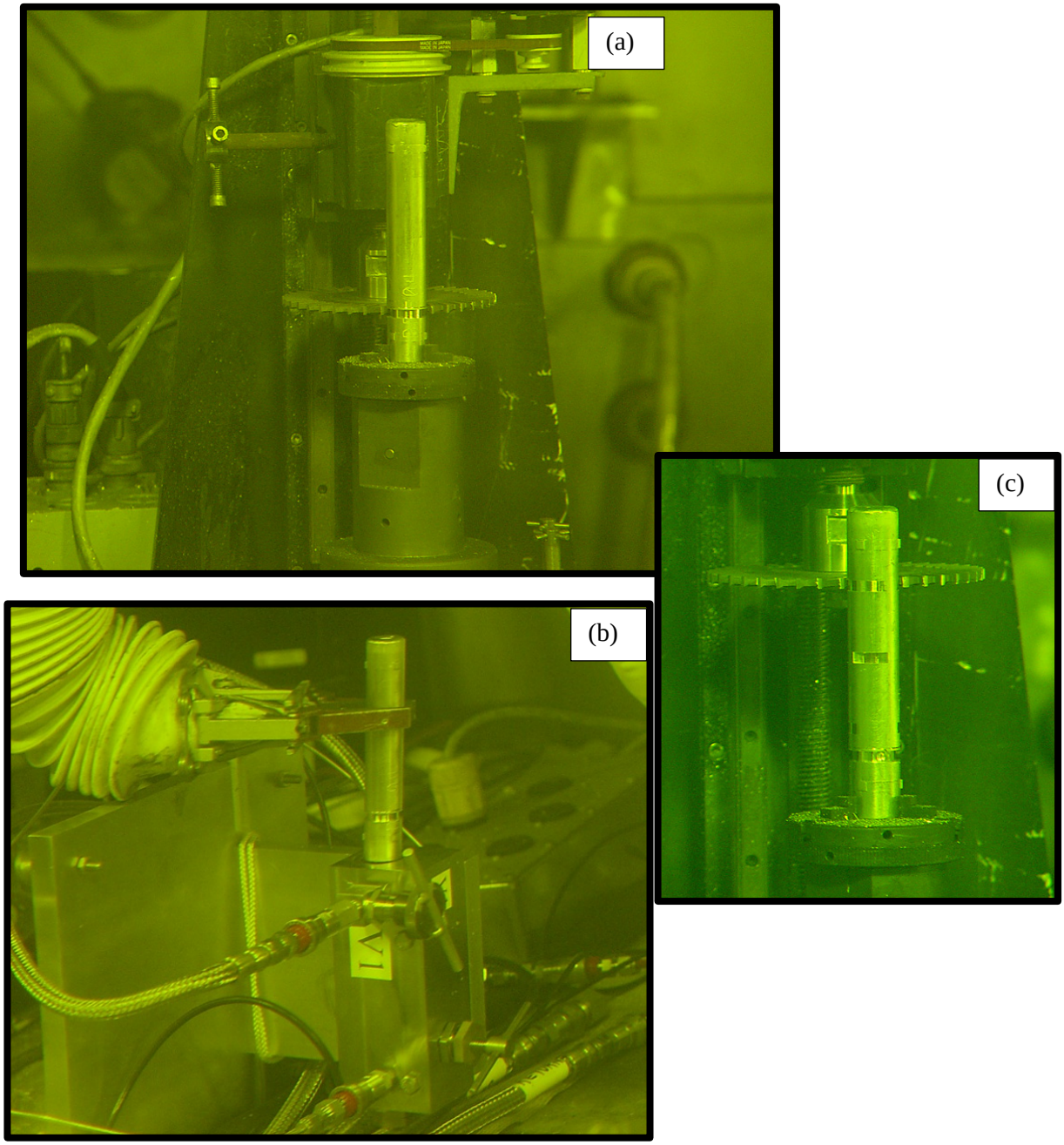

FIGURE 2. Initial capsule handling: (a) trimming the capsule wall for gas puncture; (b) placing the capsule in the gas puncture unit; (c) cutting the capsule open.

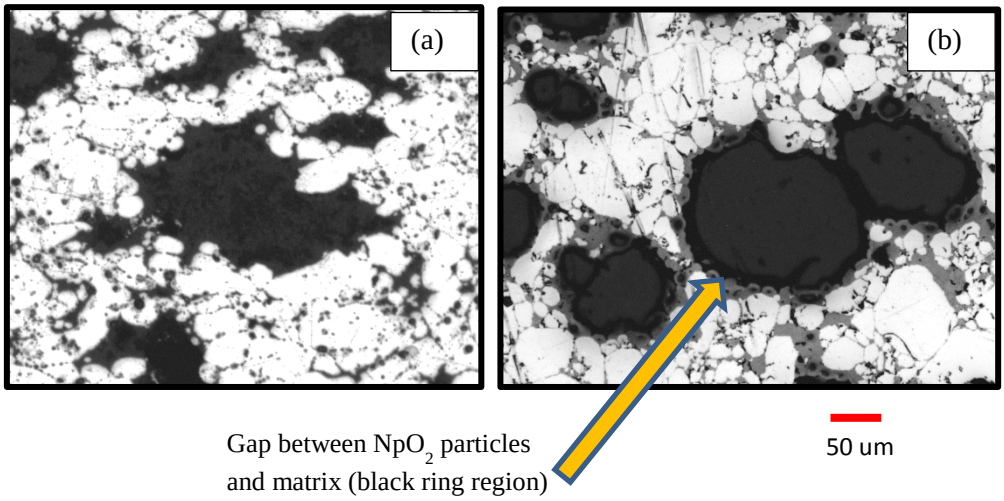

FIGURE 3. Metallographic mount of pellet showing small gap between the aluminum matrix and the NpO_2 particles due to in-pile particle sintering.

In addition to the pellet selection, the cladding performance for the candidate target design was also examined. Three capsules of similar design were constructed with sets of aluminum alloy tensile test coupons, some in direct contact with special wafer pellets, for irradiation testing of the cladding. These capsules were irradiated in a similar fashion as the single pellet capsules; see Figure 4.

After irradiation, the capsules were opened and the tensile specimens removed and visually examined; nothing unusual was noted. The specimens were then tensile tested and their tensile strength was found to have increased and their ductility decreased in accordance with expectations, both for the specimens in contact with the pellets and those not in contact with the pellets. The material irradiation changes were consistent with the literature and the cladding performance met the needs of the target irradiation; no further cladding test were needed or conducted.

PARTIAL LENGTH TARGET POST IRRADIATON EXAMINATION

A total 10 partial length targets underwent PIE. These were nearly prototypical targets containing 8 pellets in the central region of the target with spacers to fill the remaining volume in the target. Two ^{237}Np sintering temperatures were tested, the lowest having been eliminated by the single capsule testing. The central region of the target has a nearly homogeneous radiation environment so the 8 pellets saw the same irradiation conditions and thus functioned as 8 identical specimens for data collection. Both 1 and 2 irradiation cycle partial length targets were examined in the hot cell.

These targets underwent gas puncture and analysis in a manner that was similar to that of the single pellet capsules; the ^{85}Kr gas release fraction varied over a wide range, 1-13% due to different ^{237}Np sintering temperatures and irradiation conditions depending on the target location in the reactor. After disassembly, the pellets were measured and found to have shrunk by 1-4% by volume, consistent with the early tests. Cross sections of the targets were cut and polished to examine the pellet/cladding gap; they were found to be small and within the design constraints. See Figure 5.

This set of irradiations provided the information needed to complete the pellet down select, verify dimensional changes and gas release, and confirm that the full length target design would meet the irradiation goals and comply with all the safety requirements. At this stage of testing, it was apparent that the maximum powder sintering temperature, the maximum pellet pressing force, and hydrostatic compression of the cladding on the pellet stack were all needed to create a high yield target that met the reactor safety requirements. Thus, only one pellet formula, the one with the highest ^{237}Np sintering temperature, remained for the full length target testing.

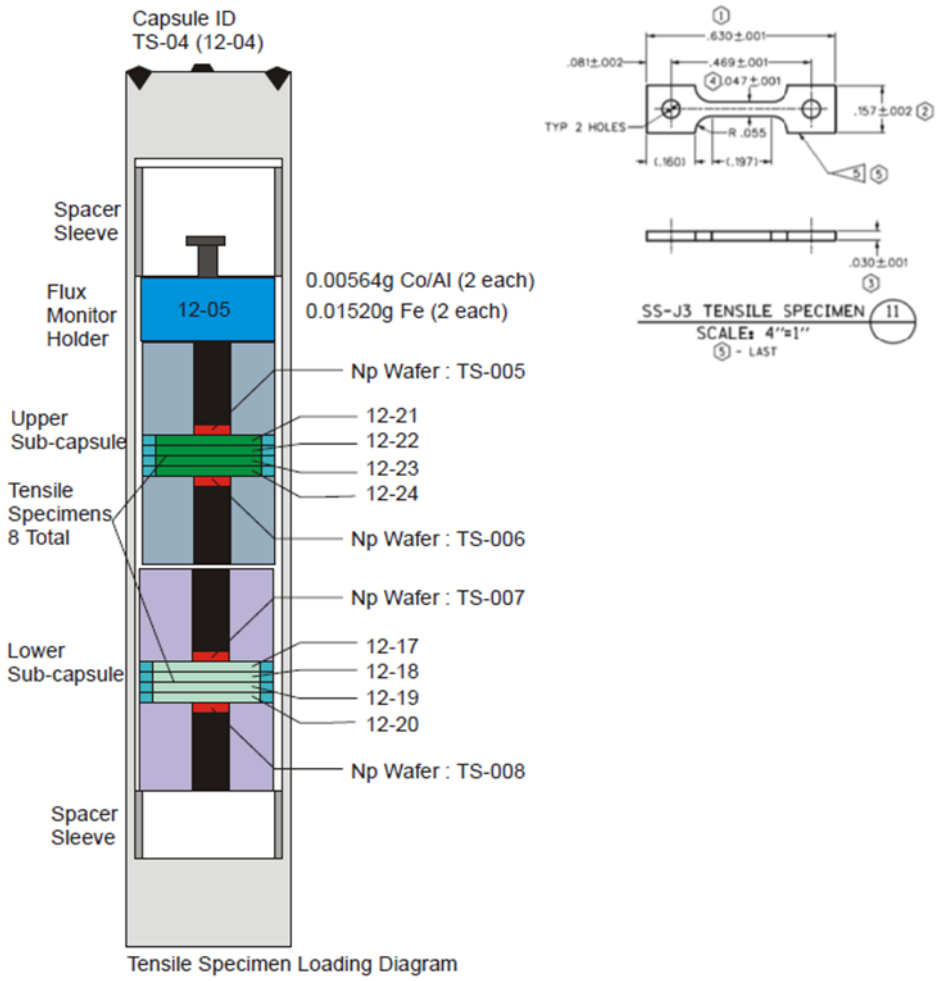

FIGURE 4. Special capsule designed for examining the radiation effects on the cladding material and the enclosed tensile specimens.

FULL LENGTH TARGET POST IRRADIATON EXAMINATION

A total 3 partial length targets underwent PIE. These were prototypical targets containing 50 pellets. These targets underwent the same examination as the previous targets with the addition of gamma scanning to determine the pre-PIE internal configuration.

The results of the gamma scanning are shown in Figure 6. As can be seen, considerable detail about the target internal structure can be determined. Small gaps between the pellets are acceptable; the major concern is that excessive pellet swelling can increase the pellet stack height and exert forces on the ends of the target. If these forces are high, target rupture is possible. However, in our case, the pellet irradiation has not gotten to the point where the pellet dimensions have exceeded their fabrication dimensions, thus for 2 cycles of irradiation swelling issues are not important. The two major issues for these targets are the point of maximum pellet shrinkage and the pellet gas release. The shrinkage opens the pellet/clad gap and the gas release adds low heat conductivity fission gases to the target internal environment. The combination of the two can increase the pellet temperature beyond acceptable levels. Dimensional data obtained on pellet diameter shrinkage and fission gas release for the full length targets is shown in Figure 7 and Figure 8. Fortunately, the design point and the selected pellet fabrication conditions result in acceptable performance with good safety margin for the general condition; the few outliners are under investigation.

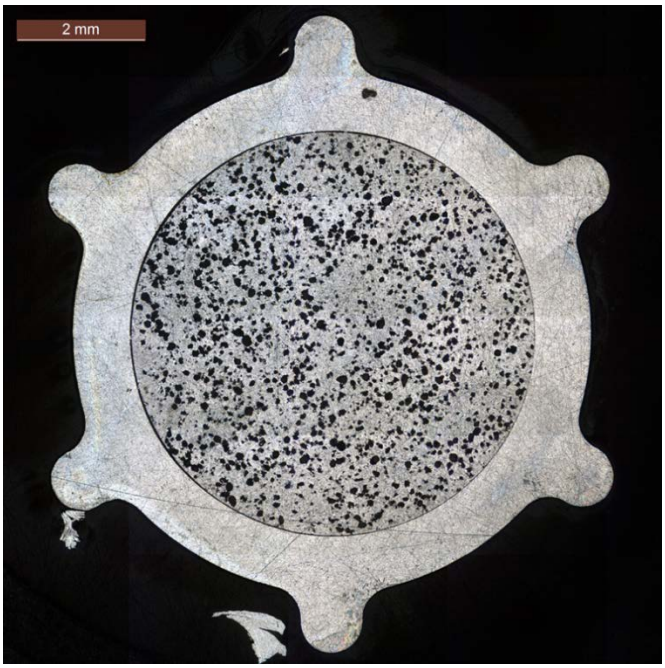

FIGURE 5. Cross section of partial length target showing the pellet clad gap after irradiation (P-94, pellet #4, mount 6395).

CONCLUSIONS

A graded approach was under taken to recover the ^{237}Np target design for US production of ^{238}Pu based on past cermet experience. The approach included the irradiation of single pellet capsules to examine the behavior of the newly fabricated cermet pellets, followed by partial length targets to collect additional information in a nearly prototypical condition to allow for pellet fabrication technic down select, followed by a full length 2 cycle irradiation to complete the data collection and verify the target design under actual irradiation conditions.

The result was a set of fabrication conditions, a target design, supporting data, and the necessary safety documentation for a high yield target. The next step is to quantify the actual ^{238}Pu production rate.

ACKNOWLEDGMENTS

The authors wish to thank the staff of the IFEL for their help with the PIE work. This work has been sponsored by NASA's Science Mission Directorate and the DOE Office of Space and Defense Power Systems.

REFERENCES

[1] Howe, S.D., “Economical Production of Pu-238”, Center for Space Nuclear Research (USRA), http://www.nasa.gov/pdf/716068main_Howe_2011_PhI_Plutonium_Production.pdf

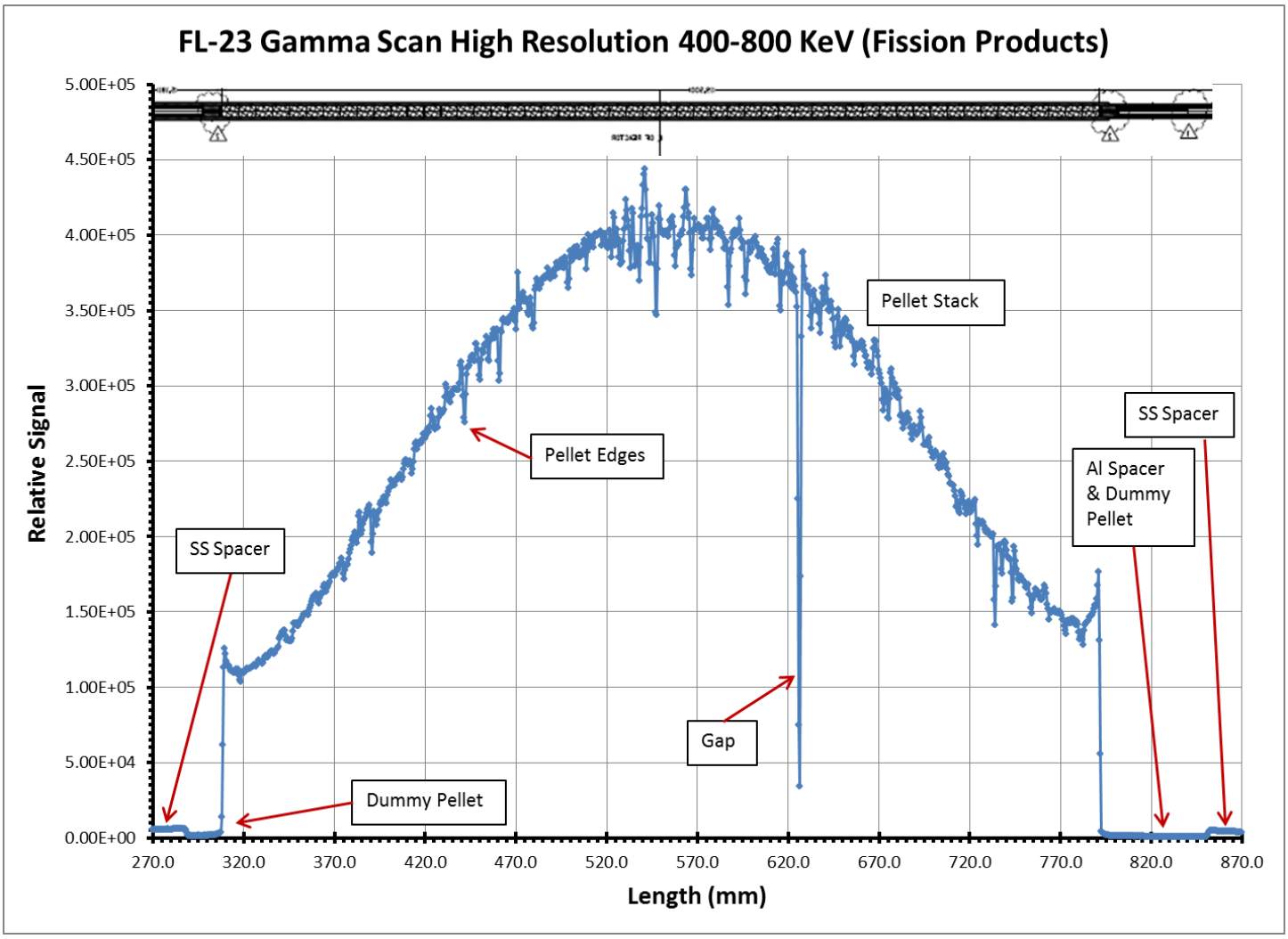

FIGURE 6. Results of gamma scanning a 2 cycle full length target.

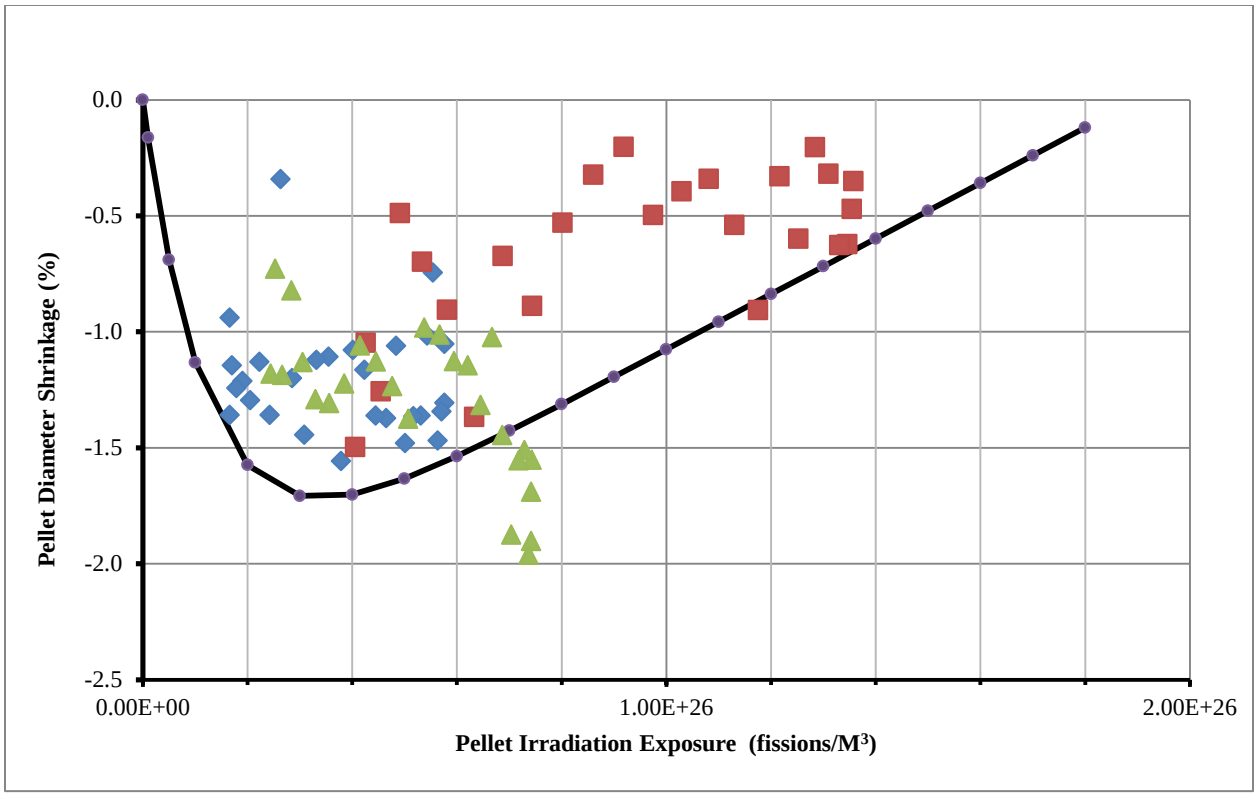

FIGURE 7. Pellet diameter shrinkage as a function of exposure. The solid line is the desired lower bound for a conservative safety analysis.

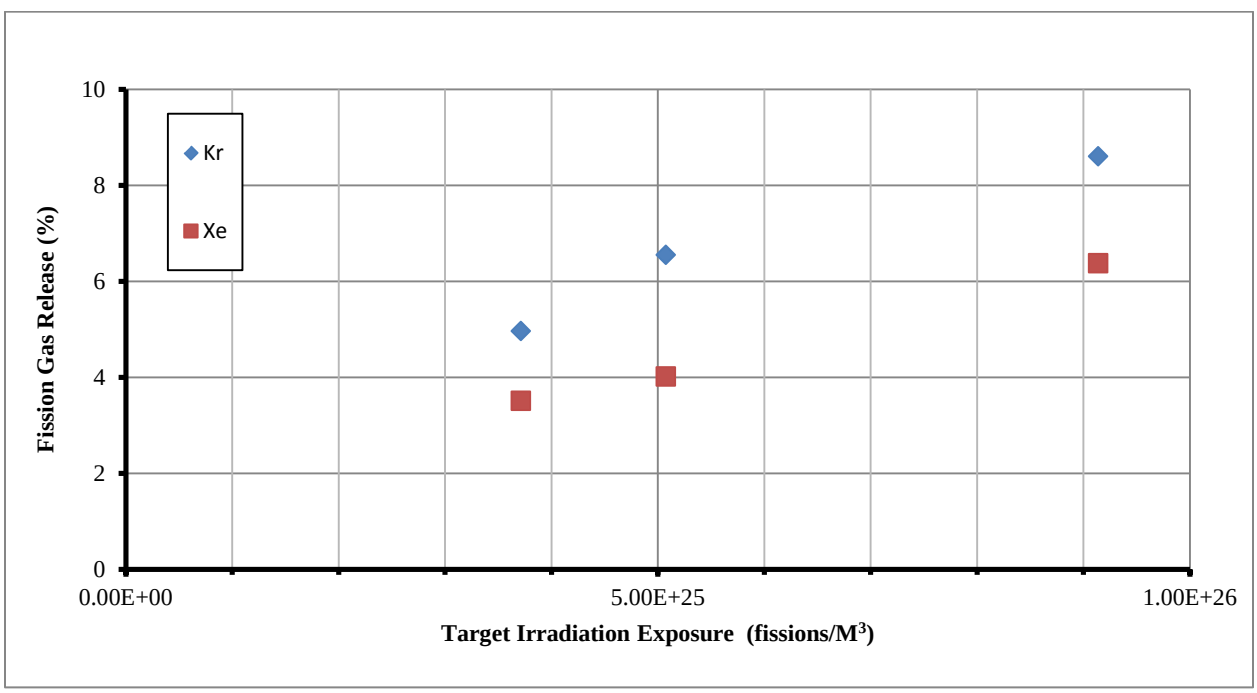

FIGURE 8. Fission gas release as a function of exposure.

Safety Analysis Models for the Irradiation of ^{237}Np Targets at the High Flux Isotope Reactor

Christopher J. Hurt[1*], James D. Freels[2a], Frederick P. Griffin[2a], David Chandler[2a], Randy W. Hobbs[2a], and Robert M. Wham[2b]

[1]Department of Nuclear Engineering, University of Tennessee, Knoxville, TN 37996
[2a]Research Reactors Division and [2b]Nuclear Science and Engineering Division, Oak Ridge National Laboratory, 1 Bethel Valley Road, Oak Ridge, TN 37831
859-358-5249; hurtcj@ornl.gov

Abstract. A campaign is underway to provide a new domestic supply of plutonium-238 using existing nuclear research reactors at the Oak Ridge National Laboratory (ORNL) and Idaho National Laboratory (INL) and existing chemical recovery facilities at ORNL. Validation and testing activities for new irradiation target designs have been conducted in three phases over a 2 year period to provide data to support an increased throughput toward a continuous production phase. Design, qualification, and fabrication of "fully loaded" targets of NpO_2/Al pellets have been completed, and target irradiation is ongoing at the High Flux Isotope Reactor (HFIR) at ORNL. In order to qualify experiments for irradiation at the HFIR, bounding accident conditions established in the HFIR safety analysis report (SAR) must be analyzed. Target design drawings, pellet fabrication data, and post-irradiation examination (PIE) measurements are input to computational safety analyses that calculate conservative parameters of interest in the target including maximum internal temperatures, coolant surface temperatures, and structural stress/strain maxima. Heat generation and decay rates in the target are analyzed using the neutronics codes MCNP, SCALE, and VESTA. Steady-state thermal-structural analysis of the target is performed using COMSOL Multiphysics, and transient thermal hydraulic analysis is performed using RELAP5. The primary physics phenomena explored include heat conduction, structural mechanics, thermal hydraulics, neutron transport, and isotopic transmutation with specific challenges in gas-gap/contact conductance, coupled thermal-structural responses, and pellet irradiation behavior.

Keywords: hfir, pu-238, thermal, Np-237, ornl.

SAFETY ANALYSIS OVERVIEW

Neptunium oxide (NpO_2) pellets are irradiated at the HFIR to produce the ^{238}Pu that will be used to fuel the radioisotope thermoelectric generators (RTGs) that power deep space mission technology for the National Aeronautics and Space Administration (NASA). A better overview of the project and its status can be found elsewhere [1,2], however it is illustrative to understand the phased strategy for reaching full production at the HFIR (see Figure 1) when viewing the safety analysis models and results.

*This student's research is being performed using funding received from the DOE Office of Nuclear Energy's Nuclear Energy University Programs.

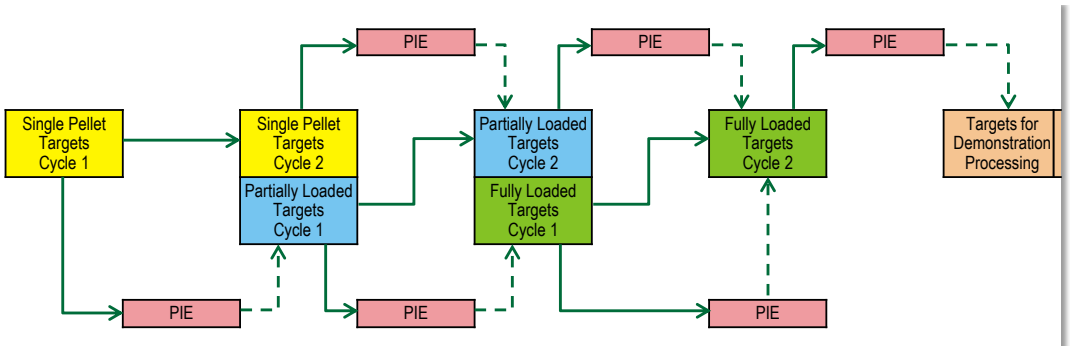

FIGURE 1. Phased target irradiation sequence.

The irradiation test program is intended to consist of four phases (as depicted by color code in Figure 1) that provide an incremental approach intended to reduce the risk of target failure during testing. Additionally, PIE results from each phase serve as a hold point and are used to guide the course of the subsequent irradiations. Ideally, safety calculations would only be performed at the start of each phase with PIE results from the previous phase informing the new set of models. However, scheduling efforts as well as unexpected pellet irradiation behavior observed in the PIE results has created the need for increasingly detailed revisions and innovative approaches to the safety analysis models.

Experiment Safety Review

Final target qualification requires an experiment authorization basis document supported by safety review references including calculations that assure target cooling in off-normal and nominal reactor operating conditions that do not result in either reactor fuel damage or damage to the experiment target as defined in the HFIR SAR[3]. The process to generate a comprehensive experiment authorization basis document is shown in Figure 2 below.

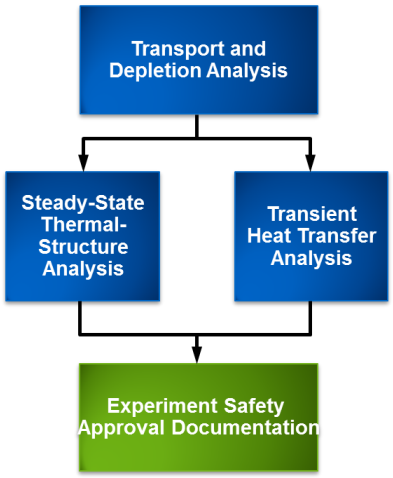

FIGURE 2. Simple diagram of the experiment safety review process.

The target cooling analyses are subdivided into bounding steady-state and transient conditions that are computed using nuclear safety software quality assurance-approved codes COMSOL Multiphysics and RELAP5, respectively, as detailed below. These analyses will be the focus of this document, as the third set of supporting calculations for neutron transport and material depletion (performed in the codes VESTA, MCNP5, and ORIGEN-S) are intended to be discussed in a separate paper.

- Steady-State Analysis in COMSOL:
  - 50% reduced coolant flow under normal reactor operating conditions,
  - 130% overpower and raised inlet temperature.
- Transient Analysis in RELAP5:
  - Small break loss of coolant accident (SBLOCA),
  - Loss of offsite power (LOOP).

The safety analysis review ensures reactor safety with respect to the experiments, specifically 1) The target internal temperatures remain below component melting temperatures, 2) The structural integrity of the target housing is such that it safely the irradiated pellet materials and prevents leakage of fission products, and 3) The target surface temperatures remain below coolant saturation temperatures. With the exception of the most recent fully loaded targets under 2 cycles of irradiation, the 1st mode of failure under steady-state 130% overpower, analyzed using coupled heat transfer and structural mechanics equations in COMSOL, has been the limiting condition from a safety review perspective [4].

The third set of supporting neutronics safety calculations are performed to establish the target heating and nuclide inventories which provide a basis for the above described calculations as well as a comparison to future PIE results.

CHALLENGING PHYSICS

In constructing, checking, and reviewing the safety analysis models, particular attention was paid to physics phenomena that had a very sensitive impact on the final safety results and whose features were particularly challenging from a modeling standpoint, due to lack of input data and computational challenges.

Contact/Gas-Gap Conductance

Peak pellet temperatures are driven by the heat transfer in the radial gap between the pellets and target cladding. The gas gap between the NpO_2 pellets and aluminum target housing is the location of the largest temperature gradient in the target and thus a crucial phenomenon to quantify when calculating the centerline (hottest) pellet temperatures. Pellet dimensional changes due to irradiation behavior have made this effect more pronounced by enlarging the gap and increasing pellet temperatures.

The heat transfer between the two surfaces (see Figure 3) consists of three effects: solid spot contact conductance between surfaces, the gas gap conductance, and a negligible radiation heat transfer term. The contact conductance is negligible when surfaces are not in contact, but nevertheless, is accounted for in the analysis for those cases where contact is made. The gas heat transfer is affected by the gas conductivity (dictated by the release of fission gases), the separation distance (dictated by dimensional irradiation behavior), and gap jump terms that account for the inefficient heat transfer between gas particles and the solid surface. The equations for the gap conductance are shown below [5]:

$$h = h_s + h_g + h_r \tag{1}$$

$$h_g = k_g/(\delta + g_1 + g_2) \tag{2}$$

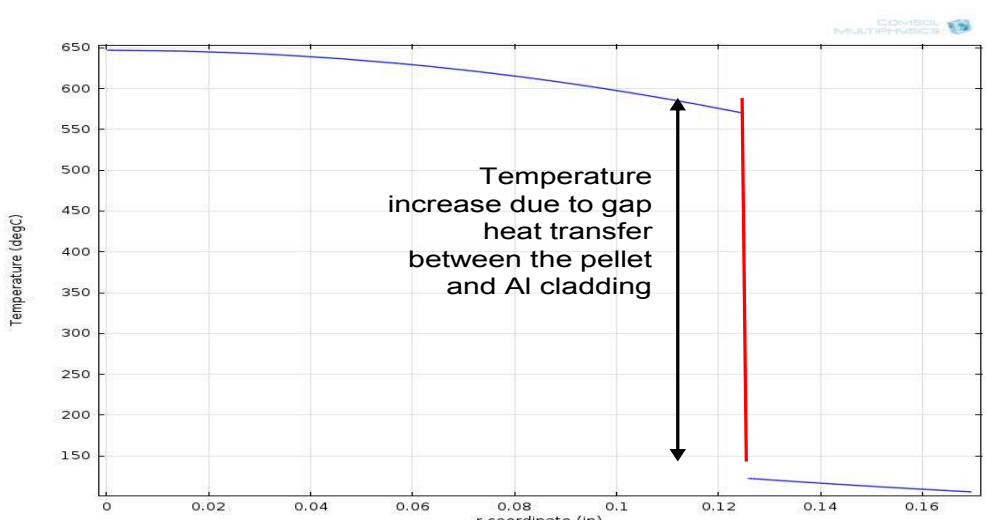

FIGURE 3. Radial temperature profile at the pellet midplane showing the temperature difference due to gap heat transfer.

Pellet Irradiation Behavior

The possibility of significant densification and swelling in the neptunium oxide pellets was discussed prior to the Phase 1 irradiations, however the expectation was that for the production burn-up levels the observed densification of the pellets would be minor and swelling would be the more measurable factor. While swelling presents a safety consideration in possible breach or failure of the target housing, densification or negative swelling presents a safety consideration as it increases the gap between the pellets and target housing, hence, reducing radial heat transfer, and elevating pellet temperatures near melting.

The behavior of irradiated fuel oxides suspended in an aluminum mixture has been measured in previous experiments [6,7,8]. The experiment results exhibit the general characteristics of densification and swelling as described in equations 3 and 4 and Figure 4 below. Fabrication void volumes experience a radiation-enhanced sintering which reduces the overall volume of the pellets for the early irradiation periods. Subsequently, the swelling due to fission gas and fission product release dominates the irradiation behavior as the reduction in void volume falls off.

$$\Delta V_{swell.} = \alpha * BU \tag{3}$$

$$\Delta V_{dens.} = P_0\left(e^{-\beta * BU} - 1\right) \tag{2}$$

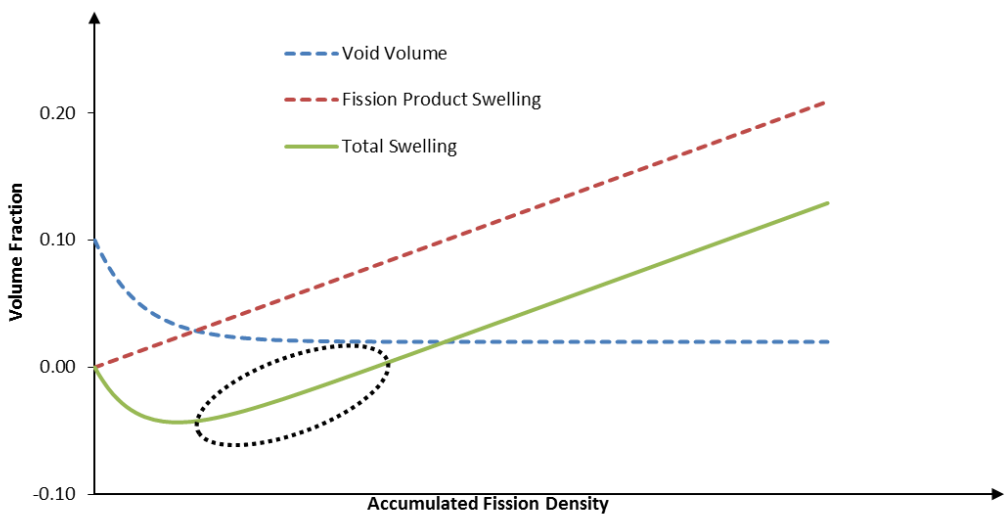

FIGURE 4. General trend and contributions to pellet irradiation behavior.

The partially and fully loaded target PIE measurements [9] provide consistent data points, enabling the creation of a trend, as shown for the 1200 °C heat-treated pellets in Figure 5. As shown in Figure 5, the irradiation behavior, as measured by the pellet dimensional changes in the PIE results, has mostly been observed in the time period after maximum densities and swelling due to fission products is recovering the negative volume change, however a trend consistent with theory in Figure 4 can be seen. The maxima densities are observed early in the irradiation periods, which is consistent with previous oxide fuel studies at around less than 4,000 MW-d/t-fuel [10,7,8].

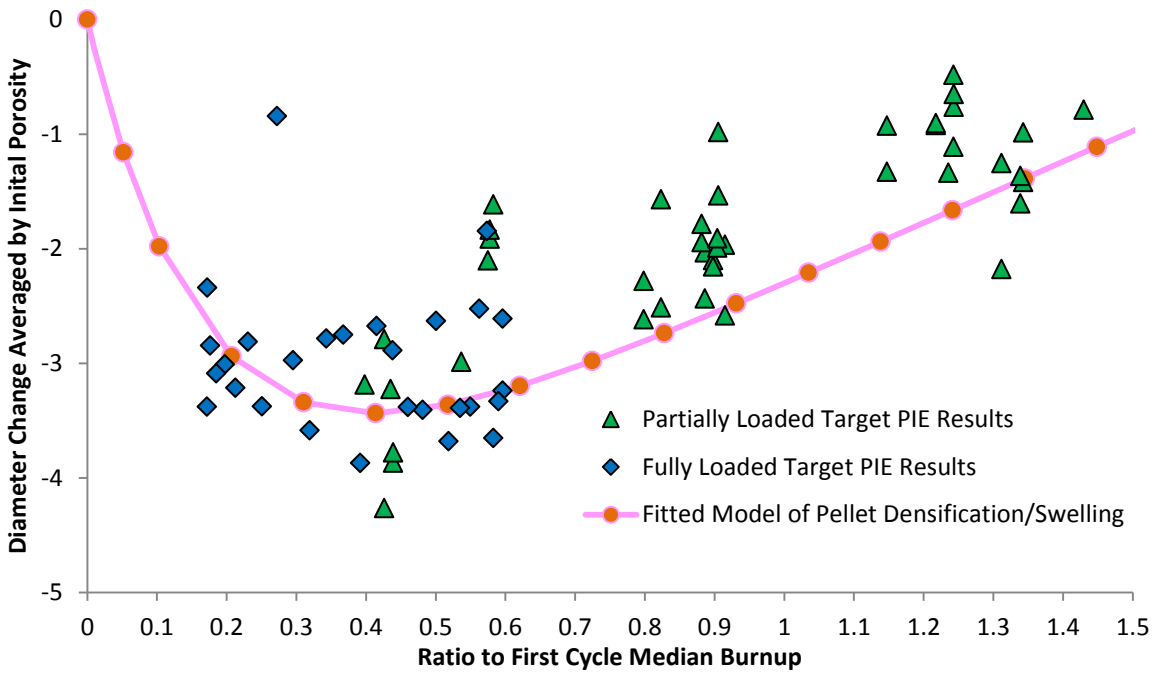

FIGURE 5. Fully and partially loaded target PIE data for 1200 °C heat-treated pellets with a fitted trendline.

SAFETY ANALYSIS MODELS

The two safety analysis model types are a steady-state thermal-structure calculation computed in COMSOL and a transient thermal hydraulic calculation computed in RELAP5. The focus will be on the COMSOL Multiphysics calculations since it results in the bounding safety condition.

Model Inputs

There are several key model inputs to the target cooling safety analysis models, as listed below. These are separated into PIE data, pellet material property data, target design information, and input data from neutron transport calculations. The PIE data was updated as measurements on irradiated targets became available, with close attention to new target designs or pellet fabrication techniques. The pellet property data has been measured as needed for the safety calculations and conservative data was assumed elsewhere. See Figure 6 for an example of recently measured unirradiated pellet stress-strain curves. Early thermophysical property and PIE measurements were made on pellets fabricated at different sintering temperatures before comparison using the safety analysis models determined a 1200 °C heat-treated pellet was the only path forward at the time. Updating the target design is a continual process but is frozen before the safety calculations are performed for each irradiation. The supporting neutron transport calculations are performed at each phase and repeated as needed to provide input to the target heating calculations.

- Post-Irradiation Examination (PIE) results
  - Shrinkage/Swelling vs. burn-up for radial and height dimensions
  - Fission gas release fractions
- Temperature- and composition-dependent material property data for the NpO_2/Al pellet (and other materials):
  - Thermal expansion coefficient
  - Thermal conductivity
  - Stress/strain curves (i.e. elastic modulus, yield strength)
  - Density, Poisson's ratio, etc.
- Target Design Drawings and Information
- Input heat generation rates (HGRs), burnup and fission gas production from neutronics calculations

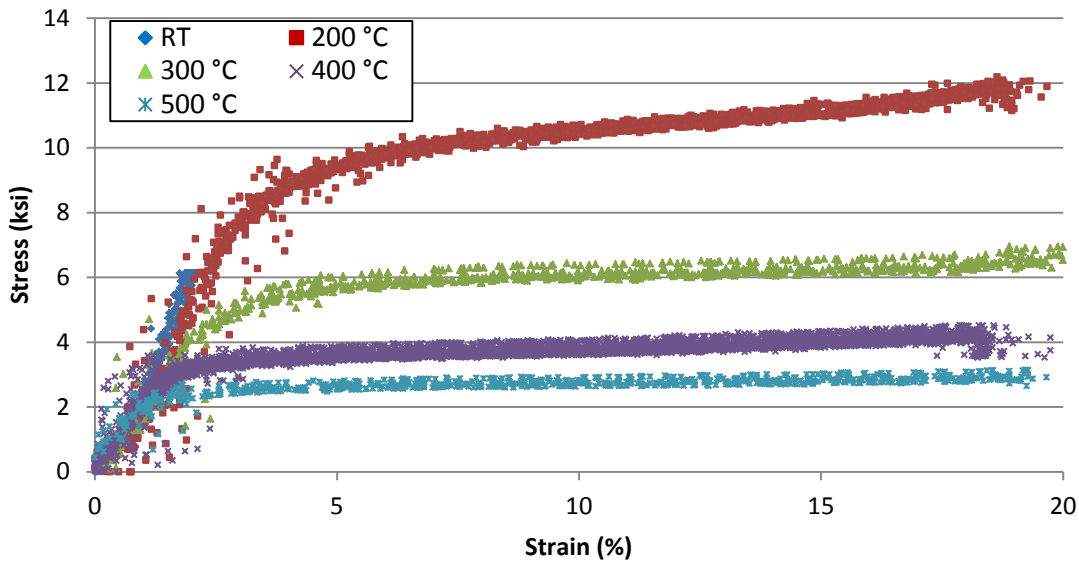

FIGURE 6. NpO_2/Al Pellet stress-strain curves measured at different temperatures.

Transient RELAP5 Model

The transient thermal hydraulics analyses completed in RELAP5 [11] generally took advantage of the verified assumption that the steady-state cases were more thermally limiting. Verifying this for the limiting case (usually conditions at the end of the reactor operating cycle with a 10% uncertainty factor in pellet HGRs) allows the transient analysis to avoid some of the complications considered for the steady-state models.

The two transients called out in HFIR procedure EG-6[12] are the LOOP and SBLOCA events as defined by the HFIR SAR. Bounding values for the cold fabrication and shrinkage gaps are chosen that will result in satisfactory thermal acceptance criteria for the model. The acceptance criteria for these events are no target failures due to (1) surface burnout or (2) excessive internal temperatures. Figure 7 below shows the LOOP transient surface temperatures against coolant saturation at end-of-cycle 2 (EOC-2) and Figure 8 shows the bounding shrinkage value for the RELAP5 analysis against the steady-state COMSOL results.

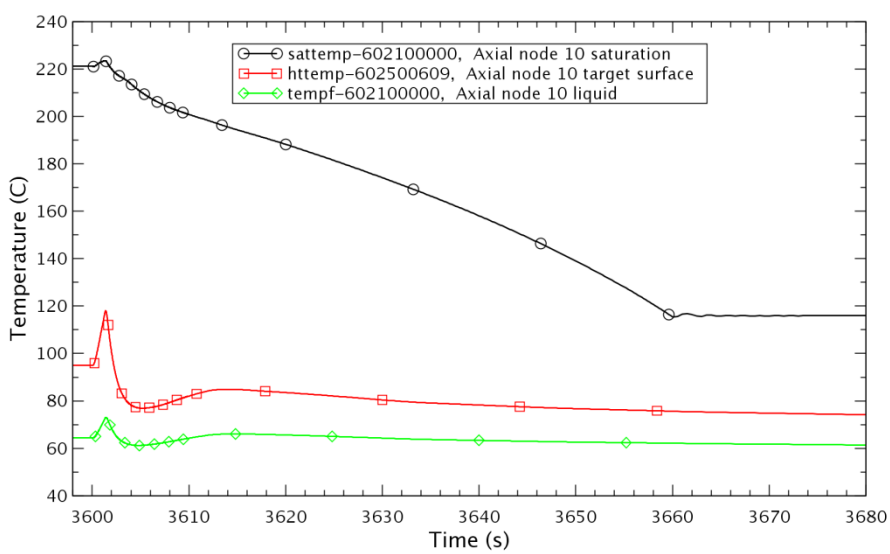

FIGURE 7. LOOP EOC-2 - Target surface temperatures never exceed adjacent coolant saturation temperatures.

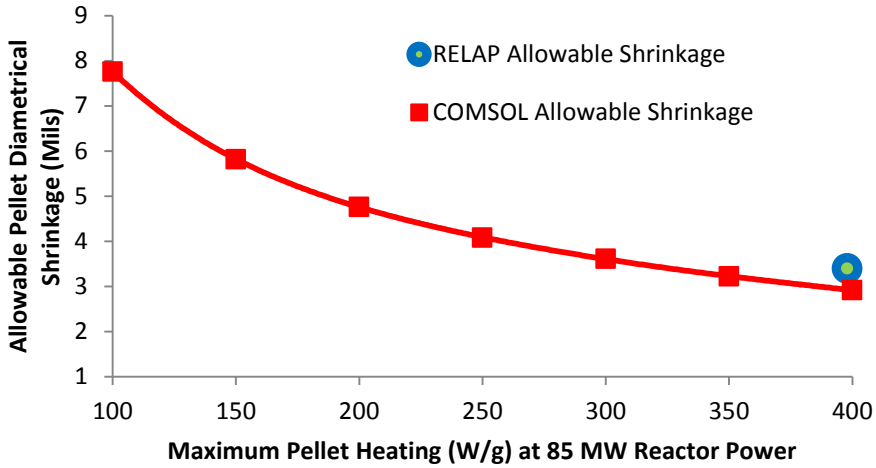

FIGURE 8. EOC-2 fully loaded allowable shrinkage for the transient analysis against the COMSOL steady-state results.

Steady-State COMSOL Model

The fully loaded target is the 3rd phase and intended prototype for the full-scale production of ^{238}Pu at the HFIR. The phase 3 fully loaded target designs contain ~ 50 NpO_2/Al pellets, NpO_2 powder heat-treated at 1200 °C, in a very similar encapsulation used in the partially loaded targets. Figure 9 shows an example of the varied results that were needed from the partially loaded target model in order to qualify target radiation on schedule using pending PIE results.

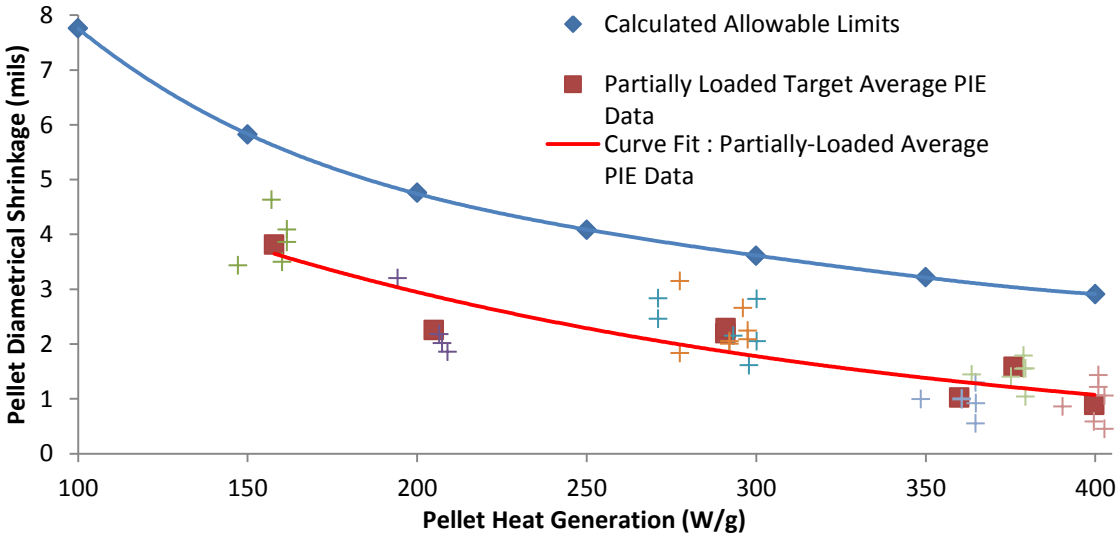

FIGURE 9. The 2nd cycle bounding allowable diametrical shrinkage in the pellet compared to measured PIE data.

Additional PIE data required a more detailed safety review for 2nd cycle irradiation of the fully loaded targets. As anisotropic swelling of the pellets [6] in the 2nd cycle begins to reach a net pellet length increase, the predicted axial swelling and thermal expansion of the pellets could exceed the irradiated target design tolerances and create axial stresses in the target housing capable of failure. In order to achieve an acceptable safety factor for the target housing structure, temperature-dependent axial stress-strain curves were measured (see Figure 6 previously) and incorporated into best-estimate calculations at different irradiation times in the second cycle. Figures 10 and 11 show the irradiation behavior effect of axially-dependent burnup on temperature profiles throughout the second irradiation cycle of the fully loaded target. A typical cosine curve, consistent with the pellet HGRs, is observed early in the cycle. However, as burnup-driven radial swelling closes the cladding/pellet gap, the higher burnup density axial center of the pellet stack cools and the hot spots shift towards the pellet stack ends.

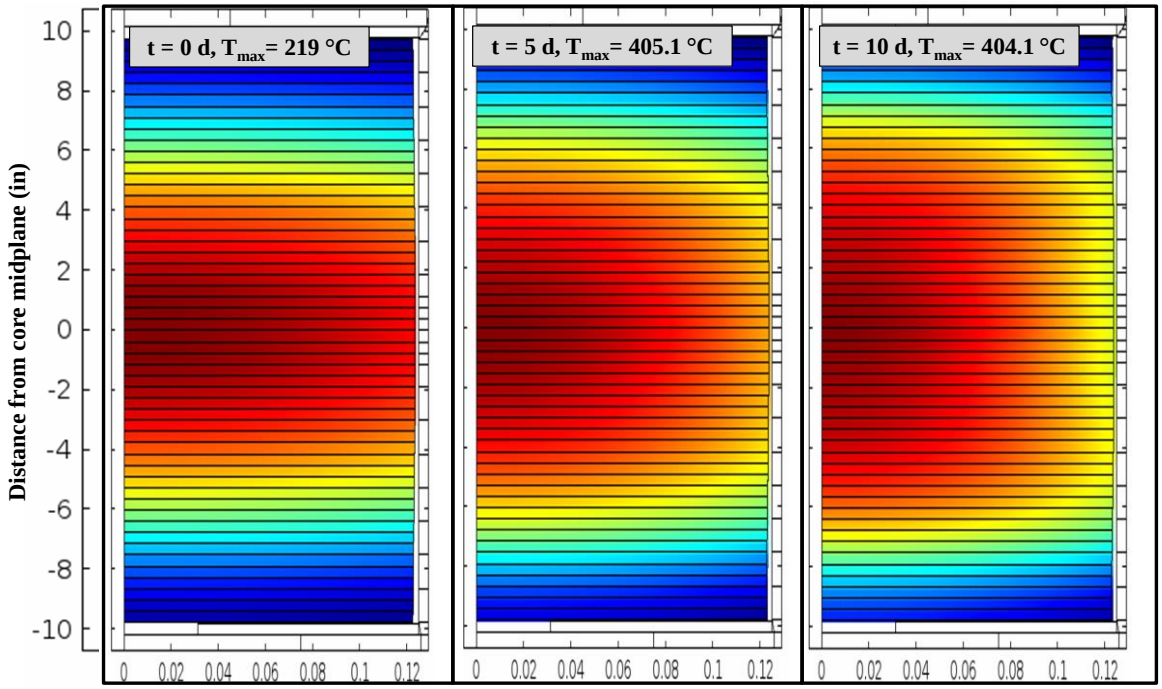

FIGURE 10. Fully loaded target temperature profile during 2nd irradiation cycle at days 0, 5, and 10.

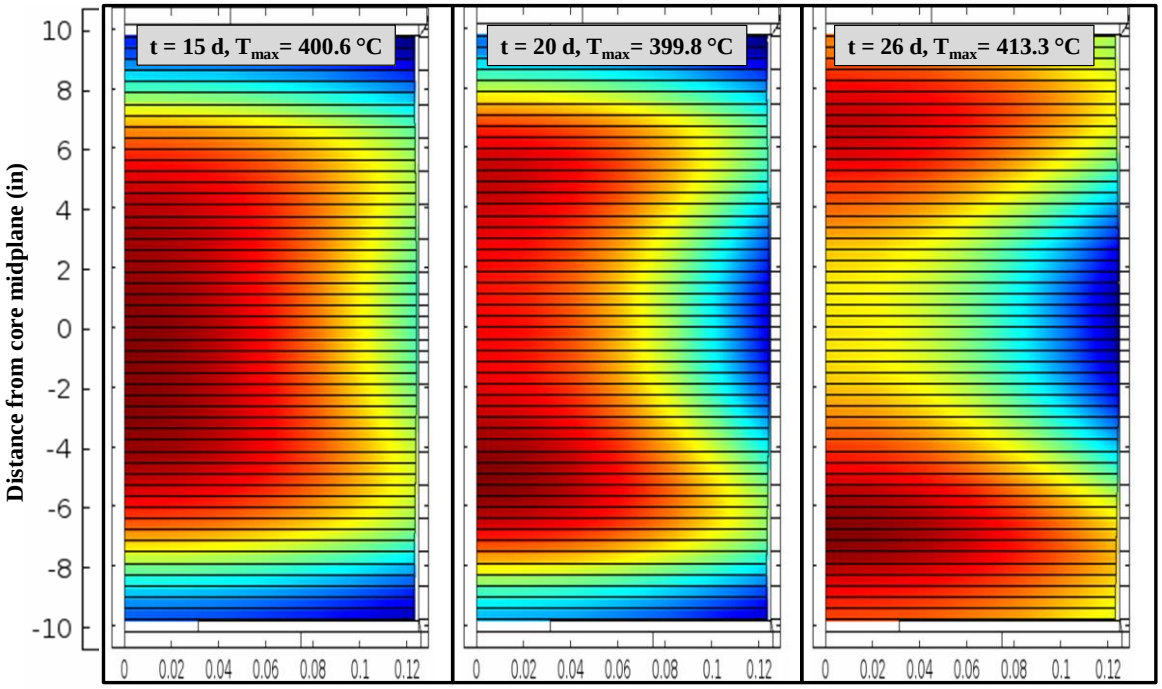

FIGURE 11. Fully loaded target temperature profile during 2nd irradiation cycle at days 15, 20 and 26.

In Figure 12, the strain caused by the axial thermal and irradiation-induced expansion of the target is compared to the elastic strain in the housing tube. An equilibrium stress is found and compared to the measured housing tube failure point to determine the safety factor for the target axial tolerances.

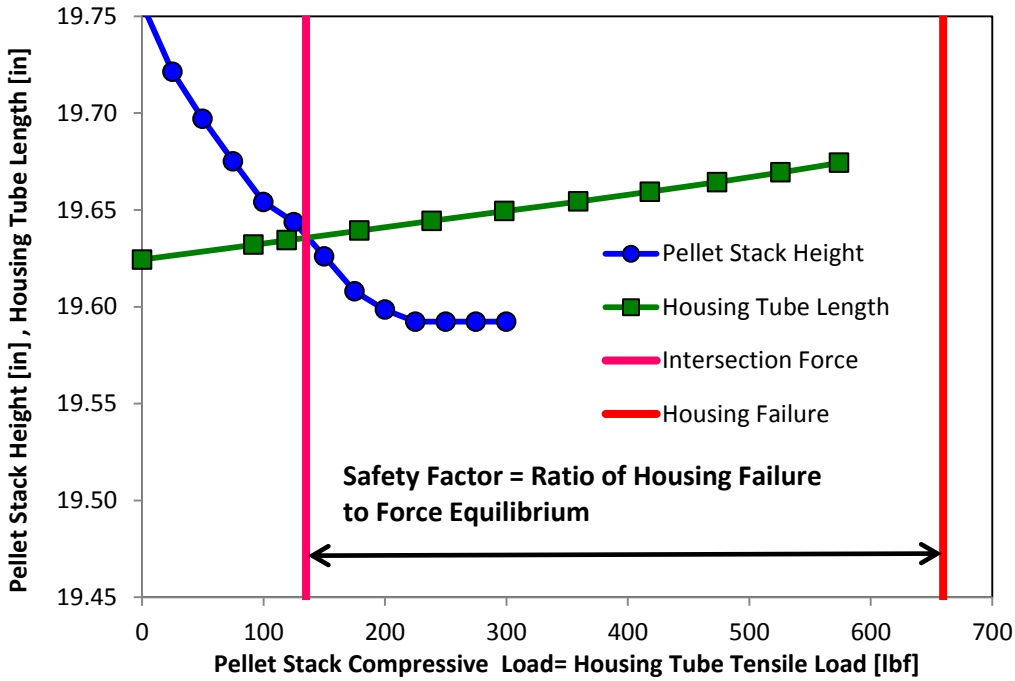

FIGURE 12. Compression of the pellet stack vs. tensile stretching of the housing tube with safety limit shown[13].

The current fully loaded target design, fabricated for future HFIR irradiations, implements a larger axial tolerance that will allow greater safety factors and potential higher loading of the targets.

CONCLUSION

A detailed set of safety analysis models have been developed and reviewed to support the irradiation of NpO_2 pellets at the HFIR. These models account for advanced and detailed physics phenomena and material behavior and their results can be used to qualify the current design of prototypical, fully loaded targets to produce ^{238}Pu. Furthermore, improvements and studies with these models can be used to optimize the ^{237}Np loading and configuration of the full-scale production targets in order to increase ^{238}Pu throughput and better meet the customer needs of NASA.

NOMENCLATURE

$\Delta V_{swell.}$	=	Volume change due to swelling	$P_{0.}$	=	Initial porosity of the pellet
$\Delta V_{dens.}$	=	Volume change due to densification	α, β	=	Experimentally fitted parameters
BU	=	Pellet burn up			
h	=	Total gap heat transfer coefficient	k_g	=	Thermal conductivity of the gap gas mixture
h_s	=	Solid-spot contact conductance	δ	=	Mean separation distance
h_g	=	Gas gap heat transfer	g_i	=	Gas gap jump value at surface i
h_r	=	Radiative heat transfer			

ACKNOWLEDGMENTS

The ^{238}Pu supply project has been tasked to the United States Department of Energy (DOE) and utilizes the resources of multiple DOE facilities. NASA provides funding for the project. This student's research is being performed using funding received from the DOE Office of Nuclear Energy's Nuclear Energy University Programs.

REFERENCES

[1] Hurt, C.J., Wham, R.M., et. al., "Plutonium-238 Production Target Design Studies," in proceedings of *The INMM 55th Annual Meeting*, Atlanta (2014).

[2] Wham, R.M., Felker, L.K., et. al., "The Plutonium-238 Supply Project," in proceedings of *The 19th Pacific Basin Nuclear Conference* Vancouver (2014).

[3] Oak Ridge National Laboratory, *HFIR Updated Safety Analysis Report*, Chapter 15, ORNL/HFIR/USAR/2344, Revision 13, 7/7/2014.*

[4] Hurt, C.J., *COMSOL Thermal-Structure Interaction Simulations of NpO2 Partially-Loaded Targets in HFIR*, reviewed by Freels, J.D., RRD calculation C-HFIR-2013-029, Revisions 0, 1, 2, 3, and 4, 8/8/2014.*

[5] Madhusudana, C. V., *Thermal Contact Conductance*, Springer-Verlag, New York, page1-page61, (1995).

[6] Yanagisawa, K., "Fuel Densification and Swelling: Relationship Between Burn-Up Induced Axial and Radial Fuel Dimensional Changes," *Nuclear Engineering and Design*, **96**, page11-page20, (1986).

[7] Hoffman, G. L., Rest, J., Snelgrove, J. L., "Irradiation Behavior of Uranium Oxide – Aluminum Dispersion Fuel", *1996 International Meeting for Reduced Enrichment for Research and Test Reactors*, Seoul, Korea, (1996).

[8] Assmann, H., Stehle, H., Thermal and in-reactor densification of UO2: Mechanisms and experimental results, *Nuclear Engineering and Design*, **48**, p49–67, (1978).

[9] Hobbs, R.W., *Analysis of Partially Loaded Np237 Target Post Irradiation Data to Support Second Cycle Irradiation of Fully Loaded Np237 Target Capsules*, reviewed by Wham, R.M., RRD calculation C-HFIR-2014-004, Revision 0, 4/24/2014.*

[10] Meyer, R.O., The Analysis of Fuel Densification – Aluminum Dispersion Fuel, , Office of Nuclear Regulatory Commission, NUREG-0085, Washington, D.C., July 1976.

[11] Griffin, F.P., *RELAP5 Transient Analyses of Pu-238 Fully-Loaded Targets*, reviewed by Valentine, J.R.., RRD calculation C-HFIR-2013-030, Revisions 0 and 1, 2/7/2014.*

[12] Oak Ridge National Laboratory, *Experiment Review Questionnaire: In-Vessel Experiments*, RRD Procedure EG-6, Revision 1, 4/5/2007.*

[13] Hobbs, R.W., *Evaluation of Axial Stresses in the Fully Loaded Np237 Targets During the 2nd Cycle of Irradiation*, reviewed by Griffin, F.P., RRD calculation C-HFIR-2014-008, Revisions 0, 1 and 2, 9/10/2014.*

*Internal ORNL Research Reactor Division (RRD) Document. Contact the RRD Document Control Center to request a copy: High Flux Isotope Reactor, Oak Ridge National Laboratory, P.O. Box 2008 MS-6398, Oak Ridge, TN 37831-6398. (http://neutrons.ornl.gov/contact/).

Development of a Prototypic Tie-Tube for Low-Enriched Uranium Nuclear Thermal Propulsion

Kelsa M. Benensky[1], Jacob W. Harry[2], Jeffrey T. Clemens[3], and Omar R. Mireles[4]

[1]*Department of Mechanical and Nuclear Engineering, Pennsylvania State University, University Park, PA 16801*
[2]*Department of Aerospace Engineering, Iowa State University, Ames, IA 50011*
[3]*Department of Nuclear Engineering, Texas A&M University, College Station, TX 77843*
[4]*NASA Marshall Space Flight Center, Huntsville, AL, 35812*

Abstract. Nuclear thermal propulsion (NTP) is under consideration for future human missions to deep space destinations such as Mars. NTP will be capable of providing a specific impulse (I_{sp}) nearly double that of the highest performing chemical engines, which significantly reduces the amount of propellant required for to complete a mission and with reduced transit time. NASA in collaboration with external partners is investigating development a low enriched uranium (LEU) engine concepts for future mission needs. The current point design calls for an array of in-core tie-tube, which function in part to pre-heat the hydrogen propellant that will drive the turbo-pump and house the zirconium hydride ($ZrH_{1:8}$) moderator to thermalize the neutron spectrum. A small development team was tasked to mature a tie tube concept by considering detailed mechanical design and materials selection based upon specific design constraints. The material and thermo-mechanical response of the system was evaluated through the construction of a sub-scale tie-tube test rig. An experimental test apparatus was developed in order to determine temperature gradients across the tie-tube, variations in inlet and outlet pressure, and potential material degradation. Nitrogen, argon, and hydrogen was used over a range of mass flow rates and furnace temperatures (-200 – 500ºC). The project culminated in the construction and preliminary testing of the test rig in addition to the creation and quantification of ZrH samples. Future work aims to scale the test rig to effectively test full-length tie-tube elements.

Keywords: Nuclear Thermal Propulsion, Tie-Tube, Low Enriched Uranium, Zirconium Hydride

BACKGROUND

In a high enriched uranium (HEU) system, stringent safety regulations require specific facilities to produce, handle, and test HEU fuels (>20 a% U-235), which adds a significant additional cost to overall development. A low enriched uranium (LEU) design for NTP applications has the potential to greatly reduce the development cost associated with nuclear systems. Because of these potential advantages, there is a current effort under NASA's Nuclear Cryrogenic Propulsion Stage (NCPS) to investigate and develop a feasible low enriched uranium (LEU) nuclear thermal rocket (NTR) for manned Mars missions. The current design, Space Capable Cryrogenic Thermal Engine (SCCTE), must be capable of producing 25,000 lbf thrust with an expected fuel enrichment of (19.75 a%).

A LEU-NTR engine for manned missions to Mars was originally investigated by the Center for Space Nuclear Research (CSNR). The system comprises of a CERMET fuel elements and a $ZrH_{1.8}$ moderator housed in tie-tube elements. In order to obtain criticality of the core, tie-tube elements surround fuel elements in a 2:1 ratio for moderation. The layout of the core systems are seen in figure 1.

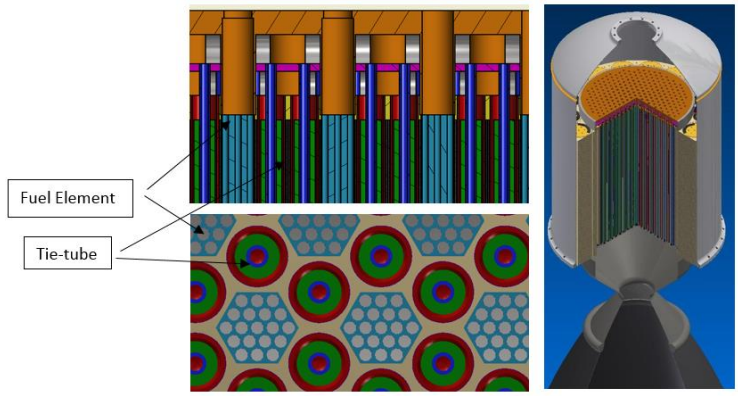

FIGURE 1. (Top Left) Tie-tubes connecting to injector head. (Bottom Left) Tie-tube and fuel element layout in core. (Right) sectioned reactor housed within pressure vessel with nozzle.

INTRODUCTION

The development of a NTR calls for unique design challenges to be met, especially for in-core reactor components. Components within the reactor core must be able to withstand large temperature and pressure gradients, interaction with the hydrogen propellant, radiation effects, as well as in-core vibrations and acoustic conditions associated with engine operation. In the current design, tie-tubes function to provide in-core cooling to the fuel, pre-heat the propellant for eventual use in the turbo-pump, and house the neutronic moderator. Therefore, the integrity of the tie-tube element is essential for safe and successful reactor operation.

Non-nuclear testing of in-core reactor components is used as an efficient and effective way to iteratively produce a mechanical design suitable to withstand the expected operating conditions of an NTP engine. Components are tested individually rather than in a full core assembly setup in order to quickly narrow down potential design candidates. Small scale tie-tube prototypes are able to be tested in gaseous nitrogen, argon, and hydrogen flows over the temperature range of interest (-200 – 500°C) to determine and validate expected temperature gradients, variations in flow, and material degradation mechanisms. This effort was undertaken through three parallel tasks: mechanical design of tie-tube components, moderator materials fabrication and production, and development of a tie-tube test rig.

MECHANICAL DESIGN

At the time of research, the core configuration for the LEU-NTR contained 291 fuel elements and 680 tie-tubes such that each hexagonal fuel element is surrounded on all six sides by the tie-tube elements (figure 1). The tie-tube elements in the system are limited by the maximum centerline temperature of the $ZrH_{1.8}$ neutron moderator. Tie-tubes supply cooling to the fuel and moderator using cryogenic hydrogen to prevent dissociation of the moderator and maintain fuel integrity during operation. The hydrogen flow leaving the tie-tube is then used to power the turbo-pump which in turn drives propellant through the engine.

The geometric constraints for tie-tube design were supplied by CSNR. The supplied design was simple and satisfied necessary neutronic and heat transfer requirements. In order for this conceptual design to function in a realistic NTR system, a feasible mechanical tie-tube design is established and satisfied the geometric constraints of the moderator and flow channel diameters. With the neutronic and thermodynamic requirements in mind, a prototypic tie-tube was

designed using CAD software to prevent tie-tube failure due to expected operating requirements of the NTR core (in-core vibrations, pressure and temperature gradients, etc.). The proposed mechanical design of the tie-tube included the moderator, flow channels, and structural components needed for a functioning tie-tube (figure 2). These components are described below:

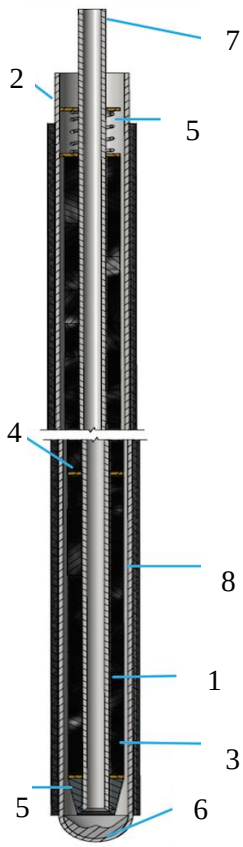

1. **Inner Tie-Tube** – provides inlet hydrogen flow to cool the neutron moderator
2. **Outer Tie-Tube** – provides outlet to hydrogen flow, allowing the tie-tube element to act as a preheater to the turbo-pump
3. **Neutron Moderator** – small (25 mm thick) $ZrH_{1.8}$ pellets are stacked axially and separated by small (1 mm thick) zircaloy spacers
4. **Moderator Spacers** – provide radial structural support and protect the moderator from vibrations by connecting the inner and outer tie-tube
5. **Bottom Support Fitting and Axial Compression Spring** – supports the moderator in axial compression and allows for the thermal expansion of the moderator elements during operation
6. **Turning Vane** – located at the bottom of the tie-tube, assists hydrogen flow during the exchange between the inner and outer tie-tube
7. **Injectifold Connector** – connects the tie-tube assembly to the reactor injectifold (injector and manifold) which governs hydrogen flow through the core
8. **ZrC Insulating Layer** – ZrC foam at 40% porosity, protects the inner assembly from the high temperature of the fuel (upwards to 2850 K)
9. **Hexagonal Graphite Element** – houses the entire tie tube assembly, provides structural support against compressive stresses within the core

FIGURE 2. Prototype tie-tube mechanical design and description.

MODERATOR PRODUCTION EXPERIMENTS

The moderator element is a critical component of the tie-tube assembly and reactor core. The moderator thermalizes the neutron spectrum, decreases leakage, and provides better fuel utilization. Because of this, the correct choice of moderator element has the potential to decrease reactor size. This is desirable in order to maximize the thrust-to-weight ratio of the core. An ε-phase zirconium hydride was chosen as the moderator of interest for a CERMET fueled LEU NTR because of its ability to provide high moderating power per unit volume and previous experience using ZrH_x for in-space and advanced terrestrial reactor designs [2,3,4,5]. Unfortunately, zirconium hydride is very brittle (especially when the δ -phase dominates) and its yield strength decreases significantly with increasing temperature [6]. The ε–phase was chosen for the moderator element because of the weaker dependence of yield strength on temperature. The zirconium-to-hydrogen ratio of 1.8 was chosen because it inherently corresponds to the lowest Young's modulus and highest malleability compared to other ratios [2]. Three methods were evaluated for production of $ZrH_{1:8}$: sintering of ZrH_2 powder, direct hydride of zirconium sponge, and direct hydride of zirconium metal. While sintering of ZrH_2

powder and direct hydride of zirconium sponge may be less time intensive processes, direct hydride of zirconium metal was chosen for our application. This was chosen for two fundamental reasons:

- Direct hydride of zirconium metal will result in a sample density with the greatest percent theoretical density and will not penalize reactor neutronics (compared to direct hydride of zirconium sponge).
- Direct hydride of zirconium metal has the potential for greater corrosion resistance than powder-based materials which typically have imperfect grain boundaries [7].

Zirconium hydride production experiments were completed by direct hydride of zirconium metal round bar and tube approximately 0.5" in diameter and 1.0" in length. Experiments were carried out in the Enclosed Hydrogen Tube Furnace (EHTF) of NASA Marshall's materials department and focused on varying time of hydride, flow rates, and gas mixtures to produce ZrH_x. Material qualification was completed using x-ray diffraction (XRD) at NASA Marshall. Ultimately, it is desired to produce the ε-phase $ZrH_{1.8}$ of interest and test small samples within the tie-tube test rig to determine the material response of the hydride to hydrogen flow at expected operating conditions. It was found that ZrH_x could be produced using a direct hydride method and that ZrH_x creation was strongly dependent upon the partial hydrogen pressure of the system. Figure 3 demonstrates the preliminary results of ZrH_x production experiments and qualification of ZrH.

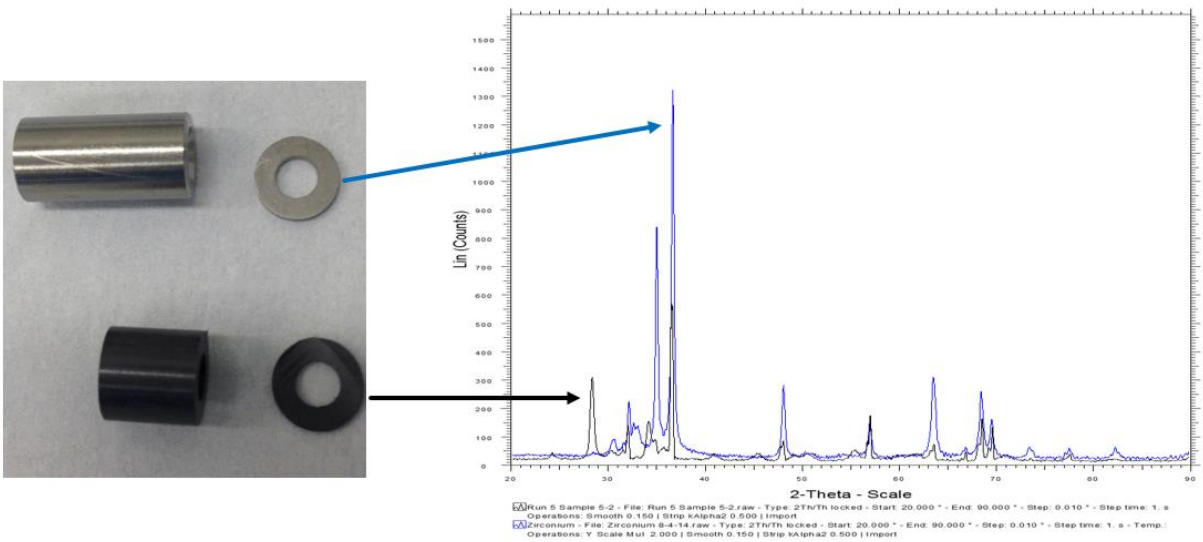

FIGURE 3. Comparison of zirconium (Blue) and zirconium hydride (Black) XRD results. The presence of low 2θ value peaks within the zirconium hydride characterization is attributed to hydrogen pickup.

TIE-TUBE TEST RIG EXPERIMENTAL SETUP AND PROCEDURE

In order to test the chosen materials and mechanical design of the tie-tube, a small-scale test assembly was developed to replicate the expected operating conditions. The use of a small-scale test rig lowers initial development costs and provides fundamental knowledge for eventual construction and testing of full-scale tie-tube elements. There are five characteristics that were identified as parameters to be examined for the tie-tube design: temperature, pressure, material compatibility, vibration, and radiation effects. The presented design, developed over a ten-week time frame, is capable of non-nuclear testing of temperature, pressure, and material compatibility for small scale tie-tube elements. The initial design constraints were based on the current system power balance requirements and included temperatures and pressures at the inlet and outlet, as well as a mass flow rate (Table 1). The assumed heat transfer to the tie-tube based on a 4% power deposition from the fuel elements. The initial constraints were calculated based upon this assumption using a coarse thermodynamic analysis. The expected pressure drop between the inlet and outlet was calculated under the assumption that all dynamic head is lost along the 180-degree turn.

TABLE 1. Initial tie-tube design constraints were determined using the current system power balance requirements. Achieved conditions were limited by the ratings of test rig components.

	Full Scale Parameters	Achieved Parameters
Maximum Temperature (K)	2850	1300
Minimum Temperature (K)	27	77
Maximum Pressure (psi)	1059	100
Mass Flow Rate (lbm/s)	0.021	0.021
Length (cm)	84	33

The tie-tube test rig is composed of a tube furnace for simulating outer tie-tube outer wall temperature, gas flow system and pump to simulate hydrogen flow through the tie tube, and a hydrogen burn stack for safe operation. The developed test rig assembly is not yet capable of achieving the design conditions for the engine (Figure 4). The small-scale rig is able to sustain pressures of 100 psi, heat the outer tie-tube surface to 1300 K, and chill the inlet gas to a temperature of 77 K. The inlet and outlet of the tie-tube is each equipped with one analog pressure gauge and one thermocouple to regulate inlet and outlet conditions. In addition, nine thermocouples are spot-welded along the outer tie-tube and infrared (IR) pyrometer readings were taken for redundancy of temperature measurements. Employing conservative procedures under safety protocol, all initial flow experiments were run well within these system bounds. Although both the heating and the cooling components have the ability to reach the aforementioned temperatures and pressures, this does not guarantee that all fittings, gauges, and materials will stand-up to the same conditions. For future work, a steady and calculated progression must be undertaken to find the true limitations of the system.

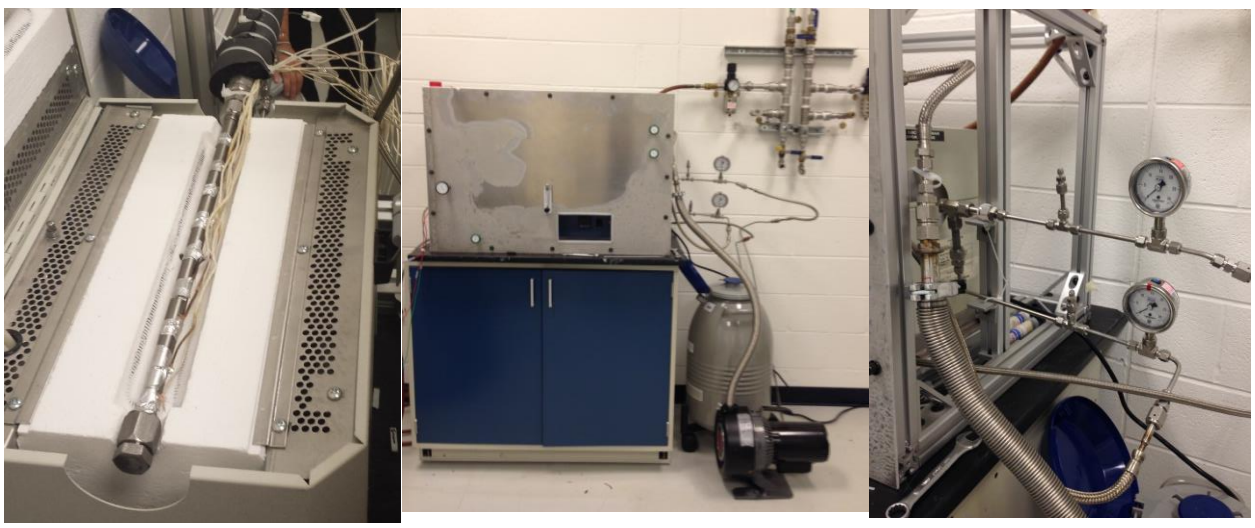

FIGURE 4. The tie-tube test rig is able to test sub-scale tie-tube elements with hydrogen flow for temperatures between 77 – 1074 K. The system uses analog pressure gages and nine thermocouples spot welded axially along the tie-tube to gather experimental data.

It should be noted that for the tie-tube test rig, the graphite hex and the thermal insulation ZrC tube were not included in the small-scale test. This approach allows for two significant advantages. First, the experiment is simplified as fewer components are required to be machined and assembled in the allotted timeframe. Secondly, the tube furnace operational temperature could be greatly reduced. The outer wall of the sub-scale tie-tube assembly is assumed to be the temperature on the inside of the thermal insulation layer.

A Lindberg/Blue Mini-Mite™ Tube Furnace was selected as the heat source for the experiments. The furnace has a maximum operational temperature of 1000^{0}C and a programmable PID controller for segmenting time durations at a given temperature [8]. For the small-scale test rig, the tube furnace was programmed to increase from 200^{0}C - 500^{0}C (474 K – 774 K) by increments of 50 K. The 500^{0}C (774 K) temperature was chosen primarily to mitigate melting concerns of the aluminum surrogate moderator, which has a melting temperature of 660^{0}C (934 K). In future

experiments with a $ZrH_{1.8}$ moderator, higher temperatures may be obtained. The system will be limited by the melting point of the moderator: 800^0C (1074 K).

The initial design called for an inlet temperature of the hydrogen propellant of 27 K. The cost and complication of using condensed hydrogen was considered too high for the purpose of the small-scale rig. As an alternative, a liquid nitrogen (LN2) bath was used to chill the inlet gas. The LN2 was kept inside a 20 liter Dewar with vacuum insulated walls and is kept at 77.2 K. The piping of the test rig is run through the Dewar in an effort to bring the gaseous hydrogen to as cold a temperature as possible. The LN2 bath is used as a heat exchanger transferring the thermal energy of the hydrogen gas to the liquid nitrogen, thus boiling off LN2 in the process.

Safety is extremely important for any system with hydrogen flow. To ensure safety, a burn stack was placed under a fume hood and hooked up to a temperature controller (figure 5). The burn stack uses a heating element to create an exhaust flame for the system that burns off the hydrogen gas before being released into the fume hood and, ultimately, the atmosphere. The burn stack consists of a flame arrestor, fine mesh (to ensure that the hydrogen flame does not go back into the piping), and thermocouple, which is connected to the temperature controller. The temperature controller is programmed to actuate a safety solenoid valve if the hydrogen flame reaches temperatures above 300^0C (574 K). The solenoid valve shuts off the hydrogen flow to prevent a potential hazard. Figure 5 shows the assembly of the hydrogen burn stack to ensure system safety during operation.

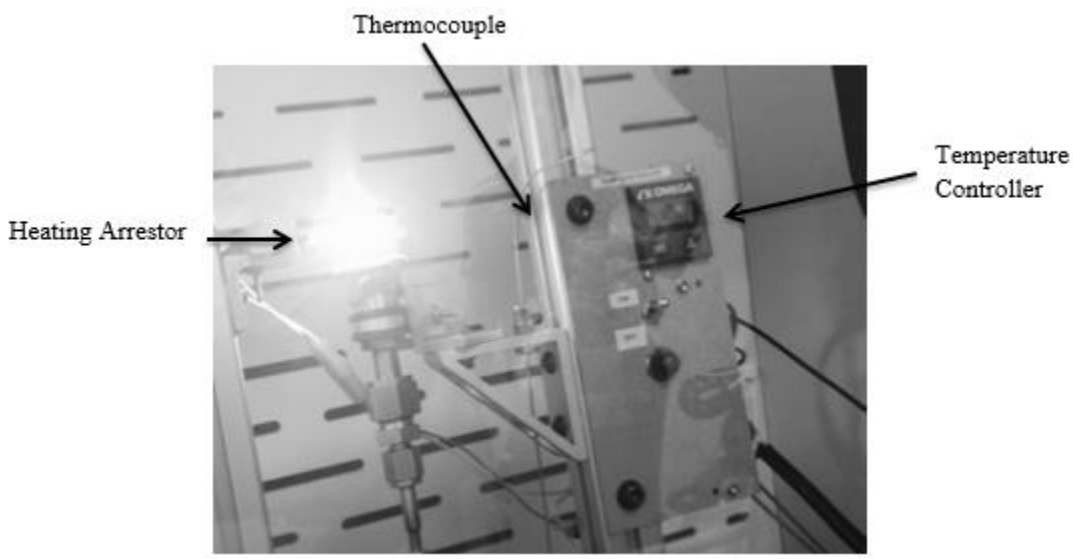

FIGURE 5. Hydrogen burn stack with heating arrestor, thermocouple, and temperature controller.

The vacuum pump is used to evacuate the gas flow system of residual oxygen, which could become dangerous when mixed with the hydrogen working fluid. A nitrogen or argon purge is performed prior to any usage of the vacuum. When developing and implementing the operational procedures for the vacuum pump, it is important to note the danger of vacuuming hydrogen gas. Vacuum pumps often use oil to dissipate the heat associated with compressing gas; the hydrogen may react with the oil violently and cause a fire. Thus it is critical to follow the established procedures and purge before vacuuming.

A piping and valve system was diagrammed and constructed based on a hydrogen flow system (figure 6). Hydrogen gas is explosive at levels as low as 4% in the atmosphere and hence mandates the utilization of a hydrogen burn stack to assure complete and safe evacuation of the pipes [9]. Leak testing was performed with nitrogen to ensure the Swagelok and flared-tube fittings were adequate for pressures up to 100 psi, the maximum pressure of the current mass flow controller. Table 2 lists a description of the valves referenced in figure 6. The system can use hydrogen as

the primary working fluid and nitrogen as the purge gas. There are two legs for the gases to pass through: the primary leg, which includes a path through the mass flow controller and the tie-tube, and the bypass leg, which can be accessed by either opening the bypass valve or by exceeding the pressure of the pressure relief valves. The mass flow controller is throttled from a range of 0 - 1 SCFM to simulate the mass flow rate that may be radially varied across the to flatten the power profile.

TABLE 2. Description of valves as seen in the tie-tube test rig gas flow system schematic (figure 6)

Valve	Description
V-1	Nitrogen k-bottle Isolation
V-2	Hydrogen k-bottle Isolation
V-3	Nitrogen Pressure Regulator
V-4	Hydrogen Pressure Regulator
V-5	Hydrogen Supply Isolation
V-6	Nitrogen to Hydrogen Line Bypass
V-7	Gas Bypass
V-8	Vacuum Pump Isolation
V-9	Burn Stack Exhaust
RV-1	Relief Valve (Pressurized to 80 psi)
RV-2	Relief Valve (Pressurized to 80 psi)

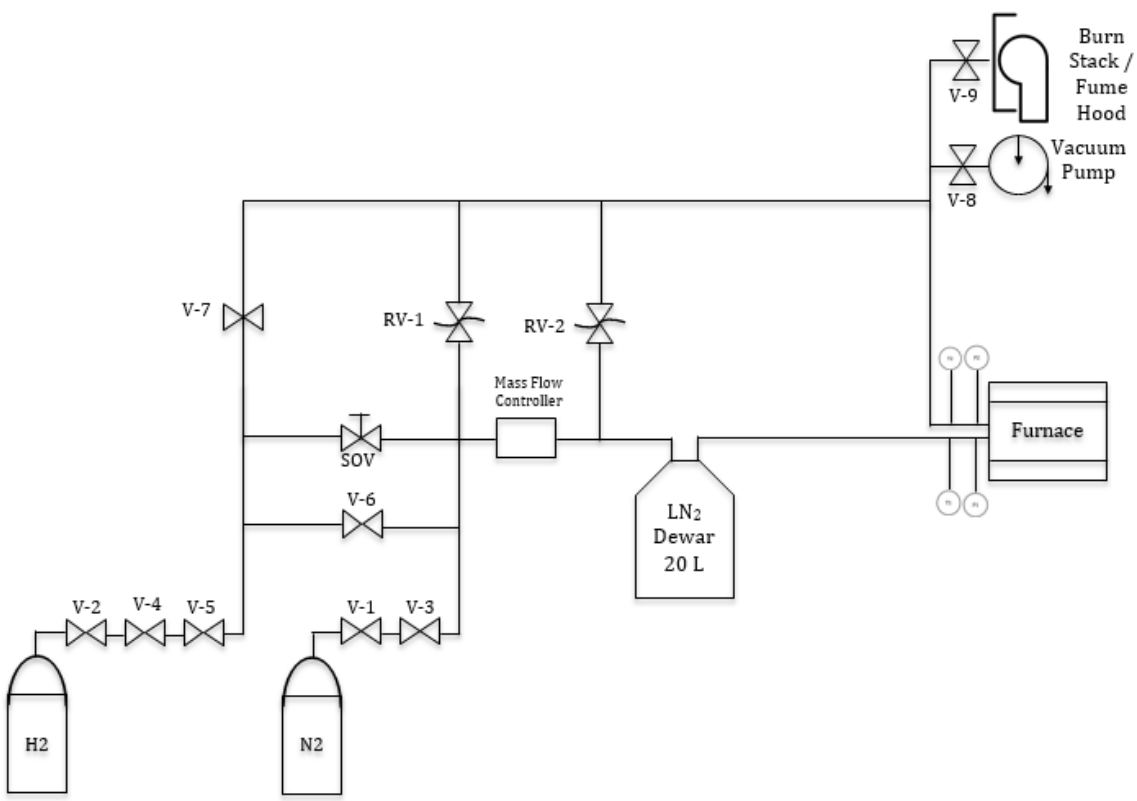

FIGURE 6. Gas flow system schematic of the tie-tube test rig. Hydrogen (H2) gas is used as the inlet gas and nitrogen (N2) gas is used as a purge gas for the system. Hydrogen is cooled by the LN2 Dewar before entering the furnace. Outlet gas escapes the system through the fume hood. A gas bypass line and burn stack are integrated into the system to ensure safe operation.

PRELIMINARY RESULTS

For the preliminary tests run using the tie-tube test rig during the rig was not fully prepared for a hydrogen gas test

run. Figure 7 displays an example of the temperature distribution of the tie-tube and test rig obtained using an infrared pyrometer when operating a 450^{0}C. For safety purposes, nitrogen gas was used as the working fluid in order to work establish preliminary procedures for when the system is prepared for hydrogen flow testing. The following section describes the preliminary results obtained using nitrogen testing and the implications of these results.

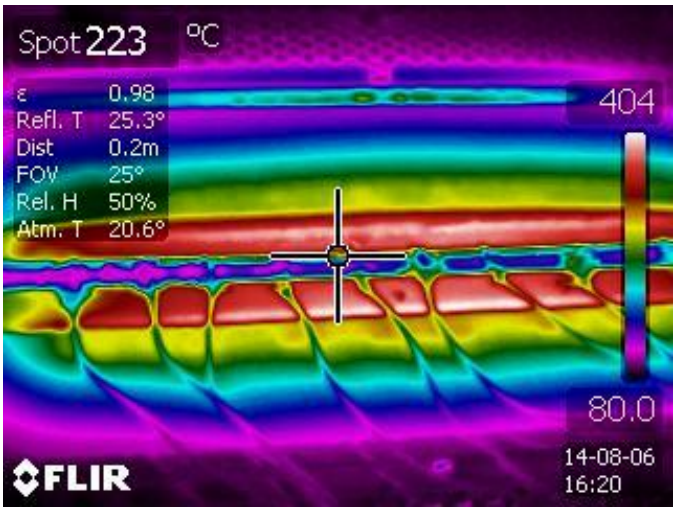

FIGURE 7. Infrared pyrometer image of the small-scale tie-tube sitting in the test rig furnace during a 450^{0}C test run is an example of the measurement capabilities of the tie-tube test rig system.

As previously described, the tube furnace is programmed to increase from 200^{0}C - 500^{0}C by increments of 50^{0}C, at each temperature increment the mass flow rate was changed from 0 SCFM – 1.0 SCFM by increments of 0.25 SCFM. The inlet and outlet temperature were recorded continuously throughout the experiment. The inlet and outlet pressure were recorded once for each temperature increment. In addition, the analog pressure gauge was the device used to determine when the system had reached a steady state operation. It is clear from figure 8 that during testing the mass flow rate had not yet come into thermal equilibrium for each temperature increment. This can be seen from the temperature spikes of the inlet gas.

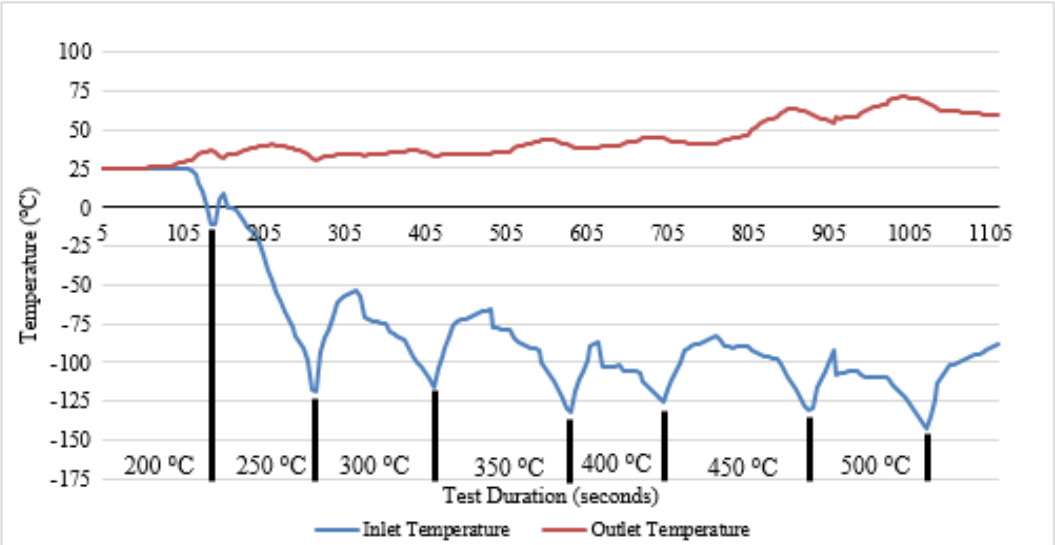

FIGURE 8. Tie-tube test rig thermocouple data during preliminary testing with nitrogen due to variation in temperature and mass flow rate. The tube furnace temperatures are indicated in black for each respective duration.

Upon examination of the inlet and outlet thermocouple data, it is evident as to how the temperature changes with the variable mass flow rate inputs as well as the increasing furnace temperature. The inlet temperature was to be examined

first as it is only affected by the mass flow rate of the system. The small plateaus that appear in the downward stair-stepping trend are the time periods where the mass flow rate is constant and the analog pressure data was recorded. In the time periods where the temperature takes large downward spikes is the time when the mass flow rate is at its highest. The cold air coming out of the liquid nitrogen Dewar is traveling quickly and doesn't have time to warm up before entering the inlet. As seen in figure 8, the inlet temperature gradually dips colder after each mass flow rate iteration. It is important to note that the outlet temperature does not appear to be affected nearly as much as the inlet temperature by either the furnace temperature or the mass flow rate. This may be a point of future investigation.

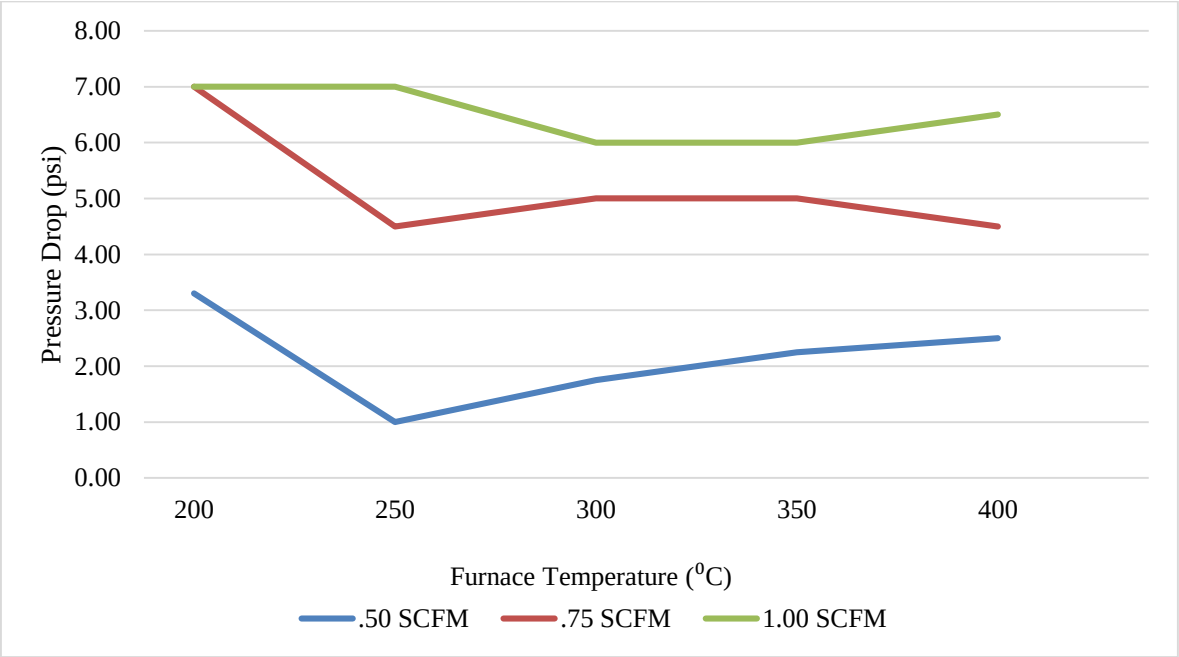

FIGURE 9. Tie-tube test assembly experimental pressure drop data for preliminary testing with nitrogen. The pressure drop data is an example of the current data collection capabilities of the tie-tube test rig.

Another parameter to investigate is how the pressure drop across the tie-tube is affected by mass flow rate changes. There does not appear to be any noticeable relationship with pressure drop and furnace temperature, more data needs to be taken over a wider range of mass flow rates. The limiting constraint with running high flow rates of hydrogen in the tie-tube test rig is that the burn stack flame may become too large for the fume hood under which it is placed. This can be mitigated by transferring the test rig to an outdoor location.

The error in these pressure measurements seen in figure 6 is too large to take into consideration that these values are accurate pressure drop numbers. Even with low accuracy, the precision of the data appears to be reasonable. What can be extracted from the data are trends that indicate that an increasing mass flow rate results in larger pressure drops through the tie-tube. Before a meaningful extrapolation of the data can be performed, a finer resolution pressure transducer needs to be utilized at the inlet and outlet.

CONCLUSIONS AND RECOMMENDATIONS

A mechanical design of a full length-tie tube prototype was proposed and is limited by the geometric and material constraints supplied to the designers via neutronic analysis. The structural integrity of the tie-tube must be ensured to maintain high performance and safe operation of the reactor. The mechanical design of the tie-tube implements several solution to securely house the moderator, support hydrogen flow, and account for thermal expansion of components. Future work should test the material response of the entire component, especially the zircaloy inner and outer tie-tubes which may experience hydrogen embrittlement due to interaction with the hydrogen propellant. Changes in design must not significantly impact neutronics to ensure enough core reactivity.

The neutronic moderator is crucial to the success of the LEU NTR system. It was found that NASA MSFC has the baseline capabilities to produce a zirconium hydride moderator if necessary. A direct hydride method was chosen to produce the moderator Future work should include:

- Post-processing: zirconium hydride phase homogenization
- Qualify the phase of zirconium hydride and identify grain structure
- Quantify the hydrogen-to-zirconium ratio of the produced moderator
- Determine the mechanical properties of interest

Using the tie-tube test rig, a range of temperatures, pressures, and mass flow rates are able to be tested to evaluate pressure drop data, temperature profiles, and material property changes in the tie-tube. From the preliminary experimental data with nitrogen gas flow, higher mass flow rates produces a scenario with a larger pressure drop across the tie-tube. In addition, a larger temperature gradient is created when the mass flow rate is high, not allowing for the chilled propellant to come into thermal equilibrium with its surroundings before reaching the tie-tube inlet. This information is only the beginning of experimental testing that will be invaluable in the further design of the LEU nuclear thermal rocket. To further the fidelity of the tie-tube test rig experimental setup, recommendations are listed below in order of chronology:

- Convert components from analog to digital data collection to improve accuracy
- Test system to prepare for hydrogen gas as the working fluid
- Replace the nitrogen purge gas with argon to ensure no propellant interactions with the tie-tube
- Increase the rating of system components to increase the pressure capability of the system
- Replace the tube furnace with a longer furnace to accommodate a full length tie-tube
- Manufacture a full length tie-tube prototype with desired materials to test material response to hydrogen gas

ACKNOWLEDGMENTS

The tie-tube component team would like to thank ***Dr. Omar Mireles*** for all of his work helping the team accomplish objectives in a timely and effective manner. A special thanks is owed to all of the employees at NASA Marshall Space Flight Center for their knowledge, patience, and altruism in helping the team throughout the summer. This summer was an invaluable learning experience; all of the mentorship and aide provided by the community deserve special recognition. Lastly, a big thank you is given to the NASA Propulsion Academy at Marshall and the Pennsylvania, Iowa, Texas, and Alabama Space Grants for in-part funding this opportunity!

REFERENCES

[1] S. K. BOROWSKI, ET. AL "Nuclear Thermal Rocket Propulsion: A Proven Game-Changing Technology for Future Human Exploration Missions," Proc. Global Space Exploration Conf., Washington, D.C., 2012.

[2] G. ROSAIRE, ET. AL "Design of a Low Enriched Nuclear Thermal Rocket*," Center for Space Nuclear Research,* Idaho Falls, ID. 2013.

[3] A. LANIN "Nuclear Rocket Engine Reactor," *Springer., St. Petersburg, Russia, 2013.*

[4] M. T. SIMNAD "The U-ZrHx Alloy: Its Properties and use in TRIGA Fuel." 1980.

[5] R. W. WEBB "SNAP 8 Experimental Reactor (S8ER) Hydrogen Barrier Coating Development," *Atomics International*, Canoga Park, CA. 1964

[6] M. P. PULS "Chapter 2: Properties of Bulk Zirconium Hydride," *Springer,* London, UK.

[7] E. ZUZEK, ET. AL "The H-Zr (Hydrogen-Zirconium) System," *Bulletin of Alloy Phase Diagrams,* Vol. 11 No. 4, 1990.

[8] "Lindberg/Blue Mini-Mite Tube Furnace Installation Manual." *Operation - UT150 Controller*: 5.

[9] "Initial Guidance for Using Hydrogen in Confined Spaces - Results from InsHyde." *SIXTH FRAMEWORK PROGRAMME NETWORK OF EXCELLENCE* (2009): 25-26. Web. 4 Jan. 2015. <http://www.hysafe.org/>.

Neutronics Simulations of ^{237}Np Targets to Support Safety-Basis and ^{238}Pu Production Assessment Efforts at the High Flux Isotope Reactor

David Chandler[1a] and Ronald J. Ellis[1b]

[1a]Research Reactors Division and [1b]Reactor and Nuclear Systems Division, Oak Ridge National Laboratory, Oak Ridge, TN 37831
chandlerd@ornl.gov

Abstract. Fueled by two highly enriched uranium-bearing fuel elements surrounded by a large concentric ring of beryllium reflector, the High Flux Isotope Reactor (HFIR) provides one of the highest neutron fluxes in the world and is used to produce unique isotopes like ^{238}Pu. The National Aeronautics and Space Administration use radioisotope thermoelectric generators powered by ^{238}Pu for deep-space missions. As part of the US Department of Energy's task to reestablish the domestic production of ^{238}Pu, a technology demonstration sub-project has been initiated to establish a new ^{238}Pu supply chain. HFIR safety-basis neutronics calculations are being performed to ensure the target irradiations have no adverse impacts on reactor performance and to calculate data required as input to follow-on thermal-structural, thermal-hydraulic, radionuclide/dose, and production yield estimation analyses. ^{238}Pu production assessments are being performed to estimate the amount of ^{238}Pu that can be produced in HFIR's permanent beryllium reflector. It is estimated that a total of 0.96–1.12 kg ^{238}Pu (~1.28–1.49 kg PuO_2 at 85% ^{238}Pu/Pu purity) could be produced per year in HFIR's permanent beryllium reflector irradiation facilities if they are all utilized.

Keywords: ^{238}Pu, HFIR, isotope, depletion, neutronics.

INTRODUCTION

^{238}Pu is a unique isotope that is used as the source of heat in radioisotope thermoelectric generators (RTG). RTGs are used by the National Aeronautics and Space Administration (NASA) for space exploration missions where solar power is inadequate due to distance from the sun or terrain limitations. RTGs work by converting heat energy produced from the alpha-decay of ^{238}Pu into electricity. The newest ^{238}Pu powered unit is the multi-mission RTG which is fueled by 4.8 kg PuO_2 and is being used to power Curiosity, a robotic rover currently exploring Mars[1]. Because the current supply of ^{238}Pu is nearly exhausted and because a domestic source of ^{238}Pu has not been available since the Savannah River Site reactors shutdown in the 1980s, NASA and the US Department of Energy (DOE) have undertaken a program to reestablish a domestic ^{238}Pu production program. As a result, a technology demonstration sub-project has been initiated using HFIR at the Oak Ridge National Laboratory (ORNL), the Advanced Test Reactor (ATR) at the Idaho National Laboratory (INL) and the Radiochemical Engineering Development Center at ORNL to develop and implement the technology required to establish a new ^{238}Pu supply chain[2]. The focus of this paper is on the neutronics studies being performed to support the safety-basis and production assessment efforts at HFIR.

Before ^{238}Pu can be produced in production quantities, a series of irradiation and chemical processing tests are required. The irradiation test program at HFIR consists of multiple irradiation phases that provide an incremental approach intended to reduce the risk of target failure during irradiation and include post-irradiation examination to

guide the course of subsequent irradiations[3]. The first irradiation phase consisted of irradiating single pellets loaded in specially-designed capsules to assess pellet swelling and pellet-clad interactions[4]. In the second irradiation phase partially loaded targets containing eight pellets (7.6 cm stack length) positioned at the reactor core horizontal midplane and in an aluminum cladding tube were irradiated to assess dimensional changes, pellet irradiation behavior and fission gas release. Fully loaded targets are being irradiated in the third irradiation phase and this design consists of an aluminum cladding tube loaded with a stack of 50 or 52 pellets (~49.5 cm stack length). The irradiation results from the fully loaded targets, which are expected to be similar to the production level targets, are extending and confirming knowledge of dimensional changes, pellet-clad interactions, fission gas release, self-shielding effects introduced within a multiple target array and production of quantities of irradiated material for larger-scale tests[3].

High Flux Isotope Reactor and ^{237}Np Target Descriptions

HFIR is a versatile 85 MW(t), pressurized, light-water-cooled and -moderated, very high flux research reactor, which is operated at ORNL. The reactor core assembly consists of a series of concentric annular regions, each approximately 61 cm high and contained in a pressure vessel: a central flux trap target region, two fuel elements separated by a small water coolant channel, a water region containing two neutron-absorbing control elements, a large beryllium reflector and a water region. A mockup of HFIR is illustrated in Figure 1. The inner (IFE) and outer (OFE) fuel elements consist of 171 and 369 fuel plates, respectively, which are curved in the shape of an involute. Highly enriched uranium fuel (U_3O_8-Al cermet) enriched to 93 wt.% ^{235}U and a total core loading of 9.4 kg ^{235}U powers HFIR for 23–26 days. The main mission of HFIR is to support neutron science experiments and activities including cold and thermal neutron scattering, isotope production, materials irradiation and neutron activation analysis.

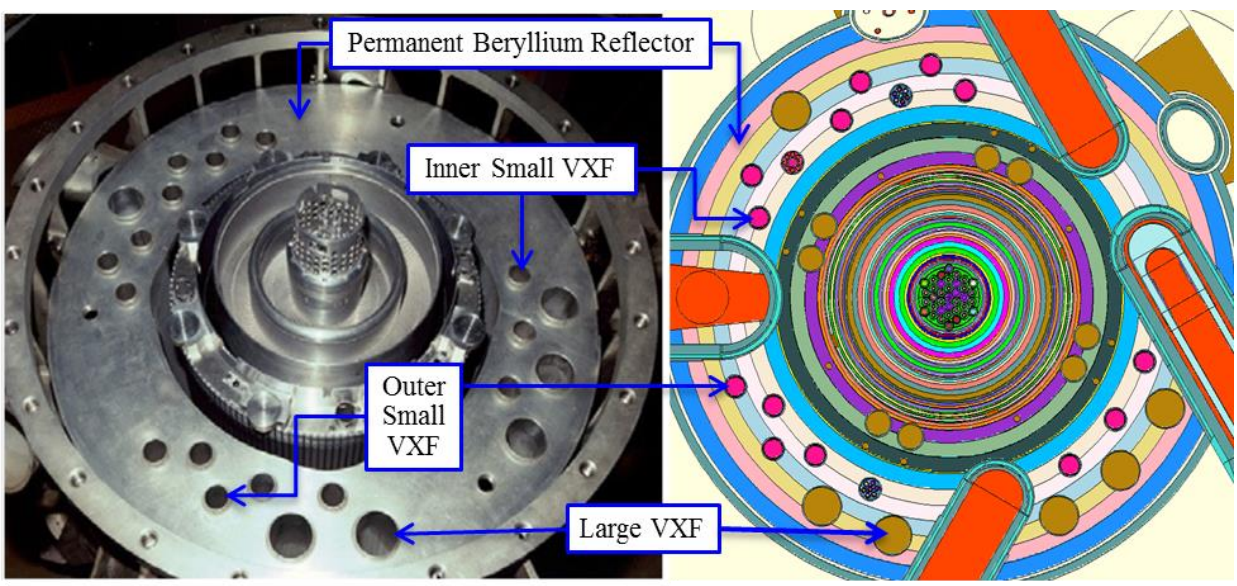

FIGURE 1. High Flux Isotope Reactor Core Mockup (Left) and MCNP Geometric Representation (Right).

HFIR's beryllium reflector is composed of three regions and the largest, outer-most radial region known as the permanent beryllium reflector (PB) is penetrated by 16 small (4.0 cm OD) vertical experiment facilities (VXF), one housing a pneumatic tube facility, and six large (7.2 cm OD) VXFs. Inner small, outer small and large VXFs are located on concentric circles with the core of radii 39.2, 44.1 and 46.3 cm, respectively. All irradiations that have been performed during the irradiation test phases described previously have taken place in inner small VXFs.

The fully loaded target design consists of an aluminum tube loaded with a stack of cermet pellets that are composed of 20 vol.% neptunium-dioxide blended with aluminum powder (NpO_2/Al) plus 10 vol.% void. Each cylindrical pellet has an OD and length of about 0.32 and 0.95 cm, respectively, and the nominal density is about 4.12 g/cm^3. The targets loaded in the small VXFs are arranged in a seven target array within an aluminum holder and when irradiated in the large VXFs, the targets are anticipated to be arranged in a 19 target array.

NEUTRONICS TOOLKIT AND METHODS

The computational tools used for the neutronics analyses include the Monte Carlo N-Particle 5 (MCNP5) version 1.5.1 code[5], the VESTA 2.0.2 Monte Carlo-based depletion tool[6] and the SCALE 6.1 nuclear safety analysis and design code package[7]. A brief description of the codes used in these studies is provided in this section.

MCNP Description

The MCNP5 code, which is a Monte Carlo-based neutron-photon-electron transport code developed and maintained at the Los Alamos National Laboratory, was used in these studies to perform neutron and photon transport calculations. Its capabilities to model complex geometries and to use pointwise cross section data for the neutron transport treatment make the code a desirable tool for analysis of highly-heterogeneous nuclear reactor systems such as HFIR. For the ^{237}Np target irradiations, MCNP was used to calculate neutron fluxes (magnitude and spectra); isotope- and reaction-type-specific reaction rates (e.g., ^{238}Pu neutron capture reaction rate); isotope-dependent effective one-group cross sections; and heat generation rates due to fission product kinetic energy and neutron, photon and beta energy deposition. Fuel element relative power densities, effective multiplication factors, and neutron fluxes to experiment facilities such as those in the flux trap target region and in the horizontal beam tubes were also calculated with MCNP in order to assess the impact ^{237}Np targets have on the performance of the reactor.

A detailed MCNP model based on the HFIR Cycle 400 input[8], which includes a detailed representation of the reactor core components and experiment facilities, was modified as needed for use in these studies. Cross section data based on the ENDF/B-VII.0[9] nuclear data evaluation was utilized for the calculations documented in this work, but ENDF/B-VII.1 and JEFF 3.1 data are also being explored. The as-modeled HFIR core, including ^{237}Np targets located in inner small VXFs 3 and 15 is illustrated in Figure 1.

VESTA Description

VESTA, a “generic” Monte Carlo-based depletion tool developed and maintained at Institut de Radioprotection et de Sûreté Nucléaire (IRSN) in France, was used for depletion analyses. VESTA has been validated against HFIR post-irradiation, spatially-dependent, uranium isotopic measurements[10]. Version 2.0.2 was used in these studies to couple the MCNP code to the point depletion and decay code ORIGEN 2.2[11]. VESTA has been selected as the primary depletion tool for HFIR core analysis because it is user friendly, it has the ability to simulate the vertical control element movement necessary to maintain critical conditions during the cycle and because extensive resources have been devoted to benchmarking MCNP and VESTA models of HFIR.

VESTA uses MCNP to determine the neutron flux in the depletion materials in an ultra-fine 43,000-group energy structure. Then, outside of MCNP, the reaction rates are calculated with pre-generated pointwise microscopic cross sections consistent with the data used in the MCNP transport calculations. The one-group data required for the ORIGEN 2.2 depletion calculations are thus determined using the ultra-fine calculated spectrum. This unique approach is called the multi-group binning approach[6]. The updated material compositions are passed to the subsequent MCNP input. This process iterates until the simulation of the desired irradiation history is complete.

SCALE Description

The SCALE 6.1 code package developed and maintained at ORNL is a comprehensive modeling and simulation suite used for nuclear safety analysis and design. The primary computational module in the SCALE “plug-and-play” framework used for these studies is the ORIGEN code, which is the only supported and most up-to-date version of ORIGEN. For these studies, the ORIGEN code was primarily used to calculate the post-shutdown nuclide inventories, decay heat data and delayed photon sources (e.g., photons emitted from radionuclide decay). Although not used for the studies described in this work, methods implementing the CSAS-MG, COUPLE and ORIGEN modules in place of VESTA have been used[4] and are currently being enhanced.

Methods Description

The first step in the simulation sequence is to setup the beginning-of-cycle (BOC) MCNP and VESTA inputs, which includes details regarding target geometry, the irradiation history and the depletion materials. During the VESTA simulation the time-dependent fission powers, neutron fluxes, isotopic inventory and isotopic cross sections are saved in the output files and the MCNP input files generated at each step are saved. The fission powers of the target materials are output in MW/cm^3 and are appropriately converted to fission rates in units of fissions/second. The

fission rate as a function of time curve is then integrated to determine the accumulated fission density (e.g., total number of fissions per unit volume) as a function of irradiation time. The end-of-cycle (EOC) nuclide inventories for each material are used as input to ORIGEN decay calculations that provide the delayed photon source for follow-on heat generation calculations in MCNP, the post-shutdown nuclide inventories and decay heats. Finally, MCNP calculations are performed in both k-eigenvalue and fixed source modes to determine the heat generation rates. The method process is illustrated in Figure 2.

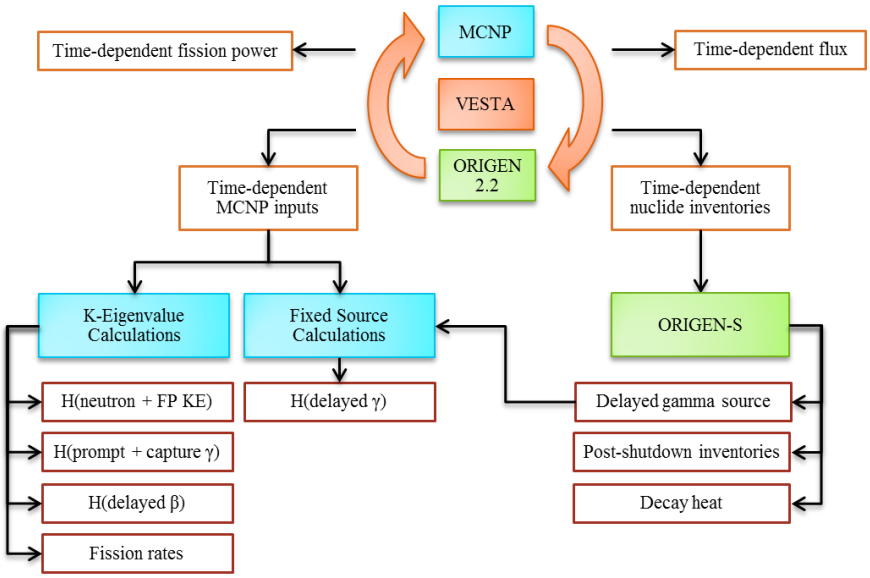

FIGURE 2. Flow Diagram of Safety-Basis Neutronics Method.

SAFETY-BASIS CALCULATIONS

Safety-basis calculations are performed to ensure the target irradiations do not have any adverse impacts on reactor performance and do not increase the probability of occurrence of or increase the consequences of an accident previously evaluated in the HFIR safety analysis report (SAR). Fission product gas inventories, fission densities, heat generation rates and decay heat data are calculated and provided to thermal-structural and thermal-hydraulic specialists who perform safety-basis analyses to demonstrate the pellets' melting temperature would not be exceeded if subjected to bounding conditions and to study other parameters of interest. Post-shutdown radionuclide inventories support post-irradiation examination, transportation, storage and dose consequence analyses.

Irradiation Target Design

For the safety-basis neutronics calculations, each full length target was subdivided into 18 axial regions by one radial region and was irradiated for 26-day cycles with 15-day outages between cycles. Only one radial region is modeled to calculate conservative centerline heat generation rates and 18 axial regions are modeled to capture the axial variation in the physics implemented in the follow-on thermal calculations. Seven target array arrangements were modeled in inner small VXFs 15 and 3 because they were calculated to experience the greatest and smallest neutron fluxes of the inner small VXFs, respectively. Twenty-six day cycle lengths were simulated because this is considered the maximum typical HFIR cycle length, which leads to greater quantities of fissile material, greater fission densities, greater heat generation rates and more conservative post-shutdown radionuclide inventories. Simulated in the VESTA calculations are the following: control element withdrawal; fuel element, ^{237}Np target and control element depletion; and one-day time steps. A graphical representation of the as-modeled targets is provided in Figure 3.

Heat Generation, Fission Density and Fission Gas Results

During irradiation, neutron capture in the ^{237}Np (e.g., feed material) nucleus produces ^{238}Np, which beta-decays with a half-life of 2.12 days[12] into ^{238}Pu. Subsequent neutron captures produce heavier plutonium isotopes, which along with ^{238}Np, have large fission cross sections. The fission events that take place in the pellets lead to heat

generation, fission product gas production and the generation of radionuclide inventories. Fission product gas production in the pellets and heat generation rates in the pellets and target structure, during irradiation and post-reactor shutdown, are calculated and provided to thermal-hydraulic specialists who perform analyses to demonstrate the maximum pellet temperature does not exceed the pellet's melting temperature and the target capsule's surface temperature does not exceed the adjacent coolant saturation temperatures during irradiation and bounding events defined in the HFIR SAR.

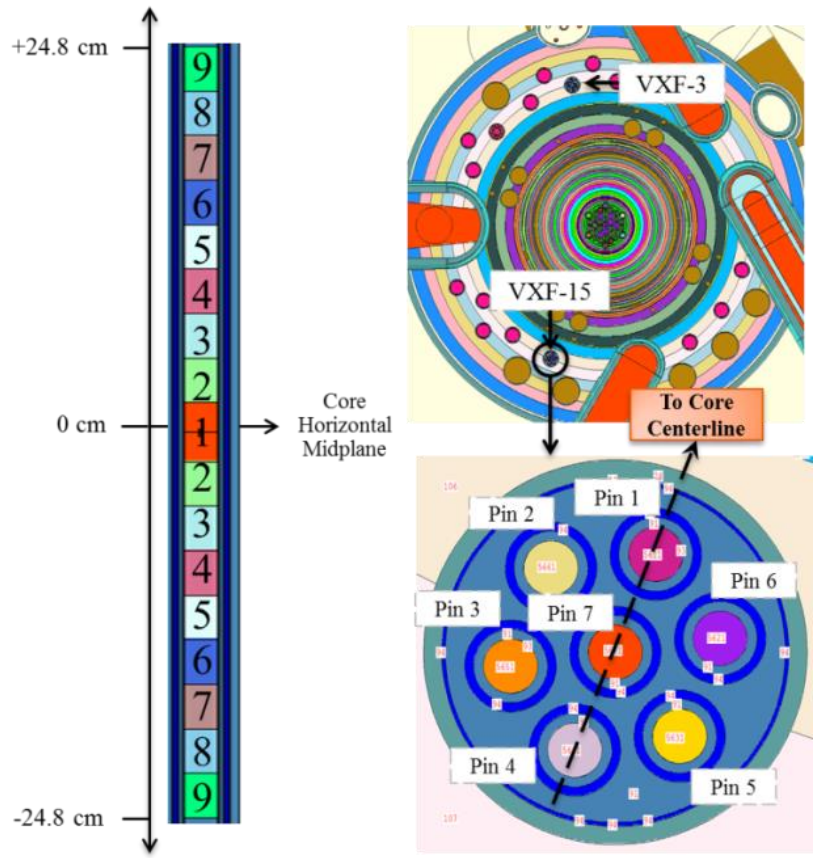

FIGURE 3. ^{237}Np Target Modeling Representation. In the Target Array, Pin 1 is Positioned to Face the Reactor Core Centerline Such that it Experiences the Greatest Fluence. The 49.5 cm Pellet Stack is Modeled as 18 Axial Regions. Material Symmetry is used Across the Core Midplane. Materials are Labeled 1-9 and Material 1 is Closest to the Midplane.

During the irradiation cycle ^{238}Np reaches equilibrium about 10 days into the cycle and then is removed during the outage between cycles as a result of its short half-life. The concentration again reaches equilibrium in the second cycle, but at a value slightly less than in the first cycle due to the consumption of some ^{237}Np in the first cycle. At the end of the first cycle most of the fission rate is attributable to ^{238}Np, but at the end of the second cycle ^{239}Pu can contribute up to about half of the total fission rate. Due to these transmutations, the heat generation rates in the targets increase with increasing irradiation time. The heat generation rates, as calculated with MCNP, are plotted at various times into the second cycle for the target materials in Figure 4. As shown in Figure 4, the maximum heat generation rates in VXFs 3 and 15 were estimated to be 362 and 398 W/g, respectively. All of the VXF-15 heat generation rates shown in Figure 4, along with VESTA-generated fission powers, are plotted as a function of fission density in Figure 5. Polynomial fits bounding this data were generated for use in follow-on evaluations.

Fission gases are required to be calculated because, when released into the helium filled plenum surrounding the pellet stack, they reduce the thermal conductivity of the gas between the aluminum clad and the pellet. This reduces the ability of the pellet to transfer heat to the clad and out to the water coolant. Typical gas release fractions vary from 0.01-0.15. The amount of xenon, krypton and helium produced during the two-cycle simulation is shown in Figure 6.

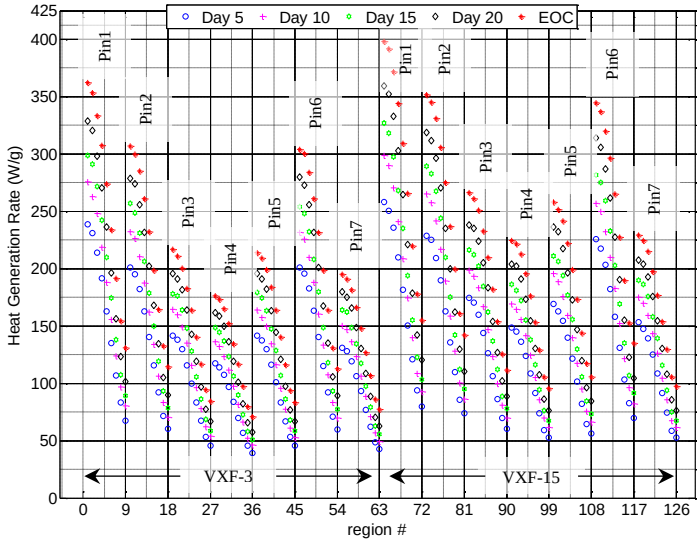

Figure 4. Safety-Basis Heat Generation Rates During Second Irradiation Cycle. Region #'s 1-63 and 64-126 Represent Materials in VXF-3 and VXF-15, Respectively. Regions 1-9 and 64-72 Represent Pin 1 Materials, Followed by Pins 2, 3, 4, 5, 6 and 7. The Greatest Value in Each Set of 9 is Material 1 Which is Closest to the Core Midplane and the Smallest Value is Material 9.

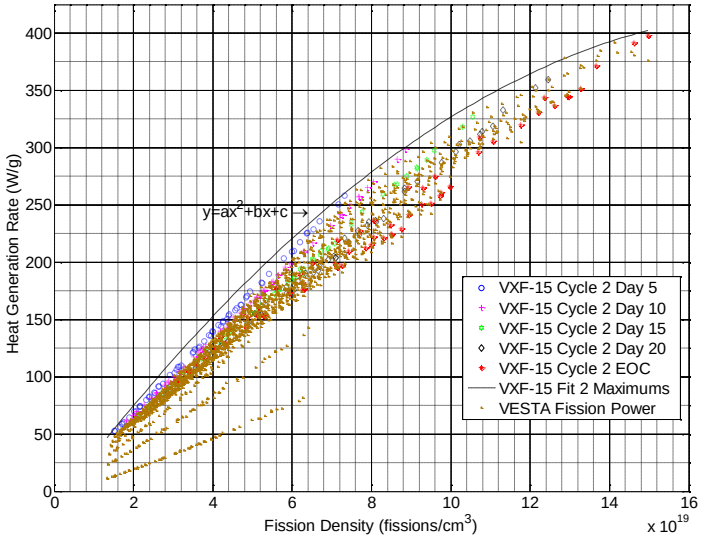

Figure 5. Safety-Basis Heat Generation Rates as a Function of Fission Density for VXF-15 Materials During Second Cycle.

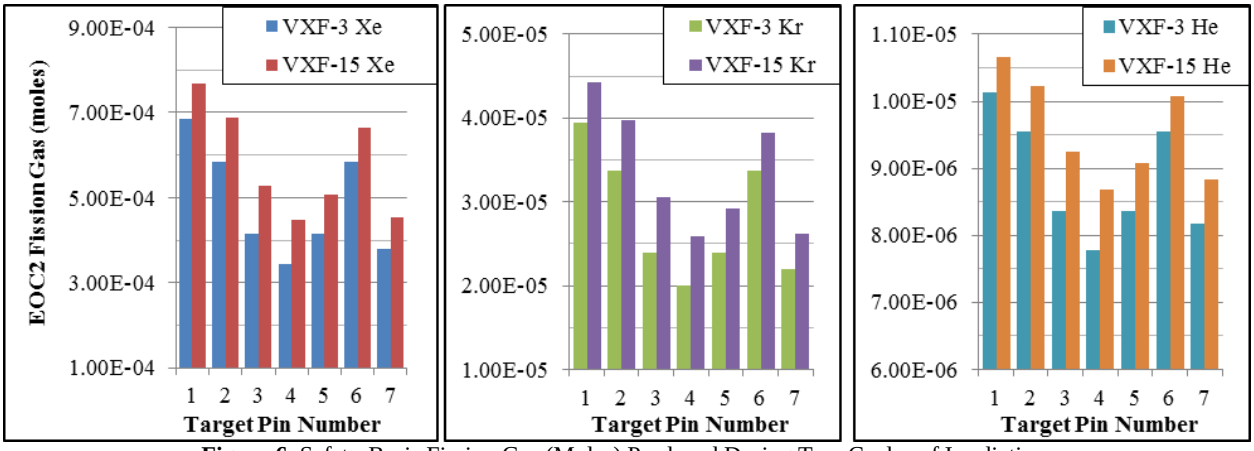

Figure 6. Safety-Basis Fission Gas (Moles) Produced During Two Cycles of Irradiation.

Impacts on Reactor Performance

In order to qualify experiments for irradiation at HFIR, bounding conditions established in the HFIR SAR must be analyzed. Safety-basis calculations are performed to ensure the target irradiations have no adverse impacts on reactor performance such as power tilts that are greater than those previously evaluated in the HFIR SAR. Because strongly-absorbing experiments can impact the power distribution profile, which in turn impacts the core thermal-hydraulics, the magnitude of the power change at the hot spot/hot streak due to experiments is limited to 9%. The core r-z fission rate density distributions at BOC (left plot) and EOC (right plot) are illustrated in Figure 7. The peak fission rate density occurs on the inner edge of the IFE at BOC because of its proximity to the over-moderated flux trap region and the peak shifts to the outer edge of the OFE at EOC because of fuel burnup at the inner edge of the IFE, control element withdrawal during the cycle and its proximity to the beryllium reflector. Due to the location of the ^{237}Np targets with respect to the core and the fact that only a few VXFs are occupied with targets, as-analyzed for the safety-basis evaluations, no statistically evident changes in the core fission density distribution due to these targets are observed.

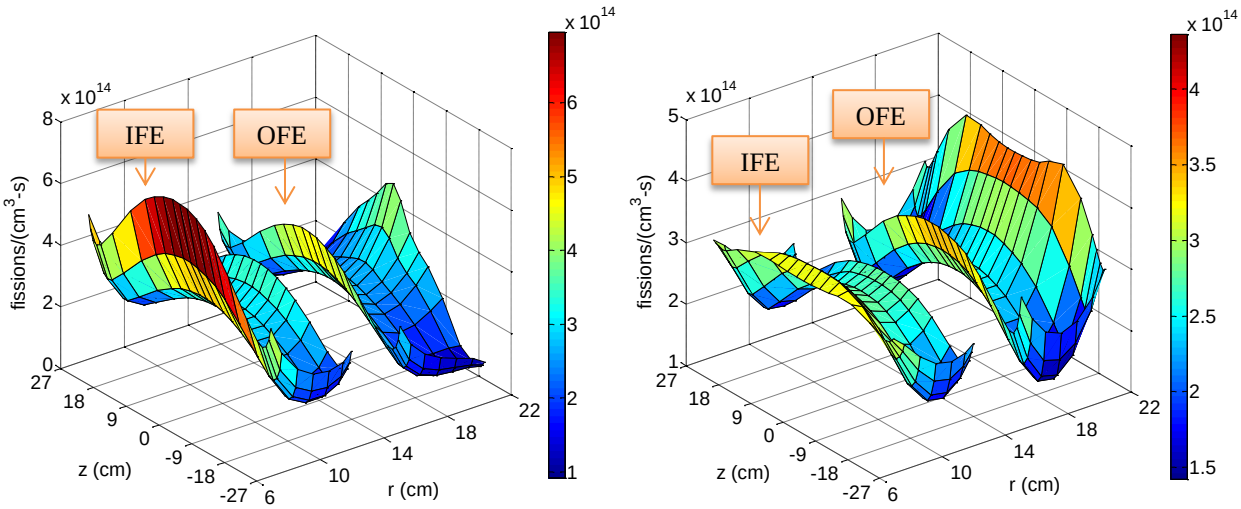

FIGURE 7. Core Fission Rate Density Distributions at Beginning-of-Cycle (Left) and End-of-Cycle (Right).

Core reactivity control is obtained by axially moving the neutron-absorbing regions of the control elements. Prior to reactor startup, the symmetrical critical control element position is estimated by accounting for the reactivity of various contributors such as experiments, as-built core data, etc. Thus, the reactivity addition due to experiments must be well characterized to ensure the estimated and actual critical positions are in good agreement. Also, if experiments are strongly-absorbing, they can reduce the cycle length and impact other HFIR missions. The reactivity attributed to these targets was found to be small-to-negligible, and thus has minimal impact on the startup critical control element position and the cycle length.

PLUTONIUM-238 PRODUCTION ASSESSMENTS

The technology demonstration project was structured to establish the target design and fabrication processes, characterize the irradiation behavior and properties of the target material, establish the chemical recovery process and to validate the computational tools and data being used to analyze the targets. Once this task is completed, ^{238}Pu production will be scaled up, and the HFIR and ATR will irradiate sufficient NpO_2/Al material to produce about 1.5 kg PuO_2 per year[3], which is equivalent to about 1.13 kg ^{238}Pu assuming the purity of the Pu material is 85% ^{238}Pu in Pu. The purpose of the studies documented in this section is to estimate the amount of ^{238}Pu HFIR can produce in the PB VXFs per year. Previous production studies modeling different array arrangements, modeling fewer VXF sites and considering one cycle of irradiation were performed[13].

Irradiation Length Determination

The target design modeled for the production studies is similar to the design modeled for the fully loaded target safety-basis studies previously described with the exception of very minor dimensional changes to pellets and small changes to the structure components of the target (e.g., dummy Al pellets, spacer tubes, etc.). The pellet stacks within the aluminum cladding tube were modeled slightly differently than discussed in the safety-basis section. For the production assessment studies, each pellet stack was discretized into three radial rings to capture the self-shielding effects into the pellet and six axial regions. Fewer axial regions are modeled for these studies because the results are not being used for follow-on thermal studies, but six axial regions is sufficient to capture the axial variation in production rates. Material symmetry across the core midplane was again used. Thus, each pellet stack was modeled with nine unique materials. The production estimate simulations modeled seven target array arrangements in the 10 inner small VXFs, seven target array arrangements in the five outer small VXFs and 19 target array arrangements in the six large VXFs.

To establish the number of cycles for which the targets should be irradiated in the three types of VXFs (e.g., inner small, outer small and large VXFs), an eight-cycle irradiation simulation was performed with VESTA. Rather than performing a detailed, time-intensive simulation as that performed in the safety-basis study, a middle-of-cycle (MOC) MCNP input, constituting cycle-averaged conditions (e.g., fuel element composition, control element position, fluxes to the reflector, etc.), was used. The eight-cycle simulation modeled 25-day irradiation cycles with 25-day outages between cycles, which is typical of HFIR operations. A transport calculation was performed at the beginning of each cycle to calculate the reaction rates to be used to deplete each uniquely identified NpO_2/Al material for that cycle. Updates were performed at the beginning of each cycle to account for the self-shielding effects introduced due to the build-in of Pu isotopes and fission products during each cycle.

^{238}Pu production and Pu purity as a function of time into the simulation curves are provided in Figure 8, and Table 1 lists the amount of ^{238}Pu produced per cycle in each of the VXF types. Due to the consumption of the feed material (e.g., ^{237}Np) during irradiation, the first cycle is the most efficient, and the efficiency reduces in each subsequent cycle. Based on these calculations, the ideal number of cycles the targets should be irradiated in the inner small, outer small and large VXFs was determined to be two, four and six, respectively. Two and four cycles were established for the inner and outer small VXFs because irradiating the targets for more cycles would lead to Pu purities below the 85% criterion upon target removal. Although the overall large VXF targets' Pu purity doesn't reach 85% until the end of the eighth cycle, six cycles was established as their irradiation length because the production during the seventh cycle is 40% less than the first cycle [e.g., 100x(36.59-61.02)/61.02].

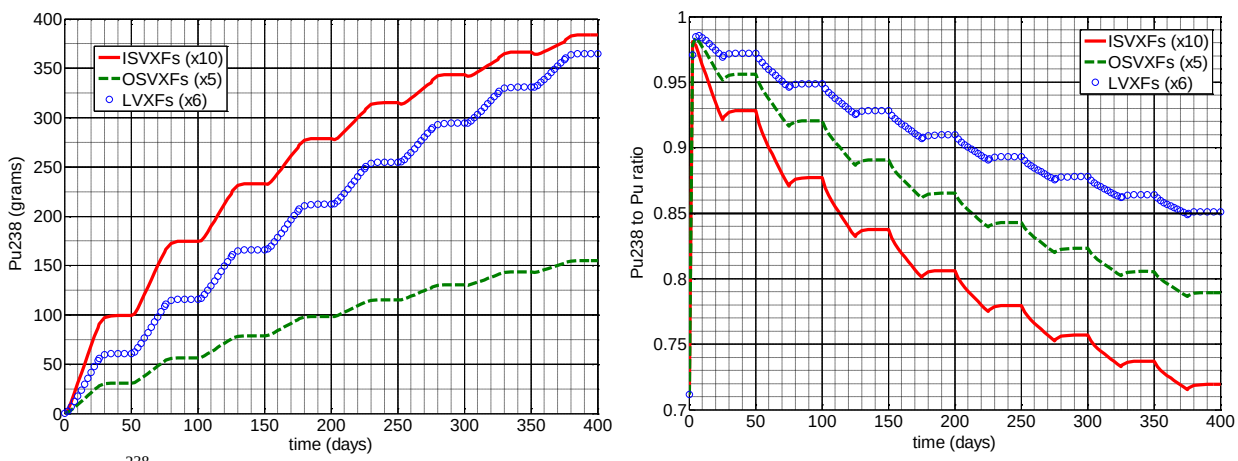

FIGURE 8. ^{238}Pu Production (Left) and Purity (Right) as a Function of Time and Vertical Experiment Facility Type During the Eight-Cycle Simulation. Ten Inner Small Facilities Each with 7 Targets, 5 Outer Small Facilities Each with 7 Targets and 6 Large Facilities Each with 7 Targets are Considered.

TABLE 1. Accumulated and Single-Cycle ^{238}Pu Production During the Eight-Cycle Simulation.

Cycle	Inner Small VXF (grams)		Outer Small VXF (grams)		Large VXF (grams)	
	Accumulated	Single Cycle	Accumulated	Single Cycle	Accumulated	Single Cycle
1	99.56	99.56	30.73	30.73	61.02	61.02
2	174.77	75.21	56.61	25.88	115.81	54.79
3	233.05	58.28	78.98	22.37	165.92	50.11
4	278.84	45.79	98.41	19.43	212.11	46.19
5	315.12	36.28	115.46	17.05	254.82	42.71
6	343.82	28.7	130.40	14.94	294.29	39.47
7	366.47	22.65	143.51	13.11	330.88	36.59
8	384.15	17.68	155.06	11.55	364.86	33.98

Assessment of Yearly Production Capability

On average HFIR operates six–seven cycles per year, and because the targets loaded in the large VXFs were determined to be irradiated for six cycles before being removed, a detailed six-cycle VESTA simulation was performed and target replacement was modeled. For this simulation, three sets of inner small VXF targets were depleted and each set was irradiated for two cycles before being replaced with fresh targets. Two sets of outer small VXF targets were irradiated, the first set for the first four cycles and the second set for the last two cycles. One set of large VXF targets was irradiated over the six-cycle period. Again, 25-day irradiations and 25-day outages were simulated, but for these studies 13 time-steps were modeled for each cycle of irradiation to better capture the pellet materials' time-dependent reaction rates. Thus, control element withdrawal and fuel element, control element and target material depletion were performed.

^{238}Pu production and Pu purity as a function of time into the simulation curves are provided in Figure 9, and Table 2 lists the amount of ^{238}Pu produced in each of the three VXF types. It is estimated that about 172, 98 and 293 grams of ^{238}Pu can be produced during two cycles of irradiation in the inner small VXFs, four cycles of irradiation in the outer small VXFs and six cycles of irradiation in the large VXFs, respectively. Thus, an average of about 0.96 kg ^{238}Pu could be produced in six HFIR cycles if all of the PB VXFs are loaded with NpO_2/Al targets. Scaling to seven cycles of irradiation per year, it is estimated that about 1.12 kg ^{238}Pu could be produced. Assuming a purity of 85% ^{238}Pu in Pu, the six and seven cycle PuO_2 production equivalents are about 1.28–1.49 kg, respectively. These estimates assume that 100% of the Pu is chemically recovered and all PB VXFs are used. However, it is important to note that not all of the Pu is recovered during the chemical recovery processes, other irradiation facilities exist in HFIR for potential ^{238}Pu production, some PB facilities may need to be reserved for other users and some facilities loaded with ^{238}Pu production targets may impact other HFIR missions such as cold and thermal neutron scattering. More work is required to investigate target irradiations in other HFIR experiment facilities and to assess target irradiation impacts on neutron flux levels down the beam tubes used for scattering experiments.

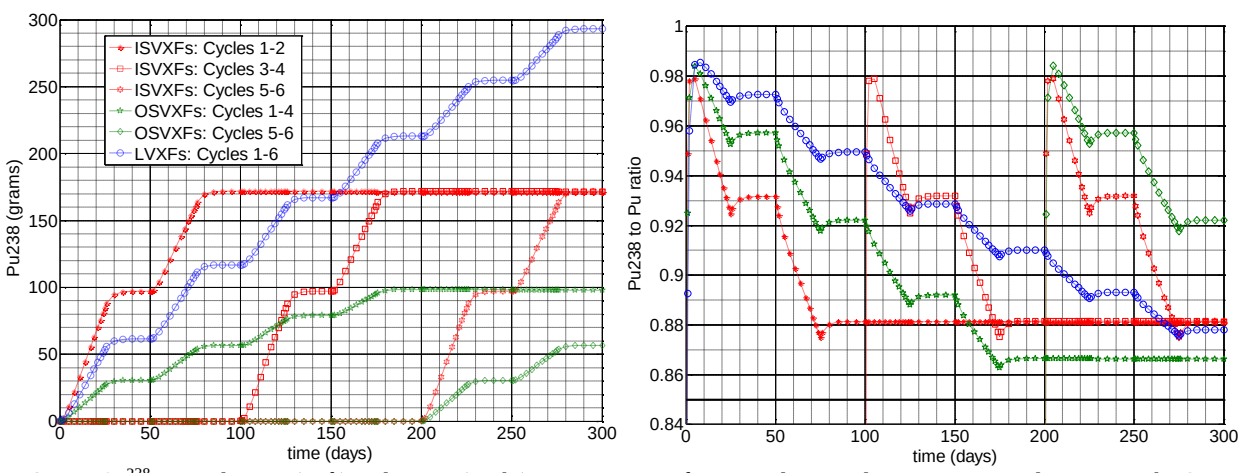

FIGURE 9. ^{238}Pu Production (Left) and Purity (Right) as a Function of Time and Vertical Experiment Facility During the Six-Cycle Simulation with Target Replacement.

TABLE 2. Accumulated ^{238}Pu Production During the Six-Cycle Simulation with Target Replacement.

Cycle	Inner Small VXFs (grams)			Outer Small VXFs (grams)		Large VXFs (grams)
	Set 1	Set 2	Set 3	Set 1	Set 2	Set 1
1	97.11	-	-	30.53	-	61.38
2	171.94	-	-	56.56	-	116.74
3	-	96.98	-	78.90	-	167.02
4	-	171.94	-	98.19	-	212.97
5	-	-	97.06	-	30.49	254.76
6	-	-	172.01	-	56.53	293.18

CONCLUSION

In an effort to reestablish a domestic ^{238}Pu production supply chain, a detailed technology demonstration sub-project has been developed to establish a safe and efficient infrastructure to fabricate and irradiate NpO_2/Al targets and to chemically recover the Np and Pu. A key task in this sub-project has been to perform neutronics simulations to support HFIR safety-basis evaluations of the target irradiations and to assess the ^{238}Pu production capability at HFIR. It is estimated that a total of about 0.96–1.12 kg ^{238}Pu, which is equivalent to about 1.28–1.49 kg PuO_2 at 85% ^{238}Pu to Pu purity, can be produced per year in HFIR assuming all of the permanent beryllium reflector vertical irradiation facilities are utilized. Post-irradiation examination isotopic measurements taken during the technology development phase will be used to help verify and validate the neutronics computational methods, data, results and conclusions.

ACKNOWLEDGMENTS

This work has been sponsored by NASA's Science Mission Directorate and the US DOE Office of Space and Defense Power Systems. The authors acknowledge R. Hobbs and C. Bryan, ORNL, for their reviews of this paper.

REFERENCES

[1] Dudzinski, L.A., "Curiosity," PowerPoint Presentation, National Aeronautics and Space Administration, Presented at the Oak Ridge National Laboratory, Oak Ridge, TN, (2012).
[2] Hurt, C.J., et. al., "Plutonium-238 Production Target Design Studies," *INMM 55th Annual Meeting*, Atlanta, GA, (2014).
[3] Wham, R.M., et. al., "The Plutonium-238 Supply Project," *The 19th Pacific Basin Nuclear Conference*, Vancouver, British Columbia, Canada, (2014).
[4] Chandler, D. and Hobbs, R.W., "Neutronics Analyses of NpO_2 Single Pellet Irradiations at HFIR to Support the Pu-238 Production Project," *Transaction American Nuclear Society*, **108**, pp. 753-755, (2013).
[5] X-5 Monte Carlo Team, "MCNP – A general Monte Carlo N-Particle Transport Code, Version 5. Volume I: Overview and Theory," LA-UR-03-1987, Los Alamos National Laboratory, Los Alamos, NM, (2003).
[6] Haeck, W., "VESTA User's Manual - Version 2.0.0," IRSN Report DSU/SEC/T/2008-331 Indice A, IRSN, France, (2009).
[7] "SCALE: A Comprehensive Modeling and Simulation Suite for Nuclear Safety Analysis and Design"," ORNL/TM-2005/39, Version 6.1, Oak Ridge National Laboratory, Oak Ridge, TN, (June 2011). Available from Radiation Safety Information Computational Center at Oak Ridge National Laboratory as CCC-785.
[8] Primm III, R.T. and Xoubi, N., "Modeling of the High Flux Isotope Reactor Cycle 400," ORNL/TM-2004/251, Oak Ridge National Laboratory, Oak Ridge, TN, (2005)
[9] Chadwick, M.B., et. al., "ENDF/B-VII.0: Next Generation Evaluated Nuclear Data Library for Nuclear Science and Technology," *Nuclear Data Sheets*, **107**, pp. 2931-3060, (2006).
[10] Chandler, D., Primm III, R.T., and Maldonado, G.I., "Burnup and Spatially-Dependent Uranium Isotopic Calculations for the High Flux Isotope Reactor," *Transaction American Nuclear Society*, **103**, pp. 768-769, (2010).
[11] "ORIGEN 2.2 – Isotope Generation and Depletion Code Matrix Exponential Method," Oak Ridge National Laboratory, Oak Ridge, TN, (2002). Available from Radiation Safety Information Computational Center at Oak Ridge National Laboratory as CCC-371.
[12] "Chart of Nuclides," National Nuclear Data Center, Brookhaven National Laboratory, <www.nndc.bnl.gov/chart>.
[13] Lastres, O., Chandler, D., Jarrell, J.J. and Maldonado, G.I., "Studies of Plutonium-238 Production at the High Flux Isotope Reactor," *Transaction American Nuclear Society*, **104**, pp. 716–718, (2011).

MEGAHIT: Conclusion of the Development of the Advanced Propulsion Roadmap for HORIZON2020

Tim Tinsley[1], Frederic Mason[2], Emmanouil Detsis[3], Enrico Gaia[4], Zara Hodgson[5], Frank Jansen[6], Alexander Semenkin[7], Jean-Marc Ruault[8], Jean-Claude Worms[9]

[1]National Nuclear Laboratory, United Kingdom, tim.p.tinsley@nnl.co.uk : [2]Centre National d'Etudes Spatiales (CNES), France: [3]European Science Foundation, France : [4]Thales Alenia Space Italia, Italy: [5]National Nuclear Laboratory, United Kingdom: [6]Institute of Aerospace Systems, Germany: [7]Keldysh Research Center, Russia: [8]Centre National d'Etudes Spatiales (CNES), France: [9]European Science Foundation, France

Abstract. A significant number of exploration missions require nuclear propulsion for which power sources are essential and enabling key assets. Associated technological developments however require important financial efforts that can probably only take place in the frame of an international collaboration, sharing the efforts as this has been the case for the International Space Station. MEGAHIT, funded by the European Commission under the 7th Framework Programme for Research and Technological Development, was a supporting action aiming at building a European roadmap for Megawatt level nuclear electric propulsion, in preparation of the Horizon 2020 programme. It concluded in September 2014. MEGAHIT was driven by a consortium coordinated by the European Science Foundation and included CNES, DLR, Keldysh Research Center, the National Nuclear Laboratory from U.K. and Thales Alenia Space Italia. The consortium favoured an open and participative approach in order that all interested stakeholders - research centers, agencies and industry- within consortium or not, can establish common research objectives and initiate research alliances. This approach allowed the building of a scientific and technical community on the topic in Europe and Russia. Potential collaboration opportunities at international level with other space fairing nations were also explored.

Megahit adopted an approach in 4 phases.

- **Phase 1: High level requirements.** Collected inputs from space agencies and research centers on mission-related high level requirements.
- **Phase 2: Reference vision.** Built a reference vision of what system we aim at, and what would be the best technological options.
- **Phase 3: Technological plans.** The rationale was that the best people for establishing technological plans are the stakeholders identified as being able to carry out the development. These stakeholders were associated through discussions and workshops on technologies they have expertise in. Main workshop was held in Brussels on December 2013 and was attended by about a hundred specialists.
- **Phase 4: Road-maps.** Aims at a synthesis of the three previous phases, translating into consistent road-maps what has been established in terms of key technologies and technological plans.

The paper and presentation will provide a summary of the project and conclusions on the progress made. The follow on project named DEMOCRITIOS will be discussed in a separate paper

Keywords: MEGAHIT, electrical propulsion, reactor.

INTRODUCTION

Nuclear propulsion is an essential and enabling key asset for a significant number of exploration missions. Associated technological developments however require important financial efforts that can probably only take place in the frame of an international collaboration, sharing the efforts, as has been the case for the International Space Station.

MEGAHIT is a supporting action aiming at building a European roadmap for Megawatt level nuclear electric propulsion. It is funded by the European Commission under the 7th Framework Programme for Research and Technological Development, in preparation of the Horizon 2020 Programme, starting in 2014.

MEGAHIT is driven by a consortium that is coordinated by the European Science Foundation and that includes CNES, DLR, Keldysh Research Center, the National Nuclear Laboratory from U.K. and Thales Alenia Space Italia. The consortium favors an open and participative approach in order that all interested stakeholders - research centers, agencies and industry- within consortium or not, can establish common research objectives and initiate research alliances. This approach will allow building a scientific and technical community on the topic in Europe and Russia. Potential collaboration opportunities at international level with other space faring nations will be included.

APPROACH

Megahit adopted an approach in 4 phases.

- **Phase 1: High level requirements.** Collected inputs from space agencies and research centers on mission-related high level requirements.
- **Phase 2: Reference vision.** Built a reference vision of what system we aim at, and what would be the best technological options.
- **Phase 3: Technological plans.** The rationale was that the best people for establishing technological plans are the stakeholders identified as being able to carry out the development. These stakeholders were associated through discussions and workshops on technologies they have expertise in. Main workshop was held in Brussels on December 2013 and was attended by about a hundred specialists.

Phase 4: Road-maps. Aims at a synthesis of the three previous phases, translating into consistent road-maps what has been established in terms of key technologies and technological plans.

MISSIONS REQUIREMENTS

Mission analysis was based on the following hypothesis/requirements:

- Departure will be from a sufficiently high orbit (800km or more).
- Spacecraft will be composed of at least 2 modules assembled in orbit: the transport power module (20 tons) and the module with payload (20 tons). Radiators can be foldable.
- System can function 5 years in full power on a total lifetime of 10 years.
- A strong requirement would be safety: the reactor shall remain subcritical at all times during launch, even in case of a launch failure.

Three families of missions emerged as the most promising:

- Near Earth Orbit (NEO) deflection: deflection would be done acting as a gravity tractor. System could deflect a NEO of Apophis size.

- Outer solar system missions: several tons of payload could be sent to Europa or Titan within 3 years. A chemical stage, without gravity assist manoeuvre, would put only 300kg of payload in this orbit.
- Cargo missions: Lunar orbit tug or manned Mars mission cargo support mission.

SYSTEM ARCHITECTURE

In addition to the mission requirements, some general configuration requirements / recommendations for the architecture are given:

- The separation distance in-between the reactor and the payload shall be as much as possible.
- Spacecraft subsystems and payloads must be contained within the shielded volume.
- Radiator panels shall be foldable (radiator area ~1000m² taking into account both sides of the radiator), arrangement >90°.
- Propellant tanks may be placed near to centre of gravity (if possible) and to be utilized to shield radiation vulnerable components.
- Thruster plumes (exhaust) should not interact with the S/C.
- The thrust direction shall be parallel to main structural axis.
- Conversion system shall be integrated near reactor.
- Radiation dose e.g. to subsystems and payload can be minimized by separation and shielding. This has a large impact on spacecraft design e.g. distance reactor to payload of 30 m leads to a shield mass of ca. 1-2t.

A trade off study was conducted between possible technologies, figure 1, leading to down select 1 to 3 options for each main subsystem. A very preliminary « high level » concept was established, to give rough order of magnitude of mass and thermodynamic maps.

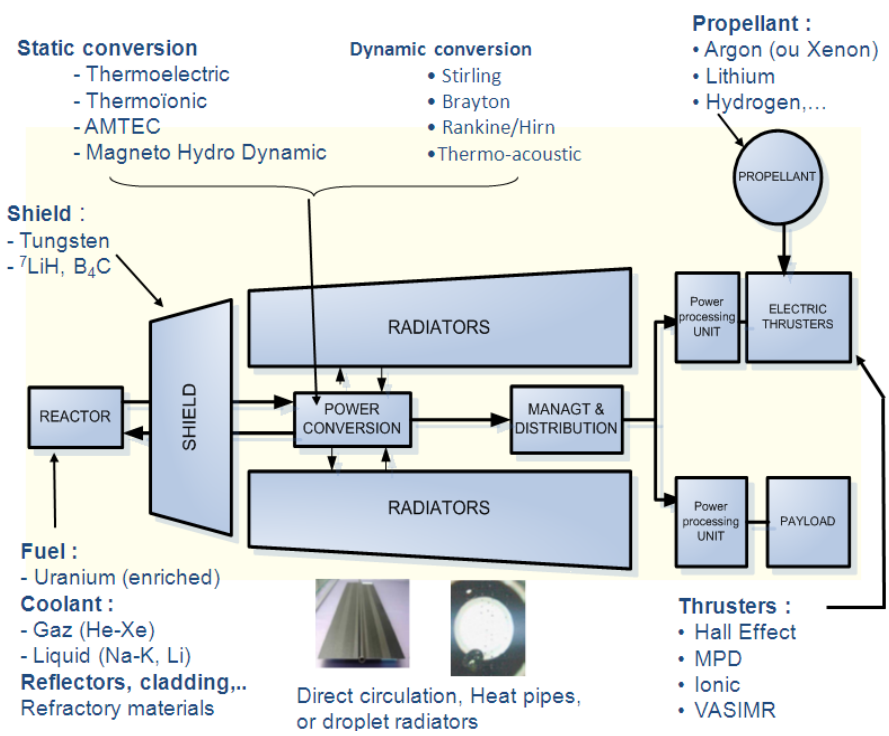

FIGURE 1. general architecture and list of candidates for subsystems.

FUEL AND CORE

There are two candidates for the MEGAHIT fast spectrum reactor concept, required to generate thermal power (greater than 3MW, ~1300K) for the nuclear electric propulsion system (target 1MW electrical power overall) over a 5-10 year operational life[1]. They are:

- Direct, gas cooled reactor loaded with coated particle/composite fuel linked to Brayton conversion system
- In-direct, liquid metal cooled reactor loaded with more conventional fuel, e.g. metallic encapsulated pins filled with fuel pellets, linked to Brayton conversion system.

Both reactor concepts warrant further assessment, together with assessment of power conversion system choices, until sufficient data are available to support a trade off study of mass versus technological risk that can determine the preferred reactor choice. With the completion of this Trade-off Study of Reactor and Conversion systems, a choice of the candidate fuel and core configuration for the reactor can be made. The following critical technologies have been identified for the Reactor, Fuel and Core system:

1. Fuel & Core Configuration: At this time there are several candidate technology options, dependent on the ultimate reactor system choice. Potential critical technologies identified are U oxides, nitrides, carbides or oxycarbide fuels in the form of pellets (clad in refractory metal pins), coated particles or composites. High enrichment and fast spectrum were retained to optimize the mass, but also to follow UN recommendation to avoid Pu239 formation linked to thermal spectrum [1].
2. Power Conversion Interface:
   - high temperature Heat Exchanger materials (for an indirect cycle choice)
   - cobalt free turbine materials (for a direct cycle choice).
3. Primary Boundary Protection:
   - Materials and advanced manufacturing techniques
4. Reflector & Control:
   - Moving parts (e.g. Drums) reliability
   - Passive control system technology, such as gas expansion modules
5. System Architecture:
   - Diverse heat removal systems;
   - Coolant purification, make-up and loops;

Additionally, there are several enabling activities for establishing this sub-system associated with System Performance and Safety Assessment. Specifically these include safety assessment methodology and processes for start-up/shutdown and mission operating requirements, Whole core performance modeling and simulation, Thermal hydraulic feedback code development, Reflector /Absorber code development Shielding code development and System transient analyses ,

At an appropriate point further down selection will be required to focus efforts on preferred, credible technologies.

CONVERSION

The leading candidate for power conversion and the choice for reference system is Direct Brayton cycle with 1300K as hot source temperature, as seen in figure 2. A mixture of gaseous He-Xe cools down the reactor, and then drives a turbine coupled to an alternator. Efficiency is good for such a conversion system (~30%) and a lot of experience is available from aeronautics engine.

With such a cycle the 20kg/kWe target for the system would be achievable, but there is still possibility to improve performance:

- Either by increasing the temperature at turbine inlet (up to 1600K)
- Or by using an indirect cycle. There would be 2 fluidic loops, one to cool down the reactor, the other one to drive the turbine. Thus, by cooling down the reactor with a liquid a lighter and more compact reactor could be used.

It is estimated that with an 1600K Indirect Brayton cycle, the system would be twice lighter than with a 1300K Indirect Brayton cycle.

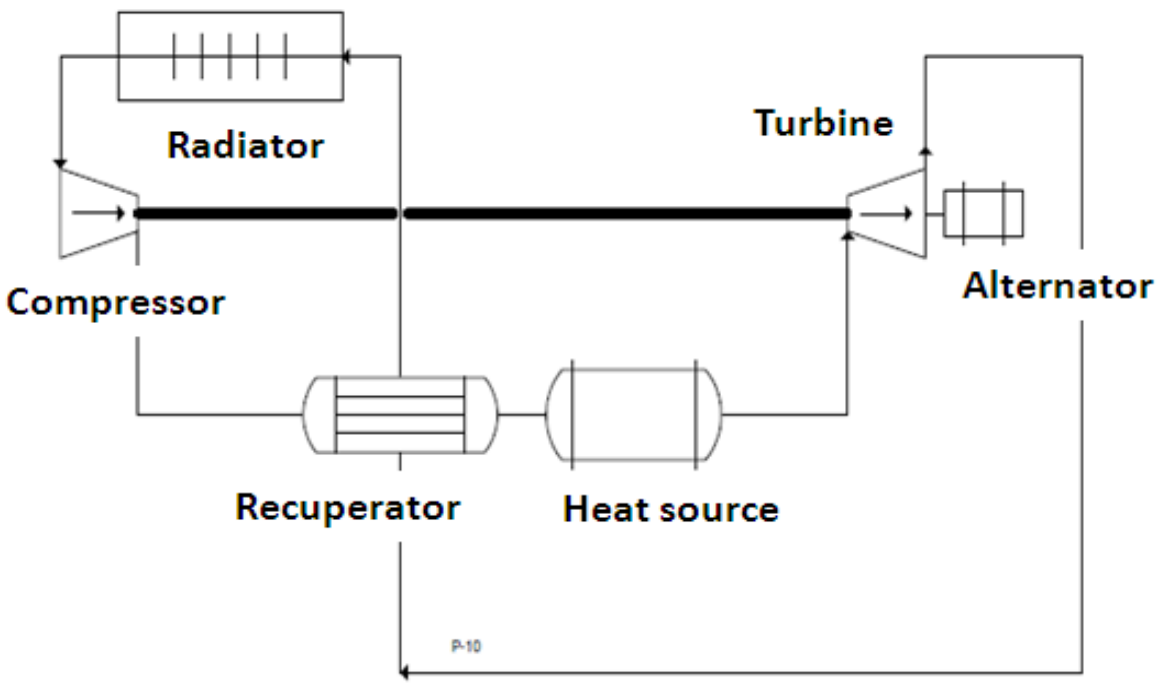

FIGURE 2. Example Direct Brayton subsystem

THERMAL CONTROL

The Radiator provides the cold source for the Brayton cycle. For radiator technology, a heat pipe system was selected due to its simplicity and good performance [3]. Droplet radiator is a promising technology under maturation, and will be used as a back-up option. For other heat exchangers, plate heat exchanger was selected. The thermal control system includes:

- Radiators.
- Heat exchangers (HX); HX1 is the heat exchanger between primary loop (reactor) and secondary loop (conversion by the turbine) if an indirect cycle is selected. HX2 is the heat exchanger between the conversion loop and the heat pipes of the radiator.
- Thermal shields.

The selected technologies are:

- Radiators based on high temperature heat pipes system.
- Plate-type heat exchangers as well for gas-gas as for gas-fluid heat transfer.
- Multi-layers Insulation mounted-on / supported by light structures for thermal shielding. The shield could be improved with micro-meteoroids blocking capabilities to protect the behind located sensible parts of MEGAHIT spacecraft.

ELECTRICAL THRUSTERS

For electric thrusters, solutions with higher TRL levels were down-selected: There are two leading candidates.

1. Hall Thrusters. Application of Hall thrusters is justified in the specific impulse range of 2000-4000s (up to 5000 for Ar). Available technologies allows thrusters with power level up to dozens kW. Increasing specific impulse may have negative effect on the operation stability and lifetime of Hall thrusters.

2. Ion Thrusters. Building of an ion thruster with power of 50 kW is possible (Cf. Russian and US background) at the existing technology level at specific impulse of 8000 (for Kr) and higher.

Other technology, such as Magnetoplasmadynamic (MDH) thrusters, may also be considered. Such thrusters can achieve higher thrust, up to 500kW. But life duration may not achieve the desired 5-10 years lifetime.

POWER MANAGEMENT AND DISTRIBUTION

Power Management and Distribution, PMAD critical technologies are:

- Electrical, Electronic, and Electromechanical (EEE) parts adequate for High Voltage
- Regenerative Fuel Cells
- Architecture: handling of different sources
- Heat dissipation of EEE devices;
- Harness
- AC/DC converters capable of integrating Power Processing Unit (PPU) for electric propulsion
- EEE parts tolerant to radiations;
- Materials for isolation of cables and electronic equipment.

CRITICAL TECHNOLOGIES DEMONSTRATION

It is proposed that selected critical technologies will be assessed for demonstration (on the ground or/and in space) in the frames of DEMOCRITOS project [4]; this project proposes 2 ground demonstrators. The First demonstrator would be for energy conversion system, and could include the electrical thrusters :

- gas heater instead of reactor with power up to several hundred kW, simulating a nuclear core
- turbo machine with “hundred kW class” electric generator with output power up to kW
- Power Management And Distribution (PMAD) of a corresponding power with electric load
- basic elements of thermal control system, including a heat pipe radiator

- electric thrusters (Hall or Ion type).
- Power and number of thrusters will be consolidated within the DEMOCRITOS project and deployable structures.

The second demonstrator would be dedicated for the nuclear reactor, and may include the demonstration of core components in existing or planned terrestrial materials testing and research reactors, as well as theoretical or 'virtual' whole core simulations.

The space demonstrators will mainly concentrate on the validation of some technologies that need zero-g conditions and cannot be validated on ground, such as the deployment of the system and some thermal control and power conversion parts.

CONCLUSIONS

A significant number of exploration missions require nuclear propulsion for which power sources are essential and enabling key assets. Associated technological developments however require important financial efforts that can probably only take place in the frame of an international collaboration, sharing the efforts as this has been the case for the International Space Station. MEGAHIT, funded by the European Commission under the 7th Framework Programme for Research and Technological Development, is a supporting action aiming at building a European roadmap for Megawatt level nuclear electric propulsion, in preparation of the Horizon 2020 programme. The MEGAHIT approach is driven by the involvement of all interested European and Russian stakeholders (research, industry and agencies) in this road-mapping exercise. This approach will allow building a scientific and technical community on the topic in Europe and Russia. Potential collaboration opportunities at international level with other space faring nations will be included.

During the first part of the project a reference vision for the spacecraft has been developed. The reference vision included reference missions, general architecture, thermodynamic map, mass budget, and identification of the most promising technologies. A choice of technologies was made in order to achieve the performance targets of 20 kg/kWe for the nuclear power system.

The reference vision was amended during the workshop in Brussels, December 2013, where a hundred specialists from European and Russian stakeholder organizations were gathered. In addition, other international experts were also invited and attended.

During the MEGAHIT project, a reference architecture was established for 1MWe nuclear-electric propulsion and a roadmap was proposed to have a spacecraft available by the early 30's. In early 2015 a follow on project will start, DEMOCRITOS. The DEMOCRITOS project aims at preparing the demonstrators for a mega-watt class nuclear-electric space propulsion. It is funded by Horizon 2020, the R&T program of the European Community. It is a new European and Russian project, including as partners: Nuclear National Laboratory (U.K.), DLR (Germany), The Keldysh Research Center (Russia), Thales Alenia Space Italia (Italy), Snecma (France), ESF (France) and CNES (France). IEAV (Brazil) will join as an observer.

The main aim of DEMOCRITOS is to start implementing the MEGAHIT roadmaps by preparing demonstrators for some of the necessary technologies. DEMOCRITOS features a technical part, with preliminary design of the demonstrators and their test benches. It features also a programmatic part, which will deal with financial and organizational aspects of such an endeavour: the ambition of the project is to initiate or join international cooperations, as broad as possible, which will lead to the implementation of the demonstrators.

ACKNOWLEDGEMENTS

The work leading to this document has received funding from the European Union Seventh Framework Programme [FP7/2007-2013] under grant agreement n° CSA-CA313096. This paper reflects only the authors view and the European Union is not liable for any use that may be made of the information contained therein.

The following are members of the Megahit project and acknowledged for their contribution to this paper:-

- Emmanouil Detsis, European Science Foundation
- Enrico Gaia, Thales Alenia Space Italia
- Zara Hodgson, National Nuclear Laboratory
- Frank Jansen, Institute of Aerospace Systems
- Gaetano Poidomani, Thales Alenia Space Italia, Italy
- Jean-Marc Ruault, Centre National d'Etudes Spatiales
- Frederic Masson, Centre National d'Etudes Spatiales
- Jean-Claude Worms, European Science Foundation

REFERENCES

[1] 47-68 UN-COPUOS Resolution « Principles relevant to the use of nuclear power sources in outer space »

[2] MEGAHIT. Deliverable D2.2: High Level Requirements, Main authors: V.N Akimov (KeRC), A.V. Semenkin (KeRC).

[3] "Intermediate Temperature Heat Pipe Life Tests" by W.G. Anderson of Advanced Cooling Technologies, Inc. and D.L. Ellis, NASA Glenn Research Center

[4] DEMOCRITOS proposal (PART B), ID SEP-210156395. Jean-Claude Worms.

Preliminary Design Study of an Innovative High-Performance Nuclear Thermal Rocket Utilizing LEU Fuel

Seung Hyun Nam[1], Paolo F. Venneri[1], Jae Young Choi[1], Yong Hoon Jeong[1], and Soon Heung Chang[1,2]

[1]Department of Nuclear and Quantum Engineering, Korea Advanced Institute of Science & Technology, 291 Daehak-ro, Yuseong-gu, Daejeon, Korea
[2]Handong Global University, Pohang-si, Gyeongbuk, Korea
+82-42-350-3891; rashkid@kaist.ac.kr

Abstract. A Nuclear Thermal Rocket (NTR) is a viable and efficient option for manned deep-space missions such as to Mars and beyond. The NTR technology has already been investigated and tested by the United States (US) and Russia. The representative US NERVA type reactors traditionally load hexagonal shaped fuel elements utilizing High Enriched Uranium (HEU) due to the imperative of making a high power reactor with a minimum size. This state-of-the-art NTR technology could be applicable with contemporary space vehicles. However, even though the NTR designs utilizing HEU is the best choice in terms of rocket performance and technical maturity, they inevitably arouse nuclear proliferation obstacles on all Research and Development (R&D) activities by civilians and non-nuclear weapon states, and potential commercialization. To cope with the security issue to use HEU, an innovative and high-performance NTR engine for future generations, Korea Advanced NUclear Thermal Engine Rocket utilizing Low Enriched Uranium fuel (KANUTER-LEU), is currently being designed at Korea Advanced Institute of Science and Technology (KAIST). The major design goals are to make use of a LEU fuel for its fairly compact reactor, but not to sacrifice the rocket performance relative to the traditional NTRs utilizing HEU. KANUTER-LEU mainly consists of a moderated Extremely High Temperature Gas cooled Reactor (EHTGR) utilizing a LEU fuel and H_2 propellant, a propulsion system housing a propellant feeding system, a regenerative nozzle assembly, and an optional electricity generation system as a bimodal engine. To implement a LEU fuel for the EHTGR, the KANUTER adopts W-UO_2 CERMET fuel to increase uranium density drastically and metal hydride moderators to thermalize neutrons in the core consequentially having a high neutron economy. The moderator and structural material selections also consider neutronic and thermo-physical characteristics to reduce non-fission neutron loss and reactor weight. The geometry design of fuel element and reactor focuses on protective cooling capability, fabricability and compactness. This paper presents the preliminary design study of KANUTER-LEU focusing on the neutronic and thermohydraulic features. The result shows comparable characteristics of high efficiency, compact and lightweight system despite the heavier LEU fuel utilization. The reference performance is theoretically estimated at a thrust of 50.0 kN, a thrust to weight ratio of 5.2 and a specific impulse of 912 s at the maximum power of 250 MW_{th}.

Keywords: nuclear propulsion, nuclear thermal rocket, innovative space reactor, low enriched uranium

INTRODUCTION

Nuclear propulsion brings the best benefit to human beings for the exploration, exploitation, commercialization, and eventual colonization of outer space. Nuclear rockets improve the propellant efficiency more than twice compared to conventional Chemical Rockets (CRs) and thus notably reduce the propellant requirement. Particularly, a NTR represents the most promising and near-term method for manned solar system missions because of a relatively high thrust as well as a high propellant efficiency. NTRs can also be configured to operate bimodally by converting the surplus nuclear energy to auxiliary electric power required for the operation of a spacecraft. Moreover, the concept

and technology of NTRs are fairly well understood, ground demonstrated, and with additional development will be safe by modern standards [1,2]. To date, NTRs have been researched and developed mainly in two countries: the United States of America (USA) and the former Soviet Union. The best known NTR development effort was conducted from 1955 to1974 under the ROVER and NERVA programs in the USA. These programs had successfully designed and tested many different reactors and engines [1]. After these major projects, the research on NERVA derived NTR engine has continued as a main stream based on the mature technology until today. The state-of-the-art NTR designs mostly use a fast or epithermal neutron spectrum core utilizing a HEU fuel to make a high power reactor with a minimum size reducing heavy metal volume and a simple core geometry. However, the use of a HEU fuel severely restricts not only the scope of R&D activities on NTRs, but also their practical uses due to the nuclear nonproliferation constraints, even though the HEU fuel is the best option for a NTR regarding high performance. In terms of the nuclear proliferation obstacles, the commercialization of NTRs will be almost impossible. Additionally, all non-nuclear weapon states are excluded from participating significantly in a foreign research as well as a self-R&D for a NTR [3]. To conquer the obstacles and resultantly to accelerate the technical advancement and the commercialization of NTRs, a new NTR design utilizing a LEU fuel is required, but it minimizes performance degradation due to the heavy LEU fuel loading. Hence, this paper proposes an innovative and futuristic NTR engine concept on KANUTER-LEU to implement a LEU fuel, and also includes the preliminary design analysis of neutronics and thermohydraulics to estimate the referential performance of KANUTER-LEU.

SYSTEM DESCRIPTION

The primary design goals of the innovative NTR engine are to implement an LEU fuel, but not to cede the merits of a NTR particularly in terms of higher rocket performance than conventional CRs. To achieve these goals, the key modifications in its reactor design are required as follows:

A. Increase of Uranium (U) density in the fuel, but preserving resistance to ultra-high heating and H_2 corrosion.
B. Improvement of neutron economy by neutron spectrum thermalization and minimization of non-fission neutron loss [4].
C. Protective cooling capability to safeguard the major components such as the fuel and moderator from the severe thermal attacks of fuel and radiation induced heating.
D. Compact reactor design efficiently arranging the complex and heterogeneous reactor components, and ensuring the structural integrity.

Overall, KANUTER-LEU mainly consists of an EHTGR utilizing a LEU fuel and H_2 propellant, a propulsion system, and an optional electricity generation system as depicted in Figure 1.

Moderated EHTGR utilizing LEU Fuel

The nuclear fuel-type selection is one of the key issues to utilize LEU in the fuel. The fuel should be able to keep not only high U density, but also great resistance to ultra-high thermal and H_2 corrosion attacks in the core. To satisfy the considerations, the Uranium Dioxide imbedded in Tungsten matrix (W-UO_2) CERMET fuel is one of the promising options for the EHTGR because of its high U density and the enhanced safety margin due to a comparably high melting point, high thermal conductivity, improved creep strength, excellent hot H_2 corrosion endurance and fission product retention [5,6]. The CERMET fuel consists of a 45 vol% W with the remainder being UO_2 with a 6 mol% ThO_2 bonding agent and thus has a great U density of about 5 g/cm^3. The ^{235}U enrichment of the fuel is assumed to be 19.5 w/o as a LEU typically used in research reactors. Additionally, to mitigate the neutron absorption by the W matrix, the W is needed to be enriched to 95 a/o ^{184}W whose thermal absorption cross-section is significantly lower than that of other W isotopes [4]. The ^{184}W-UO_2 CERMET fuel is manufactured and fabricated in the peculiar square lattice fuel assembly design, which is originally proposed by the Innovative Nuclear Space Power & Propulsion Institute (INSPI), to enhance the heat transfer capability and to reduce the fabrication difficulties as shown in Figure 2 [7]. The square lattice geometry creates numerous Square Flow Channels (SFC), which are Fuel Cooling Channels (FCC) occupying 30% cross-sectionally void area among the fuel wafers in the fuel assembly to ensure both sufficient coolant passages and a critical fuel mass. In particular, the convective heat transfer capability of the SFC is better than that of the circular channel with the same hydraulic diameter and fuel heating because the heat transfer surface area of the SFC is as much as 27% larger, even though the averaged heat transfer coefficient of the SFC is about 10% lower [8].

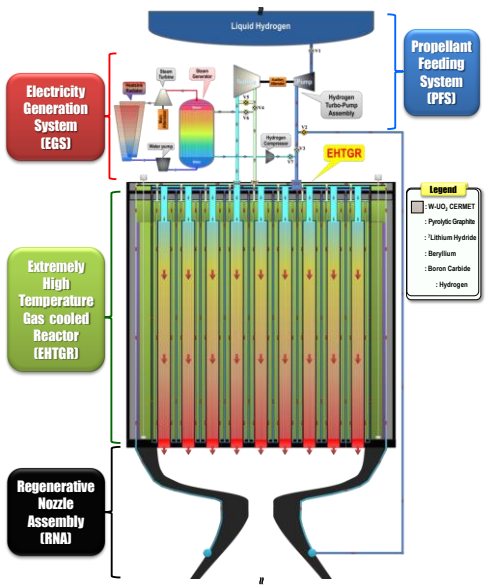

FIGURE 1. Schematic View of KANUTER-LEU.

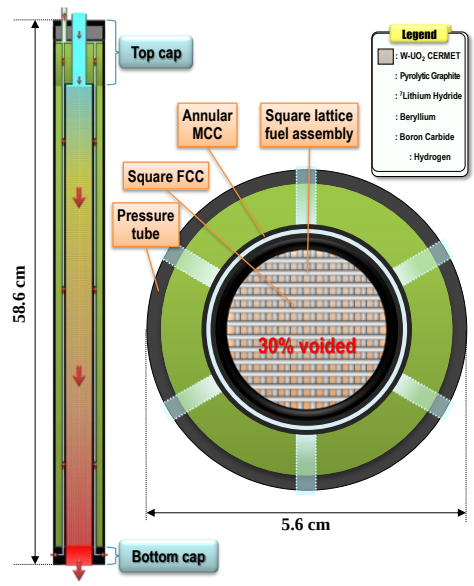

FIGURE 2. Configuration of the Integrated Fuel Element.

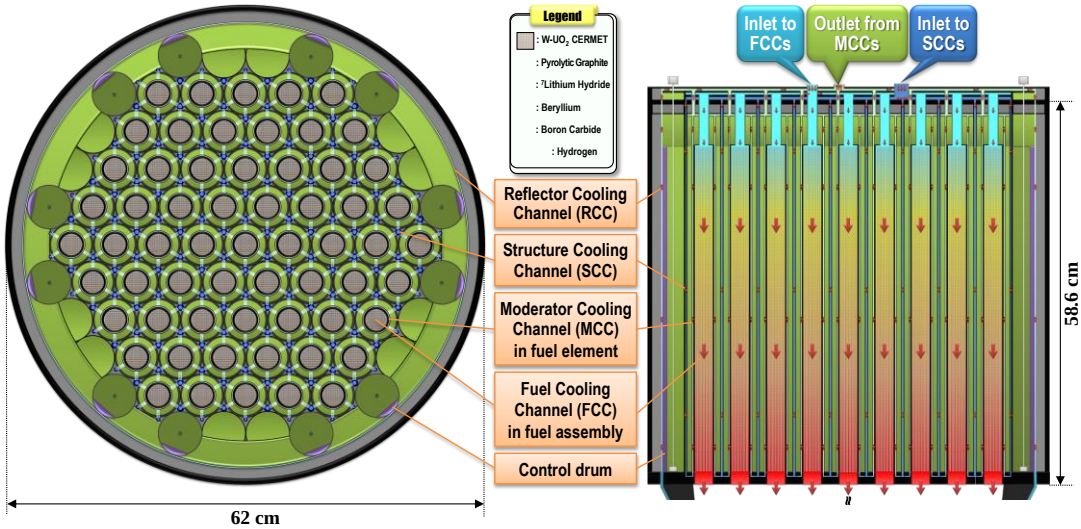

FIGURE 3. Configuration of the EHTGR-LEU.

The integrated fuel element uniquely comprises the square lattice fuel assembly, the main moderator block, the individual pressure tube and their cooling channels. As depicted in Figure 2, the ultra-heat resistant fuel assembly is supported and surrounded by three layers of moderator and pressure tubes according to the structural and thermal design considerations in order of first, the Carbon fiber-reinforced Carbon composite (C/C) shroud protectively coated with Zirconium Carbide (ZrC) to support the fuel assembly, second, the metal hydride moderator block protected by the thin ZrC-coated C/C jacket, and third, the individual C/C pressure tube. The main moderator is absolutely crucial to enable the LEU fuel use in the EHTGR because it is able to strongly thermalize neutron spectrum and ensuing largely reduce heavy metal demand to be a critical reactor. The suitable moderator candidates are the metal hydrides such as ^{7}Lithium Hydride (^{7}LiH) or Zirconium hydride ($ZrH_{1.8}$) [9,10]. A serious challenge to use these hydride moderators in the extremely high temperature (about 3,000 K) core is to sufficiently cool them for prevention of melting and large H_2 dissociation. So, the fuel element contains the annular Moderator Cooling Channel (MCC) between the first and the second layers to protect the hydride moderator from the thermal attacks of the fuel and radiation induced heating.

The 61 integrated fuel elements arranged in the hexagonal prism pattern mainly compose the compact and heterogeneous core with the Beryllium (Be) spacers of the EHTGR as shown in Figure 3. The Be spacers also have

the Structure Cooling Channels (SCC) to cool the structural components and the moderator at the outside of the fuel elements. The compact core is surrounded by the reflector composed of the ^{7}LiH – Be – C/C layers to reduce neutron leakage. Particularly, the Be – C/C reflector also serves as the reactor's Pressure Vessel (PV) [11]. The reflector has the annular Reflector Cooling Channel (RCC) as well between the ^{7}LiH and Be. The main structural materials of C/C and Be reduce non-fission parasitic neutron absorption. To control the reactor's reactivity, cylindrical control drums are symmetrically placed in the reflector and comprise partially of Boride Carbide (B_4C) neutron absorber.

To create better rocket performance, the EHTGR needs a compact and protective cooling design. The EHTGR adopts a compact design that houses the integrated fuel elements, lightweight structural components, bi-functional reflector (also PV) with the various cooling channels, to efficiently arrange the complex components in the small-size core and to minimize the reactor mass. In addition, the EHTGR evenly distributes the protective and regenerative cooling channels in the core such as the FCCs for fuel, MCCs and SCCs for moderator and structure, and RCC for reflector. The various cooling channels mitigate severe heating of the reactor components, whereas increase the coolant temperature to regeneratively transfer the thermal energy to the power conversion systems for both propulsion and electricity generation. The EHTGR could be operated in two modes of propulsion and electricity generation by adjusting the control drums for the bimodal capability. In the propulsion mode, the reactor powers are diverse in the range of 200 ~ 250 MW_{th} according to a mission requirement for both propulsion and electricity generation. In case of the electricity generation mode, the reactor is operated at 350 kW_{th} power for electricity generation. Table 1 lists the reference design parameters of the EHTGR-LEU.

TABLE 1. Design Parameters of the EHTGR-LEU.

Reactor power (electric power mode)	**200 ~ 250 MW_{th} (350 kW_{th})**
Fuel element P/D	1.60 ~ 1.62
Number of fuel elements	61
Average fuel power density	8.89 ~ 11.39 MW_{th}/L
Fuel type	^{184}W-UO_2 CERMET
(^{235}U enrichment)	(19.5wt%)
Fuel mass	303.6 ~ 296.2 kg
(^{235}U mass)	(20.1~ 19.6 kg)
Main moderator type	^{7}LiH (or $ZrH_{1.8}$)
Main moderator mass (as for ^{7}LiH)	16.4 ~ 17.2 kg
Structural material types	C/C and Be
Structural materials mass	53.7 ~ 53.3 kg
Reflector (PV) type	^{7}LiH – Be – C/C
Reflector (PV) mass	114.5 kg
Reactivity control type	Control drums with B_4C absorber
Total reactor mass	509 ~ 502 kg
Reactor diameter and height (for the core)	62 & 58.6 cm (50.4 & 50.4 cm)
Max. fuel temperature (150 K margin to UO_2 melting)	2,990 K
Avg. exit H_2 temperature	Around 2836 K
Core pressure drop	under 2.80 MPa

Estimated at a fuel wafer thickness of 0.50 mm.

TABLE 2. Design Parameters of KANUTER-LEU.

Reactor power	**200 ~ 250 MW_{th}**
Engine mass budgets *(excluding the EGS)*	
EHTGR-LEU	509 ~ 502 kg
Shadow shield & auxiliaries	254 ~ 251 kg
Propulsion system*	224 kg
- Turbo-pump assembly	30 kg
- Propellant management	39 kg
- Thrust vector control	27 kg
- Instrumentation	30 kg
- C/C nozzle assembly	98 kg
Total engine	987 ~ 976 kg
Rocket performance	
Pump discharge pressure	13.48 ~ 15.96 MPa
System pressure drop	6.85 ~ 9.06 MPa
Avg. chamber temperature	around 2826.5 K
Avg. chamber pressure	6.895 MPa
Thrust	40.1 ~ 50.0 kN
T/W_{eng}	4.14 ~ 5.22
I_{sp}	913.0 ~ 911.8 s

Estimated at a fuel wafer thickness of 0.50 mm, a nozzle expansion ratio of 200, and 5.5% losses from ideal performance.
* The same mass budgets estimated at 250 MW_{th} power.

Bimodal Engine System

One of the NTR merits is that the system could be configured for the bimodal function of both propulsion and electricity generation to reduce the mass of a spacecraft. The bimodal NTR engine schematically shown in Figure 1 consists of the EHTGR-LEU, the propulsion system, and the optional Electric Generation System (EGS). Table 2 presents the reference design parameters and performance in propulsion mode of KANUTER-LEU.

The propulsion system is made up of the propellant Feeding System (PFS) comprising a Turbo-Pump Assembly (TPA) and a propellant management unit, the Regenerative Nozzle Assembly (RNA), a thrust vector control, an instrumentation package, etc. The key element of the propulsion system is the TPA to feed the propellant to the EHTGR and in turn to the RNA. The TPA converts a small portion of thermal energy of the EHTGR into dynamic power to make the flow continue in the system. Uniquely, the TPA is equipped with an auxiliary alternator to generate electricity in the propulsion mode or emergency of the EGS malfunction. The RNA expands and accelerates the H_2 heated in the EHTGR so that the exhaust gas exits the nozzle at hypersonic velocities to produce thrust. To protect the nozzle from the high temperature H_2, a small portion of the unheated propellant is passed through a regeneratively cooing jacket of the RNA. The primary material options of the RNA are Aluminum with C/C liner, Inconel with NARloy liner or a refractory carbide-coated C/C. Particularly, the coated C/C nozzle, which was proposed at the SNTP [12], is an innovative and feasible design because of its low weight and superior high-temperature strength largely reducing cooling requirement [13]. For the preliminary study, the expander cycle is selected for the propulsion system. In the expander cycle, the H_2 propellant flows through the various components of the system both to cool the EHTGR and the RNA, and to convert the thermal energy to the powers for thrust, propellant feeding and electricity. The cold H_2 stream is pumped through the TPA and then splits up into both of the SCCs in the core, and the regenerative cooling channel of the RNA and following the RCC. Most of the coolant flows into the core and the rest with a small portion of it is used to cool the RNA and the reflector. The main stream after passing through the SCCs is connected with the MCCs in the fuel elements. In the fuel elements, the coolant flows up through the annular MCCs, then gathers into the reactor outlet head. Another core bypass stream also comes into the reactor outlet head and is mixed with the main stream after cooling the RNA and the reflector. Then, the heated H_2 (around 300 K) flows out to the TPA for both propellant feeding and electricity generation. After the power conversion in the TPA, the H_2 streams down into the FCCs of the square lattice fuel assemblies in the core to be heated, and then expands out through the RNA to produce thrust.

The EGS included in Figure 1, which operates only in the electric power mode with 350 kW_{th} reactor power, converts the thermal energy of the EHTGR into the electric power required for spacecraft operation. In terms of high power and efficiency on the basis of proven technology, both Brayton and Rankine cycles are the primary options for the EGS [14,15]. In a prospective study with simplifying assumptions, the theoretical thermal efficiencies in a similar radiator sizes of around 180 m^2 are respectively estimated at 6.4% at a pressure ratio of 1.50 and a limited turbine inlet temperature of 850 K for the Brayton cycle utilizing Argon working fluid, and 18.8% at a pressure ratio of 81 and a limited turbine inlet temperature of 670 K for the Organic Rankine cycle utilizing Toluene working fluid. Then, the radiator sizes per electric power are 8.9 m^2/kW_e of the Brayton and 3.0 m^2/kW_e of the Rankine. The low performance for power conversion is mainly due to the systemic constraint that the maximum temperature at the turbine inlet (EHTGR outlet) is limited by the moderator's melting points (962 K of ^7LiH and 1,073 K of $ZrH_{1.85}$). The result indicates that the thermal efficiency of the Brayton cycle is about 3 times lower than that of the Rankine cycle with the similar radiator areas. However, the Rankine cycle must overcome the handling and separation issues of two-phase flow, which are problematic in zero-gravity. Although some direct-condensing radiator concepts even operating in zero-gravity for the Rankine cycle were proposed, reliable and long-life operation has not been fully established [16,17]. To put these particular conditions in perspective, more studies in depth on the bimodal system are needed to determine whether the EGS is profitable or not in the severe limitations of the moderated EHTGR.

PRILIMINARY DESIGN STUDY

To estimate the reference design performance parameters of the EHTGR-LEU and the engine preliminary design studies of neutronics and thermohydraulics were carried out. First, the sizes of the core and reactor are roughly predicted by comparing those of the other NTR reactors. When a reference size of the core is assumed, the key variables to determine reactivity, mass, fuel temperature, and coolant flow states are reactor power, Pitch to Diameter ratio (P/D) of fuel element and FCC size (fuel wafer thickness and SFC width) in the square lattice fuel assembly. The reactor power affects power density, burn-up, poisoning by fission products, mass flow rate and pressure drop of the system. Particularly, the P/D regulates the volume ratio between the fuel and moderator in the constant diameter and height of the fuel element. So, the P/D variable is able to tailor the neutron spectrum and the total cross-sectional flow area of the fuel assemblies in the core. Additionally, the FCC size affects a heat transfer and a pressure drop in the fuel assembly.

Neutronic Analysis

The preliminary neutronic analysis was conducted to estimate the reference design parameters of the EHTGR. For the reactor design to be feasible, the criticality and sizing of the EHTGR must be achieved. In addition, the EHTGR has to ensure sufficient lifetime (burn-up) and non-stop operation regardless of reactor poisoning during the bimodal mode. The power distribution of the EHTGR is also a significant issue because severe power peaking could cause local fuel failure by hot spot and thermal stress.

Methodology

The neutronic study uses the Monte Carlo codes, MCNPX 2.7 [18] and Serpent [19] to simulate the reactor physics and resultantly to estimate the criticality, burn-up, and power distribution of the moderated EHTGR-LEU. In the analysis, the main moderator is assumed to be ^{7}LiH with high Hydrogen content [10]. The major variables are the P/D of fuel element and reactor power, which govern the volume ratio of fuel to moderator, and cumulative concentrations of fission product poisons as a function of power density.

Results and Discussion

Figure 4 shows the K_{eff} and mass variations as a function of the fuel element P/D. When the P/D increases, both fuel and reactor masses decrease due to the heavy fuel volume reduction. The K_{eff} plots a negative quadratic behavior according to increasing P/D, with the peck point of 1.124 at the P/D of 2.00 due to the moderator volume increment, which results in neutron spectrum softening. The K_{eff} decline after the P/D apex is due to the over-moderated neutron spectrum versus the reduced fuel mass. In terms of high reactivity and low weight, a P/D of around 2.00 is the optimal design point. However, when considering reactivity control margin and power density mitigation, a P/D of around 1.60 is the best design point.

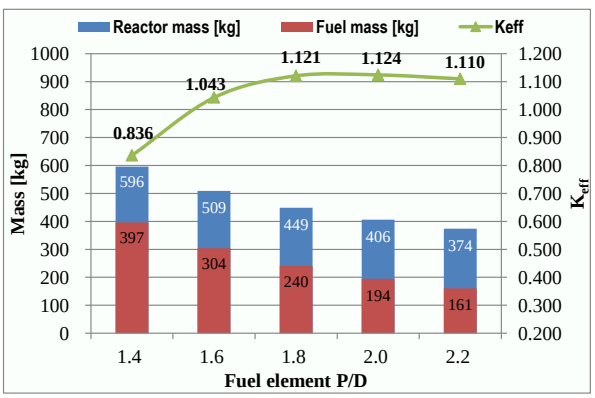

FIGURE 4. K_{eff} and Mass Variations as a Function of P/D.

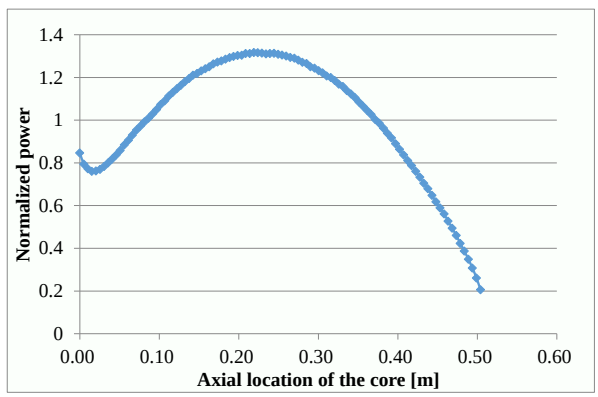

FIGURE 5. Axial Power Profile of the Core.

In principle, the EHTGR-LEU loads more than enough fuel to operate for the required two hours of the full power mode and 600 days of the idle power mode (for only electricity generation) of a single mission to Mars, and also to feasibly operate for multiple missions. However, the build-up of fission product poisons in the EHTGR with thermal neutron spectrum and high power density creates a much larger negative reactivity insertion. This could incur temporary malfunction of the reactor (due to the Xenon dead time), when large downward power change occurs to switch the modes from propulsion to electric power. Thus, the reactor poisoning is a critical issue to determine both P/D and power of the bimodal reactor. To put the reactor poisoning impact in perspective, the optimum P/Ds are estimated to be 1.60 ~ 1.62 at the reactor powers of 200 ~ 250 MW_{th}, respectively. The radial and axial power distributions of the EHTGR are also analyzed for the thermohydraulic analysis. As a preliminary analysis, the power profiles are not optimized to flatten the power peaking. Figure 5 shows the axial power profile of the core. The power peaking factors are 1.317 in the axial and 1.436 in the radial directions. These large power peaking factors limit the maximum outlet temperature of the core and the resultant rocket performance. To lessen power peaking, further optimization analysis is required.

Thermohydraulic Analysis

The rocket performance depends on some thermohydraulic constraints. To increase thrust and T/W, the EHTGR needs high power and power density. The higher power density also augments Mass Flow Rate (MFR) of the coolant to satisfy its thermal design limit, core pressure drop and ensuing pump discharge pressure (maximum system pressure), which affect the structural integrity and mass of the system. In addition, to raise propellant efficiency (I_{sp}), maximization of the core temperature is the most important factor. In that respect, the ^{184}W-UO_2 CERMET fuel has excellent heat-resistance, and the protective cooling channels are evenly distributed in the EHTGR. In particular, the square lattice fuel design creates the numerous FCCs (SFCs) with a relatively large heat transfer surface area in the fuel assemblies. This design improves heat transfer and resultantly decreases fuel temperature compared with that of a conventional hexagonal fuel design with circular channels. In the square lattice fuel design, the Fuel Wafer Thickness (FWT) is directly correlated with the size, number and heat transfer area of SFCs, and thus it affects mechanical strength as well as thermohydraulic capability of the fuel assembly. As the fuel wafers get thicker, the mechanical strength against both thermal and shear stresses improves, but the heat flux and resulting fuel temperature increase due to the heat transfer area reduction. Therefore, the thick fuel wafers are mechanically strong with low pressure drop, while the thin fuel wafers are thermally robust with less mechanical strength and higher shear stress [7]. Hense, the major variables for the analysis are reactor power and FWT of the square lattice fuel assembly. In this analysis, the major constraints are peak centerline temperature of fuel, and maximum system pressure and core pressure drop. The first design criterion was determined so that the peak temperature in fuel's centerline should be below the melting point of UO_2 (3,140 K). In the consideration of 150 K margin, the peak temperature limit of fuel's centerline is set to be 2,990 K. The pressure limit setting depends on structural considerations of the system, but there is currently no structural analysis. So, as a referential study, the maximum system pressure limit is set to be 16 MPa considering 80% margin for a high-level pump discharge pressure (20 MPa) at the constant chamber pressure (6.895 MPa) of typical expander engines [20].

Summary of Engine System Modeling

In the thermohydraulic analysis, a new numerical NTR engine model, Nuclear Square-channel-core in Expander-cycle Simulation (NSES), is used to simulate and to analyze the expender cycle engine with the complex EHTGR in propulsion mode. The numerical model focuses on thermohydraulic design analysis of the unique EHTGR comprising the square lattice fuel configuration, and the various protective and regenerative cooing channels to estimate feasible design points and resultant rocket performance. The NSES includes 1-D thermodynamic model to predict coolant state points of the entire system and 2-D radial thermal conduction model to precisely estimate temperature distribution in fuel. The NSES is written in MATLAB [21].

The engine system described in the NSES consists of the liquid H_2 (LH_2) propellant tank, the PFS (BOP), the EHTGR and the RNA as shown in Figure 6. The PFS mainly includes the TPA with a centrifugal pump, a turbine and an auxiliary alternator mounted on a same shaft for both propellant feeding and electricity generation. The RNA houses a converging-diverging nozzle and its regeneratively cooling jacket. The EHTGR's components are characterized with the equivalent coolant flow channels such as the FCC, MCC and SCC in the core, and the RCC in the reflector. The analysis of the unit cooling channels is performed by axially dividing them into many segments of constant wall temperature and numerically integrating the effects of heat addition and friction along the channel. The unit channels are respectively represented by both the hot and the averaged channels to consider the radial power distribution, and thus to estimate both the maximum pressure losses and the average temperature rises of coolant. To analyze the temperature distribution in fuel, the unit hot-FCC includes the solid fuel domain which is used to describe the heat transfer by both convection and conduction. The components of the engine system are connected with each other by the various pipes, fittings and head plenums, and the bypass flows are adjusted with control valves. For the preliminary analysis, the spatial heat depositions of the reactor components are roughly assumed according to the considerations of the recoverable energies in the fission reactor and the thermal conduction from the fuel assemblies into their C/C shrouds in the fuel elements. The amount of energy transferred from the nozzle wall to the coolant in the regeneratively cooling jacket is derived from the result of the previous CFD analysis [22]. The computational model assumes a steady-state and adiabatic system, and automatically calculates the 1-D coolant thermodynamic and heat transfer equations corresponding to each component with the initial conditions. In summary, the 1-D coolant thermodynamic model consist of the conservation of continuity, momentum and energy, pressure loss, power conversion, and ideal rocket equations. In this analysis, both the normalized power profile along the axial location and the power peaking factor at the radially central position are applied to describe the power distribution according to the location in the core. Additionally, non-uniform local mass flow rates in the core were employed according to the radial locations of the fuel

elements to mitigate the non-optimized radial power peaking and ensuing local heat concentration [23]. To estimate pressure losses in the various channels, pipes, fittings and valves, the Darcy–Weisbach equation is basically used. The friction factors of the components are predicted by the Colebrook approximation for major pressure losses [24] and the geometric resistance coefficient (K) for minor pressure losses. The geometric coefficient is derived or directly referenced by the CRANE engineering data [25]. The values of surface roughness for the Colebrook approximation are conservatively assumed to be 1E-03 mm for the FCC and 3E-02 mm for the other cooling channels and pipes in the system. The efficiencies of the pump, the turbine and the alternator are assumed to be 0.65, 0.70 and 0.85, respectively, and a thrust correction factor of 0.945 is employed to approximate the performance of nozzle. The Equation Of State (EOS) is taken from the NIST REFPROP 9.0 at the temperature range down to 900 K [26] and the NASA Lewis chemical equilibrium based on the ideal gas assumption at the temperature range of over 900 K [27]. The heat transfer model between the coolant and the fuel in the square FCC comprises the convection equations including the empirical heat transfer correlation [8] and the Finite-Difference Equations (FDEs) for 2-D radial thermal conduction derived by the energy balance method in steady-state condition. The effective thermal conductivity of the W-UO_2 CERMET fuel is analytically predicted [28]. Figure 6 briefly presents the computational analysis process of the NSES. The code iteratively solves the system component models (steady state) in order based on initial conditions. The input data includes reactor power, required electric power, both coolant bypass ratios before the inlets of the core and the turbine, P/D of the fuel element, size of the unit FCC, base dimensions of the system components, etc. In this analysis, the constant values in the input data are the required electric power of 50 kWe, the same bypass ratios of 0.10 and the base dimensions of the system. Then, the variables are the reactor powers of 200 ~ 250 MW_{th} and the corresponding P/Ds of 1.60 ~ 1.62, and the unit FCC sizes of the square lattice fuel assembly: five FWT samples of 0.50 ~ 1.50 mm. The iterative calculation ends when both peak centerline temperature of the hot FCC and average chamber pressure meet their target values of 2,990 K and 6.895 MPa, respectively. Then, the final outputs are MFR, thermodynamic states of the components and resultant rocket performance such as thrust, T/W and I_{sp}.

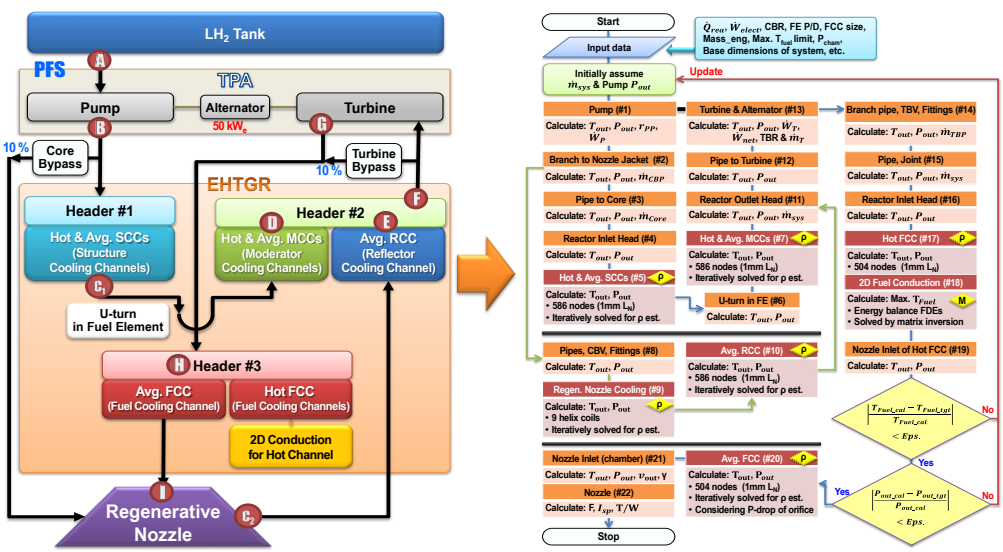

FIGURE 6. Computational Analysis Process in the NSES.

Results and Discussion

The reactor power analysis was performed in the power ranges of 200 ~ 250 MW_{th} and the corresponding fuel elements' P/Ds of 1.60 ~ 1.62 to mainly estimate proper system pressure, core pressure drop and resultant rocket performance. In this analysis, the constant FCC size with the thinnest FWT of 0.50 mm of the fuel assembly, which is able to maximize the number of SFCs and the related heat transfer area in the core, is applied to check the largest pressure loss and the highest rocket performance of the system. Figure 7 presents the MFR and the pressure in the system as a function of the reactor power. The increase of the reactor power induces the rise in the MFR to cool the fuel with higher power density to the temperature limit (2,990 K), the ensuing higher core pressure drop and pump discharge pressure. The maximum system pressure and core pressure drop are 15.96 MPa and 2.80 MPa at the highest power of 250 MW_{th}. The maximum system pressure is also lower than the hypothetical pressure limit of 16.00 MPa. The thrust chamber states are almost similar as around 2826 K and 6.895 MPa, regardless of the power

changes because of the corresponding MFR changes to maintain the limited peak fuel temperature. Therefore, thrust and T/W are linearly augmented by the rises of the power and the ensuing MFR, whereas the values of I_{sp}, which mainly depend on chamber temperatures, are almost constant at the ranges of 911.8 s ~ 913.0 s regardless of the power changes as observed in Figure 8.

Next, the fuel geometry analysis was carried out on the various sizes of FCC with the FWTs from 0.50 mm to 1.50 mm to verify the cooling capability of the square lattice fuel design. This process estimates the states of the core and the thrust chamber and the resultant rocket performance. The reactor power is also assumed to be the highest value of 250 MW_{th} to find the design points ensuring the maximum rocket performance of the system. As the characteristic of the square lattice fuel design, the size of FCC determines the number of SFCs and the related heat transfer area per unit fuel volume. The thicker FWT of FCC decreases the number of SFCs and the ensuing heat transfer area in the form of a negative exponential curve. Both drop of the heat transfer area and corresponding growth of the distance between the fuel centerline and coolant by the thicker FWT strongly increase the peak temperature in the fuel centerline. Accordingly, the MFR of system and the average temperature of chamber are changed depending on the FWTs in the limited peak fuel temperature as depicted in Figure 9. The maximum temperature difference between the fuel and the chamber also exponentially increases with the FWT thickening. The highest temperature of the chamber (2826.6 K) is rated at the thinnest FWT of 0.50 mm and the lowest MFR of 5.587 kg/s. The maximum system pressure and core pressure drop are also 15.96 MPa and 2.80 MPa at the thinnest FWT of 0.50 mm, respectively, while their minimum values drop to 13.82 MPa and 1.51 MPa at the FWT of 1.00 mm. In case of the rocket performance, according to the growth of the FWT, the thrust and the T/W slightly increase mainly due to the MFR rise, whereas the I_{sp} rapidly decreases primarily due to the temperature drop of the chamber as presented in Figure 10. Overall, the maximum chamber temperature and corresponding I_{sp} are 2826.6 K and 911.8 s at the thinnest FWT of 0.50 mm, whereas the minimum system pressure and the relatively high thrust and T/W are 13.82 MPa, 51.2 kN and 5.34, respectively, at the FWT of 1.00 mm. Therefore, in the viewpoint of high propellant efficiency, the thinnest FWT of 0.50 mm is the best choice. On the other hand, in both viewpoints of lower system pressure and relatively high thrust, the FWTs of 0.50 ~ 1.00 mm are adequate.

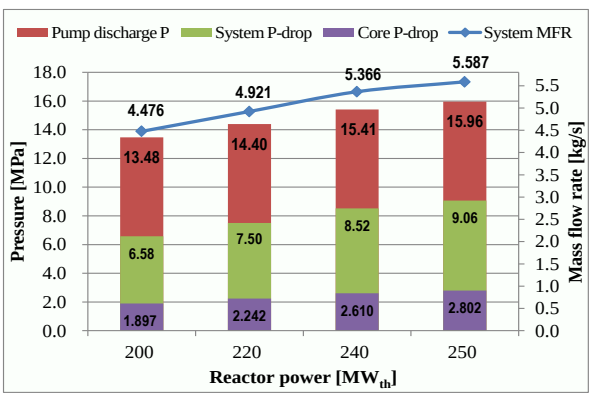

FIGURE 7. Pressure vs. MFR as a function of the Power.

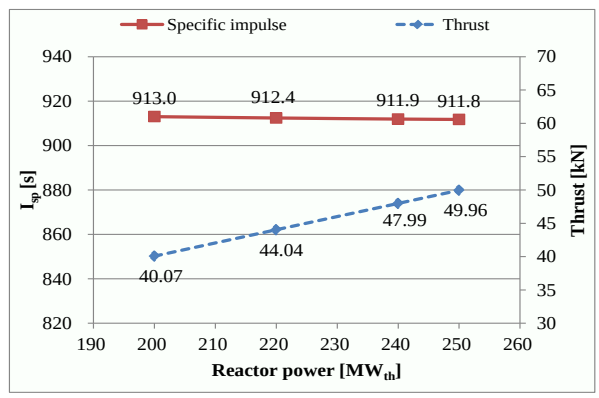

FIGURE 8. Thrust and I_{sp} as a Function of the Power.

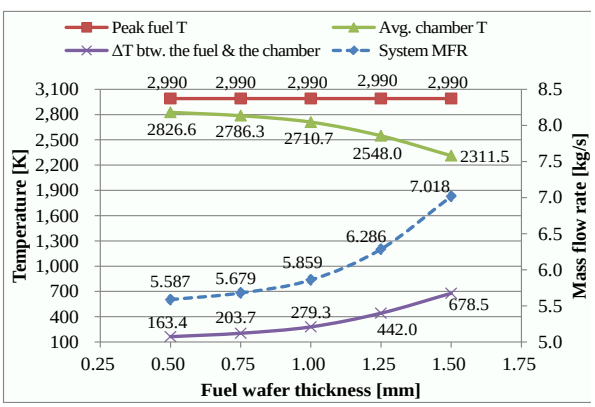

FIGURE 9. Temperature vs. MFR as a Function of the FWT.

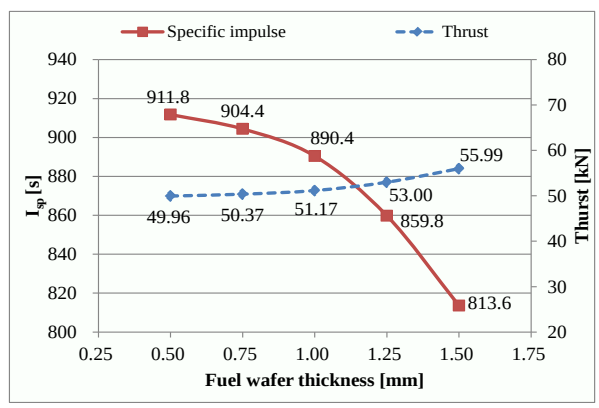

FIGURE 10. Thrust and I_{sp} as a Function of the FWT.

CONCLUSION

Most of the conventional NTR designs use HEU fueled reactors for better performance and small size. However, they inevitably provoke nuclear proliferation obstacles on all R&D activities and its eventual commercialization. To overcome these obstacles, KANUTER-LEU adopts the innovatively modified reactor concepts, which include the ^{184}W-UO_2 CERMET fuel with high U density, the metal hydride moderators to thermalize the neutron spectrum, the compact and efficient core design with the protective cooling channels, etc. The non-proliferative NTR engine mainly consists of the moderated EHTGR loading the LEU fuel, the propulsion system housing the PFS, RNA, etc., and the optional EGS for the bimodal function. In the preliminary neutronic analysis, the combination of the CERMET fuel and the hydride moderator are able to achieve the implementation of the LEU fuel in the EHTGR with relatively small size and weight, sufficient life time, etc. The design parameters of KANTUER-LEU, which are mainly estimated by the thermohydraulic analysis using the NSES code, imply very comparable performance for future applications, even though it uses the heavier LEU fuel. If a few challenges are surmounted, the innovative NTR design will provide the driving force to advance NTR technology and ensuing to move up space exploitation by human beings. In future, more extensive design analysis of neutronics, thermohydraulics and their coupling will be conducted to validate design feasibility and to optimize the reactor system enhancing the rocket performance.

REFERENCES

[1] S. Gunn, Nuclear propulsion - a historical perspective, Space Policy. 17 (2001) 291–298.
[2] P.M. Sforza, M.L. Shooman, D.G. Pelaccio, A safety and reliability analysis for space nuclear thermal propulsion systems, Acta Astronautica. 30 (1993) 67–83. doi:10.1016/0094-5765(93)90101-2.
[3] P. Venneri, Implementation of LEU Fuels in NERVA type Nuclear Thermal Rockets, KAIST, 2013.
[4] G. Rosaire, P. Husemeyer, P. Venneri, W. Deason, Design of a Low_Enriched Nuclear Theraml Rocket, ID, USA, 2013.
[5] S.K. Bhattacharyya, An Assessment of Fuels for Nuclear Thermal Propulsion, Argonne, IL, USA, 2001.
[6] D. Burkes, D. Wachs, J. Werner, S. Howe, An Overview of Current and Past W-UO2 CERMET Fuel Fabrication Technology, in: Proceedings of Space Nuclear Conference 2007, INL, Boston, MA, USA, 2007: pp. 207–216.
[7] S. Anghaie, T.W. Knight, J. Plancher, R. Gouw, Development of a Robust Tri-Carbide Fueled Reactor for Multi-Megawatt Space Power and Propulsion Applications, INSPI, University of Florida, Gainesville, FL, USA, 2004.
[8] E. Battista, H. Perkins, Turbulent heat and momentum transfer in a square duct with moderate property variations, International Journal of Heat and Mass Transfer. 13 (1970) 1063–1065.
[9] R. E. Hyland, Reactor-Weight Study of Beryllium Oxide, Beryllium, Lithium-7 Hydride, and Water as Moderators with Tungsten184 Structural Material and Uranium Dioxide Fuel, NASA/TN D-1407, 1962.
[10] C.D. Montgomery, Fabrication and properties of lithium hydride, Nuclear Engineering and Design. 25 (1973) 309–314.
[11] J. Powell, J. Paniagua, G. Maise, H. Ludewig, M. Todosow, The Role of Compact Nuclear Rockets in Expanding the Capability for Solar System Science and Exploration, State University of New York at Stony Brook/TR-740, Stony Brook, NY, USA, 1997.
[12] R. Haslett, Space Nuclear Thermal Propulsion Program - Final Report, Bethpage, NY, USA, 1995.
[13] S. Locke, R. Ahearn, Material Design Concepts for Uncooled Nuclear Rocket Nozzles, Materials Science Research. (1965) 287–310.
[14] A.K. Hyder, R.L. Wiley, G. Halpert, D. f. Flood, S. Sabripour, Chapter 7. Dynamic Energy Conversion, in: Spacecraft Power Technologies, Imperial College Press, London, UK, 2000: pp. 323–351.
[15] G.L. Bennett, R.J. Hemler, A. Schock, Status report on the U.S. space nuclear program, Acta Astronautica. 38 (1996) 551–560.
[16] H. Haller, Analysis of a Double Fin-Tube Flat Condenser-Radiator and Comparison with a Central Fin-Tube Radiator, 1964.
[17] J. Powell, G. Maise, J. Paniagua, SUSEE - Ultra Light Nuclear Space Power Using the Steam Cycle, in: 2003 IEEE Aerospace Conference Proceedings, IEEE, Big Sky, MT, USA, 2003: pp. 491–507 Vol.1. doi:10.1109/AERO.2003.1235078.
[18] X-5 Monte Carlo Team, MCNP – A General Monte Carlo N-Particle Transport Code, Version 5, 836 (2003).
[19] J. Leppänen, Serpent–a Continuous-energy Monte Carlo Reactor Physics Burnup Code, VTT Technical Research Centre of Finland. (2013).
[20] E.S. Pedersen, Chapter 6. Nuclear Rocket Engine Design, in: C.W. Besserer, F.E. Nixon, Nuclear Energy in Space, Prentice-Hall, Inc., Englewood Cliffs, NJ, USA, 1964: pp. 184–252.
[21] MathWorks, MATLAB, (2014).
[22] S.H. Nam, K.Y. Suh, Conceptual Design of Thermal Engine Rocket Adventurer for Space Nuclear Application., SNU, 2009.
[23] S.H. Nam, J.I. Lee, S.H. Chang, Preliminary Thermo-hydraulic Core Design Analysis of Korea Advanced Nuclear Thermal Engine Rocket for Space Application, in: Transactions of the Korean Nuclear Society Spring Meeting, KNS, Jeju, Korea, 2014.
[24] G. Papaevangelou, C. Evangelides, C. Tzaimopoulos, A New Explicit Relation for the Friction Coefficient in the Darcy-Weisbach Equation, in: Protection and Restoration of the Environment, Corfu, Italy, 2010.
[25] Crane Co., Flow of Fluids Through Valves, Fittings, and Pipe (TP-410), Crane, 2009.
[26] NIST, NIST Reference Fluid Thermodynamic and Transport Properties Database (REFPROP), (2010).
[27] S. Gordon, B.J. Mcbride, Computer Program for Calculation of Complex Chemical Equilibrium compositions and Applications, NASA, RP-1311, 1994.
[28] J. a. Webb, I. Charit, Analytical determination of thermal conductivity of W–UO2 and W–UN CERMET nuclear fuels, Journal of Nuclear Materials. 427 (2012) 87–94. doi:10.1016/j.jnucmat.2012.04.020.

Democritos: Preparing Demonstrators for High Power Nuclear Electric Space Propulsion

Mr. Frédéric Masson, Mr. Jean-Marc Ruault [1]
Dr. Jean-Claude Worms, Dr. Emmanouil Detsis [2]
Mr. André Beaurain, Mr. Francois Lassoudiere [3]
Dr. Enrico Gaia, Mrs Maria Cristina Tosi [4]
Dr. Frank Jansen, Mr. Waldemar Bauer [5]
Dr. Alexander Semenkin [6]
Mr. Tim Tinsley, Mrs Zara Hodgson [7]

[1a]CNES, launcher directorate, 52 rue Jacques Hillairet, 75612 Paris Cedex, France
[2]ESF, France
[3]Snecma, France
[4]Thales Alenia Space Italia
[5]DLR, Germany
[6] Keldysh Research Center, Russia
[7]National Nuclear Laboratory, United Kingdom
Contact: frederic.masson@cnes.fr

Abstract. The Democritos project aims at preparing demonstrators for a megawatt class nuclearelectric space propulsion. It is funded by Horizon 2020, the R&T program of the European Community. It is a new European and Russian project, including as partners: Nuclear National Laboratory (U.K.), DLR (Germany), The Keldysh Research Center (Russia), Thales Alenia Space Italia (Italy), Snecma (France), ESF (France) and CNES (France). IEAV (Brazil) will join as an observer. Democritos is the follow-up of the Megahit project (www.megahit-eu.org).

During Megahit project, a reference architecture was established for 1MWe nuclear electric propulsion INPPS (International Nuclear Propulsion and Power System) , and a roadmap was proposed to have a spacecraft available by the early 30's. The main aim of Democritos is to start implementing the Megahit roadmaps by preparing demonstrators for some of the necessary technologies. Democritos features a technical part, with preliminary design of the demonstrators and their test benches. It features also a programmatic part, which will deal with financial and organizational aspects of such an endeavour: the ambition of the project is to initiate or join international cooperations, as broad as possible, which will lead to the implementation of the demonstrators.

Keywords: Nuclear, electric, space propulsion, Democritos, Megahit.

THE CASE FOR MWE NUCLEAR ELECTRIC PROPULSION

Megahit project has dealt with 1 MWe level nuclear electric propulsion. As Megahit results confirmed it, this technology would yield increased capabilities for Earth protection and exploration missions.

The interest in such system depends mainly of its power (1MWe), the specific mass of the power system, and the specif impulse of the electric thrusters.
For the specific mass, the target was to get 20 kg/kWe, including the mass of the fission reactor, the shield, the thermal/electric conversion system, the radiator, the PMAD, the electric thrusters. This target of 20 kg/kWe was deemed achievable with medium term technological maturation and development.
For the electric thrusters, parametric studies were conducted ranging from 2000 sec to 9000 sec, which are specific impulse deemed achievable with hall effect thrusters and ion thrusters with medium term technological maturation and development for the highest values.
Typically, existing hall effect thruster can reach 3000 sec using Xenon, 4500 sec using Argon. Existing ion thrusters can reach higher specific impulse, up to 7500 sec, but at a cost of maximum thrust achievable.

With such hypothesis, four missions were considered as the most promising for such a system:

NEO (Near Earth Orbiter) deflection:
Asteroids are a potential threat to life on Earth. Unfortunately, most of the potentially dangerous asteroids are not known yet. Thus the ideal would be to have a system ready to be launched to deflect big asteroids.
Best strategy would be to deflect it by acting as a gravity tractor: we avoid then more complex and risky and complex strategy, such as harpooning or destruction of the asteroid
The exercise was done on the deflection of Apophis which was thought to be a serious hazard until recent observation in January 2013 discarded the risk of impact in 2036. A 1MWe nuclear electric propulsion system with a specific impulse of 7000s would have allowed deflecting Apophis trajectory by 1 million kilometer (at its passage near Earth in 2036). If spacecraft leaves Earth in 2021, would reach Apophis in 200days and deflect it by staying a distance of 300m during 40 days.

Outer solar system missions
For **Europe** orbit: we could bring 3 to 10t of payload in 2.5 to 3.5 years depending on the specific impulse of the thrusters (6000s to 8000s).
In case of chemical propulsion using for direct scheme of transfer from the Earth surface to the near Jupiter orbit (without gravity maneuvers) with the same transfer duration (T = 2.5 years) the delivered payload mass will be in 10…20 times less (about 300 kg) in comparison with case of electric propulsion utilization. Some improvement in ballistic efficiency of chemical propulsion application may be achieved by using transfer schemes with gravity maneuvers.
For Titan orbit: similarly, from 3 to 12 t of payload could be brought in 3.5 to 6 years (specific impulse Isp 6000 sec to 9000 sec).

Lunar orbit tug
With a 1MWe tug and a launcher capable of launching 80t in a 800km orbit two times per year, 650t of payload can be brought in lunar orbit in 10 years.

Cargo support mission for manned Mars mission
Megahit spacecraft could bring 15t in near Mars orbit in 400 days with an Isp = 6000 sec. A chemical propulsion systems would make it possible to deliver for 200 days to near-Mars orbit the spacecraft with 9 t mass, which is approximately half as many as that of payload, delivered by the tug with the NPPS.

It should be noted that, apart from the payload mass, the spacecraft delivers to Mars the 1MW power source, that can be used for the payload power supplying (for instance, the radar complex).

As a conclusion we can say that 1MWe nuclear electric propulsion:

- Is a multipurpose system that will enable new breakthrough missions, related to earth protection, deep space exploration and support to manned lunar or mars missions.
- Will offer significant gain of payload mass compared to chemical propulsion. The gain gets even higher if we consider that in addition to a classical payload, the spacecraft brings with it a nuclear power system that can be used for purposes other than propulsion (electrical alimentation for radars for instance).

Within Megahit project, no comparison was performed between the performances of nuclear electric propulsion and thermonuclear propulsion. Such comparison was performed in other studies, such as the one in [3].
It is concluded that thermonuclear propulsion features a lower Isp in the range of 900 sec, but a much higher thrust, comparable with chemical propulsion. Therefore, compared with thermonuclear:

- Because of higher Isp, nuclear electric may offer either a higher payload, or a less heavy (and more affordable) spacecraft to transport the same payload.
- Because of lower thrust, with nuclear electric propulsion, the flight time to destination will be longer, which may be an issue for manned mission.

To sum up to the extreme, and if we focus only on a performance/cost aspect, thermonuclear propulsion seems best suited for faster manned mission, nuclear electric propulsion has many advantages as a cheap and efficient cargo/robotic exploration missions.

TECHNICAL CHALLENGES AND ROADMAP

To be attractive with regard to more conventional propulsion system, nuclear electric must achieve the best specific mass for the power system. A target of 20 kg/kWe has been chosen as realistic, provided medium term maturation and development.

The Megahit consortium considered to this target a thermodynamic map with a rough mass budget.
First contributor is the radiator, which accounts for 30% of the mass and a surface of 500 m^2.

The most important point in the thermodynamic map is the temperature of the hot source (exit of the reactor/ inlet of the turbine).
Indeed, because of this high temperature that must be sustained during a very long lifetime (10 years to cover all possible missions), **some maturations/ new development will be required for:**

- The nuclear reactor (fuels, mechanical commands, absorbers, reflectors).
- The turbine blade and disk (turbine blades, especially, are subject to creep).
- The heat exchanger between primary and secondary circuit (if we choose an indirect cycle a heat exchanger is required).

The exact technological gap will be consolidated with more detailed design of these components. However, we expect that resistance of existing materials/technologies should be improved by 50 K – 100 K to meet the 1300 K target.

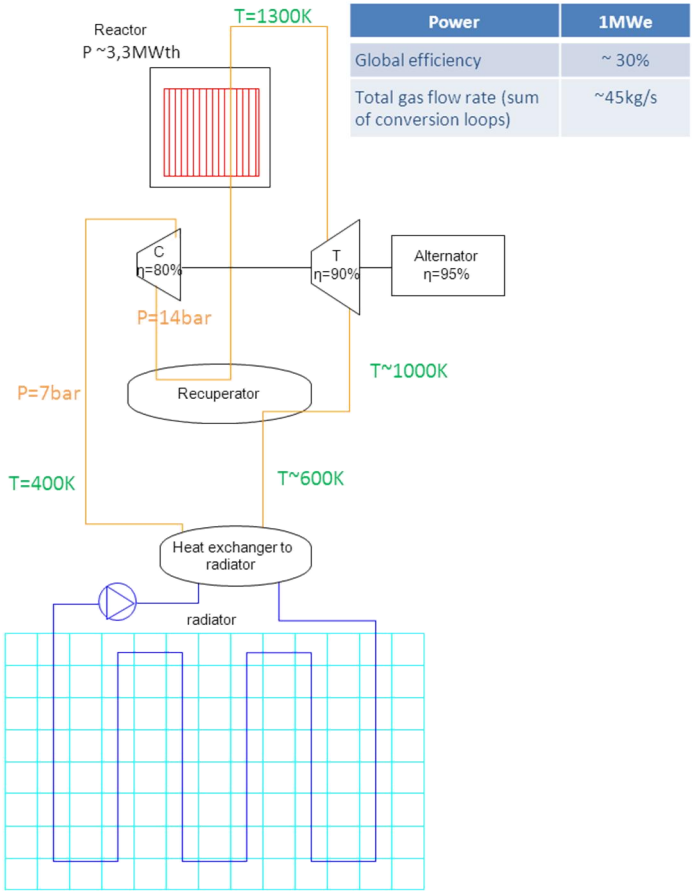

Power	1MWe
Global efficiency	~ 30%
Total gas flow rate (sum of conversion loops)	~45kg/s

FIGURE 1: Megahit reference thermodynamic map

In case of a temperature close to the expected 1300 K target, technological maturation remains interesting: as the highest temperature is achieved, the better specific mass for the power system can be reached.
With a temperature of 1600Kand an indirect cycle, for instance, it can be approached a specific power lower than 10 kg/kWe.

Existing conversion bearings will also need improvement to sustain 10 years of lifetime without maintenance.

A challenge will also be to demonstrate the **safety of the reactor**, even in case of launch failure.

The need to assemble many parts in orbit may require **advances in robotics**.

We concluded that, due to the many challenges and before building and testing the nuclear electric spacecraft INPPS, we will need lower power demonstrators, as part of technologies maturation and also to demonstrate the correct functioning of the system (for instance, a strategy for transient phases should also be defined, allowing coherent functioning between core, turbine, radiator and thrusters).
Because of this need for lower power demonstrators, Megahit consortium initiated the Democritos project.

DESCRIPTION OF THE DEMOCRITOS PROJECT

Democritos is the follow-up of the Megahit project. Its aim is to start implementing Megahit roadmaps, by preparing demonstrators for a MWe class nuclear electric space propulsion.

Democrtios is funded by Horizon 2020, the R&T program of the European Commission . It is a new European and Russian project, including as partners: Nuclear National Laboratory (U.K.), DLR (Germany), The Keldysh Research Center (Russia), Thales Alenia Space Italia (Italy), Snecma (France), ESF (France) and CNES (France). IEAV (Brazil) will join as an observer.

Democritos will feature a technical partand a programmatic part.

Technical Part

For the technical part, three sub-projects are considered:

DEMOCRITOS-GC (Ground Component). Aim is to perform preliminary design studies of ground demonstrator, including all the parts that are not nuclear. It will include design and drawings of all subsystems and ground based test benches. It will also investigate interaction of the major subsystems (thermal, power management, propulsion, structures and conversion) between each other and with a (simulated) nuclear core providing high power (about 200kW).

DEMOCRITOS-CC (Core Component): Aim is to perform preliminary design studies of ground demonstrator, for the nuclear part. It will include design and drawing of the nuclear space reactor, together with an analysis of the regulatory and safety framework.

DEMOCRITOS-SC (Space Component): Aim is to provide preliminary design of a nuclear electric spacecraft, with a detailed assembly and servicing strategy in orbit.

Programmatic Part

Programmatic part will be addressed in the sub-project DEMOCRITOS-PO (Programmatic):

Ambition is to build or join a broader consortium to implement the demonstrator project. The DEMOCRITOS-PO aims are to put in common the best technical talents, to share technical and financial resources with other organizations and to find synergies with space and non-space existing programs. Once this broader consortium is built, Democritos will propose an organizational and financial structure for the future demonstrators.

An important input for the financial structure will be to establish preliminary costs for the demonstrators and for the final spacecraft (development and production costs). Although it is not expected, that the development cost to be radically different from the cost of a cryogenic propulsive stage, this topic needs further investigation.

To achieve these goals, it will **be** used industrial and space agencies networks including the organization of a workshop with possible stakeholders by the end of 2015. It is also intended to benefit from coordination with ISEF and ISEC-G. It is also planed to present the DEMOCRITOS progress status at next ISEF meeting.

Final target is to have all the elements ready the end of 2016, in order to launch a demonstrator program in case a political consensus is reached at international level.

Opportunities for cooperation

Its is the belief of the Democritos consortium that such an international political consensus is possible within the following years.

Indeed, one can notice a rising interest in the international community for nuclear electric space applications

- ISEC-G has identified nuclear power for electric propulsion and planetary surface application as a critical technology that could "yield novel approaches to and significantly increased capabilities for exploration mission" [1]
- In Russia, with the participation of Roscosmos and Rosatom [the state agencies for space exploration and nuclear power, respectively], the Keldysh Research Center is developing a spacecraft using a megawatt class nuclear power propulsion system (NPPS)and the ground based tests of a prototype is expected to be completed in 2018.
- NASA released in 2014 a new Design Reference Architecture (DRA) for Human Exploration of Mars [2]. This DRA now includes an electronuclear design reference and chemical + solar design reference, and underscores the potential for both. Although no definitive choice is made between all the possible architectures, it appears that the 2.5MW electronuclear design allows the lowest number of SLS launches for a trip duration that is a bit higher than chemical or thermonuclear propulsion, but much lower than the chemical and solar propulsion.
- Apart from propulsion, NASA is developing Fission Power Systems (FPS) for use on the surface of the Moon, Mars, or other moons and planets of our solar system. As part of the FPS development, NASA is building and will test two demonstrators: one for the nuclear core (KRUSTY), one for the conversion system (TDU) [4], [5]. Although these demonstrators differ from what DEMOCRITOS proposes (10 kWe instead of 200 kWe, Stirling conversion instead of Brayton conversion), similarities exist in the logic and the objectives. These similarities may lead to possible cooperation.
  Although few details are available on this project, China also claims to develop its own FPS [6].

STRATEGY FOR TECHNOLOGY MATURATION

Reference technologies were identified during Megahit [2] for high power electric propulsion (for the European low power electric propulsion roadmap see under DiPoP www.DiPoP.eu). The Megahit are high TRL technologies (TRL>4), that can be available when the three demonstrators are built.

- Gas-cooled, highly enriched reactor, derived from ground applications.
- Brayton conversion, using turbines and alternators from aeronautics, able to sustain 1200K-1300K
- Heat pipes radiators.
- Low thrust Hall effect or ion thrusters, used in clusters.
- In orbit assembly similar to ISS.

The first goal of the DEMOCRITOS demonstrators will be to demonstrate all reference technologies can work together as the INPPS, and that this system can be operated efficiently and safely, during start, continuous mode, and shut down.

However reference technologies may have limited performance. Additional technological maturity could then be an asset.

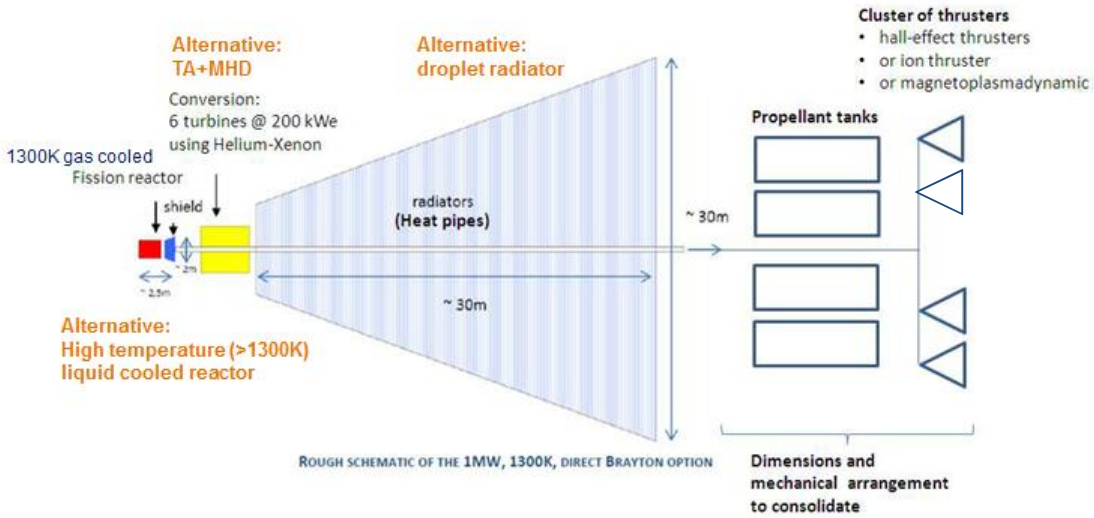

FIGURE 2: Megahit general architecture of the INPPS with reference and alternative technologies

In that perspective, alternative technologies have been identified during Megahit: those are lower TRL technologies that have improved performance and would increase the assets of nuclear electric propulsion. Most of these technologies present possible synergies with aeronautics, energy production on ground and other space programs.

- Liquid-cooled reactor, able of higher temperature, from 1300 K up to 1600 K.
- Brayton conversion, with turbine using new materials (ceramics, nobium alloys) able of higher temperature, from 1300 K up to 1600 K during five years of operation.
- Thermoacoustics + MHD as a more reliable and efficient alternative to Brayton.
- Droplet radiators.
- High thrust Electric thrusters, including MPD thrusters (Vasimir).
- Advanced and autonomous robotic in-orbit assembly.

Second goal of the demonstrator will be to participate to new technologies maturation. The Democritos members will then strive to make the Demonstrator as modular as possible, to first accommodate reference technologies, then to accommodate alternative technologies, as soons as they become available.

In parallel to Democritos, alternative technologies maturation will be proposed by the consortium in the frame of horizon2020.

CONCLUSION

High power space nuclear electric propulsion is an exciting challenge on technological and system level. ISEC-G has identified it as a critical technology that could yield significantly increased capabilities for exploration mission new missions. Among these new missions, Megahit had identified deep space exploration, cargo mission to support mars manned missions, and Earth protection against asteroids.

Democritos is an opportunity to enhance our ability to design and build nuclear electric propulsion. A core consortium already exists in Europe and Russia with Megahit partners, plus Snecma (France) that became Democritos member, similar like the Brazilian observer IEAV. Within Democritos, it will strive to make larger, attractive international consortiums emerge, to put in common technical and scientific talents, as much as technical and financial resources.

ACKNOWLEDGEMENTS

The work leading to this document has received funding from the European Union Seventh Framework Programme [FP7/2007-2013] under grant agreement n° CSA-CA313096. This paper reflects only the authors view and the European Union is not liable for any use that may be made of the information contained therein.

The following are members of the Megahit project and acknowledged for their contribution to this paper:

- Emmanouil Detsis, European Science Foundation
- Enrico Gaia, Thales Alenia Space Italia
- Alexander Semenkin, Keldysh Research Center
- Maria Cristina Tosi, Thales Alenia Space Italia
- Zara Hodgson, National Nuclear Laboratory
- Frank Jansen, Institute of Space Systems
- Waldemar Bauer, Institute of Space Systems
- Gaetano Poidomani, Thales Alenia Space Italia, Italy
- Jean-Marc Ruault, Centre National d'Etudes Spatiales
- Tim Tinsley, Nuclear National Laboratory
- Jean-Claude Worms, European Science Foundation

REFERENCES

[1] ISECG, *The global exploration roadmap, august 2013*, http://www.globalspaceexploration.org/wordpress/wp-content/uploads/2013/10/GER_2013.pdf

[2] NASA, Human Explorationof Mars, Design Reference Architecture 5.0, Addendum #2, http://www.nasa.gov/sites/default/files/files/NASA-SP-2009-566-ADD2.pdf

[3] Masson F., Tinsley T., Cliquet E., "MEGAHIT: Update on the advanced propulsion roadmap for HORIZON2020", NETS 2014,

[4] S.M. Geng, J. Stanley, J.G. Wood, E. Holliday, NASA Glenn Research Center, Cleveland, OH44135, "Development of a 12 kWe stirling power conversion unit for fission power systems – status update", NETS 2014.

[5] M.A. Gibson, L. Mason, C. Bowman, D.I. Poston, P.R. McClure. J. Creasy, C. Robinson; NASA Glenn Research Center "Development of NASA's Small Fission Power System for Science and Human Exploration", NETS 2014.

[6] Hu Gu1 and Xie Jiachun2, Department of Reactor Engineering Design, China Institute of Atomic Energy, P.O.Box 275(33) Beijing, "A new nuclear power system concept for manned lunar base application", NETS 2014.

Benchmark Experiment for Fast Neutron Spectrum Potassium Worth Validation in Space Power Reactor Design

John D. Bess

Idaho National Laboratory, 2525 N. Fremont Ave., MS 3855, Idaho Falls, ID 83415
208-526-4375; john.bess@inl.gov

Abstract. In the early 1960s a series of experiments were performed at the Oak Ridge Critical Experiments Facility (ORCEF) to support validation of reactor calculations and reactor physics methods for the design of small, potassium-cooled space power reactors. Various mock-up critical assemblies were performed using a vertical assembly machine. A separate experiment was performed to specifically test the fast neutron cross sections of potassium, as it was a candidate for coolant in some early space power reactor designs. The experiment was performed on the vertical assembly machine using a bare uranium (93.2 % ^{235}U) annulus constructed from multiple stacked rings of varying heights. The annulus outer diameter was approximately 13 inches (33.02 cm) and the inner diameter was approximately 7 inches (17.78 cm). The stacked critical height was approximately 5.6 inches (14.224 cm). Within the center of the annulus was placed two stainless steel cans. Two configurations of this experiment were measured, one with empty steel cans, and the other with potassium-filled cans. The measured difference in reactivity worth of the two near-critical configurations provided the worth of adding potassium to the system.

These two critical configurations were evaluated according to the guidelines of the *International Handbook of Evaluated Reactor Physics Benchmark Experiments* (IRPhEP Handbook). Physical uncertainties in the experiment, such as mass, enrichment, impurity content, and dimensions, were minimized to increase the accuracy of the results. The total evaluated uncertainty in the near-critical configurations is 37 pcm, of which 32 pcm of the total uncertainty pertains to the uncertainty in the measurement of the system reactivities. The benchmark experiment worth for the addition of approximately 2.4 kg of potassium metal was approximately 11 ± 1 ¢ (~0.0047 ± 0.0006 ¢/g). Calculations were then performed using the benchmark models and the neutron physics code Monte Carlo N-Particle (MCNP6.1) with contemporary neutron cross section libraries. Calculated results for the worth of the potassium were between 70 to 80 % lower than the benchmark values. Efforts continue to finalize benchmark assessment of this experiment for inclusion in the IRPhEP Handbook and identification of errors either in the experimental data or neutron cross section data for potassium.

Keywords: Benchmark, Potassium, Validation.

INTRODUCTION

In the early 1960s a series of experiments were performed at the Oak Ridge Critical Experiments Facility (ORCEF) to support validation of reactor calculations and reactor physics methods for the design of small, potassium-cooled space power reactors. A series of small, compact critical assembly (SCCA) experiments [1] had been performed in support of the Medium-Power Reactor Experiments (MPRE) program [2]. Efforts were made to study "power plants for the production of electrical power in space vehicles." The MPRE program was a part of those efforts and studied the feasibility of a stainless-steel system, boiling potassium 1 MWt, or about 140 kWe, reactor. This program was carried out until 1967. Experiments at ORCEF supported a UO_2 variant of the SNAP reactor fuel, and were indicated as the SNAP UO_2 experiments.

A pair of near-critical experiments was performed consisting of highly enriched uranium (HEU), 93.2 .% ^{235}U, metal annuli surrounding a pair of type 304 stainless steel cans: empty in the first case and potassium-filled, ~2.4 kg, in the second. The primary purpose of these experiments was to test the fast neutron cross sections of potassium [3]. These configurations, and the derived measurement of the potassium worth, were evaluated according to the guidelines of the *International Handbook of Evaluated Reactor Physics Benchmark Experiments* (IRPhEP Handbook) [4].

DETAILS OF BENCHMARK EXPERIMENT

The experiments were performed on a vertical lift machine located in a large, concrete room at ORCEF. The annular experiments consisted of a stack of uranium annuli with a nominal inside diameter of ~7 inches (~17.78 cm), surrounding the steel cans with nominal outer diameter of ~7 inches (~17.78 cm). The outer diameter of the uranium annuli was ~13 inches (~33.02 cm) with a total stack height of ~5.6 inches (~14.224 cm). Approximately half of the experiment was placed upon a thin stainless steel diaphragm. The other half was raised via a hydraulic lift into contact with the underside of the diaphragm. Figure 1 provides a cutaway diagram of the second experiment configuration with potassium-filled cans; the initial experiment used empty steel cans.

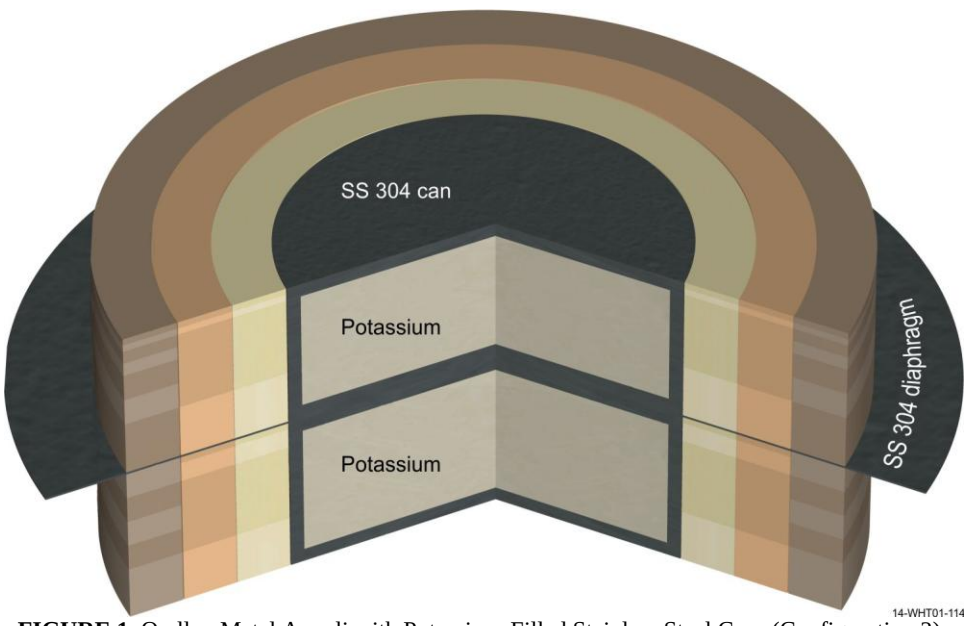

FIGURE 1. Oralloy Metal Annuli with Potassium-Filled Stainless Steel Cans (Configuration 2).

The HEU components were measured with high precision [5] in order to reduce uncertainties in their geometry and composition. The minimization in uncertainty in experimental parameters served to improve the quality of the benchmark data derived from these experiments. In addition to the stainless steel diaphragm, the support structure for the experiment included a low-mass aluminum support stand and diaphragm clamping rings. The reactivity of the support structure was evaluated experimentally by assembling the experiment to a near-critical configuration and then adding additional support structure. The difference in measured reactor period for the modified assembly was then utilized to correct the benchmark worth of the assembly for support structure removal. The reported measured worth of potassium was +10.32 ± 0.40 ¢, +4.30 × 10^{-3} ¢/g. The measured worth was obtained as the difference in measured reactivity between Configuration 1 (empty steel cans) and Configuration 2 (potassium-filled cans).

Both detailed and simple benchmark models (see Figures 2 and 3, respectively) were developed for evaluation of benchmark experiment uncertainties and calculation of the potassium worth.

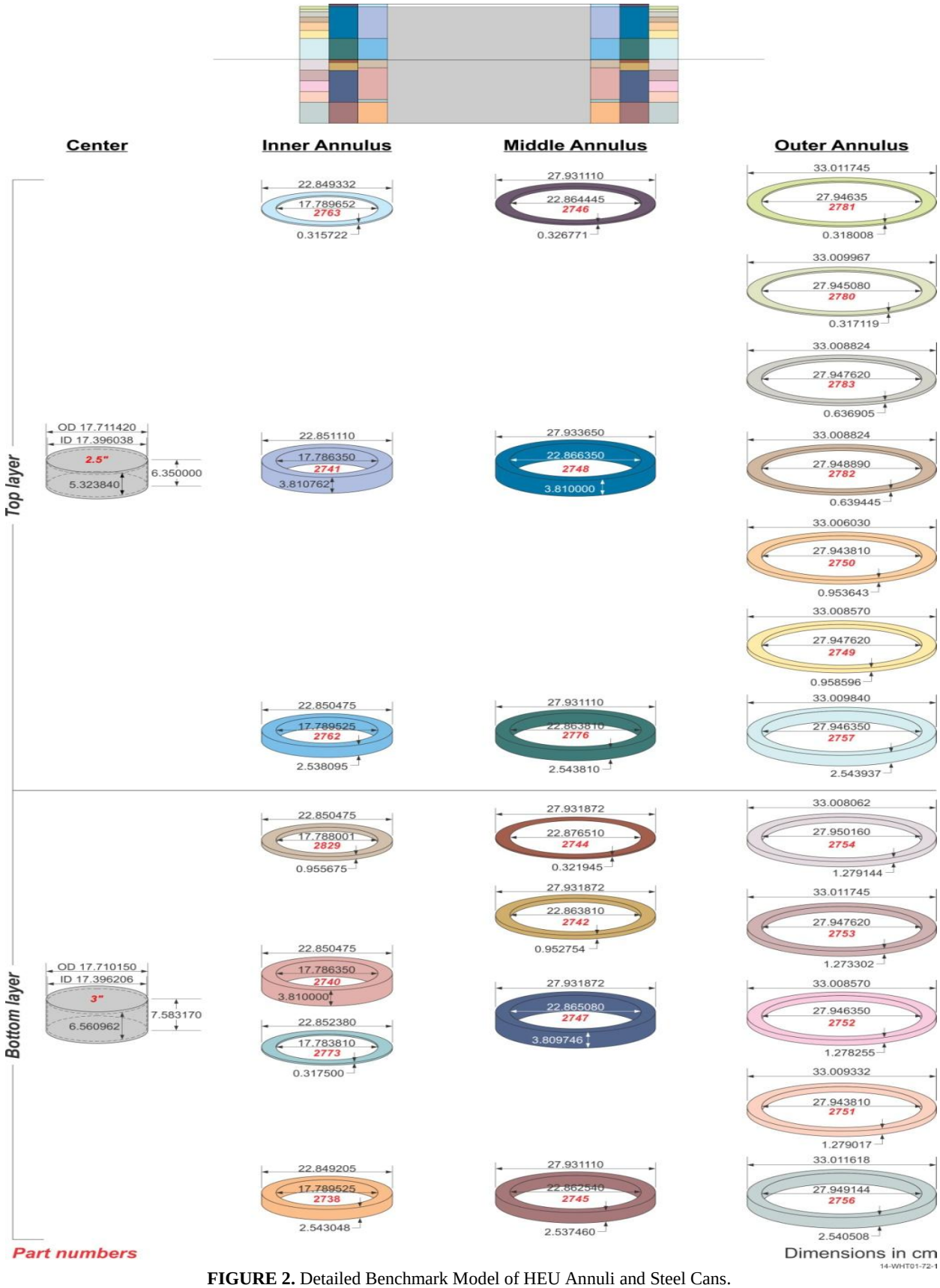

FIGURE 2. Detailed Benchmark Model of HEU Annuli and Steel Cans.

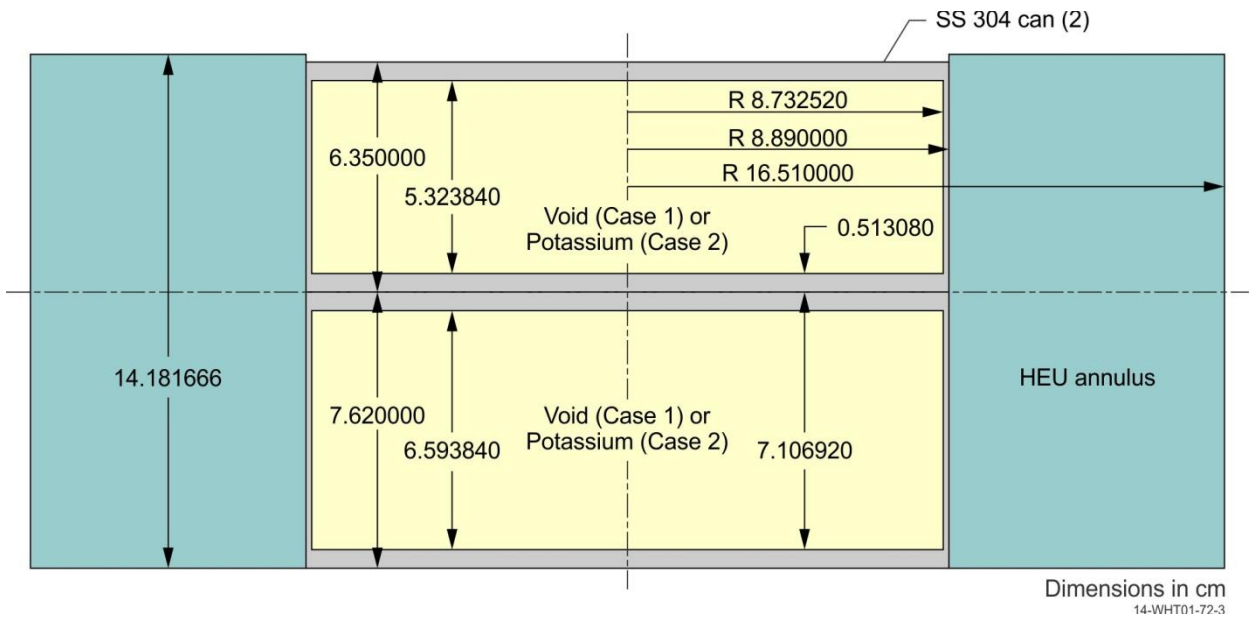

FIGURE 3. Simple Benchmark Model of Potassium Benchmark Experiment.

Uncertainties in the geometric and material properties of the experiment configurations were evaluated using the developed benchmark models. Because of the accuracy to which these experiments were measured [5] many of the uncertainties are considered negligible (< 0.00003 Δk_{eff}). The dominant uncertainty in the experiments themselves is the uncertainty in the measurement of the reactivity, and thus effective worth, of the changes in the experimental configurations. Table 1 provides a summary of the evaluated uncertainties for these measurements; more comprehensive details regarding the analysis can be found detailed in the benchmark evaluation report: ORCEF-SPACE-EXP-001 [4]. Calculations were performed using MCNP6.1 [6] with the ENDF/B-VII.1 neutron cross section data library [7]. The Monte Carlo statistical uncertainty was ±0.00002; however, uncertainties were scaled during the analysis such that the contribution from using Monte Carlo methods was much less than 0.00001 Δk_{eff}. Due to the similarity in the two experimental configurations, many of the uncertainties are highly correlated; only those uncertainties considered having an impact on the worth measurement are retained. The negligibility criterion is not applied for the measurement of the potassium worth.

Biases were also calculated using the benchmark models to account changes incurred during the simplification steps such as removal of room return effects, experiment support structure, material impurities, homogenization and removal of gaps, and slight modifications to the geometry. The complexity of the simple benchmark model is significantly reduced, as seen when comparing Figures 2 and 3. The computed biases for model simplifications are provided in Table 2. The dominant biases come from the measured worth corrections for support structure removal and the calculated effect for removal of the surrounding concrete walls of ORCEF. Only total benchmark model bias simplifications were determined for the potassium worth measurement. The uncertainties in the measured corrections for support structure removal were included in the experimental uncertainty (part of the dominant measurement uncertainty contribution). All other bias uncertainties were approximately ±0.00003 Δk_{eff} from the Monte Carlo statistical uncertainty. The bias uncertainties are propagated through to the final benchmark values, which are shown in Tables 3 and 4 for the critical configurations and potassium worth measurement, respectively.

TABLE 1. Total Experimental Uncertainty in the Potassium Worth Measurement Experiments.

Parameter	**Configuration 1 (Empty Cans) [Δk_{eff}]**	**Configuration 2 (Potassium-Filled) [Δk_{eff}]**	**Potassium Worth Measurement [Δk_{eff}]**
Temperature (K)	0.00004	0.00004	--
Experiment reproducibility (¢)	0.00013	0.00013	0.00004
Measured reactivity worth (¢)	0.00032	0.00032	--
β_{eff}	0.00005	negligible	--
Uranium diameter (cm)	negligible	negligible	--
Uranium height (cm)	negligible	negligible	--
Uranium stack height (cm)	0.00006	0.00006	--
Steel can diameter (cm)	negligible	negligible	0.00001
Steel can radial thickness (cm)	0.00003	negligible	0.00003
Steel can height (cm)	negligible	negligible	0.00002
Steel can end thickness (cm)	negligible	negligible	0.00003
Steel can lateral placement (cm)	negligible	negligible	--
Lateral assembly alignment (cm)	negligible	negligible	--
Vertical assembly alignment (cm)	negligible	negligible	--
Gaps between parts (cm)	negligible	negligible	--
Assembly separation (cm)	negligible	negligible	--
Uranium mass (g)	negligible	negligible	--
^{234}U content (wt.%)	negligible	negligible	--
^{235}U content (wt.%)	0.00010	0.00010	--
^{236}U content (wt.%)	negligible	negligible	--
Uranium impurities (ppm)	negligible	negligible	--
Stainless steel mass (g)	negligible	negligible	0.00002
Stainless steel Cr content (wt.%)	negligible	negligible	--
Stainless steel Ni content (wt.%)	negligible	negligible	--
Stainless steel Mn content (wt.%)	negligible	negligible	--
Stainless steel (C, Si, P, S, & N) content (wt.%)	negligible	negligible	--
Stainless steel impurities (ppm)	negligible	negligible	--
Potassium mass (g)	NA	negligible	<0.00001
Potassium impurities (ppm)	NA	negligible	<0.00001
Potassium bubbles or voiding	NA	negligible	<0.00001
Total Experimental Uncertainty	**0.00037**	**0.00037**	**0.00006**

TABLE 2. Calculated Biases for the Potassium Worth Measurement Experiments.

Bias/*Correction*	**Configuration 1 (Empty Cans) [Δk_{eff}]**	**Configuration 2 (Potassium-Filled) [Δk_{eff}]**	**Potassium Worth Measurement [Δk_{eff}]**
1. Room Return Effects	-0.00093	-0.00086	--
2. Removal of Stainless Steel Diaphragm	+0.00054	+0.00054	--
3. Removal of Support Structure	-0.00106	-0.00106	--
4. Temperature Effects	negligible	negligible	--
5. Removal of Steel Can Impurities	negligible	negligible	--
6. Removal of Potassium Impurities	NA	negligible	--
Total Bias for Detailed Model (1-6)	**-00.00145**	**-0.00138**	**+0.00007**
7. Removal of HEU Impurities	-0.00021	-0.00022	--
7+8. Removal of HEU Impurities and Homogenization of Annuli	-0.00027	-0.00023	--
9. Simplification of Can Geometries	+0.00013	+0.00006	--
7-9. Combined Simplification Calculation	-0.00012	-0.00015	--
Total Bias for Simple Model (1-9)	**-0.00157**	**-0.00153**	**+0.00004**

TABLE 3. Experimental and Benchmark Eigenvalues for Critical Configurations.

Case	**Steel Can Content**	**Experimental**			**Bias**			**Benchmark Experiment**		
		k_{eff}	**±**	**1σ**	**Δk_{eff}**	**±**	**1σ**	**k_{eff}**	**±**	**1σ**
1 Detailed	Void	0.99957	±	0.00037	-0.00145	±	0.00004	0.9981	±	0.0004
2 Detailed	Potassium	1.00025	±	0.00037	-0.00138	±	0.00005	0.9989	±	0.0004
1 Simple	Void	0.99957	±	0.00037	-0.00157	±	0.00005	0.9980	±	0.0004
2 Simple	Potassium	1.00025	±	0.00037	-0.00153	±	0.00006	0.9987	±	0.0004

TABLE 4. Experimental and Benchmark Potassium Worth.

Case	**Experimental**			**Bias**			**Benchmark Experiment**		
	ρ	**±**	**1σ**	**Δρ**	**±**	**1σ**	**ρ**	**±**	**1σ**
Detailed (Δk/k)	0.00068	±	0.00006	0.00007	±	0.00003	0.00075	±	0.00007
Detailed (¢)	10.3	±	1.1	1.1	±	0.4	11.4	±	1.2
Simple (Δk/k)	0.0068	±	0.00006	0.00004	±	0.00005	0.00072	±	0.00008
Simple (¢)	10.3	±	1.1	0.6	±	0.7	11.0	±	1.3

COMPUTATIONAL ANALYSES

Sample calculations are the simple benchmark model are presented in Table 5 for the critical configurations; these were obtained using MCNP6 with other neutron cross section libraries such as ENDF/B-VII.1, ENDF/B-VII.0, JEFF-3.1 [8], and JENDL-3.3 [9] for a comparison between nuclear data sets. Additional calculations were performed using SERPENT2.1.13 [10] and KENO-VI [11] for comparison. Calculations for both configurations are low, which is typical for calculations of HEU annuli and cylinder experiments from ORCEF [12]. Results for the detailed benchmark model are very similar and available in the full benchmark report [4].

Comparison of the calculated eigenvalues for both configurations provides the calculated potassium worth (see Table 6). The calculated worths are approximately 70 to 80 % lower than the benchmark experiment worth. The discrepancy between calculated and benchmark results indicated two possible problems: 1) there is an unknown error in this pair of experiments resultant in an incorrect benchmark value, or 2) there are inadequacies in the nuclear data for potassium that need further investigated and resolved. Currently there are no other benchmark experiment data currently evaluated to test potassium cross section data.

Current activities focus on completion of this benchmark evaluation for inclusion in the IRPhEP Handbook with additional investigation into uncertainties in the cross section data for potassium and identification of sensitivities to the nuclear data to potassium. The SCCA experiment series ended with a similar measurement of potassium, where the aluminum core is replaced with an empty steel calandria and then a steel calandria filled with potassium. This experiment can also be similarly utilized as a measurement of potassium worth in a fast-reactor system. Logbooks from the SCCA experimental series are also been investigated for possible additional measurements where fuel rods were replaced with potassium-filled rods. Additional nuclear reactor and criticality safety experiments with either potassium or sodium-potassium eutectic material need identified for additional benchmark evaluation. Contribution of multiple sources of benchmark experiment data for potassium will assist in the validation of its nuclear data.

TABLE 5. Comparison of Simple Benchmark and Calculated Eigenvalues.

Case	Code	Neutron Cross Section Library	Calculated			Benchmark Experiment			$\frac{C-E}{E}$%		
			k_{eff}	±	1σ	k_{eff}	±	1σ			
1	MCNP6	ENDF/B-VII.1	0.99542	±	0.00002	0.9980	±	0.0004	-0.26	±	0.04
		ENDF/B-VII.0	0.99556	±	0.00002				-0.24	±	0.04
		JEFF-3.1	0.99227	±	0.00002				-0.57	±	0.04
		JENDL-3.3	0.99982	±	0.00002				0.18	±	0.04
	SERPENT2	ENDF/B-VII.0	0.99558	±	0.00003				-0.24	±	0.04
	KENO-VI	ENDF/B-VII.0	0.99528	±	0.00003				-0.27	±	0.04
2	MCNP6	ENDF/B-VII.1	0.99564	±	0.00002	0.9987	±	0.0004	-0.31	±	0.04
		ENDF/B-VII.0	0.99577	±	0.00002				-0.30	±	0.04
		JEFF-3.1	0.99242	±	0.00002				-0.63	±	0.04
		JENDL-3.3	0.99996	±	0.00002				0.12	±	0.04
	SERPENT2	ENDF/B-VII.0	0.99581	±	0.00003				-0.29	±	0.04
	KENO-VI	ENDF/B-VII.0	0.99549	±	0.00003				-0.32	±	0.04

TABLE 6. Comparison of Simple Benchmark and Calculated Potassium Worth.

Code	Neutron Cross Section Library	Calculated			Benchmark Experiment			$\frac{C-E}{E}$%		
		ρ(¢)	±	1σ	ρ(¢)	±	1σ			
MCNP6	ENDF/B-VII.1	3.4	±	0.4	11.0	±	1.3	-69	±	5
	ENDF/B-VII.0	3.2	±	0.4				-71	±	5
	JEFF-3.1	2.3	±	0.4				-79	±	4
	JENDL-3.3	2.1	±	0.4				-81	±	4
SERPENT2	ENDF/B-VII.0	3.6	±	0.6				-67	±	7
KENO-VI	ENDF/B-VII.0	3.2	±	0.6				-71	±	6

CONCLUSION

Experiments were performed in the 1960s to support fast reactor design and validation. A pair of experiments was utilized to specifically validate the worth of potassium in a fast neutron spectrum for space power reactor design. Benchmark models were prepared for submission to the IRPhEP Handbook. The experiments were performed with high accuracy and precision, where the majority of the uncertainty in the experiments derives from the measurement of the system reactivity. While the benchmark worth for 2.4 kg of potassium metal was approximately 11 ± 1 ¢, calculations with various Monte Carlo codes and neutron cross section libraries are between 70 to 80 % lower than the benchmark values. Efforts continue to finalize the benchmark evaluation and identify additional potassium-sensitive experiments to support validation of potassium neutron cross section data.

ACKNOWLEDGMENTS

The ICSBEP and IRPhEP are collaborative efforts that involve numerous scientists, engineers, and administrative support personnel from over 20 different countries. The author would like to acknowledge the efforts of all of these dedicated individuals without whom these projects would not be possible. Special appreciation is expressed for M. A. Marshall and J. B. Briggs (retired) from INL and Y. Rozhikhin from IPPE for their service as reviewers. This paper was prepared at the Idaho National Laboratory for the U.S. Department of Energy under Contract Number (DE-AC07-05ID14517).

REFERENCES

[1] Mihalczo, J. T., "A Small Beryllium-Reflected UO_2 Assembly," ORNL-TM-655, Oak Ridge National Laboratory, TN, (1964).
[2] Fraas, A. P., "Summary of the MPRE Design and Development Program," ORNL-4048, Oak Ridge National Laboratory, TN, (1967).
[3] Mihalczo, J. T., and Wyatt, M. S., "Potassium Reactivity Worth in a ^{235}U Fission Spectrum Critical Assembly," *Trans. Am. Nucl. Soc.*, **76**, 359-360, (1997).
[4] *International Handbook of Evaluated Reactor Physics Benchmark Experiments*, OECD-NEA, Paris, France, (2015).
[5] Mihalczo, J. T., and Schaaff, G., "Uncertainties in Masses, Dimensions, Impurities, and Isotopics of HEU Metal Used in Critical Experiments at ORCEF," ORNL/TM-2012/32, Oak Ridge National Laboratory, TN, (2011).
[6] Goorley, J. T., et al., "Initial MCNP6 Release Overview – MCNP6 version 1.0," LA-UR-13-22934, Los Alamos National Laboratory, NM (2013).
[7] Chadwick, M. B., et al., "ENDF/B-VII.1: Nuclear Data for Science and Technology: Cross Sections, Covariances, Fission Product Yields and Decay Data," *Nucl. Data Sheets*, **112**, 2887-2996, (2011).
[8] Koning, A. Forrest, R., Kellett, M., Mills, R., Henriksson, H., and Rugama, Y., "The JEFF-3.1 Nuclear Data Library," JEFF Report 21, OECD-NEA, Paris, France, (2006).
[9] Shibata, K., et al., "Japanese Evaluated Nuclear Data Library Version 3 Revision 3: JENDL-3.3," *J. Nucl. Sci. Tech.*, **39**, 1125-1136, (2002).
[10] Leppännen, J., "Development of a New Monte Carlo Reactor Physics Code, D. V. Thesis, Helsinki University of Technology, VTT Publications 640, VTT Technical Research Centre, Finland, (2007).
[11] Hollenbach, D. F., Petrie, L. M., Goluoglu, S., Landers, N. F., and Dunn, M. E., "KENO-VI: A General Quadratic Version of the KENO Program," ORNL/TM-2005/39 Version 6 Vol. II, Sect. F17, Oak Ridge National Laboratory, (2009).
[12] Bess, J. D., Marshall, M. A., Briggs, J. B., "The ORSphere Benchmark Evaluation and Its Potential Impact on Nuclear Criticality Safety," *Proc. NCSD 2013*, Wilmington, NC, September 29 – October 3, 2013.

Assessment of Space Nuclear Thermal Propulsion Facility and Capability Needs

James E. Werner[1], Anthony D. Belvin[2],

[1]*Space Nuclear Systems and Technology Division,*
Idaho National Laboratory, Idaho Falls, ID 83415
[2]Office of Space and Defense Power Systems, Office of Nuclear Energy
Department of Energy, Washington DC
Telephone: 208-526-8378
Email: james.werner@inl.gov

Abstract. The development of a Nuclear Thermal Propulsion (NTP) system rests heavily upon being able to fabricate and demonstrate the performance of a high temperature nuclear fuel as well as an integrated reactor system prior to launch. A number of studies have been performed in the past which identified the facilities needed and the capabilities available to meet the needs and requirements identified at that time. Unfortunately, many facilities and capabilities within the Department of Energy have been rebuilt for other projects and missions, decommissioned or completely demolished. Any current or future NTP development effort will be subject to vary different constraints under which the Rover/NERVA program was conducted. Nuclear fuel tests and ground test operations of a reactor system will require an exhaust effluent treatment system to ensure only permitted releases of radioisotopes become airborne. Second, significant changes to the federal regulations governing the acquisition of major capital assets have occurred. These regulations will affect the coordination, review and management of design, construction and operation phases of the test facilities. DOE Order 413.3B establishes a sequence of major milestones identified as Critical Decisions from approval of mission need to start of operations. This paper provides a brief overview of the anticipated facility needs and identifies some promising concepts to be considered which could support the development of a nuclear thermal propulsion system. Detailed trade studies will need to be performed to support the decision making process.

Keywords: Nuclear, testing, facilities.

INTRODUCTION

Nuclear Thermal Propulsion (NTP) rocket stages have been shown, in past and recent mission studies, to greatly reduce the propellant mass and number of launches from earth for deep space missions and manned missions to Mars. This is because NTP systems have a large specific impulse (Isp) advantage over the best chemical rocket engines. The Isp for NTP systems is about double that of the best liquid oxygen/liquid hydrogen rocket engines. NTP systems also have an advantage in that the required velocity to perform the transient to Mars from Earth orbit and the required deceleration at Mars can be accomplished with much smaller propellant load and a shorter transient time. The propellant load reduction in turn translates to fewer heavy lift flights from the Earth's surface to assemble a Mars mission vehicle. Reducing the number of lifts from the Earth reduces the risk of delay and potentially missing a departure window. The development of an NTP system rests heavily upon being able to fabricate and demonstrate the performance of high temperature nuclear fuel as well as demonstrating an integrated system prior to

launch. A number of studies have been performed past identifying the facilities needed and the capabilities available to meet the needs and requirements identified at that time. Since that time a number facilities and capabilities within the Department of Energy have been removed or decommissioned and new requirements for construction, permitting and operations emplaced.

BACKGROUND

Since the early 1970's very little development of NTP fuels and materials or fabrication and test capabilities that could support such a system have occurred. While the debate continues between mission pull and technology push, two key questions that need to be answered are: (1) What facilities and equipment are needed to fabricate the various fuels, materials and sub-systems of an NTP; and (2) How do we identify the critical set of requirements needed to qualify a nuclear rocket engine for launch in the most cost effective and realistic timeframe?

An extensive nuclear thermal rocket technology development effort was conducted between 1955 and1973 under the Rover/NERVA Program. Candidate fuels for NTP applications included both graphite based fuels and CERMET (W-UO2) fuel) types. The major design effort was on the NERVA graphite fuels and reactor systems. Numerous engine ground tests were conducted during the NERVA program. Fuels development and engine development activities were carried on in parallel early in the program with complete engine tests effectively serving as fuels development tests. The desire for lower costs, shorter lead times and less release of radioactive materials into the environment encouraged development of the Nuclear Furnace test reactor. The Nuclear Furnace tests required a smaller number of fuel elements for a critical reactor configuration and multiple fuel element types could be tested simultaneously. Fuel performance could be demonstrated before conducting a full engine test. The facility also demonstrated an effluent treatment system.

In the Early 1990's a team of experts from NASA, DOE, DOD, and the private industry assembled to:

- Define NTP test facility requirements,
- Evaluate existing facility capabilities to meet these requirements,
- Identify new facility development or existing facility modification needs,
- Identify critical path facility development requirements, and
- Recommend facility development strategies.

The team identified a list of facilities and capabilities that were needed to support NTP development effort [1]. An initial assessment of the availability of facilities that can currently meet the identified facility categories is provided:

Table 1. NTP Facility Need and Current Capability Assessment[1]

Facility Category	Definition	Current Capability
Fuel Fabrication Facilities	Facilities for development and eventual production of enriched uranium nuclear NTP fuel materials and fuel elements.	Fuel production facilities do not exist. Limited laboratory scale equipment is available for fabrication of material coupons and segments and coatings.
Test Facilities for Unirradiated Fuel and Materials	Fuel and material testing and characterization laboratories capable of handling unirradiated uranium fuel and materials.	Capability exists at DOE and NASA centers.
Hot Hydrogen Flow Test Facilities	Facilities featuring materials or subsystems in a flowing hot hydrogen environment without nuclear heating. The facility should be able to heat elements or components up to 3200 K. Hot hydrogen flow test facilities include the following three types: 1) Fuels and Materials / low flow rate used for material and fuel coupon or segment tests 2) Equipment Development / high flow	Compact Fuel Element Environmental Tester (CFEET) and the other is the Nuclear Thermal Rocket Element Environmental Simulator (NTREES) at NASA facilities for unirradiated material. None exist at DOE facilities or for irradiated material.

	rate used for testing of partial or full length components. 3) Equipment Development / Low and High flow rate for testing of irradiated fuel and components	
Fuel and material Irradiation Test Facilities	Reactor or radiation source facilities that provide a gamma or neutron fluence to a test specimen of uranium fuel material and structural or non-fuel-bearing material.	Advanced Test Reactor and High Flux Isotope Reactor are available. The Transient Reactor Test Facility should be available. No fast reactors are available within the US. Lead test assembly capabilities exist at both INL and ORNL.
Low Power Critical Assembly Test Facilities	Low power, flexible geometry, variable material volume fraction reactor facility for physics benchmark, design confirmation, and safety tests.	Critical facilities have been established at the Device Assembly Facility at the Nevada National Security Site.
Prototypic Fuel Element Test Reactor	Test reactor in which all desired performance parameters (time, temperature, pressure, power density, etc.) can be achieved together for experiments on one or more prototypic fuel elements.	None
Reactor Test Cell	Portion of a Reactor/Engine Test Facility where early "engine-like" reactors would be tested at high powers on the ground.	None
Engine Test Cell	Portion of a Reactor/Engine Test Facility where "flight-like" nuclear rocket engines would be tested at high powers on the ground.	None
Remote Inspection/Post-Irradiation Examination Facilities	Hot cell facilities where post-test examinations of radioactive fuel, reactor, and engine components will be conducted.	Hot Fuel Examination Facility at INL is capable of performing PIE examinations of fuel elements and fuel segments. Hot cells are also available at ORNL and PNNL No facilities exist for engine assembly or disassembly of engine components.
Component Test Facilities without Hot Hydrogen or Irradiation Environment	Facilities that can simulate structural, thermal, and cycling environments during startup, continuous lifetime operation, and shutdown on system components. However, environments would not include irradiation or hot hydrogen.	Most rocket engine components can be tested in a variety of places. MSFC and SSC have that capability as well as many component level or integrated engine manufacturing aerospace prime contractors. The viability for nuclear reactor components needs to be determined
Control System Test Facilities	Simulation laboratory to develop and test engine/system control system.	Systems integration facilities and the expertise exist within the NASA centers. The facilities would have to be modified to accept the test article.
Component Safety Test	Test facilities that can subject system	None

Facilities	components to anticipated malfunctions or accident environments.	
System-Level Safety Test Facilities	Test facilities that can simulate on the complete engine all realistic malfunctions and severe or accident environments.	None
Training and Simulator Test Facilities	Facilities for operator/astronaut training. Emergency sequences would be simulated for training.	None
Engine Integration Test Facility	Cold flow test facility for complete engine system. Facility would use a hot gas to simulate nuclear heating and to evaluate potential pre-flight and flight problems. No nuclear critical operations or nuclear heating would occur.	Facilities that can accommodate this testing are located at SSC for cold flow testing. An assessment of what capabilities can be applied or modified to be used is needed.
Flight Test Facilities	Ground facilities at launch site or operations control center required for launch support or operations specifically as a result of having nuclear propulsion systems	None

The 1990 assessment concluded "This study revealed that the United States has a wealth of test facilities available for supporting NTP development. While some modifications will be required to support specific NTP development actions, there is a solid base of existing facilities available to satisfy a large majority of the test needs. Of the six test categories where no existing facilities were clearly identified, three are anticipated to either not be needed (e.g. system-level safety test facilities) or could be incorporated into other categories, or modifications to existing facilities (e.g., flight test support facilities or training and simulator test facilities) could be made."[1]

Present Day Assessment

Much of the report's findings regarding the type of infrastructure and equipment needed are valid today. However, since the time of this assessment much has changed regarding the availability and operation of the facilities and infrastructure to support the development of an NTP system today. Some facilities identified in the study no longer exist or have changed enough in capability that they are not viable for use. Three facility and capability needs central to any renewed NTP development effort have been identified in all historical and recent assessments. They are:

- NTR fuel fabrication capabilities to include process methods,
- Test facilities for fuel and material design, development and qualification, and
- A ground test facility for a system reactor and engine development and qualification effort.

The following paragraphs provide a general assessment of existing capabilities and future needs in these three areas.

FUEL FABRICATION FACILITIES

The top level facility requirement is that it must be a Category I Nuclear Facility capable of processing core load quantities of high enriched uranium (HEU) fuel elements per year while fully complying with all environmental, safety and health requirements. The fuel fabrication procedures must be defined and demonstrated, the technical basis for the specification identified and techniques to demonstrate compliance and quality assurance understood. There currently are two existing HEU facilities that are capable of supporting such an effort. However, additional floor space and equipment would be needed in either facility. Oak Ridge National Laboratory is currently working to recapture the extrusion and coating processes for NERVA fuel and the Marshall Space Flight Center is developing process fabrication techniques for a W-UO2 CERMET fuel. Both of these efforts are limited to using either a uranium surrogate or depleted Uranium. Both are using laboratory scale equipment for their development efforts. Once a fabrication process has been defined and demonstrated, the production facility requirements

regarding equipment scale and production specification and measurement techniques will need to be defined. It is estimated that it would take 8 years before the first fuel production runs could be established.

TEST FACILITIES FOR FUEL, MATERIAL AND REACTOR SYSTEMS

Facilities and equipment are needed to characterize the fuel and material for its chemical, thermal, and structural properties and for evaluations needed to improve performance and design data and to understand how the fabrication process affects these parameters. Equipment such as measuring the thermal stability of the fuel and coatings at elevated temperatures (3000 - 3500 K), stress resistance, material creep, component compatibility, and effects of hydrogen penetration, chemical interaction and formation, and mass loss are needed. In addition, as identified in earlier studies, nuclear system component development and testing (instrumentation, control, materials, valves, pumps, etc.) facilities will be needed. Some of this equipment may be available at DOE Labs or NASA research centers, but none as of yet are dedicated to this project. A program systems study is needed to determine what types of experiments and facility equipment is needed and how it would fit into a complete fuel and reactor system development effort. An integral part of any testing program will need to be the development of a number of fuel modeling codes to predict fuel and material performance and guide the types of tests as well as the neutronic, thermal, mechanical and chemical measurements needed.

Hot Hydrogen Test Facilities

The use of electrical heating in combination with exposure to hot hydrogen gas can be very beneficial in the early development phases of fuel behavior, reactor-propellant surface interactions, component design, and system design. But these methods must be verified and validated in some manner. Since these approaches use externally-generated inductive, resistive, or convective heating methods, the energy deposition profile within the fuel elements will not match the energy deposition profile that corresponds to internal fission-generated heating. The use of those electrical heating methods also includes some risk of introducing new failure modes that would not be present in the real operating environment. Some progress has been seen in this area in the past decade. MSFC has developed two systems to support hot hydrogen testing. One is the Compact Fuel Element Environmental Tester (CFEET) and the other is the Nuclear Thermal Rocket Element Environmental Simulator (NTREES)[2]. The purpose of the NTREES facility is to perform hot hydrogen non-nuclear testing of NTR fuel elements and fuel materials at prototypic high flow rates and temperatures. Electrical heating and other conventional test methods cannot duplicate the effects of irradiation and the effect of fission fragments accelerating fuel migration or breakdown of the fuel structural integrity so irradiation testing is essential to the development of nuclear fuel for NTP. Hot hydrogen test capabilities need to be developed to allow testing of fuel that contain enriched uranium as well as fuel that has been irradiated in a test reactor.

Fuel and Material Irradiation Test Facilities

The irradiation test facilities and capabilities in the United States have dramatically reduced since the 1990 assessment. The remaining operational test reactors are the Advanced Test Reactor at Idaho National Laboratory and the High Flux Isotope Reactor at Oak Ridge National Laboratory[2]. There are no fast spectrum test reactors operational in the United States. The primary challenge in irradiation test design for NTP fuels and materials will be designing the test assemblies to operate at the very high temperatures at which an NTP system operates and matching as closely as possible the neutron energy spectra and the fuel energy density. It is unlikely that a low flow or purge hydrogen flow rate can be accommodated into the reactor test assembly due to safety concerns. Capabilities exist at both ORNL and INL to design, build, instrument, and install the test assemblies into the test reactors. Significant time may be needed to complete the design and safety analysis to permit there types of tests to be conducted. However, the ability to build and understand fuel performance through computational analysis and models is one area where today's capabilities and understanding far exceed what was available in the 1970s and even 1990s. Using multi-physics codes such as the INL's BISON can be used to effectively model the fuel performance and to determine the effect material or fabrication processes have on fuel performance. Using such analytical codes enable the use of separate effects fuel data to be used to determine the fuels system performance. The number and types of nuclear irradiations and PIE analysis may be sufficient to determine the performance and boundaries of a certain fuel type so as to qualify it for use in a larger reactor core or engine systems test. However, the development and benchmarking of the model need to proceed jointly with the fuel fabrication and fuel testing

efforts.

Ground Test Facilities

Developing the capability to conduct large system testing of an NTP flight system has been recognized as one of the largest and most costly aspects associated with developing an NTP flight system. Any current or future NTP development effort will be subject to vary different constraints than what was conducted in the past Rover/NERVA program. An exhaust effluent treatment system to trap fission products and radioactive noble gases released from the fuel during power testing will be required due to federal state regulations, in particular the National Emission Standards for Hazardous Air Pollutants (NESHAP), that respond to increased awareness of the consequences of environmental releases.

In the late 1980s and early 1990s, as part of the Space Nuclear Thermal Propulsion (SNTP) Project, Sandia National Laboratory evaluated a number of effluent treatment systems for the SNTP ground test facility. Based on the operating environment for the SNTP Program, Sandia selected a process that minimized the use of water in cleaning up the effluent [3]. Due to the extensive conceptual design effort performed by Sandia, this concept has subsequently been accepted as a baseline for future evaluations of nuclear thermal propulsion systems (Figure 1). This concept used a large amount of liquid hydrogen and liquid nitrogen. For every pound of hydrogen flowing through the reactor, three additional pounds were needed to cool the effluent and allow the trapping of the noble gases in the cryogenic traps. Though the test program was also based on a 550 MWt reactor, the test period was relatively short, ~1000 sec at full power. [4]

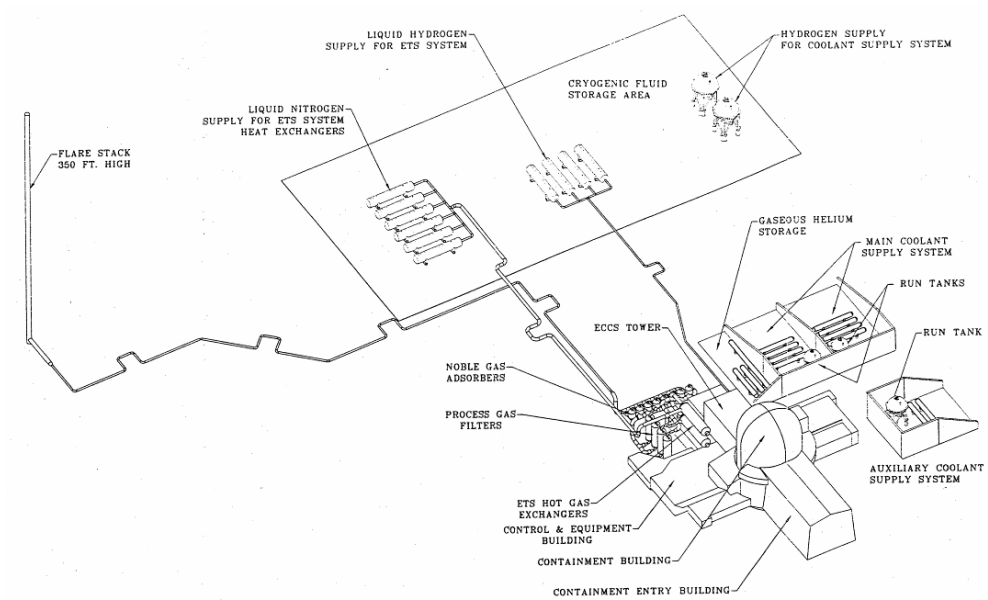

FIGURE 1. NTP Ground Test Facility and Effluent Treatment System

In 1995, DOE supported a study of a system to trap and collect the hot hydrogen effluent and store it during the test duration. The study was based on an 11.5 MWt reactor operating for 5 hours (Fluor, 1995). Based on this design case, other options were scaled, including a 550 MWt reactor operating for 500 sec. The hydrogen was stored in large steel tanks until the effluent could be treated and liquefied for recycling in the next test. The effluent treatment collection system was limited in size and depending on the test duration, the pressure in the effluent treatment system could build to 200 psig. For the baseline study of a 5 hour test, hydrogen recovery was expected to take 5 days.

The effluent treatment system for the NTP system has very few development needs, but system studies to evaluate the scale-up costs, operations and technical viability of these options are needed. The Subsurface Active Filtration of Exhaust (SAFE) concept has the potential to significantly reduce the capital costs for a nuclear ground test, but

several sub-scale feasibility tests are needed to understand the feasibility and performance of such a system before it is considers a viable alternative. [4]

Additional facilities and operations would be needed in addition to the reactor test facility. A control room or building with associated instrumentation, controls, and data acquisition system will be required. A facility for engine assembly, checkout and storage prior to placement in the test cell would also be needed. For disassembly, examination, and preparation for disposal of the NTP after completion of the test program, access to a shielded hot cell facility will be required. A shielded enclosure would also be required to load the NTP reactor or reactor fuel and components into shipping containers for transfer to a hot cell for examination.

An alternative to the complex effluent treatment system described above is the Subsurface Active Filtration of Exhaust (SAFE) Facility [5]. The NTP concept for SAFE would be sealed at the surface, and as effluent is discharged into a bore-hole, the pressure would build to the point where the gas and water vapor from the effluent cooling system would be driven into the porous soil or rock at a rate equal to the mass flow from the NTP. At equilibrium pressures, the NTP could be operated for long periods over a wide range of power levels (Figure 2).

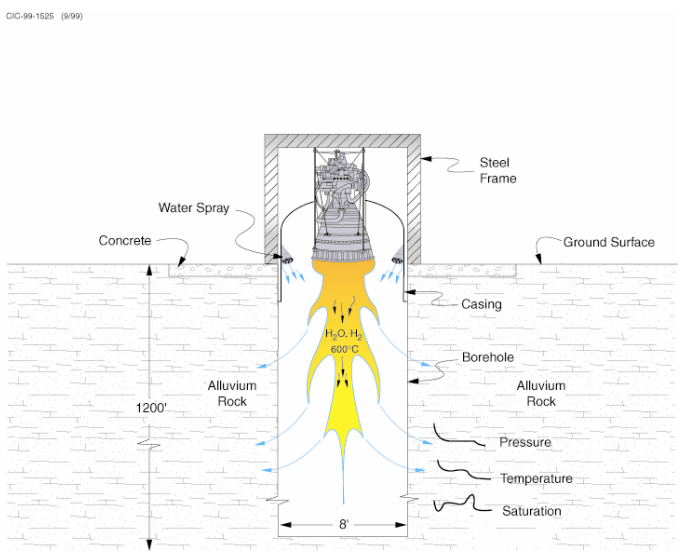

FIGURE 2. Subsurface Active Filtration of Exhaust Concept[5]

Initial studies of the SAFE concept indicate it would need a borehole eight feet in diameter by 1200 feet deep. This is a typical borehole used for underground weapons tests. The upper 100 feet would be steel encased, with the remainder of the borehole uncased and open to the NTS alluvial soils. Cooling water would be sprayed into the borehole to limit the exhaust temperature and prevent damage to the steel structure. Simulations indicate that a maximum back pressure buildup in the borehole would be 36 psi.[4]

Facilities That Do Not Exist

The following facilities do not currently exist. It is unknown at this time how much of this would need to be built or its function assimilated into a new complex such as the ground test facility or facilities for the fabrication of flight unit or engine integration with a launch system.

- Prototypic Fuel Element Test Reactor
- Component Safety Test Facilities in a nuclear environment
- System-Level Safety Test Facilities
- Training and Simulator Test Facilities
- Flight Test Facilities

CONCLUSION

A detailed systems study is needed to determine the three critical facility capabilities (from the facilities listed above) that are needed to support a mission or can be incorporated into a facility to be built or added to existing structures that will be used in support of an NTP program. This study should also provide a thorough assessment of NASA facilities and capabilities to determine how they can best be used or the modifications needed to support NTP development. A separate effort is needed to identify, define, and obtain some uniform consensus of the test, qualification, safeguards and safety requirements needed to: (1) qualify a nuclear rocket engine; and (2) obtain a clear understanding of the required facility operations, analysis, and approval process for the launch of a reactor system. Pursuing these efforts early in the development program allows for effective integration of these requirements and facility options into the design of new facilities and ensures that appropriate cost and schedule management techniques can be applied so that coats are identified upfront and developed as needed.

REFERENCES

[1] Allen, G.C., et al, 1993, "Space Nuclear Thermal Propulsion Test Facilities Subpanel Final Report," NASA Technical Memorandum 105708, April.
[2] Werner, J.W. et al, 2011, "An Overview of Facilities and Capabilities to Support the Development of Nuclear Thermal Propulsion," Proceedings of Nuclear and Emerging Technologies for Space 2011 Paper 3309
[3] Beck, D.F., et al, 1992, "SNTP PIPET Preliminary Design Review Data Package," Sandia National Laboratory, Albuquerque, NM, February.
[4] Hill, T.J., 2003, "Space Nuclear Thermal Propulsion Test Facilities Accommodations at the INEL," EFF-SNS-10526, October.
[5] Howe, S.D., et al, 2002, "SAFE Testing Nuclear Rockets Economically," Los Alamos National Laboratory, Los Alamos, NM.

Summary of the Nuclear Risk Assessment for the Mars 2020 Mission Environmental Impact Statement

Daniel J. Clayton[1], John Bignell[1], Christopher A. Jones[1], Daniel P. Rohe[1], Gregg J. Flores[1], Timothy J. Bartel[1], Fred Gelbard[1], San Le[1], Charles W. Morrow[1], Donald L. Potter[1], Larry W. Young[1], Nathan E. Bixler[1] and Ronald J. Lipinski[1]

[1]*Sandia National Laboratories, P.O. Box 5800, MS-0747, Albuquerque, NM 87185*
Contact Author at (505) 284-5360; djclayt@sandia.gov

Abstract. In the summer of 2020, the National Aeronautics and Space Administration (NASA) plans to launch a spacecraft as part of the Mars 2020 mission. One option for the rover on the proposed spacecraft uses a Multi-Mission Radioisotope Thermoelectric Generator (MMRTG) to provide continuous electrical and thermal power for the mission. NASA has prepared an Environmental Impact Statement (EIS) in accordance with the National Environmental Policy Act. The EIS includes information on the risks of mission accidents to the general public and on-site workers at the launch complex. The Nuclear Risk Assessment (NRA) addresses the responses of the MMRTG option to potential accident and abort conditions during the launch opportunity for the Mars 2020 mission and the associated consequences. This information provides the technical basis for the radiological risks of the MMRTG option for the EIS. This paper provides a summary of the methods and results used in the NRA.

Keywords: nuclear risk assessment, environmental impact statement, Mars 2020 mission.

INTRODUCTION

In the summer of 2020, the National Aeronautics and Space Administration (NASA) plans to launch a rover to the surface of Mars as part of the Mars 2020 mission. One option for the proposed rover includes the use of radioactive materials in a single Multi-Mission Radioisotope Thermoelectric Generator (MMRTG) to provide continuous power for the mission. NASA prepared an Environmental Impact Statement (EIS) for the mission in accordance with the National Environmental Policy Act (NEPA). The EIS includes information on the risks of mission accidents to the general public and on-site workers at the launch complex. The Nuclear Risk Assessment (NRA) addresses the responses of the proposed MMRTG option to potential accident and abort conditions during the launch opportunity for the Mars 2020 mission and the associated consequences [1]. This information provides the technical basis for the radiological risks of the MMRTG option for the EIS. This paper provides a summary of the methods and results used in the NRA [1].

The purpose of the proposed Mars 2020 mission would be to conduct comprehensive science on the surface of Mars and demonstrate technological advancements in the exploration of Mars. Mars 2020 mission investigations would reflect several of the high-priority scientific investigations recommended to NASA by the planetary science community. The overall scientific goal would be to address the questions of habitability and the potential origin and evolution of life on Mars.

The Mars 2020 mission spacecraft would be launched from Cape Canaveral Air Force Station (CCAFS), Florida. NASA has not yet selected the launch vehicle for the mission. However, there are four candidate Launch Vehicles (LVs) being considered for the Mars 2020 mission based upon the stated launch opportunity, spacecraft mass and mission requirements: the Atlas V 541, the Atlas V 551, the Delta IV Heavy, and the Falcon Heavy. The Atlas V,

the Delta IV, and the Falcon would be launched from CCAFS Space Launch Complex (SLC)-41, SLC-37, or SLC-40, respectively. The potential consequences of the Atlas V 541 are assumed to be enveloped by those of the Atlas V 551. The 551 has similar accident modes and uses an additional solid rocket motor compared with the 541. As of the writing of the NRA [1], for the Falcon Heavy LV, flight history, detailed design and in-flight performance data do not exist. Therefore, assumptions have been made regarding the vehicle design and number of successful flights prior to the Mars 2020 launch date. These assumptions reflect the expectation that the Falcon Heavy will achieve the degree of success and documented reliability prior to its use for missions carrying radioisotope power sources. Further, it is assumed that, to the first order, the Falcon Heavy accident modes and probabilities are equivalent to the Delta IV Heavy.

There would be one primary launch period of opportunity: July 7, 2020 to August 5, 2020 and one backup in August 2020. If the mission needs to be delayed to 2022, there is a launch opportunity within August and September of 2022. The analyses for the NRA sample weather data from several recent years for the months of July, August, and September in order to span the range of possible launch conditions [1]. In addition, since NASA has not selected the time of launch on a given day, the NRA assumes a daytime launch [1]. The planned mission trajectory would place the spacecraft in a heliocentric orbit prior to completion of the Stage 2 second burn. After separation from Stage 2, the spacecraft would be in a heliocentric interplanetary trajectory. If the spacecraft fails to intersect Mars, there is a very small but finite probability that it might return to Earth over the next several centuries.

The baseline Mars 2020 rover would use one MMRTG to provide continuous power. The MMRTG would contain eight General Purpose Heat Source (GPHS) modules. The MMRTG would contain 4.8 kg of plutonium dioxide (PuO_2) in ceramic form, with an estimated inventory of 60,000 curies (Ci), due primarily to plutonium-238 (Pu-238), an alpha-emitting radioisotope with a half-life of 87.7 years. The MMRTG would be provided by the U.S. Department of Energy (DOE). Due to the radioactive nature of this material and the potential for accidents resulting in its release to the environment, safety is an inherent consideration in all steps from mission design through launch.

DOE is responsible for quantifying the risks of its nuclear hardware subjected to the effects of potential launch accidents. The purpose of the NRA is to provide this information in support of the EIS for the mission, being prepared by NASA in accordance with requirements under the NEPA. There would also be a Presidential Nuclear Launch Approval Process for the mission subject to the requirements of Presidential Directive / National Security Council Memorandum Number 25 (PD/NSC-25), for which DOE would prepare a Final Safety Analysis Report (FSAR).

The EIS-supporting assessment presented herein is based in part on 1) spacecraft descriptions, accident environments, and LV information provided by NASA [2], 2) information regarding accident probabilities provided by NASA [3] and 3) information available from the LV manufacturers' User's Guides [4,5,6,7]. A composite approach has been taken in reporting the results in the NRA for accident probabilities, airborne portion of potential releases of PuO_2 in case of an accident (source terms), radiological consequences, and mission risks [1]. In the composite approach, the results for the Atlas V 541, the Atlas V 551, the Delta IV Heavy, and the Falcon Heavy would be combined in a probability-weighted manner with equal weight being given to each launch vehicle (25% each). Since the detailed calculations for the Atlas V 551 are being used to represent the Atlas V 541, and since the detailed calculations for the Delta IV Heavy are being used to represent the Falcon Heavy, the net result is that the Atlas V 551 calculations and the Delta IV Heavy calculations will be weighted 50% each. This approach reflects the state of knowledge at this early planning stage in the mission with respect to the candidate LVs being considered for the Mars 2020 mission. Differences in results among the various candidate LVs are not considered significant, given the uncertainties in the estimates being made in the nuclear risk assessment.

ACCIDENT PROBABILITIES AND SOURCE TERMS

The NRA considers: 1) potential accidents associated with the launch, and their probabilities and accident environments; 2) the response of the radioisotope hardware to accident environments with respect to source terms (that portion of the release that becomes airborne) and their probabilities, and 3) the radiological consequences and mission risks associated with such releases. The radioactive material inventory of interest, for a single MMRTG, is about 60,000 Ci of primarily Pu-238 [1]. The activity includes minor contributions from other related plutonium and actinide radionuclides in the fuel. This section addresses the potential accidents and hardware response; the

next section addresses potential consequences and risks. The methodology used in developing the accident probabilities and source terms is detailed in the NRA [1].

For the purpose of the risk analysis, the Mars 2020 mission is divided into five mission phases on the basis of the mission elapsed time (MET, the time (T) relative to launch), reflecting principal events during the mission as follows:

- Phase 0: Pre-Launch, $T < t_1$, from installation of the MMRTG to just prior to start of the Stage 1 Liquid Rocket Engines (LREs) at t_1.
- Phase 1: Early Launch, $t_1 < T < t_x$, from start of Stage 1 LREs, to just prior to t_x, where t_x is the time after which there would be no potential for debris or intact vehicle configurations resulting from an accident to impact land in the launch area, and water impact would occur.
- Phase 2: Late Launch, from $t_x < T$ to when the LV reaches an altitude of nominally 30,480 m (100,000 ft), an altitude above which reentry heating could occur.
- Phase 3: Suborbital Reentry, from nominally 30,480 m (100,000 ft) altitude to the end of Stage 2 burn 1 and the Command Destruct System (CDS) is disabled.
- Phase 4: Orbital Reentry, from end of Stage 2 burn 1 to Stage 2 / spacecraft separation.
- Phase 5: Long-Term Reentry, after spacecraft separation until no chance of Earth reentry.

The information on accidents and their probabilities has been based on information presented in [3].

MMRTG Response to Accident Environments

The response of the MMRTG to accident environments is based on consideration of:

- Prior safety testing of the General Purpose Heat Source Radioisotope Thermoelectric Generator (GPHS-RTG) and its components.
- Modeling of the response of the MMRTG and its components to accident environments using a continuum mechanics code.
- A comparison of the MMRTG with the GPHS-RTG in terms of structural features and accident environment responses.
- The types of LV accidents and their environments.

This information allows estimates to be made of the probability of release of PuO_2 and the amount of the release for the range of accident scenarios and environments that could potentially occur during the mission. The protection provided by the aeroshell module, its graphitic components and the iridium clad encapsulating the PuO_2 fuel, minimizes the potential for release in accident environments. Potential responses of the MMRTG and its components in accident environments are summarized as follows:

- Explosion Overpressure and Fragments: Liquid propellant explosions from LV destruct and resulting fragments are estimated to result in some MMRTG damage but no fuel release.
- Impact: Fracturing of the GPHS module and its graphitic components under mechanical impact conditions provide energy-absorbing protection to the iridium clad. Most impacts of an intact MMRTG or GPHS modules on steel or concrete near the launch pad could result in zero or small releases of PuO_2, depending on the impact velocity. Similarly, should Suborbital or Orbital Reentry accident conditions lead to GPHS modules impacting hard rock following reentry, a small release could occur. Grounds impact of an intact Space Vehicle (SV) for an early launch accident is expected, since the SV back shell and heat shield prevents the LV breakup during a destruct event. The combined effect of the SV hitting the ground and the MMRTG subsequently being hit by the SV components above it occasionally results in a fuel release, depending on the impact velocity and orientation. Larger intact configurations could result in higher releases for certain orientations in which launch vehicle and/or SV components impact directly onto the MMRTG.
- Thermal: Exposure of released PuO_2 to a liquid propellant fireball environment would be of short duration (nominally 20 s or less). Minor vaporization of exposed particulate would occur depending on the timing of the ground impact release and the fireball development. The fireball temperature would decrease in temperature to nominally 2,177 ^{o}C in less than 1 s (below which PuO_2 vaporization is negligible), and continue dropping as the fireball expands. For the Atlas V 551, exposure of released PuO_2 fuel to the higher-temperature (up to 2827 ^{o}C), longer burning (up to 250 s) solid-propellant from the Solid Rocket

Booster fragments could lead to more substantial vaporization of exposed PuO_2. In addition, exposure of a bare (or breached) iridium clad could result in clad degradation either through chemical interactions or melting, resulting in partial vaporization of the PuO_2. The aeroshell graphitic components could be damaged in accident environments, which would allow such an exposure of the iridium clads. In addition, minor PuO_2 vapor releases from intact aeroshell modules are possible in certain exposure conditions (e.g., underneath large pieces of burning solid propellant). Under such conditions, temperatures inside the module could be high enough to degrade the iridium clads and vaporize some PuO_2, which in turn could permeate through the somewhat porous graphitic materials.

- Reentry: Most suborbital reentries result in intact impact of the SV due to the presence of the SV back shell and heat shield. Most of these impacts occur in water with no release. Land impact can result in releases that are similar in nature to those from impact near the launch pad, but without the presence of solid propellant fires. Releases in these cases are similar in nature to those from impact near the launch pad. Reentry from circular orbital decay or long-term reentry will cause breakup of the SV and the MMRTG with subsequent release of the GPHS modules. This will result in some heating and ablation of the surface of the GPHS modules, but no containment failure or release in the air. When these separated components impact land, there is a potential for release from the GPHS module during impact on hard rock. No release is expected from a water impact or soil impact.

The response of the MMRTG to accident environments can be summarized as follows:

- Most launch accidents in Phases 0 and 1 would lead to one of several types of ground impact configurations. Ground impacts of the SV on steel or concrete can occasionally lead to a release. For larger impacting configurations, larger fuel releases are expected. Exposure to a liquid propellant fireball could lead to some vaporization of released PuO_2 depending on the relative timing of the impact release and the fireball development. Subsequent exposure of MMRTG hardware and PuO_2 to burning solid propellant could result in considerably larger releases through melting of the iridium clad and partial vaporization of the PuO_2.
- Nearly all Phase 2 accidents lead to impact of debris in the Atlantic Ocean with no releases. There could be some small in-air releases from blast-driven in-air fragment impacts.
- Phase 3 accidents lead to suborbital reentry and usually ground impact of the intact SV and MMRTG. Some small releases are likely due to impact of the MMRTG by SV hardware. There would be a hydrazine fire and a potential minor vaporization from it. There would be no solid propellant fires or releases due to them.
- Phase 4 and 5 accidents lead to orbital and long-term reentry heating and ground impact environments. The GPHS modules are designed to survive reentry; however, any ground impact on hard rock could result in small releases of PuO_2.

Source Terms and Probabilities

A summary of the composite accident and source term probabilities by mission phase, along with mean and 99th percentile source terms, are presented in Table 1 for the MMRTG. These results were determined by a Monte Carlo simulation using 150,000 trials or more for each of the various accident scenarios and launch vehicle options. In these simulations, 100 percent of released material with a physical diameter less than 100 microns was assumed to be airborne, which may be conservative since much of the released fuel would be trapped by the graphitics and other debris. Simulations show that particles larger than 100 microns would fall to the ground within a few meters of the source.

Two mean values are displayed: one is based on the average of all release amounts when an accident occurs (including accidents with no release), the other is based on the average release amount considering only non-zero releases. Most accidents do not result in a release; hence the mean release given an accident is lower than the mean release given a release.

The 99th percentile release is obtained by sorting the trials by the total amount released. Then the release amount for which 1% of the trials are greater is defined as the 99th percentile. The 99th percentile source term is the value predicted to be exceeded with a probability of 0.01 (1 in 100), either given an accident, or given a release. In this context, the 99th percentile release value reflects the potential for larger radionuclide releases at lower probabilities.

Most accidents do not result in a release; hence the 99th percentile release given an accident is lower than the 99th percentile release given a release. For some launch phases, the probability of a release is so low that the 99th percentile release is zero, given an accident.

TABLE 1. Source Term Summary for the MMRTG[a,b,c]

Mission Phase	Accident Probability	Conditional Probability of Release	Total Probability of Release	Source Term (Ci)			
				Mean Given an Accident	Mean Given a Release	99th Percentile Accident	99th Percentile Release
0 (Prelaunch)	3.28E-05	3.27E-01	1.07E-05	9.20E-02	2.82E-01	4.75E-02	6.68E+00
1 (Early Launch)	3.12E-03	2.81E-02	8.77E-05	1.66E+00	5.90E+01	1.64E+01	6.33E+02
2 (Late Launch)	3.63E-03	2.12E-03	7.71E-06	3.40E-05	1.60E-02	-	2.31E-01
3 (Suborbital)	1.31E-02	1.13E-03	1.48E-05	4.70E-02	4.16E+01	-	9.29E+02
4 (Orbital)	4.66E-03	5.62E-02	2.61E-04	2.96E-02	5.27E-01	6.51E-01	6.15E+00
5 (Long-Term)	1.00E-06	9.43E-02	9.43E-08	7.29E-02	7.73E-01	1.48E+00	7.82E+00
Overall Mission	2.46E-02	1.56E-02	3.83E-04	2.42E-01	1.55E+01	9.49E-03	3.41E+02

a. The table presents composite results for the LVs under consideration, determined by taking the probability-weighted value of each set of results.
b. Mean release and 99th percentile release are for all accidents in which a release occurs. 99th percentile accident is the 99th percentile release given an accident.
c. Overall mission values weighted by total probability of release for each mission phase.

Essential features of the results for the MMRTG are as follows:

- Phase 0 (Prelaunch): During the Prelaunch period, prior to ignition of the Stage 1 liquid rocket engine, on-pad accidents could result in a release at a total probability of 1.07×10^{-5} (1 in 93,000). The mean source term given an accident is estimated to be 0.09 Ci, the mean source term given a release is estimated to be 0.28 Ci, the 99th percentile given an accident is estimated to be 0.048 Ci, while the 99th percentile source term given a release is estimated to be 6.7 Ci.
- Phase 1 (Early Launch): During Phase 1 from ignition to t_x s, after which there would be no potential for land impacts in the launch area, the total probability of release is 8.8×10^{-5} (1 in 11,000). The mean source term given an accident is estimated to be 1.7 Ci, the mean source term given a release is estimated to be 59 Ci, the 99th percentile given an accident is estimated to be 16 Ci, while the 99th percentile source term given a release is estimated to be 630 Ci.
- Phase 2 (Late Launch): In Phase 2 all accidents lead to impact of debris in the Atlantic Ocean. However, there are some very small releases in air from blast-generated debris. The total probability of release is 7.7×10^{-6} (1 in 130,000). The mean source term given an accident is estimated to be 0.000034 Ci, the mean source term given a release is estimated to be 0.016 Ci, the 99th percentile given an accident is estimated to be 0 Ci, while the 99th percentile source term given a release is estimated to be 0.23 Ci.
- Phase 3 (Suborbital Reentry): Accidents during Phase 3 include suborbital reentries. Prior to the attainment of Earth park orbit, these conditions could lead to prompt suborbital reentry within minutes. This could result in impacts of the intact SV entry vehicle and MMRTG along the vehicle flight path over the Atlantic Ocean and southern Africa. Additional suborbital land impacts are possible after crossing over Africa, depending on the launch vehicle selected and its nominal mission timeline. Should the SV impact land, releases are possible. The total probability of release in Phase 3 is estimated to be 1.5×10^{-5} (or 1 in 67,000). The mean source term given an accident is estimated to be 0.047 Ci, the mean source term given a release is estimated to be 42 Ci, the 99th percentile given an accident is estimated to be 0 Ci, while the 99th percentile source term given a release is estimated to be 930 Ci.
- Phases 4 (Orbital Reentry): Accidents which occur after attaining park orbit could result in orbital decay reentries from minutes to years after the accident, affecting Earth surfaces between approximately 29° North Latitude and 29° South Latitude. The SV and MMRTG would break apart during reentry, releasing the GPHS modules. The modules would survive reentry, but could release fuel if they impact hard rock. The total probability of release is estimated to be 2.6×10^{-4} (or 1 in 3,800). The mean source term given an accident is estimated to be 0.030 Ci, the mean source term given a release is estimated to be 0.53 Ci, the 99th percentile given an accident is estimated to be 0.65 Ci, while the 99th percentile source term is estimated to be 6.2 Ci.

- Phase 5 (Long-Term Orbital Reentry): There is a set of reentry accidents which occur after attaining Earth escape. This could result in return to Earth from a heliocentric orbit many years after the accident if the spacecraft misses Mars, affecting Earth surfaces at any latitude. The reentry velocity would be larger than in Phase 4 and the heating environment would be more severe. The total probability of release is estimated to be 9.4×10^{-8} (or 1 in 11,000,000). The mean source term given an accident is estimated to be 0.073 Ci, the mean source term given a release is estimated to be 0.77 Ci, the 99th percentile given an accident is estimated to be 1.48 Ci, while the 99th percentile source term is estimated to be 7.8 Ci.

RADIOLOGICAL CONSEQUENCES, MISSION RISKS AND UNCERTAINTIES

The radiological consequences and mission risks due to the potential PuO_2 releases presented above are presented below. Uncertainties in the reported results are also discussed. The methodology used in developing estimates for the radiological consequences and mission risks is presented in the NRA [1].

Radiological Consequences

The radiological consequences resulting from the given accident scenarios have been calculated in terms of: 1) maximum individual dose, 2) collective dose, 3) health effects, and 4) land area contaminated at or above specified levels. The radiological consequences are based on atmospheric transport and settling simulations. Biological effects models, based on methods prescribed by the National Council on Radiation Protection and Measurements (NCRP) and the International Commission on Radiological Protection (ICRP), have been applied in past missions to predict the number of incremental latent cancer fatalities over 50 years (health effects) induced following a fuel release accident and assuming no mitigation measures. This present analysis uses scaling laws (consequences per Ci of fuel released) developed from more detailed calculations.

Multiple exposure pathways are considered in these types of analysis. One pathway is direct inhalation of the released cloud, which could occur over a short duration (minutes to hours), accompanied by the dose received due to direct immersion within a passing cloud (cloudshine). The other exposure pathways result from deposition onto the ground and are calculated over a 50-yr exposure period. These pathways include groundshine, ingestion, and additional inhalation from resuspension. A 50-year committed dose period is assumed for PuO_2 that is inhaled or ingested.

The maximum individual dose is the mean (for historical meteorological conditions) maximum (for location) dose delivered to a single individual for a given accident, considering the probability distribution over all release conditions. Collective dose is the sum of the radiation dose received by all individuals exposed to radiation from a given release in units of "person-rem." Internal doses are determined using particle-size dependent dose conversion factors based on ICRP-66/67 [8,9] and ICRP-60 [10].

The health effects represent incremental cancer fatalities over 50 years induced by releases, determined using a health effect estimator of 6×10^{-4} fatalities per person-rem for the general population based on recommendations by the Interagency Steering Committee on Radiation Standards (ISCORS) [11]. This is an update to the previous values of the ICRP-60 estimators of 5×10^{-4} fatalities per person-rem for the general population and 4×10^{-4} for workers [10]. The health effects estimators are based on a linear, no-threshold model relating health effects and effective dose. This means that health effects scale linearly as the dose decreases down to zero, rather than assuming a threshold dose below which there would be no health effects. To estimate the total health effects within the population, the probability of incurring a health effect is estimated for each individual in the exposed population, given a release, and then the probabilities are summed over that population.

Potential environmental contamination criteria for assessing contaminated land areas are 1) areas exceeding given screening activity concentration levels (0.1 and 0.2 $\mu Ci/m^2$), and 2) dose-rate related criteria (15, 25, and 100 mrem/yr) considered by the U.S. Environmental Protection Agency (EPA), the Nuclear Regulatory Commission (NRC), and DOE in evaluating the need for land cleanup following radioactive contamination [12]. The results for land area contaminated are reported in terms of the area contaminated at or above a level 0.2 $\mu Ci/m^2$, a reference contamination level considered in the risk analyses of previous missions. The area of land contaminated above the

EPA lifetime-risk criterion, associated with an average annual dose rate criterion of 15 mrem/yr, could be higher or lower than the land area contaminated above the 0.2 $\mu Ci/m^2$ level in the first year following the release, depending on the particle size distribution of the release and the time-dependent resuspension factor (the ratio of the airborne concentration to the ground concentration). The resuspension contribution to dose assumes that no mitigation measures are taken. Following the first year, areas contaminated above the 15 mrem/yr criterion would be expected to decrease to values comparable to that associated with the 0.2 $\mu Ci/m^2$ level as the resuspension factor decreases in time.

The potential for crop contamination is based on the Derived Intervention Limit (DIL), as defined by the Food and Drug Administration (FDA) [13]. An average DIL of 2.5 Bq/kg (edible portion of the crop) is assumed. The DIL is converted to a cropland deposition threshold by considering the annual average uptake factor of deposited radionuclides and annual crop yields (kilogram of edible food per square meter of land). The number of square kilometers of cropland that exceeds this value for each crop type is determined from atmospheric transport calculations, cropland location maps, and the average fraction of each crop type in the Kennedy Space Center vicinity or the state of Florida, depending on the extent of the plume.

A summary of the radiological consequences by mission phase is presented in Table 2 and Table 3 in terms of the mean and 99th percentile values, respectively. Two mean values are displayed: one is based on the average of all release amounts when an accident occurs (including accidents with no release), the other is based on the average release amount considering only non-zero releases. Most accidents do not result in a release; hence the mean consequence given an accident is lower than the mean consequence given a release.

The 99th percentile radiological consequence is the value predicted to be exceeded 1 percent of the time. In this context, the 99th percentile value reflects the potential for higher radiological consequences to the exposed population at lower probabilities than would normally be expected from accidents involving a release to the environment. Again, two 99th percentile values are displayed: one is based on the 99th percentile of all release amounts when an accident occurs (including accidents with no release), the other is based on the 99th percentile release amount considering only non-zero releases. Most accidents do not result in a release; hence the 99th percentile consequence given an accident is lower than the mean consequence given a release. For some launch phases, the probability of a release is so low that the 99th percentile release is zero and the 99th percentile consequence is zero (given an accident).

TABLE 2. Mean Radiological Consequence Summary for the MMRTG[a,b,c]

Mission Phase	Accident Probability	Release Proba-bility	Maximum Individual Dose (rem)		Collective Dose (person-rem)		Health Effects		Land Contamination (km^2)		Cropland Intervention (km^2)	
			Given an Accident	Given a Release	Given an Accident	Given a Release	Given an Accident	Given a Release	Given an Accident	Given a Release	Given an Accident	Given a Release
0 (Prelaunch)	3.28E-05	1.07E-05	9.42E-05	2.88E-04	7.50E-01	2.29E+00	4.50E-04	1.38E-03	1.15E-02	3.52E-02	2.02E-04	6.17E-04
1 (Early Launch)	3.12E-03	8.77E-05	1.70E-03	6.04E-02	1.35E+01	4.81E+02	8.12E-03	2.89E-01	2.07E-01	7.37E+00	3.64E-03	1.29E-01
2 (Late Launch)	3.63E-03	7.71E-06	3.48E-08	1.64E-05	2.77E-04	1.30E-01	1.66E-07	7.84E-05	4.24E-06	2.00E-03	7.45E-08	3.51E-05
3 (Suborbital)	1.31E-02	1.48E-05	4.81E-05	4.26E-02	3.83E-01	3.39E+02	2.30E-04	2.04E-01	5.88E-03	5.20E+00	1.03E-04	9.12E-02
4 (Orbital)	4.66E-03	2.61E-04	3.03E-05	5.39E-04	2.41E-01	4.30E+00	1.45E-04	2.58E-03	3.70E-03	6.59E-02	6.49E-05	1.16E-03
5 (Long-Term)	1.00E-06	9.43E-08	7.46E-05	7.91E-04	5.94E-01	6.30E+00	3.57E-04	3.78E-03	9.10E-03	9.66E-02	1.60E-04	1.69E-03
Overall Mission	2.46E-02	3.83E-04	2.47E-04	1.59E-02	1.97E+00	1.26E+02	1.18E-03	7.59E-02	3.02E-02	1.94E+00	5.30E-04	3.40E-02

a. The table presents composite results for the LVs under consideration, determined by taking the probability-weighted value of each set of results.
b. Land area contaminated above a screening level of 0.2 $\mu Ci/m^2$.
c. Overall mission values weighted by total probability of release for each mission phase.

TABLE 3. 99th Percentile Radiological Consequence Summary for the MMRTG[a,b,c]

Mission Phase	Probability of 99th Percentile	Release Proba-bility	Maximum Individual Dose (rem)		Collective Dose (person-rem)		Health Effects		Land Contamination (km^2)		Cropland Intervention (km^2)	
			Given an Accident	Given a Release	Given an Accident	Given a Release	Given an Accident	Given a Release	Given an Accident	Given a Release	Given an Accident	Given a Release
0 (Prelaunch)	3.28E-07	1.07E-07	4.86E-05	6.83E-03	3.87E-01	5.44E+01	2.32E-04	3.27E-02	5.93E-03	8.34E-01	1.04E-04	1.46E-02
1 (Early Launch)	3.12E-05	8.77E-07	1.67E-02	6.48E-01	1.33E+02	5.16E+03	8.01E-02	3.10E+00	2.04E+00	7.91E+01	3.59E-02	1.39E+00
2 (Late Launch)	3.63E-05	7.71E-08	-	2.36E-04	-	1.88E+00	-	1.13E-03	-	2.88E-02	-	5.05E-04
3 (Suborbital)	1.31E-04	1.48E-07	-	9.51E-01	-	7.57E+03	-	4.55E+00	-	1.16E+02	-	2.04E+00
4 (Orbital)	4.66E-05	2.61E-06	6.66E-04	6.30E-03	5.30E+00	5.01E+01	3.19E-03	3.01E-02	8.13E-02	7.69E-01	1.43E-03	1.35E-02
5 (Long-Term)	1.00E-08	9.43E-10	1.51E-03	8.01E-03	1.20E+01	6.37E+01	7.23E-03	3.83E-02	1.85E-01	9.77E-01	3.24E-03	1.72E-02
Overall Mission	2.46E-04	3.83E-06	9.71E-06	3.49E-01	7.73E-02	2.78E+03	4.65E-05	1.67E+00	1.19E-03	4.26E+01	2.08E-05	7.48E-01

a. The table presents composite results for the LVs under consideration, determined by taking the probability-weighted value of each set of results.
b. Land area contaminated above a screening level of 0.2 $\mu Ci/m^2$.
c. Overall mission values weighted by total probability of release for each mission phase.

Mission Risks

A summary of the mission risks is presented in Table 4. For the purpose of the NRA [1], risk is defined as the expectation of health effects in a statistical sense (i.e., the product of total probability times the health effects resulting from a release, and then summed over all conditions leading to a release). The risk is determined for each mission phase and the overall mission. Since the health effects resulting from a release equals the sum of the probability of a health effect for each individual in the exposed population, risk can also be interpreted as the total probability of one health effect given the mission (for risk much less than one). All of the Phases 0 and 1 releases are within a few km of the launch pad. Nearly all of the Phase 3 releases are within southern Africa. All of the Phase 4 releases are between 29° N and 29° S latitude. Phase 5 releases can occur anywhere on the globe where there is land. The mission risk for the MMRTG configuration is 2.9x10^{-5}.

TABLE 4. Mission Risk Summary for the MMRTG[a]

Mission Phase	Accident Probability	Mean Health Effects, Given an Accident	Mission Risks
0 (Prelaunch)	3.28E-05	4.50E-04	1.48E-08
1 (Early Launch)	3.12E-03	8.12E-03	2.53E-05
2 (Late Launch)	3.63E-03	1.66E-07	6.04E-10
3 (Suborbital)	1.31E-02	2.30E-04	3.02E-06
4 (Orbital)	4.66E-03	1.45E-04	6.75E-07
5 (Long-Term)	1.00E-06	3.57E-04	3.57E-10
Overall Mission	2.46E-02	1.18E-03	2.90E-05

a. The table presents composite results for the LVs under consideration, determined by taking the probability-weighted value of each set of results.

For the Mars 2020 configuration with an MMRTG, Phase 1 accidents contribute 87 percent of the risk. Another descriptor used in characterizing risk is the maximum individual risk, presented in Table 5. The maximum individual risk is defined in the NRA [1] to be the risk to the person receiving the maximum individual dose in a given mission phase.

TABLE 5. Maximum Individual Risk for the MMRTG[a]

Mission Phase	Accident Probability	Mean Maximum Individual Dose, Given an Accident (rem)	Maximum Individual Risk
0 (Prelaunch)	3.28E-05	9.42E-05	1.86E-12
1 (Early Launch)	3.12E-03	1.70E-03	3.18E-09
2 (Late Launch)	3.63E-03	3.48E-08	7.59E-14
3 (Suborbital)	1.31E-02	4.81E-05	3.80E-10
4 (Orbital)	4.66E-03	3.03E-05	8.47E-11
5 (Long Term)	1.00E-06	7.46E-05	4.48E-14

a. The table presents composite results for the LVs under consideration, determined by taking the probability-weighted value of each set of results.

Uncertainties

An analysis to estimate uncertainties in probabilities, source terms, radiological consequences, and mission risks has not been performed as part of the NRA [1]. Such an analysis will be performed in the FSAR. Based on experience with uncertainty analyses in the risk assessment of past missions (e.g., the Cassini, Mars Exploration Rover 2003, Pluto New Horizons, and Mars Science Laboratory), the uncertainty in the mission risk for the Mars 2020 mission can be estimated. Those analyses have shown that the uncertainty in the mission risk is dominated by uncertainties in the launch accident probability and the overall probability is about a factor of 25 higher or lower than the median for the 5th and 95th percentiles. For the MMRTG option, treating the best estimate of the Mars 2020 mission risk of 2.9x10^{-5} as the median of the uncertainty probability distribution (i.e., it is equally probable that the mission risk could be higher or lower than this value), the mission risk at the 5th and 95th percentile confidence levels are estimated to be 1.2x10^{-6} and 7.3x10^{-4}, respectively.

CONCLUSION

In the summer of 2020, NASA plans to launch a rover to the surface of Mars as part of the Mars 2020 mission. One option for the proposed rover includes the use of radioactive materials in a single MMRTG to provide continuous power for the mission. NASA has prepared an EIS for the mission in accordance with the NEPA. The EIS includes information on the risks of mission accidents to the general public and on-site workers at the launch complex. The NRA addresses the responses of the proposed MMRTG option to potential accident and abort conditions during the launch opportunity for the Mars 2020 mission and the associated consequences [1]. This information provides the technical basis for the radiological risks of both options for the EIS.

All of the Phases 0 and 1 releases are within a few km of the launch pad. Nearly all of the Phase 3 releases are within southern Africa. All of the Phase 4 releases are between 29° N and 29° S latitude. Phase 5 releases can occur anywhere on the globe where there is land. For the Mars 2020 configuration with an MMRTG, Phase 1 accidents contribute 87 percent of the risk. The mission risk for the MMRTG configuration is 2.9×10^{-5}, and the 5th and 95th percentile confidence levels are estimated to be 1.2×10^{-6} and 7.3×10^{-4}, respectively.

ACKNOWLEDGMENTS

Sandia National Laboratories is a multi-program laboratory managed and operated by Sandia Corporation, a wholly owned subsidiary of Lockheed Martin Corporation, for the U.S. Department of Energy's National Nuclear Security Administration under contract DE-AC04-94AL85000.

REFERENCES

[1] Clayton, D.J., Bignell, J., Jones, C.A., Rohe, D.P., Flores, G.J., Bartel, T.J., Gelbard, F., Le, S., Morrow, C.W., Potter, D.L., Young, L.W., Bixler, N.E. and Lipinski, R.J., *Nuclear Risk Assessment for the Mars 2020 Mission Environmental Impact Statement*, SAND2013-10589, Sandia National Laboratories, Albuquerque, NM, January 2014.

[2] National Aeronautics and Space Administration, *Final Environmental Impact Statement for the Mars Science Laboratory Mission, Volume 1, Executive Summary and Chapters 1 through 8*, Science Mission Directorate, National Aeronautics and Space Administration, Washington, DC, November 2006.

[3] ASCA, Incorporated, *Mars 2020 Launch Accident Probability Data for EIS Risk Assessment, Revision Draft*, AR 13-02, Prepared for National Aeronautics and Space Administration, Kennedy Space Center, September 2013.

[4] United Launch Alliance, *Atlas V Launch Services User's Guide*, United Launch Alliance, Centennial, CO, March 2010.

[5] United Launch Alliance, *Delta IV Launch Services User's Guide,* United Launch Alliance, Centennial, CO, September 2013.

[6] Space Exploration Technologies, *Falcon 9 Launch Vehicle Payload User's Guide, Rev 1*, SCM-2008-010-Rev-1, Space Exploration Technologies Corporation (SpaceX), Hawthorne, CA 2009.

[7] Space Exploration Technologies, *Falcon Heavy Launch Vehicle Payload User's Guide, Rev 0*, Space Exploration Technologies Corporation (SpaceX), Hawthorne, CA 2013.

[8] ICRP. International Commission on Radiological Protection, *Human Respiratory Tract Model for Radiological Protection*, ICRP-66, 1994.

[9] ICRP. International Commission on Radiological Protection, *Age-dependent Doses to Members of the Public from Intake of Radionuclides: Part 2, Ingestion Dose Coefficients*, ICRP-67, 1993.

[10] ICRP. International Commission on Radiological Protection, *1990 Recommendations of the International Commission on Radiological Protection*, ICRP-60, 1990.

[11] ISCORS 2002-02. Interagency Steering Committee on Radiation Standards, *A Method for Estimating Radiation Risk from Total Effective Dose Equivalent (TEDE) Final Report*, ISCORS Technical Report 2002-02, ISCORS, Environmental Protection Agency, Washington, DC 2002.

[12] U.S. EPA, *Radiation Site Cleanup Regulations: Technical Support Document for the Development of Radionuclide Cleanup Levels for Soil*, EPA 402-R-96-0111 A, Environmental Protection Agency, 1994.

[13] D. Thompson, *Accidental Radioactive Contamination of Human Food and Animal Feeds: Recommendations for State and Local Agencies*, U.S. Department Of Health and Human Services Food and Drug Administration Center for Devices and Radiological Health Rockville, MD, 1998.

Characterization of Pu-238 Heat Source Granule Containment

Paul D. Richardson[1], Joey Sanchez[1], Angelique D. Neuman[2], Rene Chavarria[3]

[1]NCO-5, Los Alamos National Laboratory, P.O. Box 1663, Los Alamos, NM 87545
[2]MST-16, Los Alamos National Laboratory, P.O. Box 1663, Los Alamos, NM 87545
[3]MET-1, Los Alamos National Laboratory, P.O. Box 1663, Los Alamos, NM 87545

Abstract. The Milliwatt Radioisotopic Themoelectric Generator (RTG) provides power for permissive-action links. Essentially these are nuclear batteries that convert thermal energy to electrical energy using a doped silicon-germanium thermopile. The thermal energy is provided by a heat source made of 238Pu, in the form of 238PuO2 granules. The granules are contained by 3 layers of encapsulation. A thin T-111 liner surrounds the 238PuO2 granules and protects the second layer (strength member) from exposure to the fuel granules. An outer layer of Hastalloy-C protects the T-111 from oxygen embrittlement. The T-111 strength member is considered the critical component in this 238PuO2 containment system. Any compromise in the strength member seen during destructive testing required by the RTG surveillance program is characterized. The T-111 strength member is characterized through Scanning Electron Microscopy (SEM), and Metallography. SEM is used in the Secondary Electron mode to reveal possible grain boundary deformation and/or cracking in the region of the strength member weld. Deformation and cracking uncovered by SEM are further characterized by Metallography. Metallography sections are mounted and polished, observed using optical microscopy, then documented in the form of microphotographs. SEM mat further be used to examine polished Metallography mounts to characterize elements using the SEM mode of Energy Dispersive X-ray spectroscopy (EDS).

Keywords: Characterization, Metallography, Scanning Electron Microscopy

INTRODUCTION

This paper describes the characterization of the metallurgical condition of decommissioned Radioisotopic Thermoelectric Generator (RTG) heat sources. The heat generating component of the heat source is $^{238}PuO_2$ in the form of granules. Due to the emission of radiation and its highly corrosive nature the metal selected for its containment was T-111, an alloy of Tantalum and Hafnium. A thin layer of T-111 called a liner surrounds the $^{238}PuO_2$ granules and protects the second thicker layer of T-111 called a strength member. Since T-111 can be subject to oxygen embrittlement, a layer of Hastelloy C is a third layer of containment to protect the T-111 from this. The strength member is the critical component in the containment system and is the focus for characterization of its metallurgical condition.

The techniques used for characterization are Scanning Electron Microscopy (SEM) and Metallography. The heat source is dismantled, and the $^{238}PuO_2$ granules are removed. The strength member weld is characterized by SEM used in Secondary Electron mode to reveal possible grain boundary deformation and/or cracking in the region of the strength member weld. The weld only is characterized since the weld is considered the weakest part of the strength member. If deformation and/or cracking are found, the weld is further characterized by Metallography. The polished metal surfaces in the Metallography mounts may be subject to elemental analysis of the metal surface using SEM in the Energy Dispersive X-ray Spectroscopy (EDS).

HEAT SOURCE DISASSEMBLY

The first step in the disassembly process is to remove the Hastelloy C outer clad. This is accomplished by using a high speed saw with a carborundum blade to cut the outer clad off circumferentially. The cut is made only deep enough to penetrate the outer clad of the heat source so that the second layer (strength member) is intact. Optical photographs are taken of the strength member exterior. The strength member and liner are de-fueled by drilling through the strength member and liner with a drill press while the strength member is held in a fixture. Once both layers of containment have been penetrated the fuel can be emptied from the strength member and liner. The resultant fuel is weighed, and placed in a fuel storage container. A cut is made through the circumference of the second layer (strength member) in order to remove it from the liner leaving the liner intact. Optical photographs are taken of the third layer (liner) exterior after which the liner is cut in half circumferentially. Optical photographs are taken of the strength member and liner interiors. Figures 1, 2, and 3 are optical images of the outer clad, strength member, and liner respectively.

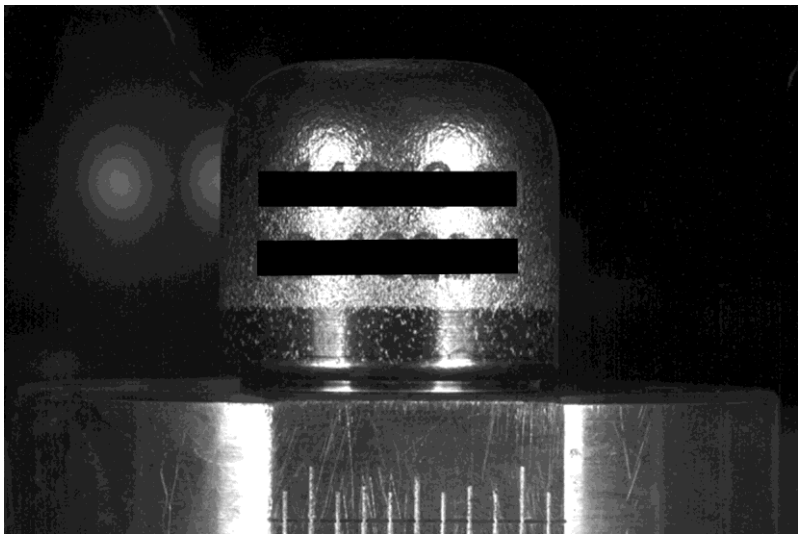

FIGURE 1. Heat Source Outer Clad.

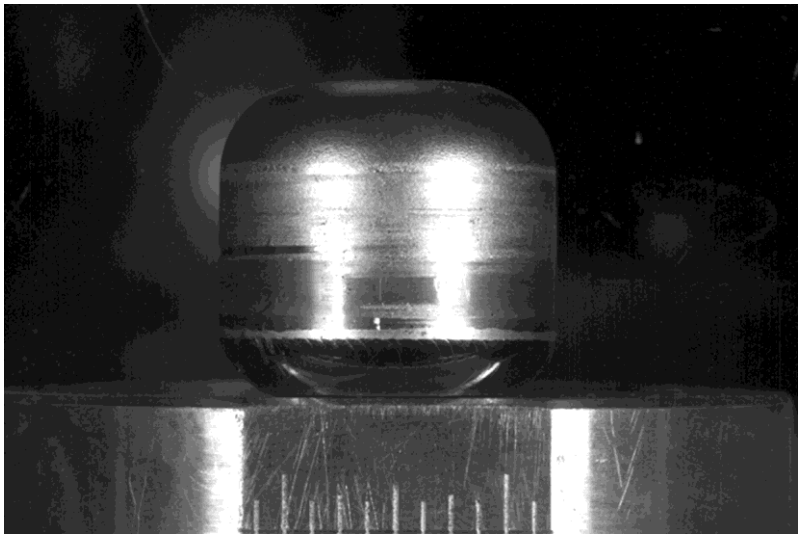

FIGURE 2. Strength Member

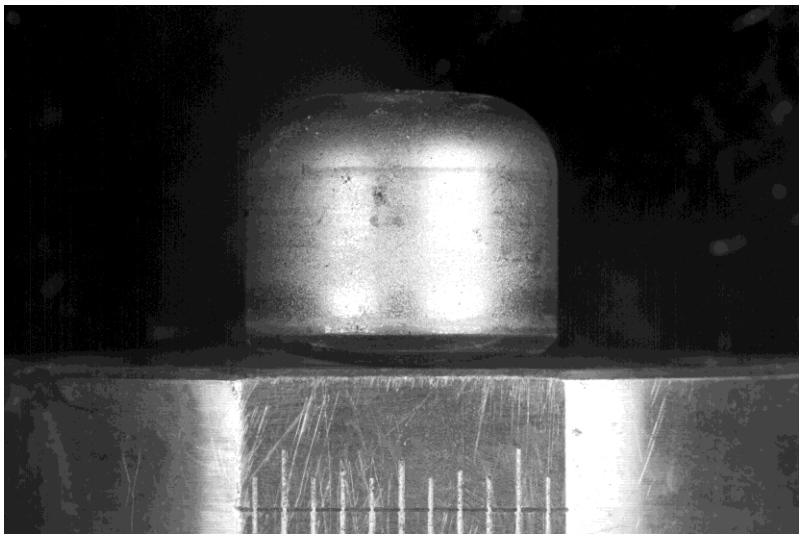

FIGURE 3. Liner

STRENGTH MEMBER PREPARATION FOR SEM ANALYSIS

The lid portion of the strength member is separated from the side wall as close as possible to the weld connecting the respective components. This is done in order for the SEM mount positioning system to be adjusted to allow the detector to analyze the weld and a small portion of the sidewall without remounting the part several times (remounting the part is avoided due to $^{238}PuO_2$ contamination). The interior weld surface (which would be exposed to the $^{238}PuO_2$ granules in the case of a liner failure) will be examined in its entirety with SEM (in secondary electron mode). The separated lid is submitted to the Interfacial Science team of our Materials Science & Technology division for the SEM analysis. Figure 4 identifies exterior strength member components, while figures 5 and 6 are optical photos of the interior and exterior strength member lid.

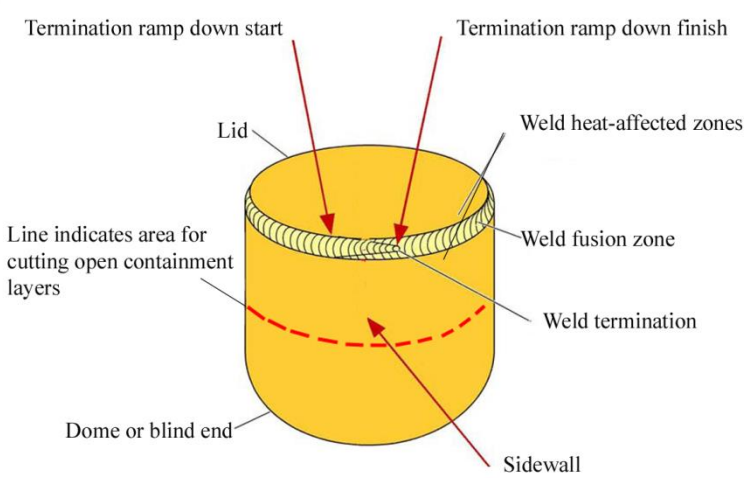

FIGURE 4. Identification of strength member components

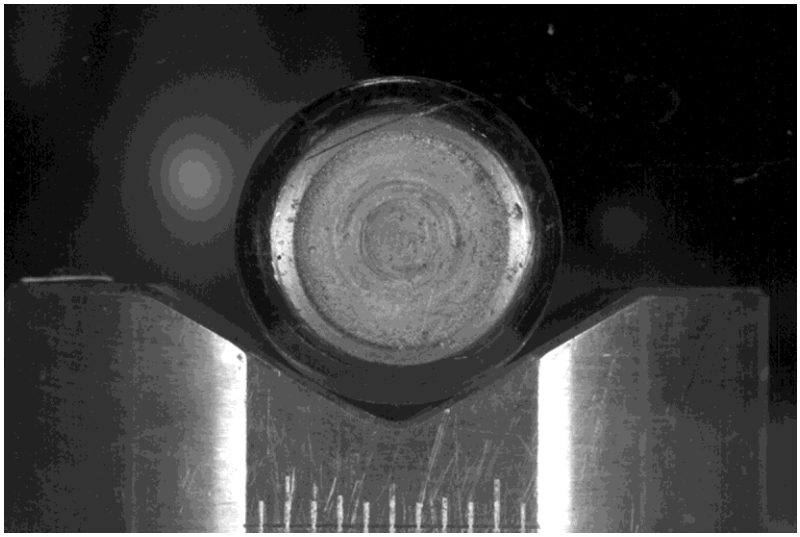

FIGURE 5. The Exterior of the Strength Member Showing the Lid and Exterior Weld Surface.

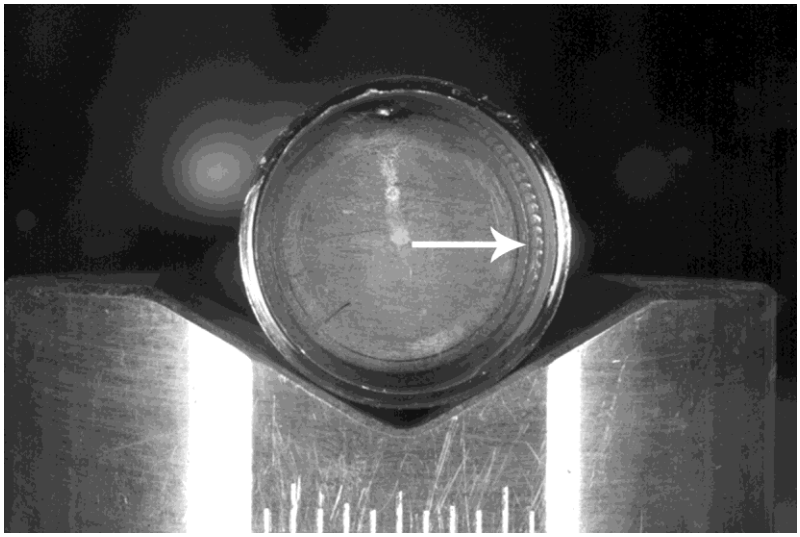

FIGURE 6. The Interior of the Strength Member Showing the Lid and Interior Weld Surface. Arrow Indicates the Interior Weld Surface Which will be Examined by SEM.

SEM ANALYSIS

Examination of the interior weld surface will indicate anomalous areas such as cracks and other degradation of the weld surface. The types of cracking that may be expected to occur are: intergranular stress-rupture cracks, intergranular fracture, intergranular secondary cracking, and subcritical cracking. The relative positions of anomalous cracking are noted within the following areas: weld fusion zone, weld heat affected zone, and the area within a position defined by the weld ramp down termination start and the weld ramp down termination finish. The weld heat affected zone extends from both sides of the weld fusion zone into the strength member lid, and the strength member sidewall. Results are reported back to our team and are used to indicate positions where the strength member lid can be sectioned for metallography.

Figures 7 and 8 are examples of SEM images; in this case portions of non-anomalous results for a strength member.

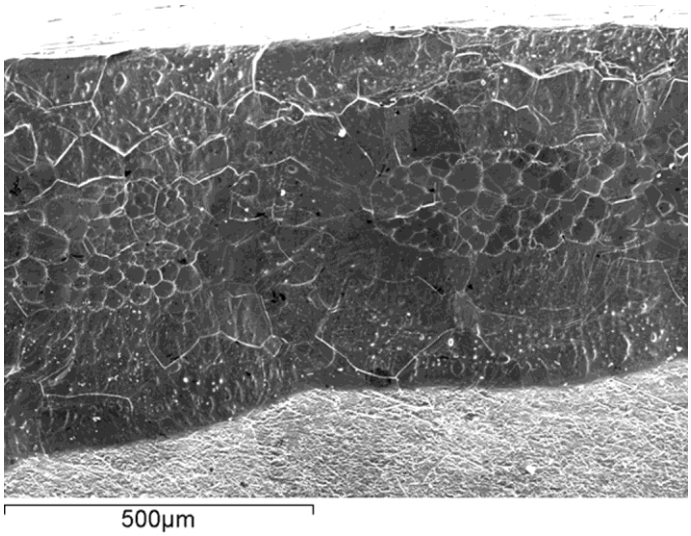

FIGURE 7. SEM Image of a Strength Member Non-Anomalous Weld Fusion Zone.

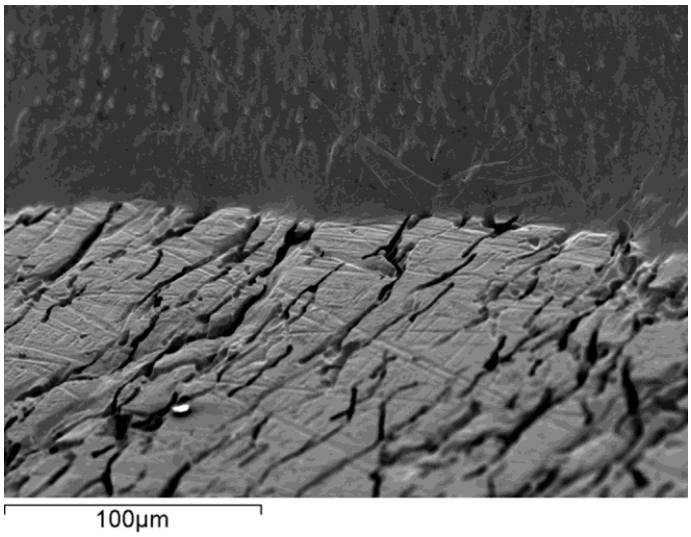

FIGURE 8. SEM Image of a Strength Member Non-Anomalous Weld Fusion Zone with Part of the Weld Heat Affected Zone.

METALLOGRAPHY

Anomalous areas indicated by SEM analysis are sectioned out of the strength member lid, mounted in epoxy, ground, polished and etched following a metallographic preparation procedure developed for T-111 alloy. Photomicrographs of the prepared mounted surfaces will produced to document the metallography results. Figures 9 and 10 are examples of non-anomalous metallography photomicrographs from a strength member, while figure 11 is an anomalous metallography photomicrograph from a strength member.

FIGURE 9. Metallography Microphotograph of a Strength Member Non-Anomalous Weld Heat Affected Zone with Part of the Weld Fusion Zone.

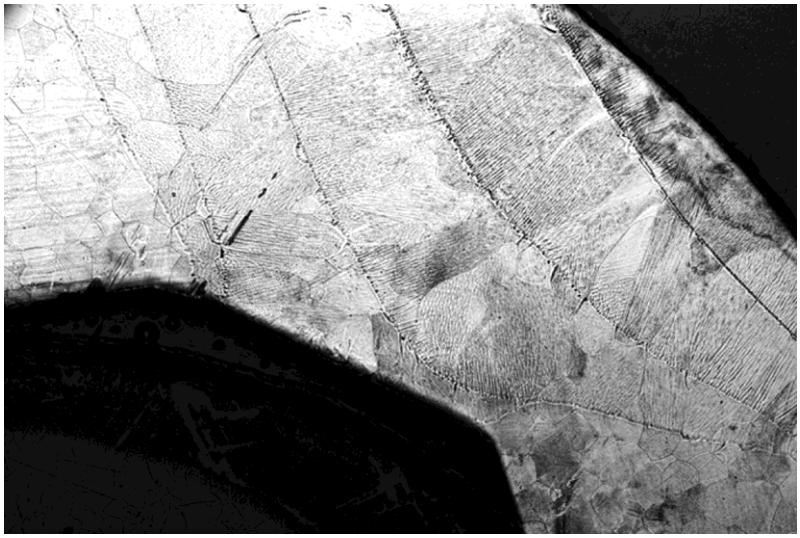

FIGURE 10. A Metallograph Microphotograph of a Non-Anomalous Weld Fusion Zone with the Weld Heat Affected Zones.

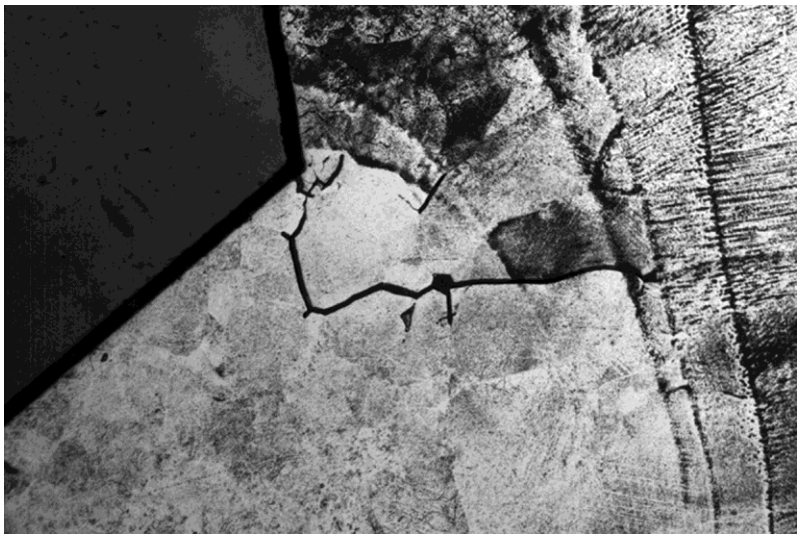

FIGURE 11. A Metallography Microphotograph of an Anomalous Strength Member Weld Fusion Zone.

SEM ENERGY DISPERSIVE X-RAY SPECTROSCOPY (EDS)

Anomalous areas seen in the photomicrographs require the metallography mounts to be resubmitted to the Interfacial Science team of our Materials Science & Technology division for SEM Energy Dispersive X-ray Spectroscopy (EDS) to characterize possible contaminates. An elemental distribution map of up to four elements or contaminants is provided to our team. Figures 12 and 13 are examples of EDS results from a strength member.

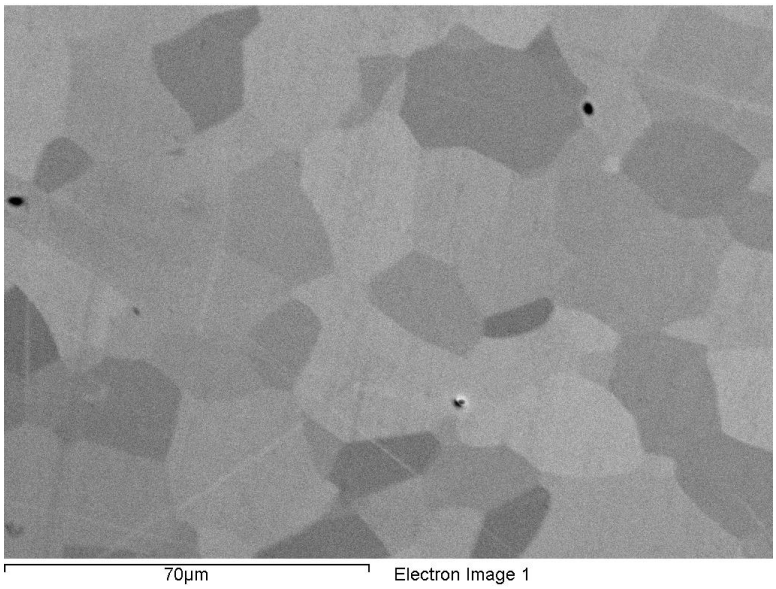

FIGURE 12. SEM EDS Electron Image

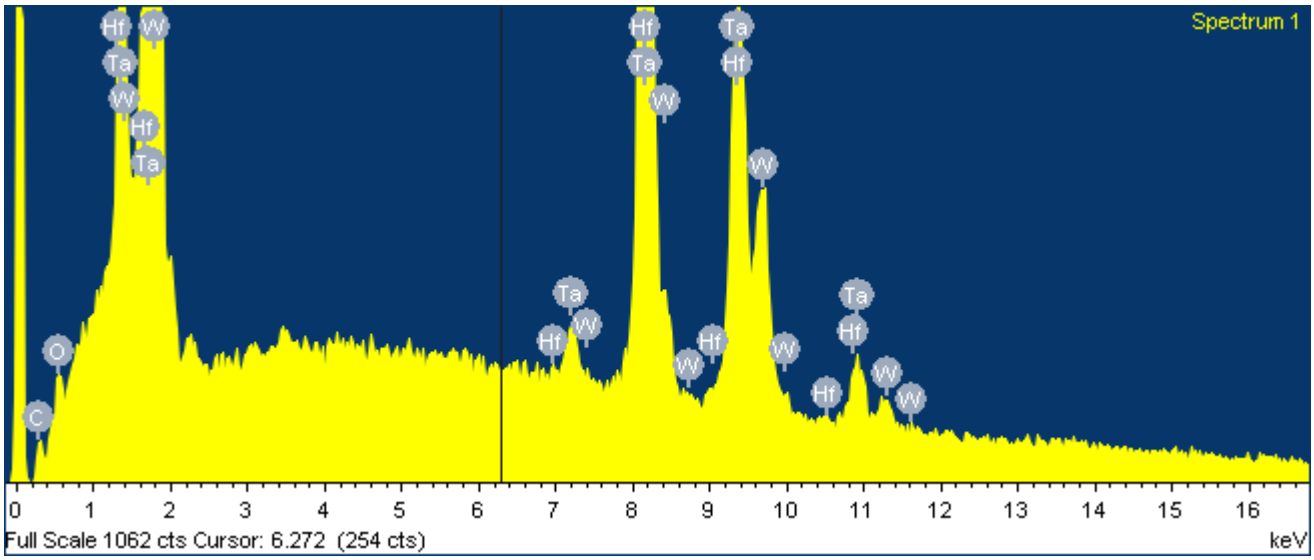

FIGURE 13. SEM EDS Elemental Distribution Indicating High Concentrations of Tantalum and Hafnium

CONCLUSION

Scanning Electron Microscopy (SEM) and Metallography are the techniques used in the characterization of the metallurgical condition of decommissioned Radioisotopic Thermoelectric Generator (RTG) heat sources. The T-111 heat source strength member weld is characterized by SEM used in Secondary Electron mode to reveal possible grain boundary deformation and/or cracking in the region of the strength member weld. If deformation and/or cracking are found, the weld is further characterized by Metallography. The polished metal surfaces in the Metallography mounts may be subject to elemental analysis of the metal surface using SEM in the Energy Dispersive X-ray Spectroscopy (EDS).

Design-Based Model of a Closed Brayton Cycle for Space Power Systems

Guilherme B. Ribeiro[1], Lamartine N. F. Guimarães[1,2] and Francisco A. Braz Filho[1]

[1] *Institute for Advanced Studies, Department of Aerospace Science and Technology, São José dos Campos, Brazil*
[2]*Department of Control and Automation Engineering, UNIESP, Jacareí*
+55 012 39475484; gbribeiro@ieav.cta.br

Abstract. Nuclear power systems turned to space electric propulsion differs strongly from usual ground-based power systems regarding the importance of overall size and weight. For propulsion power systems, size/weight are essential drivers that should be minimized during conception processes. Considering that, this paper aims the development of a design-based model of a closed Brayton cycle that applies the thermal conductance of the main components in order to predict the energy conversion performance, allowing its use as preliminary tool for the heat exchangers and the radiator panel sizing. The centrifugal-flow turbine and compressor characterization were achieved using algebraic equations from literature data. The binary mixture of He-Xe with molecular weight of 40 g/mole is applied and the impact of the components sizing in the energy efficiency is evaluated in this paper, including the radiator panel area. Moreover, an optimization analysis based on the final area/size of these components is performed.

Keywords: Simulation, Brayton, Optimization

INTRODUCTION

Space power systems present a set of novel aspects, when compared to ground-based power systems such as low power level, lightweight and a radiant heat rejection from the energy conversion scheme. For propulsion purposes, lighter power systems for the same power output promote more available mass for the payload. Furthermore, the high cost involved in sending the power systems into the space by current launch technologies makes its weight and size critical factors that can constrain the feasibility of nuclear power systems for space propulsion [1]. Therefore, a special attention should be focused on these aspects, since they perform high influence on the viability of use of such power systems.

The proposed Closed Brayton Cycle (CBC) is described schematically in Fig. 1. The generated heat of the fission power system is considered as heat source of the CBC. The outter space is applied as heat sink and a large radiator panel is used to remove the heat from the CBC by thermal radiation. The heat radiator panel plays an important role in the power system size, being the largest component. The gas turbine and compressor operate at very high speeds and are mounted with the electrical generator on a single shaft.

For ground-based power plants, gas Helim (He) has been selected as working fluid mainly because of its thermo-physical properties and chemical inertness. However, the mixture of He with other noble gases as Xenon (Xe) and Krypton (Kr) produces transport properties that are superior to those of the pure gases with similar molecular weights [2]. A He-Xe mixture with molecular weight of 40 g/mole has only 10% of turbomachinery loading and the same heat transfer coefficient, when compared with He [3].

The thermal-hydraulic management of the space reactor core applied in this study is supplied by several heat pipes placed inside the core as indicated by Fig. 2, where these heat pipes are surrounded by packed spheres of uranium

nitride (UN) immersed in liquid lead [4]. By the same token, heat pipes are applied to transfer the heat from the cold heat exchanger to the radiator panel. Thus, heat pipes are used as intermediate heat exchangers in order to couple thermally the heat source (reactor core) and heat sink (space) to the CBC.

For unmanned space applications, heat exchangers present the largest fraction of the total system mass (29.3%) [1]. Thus, a size optimization of both heat exchangers is vital for the design of an efficient and achievable CBC for space exploration purposes.

Considering all this aspects, the purpose of this work is to present a design-based steady state model of a CBC applied for nuclear space reactors. In the recent years, much attention is given for the development of nuclear space power plants, and in cases where CBC is considered as the energy conversion method, the performance modelling is commonly based on simplified thermodynamic models where the inlet pressure and temperature of the turbine and compressor were used as input [5]. Contrarily, this design-based model intends to apply the geometrical characteristics in order to estimate the performance and temperature along the cycle.

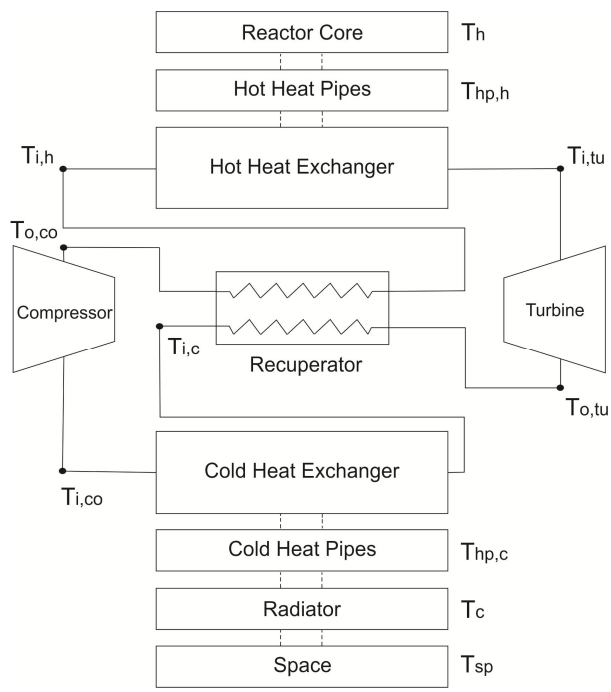

FIGURE 1. Proposed Space Power System.

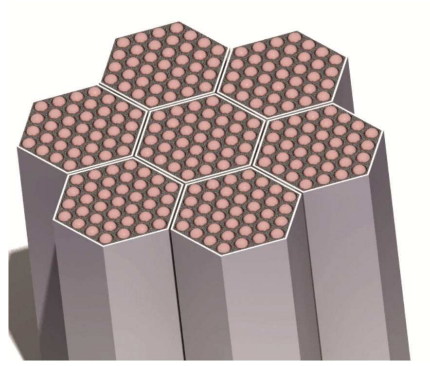

FIGURE 2. Cross-sectional view of nuclear reactor core.

A sensitivity analysis of the sizing of the main system components on the final efficiency will be discussed in details. Furthermore, an optimization approach is suggested in this paper, allowing the match between nuclear power system size and energy conversion efficiency.

MODEL DESCRIPTION

Cycle Components

As described, heat pipes are the components responsible for the heat transport from the reactor core to the hot heat exchanger and from the cold heat exchanger to the radiator panel. Considering these components as heat exchangers with constant thermal conductance and no heat transfer limits, the temperature drop along each heat pipe are proportional to the heat transfer rate and determined as

$$\dot{Q}_h = UA_{hp,h}(T_h - T_{hp,h}) \tag{1}$$
$$\dot{Q}_c = UA_{hp,c}(T_{hp,c} - T_c) \tag{2}$$

where $UA_{hp,h}$ and $UA_{hp,c}$ are the thermal conductance of the hot leg and cold leg heat pipes, respectively. The reactor core thermal power $\dot{Q}_h$ and temperature T_h are input with fixed values, independent of $UA_{hp,h}$. The hot and cold heat exchangers are defined based on effectiveness-NTU method [6]. Thus,

$$\dot{Q}_h = \dot{m}\, c_p \left(T_{hp,h} - T_{i,h}\right) \tag{3}$$
$$\dot{Q}_c = \dot{m}\, c_p \left(T_{i,c} - T_{hp,c}\right)\left[1 - e^{\frac{UA_c}{\dot{m}c_{p,c}}}\right] \tag{4}$$

where $\dot{m}$ is the gas mass flow rate and UA_h and UA_c are the overall thermal conductance of hot and cold heat exchangers, whereas the specific heat $c_{p,h}$ and $c_{p,c}$ were obtained based on temperatures $T_{i,h}$ and $T_{i,c}$, respectively. The energy balance from the CBC working fluid side is also applied for both heat exchangers as follows

$$\dot{Q}_h = \dot{m}\left(h_{i,tu} - h_{i,h}\right) \tag{5}$$
$$\dot{Q}_c = \dot{m}\left(h_{i,c} - h_{i,comp}\right) \tag{6}$$

where $h_{i,tu}$ and $h_{i,comp}$are entalpies at the turbine and compressor inlet, respectively. The gas enthalpy at the cold heat exchanger inlet $h_{i,c}$ and at the compressor outlet $h_{o,co}$ are obtained consecutively according to the recuperator effectiveness ε_r. Hence,

$$\varepsilon_r = \frac{h_{o,tu} - h_{i,c}}{h_{o,tu} - h_{o,co}} \tag{7}$$
$$h_{i,h} - h_{o,co} = h_{o,tu} - h_{i,c} \tag{8}$$

The turbine and compressor presented in the CBC can be defined as polytropic processes with expansion and compressor efficiencies (i.e η_{tu} and η_{co}) as follows

$$\frac{T_{i,tu}}{T_{o,tu}} = PR^{\left(\frac{\gamma_{tu}-1}{\gamma_{tu}}\right)\eta_{tu}} \tag{9}$$
$$\frac{T_{o,co}}{T_{i,co}} = PR^{\left(\frac{\gamma_{co}-1}{\gamma_{co}}\right)\frac{1}{\eta_{co}}} \tag{10}$$

where the term γ_{tu} and $\gamma_{co}$are the specific heat ratio of the working fluid calculated according to $T_{i,tu}$and $T_{i,co}$, respectively. The cycle pressure ratio, as well as the turbomachinery shaft speed ratio SR, are obtained via algebraic equations representing the performance map of the turbine and compressor [7]. Third-order polynomial regressions

with crossed-terms were performed based on the turbomachinery data available for a He-Xe mixture of 40 g/mole [8]. Thus,

$$\dot{m} = A_{tu} + B_{tu}.PR + C_{tu}.PR^2 + D_{tu}.PR^3 + E_{tu}.SR + F_{tu}.SR^2 + G_{tu}.SR^3 + H_{tu}.PR.SR + I_{tu}.PR^2.SR + J_{tu}.PR.SR^2 + K_{tu}.PR^2.SR^2 \quad (11)$$

$$\dot{m} = A_{co} + B_{co}.PR + C_{co}.PR^2 + D_{co}.PR^3 + E_{co}.SR + F_{co}.SR^2 + G_{co}.SR^3 + H_{co}.PR.SR + I_{co}.PR^2.SR + J_{co}.PR.SR^2 + K_{co}.PR^2.SR^2 \quad (12)$$

A coefficient of determination of no less than 98.8% was achieved for all four algebraic equations. Applying these representative equations for an arbitrary mass flow rate, a single value of PR and SR is achieved via Newton-Raphson method. Likewise, the efficiencies η_{tu} and η_{co} are also calculated algebraically dependent of mass flow rate and speed ratio as

$$\eta_{tu} = L_{tu} + M_{tu}.PR + N_{tu}.PR^2 + O_{tu}.PR^3 + P_{tu}.\dot{m} + Q_{tu}.\dot{m}^2 + R_{tu}.\dot{m}^3 + S_{tu}.PR.\dot{m} + T_{tu}.PR^2.\dot{m} + U_{tu}.PR.\dot{m}^2 + V_{tu}.PR^2.\dot{m}^2 \quad (13)$$

$$\eta_{co} = L_{co} + M_{co}.PR + N_{co}.PR^2 + O_{co}.PR^3 + P_{co}.\dot{m} + Q_{co}.\dot{m}^2 + R_{co}.\dot{m}^3 + S_{co}.PR.\dot{m} + T_{co}.PR^2.\dot{m} + U_{co}.PR.\dot{m}^2 + V_{co}.PR^2.\dot{m}^2 \quad (14)$$

The work resulted from the expansion and compression processes are obtained the energy balance. Therefore,

$$\dot{W}_{tu} = \dot{m}\left(h_{i,tu} - h_{o,tu}\right) \quad (15)$$

$$\dot{W}_{co} = \dot{m}\left(h_{o,co} - h_{i,co}\right) \quad (16)$$

The radiative heat transfer charged to extract the wasted heat from the cold heat pipe is represented as fin-tube geometry as follows

$$\dot{Q}_c = \sigma\epsilon A_r \eta_f \left(T_c^4 - T_{sp}^4\right) \quad (17)$$

where σ is the Stefan-Boltzmann constant, ϵ is the radiator emissivity, η_f is the fin efficiency and A_r is the area of radiating surface. The heat sink is represented by the outter space and presents a fixed temperature T_{sp}. The CBC mass flow rate is found iteratively through Newton-Raphson method [7], where the final solution is achieved when heat transfer rate $\dot{Q}_c$ is obtained from Eqs. 2 and 16. Lastly, the space power system efficiency is calculated as

$$\eta_{sys} = \frac{\left(\dot{W}_{tu} - \dot{W}_{co}\right)\eta_a}{\dot{Q}_h} \quad (18)$$

where η_a represents the alternator efficiency.

Fluid Thermodynamic Properties

Thermodynamic properties of He and Xe were obtained according to NASA library applied for ideal gases [9]. Gases He and Xe under high temperatures ($\geq$ 400 K) and low pressures ($\leq$ 2 MPa) present an ideal gas behavior and the effect of pressure on their compressibility factor, specific heats and transport properties can be neglected [3].

The molecular weight of 40 g/mole corresponds to a molar fraction of approximately 72% and 28% to Helium and Xenon, respectively. Each specie was calculated independently, as function of temperature whereas the He-Xe thermodynamic properties were evaluated within an ideal gas mixture approach.

Hypotheses and Settings

The model was implemented in the software Engineering Equation Solver (EES) to solve the equation set [10]. A thermal power $\dot{Q}_c$ of 160 kW and a surface temperature T_c of 1150 K were considered for the nuclear reactor core, whereas the temperature T_{sp} of 200 K is applied for the outter space. The recuperator effectiveness ε_r was arbitrated in 0.95, typical value for this type of equipment. For the same reason, the alternator efficiency η_a is set in 0.9.

In this model, it was assumed that no temperature drop occurs between the heat pipe and fin root and along the fin set. Hence, the fin efficiency η_f of 1.0 was applied, providing a minimum radiator area A_r, which is the ideal case for propulsion purposes. A typical radiator coating is considered, with a high emittance characteristic. Coatings with emissivity ϵ around 0.9 are usually found for this application [11] and as reference, this same value is employed for this study.

As a reference case, it has been arbitrated for heat pipes thermal conductance a value that represents a temperature drop of 50 K along heat pipes from the hot leg. Similarly, a 50 K temperature difference was applied between heat exchangers outlet and heat pipes as a manner to obtain heat exchangers thermal conductance. Furthermore, a radiator area A_r was chosen in order to satisfy the criteria of 0.3 for the power system efficiency η_{sys}. Based on these conditions, the reference case was calculated and its inputs and outputs can be seen in Tables 1 and 2, respectively.

In this study, it is considered the same type of heat exchanger for both legs and, also, the hypothesis of equal and constant heat transfer coefficient for heat exchangers is applied. Additionally, it is assumed that the thermal conductance UA_h and UA_c are function of heat transfer available area and consequently, heat exchanger volume and weight. Therefore, changes on the heat exchanger thermal conductance can be inferred as changes on the heat exchanger weight.

TABLE 1. Inputs from the reference case.

$\dot{Q}_h$	160 kW
T_h	1150 K
T_{sp}	200 K
ε_r	0.95
ϵ	0.9
η_f	1.0
η_a	0.9
$UA_{hp,h}$	3140 W/K
$UA_{hp,c}$	3140 W/K
UA_h	1430 W/K
UA_c	1139 W/K
A_r	122.4 m2

TABLE 2. Outputs from the reference case.

$\dot{Q}_c$	106658 kW
$\dot{W}_{tu}$	141972 kW
$\dot{W}_{co}$	88631 kW
$T_{i,tu}$	1049.0 K
$T_{o,tu}$	906.0 K
$T_{i,c}$	561.0 K
$T_{i,co}$	453.6 K
$T_{o,co}$	542.9 K
$T_{i,h}$	887.9 K
T_c	369.7 K
$T_{hp,h}$	1100.0 K
$T_{hp,c}$	403.6 K
PR	1.471
$\dot{m}$	1.91 kg/s
η_{tu}	0.94
η_{co}	0.86
η_{sys}	0.3

RESULTS AND DISCUSSION

A sensitivity analysis were performed, where the power system efficiency is evaluated under different components parameters. Figure 3 presents the influence of the hot heat exchanger thermal conductance UA_h on the system efficiency η_{sys}. As can be seen, the increase of thermal conductance provides an increase of the power system efficiency. Moreover, the system efficiency increases asymptotically, reaching a maximum value of 0.32 for the thermal conductance range. According to Figure 4, the design of a hot heat exchanger with UA_h higher than 1500 W/K will not bring worthy results, since a slightly increase of efficiency comes at the expensive of strong size/weight changes.

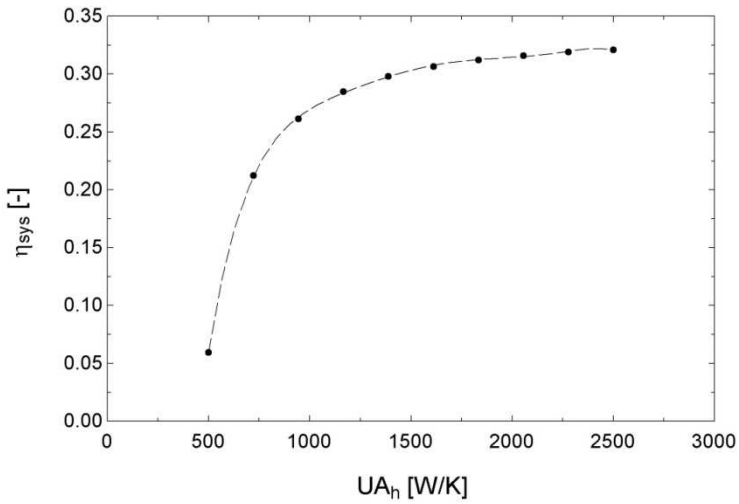

FIGURE 3. Power system efficiency as function of hot heat exchanger thermal conductance.

Figure 4 shows the influence of the cold heat exchanger thermal conductance UA_c on the system efficiency. Likewise the UA_h, the increase of UA_c resulted in an increase of η_{sys}. Furthermore, a commitment between cold heat exchanger weight and efficiency should also be performed in a power system conception phase, since higher values of UA_c resulted in a negligible η_{sys} increase. Comparing Figures 3 and 4, it can be seen that higher efficiencies η_{sys} are achievable when the cold heat exchanger is favored with thermal conductance (and consequently weight) increase. For the evaluated ranged, changes in the UA_h resulted in a maximum η_{sys} of around 0.325, whereas a maximum η_{sys} of 0.35 is obtained varying UA_c.

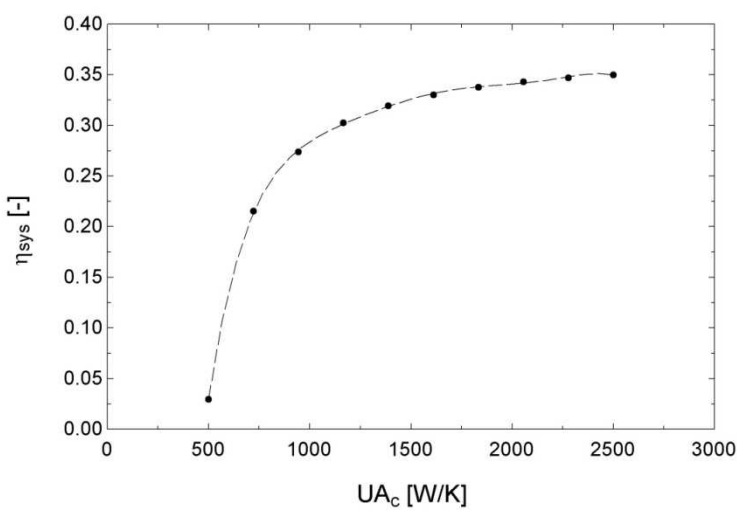

FIGURE 4. Power system efficiency as function of cold heat exchanger thermal conductance.

The effect of the radiator panel area A_r on the system efficiency η_{sys} is presented in Figure 5. As can be seen, an increase of the power system efficiency can be obtained for larger radiator panel. As can be seen, an increase of 25% of reference area panel results in a system efficiency η_{sys} of approximately 0.325, which represents an efficiency increase of 8.33% when compared to the reference case.

It is important to bear in mind that the radiator panel area is based on an assumption which the fin set presents an ideal performance and the actual area of a typical space radiator ranges from 1.2 to 1.6 times the ideal area [12]. Also, the radiator panel usually represents the largest contribution of space power system footprint, turning the A_r a crucial design parameter that should be mitigated. However, as shown in Figure 5, the increase of radiator area A_r enables a higher level of η_{sys} that cannot be reached by varying other components physical parameters.

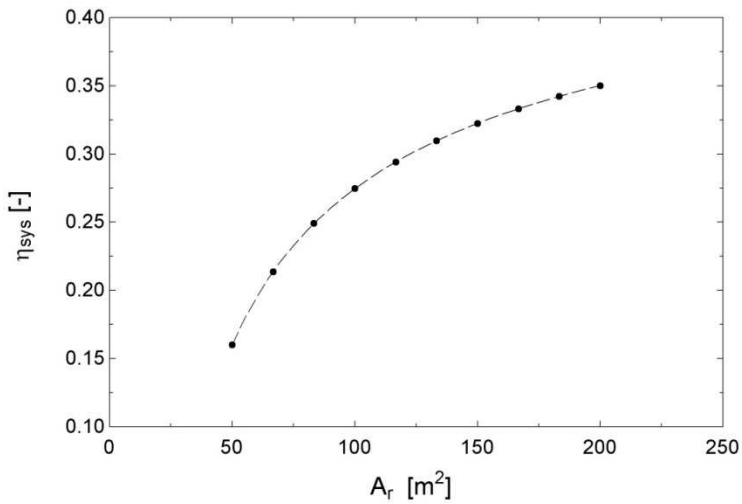

FIGURE 5. Power system efficiency as function of radiator panel area.

Figure 6 presents the influence of the hot heat exchanger thermal conductance UA_h on the power system efficiency η_{sys} for different sum values of heat exchangers thermal conductance UA_{total} (i.e hot and cold heat exchangers combined). The sum of hot and cold thermal conductance ranged from 2000 to 3500 W/K. As shown in the Figure 6, there is a maximum system efficiency for each UA_{total}. Hence, there is a maximum efficiency η_{sys} achievable for a specific total heat exchangers size and weight. Also, according to Figure 6, the maximum efficiency increases with the increasing total heat exchangers weight. Thus, conciliation between total heat exchanger weight and desired system efficiency should be performed during the design phase.

Further than total heat exchanger weight, its proportion for each heat exchanger should be evaluated in order to accomplish the optimized system efficiency. Therefore, it can be seen that a distribution of the overall weight should be performed in order to accomplish the optimized CBC power system.

The peak values of power system efficiency seen in Figure 6 were plotted as a function of the total heat exchangers thermal conductance in Figure 7. It can be noticed that possible power systems sizing are positioned below the optimized curve, whereas any point above the optimized curve are not feasible according to the applied size restrictions. Therefore, a space power system should be designed as a manner to place its point as close as possible to the optimization boundary.

The reference case considered in this study is shown in Figure 7 and as expected, there is opportunity for a proper optimization. As can be seen, a size optimization can be performed by relocating the heat exchangers thermal conductance in order to achieve lower weight for the same power system efficiency. Likewise, heat exchanger thermal conductance can also be relocated for efficiency optimization, where the best efficiency is obtained for a constant power system weight.

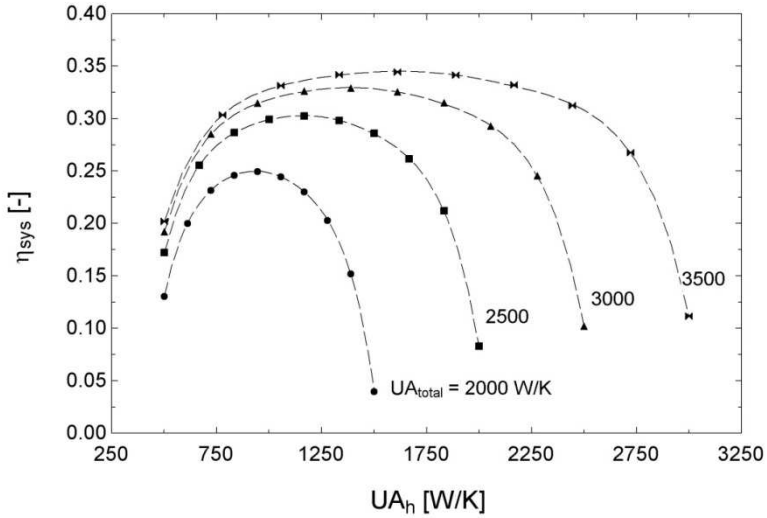

FIGURE 6. Power system efficiency for different heat exchangers total thermal conductance.

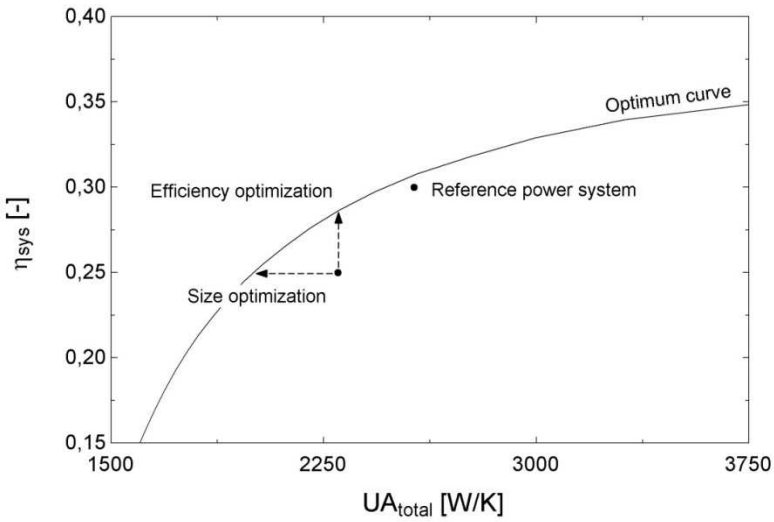

FIGURE 7. Power system optimization map.

CONCLUSION

A computational model was developed for the thermal prediction of a closed Brayton cycle applied for space needs. The model considers global parameters for each component and is used during the project conception phase, since weight and size are key drivers that allow the use of nuclear energy for aerospace propulsion.

A mixture of Helium/Xenon with molecular weight of 40g/mole was applied during this study, using the classic ideal-gas thermodynamic behavior. The turbine and compressor were characterized by algebraic equations extract from previous work [8].

It was concluded that higher heat exchangers thermal conductance (and consequently, weight) improves the final Brayton cycle efficiency. However, a proper matching between cold heat exchanger weight and efficiency should be considered, since the efficiency rate declines for high thermal conductance. Moreover, results showed that an

increase of 25% of reference area panel provides an efficiency improvement of 8.33%. When compared to other components, the increase of radiator panel area enables the highest system efficiency level.

Finally, it has been concluded that for each total heat exchangers weight (represented by the total thermal conductance), there is a maximum system efficiency. Thus, an efficiency optimization can be performed, changing each heat exchanger proportion on the final volume in order to accomplish the optimized efficiency. By the same token, the size optimization consists in achieve the lowest total heat exchanger volume keeping the same system efficiency, redistributing heat exchangers volume.

NOMENCLATURE

$A \cdots V$	=	Coefficients	$\dot{Q}$	=	Heat transfer rate, W
A	=	Area, m^2	SR	=	Speed ratio
c_p	=	Specific heat, J/kg K	T	=	Temperature, K
h	=	Enthalpy, J/kg	UA	=	Thermal conductance, W/K
$\dot{m}$	=	Mass flow rate, kg/s	$\dot{W}$	=	Work, W
PR	=	Pressure ratio			

Greek Symbols

ε	=	Recuperator effectiveness	η	=	Polytropic efficiency
ϵ	=	Emissivity	σ	=	Stefan-Boltzmann constant
γ	=	Gas specific heat ratio, c_p/c_v			

Subscript

a	=	Alternator	i	=	Inlet
c	=	Cold	r	=	Radiator
co	=	Compressor	sp	=	Space
f	=	Fin	sys	=	System
h	=	Hot	o	=	Outlet
hp	=	Heat pipe	tu		Turbine

ACKNOWLEDGMENTS

This study is part of TERRA program (acronym for Advanced Fast Reactors Technology), sponsored by the Ministry of Defense and Air Force Command. Suggestions and comments of Alexandre D. Caldeira were highly appreciated.

REFERENCES

[1] Ashe T. L., Baggenstoss W. G., Bons R., "Nuclear Reactor Closed Brayton Cycle Power Conversion System Optimization Trends for Extra-Terrestrial Applications", *Intersociety Energy Conversion Engineering Conference*, Reno, 1990.

[2] El-Genk M. S., Tournier J. M, "Noble Gas Binary Mixtures for Gas-Cooled Reactor Power Plants", *Nuclear Engineering and Design*, **v. 238**, pp. 1353-1372, 2008.

[3] Tournier J. M., El-Genk M. S., Gallo B. M., "Best Estimates of Binary Gas Mixtures Properties for Closed Brayton Cycle Space Application", *International Energy Conversion Engineering Conference*, San Diego, 2006.

[4] Guimarães L. N. F., Camillo G. P., Placco G. M., Barros Jr. A. G., Nascimento J. A., Borges E. M., Lobo P. D. C., "Basic Research and Development Effort to Design a Micro Nuclear Power Plant for Brazilian Space Application", *Journal of British Interplanetary Society*, **v. 64**, pp. 1-6, 2012.

[5] Mason L. S., Shaltens R. K., Dolce J. L., Cataldo R. L., "Status of Brayton Cycle Power Conversion Development at NASA GRC", *Proceedings of Space Technology and Applications International Forum*, edited by M. El-Genk, Melville, 2002.

[6] Shah R. K., Sekulic D. P., *Fundamentals of Heat Exchanger Design*, John Wiley & Sons, Hoboken, 2003.

[7] Stoecker W. F., *Design of Thermal Systems*, McGraw-Hill, New York, 1980.
[8] Gallo B. M., El-Genk M. S., "Brayton Rotating Units for Space Reactor Power Systems", *Energy Conversion and Management*, **v. 50**, pp. 2210-2232, 2009.
[9] McBride B. J., Zehe M. J., Gordon S., *NASA Glenn Coefficients for Calculating Thermodynamic Properties of Individual Especies*, NASA/TP – 2002 – 211556, 2002.
[10] Klein S. A., Alvarado J. L., *Engineering Equation Solver*, F-Chart, 1993.
[11] Crosby J. R., *The Development and Qualification of Thermal Controls Coatings for SNAP Systems*, NAA-SR-9908, 1965.
[12] Lubarsky B., *Nuclear Power Systems for Space Applications*, Adv. Nucl. Sci. Tech., 5, 1969.

The Performance of an Accident-tolerant Control Drum System for HEU-fueled Space Reactors

Hyun Chul Lee, Tae Young Han, Hong Sik Lim, and Jae Man Noh

Korea Atomic Energy Research Institute, 989-111, Daedeok-daero, Yuseong-gu, Daejeon, Korea
+82-42-868-4807; lhc@kaeri.re.kr

Abstract. The performance of the accident-tolerant control drum system adopted in HEU-fueled space reactors was investigated. The HEU-fueled space reactors with an accident-tolerant control drum system remains subcritical even when all the control drums are missing while the reactor with a control rod system becomes unconditionally supercritical when the control rod is missing without any damage in the reflector. The HEU-fueled space reactor with an accident-tolerant control drum system remains subcritical even when it is immersed in various surrounding materials with one or two control drums rotated to the operation position depending on the thickness of the reflector. Considering the fact that the probability of drum rotation without any damage to the reactor is much lower than that of losing control drums or control rods during launch accidents such as rocket explosion and crash of the reactor, we can conclude that the reliability of the accident-tolerant control drum system is much higher than that of a conventional control rod system or a conventional control drum system.

Keywords: Space Reactor, Reactivity Control System, Accident-tolerant Control Drum System.

INTRODUCTION

A small thermal reactor with low enriched uranium (LEU) fuel is being studied at Korea Atomic Energy Research Institute (KAERI) as a possible electric power supplier for deep space probe [1]. A control rod (CR) system was adopted as the reactivity control system of the reactors in the study and the reactors in the study were designed so that they remain subcritical when they were immersed in water, wet sand or dry sand regardless of whether they had no or minor damage (as launched or coolant pipes broken) or they had major damage (reflector and some of control rods are missing). However, it is inevitable for the reactors with a control rod system to become supercritical in the worst-case accident scenarios in which the control rods are missing without any damage in the reflector [1].

Besides the control rod system which has been widely used for nuclear reactors since Chicago Pile-1, many concepts of reactivity control system for space reactor such as the control drum (CD) system [2], the sliding reflector or the control shutter concept [3], and the hinged reflector or the petals reflector concept adopted in SP-100 space reactor [4] have been proposed and studied widely [5,6,7,8,9].

As mentioned above, the loss of control rods during launch accidents inevitably results in an increase of core reactivity and so does the loss of conventional control drums. In case of a reactor with a sliding reflector or hinged reflector system, on the contrary, the loss of the reactivity control system (the reflector itself) results in a decrease of core reactivity. However, the reflector can accidently move to its operation position when there is an external impact on the reactor. For example, a crash on the ground can move the sliding or hinged reflector to its operation position due to the inertia of the reflector or the core. With any of the reactivity control system mentioned above, the event in which the reactor becomes supercritical is still likely to happen though the absolute value of the probability is quite small.

In our previous work [10], the concept of an accident-tolerant control drum (ATCD) system as a reactivity control

system of a space reactor was proposed and its neutronic performance during the reactor's life time and the safety performance in various launch accident scenarios were demonstrated when the ATCD system was adopted in LEU-fueled space reactors. The accident-tolerant control drum consists not only of a reflector part and an absorber part but also of a fuel part which comprises the reactor core when the drums are in operation position while the conventional control drum consists of a reflector part and an absorber part [10]. The neutronic performance of reactors with an ATCD system was similar to that with a control rod system during their life time except for the drum/rod worth at the beginning of life cold zero power state. The accident-tolerant control drum has a large drum worth not only because the absorber part is inserted deep into the core and the fuel part is moved to a position far from the core when the drum is in shutdown position. The reactors with an ATCD system remained subcritical even when some or all the control drums are missing without any damage in reflector as a result of launch accident while the reactors with a control rod system became supercritical when some or all the control rods are missing without any damage in reflector, which means that the ATCD system is much more reliable than the control rod system during various launch accidents.

In this study, the performance of the accident-tolerant control drum system was investigated when it was adopted as the reactivity control system of a HEU-fueled space reactor. The performance of the HEU-fueled space reactors with a control rod system and that of the HEU-fueled space reactors with a ATCD system were compared.

PERFORMANCE OF THE ATCD SYSTEM IN A HEU-FUELED SPACE REACTOR

The neutronic performance during the life time and the safety performance in various launch accident scenarios were investigated for three designs of HEU-fueled space reactors. Figure 1 shows the radial and axial configuration of the three cases. The first one (Case A) adopted the control rod system as a reactivity control system with a thick Be reflector. The second one and the third one (Case B and C, respectively) adopted the ATCD system with a thin Be reflector and a thick Be reflector, respectively. Table 1 shows the design parameters of the three design cases. The target life time of the three HEU-fueled reactors is 15 years with a thermal power of 5 kW at an operation temperature of 1100K. No moderator is used in the three designs to minimize the total reactor mass [1]. Boron carbide (B_4C) with 89.11 weight % enriched ^{10}B is used as an absorber material. Twelve heat pipes with NaK coolant are equipped to remove the heat generated in the core. In case A, a control rod system and a very thick reflector were adopted as they were in KRUSTY [11]. The thick reflector in this case was required to meet the safety criteria (k_{eff}<0.98) for all the accident scenarios other than "the worst case accident scenario" in which the control rod is missing without any damage in the reflector. An accident-tolerant control drum system was adopted in case B and C. A relatively thin reflector was adopted in case B while a thicker reflector with a slightly smaller core radius was adopted in case C to enhance the safety during launch accident. Table V lists the design parameters of three HEU-fueled space reactors. The reactors with an accident-tolerant control drum system have smaller total reactor mass. Especially, the total reactor mass in case B is less than a half of the reactor mass in the control rod case, case A.

Neutronic Performance during Life Time

Table 2 compares the neutronic performance of the three reactors during their life time from the beginning of life (BOL) cold zero power state to the end of life (EOL) hot full power (HFP) state. The three reactors show very similar neutronic performance during their life time except for the beginning of life cold zero power shutdown state. The total drum worth in case B and C (about 24,000pcm and 17,000pcm, respectively) is much larger than the total rod worth (about 10,000pcm) in the control rod case, case A. The relatively large total drum worth is achieved not only because a large amount of absorber is inserted deep into the core but also because some fuel is moved to a position far from the core. The total drum worth in the thin reflector case, case B, is much larger than that in the thick reflector case, case C. When the control drums are rotated to the shutdown positions, the distances of the fuel parts from the reactor center in the two cases are similar because the drum radii are the same for the two cases. However, the distances of the fuel parts from the reactor outer boundary in the two cases are quite different because the reflector thicknesses in the two cases are different. The fuel parts in case B are located at the positions near the reactor outer boundary where the neutron importance is quite low due to a high leakage probability when the drum is rotated to the shutdown position while the fuel parts in case C are located at the positions far from the reactor outer boundary where the neutron importance is still high due to a low leakage probability. This explains the large difference between the drum worth in the two cases. Unlike the LEU-fueled reactors, the temperature reactivity

defects is very small for the three cases because the reactors have fast spectrums and the reactivity effect of resonance absorption which depends on the fuel temperature is quite limited. The reactivity defect due to thermal expansion is about -1600pcm ~ -1800pcm for the three cases. The reactivity swing during the life time is less than -100pcm while it was about -800pcm ~ -900pcm in the LEU-fueled thermal space reactors above. The excess reactivity at the end of life time are about 600pcm ~ 700pcm for the three cases.

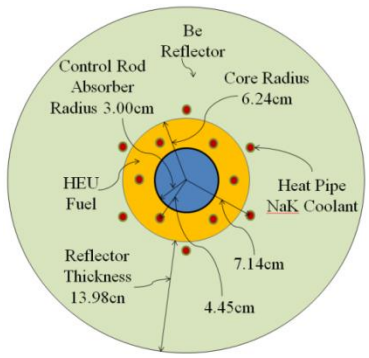

(a) Top View of the Reactor in Case A

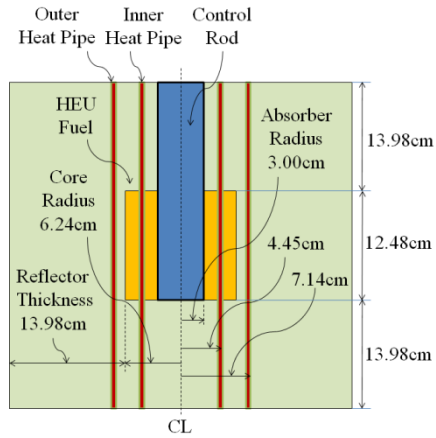

(b) Side View of the Reactor in Case A

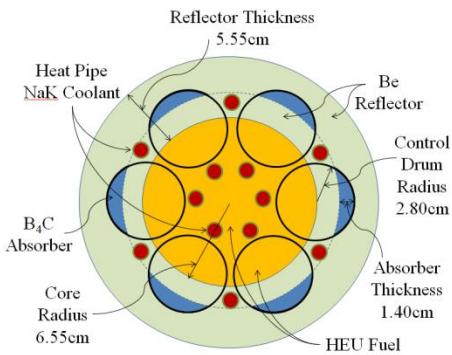

(c) Top View of the Reactor in Case B

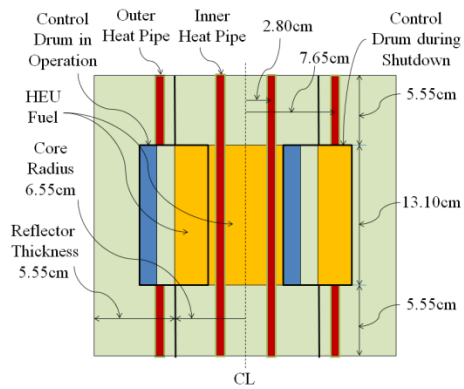

(d) Side View of the Reactor in Case B

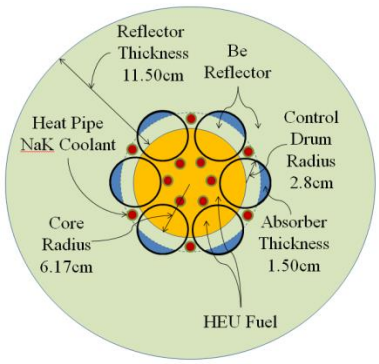

(e) Top View of the Reactor in Case C

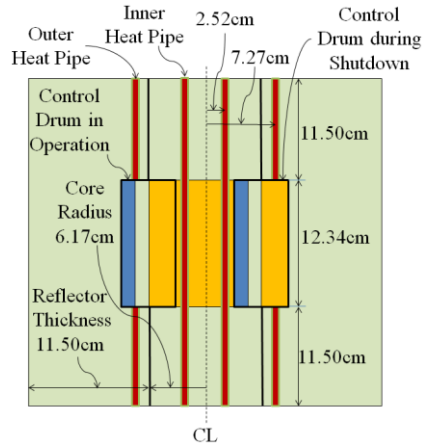

(f) Side View of the Reactor in Case C

FIGURE 1. HEU-fueled Space Reactors with a Control Rod system and an ATCD system

TABLE 1. Design Parameters of the HEU-fueled Space Reactors

Parameters	Control Rod	ATCD	
	Case A	Case B	Case C
Thermal Power (kW)	5.0	5.0	5.0
Life Time (year)	15.0	15.0	15.0
Operation Temperature (K)	1100	1100	1100
Fuel Material	HEU metal	HEU metal	HEU metal
Reflector Material	Be	Be	Be
Active Core Height/Diameter Ratio	1.00	1.00	1.00
Number of Heat Pipes	12	12	12
Heat Pipe Inner Radius (cm)	0.4	0.4	0.4
Heat Pipe Thickness (cm)	0.1	0.1	0.1
Heat Pipe Material	Zr	Zr	Zr
Coolant Material	NaK	NaK	NaK
Inner Heat Pipe Position from the Core Center (cm)	4.45	2.80	2.52
Outer Heat Pipe Position from the Core Center (cm)	7.14	7.65	7.27
Number of Control Elements	1 Rod	6 Drums	6 Drums
Control Rod/Drum Absorber Material	B_4C	B_4C	B_4C
^{10}B Enrichment in B_4C (w/o)	89.11	89.11	89.11
Control Rod/Drum Can Thickness (cm)	0.10	0.10	0.10
Control Rod/Drum Gap Thickness (cm)	0.05	0.05	0.05
Control Rod/Drum Can Material	Be	Be	Be
Control Rod Absorber Radius (cm)	3.00	-	-
Control Drum Radius (cm)	-	2.80	2.80
Control Drum Absorber Thickness (cm)	-	1.40	1.50
Reflector Thickness (cm)	13.98	5.55	11.50
Core Radius (cm)	6.24	6.55	6.17
Fuel Mass (kg)	20.60	30.75	25.45
Reflector Mass (kg)	91.73	15.96	59.84
Reactor Total Mass (kg)	114.9	48.47	87.34

TABLE 2. Neutronic Performance of the HEU-fueled Space Reactors during Their Life Time

Reactor State	k_{eff}		
	Control Rod	Accident-tolerant Control Drum	
	Case A	Case B	Case C
BOL, CZP, Shutdown Rod/Drum Position	0.92713±0.00007	0.81994±0.00006	0.87228±0.00007
BOL, CZP, Operation Rod/Drum Position	1.02601±0.00009	1.02507±0.00007	1.02374±0.00007
BOL, HFP, Operation Rod/Drum Position [a)]	1.02601±0.00007	1.02499±0.00007	1.02353±0.00007
BOL, HFP, Operation Rod/Drum Position [b)]	1.00707±0.00007	1.00732±0.00007	1.00699±0.00007
EOL, HFP, Operation Rod/Drum Position [b)]	1.00609±0.00008	1.00672±0.00007	1.00629±0.00008

a) No thermal expansion was considered.
b) A thermal expansion of 1% was considered.

Safety Performance during Launch Accidents

Table 3 shows the criticality of the HEU-fueled reactor with a control rod system during various launch accidents. The effective multiplication factors are less than 0.98 except for "the worst-case accident scenarios" in which the control rod is missing without any damage in the reflector. In such a scenario, any reactor with a control rod system should become supercritical regardless of the surrounding materials. The reactivity analysis for “the worst-case accident scenario” was omitted because it is trivial. The coolant holes and the control rod hole were assumed to be filled with surrounding materials except for the "As Launched" scenario in Table 3. The dry and wet sand were assumed to be SiO_2 with 36% porosity and a homogeneous mixture of 64% SiO_2 and 36% water, respectively. A

water density of 1.0g/cm3 and a temperature of 300K were also assumed. The standard deviations of the effective multiplication factors were around 10 pcm but they were omitted from Table 3.

Table 4 shows the criticality of the HEU-fueled reactors with an accident-tolerant control drum system for various accident scenarios in which some parts of the reactor is missing. Fifteen scenarios were investigated for each surrounding materials (water, wet sand, or dry sand). They cover various situations in which the reactor has no or minor damage and serious damage (some or all the control drums are missing or reflector is missing). Figure 2 shows the missing control drum positions for the scenarios listed in Table 4. It was assumed that all the control drums are missing when the reflector is missing. The coolant holes, the control drum gaps, and the control drum holes were assumed to be filled with surrounding materials except for the "As Launched" scenario in Table 4. The maximum value of the effective multiplication factors is around 0.95 for both cases. It means that the reliability of the accident-tolerant control drum system is much higher than that of the control rod system during the launch accidents.

The reactivity worth of the surrounding materials (water, wet sand, and dry sand) can be evaluated by comparing the reactivity at the beginning of life cold zero power shutdown state in Table 2 and that of the "As Launched" scenarios in Table 3 and Table 4. The reactivity worth of the surrounding materials in case B are about 12,000~16,000pcm. However, they are about 6,000~8,000pcm in case C and 3,500~4,500pcm in case A. The reactivity worth of the surrounding materials decreases as the reflector thickness increases because the effect of the surrounding materials on the core is limited due to a long distance between the core and the surroundings when the reflector is thick.

Table 5 compares the criticality of the reactors with one or two control drums rotated to the operation position. The effective multiplication factors of the reactor with a thin reflector, case B, are less than 0.98 even when it is immersed in dry sand, wet sand, or water with one control drum is rotated to the operation position regardless of whether the other drums are present or missing. The reactor with a thick reflector, case C, remains subcritical (k_{eff}<0.98) even when two adjacent control drums are rotated to the operation position regardless of the surrounding materials and the presence of the other control drums. The major difference between the two reactors is the reflector thickness as pointed above. The only possibility of super-criticality of the reactors in case B and C is the rotation of two or more control drums in case B and three or more control drums in case C, respectively, without any damage in the reflector. It is needless to say that the probability of such scenarios are much lower than that of losing control drums or control rods during launch accidents such as rocket explosion and crash of the reactor and thus the reliability of the accident-tolerant control drum system proposed in this paper is much higher than the conventional reactivity control systems for space reactors.

CONCLUSION

In this paper, the performance of the accident-tolerant control drum system adopted in HEU-fueled space reactors was investigated. The trend was similar to that in the LEU-fueled cases. The HEU-fueled space reactors with an accident-tolerant control drum system remains subcritical even when all the control drums are missing while the reactor with a control rod system becomes unconditionally supercritical when the control rod is missing without any damage in the reflector. The HEU-fueled space reactor with an accident-tolerant control drum system remains subcritical even when it is immersed in various surrounding materials with one or two control drums rotated to the operation position depending on the thickness of the reflector. Besides the safety enhancement, a reduction of the total reactor mass was achieved by adopting an accident-tolerant control drum system instead of a control rod system. When a thin reflector was used, the total mass of the HEU-fueled reactor with an accident tolerant control drum system was less than half of that of the HEU-fueled reactor with a control rod system.

Considering the fact that the probability of drum rotation without any damage to the reactor is much lower than that of losing control drums or control rods during launch accidents such as rocket explosion and crash of the reactor, we can conclude that the reliability of the accident-tolerant control drum system is much higher than that of a conventional control rod system or a conventional control drum system.

ACKNOWLEDGMENTS

This work was supported by Korea Research Council of Fundamental Science & Technology.

TABLE 3. Accident Scenario Analysis of the HEU-fueled Space Reactor with a CR System

Accident Scenario			k_{eff} (Case A)
Immersed in Water	No Damage in Reflector	As Launched	0.96782
		Coolant Pipe Broken	0.97881
		CR Missing	1.17519
	Reflector Missing	CR Inserted	0.83333
		CR Missing	0.96932
Immersed in Wet Sand	No Damage in Reflector	As Launched	0.96749
		Coolant Pipe Broken	0.97360
		CR Missing	1.13355
	Reflector Missing	CR Inserted	0.82892
		CR Missing	0.93608
Immersed in Dry Sand	No Damage in Reflector	As Launched	0.95841
		Coolant Pipe Broken	0.96091
		CR Missing	1.08719
	Reflector Missing	CR Inserted	0.72932
		CR Missing	0.78913

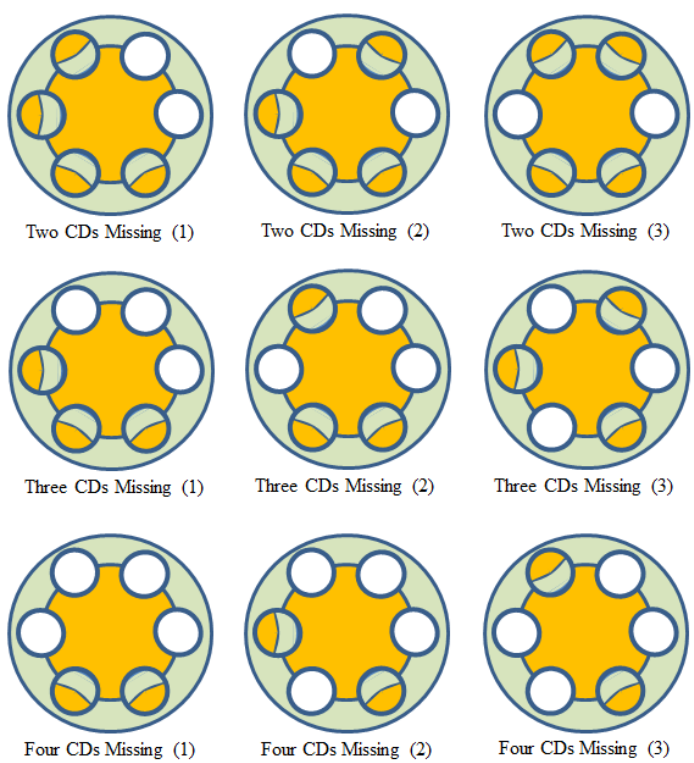

FIGURE 2. The Positions of the Missing Control Drums

TABLE 4. Accident Scenario Analysis of the HEU-fueled Space Reactor with an ATCD System

Accident Scenario		k_{eff}	
		Case B	Case C
Immersed in Water	As Launched	0.93903	0.93736
	Coolant Pipe Broken	0.94848	0.94708
	One Control Drum Missing	0.94901	0.94489
	Two Control Drums Missing (1)	0.94953	0.94208
	Two Control Drums Missing (2)	0.94950	0.94232
	Two Control Drums Missing (3)	0.94956	0.94257
	Three Control Drums Missing (1)	0.94980	0.93925
	Three Control Drums Missing (2)	0.94982	0.93954
	Three Control Drums Missing (3)	0.94960	0.93949
	Four Control Drums Missing (1)	0.94984	0.93623
	Four Control Drums Missing (2)	0.94981	0.93633
	Four Control Drums Missing (3)	0.94994	0.93623
	Five Control Drums Missing	0.95003	0.93277
	All Control Drums Missing	0.95006	0.92946
	Reflector Missing	0.88731	0.83040
Immersed in Wet Sand	As Launched	0.94176	0.93780
	Coolant Pipe Broken	0.94829	0.94389
	One Control Drum Missing	0.94187	0.93620
	Two Control Drums Missing (1)	0.93727	0.93140
	Two Control Drums Missing (2)	0.93477	0.92791
	Two Control Drums Missing (3)	0.93471	0.92769
	Three Control Drums Missing (1)	0.93218	0.92572
	Three Control Drums Missing (2)	0.92966	0.92207
	Three Control Drums Missing (3)	0.92708	0.91814
	Four Control Drums Missing (1)	0.92646	0.91914
	Four Control Drums Missing (2)	0.92396	0.91530
	Four Control Drums Missing (3)	0.92386	0.91549
	Five Control Drums Missing	0.92031	0.91154
	All Control Drums Missing	0.91606	0.90739
	Reflector Missing	0.85727	0.79078
Immersed in Dry Sand	As Launched	0.90735	0.92328
	Coolant Pipe Broken	0.91079	0.92613
	One Control Drum Missing	0.89367	0.90854
	Two Control Drums Missing (1)	0.87737	0.89194
	Two Control Drums Missing (2)	0.87490	0.88840
	Two Control Drums Missing (3)	0.87411	0.88744
	Three Control Drums Missing (1)	0.85953	0.87321
	Three Control Drums Missing (2)	0.85580	0.86805
	Three Control Drums Missing (3)	0.85309	0.86431
	Four Control Drums Missing (1)	0.83849	0.85051
	Four Control Drums Missing (2)	0.83477	0.84530
	Four Control Drums Missing (3)	0.83423	0.84432
	Five Control Drums Missing	0.81451	0.82323
	All Control Drums Missing	0.79170	0.79706
	Reflector Missing	0.72611	0.65596

TABLE 5. Criticality of HEU-fueled Space Reactors with Some Drums Rotated to Operation Position

Accident Scenario			k_{eff}	
			Case B	Case C
Immersed in Water	One Control Drum in Operation Position	No CD Missing	0.96835	0.95909
		The Other CDs Missing	0.97618	0.95441
	Two Adjacent CDs in Operation Position	No CD Missing	0.99336	0.97804
		The Other CDs Missing	1.00152	0.97835
Immersed in Wet Sand	One Control Drum in Operation Position	No CD Missing	0.96878	0.95546
		The Other CDs Missing	0.95059	0.93568
	Two Adjacent CDs in Operation Position	No CD Missing	0.99419	0.97414
		The Other CDs Missing	0.98490	0.96496
Immersed in Dry Sand	One Control Drum in Operation Position	No CD Missing	0.93907	0.94015
		The Other CDs Missing	0.85402	0.85041
	Two Adjacent CDs in Operation Position	No CD Missing	0.97102	0.96049
		The Other CDs Missing	0.91646	0.90303

REFERENCES

[1] Hyun Chul Lee, et al., "A neutronic feasibility study on a small LEU fueled reactor for space applications," *Annals of Nuclear Energy*, **77**, 35-46, (2015). (Available on-line)

[2] S. N. Barkov, "Effectiveness of rotating control drums in the radial reflector of a reactor," *Soviet Atomic Energy*, **23**, 1101-1102, (1967).

[3] D. S. Bost, "Control Worth of Sliding Reflectors for Zirconium Hydride Reactors," AI-AEC-13086, pp. 31, (1973)

[4] N.A. Dane, et al., "SP-100 reactor design and performance," in proceedings of *24th Intersociety Energy*, pp. 1225-1226, (1989).

[5] David I. Poston, "The Heatpipe-Operated Mars Exploration Reactor (HOMER)," in proceedings of *Space Technology and Applications International Forum (STAIF-2001)*, pp. 797-804, (2001).

[6] Jeffrey C. King and Mohamed S. El-Genk, "Submersion Criticality Safety of Fast Spectrum Space Reactors: Potential Spectral Shift Absorbers," *Nuclear Engineering and Design*, **236**, 238-254, (2006).

[7] Mohamed S. El-Genk , "Deployment History and Design Considerations For Space Reactor Power Systems," *Acta Astronautica*, **64**, 833-849, (2009).

[8] Aaron E. Craft, et al., "Reactivity Control Schemes for Fast Spectrum Space Nuclear Reactors," *Nuclear Engineering and Design*, **241**, 1516-1528, (2011).

[9] Shannon M. Bragg-Sitton, et al., "Ongoing Space Nuclear Systems Development in the United States," in proceedings of *2011 International Nuclear Atlantic Conference - INAC 2011*, (2011).

[10] Hyun Chul Lee, et al., "A Small Fission Reactor with an Accident-tolerant Control Drum System for Space Application," *Transactions of American Nuclear Society*, **111**, 31-32, (2014).

[11] David I. Poston, "A Simple, Low-Power Fission Reactor for Space Exploration Power Systems," in proceedings of *Nuclear and Emerging Technologies for Space 2013*, (2013).

Hot Pressing of CeO_2 Ceramic Pellets

Daniel P. Kramer, Timothy M. Pierson, Carl O. Sjöblom, Dale W. Grant, Steve M. Goodrich, Chadwick D. Barklay, and Christofer E. Whiting

University of Dayton Research Institute, 300 College Park, Dayton, Ohio, 45469
937-229-1038; daniel.kramer@udri.udayton.edu

Abstract. Over the last several years a number of different ceramic processing unit operations have been studied for fabricating sintered CeO_2 ceramic compacts as a surrogate for understanding the ceramic behavior of PuO_2, including: classical cold pressed + furnace sintering and Spark Plasma Sintering (SPS). The present work centers on the application of Hot Pressing, which is another ceramic processing technique that utilizes both temperature and pressure for obtaining sintered ceramic compacts. A series of hot press experiments were performed with CeO_2 powder employing processing temperatures of up to ~1675°C with pressures of up to ~100 MPa (~15,000 psi). Integral hot pressed CeO_2 pellets have been obtained with some examples being sectioned and polished employing typical ceramic specimen preparation techniques. Comparisons of the microstructures obtained on both hot pressed CeO_2 pellets and standard cold pressed + furnace sintered CeO_2 discs are presented and discussed.

Keywords: Hot Pressing, CeO_2, Sintering, Pellet fabrication, PuO_2

INTRODUCTION

Since the development of radioisotope thermoelectric generators at Mound Laboratories (Miamisburg, OH) over fifty years ago, several different fuel forms have been employed for the application of the radioisotope ^{238}Pu. In general, the fuel form has progressed over the years from the use of ^{238}Pu metal, to a ^{238}Pu metal-ceramic cermet, to the current $^{238}PuO_2$ ceramic pellet fuel form which has supplied all of the heat in U.S. radioisotope powered spacecraft launched over the last ~20 years. These spacecraft/missions include Ulysses/Sun, Cassini/Saturn, Curiosity/Mars Science Laboratory, and New Horizons/Pluto which is scheduled to do a fly-by of Pluto the summer of 2015.

The fabrication of the $^{238}PuO_2$ fuel pellets for radioisotope space power systems utilizes a number of standard ceramic processing techniques including ball milling, pressing, and sintering. The current pressing and sintering operations are combined via the application of hot press processing. During hot pressing the fuel powder is first loaded into a die which is then placed within the hot press. During processing a specific time-temperature-pressure (t-T-P) profile is performed which results in the consolidation/sintering of the fuel powder into a ceramic pellet.

Since ^{238}Pu is highly radioactive, great care needs to be taken in the performance of any hot pressing operation to ensure personnel safety. Therefore, the application of a non-radioactive surrogate material for performing various endeavors in support of space nuclear power efforts would result in reduced personnel exposure, and a significant reduction in associated costs. One surrogate material under investigation is cerium dioxide. Cerium dioxide has a number of chemical and crystalline structural characteristics which makes it an attractive cold surrogate. Both PuO_2 and CeO_2 are face-centered cubic with a space group of Fm-3m [1,2], and exhibit oxygen release phenomenon under various reducing atmospheres; of particular interest to an RPS system, is the tendency of these materials to reduce in the presence of carbon at high temperatures[3-6].

In terms of ceramic processing, two important physical properties of a material which need to be considered are its melting temperature and its coefficient of thermal expansion. In general, the sintering temperature of a ceramic is typically around ~0.6 to ~0.8 of its melting temperature. PuO_2 has a reported melting temperature of ~2387°C, so its sintering temperature range is ~1323°C to ~1857°C[7]. It is desirable that any ceramic surrogate for PuO_2 exhibit a similar sintering range. Cerium dioxide has a reported melting temperature of ~2341°C[8]. Employing the general rule that a ceramics sintering temperature is ~0.6 to ~0.8 of its melting temperature yields a sintering temperature range of ~1295°C to ~1818°C. Therefore, PuO_2 and CeO_2 have very similar ranges of sintering temperatures which is desirable.

A material which has a relatively high coefficient of thermal expansion will be more susceptible to thermal cracking/shock during cooling from the sintering temperature compared to a material which has a lower coefficient of thermal expansion. Therefore, it is preferable to have a surrogate material for PuO_2 which also exhibits similar thermal expansion characteristics. Figure 1 is a plot of the percent linear thermal expansions (dL/L) of PuO_2 and CeO_2 as a function of temperature developed employing data obtained in the literature[9,10]. Comparison of the expansion data shown in the figure shows that CeO_2 has a thermal expansion ~10-15% greater compared to the thermal expansion of PuO_2 at typical sintering temperatures. In general, it would be more desirable if the thermal expansion difference between the two materials was smaller, but the difference should be satisfactory for a potential surrogate.

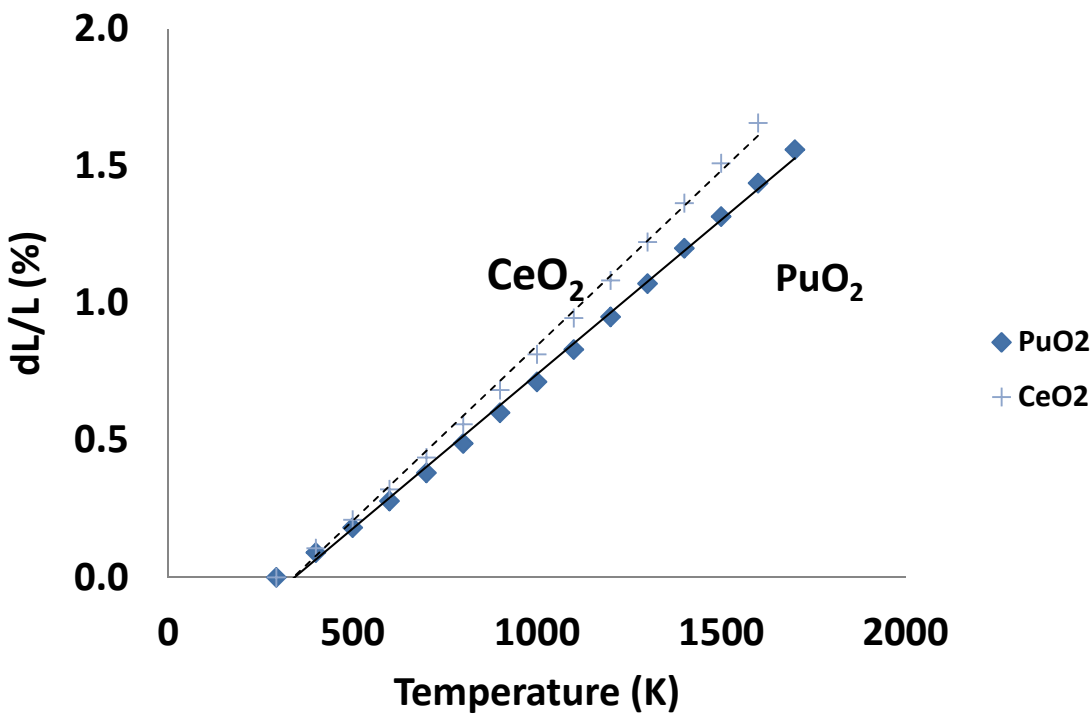

FIGURE 1. Comparison of the Percent Linear Thermal Expansion of PuO_2 and CeO_2 as a Function of Temperature.

HOT PRESSING OF CERIUM OXIDE SURROGATE PELLETS

Once it was determined that CeO_2 is a candidate surrogate material for PuO_2, a number of hot pressing experiments were performed. CeO_2 (99.9% trace metals basis) powder was obtained from Sigma-Aldrich (St. Louis, MO) with a reported particle size of <5µm. Hot pressing was performed using graphite dies and punches. Figure 2 presents a hot press die prior to assembly showing the top punch, die body, two bottom spacers, and graphite foil spacers. In most cases graphite foil and/or tantalum foil was used to line the internal surfaces of the die which would be in contact with the CeO_2 powder. The rolled "white" ceramic insulation sheet shown in Figure 2 was used to help thermally insulate the die assembly from the copper induction coil.

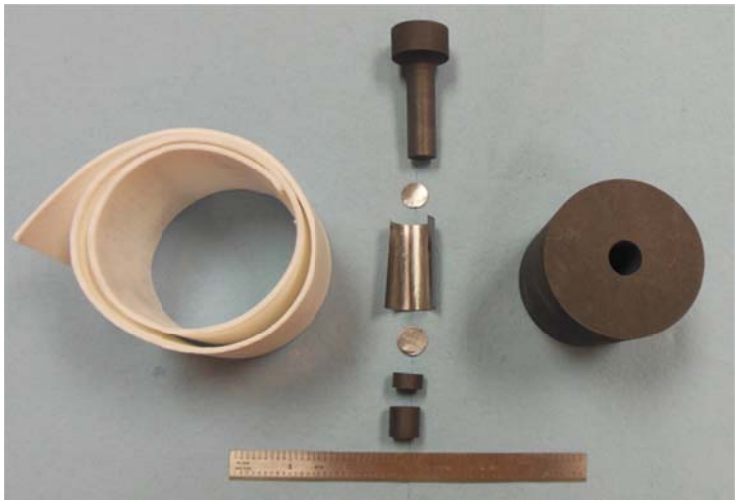

FIGURE 2. Hot Press Die Prior to Assembly Showing Various Components.

Figure 3 (left) shows the hot press employed in the experiments. The hot press is inductively heated by a motor generator system, and load is uniaxially applied via a hydraulic press. The vacuum system on the hot press consists of a diffusion pump backed up by a mechanical pump, which allows experiments to be performed down to ~10^{-5} torr. Figure 3 (right) shows the die being heated by the induction coil with the top ram loading the top die punch. During a hot press experiment, temperatures were measured via an optical pyrometer focused on the die surface around 1 cm from the edge of the top die punch. The use of the optical pyrometer did result in some variability in temperature readings as a function of focusing on the top surface of the hot die the range of up to ~75°C.

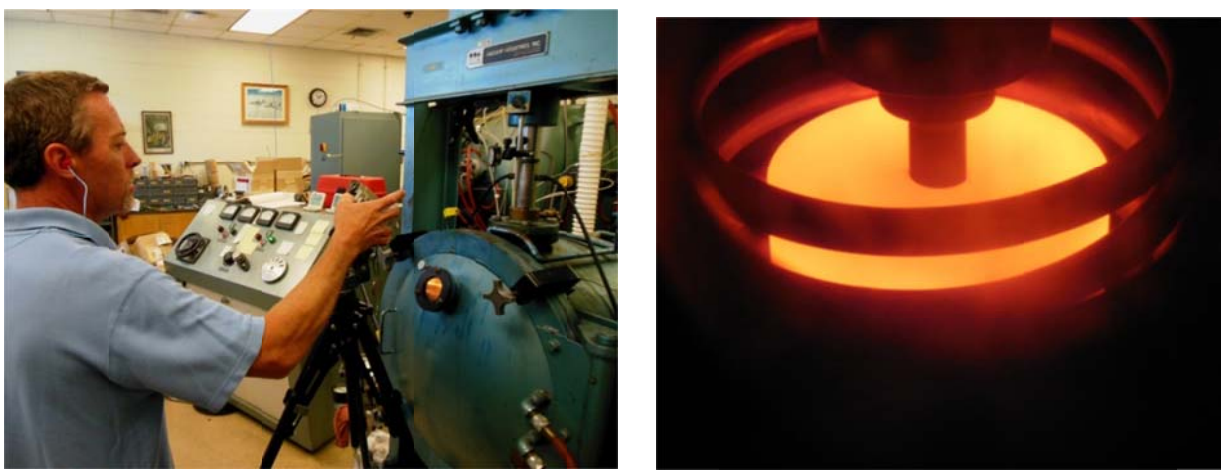

FIGURE 3. (Left) Picture of the Hot Press and Motor Generator and (Right) Heating of Die Assembly During a Hot Press run.

For the hot press experiments the graphite die was assembled and loaded with CeO_2 powder. The top punch was next loaded into the die cavity and the entire die assembly was placed into the vacuum chamber of the hot press. Care was taken to place the die assembly uniformly within the copper coils of the induction furnace. The door of the vacuum chamber was closed and the chamber was pumped overnight under vacuum. Typically, the hot press run was performed the next morning following a selected time-Temperature-Pressure (t-T-P) profile. Experiments were performed with temperatures up to ~1675°C, pressures of up to ~100 MPa (~15,000 psi), under various vacuums (~10^{-1} to 10^{-5} torr).

Figure 4 (left) shows an example of a die assembly after the completion of a hot press experiment and before disassembly. Figure 4 (right) shows a hot pressed pellet after removal from the die assembly. After removal from the die assembly, the hot pressed pellets were next cut and mounted for microstructural examination. Pellets hot pressed to date have been integral with theoretical densities, being a function of the sintering parameters, ranging from ~70% to 90+% assuming a 100% theoretical density for CeO_2 of 7.1 g/cm^3.

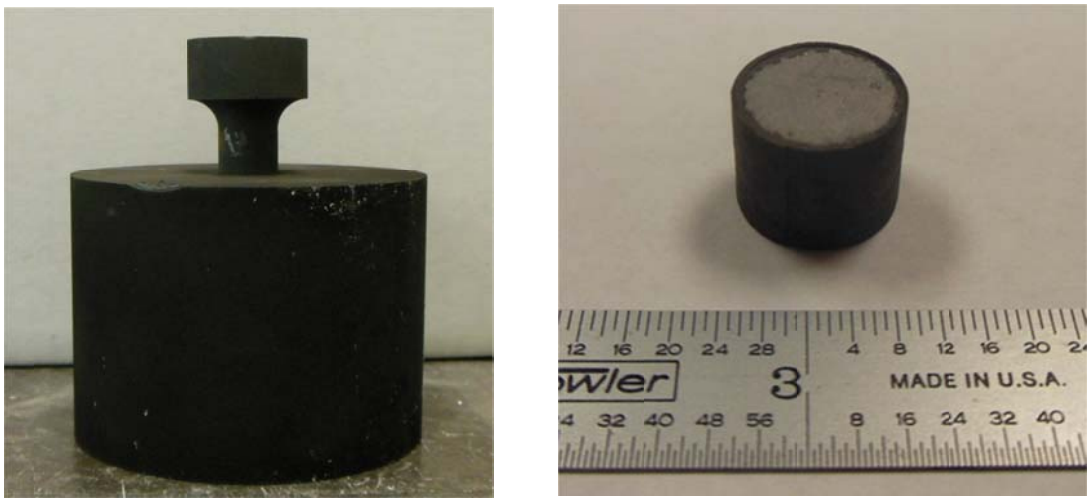

FIGURE 4. (Left) Hot Press Die Assembly After an Experiment and (Right) Hot Pressed Pellet After Removal from the Die.

OPTICAL/SEM/EDS MICROSTRUCTURAL EXAMINATION OF HOT PRESSED AND COLD PRESSED + FURNACED SINTERED CERIUM OXIDE CERAMIC PELLETS

Hot Pressed Cerium Oxide Pellet #1

Microstructural examination is an important tool for understanding how changes in hot press processing parameters directly impact various properties of the resultant ceramic pellet. Sectioning of the pellets was performed using a slow speed diamond saw. The pellets were cut dry with no application of any cutting fluids which could tend to infiltrate into pores or any cracks in the structure of the pellet making further examination more difficult. After sectioning, a pellet was vacuum impregnated cold mounted using a two part epoxy. Standard grinding and polishing techniques were employed to obtain polished mounted specimens for optical and SEM (Scanning Electron Microscopy) + Energy Dispersive Spectroscopy (EDS) examinations. Figure 5 shows two optical photomicrographs taken on a polished cross-section of hot pressed Pellet #1 that included a tantalum foil liner.

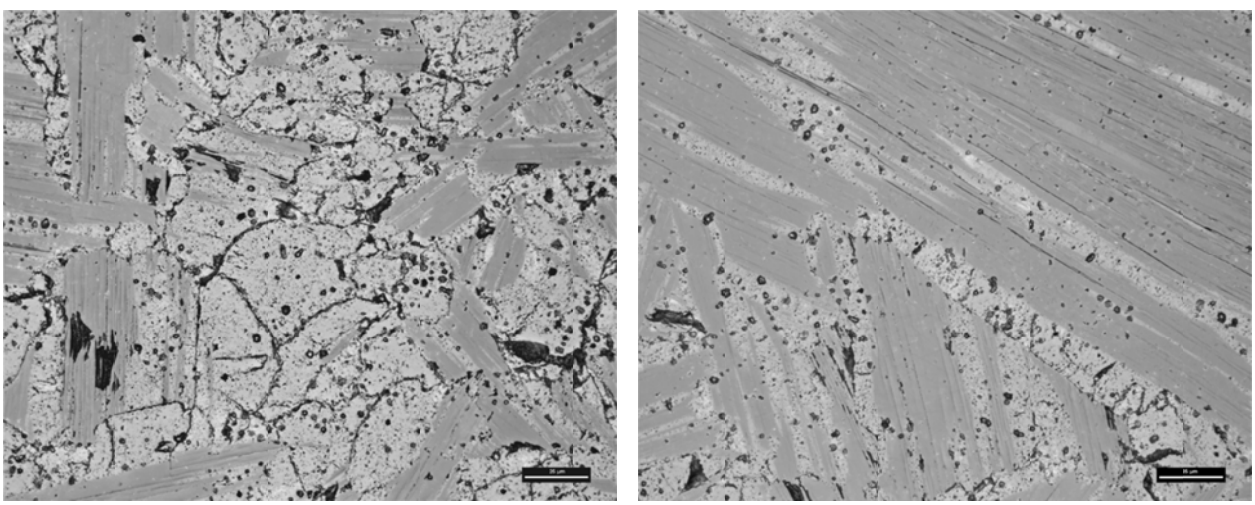

Figure 5. Optical Photomicrographs of Two Different Regions of Hot Pressed Pellet #1 Showing the Presence of Two Distinct "Light" and "Dark" Phases. The "Black" Areas are Inter-granular or Intra-granular Porosity Regions. The Scale Bar Shown in Each Photomicrograph is 25μm in Length.

As shown in Figure 5, the two microstructures exhibit two general crystallite phases ("light" and "dark") with some residual porosity ("black"). There were some variations in the amount of each phase as a function of position across the specimen along with some microcracking, which was likely due to a combination of factors including the hot press cycle and/or cutting/mounting of the specimen.

In order to determine the difference between the "light" and "dark" phases observed in the specimen, it was next positioned within an SEM (Zeiss EVO 50) with an EDS. It was not necessary to coat the ceramic specimen to reduce charging as the microscope was operated at a pressure of 10 Pa. At several "light" and "dark" phase regions of the specimen elemental spectra were obtained to determine the relative concentrations of cerium and oxygen within the two distinct phase regions. Table 1 shows a comparison of the oxygen and cerium at. % concentrations obtained on a pair of "light" and a pair of "dark" phase regions. It is interesting to note that the "light" phase Ce/O ratio is close to Ce_4O_7 while the "dark" phase is closer to a slightly sub-stoichiometric form of CeO_2 (i.e. CeO_{2-x}).

TABLE 1. EDS Results Obtained on "Light" and "Dark" Phases in Hot Pressed Pellet #1.

Phase "Type"	Oxygen (at. %)	Cerium (at. %)	Ce/O ratio
Light #1	63.63	36.37	1.75
Light #2	62.28	37.72	1.65
Dark #1	66.27	33.73	1.96
Dark #2	65.95	34.05	1.94

Hot Pressed Cerium Oxide Pellet #2

Figure 6 shows the microstructure of mounted and polished hot pressed Pellet #2 which was fabricated in the presence of a graphite liner between the hot press die and the cerium dioxide powder. The hot press processing parameters were initially set to be similar to those employed in the fabrication of Pellet #1 discussed previously. Pellet #2 presented more of a challenge during the cutting and mounting since the pellet exhibited less strength compared to Pellet #1 and was susceptible to cracking. As shown in Figure 6 (left) the microstructure of Pellet #2 was determined in some regions to be very similar to Pellet #1's microstructure with "dark" and "light" phases and "black" inter- and intra-granular regions. However, as shown in Figure 6 (right) some areas of the mounted specimen did not exhibit any "dark" phase within that particular section of the microstructure. From a ceramic perspective the difference in microstructure development between Pellet #1 and Pellet #2 is likely due to the actual hot press soak temperature being significantly less than anticipated due to operator changes in the optical pyrometer's positioning and settings.

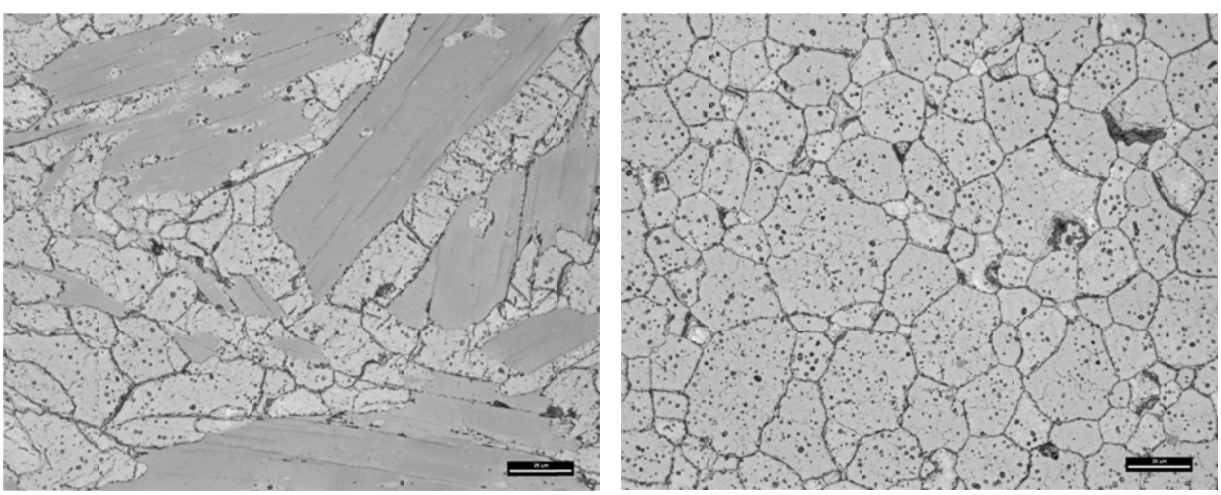

FIGURE 6. Optical Photomicrographs of Two Different Regions of Hot Pressed Pellet #2 Showing (Left) Two Distinct "Light" and "Dark" Phases and (Right) Mostly "Light" Phase. The "Black" Areas are Inter-granular or Intra-granular Porosity Regions. The Scale Bar Shown in Each Photomicrograph is 25μm in Length.

Cold Pressed + Furnace Sintered Cerium Oxide Disc #1

For comparison purposes, additional ceramic specimens were fabricated out of the same cerium dioxide powder used in the hot pressing of Pellets #1 and #2. Several specimens, such as Disc #1 shown in Figure 7, were fabricated by first cold pressing the powder in a ~2.5 cm diameter steel die using a hydraulic press at room temperature. After cold pressing, the ~0.3 cm thick disc was furnace sintered in air employing a similar thermal profile as was used in the hot pressing of Pellets #1 and #2. After completion of the furnace sintering operation Disc #1 was cut, mounted, and polished for optical microstructural examination. In order to help bring out the microstructure, after polishing the specimen was next removed from the mount and it was thermally etched. Figure 7 is an optical photomicrograph taken of Disc #1 specimen showing that its microstructure consists mainly of fine grains (<10µm)with significant amounts of inter-granular porosity with lesser amounts of intra-granular porosity. Comparing the size, shape, and characteristics of the microstructures shown in Figure 6 with Figure 7 demonstrates the significant effect of thermal + pressure on the sintering characteristics of ceramic powders.

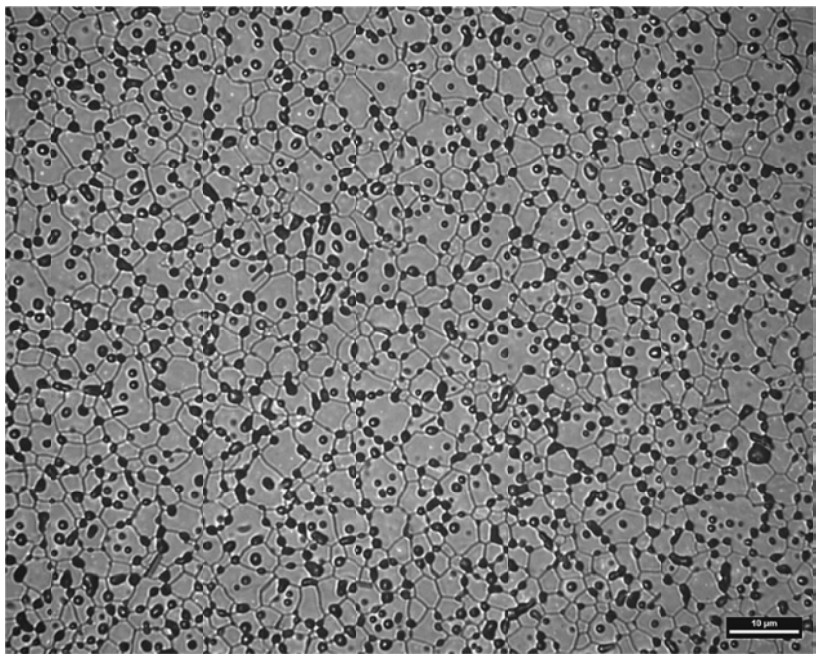

FIGURE 7. Optical Photomicrograph of a Region of Cold Pressed + Furnace Sintered Disc #1 Showing a Single Fine Grain Phase and a Significant Amount of Inter-granular Porosity "Black" Areas and Lesser Amount of Intra-granular Porosity Regions. The Scale Bar Shown in the Photomicrograph is 10µm in Length.

In addition to the differences in microstructure, Figure 7 only exhibits a single phase within the material. The "light" phase that was observed in both hot pressed pellets was not present in the cold pressed + sintered disk, suggesting that the disk contains a significantly more uniform stoichiometry compared to the hot pressed pellets. This chemical uniformity is most likely due to the different atmospheres used in the two sintering operations. In the case of the hot pressing procedure the atmosphere was a vacuum. This condition is considered to be a moderately reducing atmosphere for both CeO_2 and PuO_2 because the amount of oxygen in the atmosphere is very low. One study estimates that CeO_2 placed under these conditions will become reduced and obtain a final stoichiometry of ~$CeO_{1.84}$ if the reaction is allowed to reach equilibrium at 1500°C, with greater reduction expected at higher temperatures [5]. The cold pressed + sintered disk, on the other hand, was sintered in air, and under these conditions the same report predicts the final stoichiometry to be ~$CeO_{1.994}$. PuO_2 has been observed to follow similar trends in behavior, so the reduction in stoichiometry observed in CeO_2 is expected to translate to the PuO_2 system. As a result, a significant difference in chemistry is expected in these materials as a function of the sintering atmospheres.

The analysis of the two phase system is also corroborated by the predictions made in the literature regarding the reduction of CeO_2 in low oxygen atmospheres at high temperatures. The "dark" phase was observed to be only slightly sub-stoichiometric while the "light" phase was observed to approach the stoichiometry of the well-known Ce_4O_7 phase (i.e. $CeO_{1.75}$). In the hot pressed pellets, where the amount of oxygen in the atmosphere was very low,

the presence of the "light" phase indicates that a significant amount of reduction occurred. Meanwhile, in the cold pressed + sintered disk there was no apparent "light" phase, suggesting that very little reduction was occurring, which matches the identification of the "dark" phase as a material that was nearly stoichiometric. It is important to keep in mind that these results and observations are very qualitative. The stoichiometry where the material switches from the "dark" phase to the "light" phase is currently unknown, so we cannot draw any quantitative conclusions regarding stoichiometry. What can be said, however, is that sintering in air provides a more uniform, and controlled, stoichiometry compared to hot pressing in a vacuum. What direct effect this uniformity has on the physical/mechanical quality of the ceramic disk or pellet is currently unknown.

SUMMARY

Employing commercially produced CeO_2 powder, a series of hot press experiments have been performed which determined the feasibility of using this ceramic processing technique in the fabrication of surrogate fuel pellets. Pellets up to ~1 cm in diameter with aspect ratios of ~1 have been produced for further evaluation via a number of techniques including optical microscopy, SEM, and EDS. Examination of the microstructures of hot pressed pellets produced tend to show the presence of two crystallite phases which has been determined to differ in their relative atomic percent Ce/O ratio. Generation of these two phases is believed to be caused by exposure of the material to the reducing process parameters of high temperature and low oxygen pressure. Comparison of pellet microstructures produced by hot press processing compared to disc microstructures produced by classical ceramic cold pressed + furnace sintered processing are, as expected, significantly different. Cold pressed + furnace sintered processing relies on thermal processes for consolidation while hot press processing adds a second driving force of pressure which greatly enhances ceramic consolidation. While hot press processing is more complex and adds additional cost in the fabrication of ceramics, having both thermal + pressure as driving forces results in microstructures with significantly less porosity compared to the application of just the thermal driving forces. Additionally, the different sintering atmosphere used in the cold pressed + sintered disk resulted in a more uniform phase throughout the disk that is most likely representative of nearly stoichiometric CeO_2. The effect of this uniformity, or lack thereof, on the properties of the ceramic should be investigated in the future.

ACKNOWLEDGMENTS

This research was conducted under U.S. Department of Energy contract DE-NE0000422 and the technical support of Mr. Dirk Cairns-Gallimore (U.S. DOE) is greatly appreciated by the authors.

REFERENCES

[1] Pattern: 01-075-2011 (PuO_2), Inorganic Crystal Structure Database (ICSD), National Institute of Standards and Technology (NIST), Gaithersburg MD.
[2] Pattern: 03-065-5923 (CeO_2), Inorganic Crystal Structure Database (ICSD), National Institute of Standards and Technology (NIST), Gaithersburg MD.
[3] Knachel, H., Whiting, C.E., Barklay, C.D., and Kramer, D.P., *NETS 2015*, **5125** Albuquerque, NM (2015).
[4] Whiting, C.E., Watkinson, E.J., Barklay, C.D., Kramer, D.P., Williams, H.R., and Ambrosi, R.M. *NETS 2015*, **5032**, Albuquerque, NM (2015).
[5] Blumenthal, R.N., *J.* Solid *State Chem.*, **12**, 307-318 (1975).
[6] Morss, L.R., Edelstein, N.M., Fuger, J., Eds., *The Chemistry of the Actinide and Transactinide Elements, 4th Ed.*; Springer: Dordrecht, The Netherlands, 2010.
[7] *Engineering Property Data on Selected Ceramics*, v.3, Metals and Ceramics Information Center, Battelle, Columbus Ohio, page 5.4.10-1, 1987.
[8] *Engineering Property Data on Selected Ceramics*, v.3, Metals and Ceramics Information Center, Battelle, Columbus Ohio, page 5.4.9-1, 1987.
[9] Touloukian, Y.S., *Thermophysical Properties of Matter*, v.13, IFI/Plenum, New York, page 331-page 335, 1977.
[10] Touloukian, Y.S., *Thermophysical Properties of Matter*, v.13, IFI/Plenum, New York, page 212-page 216, 1977.

Sublimation Suppression Coatings for Thermoelectric Materials

Chadwick D. Barklay[1], Daniel P. Kramer[1], Paul R. Lichty[2], David M. King[2], and Thomas N. Wittberg[3]

[1]*University of Dayton Research Institute, 300 College Park, Dayton, OH 45469*
[2]*PneumatiCoat Technologies, 67 Tosca Dr., Stoughton, MA 02072*
[3]*Mound Technical Solutions, P.O. Box 203, Miamisburg, OH 45343-0203*

Abstract. The p-type thermoelectric material utilized in the Multi-Mission Radioisotope Thermoelectric Generator (MMRTG) is TAGS-85, which has a nominal composition of $(AgSbTe_2)_{15}(GeTe)_{85}$. Telluride materials are limited to a maximum use temperature of ~550°C. Due to the deleterious effects of oxygen on these materials and their high vapor pressures, telluride-based thermoelectric materials must be operated in a sealed generator with an inert cover gas to retard sublimation and vapor phase transport within the converter. Researchers at UDRI and PneumatiCoat Technologies have developed an atomic layer deposition (ALD) coating process for TAGS-85 that dramatically reduces the sublimation and vapor phase transport of the high vapor pressure constituents of TAGS-85. Incorporation of this coating process will potentially increase the performance and operating lifetimes of future MMRTGs. Skutterudite based thermoelectric materials have been developed by the NASA Jet Propulsion Laboratory (JPL) that will potentially offer higher-efficiency power systems with improved performance over long operating lifetimes. This coating technology platform may also prove to be beneficial once Skutterudite-based thermoelectrics become fully characterized.

Keywords: Atomic Layer Deposition, TAGS-85, Sublimation Suppression

INTRODUCTION

It is well known that degradation mechanisms associated with the thermoelectric elements based radioisotope power systems (RPS) represent a significant fraction of the overall performance degradation of the units over time. These degradation mechanisms include: sublimation of thermoelectric element materials; changes in thermoelectric element properties; increase in electrical and thermal contact resistances at the thermoelectric element interfaces; and increased conductance of the thermal insulation surrounding each thermoelectric element. Each thermoelectric element related degradation mechanism has a significant impact on overall performance degradation of RPS units over time. This study employs atomic layer deposition (ALD) coatings of alumina (Al_2O_3) that are designed to inhibit sublimation-induced deterioration of thermoelectric elements, thereby improving the long-term performance of thermoelectric-based RPS units. The application of ALD Al_2O_3 coatings to TAGS-85 thermoelectric elements inhibits the sublimation-induced deterioration of the thermoelectric elements when they are exposed to operational conditions similar to those within the MMRTG.

Background

TAGS-85 was first used as a p-type thermoelectric material for a space power application in 1968 in the Systems Nuclear Auxiliary Power Program (SNAP) 19, which powered the Nimbus-B weather satellites. Since then TAGS-85 has been employed in the SNAP 27 and the MMRTG, which is currently powering

the Curiosity Rover as part of the Mars Science Laboratory (MSL) mission (Figure 1). In the early 1970's Teledyne Energy Systems conducted a study to determine if the degradation rate of TAGS-85 thermoelectric elements could be minimized [1]. Skrabek's study employed ceramic adhesives, phosphate glasses, lead oxide based enamels, and high-temperature engine paints to coat TAGS-85 thermoelectric elements. It is important to note that Skrabek does not disclose the exact composition of the materials or the methodology of how they were applied, but a later citation by Skrabek does state that the ceramic adhesives were silica-based [2]. It is important to note that all the tested coatings failed due to rupture of the coating followed by vaporization of the thermoelectric material. However, the coated TAGS-85 thermoelectric elements exhibit very little performance degradation as long as the coating remained intact. This work demonstrated the efficacy of employing a coating to minimize the degradation rate of TAGS-85 thermoelectric elements, but the coatings employed were unreliable as a long-term solution. Thus, for over 40-years the chosen methodology to minimize the degradation rate of TAGS-85 thermoelectric elements was to pack silica-based insulation in the annulus between the thermoelectric elements and the thermal insulation in the RPS unit.

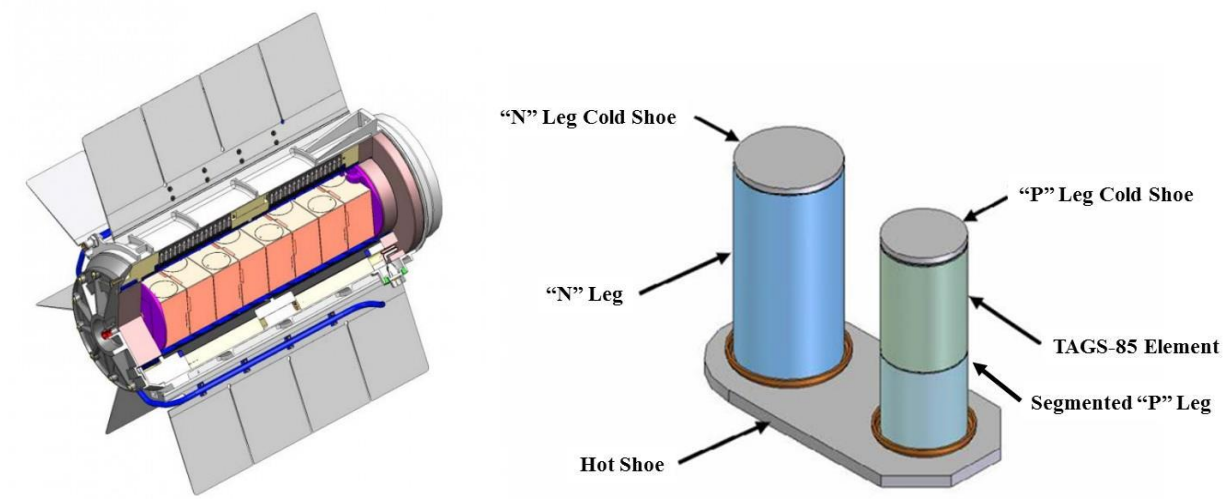

FIGURE 1. (Left) MMRTG cutaway diagram; (Right) MMRTG thermoelectric couple, which employs a segmented "P" Leg fabricated out of TAGS-85.

Atomic Layer Deposition

ALD is a gas phase coating process that is functionally superior to alternate coating approaches such as chemical vapor deposition (CVD), liquid-phase bath deposition/plating techniques, and particle-based approaches such as electrophoretic deposition. ALD reactions occur only between the gaseous precursors administered to the reactor, and the functional groups present on the surface of the substrate. The sequential nature of the process (shown in the schematic in Figure 2), and the ability to only carry out reactions on the surface functional groups, guarantees that these are self-saturating processes that cannot "overbuild" beyond one layer of a precursor. This allows for coating chemistry and thickness to be precision tailored with angstrom level precision, which is ideal for engineered components with extremely tight tolerances. The resulting coatings are chemically-bonded to the surfaces of the substrate, and have been proven to be conformal and pinhole-free, even on high aspect ratio surfaces. A typical process is sequentially repeated to build a high performance Al_2O_3 coating with a thickness that is extremely linear to the number of AB cycles. Additionally, the ALD process does not require line of sight or high substrate temperatures. The functional value of Al_2O_3 derived from an ALD coating process is the ability produce fully-dense ultra-barrier layers that can be tuned by thickness and composition to achieve maximum sublimation suppression of thermoelectric materials in an operational environment.

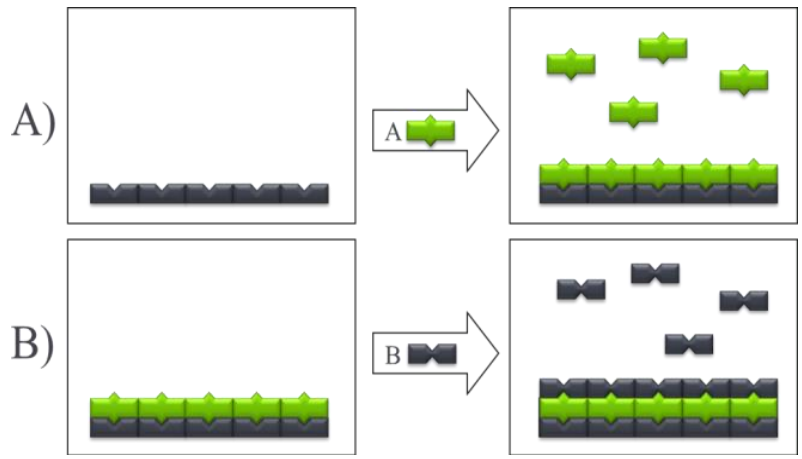

FIGURE 2: Binary reaction sequence chemistry that allows for precision-thickness films on substrates.

EXPERIMENT

A total of eight (8) TAGS-85 production elements were sequentially coated using either 200 or 400 ALD cycles to produce a 30 or 40 nm thick coating of Al_2O_3, respectively. During the ALD coating process the TAGS-85 substrate temperature was maintained at 150°C. The ALD coated TAGS-85 elements then were individually sealed in low-thermal-expansion borosilicate glass (Pyrex) ampoules using high-vacuum manifold and scientific glass blowing techniques. Each test tube was evacuated to 1 x 10^{-3} torr, then backfilled with ultra-high purity (UHP) argon to approximately 100 torr before being sealed. The encapsulated ALD coated TAGS-85 elements were then aged at 350°C for 1000, 3000, 5000, and 7000 hours. This test temperature was selected to represent the highest "worst case" hot-side temperature of the TAGS-85 thermoelectric element in a MMRTG. After aging, all coated specimens were analyzed using Auger Electron Spectroscopy (AES) to characterize the performance of the Al_2O_3 coating, and diffusion and/or sublimation of the constituent materials of the thermoelectric elements.

A Varian Auger spectrometer was used to analyze the aged TAGS-85 specimens. To analyze multiple locations on each specimen, each of the TAGS-85 elements was masked with aluminum foil before being mounted on the Auger sample tray. Thus, only a relatively small area on each sample was exposed to the ion beam during the analysis. Additionally, sputter rate standards of a 48 nm thick silicon nitride film and a 100 nm (±10%) thick silica film were employed. The sample tray loaded into the Auger vacuum chamber was baked out at 100°C and pumped overnight to achieve a vacuum of approximately 1 x 10^{-10} torr. After the analysis of each set of samples was completed, the sample tray was removed from the vacuum system and the aluminum mask on each coated TAGS-85 specimen was relocated to expose a new area for analysis. The tray was then reloaded into the vacuum system, which was again baked out and pumped overnight. In general, three profiles were recorded for each coated TAGS-85 specimen.

Auger depth profiles of the coated specimens were conducted using a 3 keV argon ion beam at 45°. The profiles of the silicon nitride and silica film standards demonstrate a sputter rate 13.0 and 15.8 nm/min, respectively. Literature indicates that the sputter rate of Al_2O_3 is half that of silica [3], and experience has shown that the sputter rate of silicon nitride and silica are similar, which is confirmed by the results. Thus, for the depth profiles of the Al_2O_3 coated TAGS-85 specimens, a sputter rate of 7.0 nm/min is assumed. The sputter rate for the TAGS-85 substrate material was not measured.

RESULTS

Virgin Uncoated TAGS-85

A detailed and systematic study of the sputtering behavior of TAGS-85 has never been conducted. Thus, before initiating any characterization activities it was first necessary to establish an AES depth profile baseline for an uncoated, untested TAGS-85 element. These results enabled the determination of potential compositional information between the near-surface (to a depth of several nanometers) and the bulk, and facilitated the proper interpretation of later AES depth profiles. Figure 3 (Left) is the AES depth profile for an uncoated, unaged TAGS-85 element. The horizontal lines show the nominal composition for TAGS-85 relative to the values associated for the depth profile. The apparent discrepancy is due to the fact that the relative sputtering yields for germanium and tellurium are significantly different. For 2 keV argon ion beam at 45°, the relative sputter yields for germanium and tellurium are 3.2 and 13.3, respectively [4]. This means that when sputtering TAGS-85, the sputtered surface will be depleted of tellurium, and thus will appear to be enriched in germanium.

Figure 3 (Right) is the AES depth profile for an uncoated TAGS-85 element aged for 3000 hours at 350°C. Based on the data there is a reduction in the levels of germanium near the surface of the TAGS-85 elements after aging. This is contrary to the belief that tellurium is the more mobile of the elemental species in the TAGS-85 system due to is high vapor pressure.

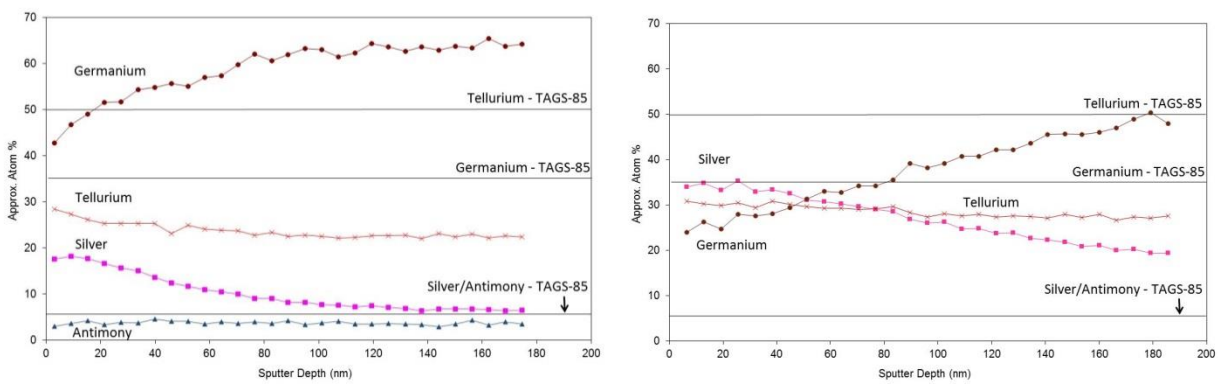

FIGURE 3. (Left) An AES depth profile for an uncoated, unaged TAGS-85 element. (Right) AES depth profile for an uncoated TAGS-85 element aged for 3000 hours at 350°C. For clarity the carbon and oxygen signals were removed from both figures.

ALD Coating Thickness

The TAGS-85 elements used to validate the coating thickness were previously used in an earlier aging experiment. Thus, the AES depth profile data associated with Figure 4 is only germane to the depth of the Al_2O_3/TAGS-85 interface. Figure 4 (Left) is the AES depth profile for an as-received ALD Al_2O_3 coated TAGS-85 element. This particular TAGS-85 element was subjected to 200 ALD cycles to produce the Al_2O_3 coating. Figure 4 (Right) is the same AES depth profile but the oxygen, aluminum, and carbon signals are removed for clarity. One methodology to determine oxide coating thickness from an AES depth profile is derived from the point where the oxygen signal is 50% of the maximum value. However, employment of this methodology would establish a coating thickness to be almost twice the calculated thickness. Thus, for this effort the coating thickness was established to be the point where the signal intensity for germanium, silver, and tellurium begin to increase. Utilizing this methodology a coating thickness for the 200 and 400 cycle ALD Al_2O_3 coating was determined to be 30 and 40 nm, respectively. This is in good agreement with the calculated Al_2O_3 coating thickness for 200 and 400 ALD cycles.

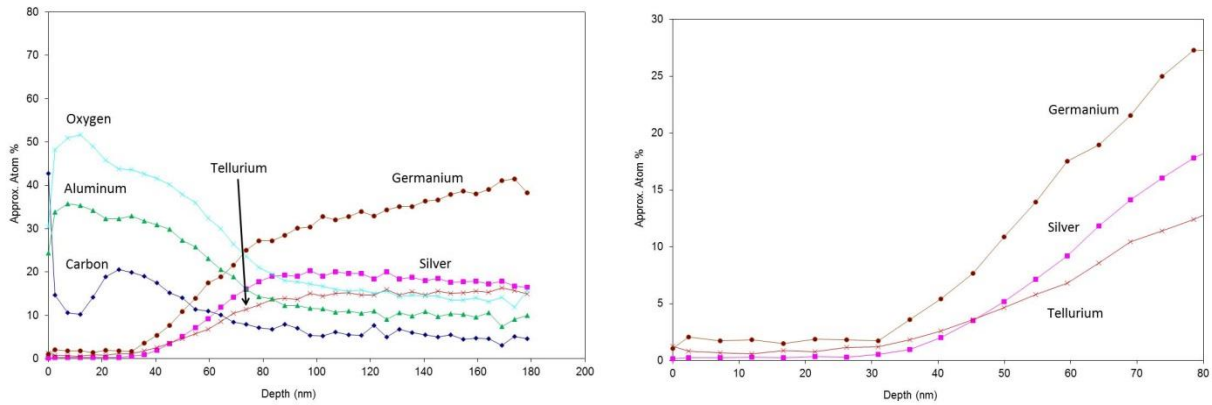

FIGURE 4. (Left) is the AES depth profile for an unaged ALD Al_2O_3 coated TAGS-85 element. (Right) is the same AES depth profile but the oxygen, aluminum, and carbon signals are removed for clarity.

ALD Coating Performance

The AES depth profiles for the ALD Al_2O_3 coated specimens aged at 350°C for durations up to 3000 hours suggest that trace amounts of germanium and tellurium have diffused through the ALD coating during the aging process. It is important to note that there is an overlap of the AES spectra for tellurium and oxygen, which confounds the measurement of low levels of tellurium in the alumina coatings. As a result, the spectra were corrected using a pure alumina spectrum as a reference. As shown in Figure 5, low levels of germanium, silver, and tellurium are present in the coating after 3000 hours of aging. These levels appear to be commensurate with those of unaged specimens shown in Figure 4 (Right) at a depth of less than 30 nm from the surface of the TAGS-85 element. However, a relatively low level of germanium has accumulated on the surface of the coated element, which is consistent with all ALD coated specimens that have been aged. This behavior is also consistent with data from previous experimentation associated with Al_2O_3 Sol-Gel coatings in 2012, but those coatings were ~100 µm thick and the diffusion of germanium was significantly more pronounced.

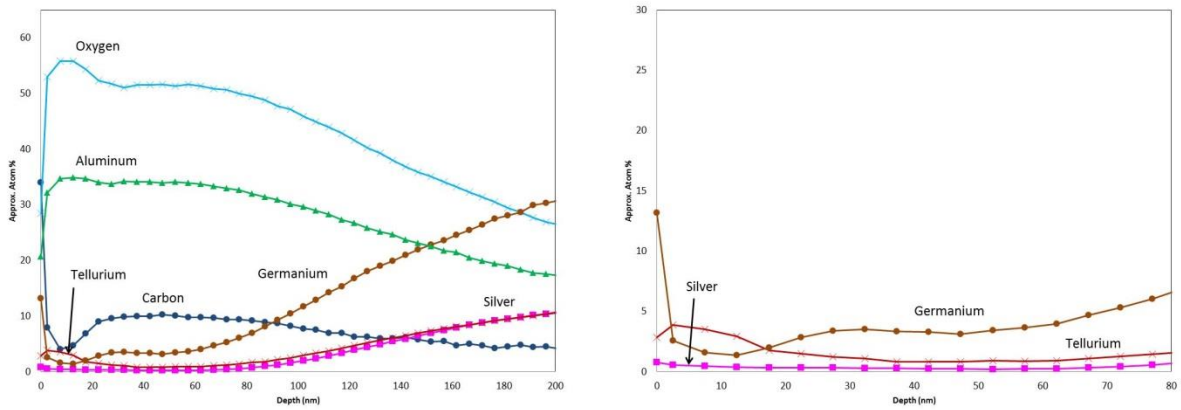

FIGURE 5. (Left) is the AES depth profile for an ALD Al_2O_3 coated TAGS-85 element aged at 350°C for 3000 hours. (Right) is the same AES depth profile but the oxygen, aluminum, and carbon signals are removed for clarity.

Figure 6 is an X-ray photoelectron spectroscopy (XPS) surface scan of the inside of a Pyrex ampoule used to age a TAGS-85 specimen at 350°C for 3000 hours. The results show that, in addition to silicon and oxygen from the Pyrex, germanium has vaporized and condensed on this surface. Tellurium, silver, or antimony was not detected. These results are consistent with coated and uncoated TAGS-85 elements. This further confirms that germanium is the most mobile of the elemental species in the TAGS-85 system.

Figure 7 represents a compilation of AES depth profiles of 200 cycle ALD Al_2O_3 coated TAGS-85 specimens that are unaged, and aged at 350°C for 1000 and 3000 hours. These compilation profiles highlight the diffusion behavior of germanium and tellurium through the ALD alumina coating.

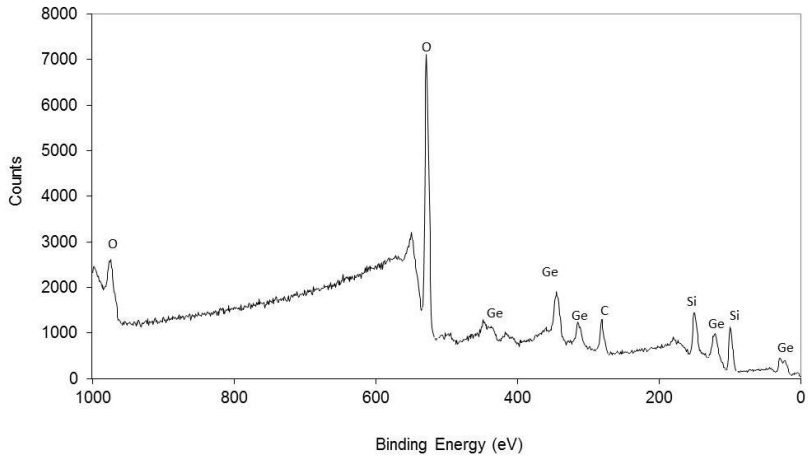

FIGURE 6. XPS surface scan of the inside of an ampoule used to age an ALD Al_2O_3 coated TAGS-85 specimen at 350°C for 3000 hours.

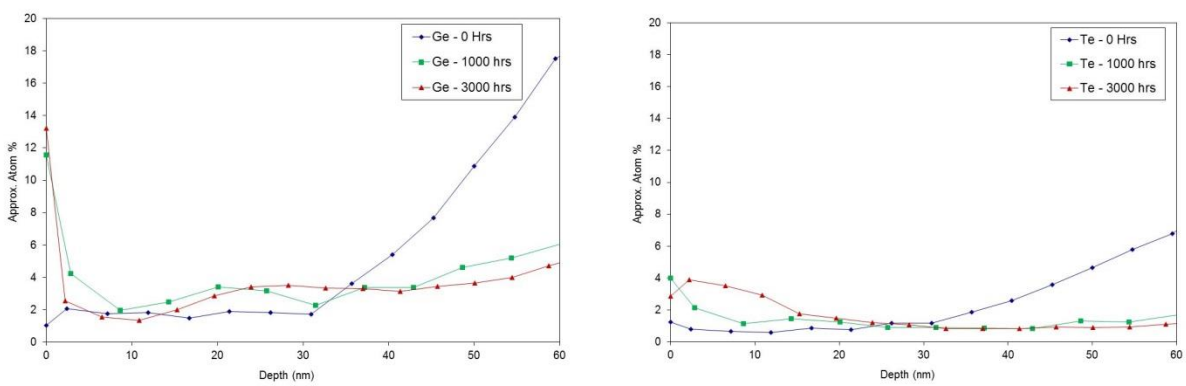

FIGURE 7. Changes in AES depth profile of ALD Al_2O_3 coated TAGS-85 specimens as a function of exposure time at 350°C. (Left) is the compilation profile for germanium, and (right) is the compilation profile for tellurium.

DISCUSSION

Any discussion regarding the quantitative aspects of this study must first center on the effects of sputtering artifacts from atomic mixing, surface roughness, and preferential sputtering in the AES depth profile results. As previously discussed, when sputtering TAGS-85, tellurium will preferentially sputter, which leads to an apparent enrichment of germanium. Mathematical models of varying sophistication do exist to deconvolute the measured AES depth profiles, and enable the correction and reconstruction of the profiles. However, employment of those models was beyond the scope of this study.

Based on a qualitative comparison of the AES depth profiles shown of the uncoated and ALD coated TAGS-85 specimens in Figure 3 (Right) and Figure 5, respectively, there is a significant reduction of the levels of germanium, tellurium and silver at the surface of the TAGS-85 element after aging. This infers that the ALD Al_2O_3 coating is inhibiting the diffusion of these elements. Additionally, comparing the AES depth profile data for germanium between 20-30 nm of the unaged ALD Al_2O_3 coated TAGS-85

element shown in Figure 4 (Right) with the ALD Al_2O_3 coated TAGS-85 element aged for 3000 hours shown in Figure 5 (Right), there is an apparent enrichment in germanium in the vicinity of the Al_2O_3/TAGS-85 interface. This suggests that germanium is migrating to the Al_2O_3/TAGS-85 interface. Similar research to characterize alumina-germanium semiconductor structures confirms that germanium can diffuse through the Al_2O_3 layer and accumulate on the surface of the oxide layer after heating to temperatures comparable to those used in the aging experiments in this study [5,6].

SUMMARY

Sublimation of the constituent elements of TAGS-85 is a leading factor in the performance degradation of the RPS units over time. Experimentation associated with this study has demonstrated a significant reduction of the diffusion of germanium, tellurium and silver from the TAGS-85 surface thru the Al_2O_3 coating at 350°C for durations greater than 3000 hours. Thus, ALD of Al_2O_3 coatings offer a novel, inexpensive, and fast technique to retard the sublimation-induced deterioration of TAGS-85 thermoelectric elements.

It is important to note that results of this study are based on first-order coupon-level demonstrations. Thus, it is difficult to derive actual RPS performance predictions from the experimental data because of the extreme differences in the physical makeup of any TAGS-85 testing apparatus and the actual RPS units. The next evolution of confirmatory testing should focus on thermoelectric couple-level validations and then extensive life testing, which could be done by Teledyne Energy Systems or the NASA Jet Propulsion Laboratory.

ACKNOWLEDGMENTS

This research was conducted under U.S. Department of Energy contract DE-NE0000422 whose fiscal support is greatly appreciated by the authors. The technical support of Mr. Dirk Cairns-Gallimore (U.S. DOE) was invaluable to the authors. Thanks to Ms. Linda Kasten for the XPS analysis. Finally, a there is immeasurable gratitude for Mr. Robert Carpenter for his patriarchal role in the RPS program and for advocating for the necessity of this research.

REFERENCES

[1] Skrabek, E.A., "Improved Long-Term Performance of TAGS Thermoelements," in proceedings of *Ninth Intersociety Energy Conversion Engineering Conference*, American Society of Mechanical Engineers, New York, pp. 160-164, (1974).

[2] Skrabek, E.A. "Effects of Coatings and Temperature on Long Term Performance of TAGS Thermoelements," in proceedings of *Eleventh Intersociety Energy Conversion Engineering Conference*, American Institute of Chemical Engineers, pp. 1567-571, (1976).

[3] Baer, D.R., Engelhard, M.H., Lea, A.S., Nachimuthu, P., Droubay, T., Kim, J., Lee, B., Mathews, C., Opila, R. L., Saraf, L.V., Stickle, W.F., Wallace, R., and Wright, B.S., "Comparison of the Sputter Rates of Oxide Films Relative to the Sputter Rate of SiO_2," *J. Vac. Sci. Technol. A - Vacuum, Surfaces and Films*, **28(5)**, 1060-1072, (2010).

[4] Seah, M.P., Clifford, C.A., Green, F.M., Gilmore, I.S., "An Accurate Semi-Empirical Equation for Sputtering Yields I: For Argon Ions," *Surf. Interface Anal.*, **37**, 444-458, (2005).

[5] Shibayama, S., Kato, K., Sakashita, M., Takeuchi, W., Taoka, N., Nakatsuka, O., and Zaima, S., "Improvement of Al_2O_3/Ge interfacial properties by O_2-annealing," *Thin Solid Films*, **520**, 3397-3401, (2013).

[6] Shibayama, S., Kato, K., Sakashita, M., Takeuchi, W., Taoka, N., Nakatsuka, O., and Zaima, S., "Understanding of Interface Structures and Reaction Mechanisms Induced by Ge or GeO Diffusion in Al_2O_3/Ge Structure," *App. Phys. Letters*, **103**, 082114, (2013).

Shielding Development for Nuclear Thermal Propulsion

Jarvis A. Caffrey[1,2], Carlos F. Gomez[2], Luke L. Scharber[2]

[1]*Department of Nuclear Engineering & Radiation Health Physics, Oregon State University, Corvallis, OR 97301*
[2]*NASA Marshall Space Flight Center, Huntsville, AL 35812*
541-227-4295; jarvis.a.caffrey@nasa.gov

Abstract. Radiation shielding analysis and development for nuclear thermal propulsion (NTP) is currently in progress and preliminary results have enabled consideration for critical interfaces in the reactor and propulsion stage systems. Early analyses have highlighted a number of engineering constraints, challenges, and possible mitigating solutions. Performance constraints include permissible crew dose rates (shared with expected cosmic ray dose), radiation heating flux into cryogenic propellant, and material radiation damage in critical components. Design strategies in staging can serve to reduce radiation scatter and enhance the effectiveness of inherent shielding within the spacecraft while minimizing the required mass of shielding in the reactor system. Within the reactor system, shield design is further constrained by the need for active cooling with minimal radiation streaming through flow channels. Material selection and thermal design must maximize the reliability of the shield to survive the extreme environment through a long duration mission with multiple engine restarts. A discussion of these challenges and relevant design strategies are provided for the mitigation of radiation in nuclear thermal propulsion.

Keywords: NTP, shielding, radiation, dose, heating

INTRODUCTION

Nuclear thermal propulsion (NTP) systems provide a dramatic improvement in performance for missions requiring both high thrust and high specific impulse, namely long duration crewed exploration missions. NTP systems can increase cargo capacity and reduce the time spent in interplanetary space, both of which will serve to reduce overall mission risk and cosmic radiation exposure. However, NTP systems present a number of additional challenges beyond those of non-nuclear propulsion, including the need to mitigate radiation generated by nuclear fission. The growing concern of long duration exposure to cosmic radiation has now brought a great deal of focus on mitigating radiation risk in crew compartment design and material selection. In light of this growing concern for a crewed Mars mission, it is now pertinent to re-approach the problem of shielding and radiation mitigation for a nuclear thermal propulsion stage.

SHIELDING CHALLENGES

Reactor shield design should, for any reactor, be intimately involved in system design from its earliest stages. Penetrating radiation tends to produce system interfaces in otherwise unrelated components. Beyond the obvious health protective requirements, radiation shields serve vital roles to minimize unwanted radiation heating and reduce degradation of electronic and mechanical components. The process of absorbing radiation energy yields heat that must be managed in some fashion, and the shields must be able to perform reliably in the face of thermal stress and high levels of radiation exposure.

Performances Requirements

Radiation shields must be designed to meet some given performance requirement. In terrestrial reactors, this is often defined by the need to minimize the ambient dose rate at a given location or the need to minimize radiation damage to the reactor pressure vessel. In the case of NTP there are three possible limiting requirements for a shield design. First, is the need to minimize radiation dose to the crew. Second, heating in the propellant must be minimized to avoid

localized boiling and pump cavitation during engine operation. Third, material damage to critical components must be held within their rated exposure limits.

Dose to Crew

Health physicists apply the principle of As Low As Reasonably Achievable (ALARA) in common practice. An emphasis is often given to the 'Reasonable' aspect of this approach, where the benefits of lower doses must be balanced against other factors such as cost, weight, and complexity. Likewise, radiation dose to personnel in or near a nuclear propelled spacecraft should be minimized to the greatest extent possible, within reason. It must be held in perspective that the doses received by astronauts on a long term expedition outside of Earth's protective magnetic field, while still largely unknown, could certainly exceed 1 Sv (100 rem) over the course of a mission due to the pervasive galactic cosmic rays (GCR) and sporadic solar particle events (SPE). Even rudimentary shielding of a nuclear engine, combined with the inherent shielding provided by the spacecraft and cargo, would likely reduce accumulated reactor-produced dose levels to an order of magnitude less than the space radiation dose.

In any case, crew dose limits for space exploration missions are not yet fully defined. However, a set of guidelines for short term and deterministic effects and long term stochastic effects were recently provided in a NASA Standard [1]. Such limits, when fully defined, will be based upon the combined effects of natural and manmade sources. Limits to radiation exposure from a nuclear engine will then need to be balanced against the anticipated dose received from cosmic rays. In terms of shielding efficiency, then, it makes better sense to allocate mass into combined shielding strategies within the crew compartment that can also serve to minimize dose from solar particles and secondary radiation produced from GCR collisions in the spacecraft. Concepts such as reconfigurable water bladders, food pantries, and waste storage can serve as slab shielding to mitigate radiation from the engines during their short periods of operation and then repurposed into 4π shielding during the long coasting stages where cosmic radiation burdens dominate. This principle does have limitations in that high-Z materials such as lead or tungsten should not be placed near the crew compartment due to the increased production rate of secondary particles produced by GCR spallation.

Radiation Heating in Propellant

Current mission architectures for nuclear thermal propulsion feature cryogenic liquid hydrogen as a propellant due to its low atomic mass that affords the highest possible specific impulse with solid core designs. Liquid hydrogen (LH_2) also serves as a reasonably effective neutron shield, although its low density mandates extremely large storage capacities. LH_2 must be actively maintained at cryogenic temperatures as heating due to sunlight and cosmic radiation results in boil-off and requires venting to avoid excess pressurization. Absorption of nuclear radiation energy dramatically increases the heating rate within cryogenic propellant, particularly during engine operation. As a simplified example case, consider an unshielded reactor adjacent to a cryogenic storage tank of very large diameter that imposes a geometry factor of one fifth of the 4π solid angle for isotropically emitting radiation. For a reactor operating at 1,000 MW with 0.5 percent of energy leaking by penetrating radiation, the tank will absorb about a full megawatt of thermal energy through nuclear radiation alone. Obviously, even in the absence of a crew or radiation sensitive equipment, shielding is needed to minimize this thermal burden in cryogenic storage.

Heating of cryogenic propellant during engine operation is not necessarily undesirable. The process of pumping from the storage tank requires that the void space, or ullage, in the tank must be repressurized to maintain a constant pressure at the pump inlet. Likewise, adding thermal energy to the propellant will not necessarily increase the system temperature, as the reducing tank pressure caused by pumping will force vaporization accompanied by cooling. From a bulk fluid perspective, then, there is a balance that may be struck between the influx of radiation energy and evaporative cooling due to pumping. In reality, though, most of the radiation is absorbed closest to the reactor. This is particularly the case for neutrons that deposit the majority of their energy within the first centimeters of LH_2 at the aft tank face. The problem, then, is the effect of localized heating in the location likely to be nearest the pump inlet. The resulting effects of localized boiling and pump cavitation would lead to failure of the turbopumps. Preventing cavitation will likely be the dominating performance requirement of a reactor shield, and establishment of radiation flux limits in this regard is ongoing.

Material Radiation Damage

Some components in a nuclear propulsion system may be sensitive to radiation damage, particularly in the case of electronic control circuits and motorized actuators. Extensive work in the field of radiation hardening for aerospace applications (electronics) and terrestrial nuclear applications (pumps, valves, and motors) will provide a wealth of options for system design. It is unlikely, then, that component radiation damage will be the largest driving factor for radiation shield design. Sensitive electronics and other components can be placed within the protection of an existing

shield or utilize spot-shielding as needed. A likely candidate for the most sensitive critical component that must be reactor-adjacent is the control drum actuator stepper motor, which will likely need to incorporate an extended coupling shaft that penetrates a layer of shielding.

Thermal Performance

Radiation shielding located near an operating reactor core will be subjected to a substantial thermal load as radiation energy is converted to heat. The shielding system must maintain temperatures within acceptable limits to maintain structural integrity. In the case of a high power reactor, active cooling is required to counteract this heat generation. If active cooling is provided by coolant flow within the shield, then radiation streaming through those flow channels must be mitigated. Of particular concern is the spatially non-uniform heat generation within the shield, in which those regions closest to the core centerline are subject to heating that is several orders of magnitude greater than elsewhere in the shield.

SHIELDING DESCRIPTION

The radiation shield system for a nuclear thermal engine needs only to shield the fraction of radiation emitted toward the vehicle and crew. This 'shadow shielding' method is possible because of the placement of the engines at the aft of the spacecraft and lack of atmosphere or other matter to facilitate scatter. The shield must be capable of attenuating the substantial source of penetrating gamma rays emitted during engine operation, and, to a lesser extent, the continued emission of gammas from fission product decay and activation. Leakage of neutrons from the core during operation must also be mitigated, particularly for fast neutrons that must be slowed and absorbed.

Neutron shielding

Neutron shielding typically occurs in multiple stages from the perspective of individual neutrons. First, in the case of a high energy neutron, the kinetic energy must be shed by nuclear collisions. Elastic collisions with heavy nuclei such as lead or tungsten will have little effect on the kinetic energy of the incident neutron due to the conservation of momentum (think of a ping pong ball against a bowling ball). Kinetic energy is more effectively shed by collisions with lighter atoms such as carbon, beryllium, and especially hydrogen. With each scattering collision, the neutron sheds more energy and subsequently increases the chance of absorption in a receptive nucleus. The probability of absorption is typically highest for the lowest energy neutrons, or 'thermal' neutrons in energy equilibrium with the thermal motion of their surrounding atoms. A purely elastic scattering shield, such as beryllium, is not considered effective as the thermal neutrons will exit the shield and be absorbed elsewhere. Thus, the neutron shield needs to both slow and capture the incident neutron flux. Inclusion of nuclides with a high absorption cross section is desirable, but neutron capture typically produces some form of secondary radiation emission. Shields that use absorbers producing high energy gammas must therefore account for a third stage in the neutron shielding process by absorbing these penetrating secondary photons.

Gamma shielding

Gammas are scattered and absorbed through electron interactions, and are best attenuated by materials with a high charge density (high-Z) such as lead, tungsten, or uranium. In the case of a combined shield in which secondary gammas are produced within the neutron shield, it may seem more efficient to place all of the neutron shield material between the reactor source and the gamma shield so that fission and secondary gammas are all captured in a single layer. This would be true in the case of one-dimensional slabs where the diameter of all shield layers is constant. In a shadow-shield, however, the diameter of the shield is roughly defined by a conical solid angle of a sphere with its origin in the reactor core (in fact, the origin of that sphere would be defined by a distribution extending below the core). The consequence of this geometry is that shield layers further from the source will have a greater diameter and mass.

Material Selection

Early development in the NERVA program featured a substantial effort in material selection in which a large number of candidate materials were considered, particularly with regard to neutron shielding [4]. Of these, only a handful can be considered viable, and two such materials consistently stand out: lithium hydride and boron carbide. Comparisons of these materials could be made at great length, but for the purposes of this paper are summarized briefly.

Lithium hydride (LiH) stands out as the most effective neutron shield material per unit mass, owing to its incorporation of hydrogen as a moderator and as an excellent neutron absorber when enriched in Li-6. Its performance suffers in

high-flux environments, however, as its poor thermal conductivity and narrow range of operating temperature make effective cooling strategies nearly impossible. Its reactive nature mandates that it be sealed within some containment, but its large volume expansion in melted liquid phase must be accounted for during casting and after containment closure.

Boron carbide (B_4C) stands out often as the most effective neutron shield per unit volume, but with a mass penalty in the neutron shield of about 20% greater than that of a practical lithium hydride shield. As a ceramic, B_4C has good thermal conductivity, mechanical integrity, and chemical stability. Although its moderating capacity is reduced by the absence of hydrogen, it does still moderate effectively and absorbs with minimal production of secondary gammas. It is currently manufactured in large quantities at relatively low cost, and although use of enriched boron-10 would increase cost above that of off-the-shelf products, those manufacturing processes would remain unchanged and are readily available.

SHIELDING ANALYSIS

Shielding design is expected to be a highly iterative process that cycles between efforts in optimizing physical effects in radiation transport and thermal performance while aiming to minimize system mass. Outer iterations in system and stage design will inevitably introduce changes to both the source term within the reactor and to performance constraints such as permissible flux. With that in mind, the best approach is to push forth with a limited set of design constraints and focus upon developing an efficient and repeatable analysis approach. The current state of shielding analysis represents a first pass at this process and the results presented herein are generally derived from non-optimized shielding designs. The processes and tools described will then be implemented within a generalized shield analysis toolkit that will enable rapid optimization based upon constraints fed by reactor design and staging parameters.

Monte Carlo Radiation Transport

Most results reported here are derived out of Monte Carlo radiation transport calculations in the MCNP6.1 transport code from Los Alamos National Laboratory (LANL) and available through the Radiation Safety Information Computational Center (RSICC) [5]. Source terms were generated in an MCNP6 model of a low-enriched reactor core design featuring tungsten composite fuel and a large fraction of moderating tie-tubes. A broad discussion of techniques relevant to dose and shielding calculations in MCNP are provided in Kiedrowski's criticality alarm primer [6].

Source Normalization

Simulation of reactor criticality in MCNP does not explicitly behave as it would in a true reactor, particularly in terms of treatments for time and power generation. Tally measurements are normalized per neutron generated in the simulation. In order to normalize any results from a simulation to a physical unit of reactor power, the user must determine a normalization constant C that relates the average number of neutrons produced in the reactor per fission, $\bar{\nu}$, to the average energy produced per fission, Q, as in Equation (1).

$$C = \frac{\bar{\nu}}{Q} \tag{1}$$

It is important to note that that these values may change depending upon fuel selection, neutron energy spectra, core life cycle, and time of reactor operation. In practice, this would be calculated with conversion factors to directly relate the neutron production rate to reactor power over a given time interval, with an example given in Equation (2).

$$1\,W \cdot s\left(\frac{1\,J/s}{1W}\right)\left(\frac{1\,MeV}{1.6E-13J}\right)\left(\frac{1\,Fission}{\sim 200\,MeV}\right)\left(\frac{2.445\,neutrons}{1\,Fission}\right) = 7.64E10\frac{n}{W \cdot s} \tag{2}$$

Surface Source Recording

MCNP permits the recording of fully characterized radiation tracks passing through a defined surface or produced within a given cell. The user can apply this 'Surface Source Write' (SSW) functionality within a criticality calculation to capture the particle fluence exiting the reactor boundaries. With careful consideration, subsequent calculations can utilize the 'Surface Source Read' (SSR) functionality to recreate the same radiation environment around the reactor with no need to track the dense population of neutrons within the core. The internal radiation environment would not be expected to change significantly between shielding design iterations, so the SSW/SSR functionality provides orders of magnitude in time savings for shielding design analysis.

Variance Reduction

Reactor shielding problems are notoriously difficult to perform in Monte Carlo analysis. The nature of a successful shield means that the total number of particles exiting the shield system is vastly lower than those entering the system, typically by many orders of magnitude. This means that out of all of the particle histories followed by the computer code, only an extremely small fraction will contribute to the scoring tallies of interest. In order to achieve reasonable statistics within those tallies, either an astronomical number of total histories must be run, or some form of variance reduction must be applied to the system. A number of such techniques were applied in these analyses, including cell importance weighting, weight windows, energy splitting, and DXTRAN, although not all concurrently. A full description of variance reduction techniques is well outside the scope of this paper, but interested readers are encouraged to consult the MCNP user's manual [7].

Time Dependent Dose Calculation

Dose rates at the crew compartment vary continuously over the duration of the mission, either through loss of shielding afforded by propellant while the engine is in operation or through the decay of fission products after engine shutdown. The time dependent behavior of dose rates in a nuclear propulsion system are of vital concern, particularly as the propellant is drained near the end of the final burn and dose rates reach a maximum before final engine cutoff. Time dependent dose rates have been modelled in MCNP by varying the propellant load within tanks of the anticipated size and shape for the current reference Mars mission profile. As could be expected, dose rates follow an exponentially increasing curve as the effective shielding thickness of propellant decreases. Gamma dose rates deviate from this trend only at points associated with the transition between stage tanks, where the geometry of the tank ends modifies the rate of change for effective shield thickness under constant flow rate conditions as seen in Figure (1a). The system can be modeled with reasonable accuracy by applying an empirical exponential function in which the dose rate is a function of remaining propellant. Alternatively, a logarithmic interpolation between the data points from the MCNP analysis can help to refine a solution.

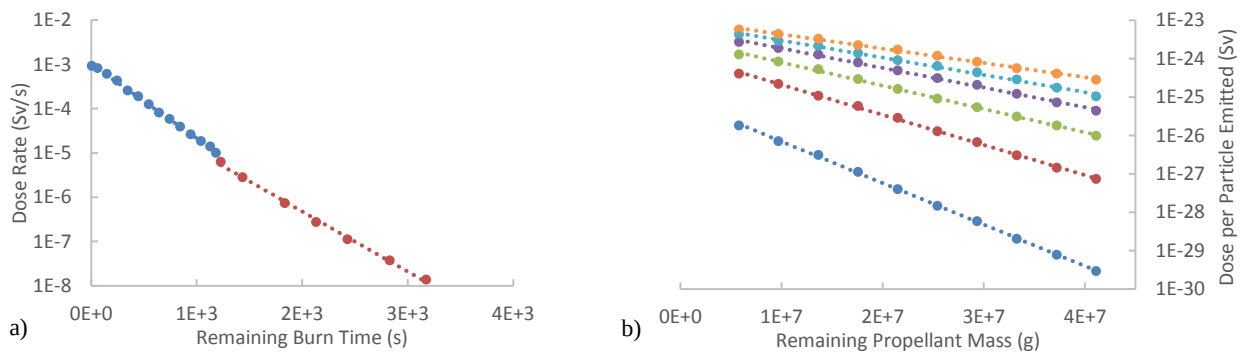

FIGURE 1. (a) Prompt dose rate during engine operation as a function of remaining burn time. (b) Dose per emitted particle for gamma rays of varying energy groups generated within the reactor core as a function of remaining propellant mass. The abscissae can be considered interchangeable, related by the total mass flow rate of propellant during operation.

Contributions to dose from delayed gammas due to buildup and decay of fission products are rather more complex and require a different approach. In one such approach, instantaneous dose rates are calculated for each of six energy groups introduced as a fixed source into the core based upon the power profile determined from analysis of the criticality run, as shown in Figure (1b). Dose contributions are then determined per emitted particle within a series of photon energy groups. Equation (3) is used to determine energy emission rate by a set of N_j multi-exponential empirical formulas for each energy group j with varying production coefficients α_{ij} and accompanying effective half-lives λ_{ij}, based upon the reactor operating time t_o and subsequent shutdown time t_s assuming a constant fission rate P_o , the behavior of which is shown in Figure (2) [8,9,10].

$$\Gamma_j(t_o, t_s) = P_o \sum_{i=1}^{N_j} \frac{\alpha_{ij}}{\lambda_{ij}} e^{-\lambda_{ij} t_s} [1 - e^{-\lambda_{ij} t_o}] \tag{3}$$

Thus, a set of six delayed gamma terms and one fission term are used to create a series of expected instantaneous dose rate contributions at discrete propellant loads. These seven terms are combined within a purpose-built MATLAB code

to analyze the dose rate throughout the mission, as shown in Figure (3). The simplified model of operation uses two conditions for calculation at discretized time steps. In the 'Engines On' condition, propellant is expended and all instantaneous dose rate components increase as the effective thickness of propellant shielding is eliminated. The fission source term is applied throughout this condition, and buildup of delayed gamma sources from fission products is added as an independent source term. In the 'Engines Off' condition, the fission source is turned off and propellant load is assumed to be static while the delayed gamma term ceases buildup and the existing inventory decays for the remainder of the calculation. Subsequent engine cycles repeat this process and all delayed gamma terms are added to the inventory built-in during the preceding runs. In the current model, no accounting is included for engine transients (startup and shutdown) and no consideration is made for absorption in fission products or bremsstrahlung radiation from beta decay.

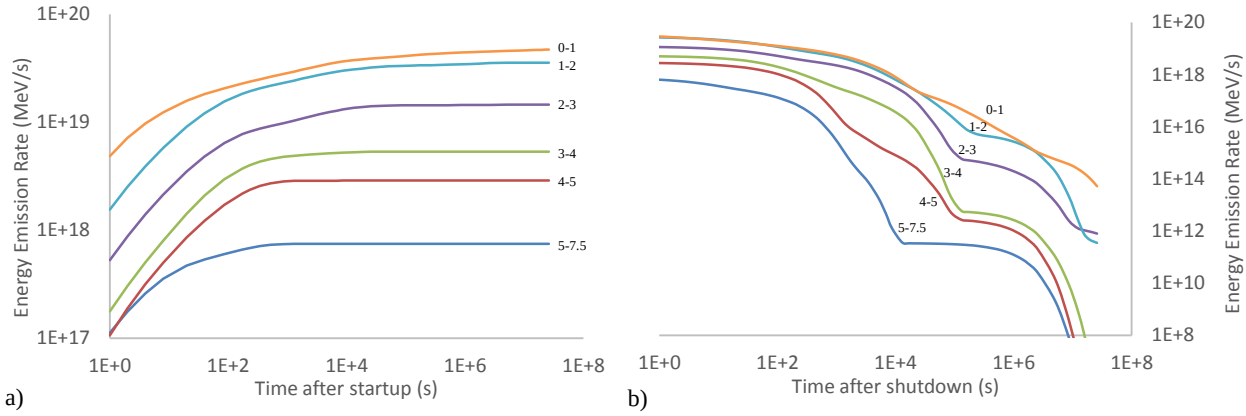

FIGURE 2. (a) Energy emission rate of fission products across 6 energy groups (labeled in MeV) building in during steady state operation at 560 MW. (b) Energy emission rate of fission products decaying after one hour of operation at 560 MW.

The upcoming model will instead use the CINDER-90 algorithm included within MCNP6 to track decay of fission and activation products. Tallies must then be discretized in time, with the resulting time-dependent distribution representing the energy release and absorption behavior after a single fission event. Further processing then yields the relevant values needed to account for source buildup and decay based upon reactor power history. Either of these methods permits flexible integration over user-defined time intervals to determine accumulated dose.

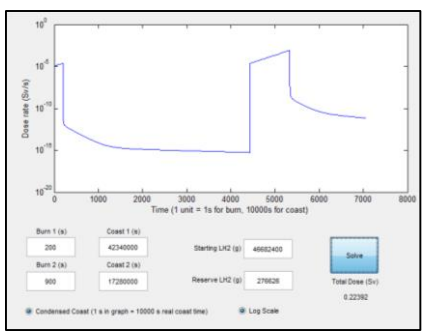

FIGURE 3. Example dose rate history calculated in the custom MATLAB code for a reactor operating at 560 MW with a basic LiH/Pb shield.

Isodose and Isoflux Contours

Early studies for component selection, sizing, and configuration in a nuclear propulsion system require a basic understanding of the radiation environment presented during engine operation. Contour plots of anticipated radiation levels are especially useful in these early phases to provide guidance for placement of sensitive components and enable simple trades between materials and cost factors. MCNP features a simple implementation of FMESH superimposed tallies that can produce spatial flux distributions. In core-centered analyses, an axisymmetric cylindrical tally is generated about the core centerline. Simple flux (F4-type) tallies may be used for flux measurements, as is often the case for neutrons separated by energy groups. However, it is often more desirable to represent these values in terms of their dose, as is often the case for photon flux. Energy dependent dose-response factors are then applied as an FM

multiplier using log-interpolated interaction coefficients, as in the left side of Figure (4) for photon dose to silicon [8]. Where crew dose is a concern, conversion coefficients were applied for ambient deep dose equivalent from neutrons and photons [11]. Silicon dose rate and neutron fast flux values are shown in Figure (4) for a reactor operating at 560 MW. Alternative representations may instead be normalized to dose/fluence per fission, dose rate/flux per $W \cdot s$, or integrated over the reactor power history to provide total dose/fluence.

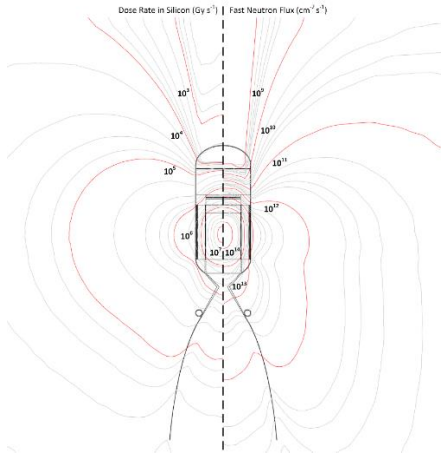

FIGURE 4. Dose rate in silicon (left) and neutron fast flux (right) profiles for a reactor operating at 560 MW with a basic LiH/Pb shield.

Thermal Analysis

Substantial heating occurs within the shield due to radiation absorption and collision processes. Bulk heating within individual cells can be calculated easily in MCNP using F6 heating tallies, which can be useful in many respects, but rigorous thermal analysis requires more detailed spatial representation of heating. Segmentation of large cells into smaller component cells is a possible solution, but such an approach is tedious and unnecessary. Instead, as in the case of dose/flux mapping, FMESH superimposed tallies can be used to resolve the spatial effects of radiation heating. An FM multiplier can be used to extract the ENDF energy dependent heating values for specified materials within a given FMESH tally. Heating mesh tallies were generated for simple representative designs featuring boron carbide neutron shield material, assumed as a pebble bed design with bulk material density adjusted to account for effective packing density. LiH was also considered earlier in the study, but brief analysis suggested that a simple cooling channel model would be inadequate to maintain sufficiently low temperatures near the reactor face and simultaneously maintain sufficiently high temperatures throughout the rest of the shield, as is needed in the case of lithium hydride. Further analysis of LiH was set aside, then, in favor of advancing the more resilient boron carbide design. LiH will likely be considered in later analyses as part of a multicomponent neutron shield to mitigate fast neutron leakage, as its poor conductivity precludes its use in locations immediately adjacent to reactor components.

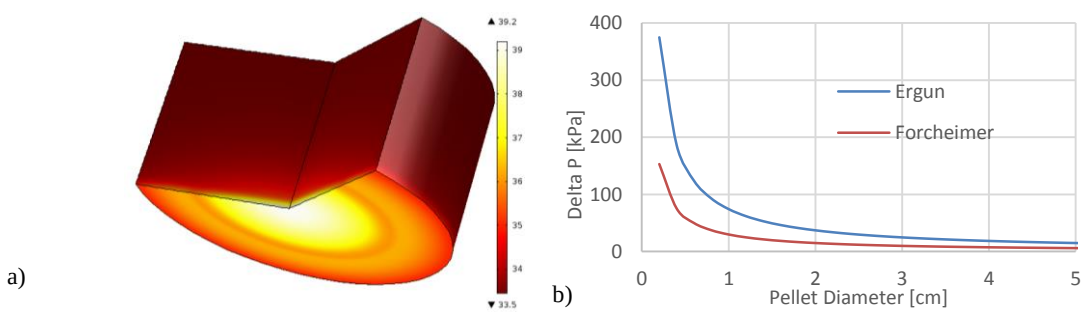

FIGURE 5. a) Hydrogen propellant temperature (°C) (assumed equal to pellet surface temperature) in a B_4C pebble bed shield for a reactor operating at 560 MW after 50 seconds. Effective packing density of 0.6 assumed. b) Pressure drop for gaseous hydrogen in a half-meter length pebble bed shield. Reference reactor operating at 560 MW with effective packing density of 0.6 assumed.

As a ceramic, B_4C features good thermal conductivity and very high temperature limits. Its hardness and chemical stability also permit more construction options. An enticing option is the use of a pebble bed design that allows generous cooling flow while minimizing radiation streaming paths. Pebble beds may also allow for ample opportunity to mix flow streams from multiple inlets prior to injection into the core. One concern for this option, however, was

the magnitude of pressure drop across the shield and its negative impact on engine system power balance. That concern was abated in analysis, though, as pressure drop for a reasonable pellet diameter of 2 cm was determined to be no more than 37 kPa (5.6 psi) using the Ergun formulation as in Equation (4), and likely on the order of 15 kPa (2.2 psi) determined by Ergun formulation including the Forcheimer drag term as in Equation (5). Each equation accounts for dynamic viscosity μ, density ρ, fluid velocity V across the flow length of the shield L. In the case of Equation (5), sphere diameter D and porosity ϵ are coupled as permeability k given in Equation (6), and effects of sphere diameter on pressure drop in either case are shown in Figure (5b) based upon input assumptions derived from early power balance analysis.

$$\Delta P = \frac{150\mu V_s L}{D^2}\frac{(1-\varepsilon)^2}{\varepsilon^2} + \frac{1.75\rho V^2}{D}\frac{(1-\varepsilon)}{\varepsilon^3} \tag{4}$$

$$\Delta P = \frac{\mu V_s L}{k} + \frac{1.75\rho V^2 L}{\sqrt{k}}\frac{\varepsilon}{\sqrt{150\varepsilon^3}} \tag{5}$$

$$k = \frac{D^2\varepsilon^2}{150(1-\varepsilon)^2} \tag{6}$$

Mass Optimization

Given a source term and a limit for exiting radiation flux, the problem of shield optimization can be made relatively straight-forward. In the absence of such well-defined limits, the problem becomes more complex. Rather than optimizing to a single point constraint, the system must be optimized in parallel for a distribution of possible performance constraints. As an example in Figure (6), a limited set of various combinations of gamma shield thickness, neutron shield thickness, and gamma shield position are plotted in terms of total mass versus dose rate. The figure demonstrates the optimal curve, or 'Pareto front', for design variables that balance dose rate against shield mass. Points that plot farther from the optimal curve are considered dominated solutions that represent non-optimal designs. Eliminating all but those non-dominated solutions results in the 'Pareto set' of optimal solutions along the Pareto front. Selection of a point design can then be made with constrained minimization once outer constraints are established. For example, if setting a maximum terminal dose rate of 8E-13 $Sv\ s^{-1}W^{-1}$ for the scenario in Figure (7), then selecting the mass-minimized point design below that point will result in a shield mass of 1,000 kg.

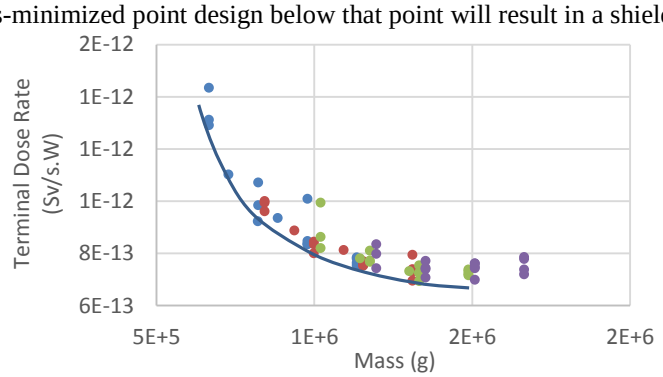

FIGURE 6. Example Pareto optimization plot for various shield designs. Points adjacent to the Pareto front represent optimal, or non-dominated, solutions.

OTHER MITIGATION STRATEGIES

Engine Placement

Standard practices of radiation protection focus upon three factors: time, distance, and shielding. In the case of a nuclear propulsion vehicle, time of exposure is already minimized by mission planning due to other inherent risks of long-duration spaceflight (including cosmic radiation exposure). Shielding is effective, but massive and costly. Distance, however, could be incorporated into a vehicle design to maximize the separation between the crew and the radiation source. For point-sources of radiation (or approximations thereof), intensity is inversely proportional to the square of distance. The current mission architecture is based upon a long-cylinder shape that houses crew opposite the engine assembly, separated by around 80 meters of propellant tanks, structure, and void space. While the length of the spacecraft may seem sufficient to minimize dose, it's important to note that a substantial portion of the radiation reaching the crew compartment is contributed by scatter in the tank assembly near the engines. Heating in propellant

near the engines is also likely to be the constraining factor if it is assumed that crew will be otherwise adequately shielded against cosmic radiation.

Distancing the reactor assembly away from the bottom face of the tank benefits the system in two ways. First, the added distance reduces the unshielded radiation exposure and thus reduces the required shield thickness to meet a given flux constraint. Second, the added distance narrows the fractional solid angle extending between the source and the propellant tank face, thus reducing the required diameter of the shadow-shield and significantly reduce the required shielding mass.

A series of viable truss designs were analyzed in order to validate the feasibility of using a distance truss in place of shielding. Each design type was tested against a maximum thrust loading of 75,000 lb_f at a maximum expected gimbal angle of 5 degrees, with lengths varying between 4 and 10 meters. For each case, the minimum required mass was determined. From this process, the most mass-efficient design was selected, shown in Figure (7a) and represented in Figure (8b), assuming construction out of Al-Mg alloy 5454. From this analysis, a polynomial expression for mass was determined as a function of length. Maximum instantaneous crew gamma dose rates were calculated at varying distances from the propellant tank using an internal shield reference design mass of approximately one metric ton.

To compare mass effectiveness of additional shielding versus that of a distance truss, a set of optimally located external disk shields of varying mass were placed between the propellant tank and engine, which was anchored at the nominal three meter distance. Figure (7b) displays the dose reduction factor, here defined as the nominal dose rate (3m, no external shield) divided over the point dose rate determined with added shield mass or with added distance in terms of truss mass.

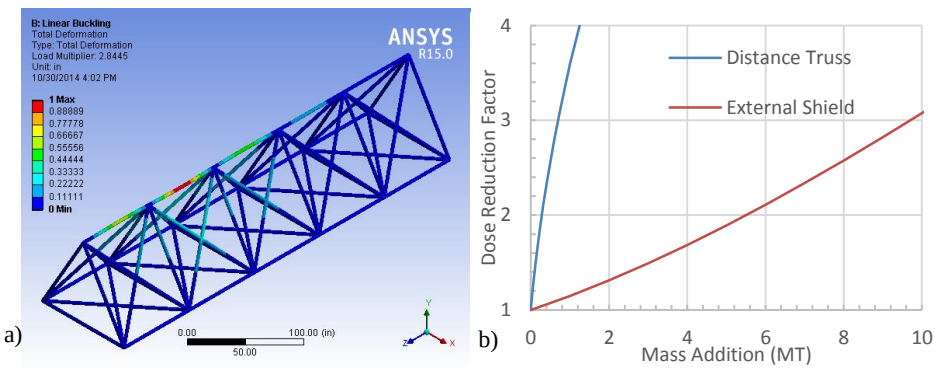

FIGURE 7. a) Buckling analysis of 10m truss determined as mass-optimal for given loading parameters. b) Comparison of gamma dose reduction factors gained by either adding simple external shield mass (cylindrical lead slabs) or a distance truss in terms of mass for a given length (i.e. 10 m ≅ 1 MT).

Tank and Stage Considerations

Careful planning of stage design with consideration for radiation effects will be necessary to minimize shielding mass. Earlier plans for the NERVA-powered nuclear shuttle implemented conical propellant storage tanks that minimized the exposed geometry, similar to that shown in Figure (8d). This served to reduce scatter source terms and propellant heating, and also improved terminal dose rates as the tank emptied by draining from a narrower column and thus increasing the effective thickness per unit mass of propellant acting as a shield. Some alternative considerations for mitigating dose effects and propellant heating also warrant investigation, including use of a smaller secondary tank, as in Figure (8c) with line routing schemes that prevent pump induction of heated propellant. Benefits of these design considerations must be weighed against other factors, such as cost, reliability, and payload envelope size.

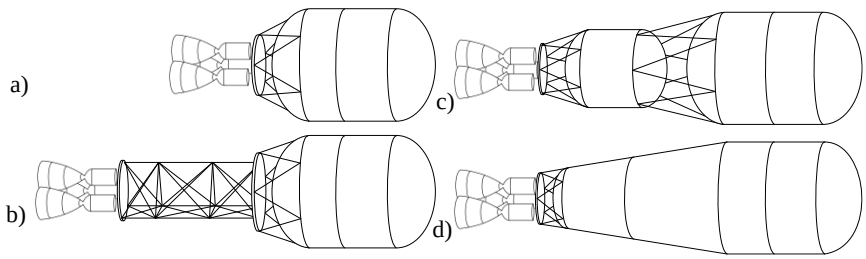

FIGURE 8. Comparison of various staging design options to mitigate radiation effects. a) Nominal core stage design. b) Distance truss. c) Thermal buffering tank. d) Conical core stage tank.

CONCLUSION

Development of radiation shielding for a nuclear thermal propulsion stage has progressed considerably in this preliminary design phase. Methods for dose and heating calculations have been refined throughout the project and continue to progress. Upcoming source terms will feature a more rigorous method of decay and activation source production using CINDER-90 production models. Thermal analysis has indicated the feasibility of implementing a pebble-bed type shield using boron carbide, and a framework has been established to quickly iterate shield designs between radiation transport and thermal analysis. Preliminary designs for a distance truss have indicated a tremendously favorable mass trade for radiation effects compared to added mass of external shielding. B_4C has been selected as a favorable material for neutron shielding, owing to its low cost of development and improved reliability compared to other materials. Pareto optimization techniques are in use to establish a broad range of mass-optimized shield designs, and required constraints for propellant heating to prevent cavitation and boiling are currently being developed.

ACKNOWLEDGMENTS

Special thanks are extended to Omar Mireles and Daniel Cavender of NASA Marshall Space Flight Center for their guidance in project integration, and to Wesley Deason and Michael Eades for providing interfaces with reactor design.

REFERENCES

[1] NASA Space Flight Human-System Standard Volume 1, Revision A: Crew Health (NASA-STD-3001).
[2] National Council on Radiation Protection and Measurements. Recommendations of Dose Limits for Low Earth Orbit. NCRP Report 132, Bethesda MD (2000).
[3] Cucinotta, F.A., Kim, M.H., Chappell, L.J., "Space Radiation Cancer Risk Projections and Uncertainties – 2012", NASA/TP-2013-217375, (2013).
[4] Poindexter, A., Ricks, L., and Disney, R., "A Survey of Potential Shield Materials," Westinghouse Astronuclear Laboratory, WANL-TME-1345 (1966).
[5] Goorley, J.T., et al. "Initial MCNP6 Release Overview - MCNP6 Version 1.0." LA-UR-13-22934 (2013).
[6] B.C. Kiedrowski, "MCNP6 for Criticality Accident Alarm Systems -- A Primer", LA-UR-12-25545 (2012).
[7] Goorley, J.T., et al. "MCNP6 User's Manual – Version 1.0." LA-CP-13-00634 (2013).
[8] Shultis, J.K., and Faw, R.E., *Radiation Shielding*. American Nuclear Society, Inc., La Grange Park IL, (2000).
[9] George, D.C., et al., "Delayed photon sources for shielding applications," *Trans. Am. Nucl. Soc.*, **35**, 463 (1980).
[10] LaBauve, R.J., England, T.R., George, D.C., Maynard, C.W., "Fission product analytic impulse source functions," *Nucl. Technol.*, **56**, 322-339 (1982).
[11] ICRP, *Conversion Coefficients for use in Radiological Protection against External Radiation*, Publication 74, International Commission on Radiological Protection, *Annals of the ICRP*, **26,** No. 3/4, Pergamon Press, Oxford, (1996).
[12] Goetz, C.A., and Billings, M.P., "Impact of radiation dose on nuclear shuttle configuration," in proceedings of *The National Symposium on Natural and Manmade Radiation in Space*, edited by E. A. Warman, NASA TM X-2440, Las Vegas, pp. 40-47, (1972).

Kinetics of the High Temperature Oxygen Exchange Reaction on $^{238}PuO_2$ Powder

Christofer E. Whiting[1*], Miting Du[2], L. Kevin Felker[2], Robert M. Wham[2], Chadwick D. Barklay[1] and Daniel P. Kramer[1]

[1] *University of Dayton – Research Institute, 300 College Park, Dayton, OH 45469-0172*
[2] *Oak Ridge National Laboratory, P.O. Box 2008, Oak Ridge, TN 37831*
[*] *Corresponding Author: (937) 229-2570, chris.whiting@udri.udayton.edu*

Abstract. Mechanisms and kinetics of the oxygen exchange reaction were studied on PuO_2. Results indicate that the oxygen exchange behavior of PuO_2 is quite complex. Exchange rates are influenced by three different mechanisms: a chemical reaction that is occurring within the bulk and not at the material surface, the surface mobility of active species/defects, and the actual exchange of surface adsorbed oxygen with lattice oxygen ions. Determining which mechanism dominates the overall exchange rate appears to be a complex function including at least temperature and specific surface area. The fastest exchange rate is controlled by an internal chemical reaction and can be obtained when the specific surface area of the PuO_2 and exchange temperatures are high. The rate of this internal chemical reaction should be independent of most particle and atmospheric characteristics, including: specific surface area, oxygen partial pressure, total pressure, particle size, and grain size. As temperature and/or specific surface area decrease, eventually the surface mobility mechanism becomes slow enough to control the exchange rate. As temperature and/or specific surface area decrease further, the exchange rate will enter a regime where the surface mobility and surface exchange mechanisms become competitive, and eventually the surface exchange mechanism will become slow enough to completely dominate the exchange rate. These two surface mechanisms are observed to have a dependence on the specific surface area of the PuO_2. Strong similarities are observed between the oxygen exchange behavior of CeO_2 and PuO_2. This suggests that CeO_2 is a very good surrogate for PuO_2 in this regard and means that the extensive oxygen exchange experiments performed on CeO_2 can be used to predict the behavior of PuO_2. Exposure of the PuO_2 to high temperatures ($\geq$ 600 ^{o}C) may cause a reduction in the specific surface area of the material due to initial phase sintering. Upon exposure to 1000 ^{o}C for ~3 hours, the surface of the PuO_2 appears to have stabilized enough that exposure to lower temperatures does not have a significant impact on the surface over the short term. Activation energies are obtained for the internal chemical reaction and the surface mobility reaction.

Keywords. plutonium (IV) oxide, oxygen exchange, reaction mechanisms, kinetics

INTRODUCTION

Isotopic oxygen exchange reactions are used in the production of $^{238}PuO_2$ based Radioisotope Power Systems (RPS) employed in space exploration to help minimize the secondary (α,n) reaction that occurs between the α-emitting ^{238}Pu and the naturally occurring ^{17}O and ^{18}O isotopes [1-7]. Neutron radiation is a significant safety concern for personnel as well as an operational concern for some spacecraft and their scientific payload. While a number of publications have proven the principle of the oxygen exchange reaction, there is very little kinetic or mechanistic information that has been published. Obtaining a better understanding of the mechanisms and kinetics that govern the oxygen exchange are valuable because they will help the RPS program apply the oxygen exchange reaction in an efficient manner and help them adapt to processing changes without the need for extensive development work.

Recently, an extensive campaign of oxygen exchange experiments was performed by the University of Dayton Research Institute using CeO_2 as a non-radioactive surrogate for PuO_2 [8,9]. Results from these experiments showed that the oxygen exchange behavior of CeO_2 is very complex. Up to three different mechanisms were observed on several different CeO_2 powders as the temperature was varied from 600 to 1100 ^oC: 1) an unidentified chemical reaction occurring within the bulk and not at the material surface, 2) the surface mobility of active species/defects, and 3) the exchange of surface adsorbed oxygen with lattice oxygen. Determining which mechanism dominated the rate appeared to be a complex function of variables including at least temperature and specific surface area (SSA). A comparison of this data with the limited literature on PuO_2 showed that some of the unique behaviors observed on CeO_2 are also observed on PuO_2, which suggests that the two materials experience very similar oxygen exchange behavior [10]. These similarities made it possible to explain some of the complexities observed in the literature and extract new kinetic and mechanistic results for the oxygen exchange on PuO_2, including the activation energy for the internal chemical reaction and identification of the surface mobility and surface exchange mechanisms.

The PuO_2 oxygen exchange experiments presented here were specifically designed to be comparable to the CeO_2 results, allowing a more direct and thorough comparison of the exchange behavior of these two materials. This will improve our understanding of the role of the internal chemical reaction, surface mobility, and surface exchange mechanisms for the PuO_2 oxygen exchange, as well as providing a better understanding of the kinetics and thermodynamics that govern these mechanisms. Additionally, previous reports on the oxygen exchange behavior of PuO_2 were performed with a very limited scope, and almost no replication of results was obtained [7]. This work will help reinforce the accuracy of these previous reports by attempting to replicate their kinetic and mechanistic results.

EXPERIMENTAL

Instrumental

Figure 1 presents a schematic of the glovebox layout and the atmosphere controlled reaction chamber used to perform the experiments described here. The quartz reaction chamber was fabricated in-house and had an approximate internal volume of 500 mL. A quartz sample vessel, also fabricated in-house, was loaded with the PuO_2 sample and positioned within ~2.5 cm of the rounded end of the reaction chamber. Quartz tubing was used to bring the inlet gases into the reaction chamber and was positioned such that the end of the quartz tube would blow the incoming gases directly over the sample bed. Incoming gases passed through a flow meter that was set to a flow rate of ~2 mL/s to minimize potential issues with the gas flow disturbing the sample bed. A series of ball valves and stainless steel tubing was used to control the flow of gases into and out of the reaction chamber, while a vacuum pump was used to remove the reagent gases after the exchange was complete. A sampling line was included in this instrumental design to allow analysis of gases in the reaction chamber, but the sampling was not utilized in this work. Neutron emission rates were monitored using an NP-2A Portable Neutron Monitor from Nuclear Research Corporation/Canberra (Meriden, CT).

Materials

A sample of plutonium (75 % as ^{238}Pu) oxalate was precipitated from a 1.3 g/L solution of plutonium nitrate in nominally 0.15 M HNO_3 by the addition of ~25-fold excess of solid oxalic acid. The solution was agitated and allowed to settle over the course of a week. After filtration of the solid plutonium oxalate, an additional ~12-fold excess of solid oxalic acid (based on original Pu concentration) was then added to improve the plutonium recovery. This solution was agitated and allowed to settle over the weekend. Calcination of the plutonium oxalate was performed at 700 ^oC for 90 min with a ramp rate of 20 ^oC/min. A calculated final sample mass of 234.0 mg PuO_2 (154.7 mg ^{238}Pu) was then transferred to the quartz sample vessel; calculations were based on the Pu concentrations in the nitrate solution before and after precipitation. All experiments were performed on this sample of PuO_2.

^{18}O gas containing 52 % ^{18}O was obtained from Isotec, Inc. (Miamisburg, OH) and was provided as a mixture of 21 % O_2 and 79 % N_2 to minimize safety concerns with utilizing pure oxygen. Compressed air and 99.999 % purity Ar were obtained from Air Liquide (Houston, TX). Oxalic acid was obtained in its dihydrate form from J. T. Baker (Center Valley, PA). 99.5 % purity -325 mesh CeO_2 was obtained from Materion (Milwaukee, WI) and had a measured SSA = 4.23 m^2/g. 99.9 % purity CeO_2 with a nominal particle size of 15–30 nm was obtained from Alfa Aesar (Ward Hill, MA) and had a measured SSA = 72.91 m^2/g. SSA measurements were performed by Particle Technology Labs (Downers Grove, IL) using a 3-point BET analysis.

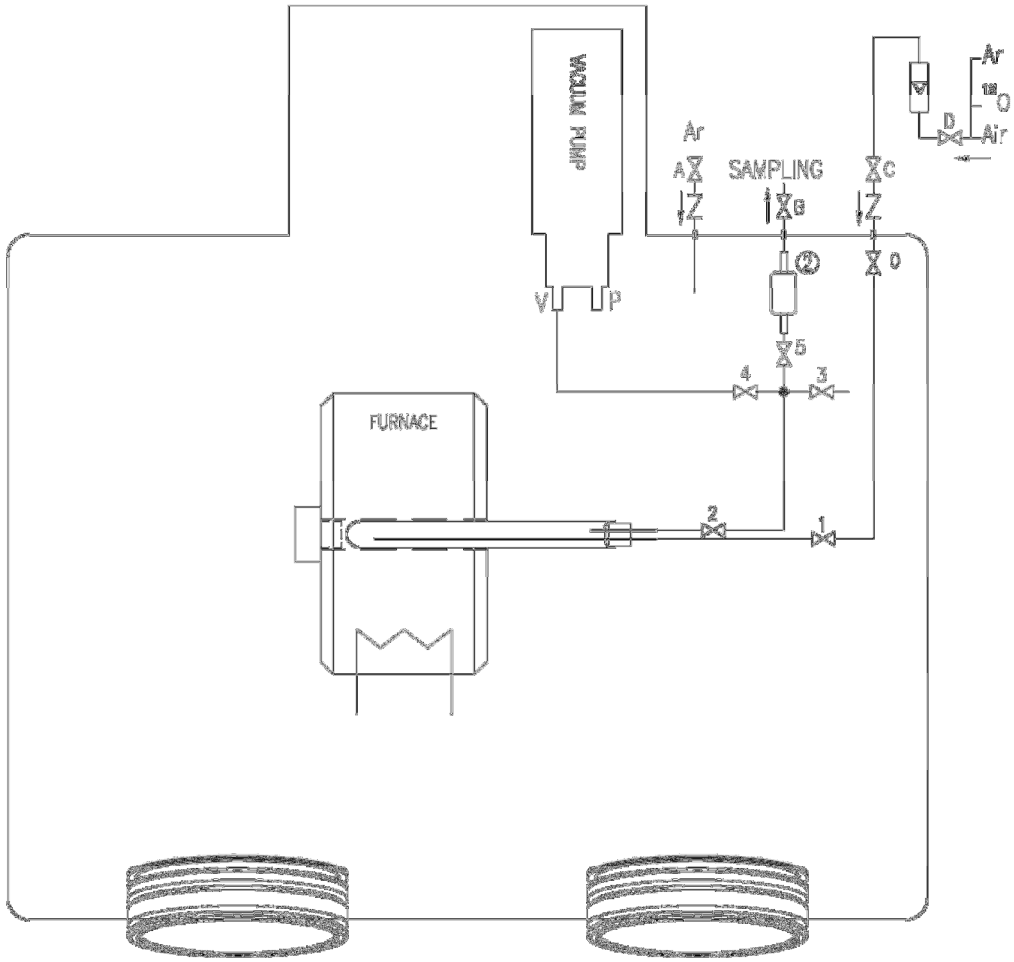

FIGURE 1. Schematic of the Glovebox and Apparatus Used to Perform the Oxygen Exchange Experiments.

Methods

After the sample was allowed to reach thermal equilibrium with the furnace, the reaction chamber was evacuated, flushed with Ar for several minutes, and then evacuated again to minimize the amount of residual glovebox air. Flowing ^{18}O gas was then passed over the sample bed in the reaction chamber and the rate of the exchange was monitored by recording the neutron emission rate from the sample as a function of time. After complete exchange with the ^{18}O gas was obtained, the reaction chamber was evacuated and the reverse reaction was performed using compressed air (i.e. ^{16}O). Upon completion of the reverse reaction, the reaction chamber was evacuated, flushed with Ar for several minutes, and then evacuated again prior to any subsequent experiments.

Previous results from CeO_2 suggest that the thermal history of the sample can have a significant impact on the exchange rate, which is most likely due to changes in SSA resulting from exposure to high temperatures. This strongly suggests the thermal experimental profile is a very important consideration when analyzing the results obtained from a single sample of PuO_2. Therefore, the order in which the experiments were performed is described here. The first two experiments were performed at 700 ^oC prior to exposure to higher exchange temperatures. This temperature is unlikely to cause significant changes to SSA because this was the calcination temperature of the material. After the 700 ^oC experiments, 4 experiments were performed at 1000 ^oC, which resulted in the sample being exposed to 1000 ^oC for ~3 hours. Subsequent experiments were performed at 900 (x2), 800 (x2), 700 (x1), 850 (x2), and 950 (x2) ^oC, in that order. Data from the second run at 800 ^oC was not utilized because the first 800 ^oC reaction was stopped before the exchange was completed. This complicated the results of the second run, but the data from the first run could be salvaged by extrapolating the neutron emission rate at the end of the reaction from other runs.

Results were analyzed using a rate law that was previously developed for CeO_2 [8]. In summary, the apparent rate of exchange was monitored on CeO_2 by measuring the isotopic ratios of the gas phase as the exchange progressed. In this report, monitoring the neutron emission rate is functionally equivalent to monitoring the solid phase isotopic ratios because the (α,n) reaction is directly dependent on the isotopic ratios of the sample. Changes in the neutron emission rate can therefore be used to monitor the apparent rate of exchange using the same rate equation developed on CeO_2, which is defined by the rate constant (k) for the true exchange rate as modified by a set of probability constants that can be defined as the fraction of reaction remaining (F):

$$\text{Rate} = k * F \tag{1}$$

It is important to note that this rate is referred to as the apparent rate of exchange because the true rate of exchange never changes. The oxygen exchange occurs at the surface of the PuO_2 material at a constant rate because the chemistry of the system is not changing, despite changes in the isotopic ratios.

RESULTS AND DISCUSSION

Mechanisms and Activation Energies

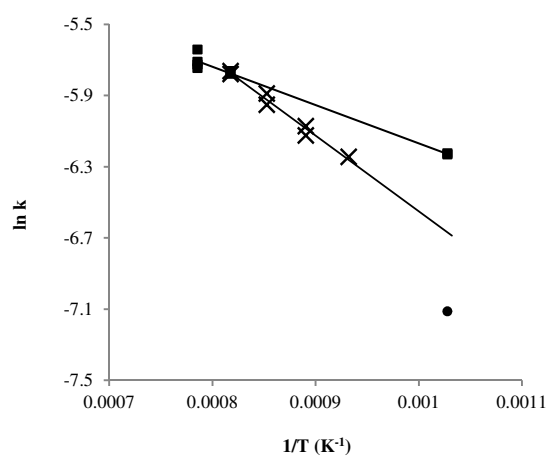

FIGURE 2. Arrhenius Plot of Data Obtained from PuO_2 Oxygen Exchange Experiments Showing that the Rate can be Governed by up to 3 Different Mechanisms: Internal Chemical Reaction (■), Surface Mobility (X), and Surface Exchange (●).

Figure 2 presents the data obtained from these experiments as an Arrhenius plot. Three different exchange mechanisms appear to be occurring over the temperature range studied. The first is represented by ■ in Figure 1, and was observed in the 1000, 950, and the non-thermally treated 700 ^oC experiments. This mechanism has an

(activation energy) E_a = 17.9 ± 0.9 kJ/mol, and is most likely the internal chemical reaction. The only previous report on the oxygen exchange behavior of PuO_2 provides data that produces an E_a = 20.6 ± 5.5 kJ/mol for the internal chemical reaction on PuO_2 [7,10], which is very similar to the E_a measured here; especially when considering the lower degree of precision obtained from the previous report.

The second mechanism observed in Figure 1 occurs during the 950, 900, 850, and 800 °C experiments, and is most likely the surface mobility of active species/defects, which is represented by X in Figure 1 and has an E_a = 35.3 ± 2.3 kJ/mol. 950 °C was used in determining the E_a for both the internal chemical reaction and surface mobility because the intersection of these trendlines occurs at exactly 950 °C. This assignment of the surface mobility mechanism is supported by a number of observations. First, the surface mobility is expected to succeed the internal chemical reaction as the dominant mechanism as the temperature decreases on both CeO_2 and PuO_2 [9,10]. Second, the surface mobility on any metal oxide is expected to occur at very high temperatures and have an $E_a \leq 40$ kJ/mol, as a general rule; this is in comparison to the surface exchange reaction on metal oxides, which is expected to have an E_a of 80–160 kJ/mol [11,12]. Finally, the E_a measured here is reasonably similar to the surface mobility E_a measured on the CeO_2 surrogate (i.e. E_a = 29.1 ± 1.2 kJ/mol). Statistically speaking ($P > 0.05$), the E_a for the surface mobility reaction is larger for PuO_2 than CeO_2, indicating that the reaction is less energetically favorable for PuO_2. Unfortunately, we know very little about the nature of the surface mobility of active species/defects on PuO_2, so we are not able to attribute the higher E_a to any specific cause at this time.

When the PuO_2 sample was exchanged at 700 °C after it had been exposed to high temperatures for ~3 hours during the 1000 °C exchange experiments (Figure 1, ●); two major observations were made. First, the rate is significantly slower than the 700 °C exchanges performed before exposure to 1000 °C. This suggests that a significant reduction occurred in the SSA of the material, which subsequently caused one of the surface reactions to slow down enough to become the rate limiting mechanism. Second, the rate did not fall on the surface mobility trendline, which strongly suggests that the exchange rate was influenced by the surface exchange mechanism. Results on CeO_2 suggest that there is a temperature range of ~300 °C where the surface mobility and surface exchange mechanisms are competitive [9]. It was also suggested that these mechanisms were observed to be competitive in the data presented by Deaton and Wiedenheft on their large hydroxide precipitated PuO_2 particles [10]. This suggests that the rate observed here at 700 °C after thermal exposure may be due to a mixture of surface mobility and surface exchange.

Temperatures below 700 °C were not studied because data presented in previous reports suggests that obtaining an E_a for the surface exchange would be impractical under the conditions presented here for several reasons [7-10]. First, the exchange behavior is complex when surface mobility and surface exchange are competitive. It is unlikely that the post-thermal exposure 700 °C data presented here is actually operating under a purely surface exchange based regime, and it is uncertain at what temperature this sample of PuO_2 would become dominated by just the surface exchange. Second, it took ~2.5 hours for the thermally exposed sample to reach 95 % completion at 700 °C. Since the instrumentation used in this work was not automated, kinetic experiments at the low temperatures necessary to study the surface exchange would result in extended exposure of the experimental staff to the radiological environment where the experiments were performed. Finally, all previous oxygen exchange experiments that were performed on PuO_2 for the purposes of (α,n) reduction were performed at temperatures ≥ 700 °C. Therefore, it was determined that value gained from obtaining the E_a for the surface exchange was not worth the required resources.

Impact of Thermal Treatment on Exchange Rates

Results presented in Figure 2 clearly indicate that thermal treatment plays a major role in the oxygen exchange behavior of PuO_2. CeO_2 results suggested that after ~2 hours at 1000 °C, a significant change in the SSA occurred [8]. Examining the exchange behavior at 700 °C suggests that this behavior is also occurring on PuO_2. The first two exchange experiments on PuO_2 were performed at 700 °C (no exposure to 1000 °C), and these experiments produced relatively fast exchange rates with similar results, as evidenced by the overlapping ■ data points in Figure 2. After ~3 hours of exposure at 1000 °C, however, performing an exchange at 700 °C produced a significantly slower rate (Figure 1, ●). This suggests that a significant reduction in SSA occurred as a result of exposure to the 1000 °C exchange temperature, and that this change caused the SSA dependent surface exchange to become so slow that it was influencing the exchange rate. While this behavior was suspected based on the CeO_2 surrogate studies, these

results confirm that thermal treatments can play a major role in the exchange rate and/or mechanism observed on PuO_2.

Fortunately, the other observation made regarding the impact of thermal treatment on CeO_2 SSA also appears to hold true for PuO_2. After exposure to 1000 ^oC for at least 2 hours, the SSA of CeO_2 appears to become stable enough that exposure to lower temperatures (i.e. $\leq$ 950 ^oC) will not significantly alter the SSA. This behavior on PuO_2 is evidenced by the fact that replicate results at $\leq$ 950 ^oC appear similar to each other (Figure 2). At each of the measured temperatures, the SSA dependent surface mobility appears to be dominating the rate of exchange. If the SSA was changing significantly during these experiments, then a more complicated rate behavior should be observed. This suggests that a high temperature thermal treatment can be used to stabilize the PuO_2 surface and help assure that more reproducible exchange rates are obtained.

Additional Impacts of Thermal Exposure

The experiments described here were performed over the course of three days. On the first day, the initial 700 ^oC and 1000 ^oC experiments were performed. The 900, 800, and 700 ^oC experiments were performed on the second day. The 850 and 950 ^oC experiments were performed on the third day. At the end of each day of experiments, the PuO_2 sample was removed from the furnace and examined. These examinations showed that the PuO_2 sample bed was always crusty and would not flow, even when the sample boat was held at a 90° angle. Breaking up the bed, and returning the sample into a more flowable powder could be accomplished with a spatula and was performed at the end of each day of experiments. Fortunately, this "caking" of the sample bed did not appear to impact the exchange rate. This is evidenced by the fact that replicate experiments performed at 1000 ^oC produced similar results, and experiments performed on subsequent days fit the expected trends.

These physical changes in the sample bed were likely occurring at the higher temperatures due to initial phase sintering. Initial phase sintering is a phenomenon where consolidation of the particles and grains begins to happen at a slow rate. Normally, initial phase sintering begins when a material is exposed to ~half of its melting point, which would suggest that initial phase sintering would start at ~1200 ^oC for both PuO_2 and CeO_2. However, some consolidation of CeO_2 can be observed to occur when the temperatures are much lower.

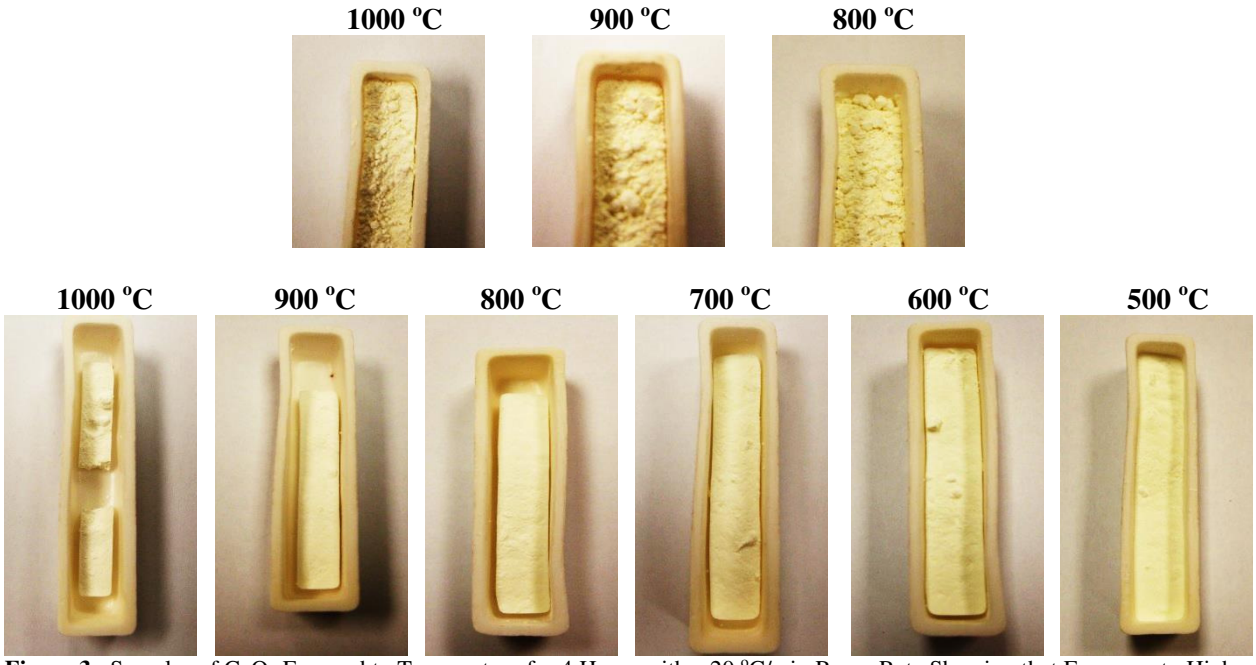

Figure 3. Samples of CeO_2 Exposed to Temperature for 4 Hours with a 20 ^oC/min Ramp Rate Showing that Exposure to Higher Temperatures Can Cause Consolidation of the CeO_2 Sample Bed. Top Row: -325 mesh CeO_2. Bottom Row: 15–30 nm CeO_2.

Figure 3 shows how exposure to high temperatures for 4 hours impacts a sample bed of CeO_2 in an alumina sample boat. The top row of Figure 3 contains samples of a larger -325 mesh (i.e. $\leq$ 44 μm) CeO_2 powder that had a SSA = 4.23 m^2/g, and it shows that at 900 and 1000 ^oC the bed of CeO_2 shrank slightly and pulled away from the walls of the alumina boat to a small degree. At $\leq$ 800 ^oC the -325 mesh CeO_2 no longer consolidated enough to have a visual effect on the sample bed. This consolidation is much more pronounced when a sample of nominally 15–30 nm CeO_2 that had a SSA = 72.91 m^2/g was exposed to the same set of conditions (Figure 3 bottom row). Consolidation was much more pronounced at the higher temperatures, and the consolidation had a visual effect on the size of the sample bed all the way down to 600 ^oC. This suggests that significant changes in the sample can occur as the result of thermal exposure and that these changes are a function of the temperature that the material is exposed to and the characteristics of the material that is exposed.

It is very likely that the proposed initial phase sintering is also the primary cause of the reductions in SSA. If initial phase sintering is occurring, then the PuO_2 surface has some mobility, allowing the material to smooth out (i.e. lower SSA), close off porosity, and consolidate. In addition, if two particles are in contact, the material can merge, creating a minor physical connection between the particles often referred to as necking. Figure 3 indicates that significant changes can occur on some samples of CeO_2 as the result of thermal exposure to surprisingly low temperatures (i.e. 600 ^oC), which suggests that thermal exposure should be kept to a minimum if retaining particle properties (like SSA) is important.

Comparison to CeO_2 Surrogate Studies

The oxygen exchange behavior of PuO_2 appears to be very similar to the behavior of CeO_2 on a qualitative level. When temperature and SSA are large, the exchange rate appears to be dominated by a chemical reaction that is occurring within the bulk and not at the surface of the material. This conclusion is primarily supported by the fact that the rate is independent of the SSA of both materials. As temperature and SSA decrease, the material becomes dominated by a different mechanism that appears to fit the expected behavior of the surface mobility of active species/defects. As temperature decreases further, the material becomes influenced by a third mechanism that appears to fit the expected behavior of the surface exchange of adsorbed oxygen with lattice oxygen ions. Both the surface mobility and surface exchange mechanisms appear to have a significant dependence on the SSA of the material, as expected, though the mathematical dependence has not yet been determined.

Both CeO_2 and PuO_2 experience a significant decrease in SSA upon initial heating to high temperatures, which is likely caused by initial phase sintering occurring at temperatures that are much lower than one would normally expect. Decreasing SSA could cause a significant change in the exchange rate and/or mechanism to occur in subsequent runs, or it could even cause a dynamic change to occur during the exchange experiments. This could result in very confusing, or inconsistent, exchange behavior that would be difficult to interpret properly. Historical literature discussing the oxygen exchange behavior on CeO_2 indicates that the exchange rate is unstable at temperatures above 700 ^oC [14,15], while prior work on PuO_2 was only able to obtain very limited kinetic information because of the complexities in the data [7]. These historical observations are most likely the result of a SSA that is dynamically changing over the course of the experiment.

While thermal treatment at high temperatures appears to cause a significant reduction in SSA, it also appears to create a surface that is relatively stable when exposed to lower temperatures. For example, after exposure to 1000 ^oC for 2-3 hours, the surfaces of CeO_2 and PuO_2 powders appear to be stable because replicate oxygen exchange experiments performed at $\leq$ 950 ^oC produce similar results. It is important to note that this stability has only been observed in the timeframe of several oxygen exchange experiments. Long term exposure to lower temperatures (i.e. more than 2-3 hours) after a 2 hour thermal treatment at 1000 ^oC has not been tested.

E_a for the surface mobility and internal chemical reaction on PuO_2 are also similar to the values obtained on CeO_2, but they are notably higher (i.e. ~60 % and ~20 % higher for the internal chemical reaction and surface mobility, respectively) [9]. This indicates that the internal chemical reaction and the surface mobility of active species/defects are less energetically favorable on PuO_2. While this clearly indicates that the exchange reaction on these two materials is similar, there are some differences in their chemistry. Unfortunately, there is not enough information on

the surface mobility or internal chemical reactions of these two materials to evaluate the reasons why there are observed differences in E_a.

Data presented in this report further solidifies the conclusion that CeO_2 is an excellent surrogate for the oxygen exchange behavior of PuO_2. Therefore, it is possible to extrapolate information obtained on CeO_2 to the PuO_2 system with a high degree of confidence. This allows more detailed exchange experiments to be performed on CeO_2 where the non-radioactive nature of the material makes experimentation easier to perform and less expensive than experiments on PuO_2.

CONCLUSIONS

Oxygen exchange reactions on PuO_2 are complex and appear to be very similar to the oxygen exchange behavior on the surrogate material, CeO_2. Exchange rates are controlled by an internal chemical reaction, surface mobility of active species/defects, or the exchange of surface adsorbed oxygen with lattice oxygen ions. Both the internal chemical reaction and the surface mobility mechanism appear to be less energetically favorable on PuO_2 than CeO_2. Determining which mechanism impacts the exchange rate appears to be a complex function including at least specific surface area and temperature. Exposure to high temperatures causes a significant reduction in SSA that is most likely the result of initial phase sintering. This suggests that performing an exchange reaction at high temperatures could cause the SSA to change dynamically during the experiment, which could result in complicated data that is very difficult to interpret. After exposure to high temperatures for at least a few hours, the surface appears to become relatively stable, allowing exchange experiments to be performed at lower temperatures without significant changes in SSA.

ACKNOWLEDGMENTS

This work was funded by the U.S. Department of Energy. Funding was supplied to the University of Dayton through contract #: DE-NE0000422. Funding was supplied to Oak Ridge National Laboratory through contract #: DE-AC05-00OR22725.

REFERENCES

[1] Rutherford, W.M.; Huffman, G.N.; and Coffey, D.L. *Nucl. Appl.*, **3**, 366-371 (1967)
[2] Plymale, D.L. *J. Inorg. Nucl. Chem.*, **30**, 886-890 (1968), doi:10.1016/0022-1902(68)80452-X
[3] Plymale, D.L. *U.S. DOE Report MLM-1462*, Mound Laboratory, Miamisburg, OH (1968), doi:10.2172/4539830
[4] Porter, J.A. and Thompson, M.C. *U.S. DOE Report DP-1153*, Savannah River Laboratory, Aiken, SC (1968), doi:10.2172/4800132
[5] Porter, J.A. and Thompson, M.C. *Inorg. Nucl. Chem. Lett.*, **5**, 129-134 (1969), doi:10.1016/0020-1650(69)80208-4
[6] Miles, J.C.; Deaton, R.L.; and Wiedenheft, C.J. *U.S. DOE Report MLM-1891*, Mound Laboratory, Miamisburg, OH (1972), doi:10.2172/4699028
[7] Deaton, R.L. and Wiedenheft, C.J. *J. Inorg. Nucl. Chem.*, **34**, 3419-3425 (1972), doi:10.1016/0022-1902(72)80236-7
[8] Whiting, C.E.; Douglas, J.M.; Cremeans, B.M.; Barklay, C.D.; and Kramer, D.P. *J. Solid State Chem.*, **218**, 116-123 (2104), doi:10.1016/j.jssc.2014.06.033
[9] Whiting, C.E.; Barklay, C.D.; Kramer, D.P.; Kaufman, E.A.; and Douglas, J.M. *Solid State Ionics*, *In Press*, doi:10.1016/j.ssi.2014.12.017
[10] Whiting, C.E. *J. Nucl. Mater.*, *Submitted*
[11] Winter, E.R.S. "The Reactivity of Oxide Surfaces," in *Advances in Catalysis*, vol. X 196-241; Eley, D.D.; Frankenburg, W.G.; Komarewsky, V.I. Eds.; Academic Press, Inc.: New York, NY, (1958), ISBN:978-0-12-007810-3
[12] Winter, E.R.S. *J. Chem. Soc. A*, **9**, 2889-2902 (1968), doi**:**10.1039/J19680002889
[13] Whiting, C.E.; Kaufman, E.A.; Kramer, D.P.; Goodrich, S.M.; and Barklay, C.D. *INMM 2014*, Atlanta, GA (2014)
[14] Sazonov, L.A.; Sokolovskii, V.D.; and Boreskov, G.K. *Kinet. Katal.*, **7**, 521 (1966)
[15] Kharton, V.V.; Yaremchenko, A.A.; Naumovich, E.N.; and Marques, F.M.B. *J. Solid State Electrochem.*, **4**, 243-266 (2000), doi:10.1007/s100080050202

A Historical Review of Cermet Fuel Development and the Engine Performance Implications

Mark E. M. Stewart

VPL, LLC at NASA Glenn Research Center, Cleveland, OH 44135
(216) 416-5679; Mark.E.Stewart@nasa.gov

Abstract. This paper reviews test data for cermet fuel samples developed in the 1960's to better quantify Nuclear Thermal Propulsion (NTP) cermet engine performance, and to better understand contemporary fuel testing results. Over 200 cermet (W-UO_2) samples were tested by thermally cycling to 2500°C (2770 K) in hydrogen. The data indicates two issues at high temperatures: the vaporization rate of UO_2 and the chemical stability of UO_2. The data show that cladding and chemical stabilizers each result in large, order of magnitude improvements in high temperature performance, while other approaches yield smaller, incremental improvements. Data is very limited above 2770 K, and this complicates predictions of engine performance at high I_{sp}. The paper considers how this material performance data translates into engine performance. In particular, the location of maximum temperature within the fuel element and the effect of heat deposition rate are examined.

Keywords: Nuclear Thermal Propulsion, fuel development, cermet fuel,

INTRODUCTION

The promise of nuclear thermal propulsion is that its high thrust and high specific impulse—twice that of the best chemical engines—significantly reduces rocket mass, size, and cost. NTP rocket engines use a nuclear reaction to heat propellant, in contrast to traditional chemical rockets, which heat propellant in a chemical reaction. High energy density nuclear fuel in high thrust engines operating at high specific impulse ($I_{sp} \geq 900$s) represents the next evolutionary step in liquid rocket engines.

To achieve high specific impulse, rockets often use materials and components near their performance limits; consequently, engine lifetimes can be short—from minutes to hours. For NTP rockets, the nuclear fuel and fuel elements operate near their structural and thermal limits. An understanding of high temperature behavior is important: What are the melting point, vaporization rate, and strength of fuel and cladding at high temperatures? Do chemical reactions appear in these extreme conditions? This paper examines historical test data for cermet fuel and attempts to clarify performance.

Nuclear thermal rockets were conceived in 1946 [1] at the beginning of the Atomic Age. The Rover and NERVA programs were initiated in 1955 and 1961, respectively, to develop NTP technology, and they were an integral part of the Space Race. NTP engines were a backup to intercontinental ballistic missile chemical propulsion, and envisioned uses included a lunar mission stage, Earth orbit-to-orbit transfer, and manned Mars missions. NTP's high I_{sp} promised significant reductions in rocket mass and size. The NERVA program was an extensive program with a budget of ~$8.9 billion (2014 $) which designed, built, and tested the KIWI, NRX, PHOEBUS, PEWEE, and NF thermal spectrum reactors. This series of 20 rocket/reactors advanced graphite-based NTP fuels to the point where the NRX-XE rocket reactor performed 28 burns with more than 3.5 hours of operation. Yet, by 1970, the Space Race was won, chemical propulsion engines were well established, and priorities were reassessed: Apollo missions 18-20 were cancelled, and plans for manned Mars missions were curtailed. The Rover/NERVA program was cancelled in 1972. From 1987 to 1994, the Space Nuclear Thermal Propulsion (SNTP) program developed

graphite-based, particle bed reactors. Currently, NASA's Nuclear Cryogenic Propellant Stage (NCPS) program is recapturing NTP fuel element fabrication techniques and design knowledge.

Although the NERVA program has become synonymous with graphite-based fuels, a second fuel type—ceramic metallic (cermet) fuel—was also investigated. Cermet fuel is used in fast and thermal spectrum reactors, and this composite material involves uranium dioxide (UO_2) particles typically in a tungsten matrix. Early in the Rover/NERVA program, tungsten was a very promising material for high temperature nuclear reactors. It has the highest melting temperature of all metals (3680 K)—graphite sublimes at 3915 K, while the compounds hafnium carbide and tantalum carbide (early coating material for graphite-based fuels) both melt near 4150 K, (Table 1). Further, tungsten has the lowest vaporization rate of all materials (Table 1). Initially, tungsten appeared to be chemically compatible with both hydrogen and UO_2. The performance of uranium dioxide fueled cermet fuels has been reviewed previously [2, 3].

TABLE 1. Melting Points and Surface Vaporization Rates (Vacuum) for NTP Materials and Fuels. From [4, 3]

Material	Melting Point (K)	Surface Vaporization Rate at 2800 K (mil/hr)	Material	Melting Point (K)	Surface Vaporization Rate at 2800 K (mil/hr)
Tungsten, W	3680	< 0.01	Uranium Dioxide, UO_2	3075	6×10^3
Graphite, C (sublimes)	3915	10	Uranium Carbide, UC_2	2835	10
Rhenium, Re	3453	0.1	Uranium Nitride, UN	Unstable	-
Tantalum, Ta	3270	0.07	UC-40ZrC	3050	2.
Molybdenum, Mo	2890	>>10	Hafnium Carbide, HaC	4160	~1.
Zirconium Carbide, ZrC	3805	>>10	Tantalum Carbide, TaC	4150	0.1

Why were much less resources devoted to cermet, rather than graphite-based fuels? Rom [4] claims that, "The potential for tungsten reactors needed intensive experimental investigation for verification. Aside from its use as a light bulb filament, very little was known about the properties of tungsten. There was essentially no data base." In contrast, graphite had been extensively used in high temperature industrial applications including crucibles and furnace electrodes. Graphite and related carbides have high melting temperatures, moderate vaporization rates, and good chemical compatibility at high temperatures (Table 1). Very high purity reactor grade graphite had been developed and could be fabricated with precision [4].

In the 1960's, Argonne National Laboratory (ANL) designed two rocket reactors based on cermet fuel. The ANL200 [5] and ANL2000 were 200 MW_t and 2000 MW_t fast spectrum propulsion reactors. The performance goals of this rocket/reactor were a maximum fuel temperature of at least 2500°C (2770 K) (I_{sp} = 821 to 832 s), ten hours of operation with at least 25 thermal cycles, and a fuel loss target of less than 1%. The program advanced to the point where many fuel samples and several fuel elements were tested in high temperature hydrogen. NASA's Lewis Research Center (LeRC) performed extensive fuel and reactor development work and designed the thermal spectrum Tungsten Water Moderated Rocket (TWMR) [6, 7] to similar performance goals. Honeycomb and concentric cylinder fuel elements were developed and a critical assembly experimental program was completed.

In 1961, General Electric (GE) started the High-Temperature Materials Program (HTMP) [8] involving extensive reactor materials development for high temperature (>2200 K), fast spectrum, gas reactors. The program involved extensive thermal cycling of material samples of UO_2 with W, Re, and Mo matrices, with various cladding, plus reactor tests of fuel samples. The 710 Reactor Project [8], a reactor design sub-element of GE's HTMP, involved developing brazing, sintering, and fabrication techniques for fuel elements, and culminated in reactor tests. Initially, it developed a design for the GE 710 reactor for NTP, but the program's focus moved to closed-cycle, land and space power systems using inert gas working fluid at lower fuel temperatures. Consequently, GE 710 sample testing is less relevant to NTP, although GE HTMP continued research into high temperature cermet fuel in hydrogen.

Although cermet fuel elements were not tested as a rocket/reactor, extensive fuel sample development and testing took place at the Department of Energy's (DOE) Argonne, Pacific Northwest, and Los Alamos National Laboratories (LANL), NASA Lewis Research Center, and General Electric. During the Nuclear Energy for the Propulsion of Aircraft (NEPA) project, W-UO_2 and Mo-UO_2 cermet materials were investigated [8]. LANL was

testing cermet fuel samples in 1957 [9], and by 1962 LeRC had a rocket reactor concept [10] and sample testing. By May 1962, when GE's 710 Reactor Project started, GE's HTMP was already performing in-pile tests of cylindrical, seven-channel, Ta- and Nb-clad W-60% UO_2 fuel system specimens. Tighter budgets terminated cermet fuel development about 1968, and final reports were published between 1966 and 1968.

The next section of this paper examines published cermet sample test results. The intent is to understand the significance to performance of surface cladding, fuel stabilizers, fuel particle coatings, and processing techniques. The final section attempts to place high temperature fuel performance in the engine context and understand the engine performance implications.

RESULTS OF HISTORICAL CERMET MATERIAL TESTING

This section summarizes over 200 cermet samples from the 1960's that were tested by thermally cycling to high temperature in hydrogen (Table 2). The following sub-sections explain the underlying mechanisms and significant design improvements. The reports show two issues at high temperatures: the vaporization rate of UO_2 and the chemical stability of UO_2. The data also show that cladding and chemical stabilizers each result in large improvements in high temperature performance, while other approaches yield smaller, incremental improvements.

The columns of Table 2 correspond to tests of different groups of samples. The design features are indicated across the top. Samples include unstable UO_2 samples (indicated in red), to stable fuel samples with greater than 5% fuel loss (indicated in yellow), to stable samples with lower, less than 5%, fuel loss (indicated in green). Unstable fuel cracks or turns to powder due to free uranium forming uranium hydride (UH_3) (see next section); stable fuel does not. The results indicate the most effective design features are surface cladding and fuel stabilizers. The following two sections consider these two issues. Other design and processing techniques are valuable, and Baker et al [11] describes process improvement.

TABLE 2. Stability and Mass Loss of Tested Cermet Samples from Historical Reports. Each column corresponds to a different sample group, and the group's features are indicated with check marks near the top of each column. From left to right cladding and stabilizers are added. Moving from left to right in the table moves from unstable fuel (indicated in red), to stable fuel samples with > 5% fuel loss (indicated in yellow), to stable samples with low (< 5%) fuel loss (indicated in green). The number of tested samples is shown at the foot of the column with a reference to the data source.

		Unstable: Cracks or Forms Powder					Stable: Mass Loss > 5 %				Stable: Mass Loss < 5 %				
Sample Group		**1**	**2**	**3**	**4**	**5**	**6**	**7**	**8**	**9**	**10**	**11**	**12**	**13**	**14**
UO_2 Only		✔						✔							
W-UO_2			✔	✔	✔	✔	✔		✔	✔	✔	✔	✔	✔	✔
Partial Clad (Not Edges)									✔			✔			
Full Clad										✔	✔		✔	✔	✔
Coated Fuel Particles				✔									✔		
Stabilizers (Various)							✔	✔	✔	✔		✔	✔	✔	✔
Temperature															
(C)	**(K)**														
2000	2273														
2300	2573														
2350	2623														
2500	2773														
2600	2873														
2650	2923														
2700	2973														
2800	3073														
Cycles Tested									25	>25				<30	<10
Fuel Samples Tested			29+14	46	19	2		25+	~30	~20	6	2	1	2	2
Reference		[17]	[11]	[11]	[11]	[18]	[18]	[17]	[13]	[13]	[9]	[18]	[18]	[18]	[18]

Table 2 samples are a fraction of all the samples tested since many additional ones are not detailed or relevant. For example, Lenz compares cooling in helium and hydrogen to detect UH_3 formation from free uranium [9]; these samples cannot be easily included within the scope of this table. GE 710 sample tests were conducted in an inert gas, not hydrogen, as the program's focus moved to closed-cycle power generation.

High Temperature Vaporization of UO_2 and the Need for Cladding

At temperatures above 2000 K, uranium dioxide vaporizes rapidly (Table 1), and cladding or coating is necessary. This need for cladding was quickly recognized as a successful method for reducing fuel loss at high temperatures. At the 1962 nuclear propulsion conference, Lenz and Mundinger [9] reported that thin tungsten coatings significantly reduced UO_2 vaporization and loss (Group 10). At the same time, Saunders et al [10] and McDonald [12] reported that fuel vaporization was a major issue with unclad samples, and could be reduced by an order of magnitude with cladding.

The cladding's permeability to oxygen is important. GE found that W-Re-W was 10^3 times less permeable to oxygen than tantalum [8, pp. 32, Vol 3], hence a much better cladding material.

Furthermore, full cladding appears to be significantly better than face cladding. Gluyas et al [13] thermally cycled face and full clad specimens with various stabilizers in hydrogen (groups 8 & 9 in Table 2). The 3.5 x 2.5 cm samples with 0.0046 cm thick face cladding had 0.045 cm thick unclad edges. The results demonstrate the need for full cladding.

Decomposition of Uranium Dioxide, Hydride Formation, and the Need for Stabilizers

Early in the cermet fuel program, uranium dioxide's instability at high temperatures was recognized. Further, thermal cycling and flowing hydrogen all accelerate the instability. In 1960, Anderson et al [14] reported that uranium dioxide decomposes (or reduces) at high temperature and becomes hypostoichiometric in oxygen, UO_{2-x}. At the nuclear propulsion conference in 1962 [15], papers from LeRC [10] and LANL [9] noted the UO_{2-x} reduction issue, free uranium formation, UH_3 formation from this free uranium, and sample cracking. A similar understanding by GE was also cited. Towards the end of the program, Baker et al [11] carefully explained this basic behavior.

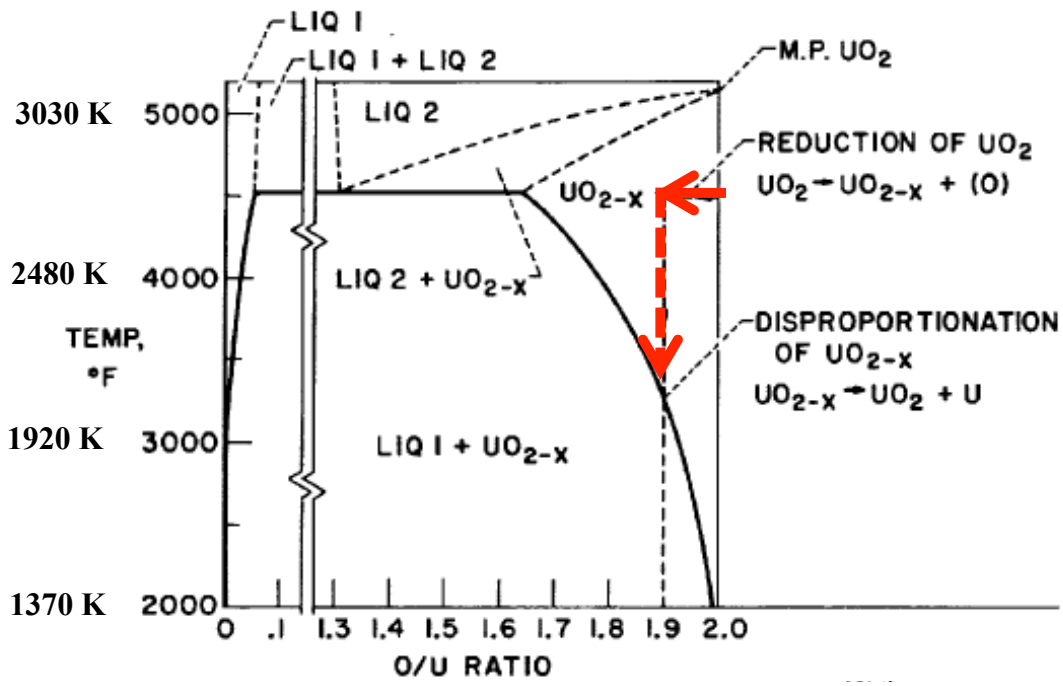

FIGURE 1. Oxygen Uranium Phase Diagram shows Reduction of Uranium Dioxide is Significant at Temperatures Above 2000 K. From [16].

What is this instability? Figure 1 shows the oxygen-uranium phase diagram, and the red path indicates the chemical changes at high temperature (solid line) and with cooling (dashed line). At temperatures above 2000 K, uranium dioxide undergoes reduction and becomes hypostoichiometric in oxygen, UO_{2-x}. The fluorite structure of UO_2 develops vacant oxygen sites compensated with reduced U^{4+} ions. Stabilizers (Gd_2O_3, Y_2O_3) interfere with this reduction, and it may be the stabilizer provides free oxygen [17]. With cooling (dashed line in Figure 1), this reduction reaction reverses, and the uranium and oxygen would recombine into uranium dioxide—but some oxygen is no longer present.

Oxygen freed during reduction diffuses out of the fuel at high temperatures. With cooling, free uranium forms if oxygen has been removed. Figure 2 shows the formation of free uranium at grain boundaries adjacent to UO_2 fuel particles. Cladding provides a barrier to hydrogen, oxygen, and water, and can slow the process.

With cooling below 770 K, uranium hydride forms from this free uranium. This large molecule forces apart grain boundaries, stresses the material, and can cause surface cracking [9] or reduce it to powder—sometimes in an explosive manner [17]. This is a specific example of hydrogen embrittlement. Some sources indicate that instead of forcing expansion, UH_3 forms a brittle hydride on grain boundaries. Unstable fuel, where structural integrity is lost, is shown in red in Table 2.

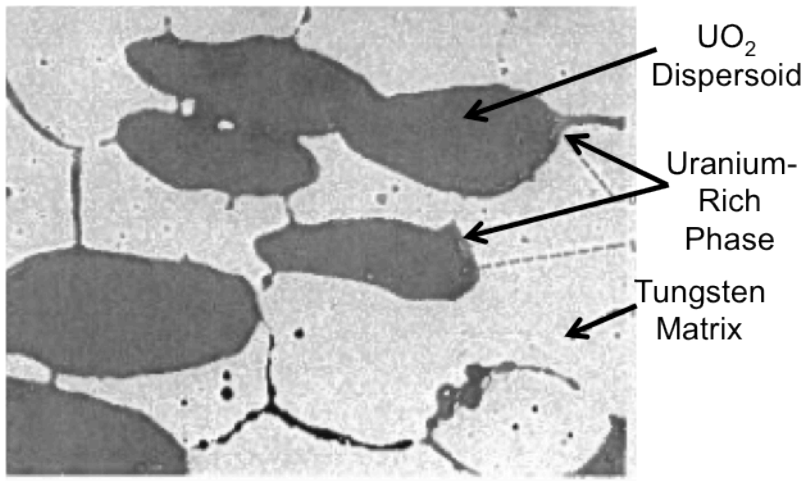

FIGURE 2. Micrograph of Thermally Cycled W-20vol% UO_2 Cermet Showing Free Uranium at Grain Boundaries. From [6] via [2].

Thermal cycling (corresponding to engine re-starts) amplifies this destructive process and eventually disrupts fuel integrity and allows rapid fuel vaporization. High pressure hydrogen (engine pressure ~1MPa (10 atm)) and flowing hydrogen accelerate fuel loss [13]. Higher temperatures should also accelerate the reaction. Cladding, stabilizers, and fuel particle coatings all slow this process, delay fuel failure (Table 2), and evidence exists of low fuel loss after many thermal cycles.

High Temperature Cermet Fuel Performance

Most of the samples in Table 2 were tested near 2500°C (2770 K)—for an I_{sp} of ~825 s—because this was the design goal for the ANL and LeRC rocket/reactors. Yet, higher temperature data would help us understand higher performance cermet engines, which demand higher fuel temperatures to achieve a higher I_{sp}. Stoichiometric instability (Figure 1), and hydrogen and oxygen permeability in tungsten all increase with increasing temperatures, hence accelerated fuel loss is expected.

Limited data is available at higher temperatures. One group of data [17] tested UO_2 with various chemical stabilizers and is not directly relevant to engine performance since it was only UO_2—matrix and cladding were not included. However, another group of 4 samples [18] (groups 13, 14) provides insight into high temperature behavior (Figure 3), and indicates drops in fuel endurance with each 100 K increase in fuel sample temperature. Baker et al [11] tested some samples to 2500°C and 2600°C in high pressure, flowing hydrogen (group 3). Again, the 100 K temperature increase shows higher fuel loss. The data [11] also show that flowing hydrogen significantly increases fuel loss, and hydrogen pressure can increase fuel loss.

For the samples in Figure 3, swelling rates of 2-9% were reported [18]. Although mass loss is typically reported and swelling/shrinkage is not, it is not clear if this swelling was exceptional.

Historical Material Property Data for Fuel Element Simulation

Material property data for cermet fuel elements and reactors includes thermal conductivity, thermal expansion, Young's modulus, yield and ultimate strength all up to maximum temperature. This information is important for simulations that predict fuel element performance. Cermet material property data is limited, but component material

(W, UO_2) is more readily available, and estimates can be made for the composite material. Stewart [19] reviews material property data for NTP fuel elements.

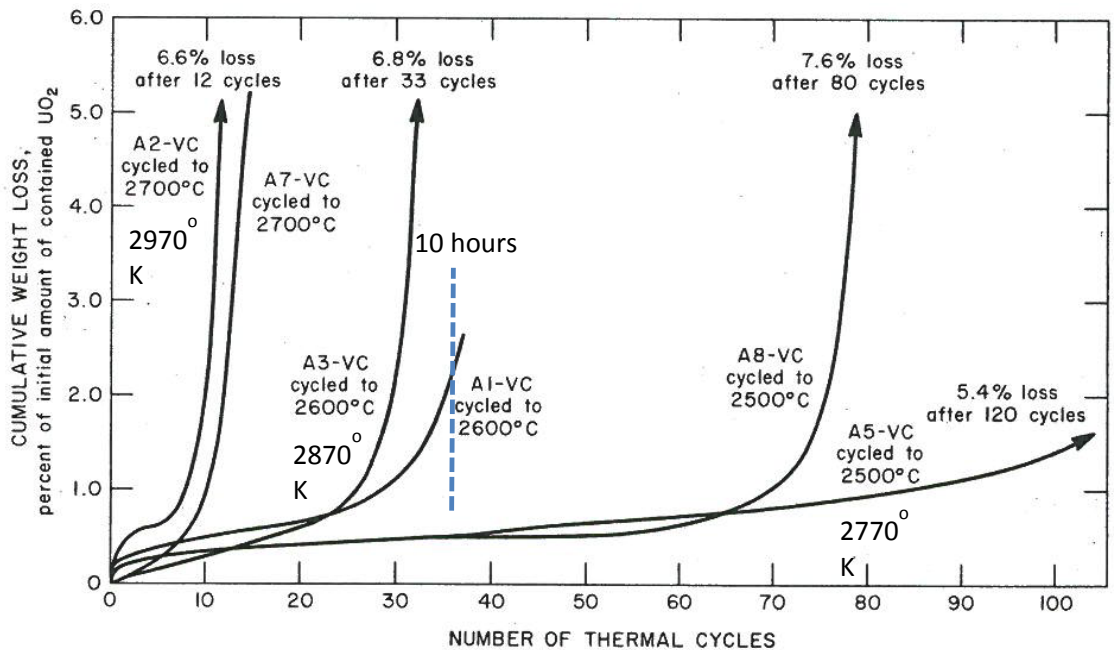

FIGURE 3: Fuel Loss Behaviors of 6 Samples of Tungsten Clad W-66v/o (10m/o $GdO_{1.5}$-stabilized UO_2) Cermet Thermally Cycled to 2770 K, 2870 K, and 2970 K in Low Pressure Hydrogen. The report suggests the hydrogen is static, or at a very low flow rate. From [18, p. 105]. Testing with flowing hydrogen at engine pressures would reduce performance.

IMPLICATIONS FOR CERMET ENGINE PERFORMANCE

What does a NTP fuel element designer do with this high temperature material performance data? The designer must achieve the highest possible propellant outflow temperature and the minimum peak fuel temperature to maintain acceptable fuel integrity, fuel loss, nuclear and system performance. Here we will consider how fuel geometry and nuclear heat deposition rates influence existing fuel element/reactor designs for the fuel temperatures discussed above.

Size and Location of Peak Fuel Temperature in a Cermet Fuel Element

In NTP engines, the peak fuel temperature occurs within the solid fuel, and the gaseous propellant has a lower peak temperature and mean exit temperature. The nuclear reaction deposits heat in the solid fuel, and this heat diffuses to coolant channels carrying propellant. In contrast, in chemical rocket engines and jet engines, a chemical reaction releases heat in the gaseous propellant—away from the solid walls which are cooled.

The size of the high temperature fuel region within the fuel element is important. Figure 4 shows the predicted temperature distribution and the regions of highest fuel temperature from a GE 711 fuel element simulation. The high temperature fuel performance issues mentioned in the previous section would only be expected in the regions indicated. This high temperature region is a minority of the fuel element. Simulations of other cermet [20] and graphite-based [21] fuel element designs have similar temperature distributions.

The Effect of Cermet Fuel Element Geometry and Heat Deposition Rate on Peak Fuel Temperature

Fuel element geometry and heat deposition rate can have a significant effect on peak fuel temperature and propellant mean outflow temperature. In particular, some fuel element geometries are better than others.

To demonstrate this effect, we perform a thermal analysis of a short length of fuel element as shown in Figure 5. A short length can be used because the temperature gradients to the coolant channels are much greater (30X) than the gradients along the fuel element's length. The fluid flow and heat transfer effects are excluded by fixing the coolant channel surface temperature, and this greatly simplifies and clarifies the problem. Fluid flow and heat transfer effects must eventually be considered. The heat deposition rate given is the uniform rate within the fuel matrix. The heat deposition rate in the cladding is scaled based on MCNP simulation results [20].

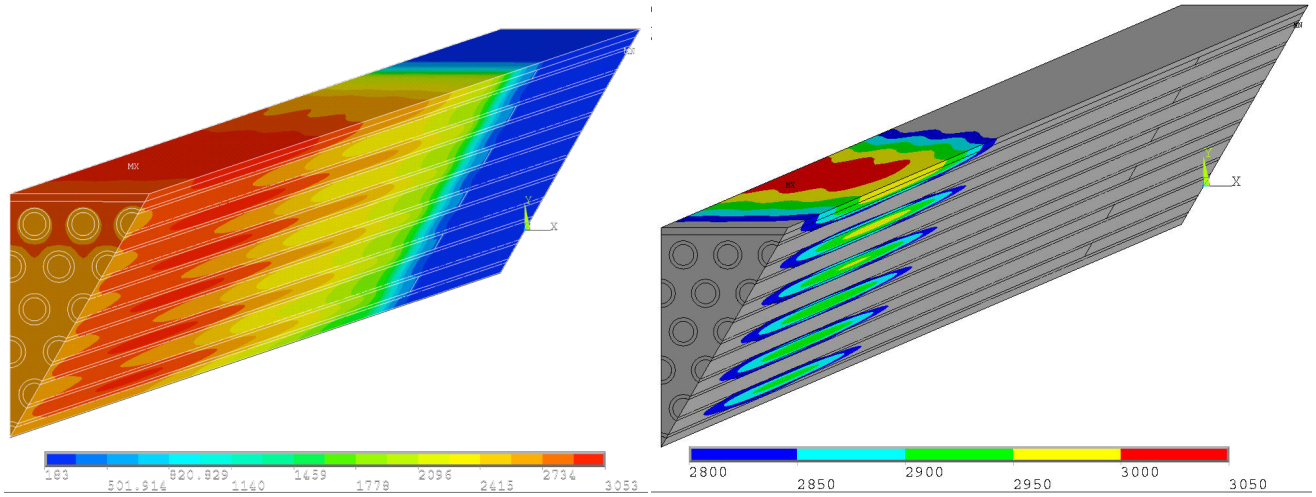

FIGURE 4. Predicted Temperature Distribution Through a GE 711 Cermet Fuel Element (left), and Detail of the Hottest 250 K Region of the Fuel Element (right). The NCPS baseline cermet fuel element geometry is a modification of the GE 710 geometry, designated GE 711. Using symmetric sectors reduces computational requirements.

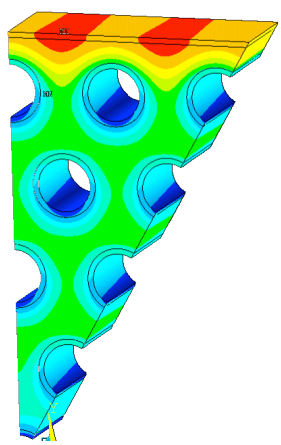

FIGURE 5. Temperature Distribution in a Fuel Element Length. Coolant Channels are Kept at a Fixed Temperature. Adiabatic External Surface.

To minimize peak fuel temperature while maximizing propellant mean outflow temperature, we are interested in two temperature differences which are plotted in Figure 6. The first, larger, temperature difference is between the fuel element edge (exterior surface) (red in Figure 5) and the coolant channel surface. These temperature differences form the solid lines in Figure 6. The second, smaller temperature difference is between the fuel matrix centerline (green) between coolant channels and the coolant channel surface. These differences form the dashed lines in Figure 6. These temperature differences are plotted against heat deposition rate (into the fuel matrix) since designers may choose to increase this rate to make a more compact reactor with heat deposited in fewer fuel elements. The engine's thrust to weight ratio increases. However, the propellant must remove the additional heat, and in smaller reactors, the nuclear reaction can be more difficult to control. As a footnote, the heat equation's mathematics confirms the linear variation of the results shown in Figure 6.

The results also show that different fuel element geometries perform differently. The ANL200 fuel element geometry has significantly larger temperature differences, than the GE 710 geometry, and, in turn the GE 711 geometry. The ANL nuclear rocket program's materials testing goal was a peak fuel temperature of 2500°C (2770 K) [18, p. 85]. Yet, the ANL200 design [5, p. 109] called for a peak centerline temperature of 3000 K at an average heat deposition of 3.27 MW/L (max. 5.16 MW/L) for an I_{sp} of 821s. Another fuel element geometry might have decreased the temperature differences and peak fuel temperature in the ANL200 design. For this and other reasons, the NCPS baseline cermet fuel element geometry is a modification of the GE 710 geometry, designated GE 711.

Stress analysis for NTP fuel elements is not a typical linear stress analysis with a margin of safety. At high temperatures, the materials will creep and plastically deform. These deformations are driven by thermal stress, thermal expansion, and differences in thermal expansion at material interfaces. Thermal cycling results in large deformations between the hot and cold shapes of each cycle. When hot, the material's ductility can accommodate deformations, but when cold or cooling, the material is less able to avoid residual stress, deformation, or fracture.

Stress analysis for the fuel elements in Figure 6, indicate that stresses are dominated by mismatch of thermal expansion at material interfaces; thermal stresses are smaller.

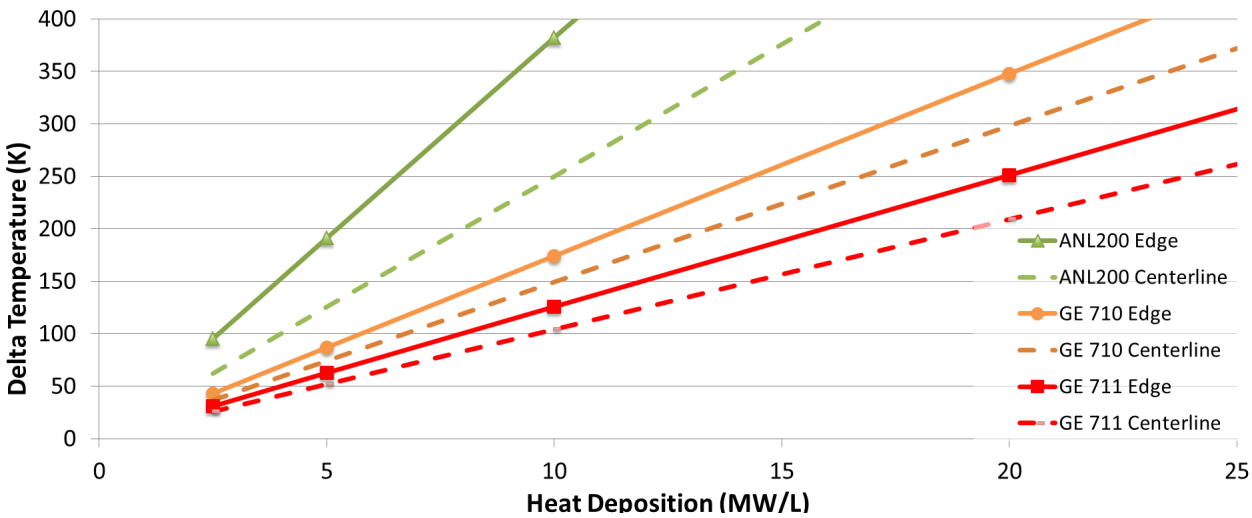

FIGURE 6. Temperature Difference, Fuel Peak at Edge to Coolant Channel Wall (Solid Line) and Fuel Centerline to Coolant Channel Wall (Dashed Line), for Several Cermet Fuel Geometries at a Range of Heat Deposition Rates.

CONCLUSION

In order to understand cermet fuel performance in NTP engines, this paper examined historical cermet material development reports. Fuel element and engine simulations were used to interpret the data. The reports indicate two issues at high temperatures: the high vaporization rate of UO_2 and the chemical stability (high temperature reduction) of UO_2. The data show that cladding and chemical stabilizers each result in large, order of magnitude, improvements in high temperature performance. Contemporary fuel samples are unlikely to achieve the best historical performance without these features. Some coated, stabilized, cermet samples were tested above 2770 K, but they are a small sample to fully assess high I_{sp} (>900s) potential. Contemporary testing of fuel samples at high temperatures is justified. Fuel element development may be complicated by the stability of UO_2 at high temperatures.

NOMENCLATURE

I_{sp} = Specific Impulse, s

T = Temperature, K

ACKNOWLEDGMENTS

The author expresses thanks to Chris Moore and John Warren at NASA Headquarters who supported this work through the Nuclear Cryogenic Propulsion Stage (NCPS) project established as part of the Advanced Exploration Systems Program. NASA Glenn Research Center (GRC) also provided funding. The author also thanks Stan Borowski and Bruce Schnitzler for their guidance and support, and Raj Sai, and Jim Fittje for many helpful discussions. The GRC library staff tirelessly located many documents, journal articles, and reports.

REFERENCES

[1] R. W. Bussard, "Nuclear Powered Rockets: A Historical Survey and Literature Summary," LANL Report LA-2036, Los Alamos, 1956.

[2] C. Haertling and R. J. Hanrahan, "Literature Review of Thermal and Radiation Performance Parameters for High-Temperature, Uranium Dioxide Fueled Cermet Materials," *Journal of Nuclear Materials,* vol. 366, pp. 317-335, 2007.

[3] L. B. Lundberg and R. R. Hobbins, "Nuclear Fuel for Very High Temperature Applications," in *Intersociety Energy Conversion Engineering Conference*, San Diego, 1992.

[4] R. E. Rom, "Review of Nuclear Rocket Research at NASA's Lewis Research Center from 1953 thru 1973," in *AIAA/NASA/OAI Conference on Advanced SEI Technologies*, AIAA 91-3500, 1991.

[5] Argonne National Laboratory, "Nuclear Rocket Program Terminal Report," ANL-7236, Argonne, IL, 1968.

[6] N. T. Saunders, R. E. Gluyas and G. K. Watson, "Feasibility Study of a Tungsten Water-Moderated Nuclear Rocket, II Fueled Materials," NASA TM X-1421, 1968.

[7] S. J. Kaufman, "Feasibility Study of a Tungsten Water-Moderated Nuclear Rocket, I Summary Report," NASA TM X-1420, 1968.

[8] General Electric, Nuclear Materials and Propulsion Operation, "710 High-Temperature Gas Reactor Program Summary Report; Volumes I-VI," GEMP-600, Vol 1 to 6, 1968.

[9] W. H. Lenz and P. R. Mundinger, "High Temperature Testing of Mo-UO2 and W-UO2 Cermets," in *Proceedings of the Nuclear Proopulsion Conference*, San Diego, CA, 1962.

[10] N. T. Saunders, G. K. Watson and R. J. Buzzard, "Investigation of Tungsten and Uranium Dioxide as a Nuclear Rocket Fuel Material," in *Proceedings of the Nuclear Propulsion Conference*, San Diego, CA, 1962.

[11] R. J. Baker, J. L. Daniel, W. J. Lackey, R. J. S. F. A. Lobsinger, E. A. Snajdr and W. E. Roake, "Basic Behavior and Property of W-UO2 Cermets," NASA CR-54840, Nov. 1965.

[12] G. E. McDonald and T. A. Moss, "Fabrication and Retention of Uranium Dioxide in Tungsten-Uranium Dioxide Composites Containing 20 Volume Percent Dispersed Uranium Dioxide," NASA TM X-473, 1961.

[13] R. E. Gluyas and M. A. Gedwill, "Stabilization of Tungsten-Uranium Dioxide Composites Under Thermal Cycling Conditions," NASA TM-X-1295, Cleveland, 1966.

[14] J. S. Anderson, J. O. Sawyer, H. W. Worner, G. M. Willis and M. J. Bannister, "Decomposition of Uranium Dioxide at its Melting Point," *Nature,* vol. 185, no. 915-916, pp. 228-229, March 26, 1960.

[15] Naval Postgraduate School, "Proceedings of Nuclear Propulsion Conference," Monterey, CA, August, 1962.

[16] A. F. Lietzke, N. T. Saunders, G. K. Watson, R. E. Gluyas and J. G. Slaby, "Fuel Elements and Fuel-Element Materials," NASA X66-51413, 1966.

[17] R. J. Beals, J. H. Handwerk and B. J. Wrona, "Behavior of Urania-Rare-Earth Oxides at High Temperatures," *Journal of the American Ceramic Society,* vol. 52, no. 11, pp. 578-581, Nov. 1969.

[18] Argonne National Laboratory, "Nuclear Rocket Program Quarterly Progress Report, Fourth Quarter 1965," ANL-7150,

Argonne, IL, 1965.

[19] M. E. M. Stewart, "Historical Material Property Data for Cermet and Graphite-Based NTP Fuels," in *Nuclear and Emerging Technologies for Space*, 2014.

[20] M. E. M. Stewart and B. G. Schnitzler, "Thermal, Fluid, and Structural Analysis of a Cermet Fuel Element," in *48th Joint Propulsion Conference*, AIAA 2012-3959, Atlanta GA, August 2012.

[21] M. E. M. Stewart and B. G. Schnitzler, "Thermal Hydraulics and Structural Analysis of the Small Nuclear Rocket Engine (SNRE) Core," in *43rd Joint Propulsion Conference*, AIAA 2007-5619, Cincinnati, July 2007.

Benchmark Evaluation of Fuel Effect and Material Worth Measurements for a Beryllium-Reflected Space Reactor Mockup

Margaret A. Marshall[1,2], John D. Bess[2],

[1] *Center for Space Nuclear Research,*
[2] *Idaho National Laboratory, PO Box1625, MS 3860, Idaho Falls, ID 83415-3860*
208-526-6826; margaret.marshall@inl.gov

Abstract. The critical configuration of the small, compact critical assembly (SCCA) experiments performed at the Oak Ridge Critical Experiments Facility (ORCEF) in 1962-1965 have been evaluated as acceptable benchmark experiments for inclusion in the *International Handbook of Evaluated Criticality Safety Benchmark Experiments* [1]. The initial intent of these experiments was to support the design of the Medium Power Reactor Experiment (MPRE) program, whose purpose was to study "power plants for the production of electrical power in space vehicles." The third configuration in this series of experiments was a beryllium-reflected assembly of stainless-steel-clad, highly enriched uranium (HEU)-O_2 fuel mockup of a potassium-cooled space power reactor. Reactivity measurements cadmium ratio spectral measurements and fission rate measurements were measured through the core and top reflector. Fuel effect worth measurements and neutron moderating and absorbing material worths were also measured in the assembly fuel region. The cadmium ratios, fission rate, and worth measurements were evaluated for inclusion in the *International Handbook of Evaluated Criticality Safety Benchmark Experiments* [2]. The fuel tube effect and neutron moderating and absorbing material worth measurements are the focus of this paper. Additionally, a measurement of the worth of potassium filling the core region was performed but has not yet been evaluated

Pellets of 93.15 wt.% enriched uranium dioxide (UO_2) were stacked in 30.48 cm tall stainless steel fuel tubes (0.3 cm tall end caps). Each fuel tube had 26 pellets with a total mass of 295.8 g UO_2 per tube. 253 tubes were arranged in 1.506-cm triangular lattice. An additional 7-tube cluster critical configuration was also measured but not used for any physics measurements. The core was surrounded on all side by a beryllium reflector.

The fuel effect worths were measured by removing fuel tubes at various radius. An accident scenario was also simulated by moving outward twenty fuel rods from the periphery of the core so they were touching the core tank. The change in the system reactivity when the fuel tube(s) were removed/moved compared with the base configuration was the worth of the fuel tubes or accident scenario.

The worth of neutron absorbing and moderating materials was measured by inserting material rods into the core at regular intervals or placing lids at the top of the core tank. Stainless steel 347, tungsten, niobium, polyethylene, graphite, boron carbide, aluminum and cadmium rods and/or lid worths were all measured. The change in the system reactivity when a material was inserted into the core is the worth of the material.

Keywords: Critical experiment, Uranium dioxide, Beryllium reflected, Reactivity measurement.

INTRODUCTION

A series of small, compact critical assembly (SCCA) experiments were completed from 1962–1965 at Oak Ridge National Laboratory's (ORNL's) Critical Experiments Facility (CEF) in support of the Medium-Power Reactor Experiments (MPRE) program. In the late 1950s, efforts were made to study "power plants for the production of electrical power in space vehicles."[3] The MPRE program was a part of those efforts and studied the feasibility of a stainless-steel system, boiling potassium 1 MW(t), or about 140 kW(e), reactor. The program was carried out in [fiscal years] 1964, 1965, and 1966. A summary of the program's effort was compiled in 1967 [3]. The delayed critical experiments were a mockup of a small, potassium-cooled space power reactor for validation of reactor calculations and reactor physics methods.

Initial experiments, performed in November and December of 1962, consisted of a core of un-moderated stainless-steel tubes, each containing 26 UO_2 fuel pellets, surrounded by a graphite reflector. Measurements were performed to determine critical reflector arrangements, fission-rate distributions, and cadmium ratio distributions. Subsequent experiments used beryllium reflectors and also measured the reactivity for various materials placed in the core. "The [assemblies were built] on [a] vertical assembly machine so that the movable part was the core and bottom reflector" [4]. The experiment studied in this evaluation was the third of the series and had the fuel in a 1.506-cm-triangular and 7-tube clusters leading to two critical configurations [5,6]. Once the critical configurations had been achieved, various measurements of reactivity, relative axial and radial activation rates of ^{235}U, and cadmium ratios were performed. These measurements were performed using the 1.506-cm-triangular pitch critical configuration. The reactivity measurements for fuel effect and material worth are the focus of this paper. The critical assembly configuration is briefly outlines for reference of the reader. The benchmark evaluations should be referenced a full description, evaluation, and discussion of the measurements [1,2].

CRITICAL CONFIGURATION

The critical configurations used for the fuel effect and material worth measurements was a core of 253 stainless steel rods each containing 26 UO_2 (93.2 wt.% U-235 enrichment) pellets. The dimensions of the fuel pellets, the fuel tubes, and the isotopic composition of the fuel is given in Table 1and 2. The tubes were arranged in a 1.506-cm-triangular-pitch arrangement and held in place using two grid plates. The fuel was contained within an aluminum core tank. The core tank was surrounded on all side by beryllium reflector. Dimensions of the reflectors are given in Table 3. The configuration was brought to critical using a vertical assembly machine; the core tank and bottom reflector were lifted into and under the side reflector and top reflector. Photographs of the vertical assembly machine and the critical configuration are given as Figure 1.

The critical configuration was evaluated and a detailed and simple benchmark model was derived. The detailed and simple benchmark models of the critical configuration were used in the evaluation of the fuel effect and material worth measurements. The detailed benchmark model of is shown in Figure 2. For more detail regarding the derivation of the critical configuration benchmark models refer to the full benchmark evaluation [1].

TABLE 1. Fuel Pellet and Tube Data

Number of Pellets per Tube	26		**Number of Fuel Tubes**	253	
UO_2 Density	9.71	g/cm^3	**Length**	30.48	cm
UO_2 Mass per Tube	295.8	g	**Outside Diameter**	1.27	cm
Pellet Diameter	1.141	cm	**Wall Thickness**	0.051	cm
Length of One Pellet	1.145	cm	**Weight with End Caps**	45.37	g
Length of 26 Pellets	29.88	cm[(a)]	**Weight of One End Cap**	0.64	g

(a) This length "includes 0.110 cm of void or ~0.0044 cm of void between each pellet".[2]

TABLE 2. Fuel Isotopic Composition

^{234}**U**	1.01	wt.%
^{235}**U**	93.15	wt.%
^{236}**U**	0.47	wt.%
^{238}**U**	5.37	wt.%

TABLE 3. Reflector Dimensions.

Top Reflector		**Bottom Reflector**	
Thickness (cm)	6.985	Thickness (cm)	7.62
Nominal Diameter (cm)[(a)]	41.2	Nominal Diameter (cm)[(a)]	41.2
Mass (kg)	17.13	Mass (kg)	18.7
Top Reflector Tank-Aluminum (Type 1100)		**Bottom Reflector Tank-Aluminum (Type 1100)**	
Side Wall Thickness (cm)	0.635	Side Wall Thickness (cm)	0.635
Height (cm)	12.95	Height (cm)	8.51
Bottom Thickness (cm)	0.22	Bottom Thickness (cm)	0.89
Mass (kg)	4.38	Mass (kg)	5.75
Side Reflector			
Height (cm)	30.63		
Thickness (cm)	11.37		
Inside Diameter (cm)	26.16		
Mass (kg)	75.7		

(a) This nominal diameter was given in the published report [4]. The top and bottom reflector were composed of 7.3- and 3.65-cm-square blocks, 2.54- or 0.635-cm-thick, and some triangular shaped pieces.

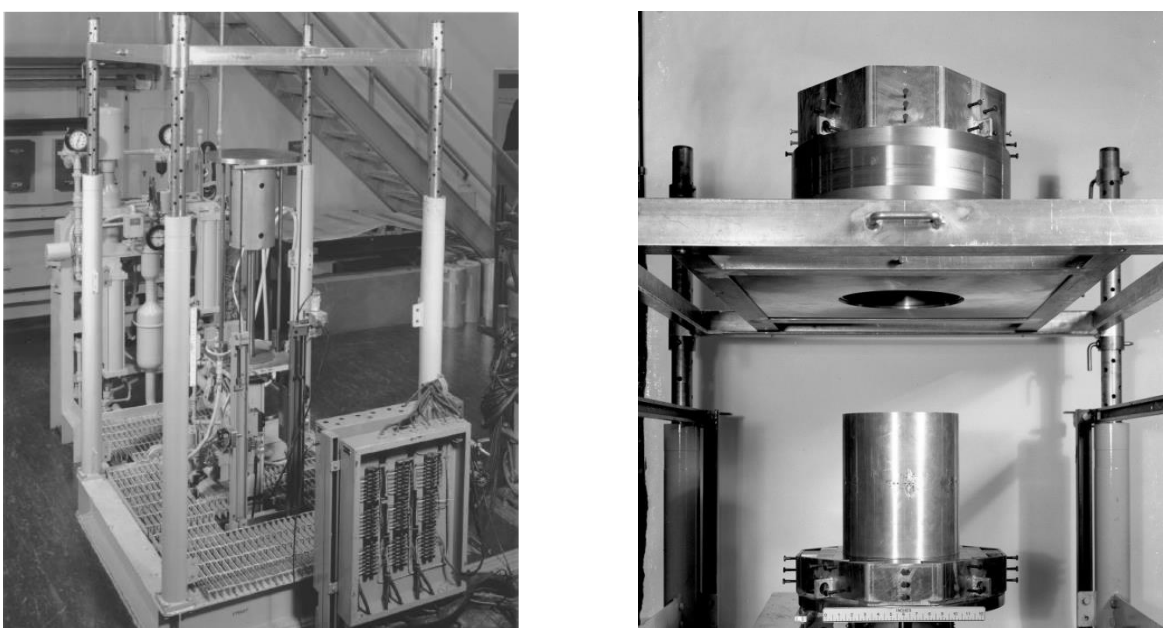

FIGURE 1. Vertical Assembly Machine and Disassembled Beryllium Reflected Core.

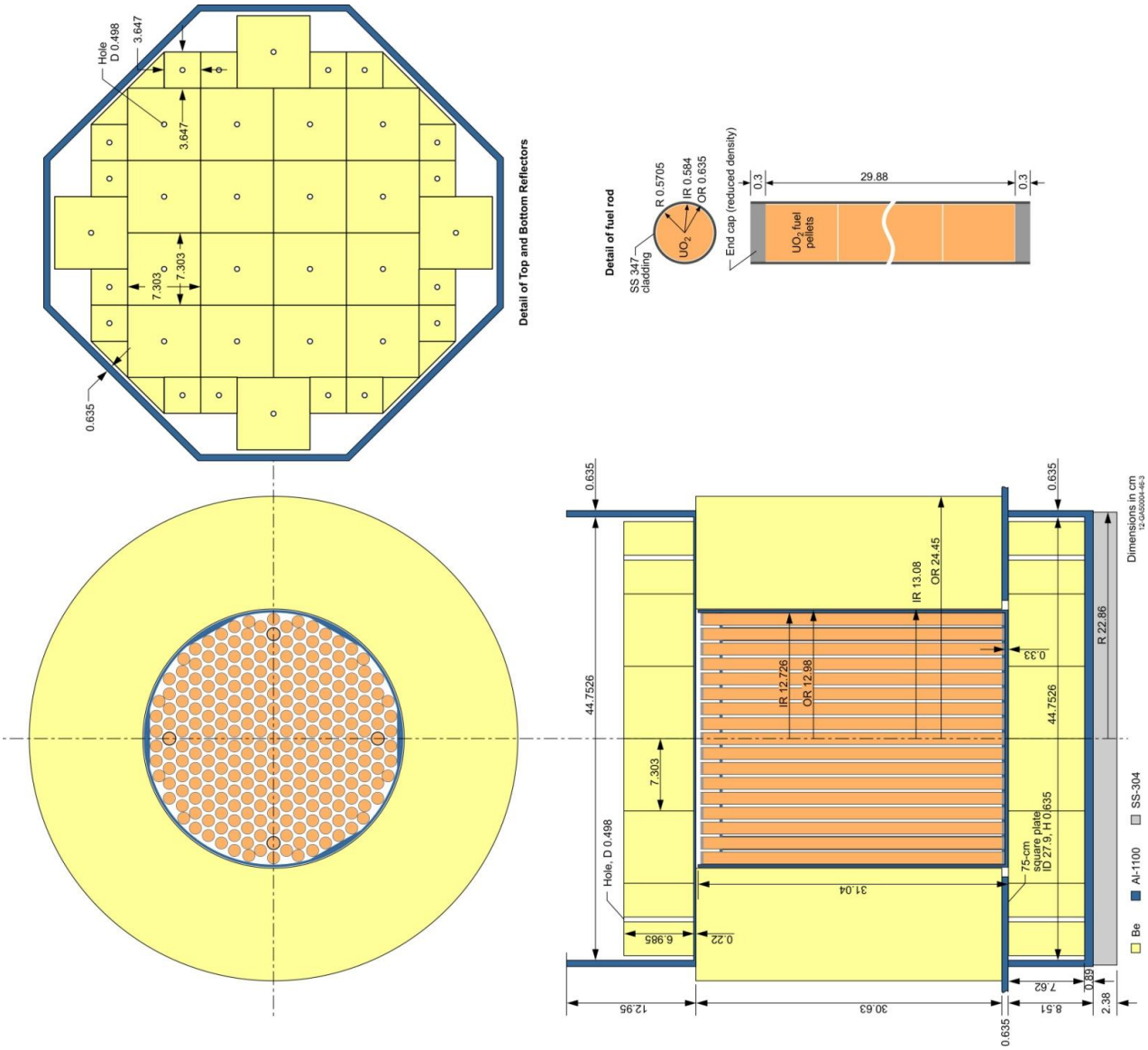

FIGURE 2. Detailed Benchmark Model of Critical Configuration.

REACTIVITY EFFECT MEASUREMENTS

Various reactivity measurements were performed. The reactivity of fuel tubes at various locations in the core and the effect of fuel tube movement at the periphery of the core were measured. The worth of various neutron absorbing and moderating materials inserted into the core and the worth of adding thickness to the top reflector were also measured. Finally the worth of adding potassium to the core was measured, which also led to some other worth measurements as the core was reconfigured to accommodate the potassium. The fuel effect and material reactivity measurements have been evaluated and are described in this paper. The potassium measurements have not yet been evaluated.

Experimental Results

Various reactivity measurements were performed. The reactivity of fuel tubes at various locations in the core and the effect of fuel tube movement at the periphery of the core were measured. The worth of various neutron absorbing and moderating materials inserted into the core were also measured. All worth measurements were

performed by measuring the stable reactor period of the system before and after the system was perturbed. The stable reactor period was then converted to a system reactivity in units of dollars. The change in the system reactivity is the worth of the perturbation.

Fuel Effect Reactivity Measurements

The worth of fuel tubes at various radial locations in the core was measured by "observing the change in the stable reactor period when the fuel tube was removed"[5]. The worth of fuel tubes versus radial position is given in Table 4. The locations of the fuel tubes are shown in Figure 3.

A credible accident condition where twenty fuel tubes at the periphery of the core were moved from their normal location in the lattice out to the edge of the core was simulated. An example of this movement is shown for two fuel tubes in Figure 3. It is clear from the grid plate, Figure 4, which twenty rods were moved. The measured reactivity effect was -8.2 ¢ for displacement of twenty fuel tubes.

TABLE 4. Fuel Tube Reactivity Worth Versus Radial Position

Fuel Tube Position[(a)]	Distance From Core Center	Reactivity (¢)
1	0	32.0
2	2.59	32.0
3	5.23	30.8
4	7.75	27.2
5	10.48	25.5
6	10.56	25.6
7	11.78	22.6

(a) Positions given in Figure 3.

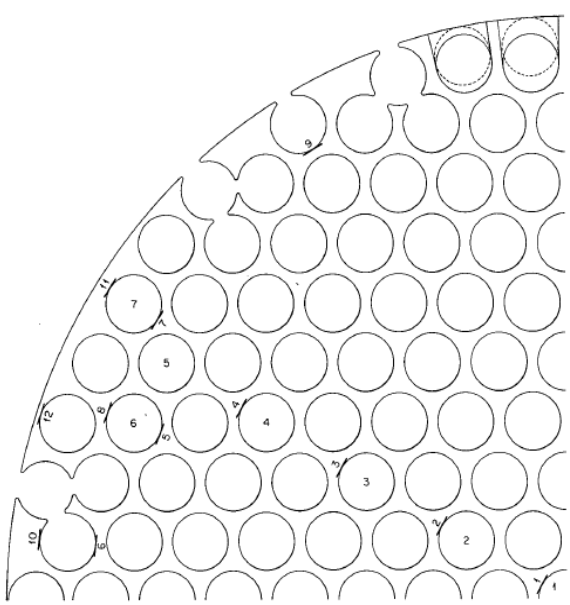

FIGURE 3. Fuel Tube Locations for Fuel Reactivity Measurements.

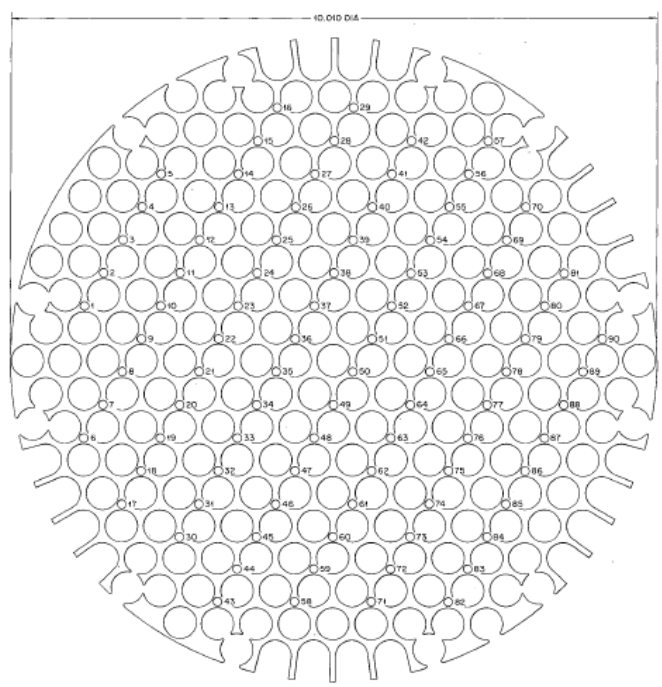

FIGURE 4. Drawing of Grid Plate with Sample Rod Locations.

Neutron Absorbing and Moderating Material Reactivity Measurements

The effect of adding various neutron absorbing and moderating materials was also measured. Materials were added to the core as rods, filled stainless steel tubes, and discs or lids that fit between the top of the fuel tubes and the top of the core tank. The results of the reactivity measurements are summarized in Table 5.

TABLE 5. Reactivity Effects of Absorbing and Moderating Material in the Core

Material	Form	Number	Location[(a)]	Total Weight (g)	Total Reactivity (cents)
Type 347 Stainless Steel	0.317 cm dia rods 30.5 cm long	90	All positions filled	1704	14.8
	0.317 cm dia rods 30.5 cm long	46	Every other position	871	7.92
W	0.317 cm dia rods 30.5 cm long	46	Every other position	2110	-4.27
Nb	3/32 inch dia rods 30.48 cm long[(c)]	90	All positions	1050	4.9
CH_2	0.317 cm dia rods 30.5 cm long	8	Odd number holes between 43-57	18.42	24.43
C	0.120 inch dia rods 30.5 cm long	23	Every 4th position	82	7.5
B_4C	Filled with B_4C[(g)]	1	Center fuel tube position	30.5	-6.65
Stainless Steel	Disc 0.317 cm thick for top of core tank	1	Top of core	1290	7.97
Al	Lid for top of core tank, 0.317 cm thick	1	Top of core	464	16.62
Al	Lid for top of core tank, 0.159 cm thick	1	Top of core	226	8.14
Cd	Lid for top of core, 0.066 cm thick	1	Top of core	286.5	-45.7

(a) Rod locations are labeled in Figure 4.

Evaluation of Experimental Results

The reactivity measurements were evaluated as benchmark experiments and found to be acceptable. The effect of the uncertainty in various experimental, geometrical, and material uncertainties was evaluated. The measurement uncertainty of the reactivity measurement was 10%√2.

Fuel Effect Reactivity Measurements

The uncertainty in the fuel and fuel tube dimensions and composition were evaluated as part of the evaluation of the critical configuration [1]. It was found that all parameters had a negligible effect on the critical system reactivity except for the fuel tube composition and the fuel mass. The fuel tube composition uncertainty was judged to be systematic across all fuel tubes. The effect of perturbing all fuel tubes simultaneously was ± 0.00025 Δk_{eff}. Because this uncertainty is rather small when perturbing all 253 fuel rods in the critical configuration and because the uncertainty is systematic across all fuel tubes, the effect of the fuel tube composition on the worth measurement of a single fuel tube would be negligible.

The uncertainty effect of the mass of fuel per fuel tube was 0.00010 Δk_{eff} or ±1.37 ¢. For the fuel tube worth measurements, this was added in quadrature to the 10%√2 measurement uncertainty.

For the accident configuration, the fuel tube composition and the fuel mass uncertainties would have a negligible effect because no fuel was removed but only moved. The fuel position uncertainty was evaluated for the critical configurations and was found to have a negligible effect. Thus, only the 10%√2 measurement uncertainty applied to the accident configuration worth measurement.

The experimental uncertainty for the fuel effect reactivity measurements is summarized in Table 6.

Neutron Absorbing and Moderating Material Reactivity Measurements

The uncertainty in dimensions, position/placement, and material composition was evaluated for all neutron absorbing and moderating materials inserted into the core. Each parameter was perturbed individually for each worth measurement. The total uncertainty for each reactivity measurement is given in Table 7. A summary of the uncertainty effect of each parameter can be found in [2].

TABLE 6. Fuel Effect Reactivity Measurements and Uncertainties

Distance from Core Center (Fuel Tube Position)	Experimental Worth with Experimental Uncertainty (¢)		
0 cm (1)	-32.0	±	4.73
2.59 cm (2)	-32.0	±	4.73
5.23 cm (3)	-30.8	±	4.57
7.75 cm (4)	-27.2	±	4.08
10.48 cm (5)	-25.5	±	3.86
10.56 cm (6)	-25.6	±	3.87
11.78 cm (7)	-22.6	±	3.48
Accident Configuration Worth	-8.2	±	1.79

TABLE 7. Material Reactivity Measurements and Uncertainties

Absorbing or Moderating Material	Experimental Worth with Experimental Uncertainty (¢)		
90 Stainless Steel 347 Rods	14.8	±	2.15
46 Stainless Steel 347 Rods	7.92	±	1.89
46 Tungsten Rods	-4.27	±	0.91
90 Niobium Rods	4.9	±	1.27
8 Polyethylene Rods	24.43	±	3.49
23 Graphite Rods	7.5	±	1.20
B_4C Filled Tube	-6.65	±	0.94
Stainless Steel Lid	7.97	±	1.38
0.3175 cm Thick Al Lid	16.62	±	2.59
0. 15875 cm Thick Al Lid	8.14	±	1.58
Cadmium Lid	-45.7	±	6.63

Evaluation of Experimental Results

Detailed and simple benchmark models were derived for the reactivity effect measurements. The simplifications made were simplifications to the critical configuration. Additionally, impurities were removed from the fuel, the tungsten rods, the niobium rods, the graphite rods, and the cadmium lid. The effect of all simplifications on the worth measurements were negligible; however, an additional bias uncertainty was required due to modeling limitations. The detailed benchmark model benchmark values for the reactivity measurements are given in Table 8 for the fuel effect reactivity measurements and Table 9 for the neutron absorbing and moderating material worth measurements.

TABLE 8. Fuel Effect Reactivity Measurements and Uncertainties

Distance from Core Center (Fuel Tube Position)	Detailed Benchmark Model Value (¢)		
0 cm (1)	-32.00	±	5.014
2.59 cm (2)	-32.00	±	5.014
5.23 cm (3)	-30.80	±	4.861
7.75 cm (4)	-27.20	±	4.411
10.48 cm (5)	-25.50	±	4.203
10.56 cm (6)	-25.60	±	4.215
11.78 cm (7)	-22.60	±	3.828
Accident Configuration Worth	-8.20	±	2.448

TABLE 9. Material Reactivity Measurements and Uncertainties

Absorbing or Moderating Material	Detailed Benchmark model Value (¢)		
90 Stainless Steel 347 Rods	14.80	±	2.716
46 Stainless Steel 347 Rods	7.92	±	2.514
46 Tungsten Rods	-4.27	±	1.840
90 Niobium Rods	4.90	±	2.094
8 Polyethylene Rods	24.43	±	3.864
23 Graphite Rods	7.50	±	2.053
B_4C Filled Tube	-6.65	±	1.919
Stainless Steel Lid	7.97	±	2.163
0.3175 cm Thick Al Lid	16.62	±	3.076
0. 15875 cm Thick Al Lid	8.14	±	2.295
Cadmium Lid	-45.70	±	6.823

Evaluation of Experimental Results

The worths were calculated using MCNP5-1.60 and ENDF/B-VII.0 neutron cross section libraries. For each run, a total of 2,150 cycles were run, skipping the first 150 cycles, with 100,000 histories per cycle. For each reactivity effect measurement the base and perturbed benchmark model eigenvalues were calculated. The change in eigenvalues was then converted to a reactivity in units of cents using β_{eff}, 0.0073± 5% [1]. The fuel effect reactivity sample calculations for the detailed benchmark model are presented in Table 10. They calculations agree well with the benchmark results. The material worth sample calculations for the detailed benchmark model are presented in 11. Some calculated results have a large deviation from the benchmark. This cause for this deviation is not known; however, all results are within 3σ of the benchmark value.

CONCLUSION

The reactivity effect measurements for the beryllium-reflected, UO_2, small, compact critical assembly have been evaluated. The fuel effect measurements, including an accident scenario configuration, and neutrol absorbing and moderation material worth measurements were measured. All measurements are acceptable as benchmark experiments. Sample calculation results, using MCNP, show that a large deviation from the benchmark model, however, all results are within 3σ.

Future work includes the evaluation of potassium worth measurements.

TABLE 10. Calculation Results for Fuel Effect Reactivity

Distance from Core Center (Fuel Tube Position)	Calculated Reactivity (¢)			(C-E)/E [(a)]			C/E Ratio[(a)]
0 cm (1)	-31.67	±	1.18	-8.7%	±	15.9%	0.91
2.59 cm (2)	-30.14	±	1.18	-5.8%	±	15.2%	0.94
5.23 cm (3)	-28.47	±	1.18	-7.6%	±	15.1%	0.92
7.75 cm (4)	-27.21	±	1.18	0.0%	±	16.8%	1.00
10.48 cm (5)	-24.57	±	1.18	-3.6%	±	16.5%	0.96
10.56 cm (6)	-23.18	±	1.18	-9.5%	±	15.6%	0.91
11.78 cm (7)	-20.40	±	1.08	-9.7%	±	16.0%	0.90
Accident Configuration Worth	-8.04	±	1.18	-1.9%	±	32.6%	0.98

(a) "E" is the experimental benchmark value. "C" is the calculated value..

TABLE 11. Calculation Results for Material Reactivity

Absorbing or Moderating Material	Calculated Reactivity (¢)			(C-E)/E [(a)]			C/E Ratio[(a)]
90 Stainless Steel 347 Rods	21.44	±	1.18	21.1%	±	27.7%	1.21
46 Stainless Steel 347 Rods	8.45	±	1.18	47.8%	±	37.0%	1.48
46 Tungsten Rods	-1.11	±	1.08	-74.0%	±	27.7%	0.26
90 Niobium Rods	8.45	±	1.18	72.4%	±	77.5%	1.72
8 Polyethylene Rods	22.83	±	1.18	2.6%	±	15.5%	1.03
23 Graphite Rods	7.76	±	1.18	3.4%	±	32.4%	1.03
B_4C Filled Tube	-8.22	±	1.18	23.6%	±	39.8%	1.24
Stainless Steel Lid	9.83	±	1.18	23.4%	±	36.6%	1.23
0.3175 cm Thick Al Lid	19.65	±	1.18	18.2%	±	23.0%	1.18
0.315875 cm Thick Al Lid	8.86	±	1.18	8.9%	±	33.9%	1.09
Cadmium Lid	-31.94	±	1.18	-30.1%	±	10.8%	0.70

(a) "E" is the experimental benchmark value. "C" is the calculated value.

ACKNOWLEDGMENTS

The author would like to acknowledge and thank the experimenter (John T. Mihalczo), the evaluation reviewers (John D. Bess, J. Blair Briggs, and Michael F. Murphy), and the ICSBEP and IRPhEP technical review groups for their countless hours of help and review.

REFERENCES

[1] M.A. Marshall, "Critical Configuration for Beryllium Reflected Assemblies of U(93.15)O_2Fuel Rods (1.506-cm Pitch and 7-Tube Clusters," *International Handbook of Evaluated Criticaltiy Safety Benchmark Experiments*, NEA/NSC/DOC(95)03/I-IX, Organization for Economic Co-operation and Development-Nuclear Energy Agency (OECD-NEA), Paris (2014).

[2] M.A. MARSHALL, "Critical Configuration and Physics Measurements for Beryllium Reflected Assemblies of U(93.15)O_2Fuel Rods (1.506-cm Pitch and 7-Tube Clusters) ," *International Handbook of Reactor Physics Benchmark Experiments*, NEA/NSC/DOC(2006)1, Organization for Economic Co-operation and Development-Nuclear Energy Agency (OECD-NEA), Paris (2015).

[3] A. P. Fraas, "Summary of the MPRE Design and Development Program," ORNL-4048, Oak Ridge National Laboratory (1967).

[4] J.T. Mihalczo, "A Small Graphite-Reflected UO_2 Critical Assembly," ORNL-TM-450, Oak Ridge National Laboratory (1962).

[5] J.T. Mihalczo, "A Small Beryllium-Reflected UO2 Assembly," ORNL-TM-655, Oak Ridge National Laboratory (1963).

[6] J.T. Mihalczo, "A Small, Beryllium-Reflected UO_2 Critical Assembly," *Trans. Am. Nucl. Soc.*, **72**, 196-198 (1995).

Liquid Metal Thermo-magnetic Systems for Space, Nuclear and Industrial Applications

Carlos O. Maidana

Chiang Mai University, Department of Mechanical Engineering, Chiang Mai 50200 - Thailand
Idaho State University, Department of Mechanical Engineering, Pocatello, ID 83209 - USA
MAIDANA RESEARCH, 2885 Sanford Ave SW #25601, Grandville, MI 49418 - USA
E-mail: maidanac@dome.eng.cmu.ac.th | maidanac@gmail.com | maidana@physics.isu.edu
Phone: +1 208 904-0401 | +66 8 3003-3910 | +41 22 575-4488

Abstract. Liquid alloy systems have a high degree of thermal conductivity far superior to ordinary non-metallic liquids and inherent high densities and electrical conductivities. This results in the use of these materials for specific heat conducting and dissipation applications. Typical applications for liquid metals include heat transfer systems, and thermal cooling and heating designs. Uniquely, they can be used to conduct heat and/or electricity between non-metallic and metallic surfaces. The motion of liquid metals in strong magnetic fields generally induces electric currents, which, while interacting with the magnetic field, produce electromagnetic forces. Thermo-magnetic systems, such as electromagnetic pumps or electromagnetic flow meters, exploit the fact that liquid metals are conducting fluids capable of carrying currents source of electromagnetic fields useful for pumping and diagnostics.

Liquid metal-cooled reactors are both moderated and cooled by a liquid metal solution. These reactors are typically very compact and they can be used in regular electric power production, for naval and space propulsion systems or in fission surface power systems for planetary exploration. Liquid metals in fusion reactors can be used in heat exchange, tritium breeder systems and in first wall protection, using a flowing liquid metal surface as a plasma facing component. Liquid metal targets and beam dumps for spallation and for heat removal will also be needed at many high power particle accelerator facilities where the severe constraints arising from a megawatt beam deposited on targets and absorbers will require complex procedures to dilute the beam, and liquid metals constitute an excellent working fluid due to its intrinsic characteristics. In the metal industry, thermo-magnetic systems are used to transport the molten metal in between processes. By developing methods to control the surface tension of liquid metals, applications can be developed in configurable electronics, microfluidic channels and MEMS.

But the coupling between the electromagnetics and thermo-fluid mechanical phenomena observed in liquid metal thermo-magnetic systems, and the determination of its geometry and electrical configuration, gives rise to complex engineering magnetohydrodynamics and numerical problems were techniques for global optimization has to be used, MHD instabilities understood -or quantified- and multiphysics models analyzed. The environment of operation adds even further complexity, i.e. vacuum, high temperature gradients and radiation, whilst the presence of external factors, such as the presence of time and space varying magnetic fields, can lead to the need of developing active flow control systems.

In this review paper we explore the different applications of liquid metal technology, we present the magnetohydrodynamics equations behind this technology and the research topics that should be addressed in the near future and currently under research by this author.

Keywords: liquid metals, magneto-hydrodynamics, thermo-magnetic systems, electromagnetic pumps.

INTRODUCTION

The coupling between the electromagnetics and thermo-fluid mechanical phenomena observed in liquid metal thermo-magnetic systems, and the determination of the device geometry and electrical configuration when appropiate, gives rise to complex engineering magnetohydrodynamics and numerical problems were techniques for global optimization has to be used, MHD instabilities understood, and multiphysics models developed and analyzed [1, 2]. The environment of operation adds even further complexity, i.e. vacuum, high temperature gradients and radiation, whilst the presence of external factors, such as the presence of time and space varying magnetic fields, also leads to the need of developing active flow control systems [3, 4, 5, 6, 7]. The development of analytical models and predictive tools to model, characterize, design and build liquid metal thermo-magnetic systems and components for space, nuclear and industrial applications are of primordial importance and represent a cross-cutting technology that can provide unique design and development capabilities besides a better understanding of the physics behind the magneto-hydrodynamics of liquid metals and plasmas.

Liquid Metal Technology for Nuclear Fission Reactors

Liquid metal-cooled reactors are both moderated and cooled by a liquid metal solution. These reactors are typically very compact and can be used for regular electric power generation in isolated places, for fission surface power units for planetary exploration, for naval propulsion and as part of space nuclear propulsion systems. Certain models of liquid metal reactors are also being considered as part of the Generation-IV nuclear reactor program. The liquid metal thermo-magnetic systems used in this type of reactors are MHD devices which design, optimization and fabrication represents a challenge due to the coupling of the thermo-fluids and the electromagnetics phenomena, the environment of operation, the materials needed and the computational complexity involved. This challenge we aim to solve [2].

A liquid metal cooled nuclear reactor is a type of nuclear reactor, usually a fast neutron reactor, where the primary coolant is a liquid metal. While pressurized water could theoretically be used for a fast reactor, it tends to slow down neutrons and absorb them. This limits the amount of water that can be allowed to flow through the reactor core, and since fast reactors have a high power density most designs use molten metals instead. The boiling point of water is also much lower than most metals demanding that the cooling system be kept at high pressure to effectively cool the core. Another benefit of using liquid metals for cooling and heat transport is its inherent heat absorption capability.
Liquid metals also have the property of being very corrosive and bearing, seal, and cavitation damage problems associated with impeller pumps in liquid-metal systems make them not an option and electromagnetic pumps are used instead. In all electromagnetic pumps, a body forced is produced on a conducting fluid by the interaction of an electric current and magnetic field in the fluid. This body force results in a pressure rise in the fluid as it passes from the inlet to the outlet of the pump.

In space reactors as well as in other types of semi-transportable small modular reactors, weight, reliability and efficiency are of fundamental importance. Furthermore, for the former, liquid metals as working fluid are the only option due to the working environment characteristics that outer space provides [1]. For space power systems, the induction electromagnetic pump, because it lacks electrodes, is inherently more reliable than the conduction electromagnetic pump. The annular linear induction pump, furthermore, has several advantages over its flat counterpart because it has greater structural integrity, is more adaptable to normal piping systems, and allows greater design freedom in the coil configuration. The annular design also has a basically greater output capability since the path followed by the induced currents has a lower resistance than the path followed in a corresponding flat pump [2].

Liquid Metal Technology for Nuclear Fusion Reactors

Research and development in nuclear fusion devices is increasing worldwide and experimental facilities and prototypes face new engineering magnetohydrodynamics challenges and needs. Among the latter are the use of liquid metals thermomagnetic systems such as electromagnetic pumps and the use of liquid metals as plasma facing material. Certain engineering MHD problems and solutions are shared by different fields but there are aspects specific to nuclear fusion devices that we aim to solve by developing mathematical, computational and experimental

methods and tools useful in the design and multi-physics analysis of engineering components and in the understanding of the MHD phenomena in place.

While fusion power is still in early stages of development, substantial sums have been and continue to be invested in research. In the EU almost €10 billion was spent on fusion research up to the end of the 1990s, and the new ITER reactor alone is budgeted at €10 billion. It is estimated that up to the point of possible implementation of electricity generation by nuclear fusion, R&D will need further promotion totaling around €60–80 billion over a period of 50 years or so (of which €20–30 billion within the EU). Nuclear fusion research receives €750 million (excluding ITER funding) from the European Union, compared with €810 million for sustainable energy research, putting research into fusion power well ahead of that of any single rivaling technology.

Despite many differences between possible designs of power plant, there are several systems that are common to most. A fusion power plant, like a fission power plant, is customarily divided into the nuclear island and the balance of plant. The balance of plant converts heat into electricity via steam turbines; it is a conventional design area and in principle similar to any other power station that relies on heat generation, whether fusion, fission or fossil fuel based. The nuclear island has a plasma chamber with an associated vacuum system, surrounded by plasma-facing components (first wall and divertor) maintaining the vacuum boundary and absorbing the thermal radiation coming from the plasma, itself surrounded by a "blanket" where the neutrons are absorbed to breed tritium and heat a working fluid that transfers the power to the balance of plant. If magnetic confinement is used, a magnet system is needed, and usually systems for heating and refueling the plasma and for driving current. In inertial confinement, a driver (laser or accelerator) and a focusing system are needed, as well as a mean for forming and positioning the pellets.

The plasma-facing material is any material used to construct the plasma-facing components, those components exposed to the plasma within which nuclear fusion occurs, and particularly the material used for the lining or first wall of the reactor vessel. The plasma facing components in energy producing fusion devices will experience 5-15 MW/m^2 surface heat flux under normal operation (steady-state) and off-normal energy deposition up to 1 MJ/m^2 within 0.1 to 1.0 ms. Refractory solid surfaces represent one type of plasma facing component option. Another option is to use a flowing liquid metal surface as a plasma facing component, an approach which will require the production and control of thin, fast flowing, renewable films of liquid metals such as lithium, gallium, or tin for particle control at diverters.

High Energy Particle Accelerator Targets and Dumps

A particle accelerator is a machine that accelerates particles to extremely high energies. These particles are elementary particles or heavy ions. Beams of high-energy particles are useful for both fundamental and applied research in the sciences, and also in many technical and industrial fields unrelated to fundamental research. It has been estimated that there are approximately 26,000 accelerators worldwide. Of these, only about 1% are research machines with energies above 1 GeV, while about 44% are for radiotherapy, 41% for ion implantation, 9% for industrial processing and research, and 4% for biomedical and other low-energy research.

The largest particle accelerators with the highest particle energies, such as the Large Hadron Collider (LHC) at the European Organization for Nuclear Research (CERN), are used for experimental particle physics for the most basic inquiries into the dynamics and structure of matter, space, and time. These typically entail particle energies of many hundreds of GeV up to several TeV. Besides being of fundamental interest, high energy electrons may be coaxed into emitting extremely bright and coherent beams of high energy photons via synchrotron radiation, which have numerous uses in the study of atomic structure, chemistry, condensed matter physics, biology, and technology. Examples include the European Synchrotron Radiation Facility (ESRF), which has recently been used to extract detailed 3-dimensional images of insects trapped in amber. Thus there is a great demand for electron accelerators of moderate (GeV) energy and high intensity.

Liquid metal targets in particle accelerators are used for spallation purposes. Liquid metal dumps are used as a machine protection mechanism to stop a beam while absorbing and diluting the power stored in the particle beam [3]. Liquid metal insertion devices are used in cooling rings to make the momentum distribution of particles more homogeneous, minimizing the lateral components [4]. Liquid metal channels are used for thermal control of solid targets, accelerator components and experimental stations dealing with high density beams or radiation that could generate a high temperature gradient.

If the spallation target is surrounded by a blanket assembly of nuclear fuel, such as fissile isotopes of uranium, plutonium or thorium, there is a possibility of sustaining a fission reaction. This is described as an accelerator-driven system (ADS). In such a system, the neutrons produced by spallation would cause fission in the fuel, assisted by further neutrons arising from that fission. Up to 10% of the neutrons could come from the spallation, though it would normally be less, with the rest of the neutrons arising from fission events in the blanket assembly. An ADS system can only run when neutrons are supplied to it because it burns material which does not have a high enough fission-to-capture ratio for neutrons to maintain a fission chain reaction. One then has a nuclear reactor which could be turned off simply by stopping the proton beam, rather than needing to insert control rods to absorb neutrons and make the fuel assembly subcritical. Because they stop when the input current is switched off, accelerator-driven systems are seen as safer than normal fission reactors. However, the target still needs to be cooled continuously due to heating caused by the accelerator beam.

For the highest power densities, it is widely expected that many facilities will need to employ liquid metal targets and beam dumps for spallation and for heat removal. A common problem encountered when using liquids is shock wave generation due to heat deposition resulting from a powerful pulsed beam. The severe constraints arising from a megawatt beam deposited on targets and absorbers will require complex procedures to dilute the beam. Liquid metals, due to their heat capacity and density, are excellent materials to heat removal and spallation.

FUNDAMENTAL EQUATIONS

The equations describing the liquid metal dynamics are given by:

$$\boldsymbol{J_i} = \sigma(\mathbf{E} + \mathbf{u} \times \mathbf{B}) \tag{1}$$

$$\rho\left[\frac{\partial \mathbf{u}}{\partial t} + (\boldsymbol{u} \cdot \nabla)\mathbf{u}\right] + \nabla p - \rho\nu\nabla^2\mathbf{u} = \mathbf{J} \times \mathbf{B} \tag{2}$$

where the current density is $\mathbf{J}=\mathbf{J}_s+\mathbf{J}_i$, s and n are the conductivity and kinematic viscosity (ratio of the viscous force to the inertial force) of the fluid, and $\mathbf{u}$ is the fluid velocity. Because the linear momentum of the fluid element could change not only by the pressure force, $-\nabla p$, viscous friction, $\rho\nu\nabla^2\boldsymbol{u}$, and Lorentz force, $\boldsymbol{J} \times \boldsymbol{B}$, but also by volumetric forces of non-electromagnetic origin; then eq. (2) should be modified and it could be expressed with an additional term $\boldsymbol{f}$ in the right hand side,

$$\rho\left[\frac{\partial \mathbf{u}}{\partial t} + (\boldsymbol{u} \cdot \nabla)\mathbf{u}\right] + \nabla p - \rho\nu\nabla^2\mathbf{u} - \mathbf{f} = \mathbf{J} \times \mathbf{B} \tag{3}$$

while the conservation of mass for liquid metals would be given by $\nabla \cdot \boldsymbol{u} = 0$, which expresses the incompressibility of the fluid. An induction equation, valid in the domain occupied by the fluid and generated by the mechanical stretching of the field lines due to the velocity field, can be written as,

$$\frac{\partial}{\partial t}\boldsymbol{B} + (\boldsymbol{u} \cdot \nabla)\boldsymbol{B} = \frac{1}{\mu\sigma}\nabla^2\boldsymbol{B} + (\boldsymbol{B} \cdot \nabla)\boldsymbol{u}\ , \tag{4}$$

describing the time evolution of the magnetic field, $\partial\boldsymbol{B}/\partial t$, due to advection $(\boldsymbol{u} \cdot \nabla)\boldsymbol{B}$, diffusion $\nabla^2\boldsymbol{B}$ and field intensity sources $(\boldsymbol{B} \cdot \nabla)\boldsymbol{u}$. Sometimes the induction equation, eq. (4), is written dimensionless by the introduction of scale variables and as a function of the magnetic Reynolds number, $R_m = \mu\sigma L u_0$, where u_0 is the mean velocity and L the characteristic length. A relatively small R_m generates only small perturbations on the applied field; if R_m is relatively large then a small current creates a large induced magnetic field. For small magnetic Reynolds numbers (R_m<<1), the magnetic field will be dominated by diffusion and perturbative methods can be used accurately. Similarly, the equation for temperature is

$$\rho c_p\left[\frac{\partial}{\partial t}T + (\boldsymbol{u} \cdot \nabla)T\right] = \nabla \cdot (\lambda\nabla\boldsymbol{T}) + \frac{1}{\sigma}\boldsymbol{J}^2 + \Phi + Q\ , \tag{6}$$

which is a convection-diffusion equation with l*:* thermal conductivity, *Q:* other sources of volumetric energy release such as radiation or chemical reactions and thermal diffusivity $k= \lambda/\rho c_p$, c_p*:* constant pressure specific heat of the flow*;* while the kinetic energy evolution is given by,

$$\frac{\partial}{\partial t}\left(\frac{1}{2}\rho u^2\right) = -\nabla\cdot\left[\boldsymbol{u}\left(p+\frac{1}{2}\rho u^2\right) - \boldsymbol{u}\cdot\boldsymbol{S}\right] + \boldsymbol{u}\cdot\left(\boldsymbol{J}\times\boldsymbol{B}\right) + \boldsymbol{u}\cdot\boldsymbol{f} - \Phi, \tag{7}$$

where **S** is the viscous stress tensor. We deduce from the latter that due to the action of the Lorentz forces an increase of the kinetic energy leads to a decrease in the magnetic energy. From the temperature equation, eq. (6), one can identify the temporal increase of enthalpy, $\rho c_p \frac{\partial T}{\partial t}$, which equals to the loss of magnetic energy due to joule dissipation, $\frac{1}{\sigma}J^2$, plus the loss of kinetic energy, F, due to viscous dissipation.

From the mathematical point of view, the coupling between Maxwell equations and Navier-Stokes equations induces an additional nonlinearity with respect to the ones already present, leading to unsolved questions of existence and uniqueness (mainly related to the hyperbolic nature of Maxwell equations). As explained by Gerbeau et al., simplified models can be analyzed but care should be taken with certain approximations:

A system coupling the time dependent incompressible Navier-Stokes equations with a simplified form of the Maxwell equations (low frequency approximation) is well-posed when the electromagnetic equation is taken to be time-dependent, i.e. parabolic form. In contrast, the same model is likely to be ill-posed when the electromagnetic equation is taken to be time-independent, i.e. elliptic form, while the hydrodynamic equations are still in a time dependent form.

The coupling of Maxwell equations with Navier-Stokes equations certainly represents a challenge. [1, 2]

COMPUTATIONAL TOOLS FOR THE STUDY AND ANALYSIS OF LIQUID METAL MHD PHENOMENA

We can investigate the effect of the time-varying electromagnetic field on an incompressible turbulent flow via direct numerical simulation and by using multi-physics analysis tools. We can upgrade CFD solvers for direct numerical simulation which solves the incompressible Navier-Stokes equations, on a staggered grid with second-order finite differencing in space and Adams–Bashforth stepping in time, to be able to compute a conducting fluid coupled with a magnetic field in arbitrary orthogonal coordinates setting foundation to develop a low dimensional model of the flow for implementation of a closed-loop flow control system.

On a staggered grid the scalar variables (pressure, density, total enthalpy etc.) are stored at the cell centers of the control volumes, whereas the velocity or momentum variables are located at the cell faces. Using a staggered grid is a simple way to avoid odd-even decoupling between the pressure and velocity. Odd-even decoupling is a discretization error that can occur on collocated grids leading to checkerboard patterns in the solutions. The Adams-Bashforth is a multi-step scheme that allows relatively easy local time-stepping on the smallest cells of the mesh.

The development of computational tools that model the flow and the magnetohydrodynamic response of flowing liquid metals is of the highest importance. The latter will help in the development of a low dimensional model of the flow which is essential for the analysis and the development of techniques for active control of liquid metal flow and stabilization in the presence of time and space varying magnetic fields.

ANNULAR LINEAR INDUCTION PUMPS

A special type of liquid metal thermo-magnetic device is the annular linear induction pump. It is known that electromagnetic pumps have a number of advantages over mechanical pumps: absence of moving parts, low noise and vibration level, simplicity of flow rate regulation, easy maintenance and so on. However, while developing a large-scale induction pump, in particular annular linear induction pumps (ALIPs), we are faced with a significant problem of magnetohydrodynamic instability arising in the device. The manifestation of the instability does not allow linear induction pump development in a certain range of flow rate or the development of high efficiencies under certain flow rates and dropping pressure conditions [2, 8, 9].

Linear induction pumps use a traveling magnetic field wave created by 3-phase currents, and the induced currents and their associated magnetic fields that generate a Lorentz force. The complex flow behavior in this type of devices includes a time-varying Lorentz force and pressure pulsation due to the time-varying electromagnetic fields and the induced convective currents that originates from the liquid metal flow, leading to instability problems along the device geometry. The determination of the geometry and of the electrical configuration of a thermo-magnetic device gives rise to an inverse magnetohydrodynamic field problem. When the requirements of the design are defined, this problem can be solved by an optimization technique. The objective function which has to be maximized in the optimization problem is derived from the main design requirement. Usually for a magnetohydrodynamic device, this is the efficiency. Other design requirements can be taken into account as constraints. For a non-linear system, such as for linear induction pumps, the main objective functions are low weight and high efficiency and so more than one maximum can exist. In this case a technique for the global optimization has to be used.

Before any optimization method can be used, design approaches should be identified and understood while mathematical and computational models developed. This leads to the study of magnetohydrodynamics instabilities, usually with negative effects on the efficiency and working fluid behavior, as well as to the study of its individual components, its fabrication methods, assembly and system integration procedures. The design process and technology evaluation of thermo-magnetic systems, with emphasis in annular linear induction pumps, can be divided in four stages. The first stage is a basic study of the main electrical, mechanical and thermal parameters. The second stage is the development of a fully integrated model using theoretical, experimental and computational tools for the design and characterization of an ALIP system and its components. The third stage is the development of programming methods and procedures for the design and construction of optimized annular linear induction pumps. At the end of the third stage a test, or proof of concept, device can be built for benchmarking and performance evaluation. The fourth stage involves further study of the magnetohydrodynamic instabilities and the development of control systems for active flow control and machine protection.

CONTROL SYSTEM DESIGN FOR ACTIVE FLOW CONTROL

Closed-loop active flow control is the capability to estimate, efficiently alter and maintain a flow rate. Closed-loop flow control is by its nature a multidisciplinary problem involving experimental and computational fluid dynamics, low dimensional modeling, control law design, and sensors and actuators development. A key to successful implementation of closed-loop flow control is the development of a simple flow model that can capture the essential dynamics of the flow. It is well known that fluid flow is governed by the Navier-Stokes equations, a set of highly non-linear partial differential equations. However, due to the infinite dimensionality, these equations are not very useful for feedback control purposes. To add more complications, a MHD flow is governed not only by the Navier-Stokes equations but also by the Maxwell equations of electromagnetism coupled to the former.

Therefore, a low dimensional model of the flow is essential for successfully implementing the closed-loop flow control. The best-known technique for deriving low dimensional models in the fluid dynamics community is Proper Orthogonal Decomposition. The method provides a spatial basis (a set of eigenfunctions) for a modal decomposition of an ensemble of data, which are obtained from experiments or from computational simulations. These eigenfunctions, or modes, are extracted from the velocity fluctuations cross correlation tensors, and can be used as basic functions to represent the flow.

It is Imperative to develop a control system for the active control of liquid metal flow and its stabilization in the presence of time and space varying magnetic fields as well as in the presence of other secondary instabilities.

CONCLUSIONS

The complexity of the MHD equations had made impossible to develop a design and optimization methodology using first-principles as well as to perform a true multi-physics analysis where the couple phenomena is studied as a whole. The approached used until today is to separate the electrodynamics from the thermos-fluid phenomena or to approximate the system behavior by using the electric-circuit-approach for electric machines which cannot give a realistic inside to the physics phenomena that takes place and can neither leads to a reliable design methodology nor to the determination of reliable operational working points by itself. The increased in computational power, at software and hardware level, as well as the theoretical, computational, and experimental effort performed during the

last years by this author and a group of people in the United States, France, Japan and South Korea has led to advances in the understanding of the phenomenology and technical challenges that the engineering of MHD devices represent. We are for first time in conditions of performing this type of work designing and optimizing liquid metal thermo-magnetic systems using first principles and multi-physics analysis.

The variety and importance of the topic leads to the need of i) developing computational tools for the study and analysis of the liquid metal MHD phenomena, ii) To a better understanding of the physics and engineering of liquid metal thermo-magnetic systems for better modeling, iii) To develop tools, procedures and CAE software for more accurate simulation of the device, iv) To develop procedures and tools for design optimization, and v) to develop control systems for active flow control.

ACKNOWLEDGMENTS

I want to thank to Dr. Hee Reyoung Kim, currently at the Ulsan National Institute of Science and Technology (UNIST), for his collaboration in the research of liquid metal thermos-magnetic systems.

REFERENCES

[1] Maidana, C.O., “Thermo-magnetic Systems for Space Nuclear Reactors: An Introduction”, Springer Briefs in Applied Science and Technology, ISBN-13 978-3319090290. (2014)
[2] Maidana, C.O. et al., “Design of an Annular Linear Induction Pump for Nuclear Space Applications”, Proceedings of Nuclear and Emerging Technologies for Space Exploration 2011 (NETS2011), Albuquerque, NM, February 7-10 (2011).
[3] Maidana, C. O., Latina, A., Jonker, M., "Failure Studies at the Compact Linear Collider: Main Linac and Beam Delivery System", International Particle Accelerator Conference 2012 – USA. (2012)
[4] Maidana, C.O., Makino, K., Berz, M., “Muon Ring Cooler Simulations using COSY Infinity”, Institute of Physics Conference Series N 175. (2004)
[5] Werner, J. et al., “An Overview of Facilities and Capabilities to Support the Development of Nuclear Thermal Propulsion”, Proceedings of Nuclear and Emerging Technologies for Space Exploration 2011 (NETS2011), Albuquerque, NM, February 7-10 (2011).
[6] Maidana, C.O., “Nuclear Technologies for Space Exploration: an overview on nuclear thermal propulsion, radioisotope power generators and fission surface power”, Mars Transactions N5 – Journal of the Italian Mars Society, ISSN: 2037-6928. (2014)
[7] Giordani, A., “Seven innovative ways to cool a scientific computer”, International Science Grid this Week, e-Science Talk, 2/2012. Contributed Article / Scientific Consultant: Carlos O. Maidana. Selected as one of the most popular articles by Google Analytics. (2012)
[8] Kim, H. R., “Design and Experimental Characterization of an EM Pump”, Journal of the Korean Physical Society, Vol. 35, No. 4, pp. 309-314. (1999)
[9] Schwirian, R. E., “Analysis of linear-induction or traveling wave electromagnetic pump of annular design”, NASA TN D-2816 , NASA Lewis Research Center, Cleveland, Ohio, United States. (1965)

High Temperature Water-Titanium Heat Pipes for Spacecraft Fission Power

William G. Anderson[1], Rebecca Hay[1]

[1]*Advanced Cooling Technologies, 1046 New Holland Ave. Lancaster, PA 17601*
717-295-6104; Bill.Anderson@1-act.com

Abstract. NASA is examining small fission reactors for future space transportation and surface power applications. The Kilopower system will use a nuclear reactor to supply energy to Stirling convertors to produce electricity. Titanium/water heat pipes will be used to carry the waste heat from the Stirling to a radiator, where the heat is rejected. Most current water heat pipe designs are for surface fission power, and use gravity aided heat pipes (thermosyphons). The Kilopower system will be designed to operate in space, which will require a different heat pipe design than the thermosyphons used in surface applications. The heat pipe design needs to support the Kilopower system through four different operating conditions: operation in space, with zero gravity; operation on earth, with a slight adverse orientation, to estimate performance in space; ground testing, with the heat pipes operating gravity aided; and launch, with the evaporator elevated above the condenser. During the last two conditions, vertical ground testing and launch, the heat pipe wick will deprime and will need to re-prime for operation in space operation after launch. Two heat pipe wick designs were identified as readily repriming after depriming: grooved wick heat pipes and self-venting arterial heat pipes. In the grooved wick design a screen or sintered wick is required in the evaporator during start-up. This hybrid-wick design is necessary to supply liquid to the evaporator during vertical operation. Two heat pipes were designed, fabricated and tested: a self-venting arterial wick and a hybrid groove-screen wick design. This paper presents the design of the two heat pipes and test results which were used to evaluate which heat pipe wick design is better suited for the Kilopower system.

Keywords: Kilopower, heat pipe, hybrid wick, self-venting arterial wick

INTRODUCTION

NASA is currently examining small fission power reactors, such as the Kilopower, which aims to provide roughly 1 kW of electric power. Kilopower plans to use alkali metal heat pipes to supply power from the reactor to a series of Stirling convertors, and titanium/water heat pipes to remove the waste heat from the cold end of the convertors. Previous water heat pipe designs for space fission power are not suitable for Kilopower, because they were designed as gravity aided heat pipes (thermosyphons) for surface fission power and are not suitable for space. Grooved heat pipe designs that will work in space have also been developed but the grooved wick is unable to prime the evaporator in a vertical orientation, which is necessary for ground testing of Kilopower. Advanced Cooling Technologies, Inc. (ACT) developed heat pipes with two different designs that are suitable for Kilopower: a hybrid grooved/screen wick and a self-venting arterial wick. The heat pipe design needs to support the Kilopower system through four different operating conditions: operation in space, with zero gravity; operation on earth, with a slight adverse orientation, to estimate performance in space; ground testing, with the heat pipes operating gravity aided; and launch, with the evaporator elevated above the condenser.

Kilopower Background

NASA is examining small fission reactors for future space transportation and surface power applications (Mason and Carmichael, 2011). The Fission Surface Power System is designed to operate from 10 to 100 kWe while current Radioisotope Power Systems operate below 1kWe. The Kilopower system would address the power gap between current RPS and FPS. A nominal Kilopower design is shown in Figure 1 [1]. The nuclear reactor supplies energy to

Brayton (or Stirling) convertors to produce electricity. Titanium/water heat pipes carry the waste heat to a radiator, where the heat is rejected. Previous spacecraft heat pipe designs have neglected ground testability, and assumed a grooved wick. The Kilopower heat pipes must accommodate four different operating conditions: Operation in space, with zero gravity. Liquid is returned from the condenser to the evaporator by capillary forces in the wick; Operation on earth, with a slight adverse orientation, to estimate performance in space. The heat pipe is operated with the evaporator slightly oriented above the condenser. The adverse orientations are typically 0.25 and 0.5 cm; Ground testing, with the heat pipes gravity aided. The heat pipes will deprime in this orientation. Liquid is returned to the evaporator by gravity; see Figure 2b; Launch, with the evaporator elevated above the condenser. The heat pipes will deprime in this condition; see Figure 2a.

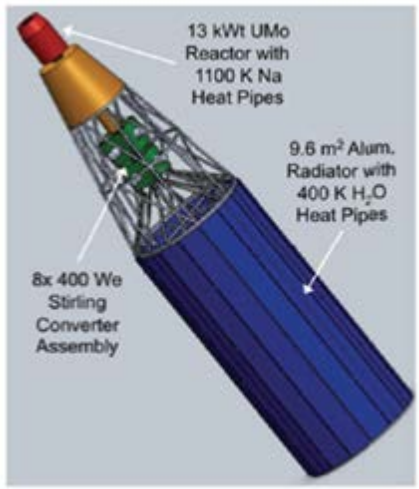

FIGURE 1. Kilopower System.

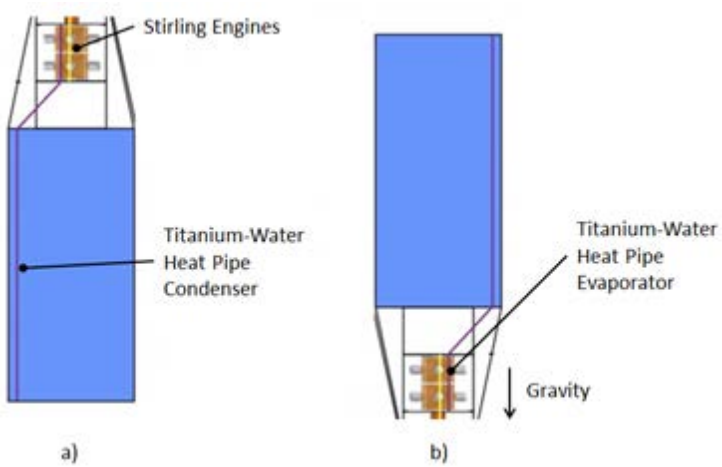

FIGURE 2. Two operating conditions for the Kilopower radiator: a) The pipe is oriented opposite gravity, during launch, causing the wick to deprime, b) the pipe operates gravity aided during testing [2].

The orientation of the heat pipes during ground testing is shown in Figure 2b. The reactor (not shown) is located below the Stirling convertors. The pipes are orientated with the evaporator (by the Stirling engines) below the condenser (radiator). Water vapor travels from the evaporator to the condenser, releasing heat. The liquid condensate returns to the evaporator by gravity. During these tests, the grooves and self-venting arteries will deprime, as discussed below. A wick in the evaporator is required during start-up, to supply liquid to the evaporator before liquid drips back down from the condenser.

When the Kilopower system is prepared for launch, the system will be oriented such that the evaporator will be above the condenser (Figure 2a), causing the pipe to deprime. Once in space the pipe will need to reprime and begin working. The hybrid-wick heat pipe is known to reprime spontaneously.

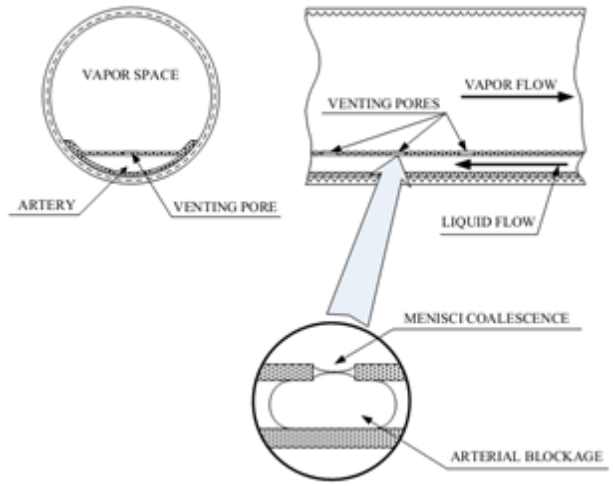

FIGURE 3. Russian developed self-venting arterial heat pipe with a screen wick.

Heat Pipe Wicks

The length of the Kilopower titanium/water heat pipes can be up to several meters. There are four types of wicks that carry significant power over these long distances in space: Arterial heat pipes with sintered powder or screen wicks; Grooved heat pipe wicks; Hybrid Grooved Screen wicks; Russian self-venting arterial heat pipes. Arterial and grooved pipes are not suitable for this application. The arterial pipes will de-prime during testing and during launch and it is not possible to reliably re-prime arterial pipes. Grooved heat pipe designs that will work in space have also been developed but the grooved wick is unable to prime the evaporator in a vertical orientation, which is necessary for ground testing of Kilopower. The two wicks that can be used for the Kilopower system are the hybrid grooved/screen wick, and the self-venting arterial heat pipe.

Grooved wicks are the standard wick used in for spacecraft Constant Conductance Heat Pipes (CCHPs) and Variable Conductance Heat Pipes (VCHPs). The benefit of the grooved wick is that it cannot be deprimed by vapor bubbles, since the bubbles can vent into the vapor space. These extruded grooves also have a very high permeability, allowing very long heat pipes for operation in zero-g, typically several meters long. Their only flaw is that they are unsuitable for the evaporator when the heat pipe is tested vertically on the ground. Instead, a hybrid wick is used, with grooved adiabatic and condenser sections, and a screen evaporator wick. The screened evaporator section is necessary for startup after the pipe has been deprimed or frozen.

The second wick design ACT investigated was a self-venting arterial heat pipe developed by Goncharov et al. at Lavochkin in Russia [3]; see Figure 3. Arterial heat pipes are a variation of a heat pipe that utilizes a single artery as well as a screen or sintered wick for liquid return. During operation, liquid condensing in the condenser flows circumferentially in the condenser to the artery. The liquid then flows through the artery to the evaporator, where the sintered (or screen) wick distributes the liquid. The combination of a single artery with a screen wick gives the heat pipe the benefit of a wick with high wick permeability as well as a small pore size and thus a high capillary limit. When the artery is primed (full of liquid), arterial heat pipes can transfer high heat loads over long distances. On the other hand, the heat pipe fails if the artery is de-primed by non-condensable gas generation or vapor generation in the artery. These standard arterial heat pipes are not suitable, since the arteries will definitely deprime during launch. To eliminate the de-priming problems seen in standard arterial heat pipes, self-venting arterial heat pipes use small venting pores that are located in the evaporator section of the heat pipe. If vapor or non-condensable gas (NCG) is introduced into the single artery the typical de-priming that would be experienced in a standard arterial heat pipe can be avoided due to the venting pores. The vapor blockage will travel through the artery and into the evaporator where the venting pores are located. The design eliminates the single point failure nature of previous arterial heat pipes.

HEAT PIPE DESIGN

Two heat pipe configurations were designed: a self-venting arterial wick, with a screen artery and vent holes and a hybrid wick design, with a screened evaporator and grooved condenser. Both heat pipes also incorporated a reservoir on the evaporator which stored any excess fluid charge during vertical operation to minimize the effects of overcharging on test results.

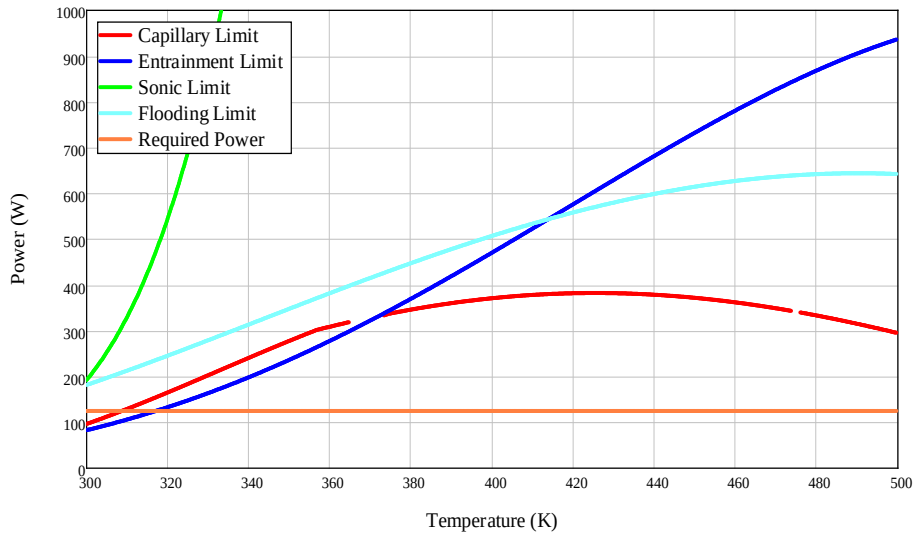

FIGURE 4. Performance Predictions for a 0.5 in OD, 40 in Hybrid Wick Heat Pipe

Hybrid Screen – Grooved Wick Design

The hybrid heat pipe design used 1.27 cm outside diameter titanium tube with 0.089 cm walls. Capillary, entrainment, sonic and flooding limits were calculated for the 1.27cm OD hybrid wick heat pipe design. The heat pipe needed to function 0.508 cm against gravity for ground testing, which was accounted for in the performance calculations. The performance predictions for the 1.27 cm OD, 0.99 m long hybrid wick heat pipe can be seen in FIGURE 4. The designed heat pipe can carry a maximum power of 375W at the target temperature of 400K.

The hybrid heat pipe was made from four 25.4 cm grooved sections and one 12.7 cm screened section. The tube section has four wraps of 150 mesh titanium screen. The four groove sections were machined from solid titanium rod using electric discharge machining (EDM).

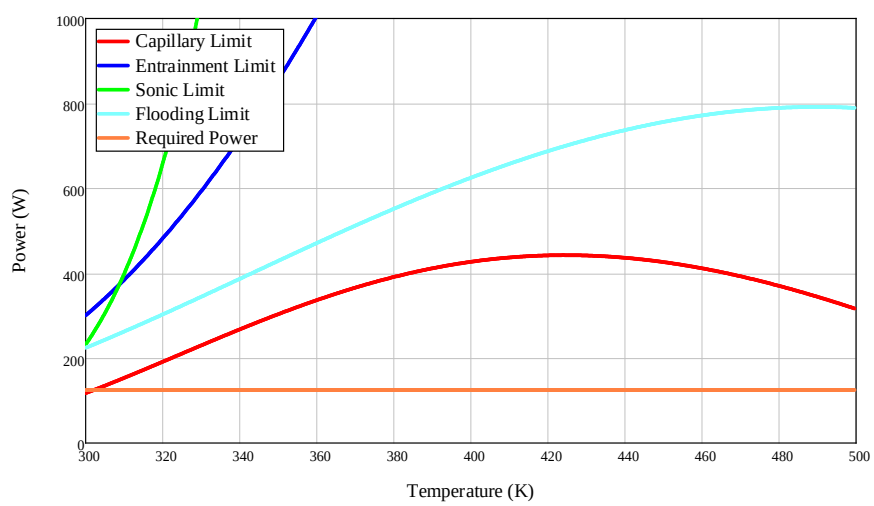

FIGURE 5. Performance Predictions for a 0.5 in. OD, 39 in. Long Self-Venting Arterial Wick Heat Pipe

Self-Venting Arterial Wick Design

The design for the self-venting arterial pipe used a 1.27 cm outside diameter titanium tube with 0.089 cm walls, the same design as the hybrid wick heat pipe. The capillary, entrainment, sonic and flooding limits were also calculated for the 1.27cm OD self-venting arterial heat pipe design. The self-venting arterial heat pipe will need to function at 0.508 cm against gravity for ground testing, which was accounted for in the performance calculations. The performance predictions for the 1.27cm OD, 1.02 m long self-venting arterial heat pipe can be seen in FIGURE 5. The designed heat pipe can carry a maximum power of 390 W at the target temperature of 400K.

The artery has one screen wrap on along the edge bounded by the pipe and two screen wraps on all other edges. The screen along the perimeter of the pipe outside of the artery has a total of three screen wraps. The pipe was fabricated from a single 40 in (0.99 m) tube with 0.035 in (0.089 cm) walls. Included in the design is a small reservoir below the evaporator. The reservoir is used to hold the working fluid during vertical operation and freezing.

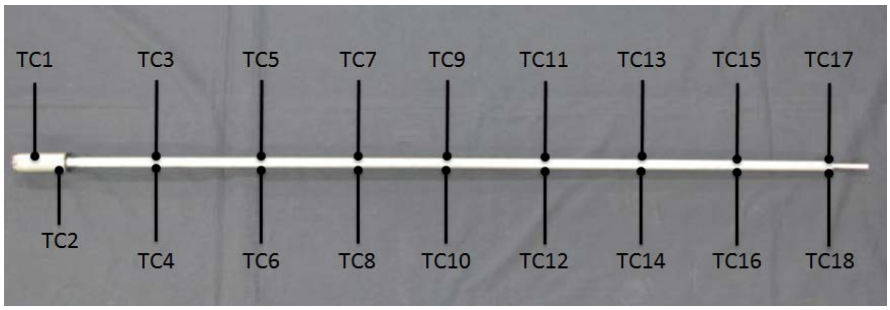

FIGURE 6. Thermocouple Map for the Self-Venting Arterial Heat Pipe

TEST RESULTS

The test set up was designed so that all tests could be performed with little or no modifications during testing. The heat pipe was mounted to a tilt table which allowed for testing at any angle. Power was applied to the evaporator using an aluminum heater block with four cartridge heaters. The heat pipe condenser was cooled using compressed air forced through a tube around the pipe. Both assembled heat pipes were instrumented according to the thermocouple map shown in FIGURE 6. Two thermocouples measured the reservoir temperature. The temperature along the heat pipe was measured every 5 in., with two thermocouples at each location for redundancy. An additional thermocouple is located on the outside of the heater block, which is labeled evaporator in the results.

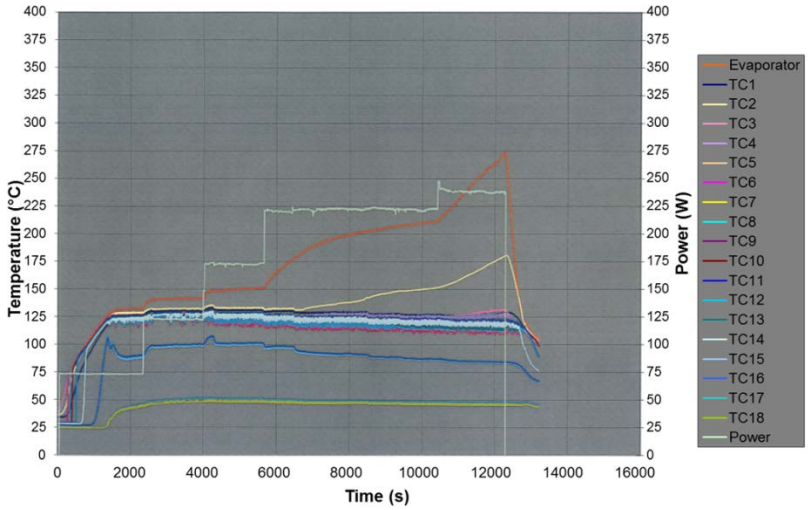

FIGURE 7. Test Results for the Self Venting Arterial Heat Pipe at 0.5 cm Adverse

Self-Venting Arterial Pipe Power Test Results

To evaluate the operation of the heat pipe in space, the self-venting arterial heat pipe was tested at 0.25 cm and 0.5 cm against gravity, with the results from the 0.5 cm test presented here in FIGURE 7. The self-venting heat pipe dried out at 225 W, which was about half of the predicted 425 W from the model but 100 W more than the required power. The heater block temperature was also offset from the pipe temperature for most of the testing. This can be attributed to thermal resistance between the heater block and the heat pipe evaporator, which increased with temperature due to the CTE mismatch between the aluminum block and titanium heat pipe.

Hybrid Screen-Groove Heat Pipe Power Test Results

The hybrid heat pipe was also tested at 0.25 and 0.5 cm against gravity to evaluate space performance. The results for the 0.2 in. adverse test of the hybrid heat pipe are shown in FIGURE 8. At 0.2 in adverse the hybrid heat pipe started up and reached steady state at each power increment until150 W, when the heater block temperature became unsteady. The heat pipe temperatures also started to fluctuate more than had been seen in previous tests, with the fluctuations matching those seen in the heater block temperature. At this point the vapor temperature control was reduced from 125°C to 90°C, which produced stable results. This is shown at the beginning of the data set in FIGURE 8. After the temperatures reached steady state, the temperature was increased while maintaining a constant power until the vapor temperature was again at 125°C. At this point the temperatures continued to be unstable for about 4000 seconds before reaching steady state, which continued until dry out at 475 W. ACT suspects this behavior is due to the pipe being undercharged, which in this case seems to be caused by fluid being trapped in the reservoir. The hybrid heat pipe carried 475 W of power, which was higher than both the predicted 375 W and the required 125 W.

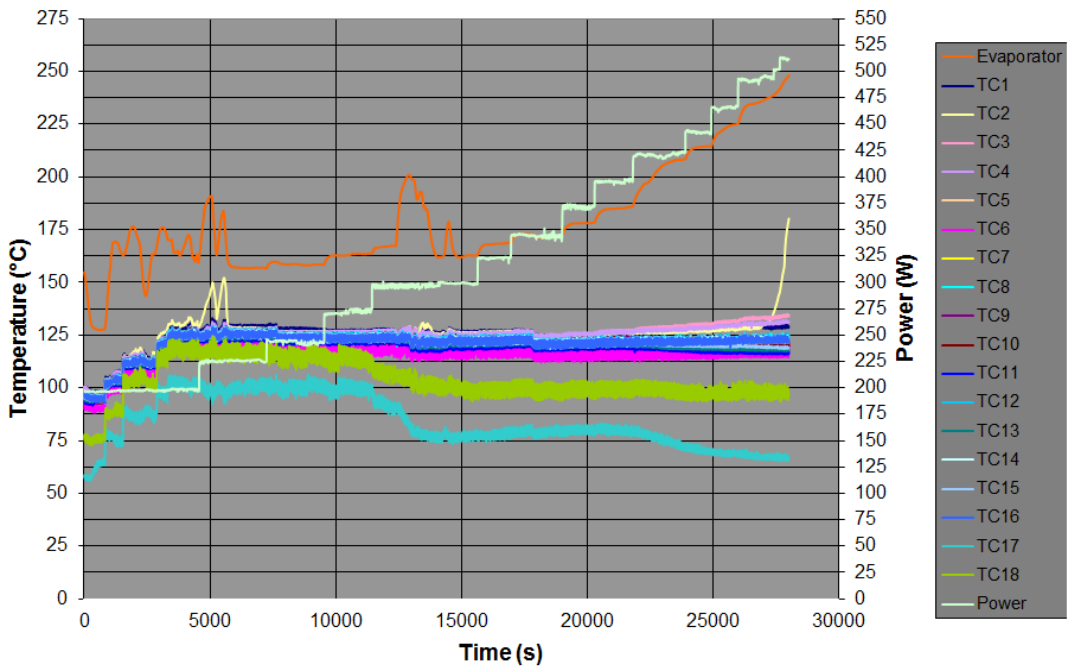

FIGURE 8. Hybrid Groove-Screen Heat Pipe 0.5 cm Adverse Test Results

Vertical Orientation and Re-priming Tests

Both heat pipe designs must operate as thermosyphons and re-prime. To test re-priming of the self-venting artery the pipe was first tested vertical and allowed to de-prime. The heat pipe was then be turned horizontal and tested to demonstrate re-priming. The hybrid heat pipe was also tested as a thermosyphon to validate the reservoir and evaporator design. The screened evaporator was necessary to ensure there was a fluid supply during start up in the evaporator and the reservoir held the excess fluid inventory to prevent pool boiling.

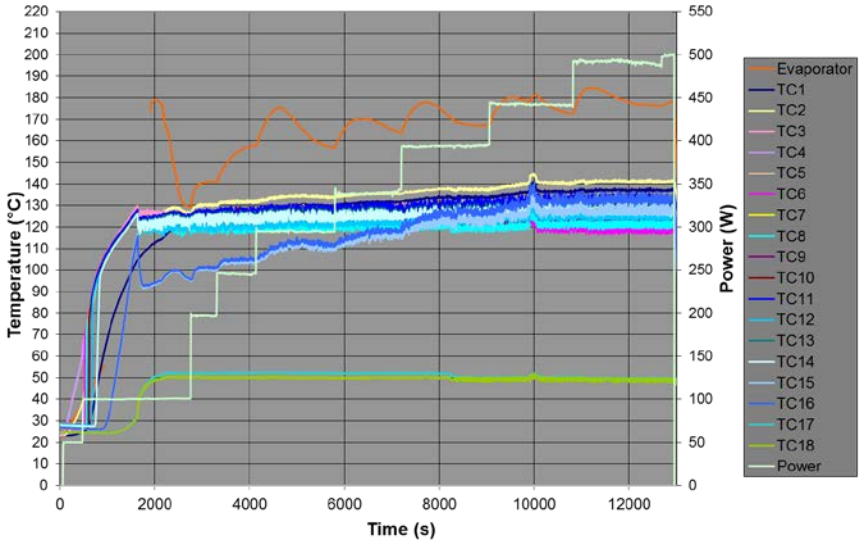

FIGURE 9. Self-Venting Arterial Heat Pipe Thermosyphon Mode Test Results

Self-Venting Arterial Heat Pipe Vertical Orientation and Re-priming Tests

The self-venting heat pipe will need to operate as a thermosyphon for ground testing. FIGURE 9 shows the test results from the vertical orientation test. The heat pipe showed no pool boiling or dry-out in the evaporator, indicating that the reservoir and evaporator were operating as expected. The power test went up to 500 W, which was the limit for cooling with the current air cooled test set up. Throughout the test the temperature of the evaporator block spiked with increases in power, due to the thermal resistance between the heater block and the heat pipe.

After the self-venting arterial heat pipe thermosyphon mode test, the heat pipe was left in a vertical orientation overnight. For the re-priming test the heat pipe was turned to 0.5 cm against gravity and power was immediately applied. The results of this re-prime test are shown in FIGURE 10. The heat pipe had no noticeable problems with startup and the performance matched the power test conducted before de-priming. The re-primed heat pipe dried out at 225 W, which was the same performance seen before de-priming.

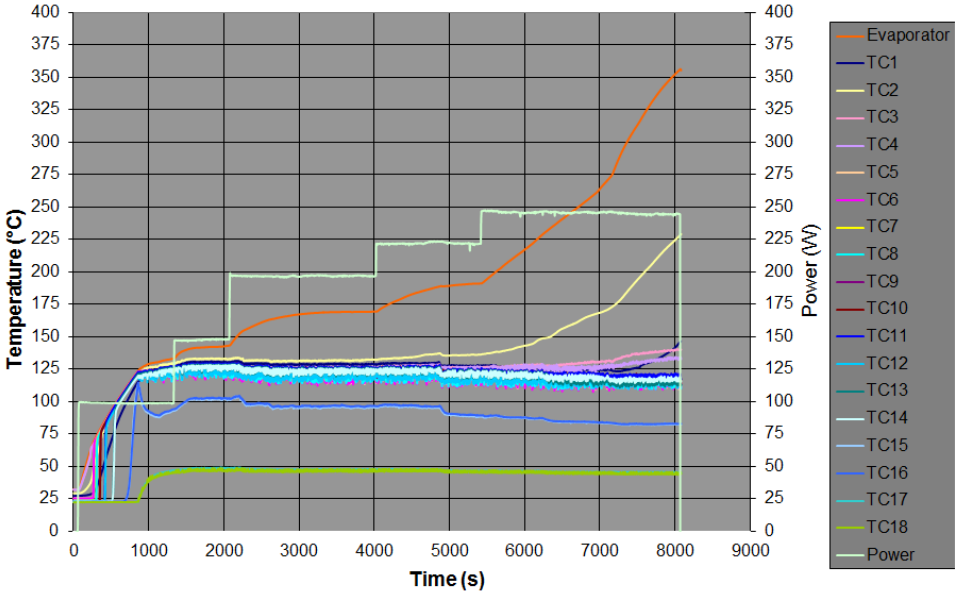

FIGURE 10. Self-Venting Heat Pipe Re-prime Test at 0.5 cm Adverse

Hybrid Screen-Groove Thermosyphon Test

The hybrid screen-groove heat pipe was tested as a thermosyphon to evaluate the screened evaporator during start up and normal operation. The results from the hybrid heat pipe thermosyphon test are shown in FIGURE 11. As in all the other tests, the heater block temperature is higher than the heat pipe temperature, due to the thermal resistance between the two. While operating as a thermosyphon the hybrid heat pipe showed no evidence of start-up issues or pool boiling during operation. The heat pipe was able to carry 500 W, at which point the cooling was becoming inadequate so the test was stopped.

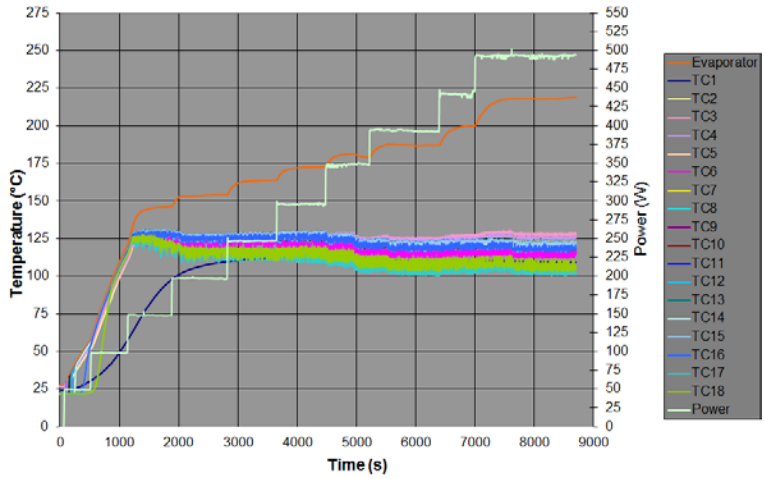

FIGURE 11. Hybrid Heat Pipe Thermosyphon Test Results

Freeze – Thaw Testing

ACT conducted freeze-thaw testing on both heat pipe designs. This testing was used to evaluate the response of the two wick designs to a freeze-thaw cycle. The freeze-thaw testing included short term freezing vertically with thawing at a slight adverse elevation, to demonstrate that the heat pipe can restart in space.

Hybrid Groove-Screen Heat Pipe Freeze-Thaw Test

The hybrid heat pipe was subjected to one freeze-thaw cycle. The heat pipe was placed in a freezer overnight in a vertical orientation so the fluid would freeze in the evaporator and reservoir. The heat pipe was then placed in the test stand at 0.25 cm adverse and heat was applied. The power was ramped up just like the previous power tests and stopped at the nominal power of 125 W. During start up the heat pipe showed no problems with the liquid supply to the evaporator and showed the expected behavior as the pipe came up to the nominal temperature of 125°C.

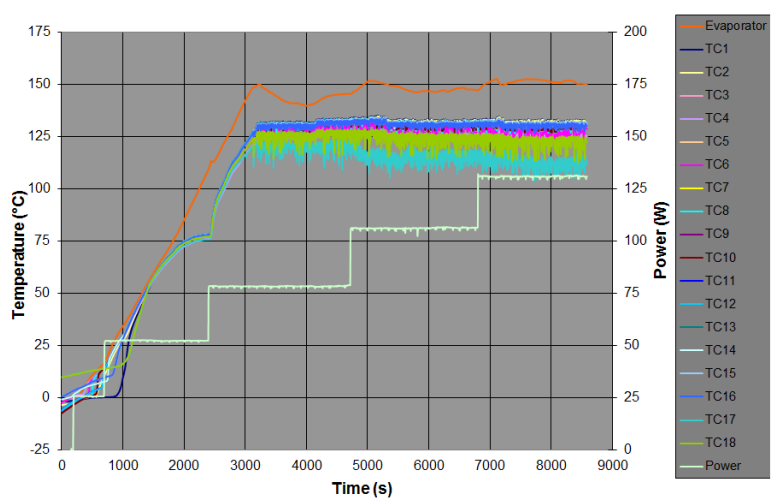

FIGURE 12. Hybrid Grooved-Screen Heat Pipe Freeze-Thaw Test Results

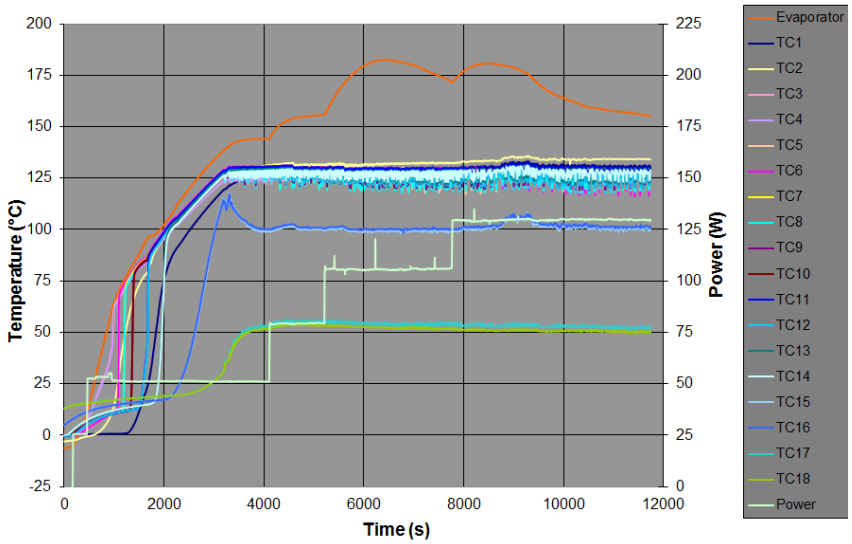

FIGURE 13. Self-Venting Arterial Heat Pipe Freeze-Thaw Test Results

Self-Venting Arterial Heat Pipe Freeze-Thaw Test

The self-venting arterial heat pipe was also subjected to a freeze-thaw cycle. Like the hybrid heat pipe, the self-venting arterial heat pipe was placed in a freezer overnight in a vertical orientation so the fluid would freeze in the evaporator and reservoir. The heat pipe was then placed in the test stand at 0.25 cm adverse and heat was applied. The power was ramped up just like the previous power tests and stopped at the nominal power of 125 W. During start up the heat pipe showed no problems with the liquid supply to the evaporator and showed the expected behavior as the pipe came up to the nominal temperature of 125°C. Each thermocouple was initially at 0°C and as the pipe thawed the temperature increased rapidly in order from the evaporator to the end of the condenser. Once the pipe was completely thawed and operating at 125°C it showed the same behavior seen during the initial power tests.

Conclusion

The two heat pipe designs were successfully tested in all modes of operation: against gravity tests, vertical and re-priming tests and freeze-thaw testing. While the self-venting arterial heat pipe successfully carried more than the required 125 W at both adverse elevations, the heat pipe only carried about half of the predicted power. This indicates there was either a problem with the manufacturing of the heat pipe or with the original model. ACT is still evaluating possible causes. The hybrid heat pipe successfully carried the required 125 W at both adverse elevations and carried more power than the model predicted. During the test at 2.5 mm adverse elevation the heat pipe operated very smoothly, quickly reaching steady state and displaying a clear dry out at about 490 W. At 5 mm adverse, the heat pipe did eventually operate smoothly after displaying unsteady temperatures, especially in the heater block temperature. Based on the performance difference between the 2.5 mm and 5 mm adverse cases, ACT believes that at 5 mm the pipe may be undercharged due to fluid becoming trapped in the corners of the reservoir. The vertical and re-priming tests showed that both wick designs are suitable for Kilopower, successfully operating as a thermosyphon for ground testing and in the self-venting case, able to re-prime with no change in performance. Both pipes also underwent a freeze-thaw cycle with no change in performance. Further research and testing is needed for both heat pipe designs to address the issues seen during the adverse testing.

References

[1] Mason, G. Gibson, and D. Poston, “Kilowatt-class Fission Power Systems for Science and Human Precursor Missions,” Nuclear and Emerging Technologies for Space (NETS-2013), Albuquerque, NM, February 25-28, 2013.

[2] L. Mason, C. Carmichael, “A Small Fission Power System with Stirling Power Conversion for NASA Science Missions,” Nuclear and Emerging Technologies for Space (NETS-2011), Albuquerque, NM, February 7-10, 2011.

[3] T. Kaya and K. Goncharov, “Analysis of a Gas-Tolerant High-Capacity Single-Artery Heat Pipe,” 15th International Heat Pipe Conference (15th IHPC), Clemson, SC, April 25-30, 2010.

Pyroshock Induced Loads Driving Electrical, Thermal, and Structural Impacts in Multi-Mission Radioisotope Thermoelectric Generators (MMRTGs)

Armen Derkevorkian, Ali R. Kolaini*, Nicholas R. Keyawa, David J. Neff, Bill J. Nesmith, and Terry J. Hendricks

Jet Propulsion Laboratory, California Institute of Technology, Pasadena, CA 91109
**Corresponding Author: Phone: +1-818-393-6006, E-mail: Ali.R.Kolaini@jpl.nasa.gov*

Abstract. Severe pyroshock environments due to several shock separation devices in the close proximity of the Multi-Mission Radioisotope Thermoelectric Generator (MMRTG) were derived for the Mars Science Laboratory (MSL) project. During the MMRTG pryoshock qualification and engineering units tests, the power output from each system temporarily decreased, but fully recovered after the shock signature subsided. An effort is underway to understand the root causes of the RTG temporary power losses, and a detailed system fault tree and associated system analyses have been developed to establish specific root-cause and recovery pathways. As part of this effort, the shock-induced loads and accompanying electrical/thermal/structural impacts within the system are currently being modeled. In this paper, the MMRTG shock qualification test results are reviewed and the preliminary shock prediction results are provided. The analysis includes predicting the dynamic, structural, and thermal responses of the MMRTG's critical internal interfaces to experimentally generated input transient shock loads. The shock analysis approach consists of two parts: First, transient normal-mode finite-element analysis is performed to predict the acceleration and the displacement responses at various RTG interfaces. Second, shock wave propagation is predicted through the interfaces, by taking advantage of the empirically defined shock impedances at the RTG internal interfaces. The potential applicability of the high-fidelity advanced-simulation codes to model the high frequency shock waves propagating through complex RTG internal interfaces is discussed. The impact of transient normal-modes and shock wave propagation on electrical circuit networks and electrical contact interfaces, thermal networks and interfaces, and structural components and interfaces within the MMRTG is being evaluated and quantified through electrical and thermal modeling, all of which is being correlated and tied to system fault tree pathways to identify and prioritize likely causes and recovery mechanisms. This study suggests that the combination of the proposed computational and empirical techniques may provide computationally-robust wave propagation prediction schemes within the MMRTG, coupled to MMRTG electrical and thermal predictive models, to track and predict pyroshock effects and impact magnitudes. The preliminary results from this study are used to understand the root causes of the pyroshock anomaly observed during MMRTG shock qualification testing. These results will be used to recommend corrective or mitigating MMRTG design techniques.

Keywords: Pyroshock environments, shock waves, shock predictions, transient analysis, pyroshock electrical analysis, pyroshock thermal analysis.

INTRODUCTION

The MMRTG pyroshock qualification tests were performed to qualify this hardware for the Mars Science Laboratory (MSL) mission. The MMRTG was built by DoE under a NASA managed contract. A series of pyroshock tests was performed as part of the multi-mission qualification testing using an Engineering Unit (EU) for this program. The first pyroshock simulation test was performed in 2006 and the results from this activity is documented in comprehensive reports [1, 2]. The EU was mounted on a ½" thick large steel plate and the required shock was simulated using primacord detonated on the bottom surface of the plate. Several steps were taken to calibrate the required shock environments using a mass mockup. However, the peak shock level with the EU

mounted on the plate exceeded the nominal requirement of 6,000 peak g's above 1,600 Hz and reached close to 20,000 g's at ~3,500 Hz [2]. This provided an over-test relative to the multi-mission shock requirement. During the EU shock test a severe power loss had occurred. The power loss was recovered after several minutes from completion of the test. The concern about the loss of EU power led to performing an additional Qualification Unit (QU) test. The QU test was performed at JPL by mounting it on the flight MSL rover chassis [3], where flight-like separation nuts were fired. The test was intended to gain more understanding about the power drop issue that the generator would experience during the MSL shock environment, which was lower than the multi-mission environment and performed using a flight-like configuration and flight-like separation devices. The results from the QU pyroshock test confirmed that the generator would respond to a flight level pyroshock event with a temporary power drop although significantly less severe than that experienced by the EU shock test and were used to risk assess the hardware for flight readiness. Due to the schedule constraint, the root causes of this anomaly were not investigated and the MSL was launched with project accepting the risk posture.

In preparation for the Mars2020 mission, the root causes of the MMRTG power drop are being investigated. An updated root-cause fault tree has been created from previous MMRTG pyroshock case studies and test reports. Figure 1 shows the current fault tree with suspect root-cause branches currently being investigated.

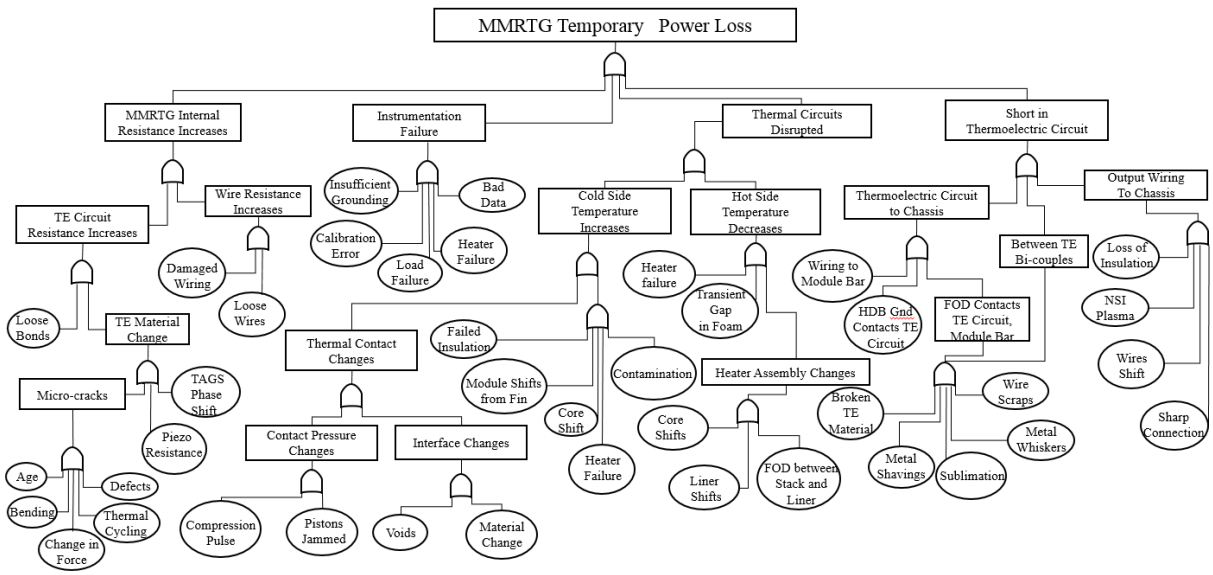

FIGURE 1. MMRTG Pyroshock-induced Root-cause Fault Tree Guiding this Study.

This fault tree shows that the power drops are most likely caused by pyroshock-induced dynamic events that trigger a combination of electrical circuit impacts, thermal network impacts, and/or TE materials impacts which may be interrelated. The current belief is that the pyroshock-induced power drops and recovery occur from a two-step process: 1) An electrically-generated or thermally-caused response in key MMRTG components having a time-constant on the order of milliseconds emanating from a pyroshock dynamic event, followed by 2) A mechanical-thermal recovery response in the MMRTG components having a time-constant on the order of 10's of minutes. This work is focused on identifying and quantifying the dynamic environments that could induce the electrically-generated or thermally-caused response in key MMRTG components. The critical MMRTG components would include the Thermoelectric (TE) couples themselves, the couple interconnect materials, the TE couple or TE module electrical connectors and current collectors, the spring-loaded pistons in the TE module bar interfacing on the cold-side, and the resulting cold-side and hot-side thermal connections to the TE couples. In order to decipher this potentially complex series of pyroshock-induced dynamic events and resulting electrical-thermal response events causing the power drops, our work is employing a combination of NASTRAN and Presto-based pyroshock dynamic models and the Jet Propulsion Laboratory's Lifetime Performance Prediction Models (LPPMs) to draw the link between the dynamic causation events and the electrical-thermal responses leading to the observed power drops.

SHOCK PREDICTION

The pyroshock simulation tests were performed using the Engineering Unit (EU) MMRTG after properly preparing the unit for thermally hot and electrically charged flight conditions. The EU was mounted on the test fixture as shown in Figure 2. The unit was left powered on until a steady temperature was reached before the shock test was resumed. The pyroshock test was performed by detonating primacord as means of simulating the required shock environment for the MMRTG. Also shown in Figure 2 is a portion of the Finite Element Model of the unit used for shock predictions discussed in this section. Figure 3 shows typical input accelerations measured at the base of the unit and responses measured on the top of the unit. The shock signatures in frequency domain indicate that the shock levels above a couple of 1000 Hz were significantly exceeded the required nominal shock levels. The high-frequency high-shock levels in general do not provide primary structural damage rather it could exert a profound impact on the functionality of the electronic parts such as diodes, resistors, etc. and could potentially break small brittle parts such as ceramics, glasses, etc. The generator power monitored during the test indicated a severe loss of power and a jump in the internal resistance. The power loss was recovered after some time.

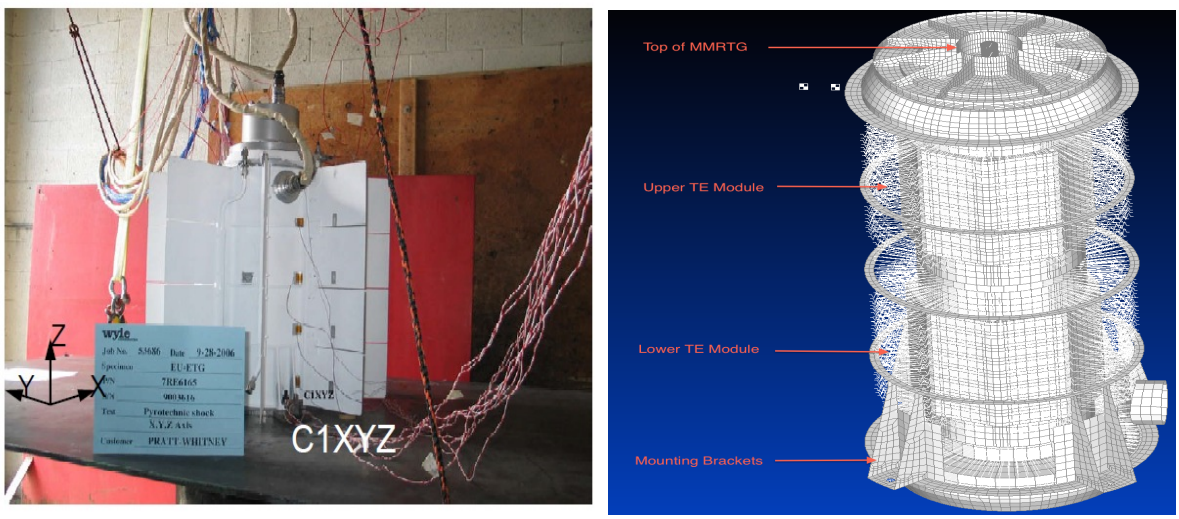

FIGURE 2. The EU MMRTG pyroshock test setup [1]. The right figure shows a segment from the finite-element model. The locations of interest for this study are marked with red arrows.

Several different paths are being considered to investigate root causes of the power loss during the shock test. This work is concentrating primarily on root causes associated with MMRTG internal electrical resistance increases; thermoelectric circuit short-circuiting within TE couples, TE module bars, or to the metal chassis / housing; or TE module bar thermal network disruptions at the TE couple cold- and hot-sides, piston and spring assemblies, and module bar to housing interfaces. This work is particularly focused on predicting pyroshock-induced dynamic environments that create significant impacts on the electrical-thermal networks within the MMRTG and developing tests to demonstrate the predicted and observed effects. One of the paths in investigating this anomaly is to assess how the shock loading affected the critical and sensitive MMRTG components. The shock prediction methodologies considered are divided into low- and high-frequency regions as the shock attenuation and/or amplification characteristics in each frequency region are known to differ. A pyroshock environment is characterized as a traveling wave response phenomenon at higher frequencies and a classical standing wave or the vibration normal modes (structural Eigen solution) at lower frequencies. The traveling waves in general cause rapid attenuation of shock level as a function of distance from the source and as it crosses structural discontinuities produced by joints and interfaces [4]. The shock wave propagation in structures has been a subject of studies in recent years and attempts have been made to predict waves transmitted and scattered from interfaces, the accuracy of which is dependent on the detailed modeling of the interfaces with proper inclusion of the physics of the contact frictions. An elaborate effort is currently underway at Jet Propulsion Laboratory (JPL) to use Presto, a Sandia developed numerical tool that uses supercomputers with multi parallel processors. In this paper, the standing wave analysis to transient input excitation forces using MSC Nastran based finite element model (FEM) of the MMRTG is performed. The structural responses both in acceleration and relative displacement are predicted and are discussed.

The FEM used for the analysis is obtained from MSL project, where the model fidelity is reasonable to several-hundreds Hz.

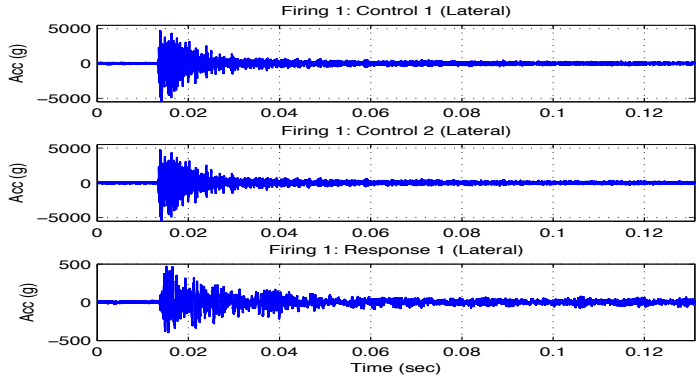

FIGURE 3. The measured input shock signatures (two locations labeled as Control 1 and Control 2) and response shock signature (labeled as Response 1) [1].

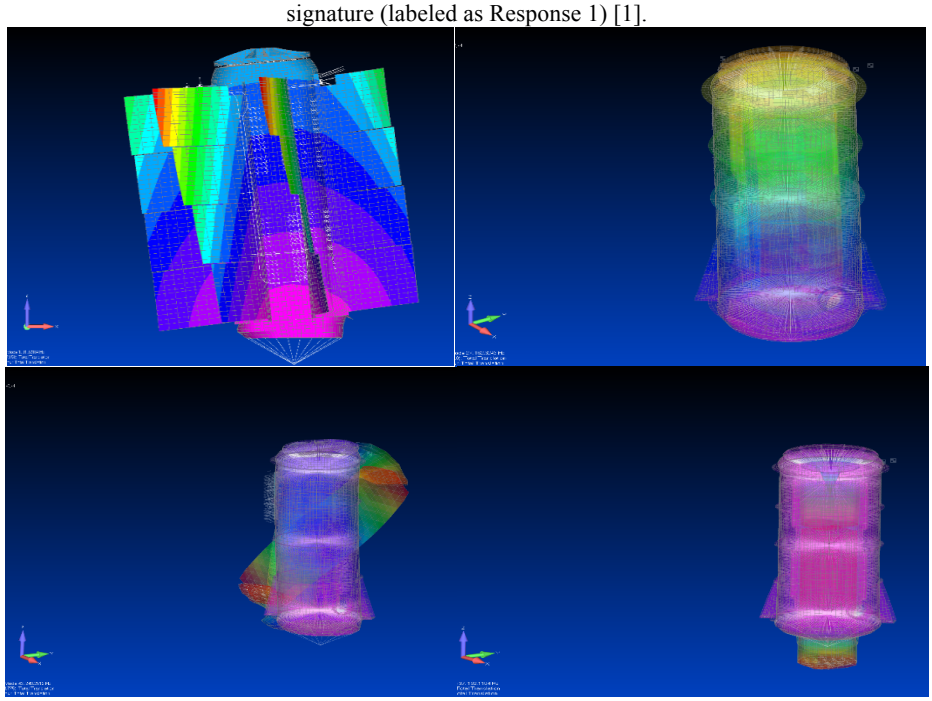

FIGURE 4. The MMRTG FEM used to obtain first few structural modes; three modes in the lateral direction (91.9.2 Hz, 162.3 Hz, and 249.2 Hz and one mode in the vertical direction (191.1 Hz) are shown.

The structural responses to the transient input below 750 Hz (a cut-off frequency above which the FEM does not have adequate fidelity) were computed and correlated to the data obtained from EU MMTRG shock test. The first few structural modes in the vertical and lateral directions that contribute the most to the displacements at critical interfaces are shown in Figure 4. First part of the analysis was performed by applying white noise acceleration as input at the base of the EU and transfer functions were recovered using MSC Nastran. Figure 5 depicts the predicted transfer functions in the lateral and vertical directions. Three dominant frequencies are identified in the lateral direction (plotted in red) and two dominant frequencies are identified in the vertical direction (plotted in black). These transfer functions are used to predict acceleration power spectral densities at the top of the MMRTG to a transient measured acceleration input as shown in Figure 6. This figure shows reasonable model correlation with the measured acceleration responses. The test-correlated MMRTG FEM then made it possible to use it to predict displacements at critical locations of the MMRTG, which may be important to the understanding of the anomalous power drop observed during the EU shock testing.

The shock input signatures obtained from EU pyro-firing test were down sampled and band-pass filtered using Finite Impulse Response (FIR) filter of 20th order to include shock signatures between 50-750 Hz. The resulting acceleration signatures were numerically integrated to obtain the velocities and displacements. The displacement time-histories were used as inputs to the FE model at the base of the MMRTG to predict its transient displacement at several critical locations. All the modes within the frequency range of 50-750 Hz were included in the predictions. A constant structural damping of 4% was assumed and included in the analysis. The displacements at three locations on the MMRTG were predicted: Top of the MMRTG, on TE modules, and the bottom of the MMRTG, where the mounting brackets are located (see Figure 2). The TE relative displacement, positioned between the outer housing and the inner heat distribution blocks of the MMRTG, was predicted both in the vertical and lateral directions.

Figure 7a shows the predicted displacement at the top of the MMRTG in the lateral direction to the transient input displacement at the base of the MMRTG shown in Figure 7b. The maximum predicted displacement is close to 0.23 inches. Figures 8a and 8b are the lateral displacements at the upper and lower TE modules, respectively where the displacements of the heat distribution block and outer housing are compared. The TE heat distribution module surfaces are connected to the outer housing by an idealized FEM (i.e. combination of bar elements and non-dimensional spring elements). The differences in the displacement between the TE module and outer housing are insignificant in the lateral direction and most likely do not contribute to the anomaly under investigation. The predicted displacements at the same locations in the vertical direction are shown in Figures 9a and 9b. Figure 9a is the displacement time-history of the outer housing and the heat distribution block connected through the idealized FE model. Figure 9b is the same as Figure 9a, except measured at the lower TE module region. The predicted responses shown in Figures 9a and 9b indicate that the TE module has a relative maximum displacement of approximately 27% (~0.03 inches) with the outer housing. The predicted relative displacement between the outer housing and the inner TE module is significant and may contribute to the anomaly observed during the pyroshock testing of the EU. The relative predicted displacements were obtained based on the contribution of the standing structural waves (i.e. normal modal excitation). These housing/TE module relative displacements are suspected to: 1) degrade the electrical contact resistances at key TE couple interconnect interfaces, 2) possibly create electrical shorts between adjacent TE couples, between TE module couples and components and the module bar which is in turn in contact with the outer metal chassis, 3) possibly create electrical shorts between current collectors and the outer metal chassis, and 4) possibly create electrical interconnect and network disruptions that cause re-distribution of currents in the TE couple series-parallel cross-strapping. Preliminary electrical network circuit analyses indicate that power drops on the order of 3-5% are possible with the reasonable and plausible electrical short resistances at these locations.

The contribution of high-shock energy and high-frequency displacement due to the wave propagation may not be significant, however, their contribution to the anomaly may be related to shorting of the circuitry parts as the high energy shock waves passes through them. The shock wave propagation analysis includes the superposition of elastic waves that propagate through the structural interfaces, where they may be reflected and transmitted at the structural discontinuities. The structural FE model used in the analysis and discussed above does not have the fidelity to use for the wave propagation analysis. The accurate mapping of the wave propagation throughout the MMRTG structure is dependent on the determination of the properties of joints, or acoustic impedance at the interfaces, and the contact mechanism. Therefore, a Presto-based model is necessary and the preliminary wave propagation through the Heat Source Liner of the MMTRG from a Presto-based analysis is shown in Figure 10. A more detailed Presto-based FEM is currently being considered and results from this effort will be reported in the near future.

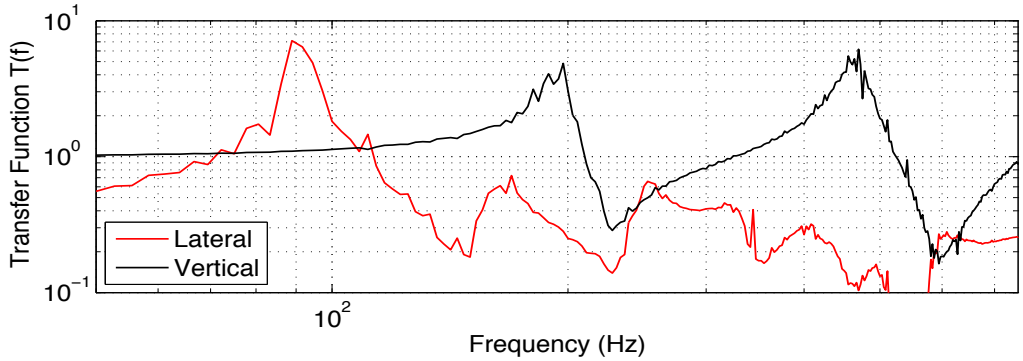

FIGURE 5. The estimated transfer functions in the lateral and vertical directions are shown. The input to the model was chosen to be white-noise transient acceleration. Three dominant frequencies are identified in the lateral direction (plotted in red) and two dominant frequencies in the vertical direction (plotted in black)

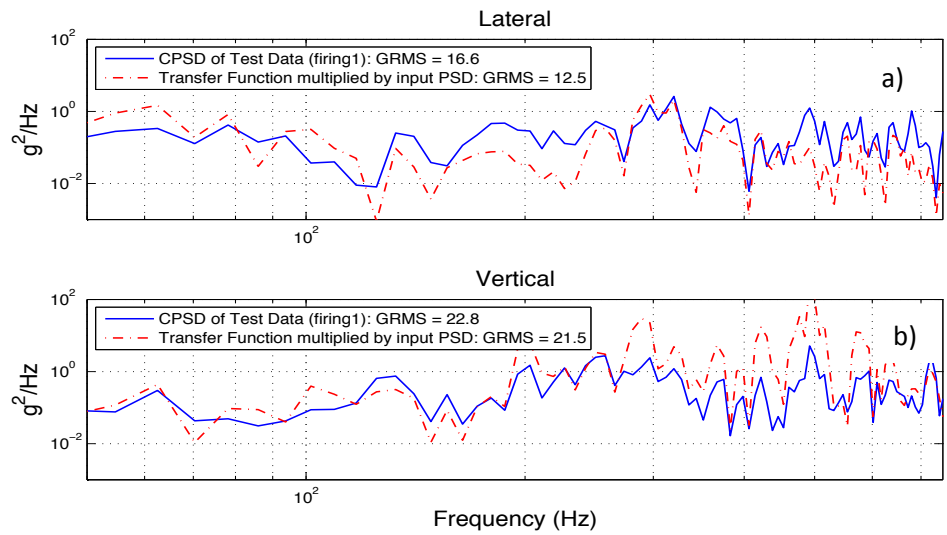

FIGURE 6. The predicted acceleration PSDs in the lateral and vertical directions are shown. The predicted results are compared with the measured acceleration responses obtained from EU MMRTG pyroshock tests.

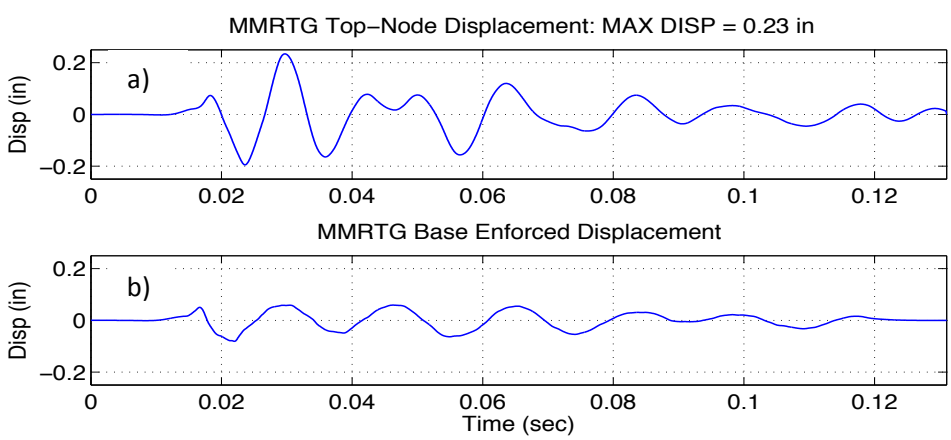

FIGURE 7. The predicted displacements in the lateral direction (X-axis) at the top and the bottom of the MMRTG, obtained using measured shock displacement as input to the model. The maximum predicted displacement at the top of the MMRTG is 0.23 in.

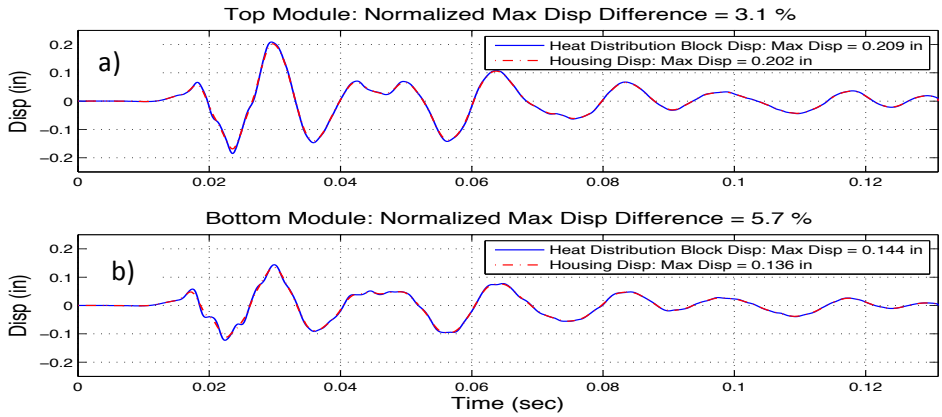

FIGURE 8. The predicted lateral displacements obtained at the upper (a) and lower (b) MMRTG TE modules. The responses at a sample outer housing node and a corresponding node on the heat distribution block are superimposed. Two nodes are connected through an idealized TE module. The relative displacements between the heat distribution block and the outer housing are insignificant and may not contribute to the anomaly under investigation.

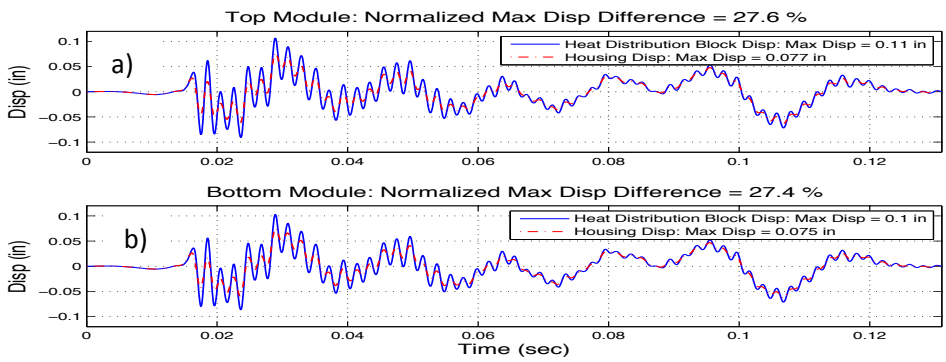

FIGURE 9. The predicted vertical displacements obtained at the upper (a) and lower (b) MMRTG TE modules. The responses at a sample outer housing node and a corresponding node on the heat distribution block are superimposed. Two nodes are connected through an idealized TE module. The relative displacements between the heat distribution block and the outer housing are significant (~27%) and may contribute to the anomaly under investigation.

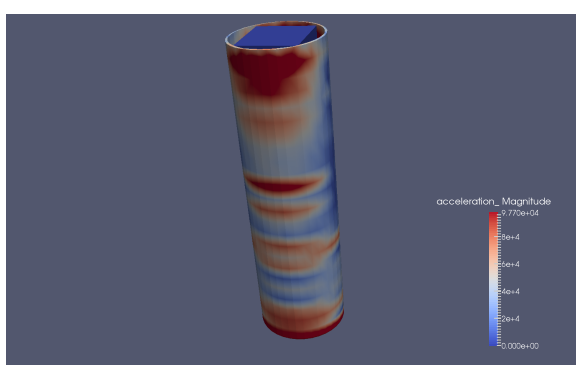

FIGURE 10. Preliminary results of the wave propagation predicted using Presto-based model. The acceleration wave propagation in the Heat Source Liner surrounding the GPHS modules is shown.

THERMAL-POWER RESPONSE PREDICTION

One portion of our pyroshock fault tree (Figure 1) deals with whether and how much pyroshock-induced degradation of the thermal conductances and thermal network could contribute to the observed MMRTG power

drops during pyroshock events. The dynamic data in Figure 9a and 9b indicates that the significant relative displacement between the TE module and outer housing, which in turn creates questions on whether changes in thermal conductances in the MMRTG cold-side thermal network could be contributing. Our team has employed the JPL Lifetime Performance and Prediction Model (LPPM) to evaluate and quantify this possibility and provide guidance on future test plans. The LPPM has a built-in thermal network model of the MMRTG and predicts its resulting power output in response to the thermal network temperature profiles through the MMRTG. The LPPM is a product of many decades of development and validation effort to predict the steady state power output as a function of time in SiGe-based RTGs like the Multi-Hundred Watt units that flew on Voyager or the General Purpose Heat Source RTGs that flew on Galileo, Ulysses and Cassini. More recently the LPPM was upgraded to incorporate PbTe RTGs like the MMRTG.

Two preliminary LPPM studies were performed in response to the pyroshock dynamics analysis results discussed above: 1) An assessment of the impact of degrading thermal conductance between the TE module bar and the outer housing, and 2) An assessment of the impact of degrading thermal conductance between the TE cold shoe and module bar. The MMRTG LPPM has a number of preset default values for various MMRTG electrical and thermal design parameters. These preset default values were determined by extensive validation testing during the MMRTG development and subsequent Mars Science Laboratory project work. In order to perform these assessments, we simply ran a number of MMRTG performance analyses with degraded thermal conductance at the interfaces described above. Figure 11 displays the impact to MMRTG power output from degrading the TE-module-bar-to-outer-housing thermal conductance by a factor of 5. Figure 11 shows that even with a thermal conductance degradation of 5X at this thermal interface the MMRTG power drop is only about 0.1 W, certainly much lower than the observed pyroshock-induced power losses. Figure 12 demonstrates the impact to MMRTG power output from degrading the TE-cold-shoe-to-module-bar thermal conductance by a factor of 7. Figure 12 shows that even with a thermal conductance degradation of 7X at this thermal interface the MMRTG power drop is less than 0.1 W, once again certainly much lower than the observed pyroshock-induced power losses.

The major conclusion from these preliminary MMRTG thermal-electrical analyses is that it is not likely that pyroshock-induced changes to MMRTG cold-side thermal conductances alone provides a sufficient explanation to the observed MMRTG power losses during pyroshock events. At the very least, it is clear that factors of change much greater than 5-7 are required to achieve the observed pyroshock-induced power losses discussed herein. Further work with the MMRTG LPPM and dynamics models is required to determine specific values for thermal and electrical resistances within the MMRTG and how these values can be used to predict changes in the power output during and after pyroshock testing.

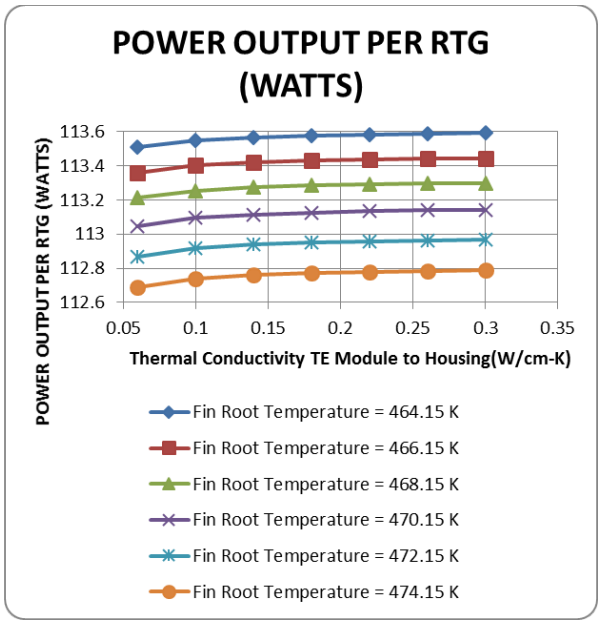

Figure 11. LPPM Prediction of MMRTG Power Increases/Decreases as TE-Module-Bar-to-Fin-Root Thermal Conductance Varies by 5X.

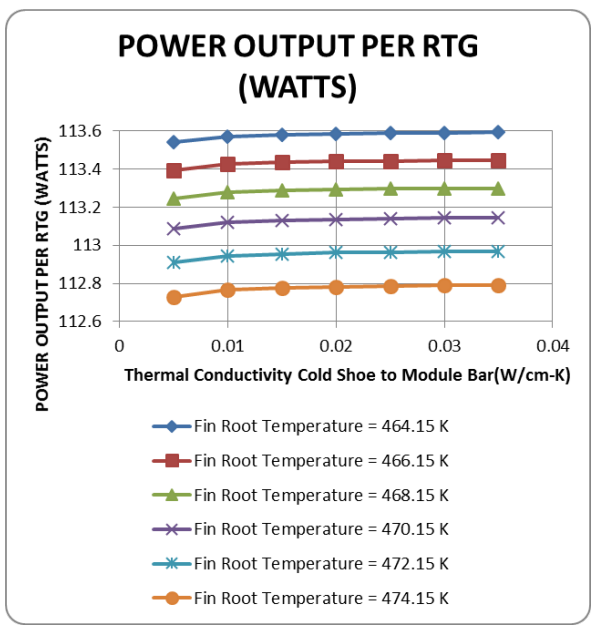

Figure 12. LPPM Prediction of MMRTG Power Increases/Decreases as TE-Cold-Shoe-to-Module-Bar Thermal Conductance Varies by 7X.

CONCLUSION

This work-in-progress provides a status report in understanding the risk or risks associated with the output power drop and recovery observed during various levels of MMRTG pyroshock testing. Every effort has been made to maximize the use of existing data, models and test facilities to minimize the cost to the program. The RTG interplanetary space program has a long history of developing models to predict all types of degradation and failure mechanisms such that with only a few years of test data, missions have been able to predict reliably the output

power that will be available to them based on the operating environment for periods up to 40 years. This approach is being used to understand even temporary degradation mechanisms like this MMRTG power loss following pyroshock testing to assure future missions will continue to have the long lifetime and success of previous missions.

The pyroshock-induced structural responses that may impact the electrical-thermal networks within the MMRTG are discussed. The shock prediction methodologies considered in this paper include both the low-frequency normal and high-frequency wave propagation analysis. The relative displacements were recovered at critical MMRTG locations to a transient input using the low-frequency FEM. The predicted responses indicate that the Heat Distribution Block has a relative maximum displacement of approximately 0.03 inches with outer housing, which is significant and may contribute to the anomaly observed during the pyroshock testing of the EU. The shock wave propagation analysis includes the superposition of elastic waves that propagate through the structural interfaces and its accuracy is dependent on the determination of the properties of joints, or acoustic impedance at the interfaces, and the contact mechanism. The existing model is being revised to increase its fidelity, where the impact of the high-frequency wave propagation on MMRTG components can be assessed and be used in the anomaly investigation.

Our preliminary thermal-power analyses using JPL's LPPM indicate that it would take factors of change significantly larger than 5-7 in key MMRTG cold-side thermal conductances to produce the observed pyroshock-induced power losses discussed herein. This calls into question whether degradation of key cold-side thermal conductances alone could be creating the observed power losses, and begins to shift thinking and emphasis toward pyroshock-induced, dynamics-driven electrical circuit or TE material changes within the MMRTG. This project is an on-going work-in-progress and further status report publications, including results from planned experimental couple and TE module bar tests, are anticipated as we increase our understanding and refine our causation-recovery scenarios of the pyroshock-induced MMRTG power losses.

ACKNOWLEDGMENTS

The authors acknowledge David Woerner, Radioisotope Thermoelectric Generator Integration Manager, Radioisotope Power System Program for his support and Aerojet Rocketdyne, Canoga Park, CA for providing the MMRTG dynamics finite element dynamics models, which were the basis for this work. The research was carried out at the Jet Propulsion Laboratory, California Institute of Technology, under a contract with the National Aeronautics and Space Administration.

REFERENCES

[1] Bromberg, M. and Otting, W., "MMRTG EU-ETG Summary Test Report," *Pratt & Whitney Test Report*, TR-00156, S/A #20931, GO #98328, (February 2007).
[2] Chang, J., "EU-ETG Vibration and Shock Test Report," *Pratt & Whitney Test Repot*, TR-00152, GO #98328, (March 2007).
[3] Lee, J.T., "Mars Science Laboratory Rover Pyroshock Test Report," *JPL* D-69262, (April 2011).
[4] Baumann, R.C., "General Environmental Verification Specification For STS & ELV Payloads, Subsystems, and Components," *NASA Goddard Space Flight Center*, (1996).

New Horizons National Environmental Policy Act Compliance and Presidential Launch Approval: Lessons Learned

Yale Chang

The Johns Hopkins University Applied Physics Laboratory, 11100 Johns Hopkins Rd, Laurel, MD 20723
240-228-5724; yale.chang@jhuapl.edu

Abstract. New Horizons, the first Principal Investigator (PI)-led and competed NASA Radioisotope Power System (RPS) mission, is on target to reconnoiter the Pluto system in July 2015. Launching an RPS mission requires compliance with two Federal mandates: the National Environmental Policy Act of 1969 (NEPA) and launch approval (LA) as directed by Presidential Directive/National Security Council Memorandum 25. The origins, planning, and development of the New Horizons project, not only in science and technology but also in policy and politics, have been described elsewhere. This paper presents the NEPA/LA aspects of New Horizons. The project's management of the NEPA/LA processes emphasized a collaborative, interactive approach among the many agencies and organizations involved, and obtained Presidential launch approval in less than 4 years. Specific accomplishments, from pre-proposal in November 2000 to launch approval and then launch in January 2006, are described and their criticality assessed. Lessons learned on various aspects and applicability to future PI-led and competed NASA RPS missions are offered. These NEPA/LA lessons learned are from the mission manager's implementation perspective.

Keywords: Lessons Learned, NEPA/LA Implementation, New Horizons, PI-led and competed NASA RPS mission

INTRODUCTION

The author's involvement in RPS and NEPA/LA-related activities for what was initially called the Pluto Kuiper Belt (PKB) mission started in November 2000. NASA opened the PKB mission to competition as an Announcement of Opportunity on 19 January 2001. On 29 November 2001, NASA awarded the New Horizons mission to Dr. S. A. Stern of the Southwest Research Institute as the PI and to The Johns Hopkins University Applied Physics Laboratory (JHU/APL) as the mission manager. New Horizons carries a General Purpose Heat Source (GPHS) Radioisotope Thermoelectric Generator (RTG), a type of RPS that uses 10.9 kg of plutonium dioxide to supply heat and electrical power to the spacecraft and its scientific instruments at 30 astronomical units or more. Launching an RTG requires fulfilling the NEPA/LA requirements; the rationale for NEPA/LA is described by Chang [1] as follows: "Preparation for NASA missions carrying nuclear material must consider the possibilities of launch accidents and the subsequent disposition of the nuclear fuel regionally and worldwide. The formal safety effort centers on compliance with the National Environmental Policy Act and Presidential launch approval processes. These processes are rooted in sound management, engineering, physics, and public safety principles, requiring significant analytical, experimental, and scientific studies."

To accomplish these goals, both processes have distinct milestone products. Briefly, the products for NEPA compliance are the Environmental Impact Statement (EIS) Databook, the Nuclear Risk Assessment, the Draft EIS, risk communications activities, the Final EIS, and the Record of Decision. Briefly, the products for launch approval

are the Safety Analysis Report (SAR) Databook (and revisions); the Preliminary SAR, the Draft SAR, and the Final SAR; the Safety Evaluation Report; and the Presidential launch approval decision.

An account of the policy, politics, science, and technology in the origins of New Horizons is provided by Neufeld [2], who describes the pursuit of a mission to Pluto starting in 1989, and ends with a narrative of the genesis, development, and validation of the New Horizons project when it was placed in the fiscal year 2003 Congressional budget. Neufeld mentions that the NEPA/LA requirements were the number two challenge (ranked behind the project budget) in NASA's award letter to the PI: "In particular the federal environmental clearance to launch nuclear material—the plutonium in the RTG—was far from easy." This was an understatement—the traditional NEPA compliance process for an RTG mission was widely accepted at the time to be up to 6 years in duration, and the traditional launch approval process was up to 9 years in duration, with the two processes starting concurrently. (For example, the launch approval process for NASA's nuclear-powered Cassini mission took 8 years, October 1989 to October 1997 [3].) The New Horizons baseline mission design specified a launch in January 2006, with a Jupiter gravity assist in 2007, and arrival at Pluto in 2015, well before its atmosphere was postulated to collapse in 2020 [4]. Thus, the New Horizons' NEPA/LA activities had to be completed in only 4 years. Strategies for doing so were presented in the mission's Concept Study Report, which were to a large extent followed. Basically, the strategies were to (1) emphasize a collaborative and interactive approach among the many agencies and organizations involved; (2) understand and improve the efficiencies in the many processes and milestones that were interrelated in dependency and sequencing; (3) avoid spacecraft design, mission design, and launch vehicle features that could negatively affect the schedule; (4) select a launch vehicle as early as prudently possible; and (5) leverage previously completed work as much as possible. Crises and issues were dealt with promptly, and decisions made quickly but judiciously.

New Horizons was "on probation" from the award date until NASA Headquarters issued its final mission confirmation in March 2003 [2]. Part of the probationary activities was to demonstrate to NASA Headquarters and Congress that sufficient progress was being made in the NEPA/LA activities to warrant official line-item funding. Thus, the New Horizons project's risk meter for NEPA/LA was continuously pegged at red from the beginning, through probation, through fulfillment of NEPA requirements by the issuance of the Final EIS in July 2005 and the Record of Decision in September 2005, until the granting of Presidential launch approval on 3 January 2006. The New Horizons spacecraft was launched on 19 January 2006.

Some activities of JHU/APL's New Horizons NEPA/LA team (the author was the deputy manager) that contributed to attainment of the NEPA/LA goals, and lessons learned from these activities, are described in this paper. These activities were a small subset of the total NEPA/LA efforts across many Government agencies, private companies, and other organizations.

NEPA compliance and Presidential launch approval are inherently Government functions, where NASA is the lead agency and the Department of Energy (DOE) is the cooperating agency. However, the mission manager can affect the level of effort required for these processes in three basic areas: launch vehicle features, spacecraft design, and mission design. These areas are also fundamental to the attainment of the project's scientific objectives and therefore must be appropriately balanced. Thus, the challenge from the mission manager's point of view in performing these tasks was to consider the nuclear safety aspects without diminishing or adversely affecting the scientific objectives.

NASA's Jet Propulsion Laboratory (JPL) is typically responsible for Launch Approval Engineering and Aerospace Nuclear Safety Engineering functions for NASA RPS missions. JHU/APL, under its Aerospace Nuclear Safety Program (the author is the program manager), has continuously supported the DOE for NASA RPS missions since 1971. JHU/APL also launched the first RPS into space in 1961 with the Transit 4A navigational satellite for the U.S. Navy.

NEPA compliance and Presidential launch approval consider any potential accidents that could result in release of the RPS's fuel into Earth's environment, even low-probability accidents. For New Horizons, the probability of a successful launch leading to a Pluto trajectory was estimated as 93.8%, the probability of accidents with no radiological releases as 5.8%, and the probability of accidents with radiological releases and potential consequences as 0.4% [5]. Potential consequences considered are health effects and land contamination, which are determined by the accident environments, and the responses of the RTG hardware to those environments. Although the nuclear fuel is protected by multiple layers of material, the accident environments—such as blast and impact from explosions,

atmospheric reentry, and liquid and solid propellant fires—can be severe. The responses of the RPS and its components to these environments are analyzed, and are based on an extensive testing database. These responses are then used to determine the consequences. The overall radiological risk for the New Horizons mission was estimated to be 5.8×10^{-4} [5].

LESSONS LEARNED

Spacecraft and Mission Design

Certain spacecraft design, mission design, and launch vehicle features could significantly affect the amount of effort and time required for the NEPA/LA processes, with closer scrutiny applied to those features that could adversely affect nuclear risk. The New Horizons' spacecraft layout was similar to that of the 1990 Ulysses mission, but as the project progressed, new test data and analyses from the concurrent development of the NASA Mars Exploration Rovers project [6] (launched in June and July 2003) provided insights pertaining to the nuclear safety implications for the New Horizons spacecraft design. These are discussed further in the "Team Contributions" section. Regarding mission design, the project was advised that an Earth gravity assist (EGA) maneuver would increase the level of effort in examining potential EGA reentry accidents, and would not be favorable to the NEPA/LA schedule. The project was also advised against a launch in other than daylight hours because this could negatively affect the mission flight control officer's response time in activating the launch vehicle's command destruct system in the event of a launch accident.

JHU/APL NEW HORIZONS NEPA/LA TEAM CONTRIBUTIONS

Twenty-one contributions from the JHU/APL New Horizons NEPA/LA team were compiled after the 2006 launch for purposes of documentation, applying lessons learned, and assessing their applicability to future RPS missions. These contributions are listed in TABLE 1, in no particular order. At the time of the initial compilation, one important item was inadvertently omitted; it has since been added in the Table as Item 5.5. The table headers are self-explanatory. The ratings of Critical, Important, Routine, and Mission-Dependent are admittedly subjective. A further delineation of the contributions is shown as items that were unanticipated at the time of mission award; these are marked with asterisks. Of the 10 unanticipated items, 5 were rated critical. Further discussion on a few select contributions will be provided.

TABLE 1. Summary of Contributions to New Horizons and Applicability to Future RPS Missions

Item	Action for New Horizons	Funded by	Rating for New Horizons	Comments for New Horizons	Rating for Future RPS Missions
1	Wrote proposal sections on nuclear safety, NEPA and launch approval plans, and radioactive materials	Bid and Proposal (B&P)	Critical	NASA press release of 29 November 2001: "New Horizons represented … the best plan to bring the spacecraft to the launch pad on time …" referring to the plan to get Presidential launch approval in less than 4 years	Critical
2	Sponsored subcontractor accident probabilities report for the EIS	B&P, NASA	Critical	Early pre-award work	Mission-dependent
3	Produced sections of the SAR Databook on Introduction, Mission Overview, Spacecraft and Third-Stage Description	NASA	Routine	These sections are the mission and spacecraft manager's responsibilities	Routine
4	Produced sections of the SAR Databook on Spacecraft and Third-Stage Fallback Impact Orientations	NASA	Important	Improved method to produce probabilities of spacecraft landing on the RTG	Important

TABLE 1. Summary of Contributions to New Horizons and Applicability to Future RPS Missions (Continued)

Item	Action for New Horizons	Funded by	Rating for New Horizons	Comments for New Horizons	Rating for Future RPS Missions
5*	Produced sections of the SAR Databook on solid propellant fire specification	DOE	Critical	The solid propellant fires environment in the SAR Databook was the risk-driver for the Final SAR	Critical
5.5*	Implemented Star 48 Breakup System (BUS)	NASA	Critical	Prevent large solid propellant fragments from crushing the RTG, or large fires from vaporizing plutonium; led to Items 6, 7, 9, and 16	Mission-dependent
6*	Wrote test proposal for conical-shaped charge (CSC) tests conducted by JPL and JHU/APL	NASA, DOE	Critical	JHU/APL test proposal included effects of obliquity of impacts, and correctly predicted the test results (little to no damage to RTG from CSC shrapnel)	Mission-dependent
7*	Produced Fallback Impact Orientations of the RTG	DOE	Important	JHU/APL report provided analytical predictions of impact orientations	Mission-dependent
8*	Advised New Horizon project to obtain contractual Price Anderson Act nuclear indemnification against third-party liability	NASA	Critical	Conforms to JHU/APL's risk mitigation plan; contractual indemnification granted	Critical
9*	Produced spacecraft reentry sequential failure analysis	NASA, DOE	Important	JHU/APL report defused concern in nuclear safety community of high-altitude release of plutonium	Mission-dependent
10	Provided Debris Impact Footprint Prediction capability and support	NASA, DOE	Critical	JHU/APL improved methodology to predict spacecraft and RTG breakup, release of GPHS modules, trajectory simulation to Earth, and footprint prediction. Part of Radiological Control Center (RADCC) activities.	Critical
11	Provided updated GPHS aerodynamics	DOE	Important	JHU/APL improved aerodynamics based on computational fluid dynamics	Routine
12*	Provided a JHU/APL Payload Representative in the Kennedy Space Center RADCC	NASA	Critical	White House Office of Science and Technology Policy granted launch approval assuming contingency plans. The RADCC was a mandatory asset for launch.	Critical
13*	Provided Heliocentric Orbit Contingency Plan	NASA	Routine	Input to RADCC activities	Routine
14	Provided Debris Impact Footprint Definition Suborbital and Orbital Contingencies Plan	NASA	Routine	Input to RADCC activities	Routine
15*	Contributed to JHU/APL Contingency Plan	NASA	Routine	Provided procedures for notification of Laboratory director, data impoundment procedures	Routine
16	Provided briefs and responses to the Interagency Nuclear Safety Review Panel	DOE, NASA	Important	Briefings and responses were mainly related to the solid propellant fire specification in the databook	Important
17	Provided drag ballistic coefficients to the range safety community and U.S. Strategic Command	NASA, DOE	Important	Provided common set of engineering data for community use	Important

TABLE 1. Summary of Contributions to New Horizons and Applicability to Future RPS Missions (Continued)

Item	Action for New Horizons	Funded by	Rating for New Horizons	Comments for New Horizons	Rating for Future RPS Missions
18	Sponsored subcontractor report of Nuclear Risk Assessment for the New Horizons EIS	DOE	Critical	Subcontract	Critical
19	Contributed to the New Horizons EIS	NASA	Routine	Mission and spacecraft descriptions, Earth impact study, alternate mission designs, alternate power sources, solar electric propulsion study	Routine
20*	Wrote console procedure for the JHU/APL Payload Representative in the RADCC	NASA	Important	Part of RADCC activities	Important

Perhaps the most prominent and controversial item in TABLE 1 is Item 5.5 and its derivative Items 6, 7, 9, and 16. The New Horizons payload shown in FIGURE 1 includes the spacecraft (observatory) with attached RTG, the payload attach fitting with two CSCs mounted internally, and the Star 48 solid propellant third-stage motor. From a mission execution standpoint, this configuration meets all the science and operational requirements. However, the RTG is placed close to the Star 48 motor, which is not desirable from a nuclear safety standpoint because (1) the RTG would be in the direct path of projected solid propellant fragments in the event of a commanded or automatic destruct action of the Star 48 motor at altitude; (2) a fallback of the intact motor or its fragments has a higher probability of impacting on top of the RTG or its internal GPHS modules; and (3) this configuration has a higher probability of allowing the GPHS modules to be in close proximity to large solid propellant fires of long duration. To lessen these risks, a Star 48 BUS was implemented, wherein its CSCs would fragment the motor into smaller pieces. The BUS, however, while decreasing the stated risks, introduced another risk in that the CSCs upon detonation would produce backside fragments that could impact the RTG. To determine that risk, CSC tests were conducted that showed these fragments were unlikely to penetrate the GPHS's protective graphitics (Item 6). As a result of these tests, boron carbide shields, which had been designed and fabricated to protect the RTG from potential CSC fragments as a risk mitigation measure, were not installed on the third stage for flight.

Another concern among the nuclear safety community involved a scenario for an accidentally reentering spacecraft and attached third-stage motor. It was postulated that, as the spacecraft was subjected to aerothermal heating during reentry, that the CSCs of the BUS might detonate upon reaching their auto-ignition temperature and impact the RTG, potentially releasing nuclear fuel at altitude. This concern was defused by JHU/APL in an analysis report showing that the spacecraft would break apart as a result of thermal and deceleration loads and separate from the RTG well before the CSCs' auto-ignition temperature was reached (Item 9).

The RTG fallback orientation analysis (Item 7) proved critical. After a commanded or automatic destruct action following an accident at altitude, the RTG attached to its mounting fixture would separate from the spacecraft, then fall back ballistically to impact the ground. Initially, the safety analysis assumed that the RTG attached to its mounting fixture would have an attitude at ground impact such that the GPHS modules would impact first at high velocities up to 150 m/s, and the remaining mass would "pile drive" the modules farther into the ground. JHU/APL then conducted six degree of freedom fallback motion simulations coupled with a Monte Carlo method, using the structures' mass and aerodynamic properties and varying the initial tip-off rates, attitudes, and altitudes to produce probabilities of impact orientations and velocities. Analysis results showed that, contrary to the initial assumptions, the mounting fixture was likely to impact the ground first, and at much lower terminal velocities of about 30.5 m/s [7].

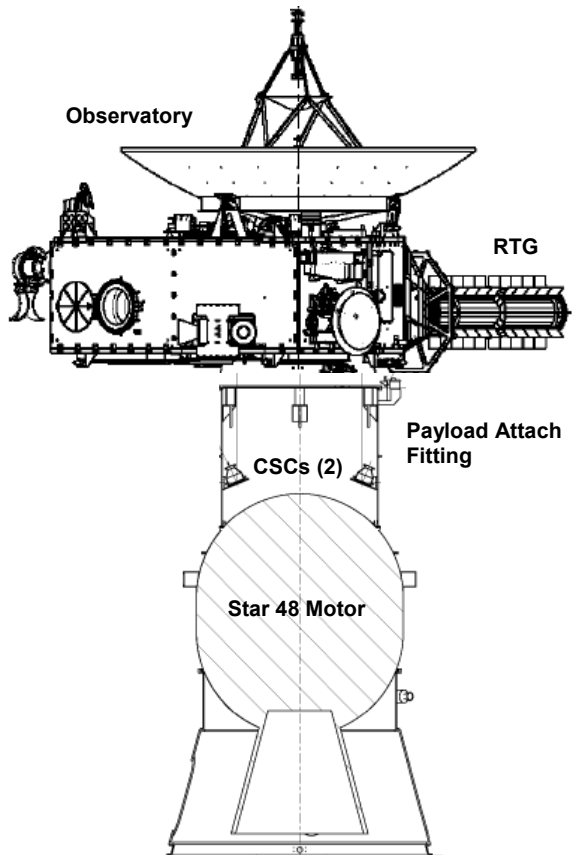

FIGURE 1. New Horizons Observatory with RTG, Payload Attach Fitting, Star 48 Motor, and CSCs of the BUS. The RTG Long Axis is Shown Rotated 45° about the Thrust Axis (Flight Configuration).

These three examples show the value of the mission manager, as the spacecraft design agent, investigating the responses of the spacecraft to accident environments, and then producing risk mitigation measures and detailed response analyses to provide better information for the risk analysis. In the case of the BUS implementation, an additional risk from the CSCs was identified and addressed by the CSC tests, with the participation of the mission manager.

Contingency plans were required for several possible anomalies. An anomaly is defined as any event that causes deviation from the spacecraft's trajectory to Pluto. For a near-pad launch accident, the Kennedy Space Center prepared a contingency plan for, among other things, public guidance such as shelter in place, using several ground-based pre-positioned remote radioactivity sensors located around the Cape Canaveral launch region to provide data and inform decisions. For a spacecraft accidentally reentering the Earth's atmosphere from an orbital or suborbital trajectory, JHU/APL prepared a Debris Impact Footprint Definition Suborbital and Orbital Contingencies Plan that described the procedures and capabilities for predicting where the spacecraft and RTG components would land on the Earth's surface (Item 14). For a spacecraft in an anomalous heliocentric orbit, JHU/APL prepared a contingency plan to address possible actions to prevent a long-term reentry (Item 13). For any type of anomaly, JHU/APL prepared a contingency plan for notification of the JHU/APL director, the president of The Johns Hopkins University, and other officials (Item 15).

The preceding discussion described launch and spacecraft operation anomalies that could result in release of nuclear material into Earth's environment with the potential for consequences such as health effects or land contamination. This brings up the issue of third-party liability. JHU/APL procured liability insurance for New Horizons, but also obtained Price Anderson Act indemnification from NASA prior to the launch (Item 8). Because of this and other laboratory programs with potential for third-party liability, JHU/APL instituted two actions after the launch. The first was to restructure the governance of the Laboratory from a division of The Johns Hopkins University to that of

a limited liability corporation. The second action was to assess and rate proactively the risk of third-party liability for all future programs prior to award to inform management decisions regarding the potential risk incurred in accepting new programs.

General NEPA/LA Lessons Learned

The infrastructure should remain intact

JPL and JHU/APL currently have roles and responsibilities for NASA missions carrying RPSs and decades of experience. These roles and responsibilities should continue whether future missions are directed or competed, and whether these missions are managed by JPL, JHU/APL, or some other team.

Allocate roles and responsibilities

Roles and responsibilities for various activities for various organizations can be simply and logically determined by who owns what. For example, all issues related to the RPS belong to DOE because DOE owns the RPS and RPS fuel throughout all phases of the mission. All issues relating to the spacecraft belong to the mission manager, including off-nominal incidents such as spacecraft breakup upon atmospheric reentry, or response to a detonation. The PI owns attainment of the mission objectives.

Integrate nuclear considerations into mission and spacecraft designs

Future competed RPS missions should include NEPA/LA and nuclear hardware considerations as integral parts of the proposed missions from the beginning. This allows the best overall proposals to be submitted as Concept Study Reports. If these considerations are added or addressed after mission award, much of the foundation for the spacecraft and mission designs will already exist and could be costly to modify or costly to address, e.g., Item 5.5 of TABLE 1.

Intellectual Property

Many of the participants were concerned about protecting their organizations' intellectual property (proprietary, confidential, or limited rights; competition-sensitive; or privileged information). The working solution turned out to be non-disclosure agreements (NDAs). Because several organizations were interacting with several other organizations requiring NDAs, one approach was to use multi-party NDAs. Another concern was conflict of interest, real or perceived. Post-launch, the NASA Program Executive indicated he saw no conflicts of interest for the author's participation in NEPA/LA activities for New Horizons [8].

Competition

Future NASA RPS missions may be PI-led and competed. Although not comprehensive, the following lessons learned are offered:

- In providing a "level playing field" for the competition, this rule should apply to the field only and not to the proposing teams. The teams on that level playing field will have varying degrees of expertise, experience, and qualifications.
- Use an NDA construct rather than a firewall. Team members should be allowed to use information from publicly available sources and past missions in their proposal. Team members should not be allowed to use any privileged or insider information obtained from outside the team. Similarly, team members should not be allowed to share any privileged or insider information obtained from inside the team to unauthorized outside parties.
- Information on any sole source item, such as an RPS or other Government-furnished equipment, should be available to all teams.
- After the mission is awarded, the competition is over. This is obvious but hard to implement because former team members may unconsciously and unwittingly retain some degree of the competitive spirit, thereby hindering progress.

- Preparing for a nuclear space mission is not like preparing for a non-nuclear space mission. Experience in the latter is not necessarily qualification for the former. Many unknowns may be encountered by even experienced practitioners (see TABLE 1). The best preparation for these anticipated and unanticipated items is to use practitioners experienced with nuclear space missions, with the programmatic and engineering capabilities to address any issue.

Closing Remarks

Some challenges of completing the NEPA/LA processes were presented herein; many more are documented elsewhere. Needless to say, many doubted it could be accomplished in 4 years; some expressed their views openly. Every major difficulty or hurdle was taken as an impetus to delay the launch beyond 2006; indeed, this was viewed as the more logical approach. However, it was the perseverance and support of the PI and the leadership at JHU/APL, NASA, and DOE to push ahead doggedly to overcome these difficulties rather than succumb to them that contributed to successful attainment of a Record of Decision from NASA to proceed with the mission and the Presidential launch approval.

CONCLUSIONS

The NEPA/LA activities for New Horizons, as with any RPS mission, ensured that informed decisions were made and the public notified of potential risks. This paper described several contributions from the mission manager's implementation perspective, along with general NEPA/LA lessons learned. The NEPA/LA activities were completed in 4 years, and contributed to validation of NASA's experiment in offering outer planets and RPS missions as PI-led and competed missions. The New Horizons spacecraft is on target to fly by Pluto with a closest approach on 14 July 2015. Recent discovery of other potential targets could lead to a follow-on mission to fly by another Kuiper Belt Object.

ACKNOWLEDGMENTS

The successful NEPA/LA activities for New Horizons were the results of efforts of dozens of dedicated people from several Government agencies, private companies, and other organizations. It is a tribute to their often heroic efforts that proper processes were conducted in achieving NEPA compliance and Presidential launch approval, in time to launch New Horizons on the scientifically most promising mission trajectory to explore Pluto and its moons.

REFERENCES

[1] Chang, Y., "Aerospace Nuclear Safety at APL: 1997–2006," *Johns Hopkins APL Technical Digest*, **27**, No. 3 (2007).
[2] Neufeld, M. J., "First Mission to Pluto: Policy, Politics, Science, and Technology in the Origins of New Horizons, 1989–2003," *Historical Studies in the Natural Sciences*, **44**, No. 3, pp. 234–276 (2014).
[3] "Space Exploration: Power Sources for Deep Space Probes," United States General Accounting Office, National Security and International Affairs Division, GAO/NSIAD-98-102 (May 1998).
[4] Guo, Y., and Farquhar, R. W., "New Horizons Mission Design," *Space Science Review*, **140**, pp. 49–74 (2008).
[5] *Final Environmental Impact Statement for the New Horizons Mission*, NASA (July 2005).
[6] *Star 48B Full-Scale Demonstration Test, Special Test Data Report*, NASA White Sands Test Facility, WSTF #02-36952 (17 June 2002).
[7] McGrath, B. E., Frostbutter, D. A., and Chang, Y., "Probabilities of Ground Impact Conditions of the New Horizons Spacecraft and RTG for Near Launch Pad Accidents," in proceedings of *Space Technology and Applications International Forum (STAIF-2007)*, edited by M. S. El-Genk, AIP Conference Proceedings **880**, Melville, NY, pp. 579–589 (2007).
[8] Lindstrom, K. L., personal communication.

Integrated Surface Power Strategy for Mars

Michelle A. Rucker[1]

[1]*National Aeronautics and Space Administration, Lyndon B. Johnson Space Center, 2101 Nasa Parkway, Houston, TX 77058*
281-244-5569; michelle.a.rucker@nasa.gov

Abstract. A National Aeronautics and Space Administration (NASA) study team evaluated surface power needs for a conceptual crewed 500-day Mars mission. This study had four goals:

1. Determine estimated surface power needed to support the reference mission;
2. Explore alternatives to minimize landed power system mass;
3. Explore alternatives to minimize Mars Lander power self-sufficiency burden; and
4. Explore alternatives to minimize power system handling and surface transportation mass.

The study team concluded that Mars Ascent Vehicle (MAV) oxygen propellant production drives the overall surface power needed for the reference mission. Switching to multiple, small Kilopower fission systems can potentially save four to eight metric tons of landed mass, as compared to a single, large Fission Surface Power (FSP) concept. Breaking the power system up into modular packages creates new operational opportunities, with benefits ranging from reduced lander self-sufficiency for power, to extending the exploration distance from a single landing site. Although a large FSP trades well for operational complexity, a modular approach potentially allows Program Managers more flexibility to absorb late mission changes with less schedule or mass risk, better supports small precursor missions, and allows a program to slowly build up mission capability over time. A number of Kilopower disadvantages—and mitigation strategies—were also explored.

Keywords: Mars, Kilopower, fission

BACKGROUND

Early crewed Mars mission concepts developed by NASA estimated that two each 40 kilowatt electric (kWe) FSP systems would be needed to support up to six crew members for a 500-day Mars surface stay. To minimize mass, the crew's return vehicle would land on Mars with empty oxygen propellant tanks and a manufacturing plant that would produce propellant from in situ Martian resources. The primary FSP would be autonomously deployed on a dedicated mobility system to support propellant production; once the return vehicle's propellant tanks were full, the crew would arrive with a spare FSP, which would only be deployed if the primary unit failed. The primary unit would be located at least one kilometer (km) from the crew habitat, providing a safe crew separation distance. The time needed to relocate the FSP depends on the mobility system and terrain factors, but was estimated to take up to 40 sols to complete[1]. FSP design[2] (Figure 1) varies with mission, but is estimated at a mass of about 7,000 kilograms (kg) for a Mars surface mission. Measuring seven meters (m) tall by 3.3 m wide when stowed, the radiator panels would extend about 34 m when deployed.

STUDY OBJECTIVES

Four potential concerns with the baseline scheme prompted this study. First, a detailed survey of powered equipment was needed to validate the 40 kWe requirement and correctly size the power system. Second, seven metric tons is a large mass allocation for a contingency item that may never nominally used. Third, the 40 sol

estimated FSP deployment timeline placed a mass burden on the cargo lander, which must be self-sufficient for power until the FSP is activated. Finally, because the FSP is one of the largest items that must be moved around the surface, it drives surface mobility design in a direction that is not necessarily compatible with other mobility system tasks.

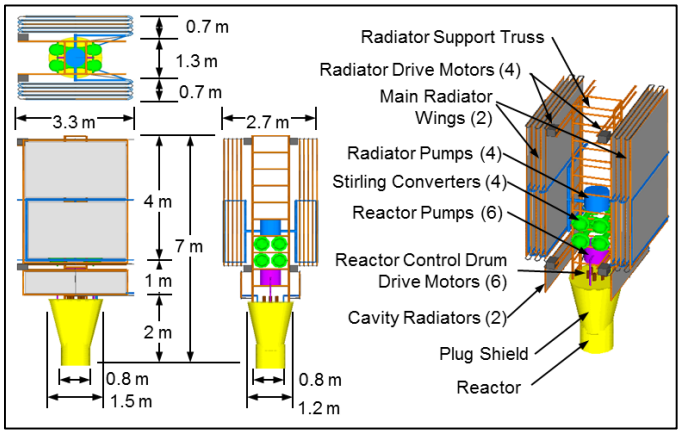

FIGURE 1. Baseline 40 kWe FSP, Stowed Configuration

To address these concerns, four objectives were identified for this study:

1. Validate estimated surface power needs.
2. Explore ways to reduce contingency mass.
3. Explore ways to accelerate FSP deployment.
4. Explore ways to minimize FSP impact on surface mobility systems.

SURFACE POWER NEEDS

After mapping the physical locations of powered items relative to the Landers, it became clear that there were three distinct categories of powered equipment:

1. Stationary Equipment: items that remain on or near the Landers, and therefore have ready access to the fission power system. This group comprises the bulk of fission surface power system users.
2. Mobile Equipment: items that move around the surface. These may be recharged from the fission system while visiting the Landers, but must be self-reliant away from the Landers, or have limited range from the Landers.
3. Deployed Equipment: relocated away from the Landers where they remain for the duration of the campaign. *Without access to the fission system they must be self-sustaining, and are therefore not addressed here.*

The Study Team found that a six crew, 500-day surface stay type of mission required a maximum of about 34 kWe during the un-crewed cargo mission and a maximum of about 33.6 kWe during the crewed surface stay; both of these estimates include 30% margin, but should be considered preliminary because the architecture is not well defined. Power could be reduced during the un-crewed phase if more time were available for propellant production. Crewed mission power needs could be reduced by phasing operations.

Stationary Powered Equipment

Table 1 summarizes estimated stationary powered equipment needs. Because stationary assets remain on or near the Landers, they define the bulk of FSP sizing. As shown in Figure 2, In-Situ Resource Utilization (ISRU) almost single-handedly sets the maximum cargo phase power requirement.

In-Situ Resource Utilization

Two ISRU systems arrive on the Cargo Lander. Once powered, the primary ISRU system extracts oxygen from the Martian atmosphere and fills the Mars Ascent Vehicle (MAV) propellant tanks. The second ISRU is a back-up, so only one ISRU would be in operation at a given time; once the MAV's propellant tanks are full, it is assumed that

ISRU can be powered down or put into standby mode. Ascent propellant load will vary with MAV crew cabin mass (which in turn varies with the number of crew and how long they must be inside the MAV[3]), and the orbit to which the MAV ascends (higher orbit requires more propellant). Using an estimate of 23,533 kg propellant for the largest MAV variant (a habitable, 6-crew vehicle bound for a one sol orbit), and a production time of 480 days, ISRU power needs are estimated at 25.2 kWe. With a 30% margin, propellant-only ISRU power for this largest MAV variant would be 32.76 kWe. For comparison, only about 19.63 kWe (including margin) would be required to produce propellant for a much smaller two-crew "taxi" MAV variant.

TABLE 1. Stationary Powered Equipment Summary

Power Consuming Equipment	Power Used (W)			Duty Cycle	Mission Phase
	Min.	Max.	Avg.		
In-Situ Resource Utilization	17,640	32,760	25,200	100%	Cargo
Mars Ascent Vehicle	623	1,157	890	100%	Cargo + Crewed
Geological/Meteorological Science Stations	20	105	69	100%	Cargo + Crewed
Surface Habitat					
Crew Accommodations	2,599	4,827	3,713	100%	Crewed
Environmental Control and Life Support	4,287	7,961	6,124	100%	
Avionics	3,375	6,267	4,821	100%	
Other	882	1,638	1,260	25%	
Extravehicular Activity	1,120	2,080	1,600	25%	
Mars Sample Laboratory					Crewed
Express Rack #1	0	720	720	100%	
Materials Science Research Rack	0	5500	550	10%	
Science Glovebox	0	1500	105	7%	
Illumination	13	130	65	100%	
Heaters	0	500	500	100%	
Control and Data Acquisition System	16	29	22	100%	
Sample Handler (Robonaut)	100	600	150	25%	
Communications	45	65	50	100%	
Planetary Protection	0	500	50	10%	Crewed

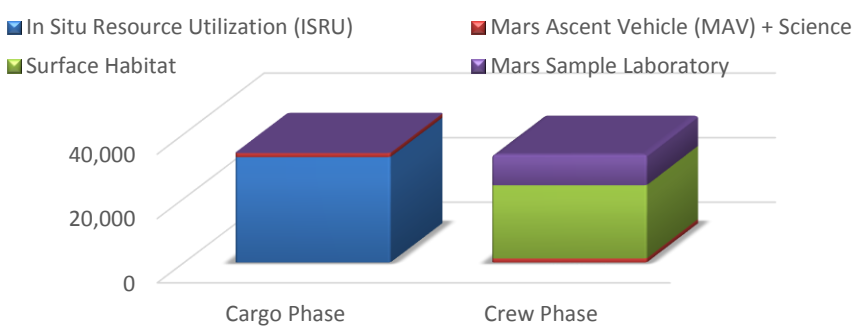

FIGURE 2. Baseline Maximum Power Needed (kWe) for Stationary Equipment

Mars Ascent Vehicle

From the time the MAV lands until it departs up to three years later, keep-alive power will be needed to heat the electronics, assess and communicate system health, and maintain propellants at proper temperature. In lieu of a detailed MAV design, keep-alive power estimates were drawn from previous ascent vehicle concepts. With 30% margin, MAV maximum keep-alive power is estimated at about 1,157 W. Note that the MAV draws power during *both* the cargo and crewed portions of the mission. One key area of uncertainty is the power required to maintain the MAV's cryogenic propellants at proper temperatures; additional studies planned for 2015 are expected to refine MAV power estimates.

Mars Surface Habitat

A 2007 Mars Surface Habitat System Sizing Report[4] suggested 12.1 kW would be needed for a four crew Habitat, derived from Lunar concepts. 2011 modelling[5] increased Habitat power up to 14.2 kW for a six crew, 500 day

surface stay. More recent[6] models suggest 17.258 kW for a six-crew, long duration surface habitat. Note that this latest model assumes partially closed regenerative air and water loops; if fully closed loops were employed, more power may be required[7].

Mars Sample Laboratory

A separate laboratory space could mitigate crew contamination of Mars science samples. The Sample Laboratory is envisioned as an unpressurized tent-like structure with a robotic manipulator (such as NASA's Robonaut) tele-operated from the Habitat to perform "hands-on" sorting, analysis, and packaging. In lieu of a laboratory design or equipment list, the Study Team used actual power requirements for three representative International Space Station racks. Because these were actuals, the 30% margin was not used for these line items.

Mobile Powered Equipment

Mobile powered equipment may be recharged from the fission system while visiting the Landers. For the purpose of this exercise, the 1,638 W "other" allocation in the Surface Habitat power budget is intended to cover mobile equipment recharging but, again, this is an area of uncertainty until mobility systems are better defined.

EXPLORING ALTERNATIVES

Having determined a fission system power budget of at least 34 kWe, the Study Team next pondered how best to minimize power system landed mass.

Kilopower Alternative

The surface power system must provide at least 34 kWe, but not necessarily in a single package. Mission needs could be met with various combinations of multiple, smaller power sources. One alternative to the single, large FSP is a smaller fission system called a Kilopower unit being developed at the NASA Glenn Research Center[8]. Like the FSP, the Kilopower concept employs Stirling power conversion; but in contrast to the FSP's pumped Sodium-Potassium heat transport system, the Kilopower concept relies on simpler heat pipes directly coupled to the Stirlings. With fewer moving parts and a smaller reactor core, the Kilopower concept offers a compact, lower mass solution as compared to the equivalent FSP design (Figure 3). With its parasol-like deployable radiator, the 10 kWe Kilopower concept stows quite compactly. Current 3 and 5 kWe concepts feature fixed radiators, but could be designed for the more compact deployable radiators. Table 4 outlines system characteristics for the family of Kilopower concepts. Although too small for this application, the 1 kWe is shown only for comparison purposes.

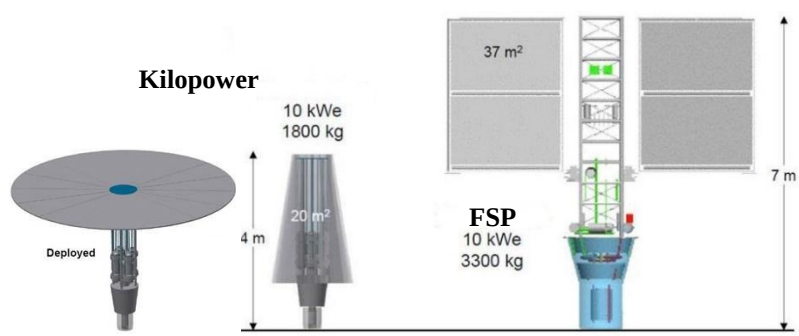

FIGURE 3. 10 kWe Kilopower vs. 10 kWe FSP Comparison.

One obvious advantage of breaking the power system up into smaller packages is that it allows power system development to proceed with lower risk, even before mission design has been finalized. For example, if the crewed surface mission requirements grow to require 43 kWe of power, the original scheme would have required a late-stage FSP redesign or a second 40 kWe unit to be manifested at a seven ton mass penalty, compared to only a 0.75 to 1.5 ton mass penalty to add an extra Kilopower unit to the manifest. Conversely, the need for only a few kilowatts on a precursor mission might drive overall program cost to develop a sub-scale FSP demonstration system, whereas even a small precursor lander could carry a full-scale Kilopower unit.

TABLE 4. Kilopower System Characteristics.

Power System Characteristics	User Power (kWe)				
	1.0	**3.0**	**5.0**	**7.0**	**10.0**
Reactor core power (kWt)	4.3	13.0	21.7	30.3	43.3
Separation Distance for a single unit dose <3mR/hr (m)	100	200	300	400	500
Radiator area (m^2)	3.2	9.6	13.5	17.1	20.0
Stowed diameter (m)	1.1	1.2	1.3	1.4	1.5
Stowed height (m) with fixed radiator	3.0	4.9	5.9	6.7	7.3
Stowed height (m) with deployable radiator	N/A	2.2	2.7	3.0	3.3
Mass Summary (kg)					
Reactor	136	175	198	215	235
Shield	148	272	364	443	547
Balance of Plant	122	304	449	589	763
Kilopower Unit Total Mass (kg)	**406**	**751**	**1011**	**1247**	**1545**

Optimizing Spares Mass

One option for reducing contingency mass is to increase FSP reliability and eliminate spares altogether. But the FSP could fail from external damage (such as debris plume from another Lander or a robotic rover mishap) and that could be catastrophic during a dust storm that prevents the crew from simply returning to orbit. If a single FSP were replaced with, for example, four each 10 kWe Kilopower systems, it's unlikely that all four would fail; therefore it isn't necessary to carry four spares. To obtain an "apples to apples" mass comparison between options, the following assumptions were used:

a. The combination of primary power units must meet or exceed 34 kWe.
b. Contingency power must meet or exceed 10 kWe total (arbitrarily selected as the largest Kilopower increment).
c. High voltage transmission cable is assumed at 60 kg per km, while low voltage DC cable ranges from 1,028 kg for a basic 3:2 copper conductor to 1,349 kg for 1 km of armored cable; this study assumed 1,100 kg.
d. In lieu of a specific design, it was assumed that an Inverter/Junction box would be about 150 kg for all options.
e. In lieu of a detailed design, it was assumed that the jumpers ganging Kilopower units together were 10 m long (arbitrarily selected to be longer than the worst-case distance between units, plus margin to navigate around surface obstacles). Connectors were assumed to be 5 kg each to account for robotic handling and dust resistance.

As shown in Figure 4, all four Kilopower options result in lower cumulative mass when contingency power and cables are included. Even without contingency power, all but the 3 kWe Kilopower options have lower cumulative system mass than a 40 kWe FSP. In fact, four each primary plus one contingency 10 kWe Kilopower unit (50 kWe total), is about 200 kg lower cumulative mass than a single 40 kWe FSP with no contingency. Of the Kilopower options, the 10 kWe trades best for cumulative system mass. Sparing strategy will depend on risk tolerance but if only one or two spares are needed, overall landed mass could be reduced by as much as eight metric tons.

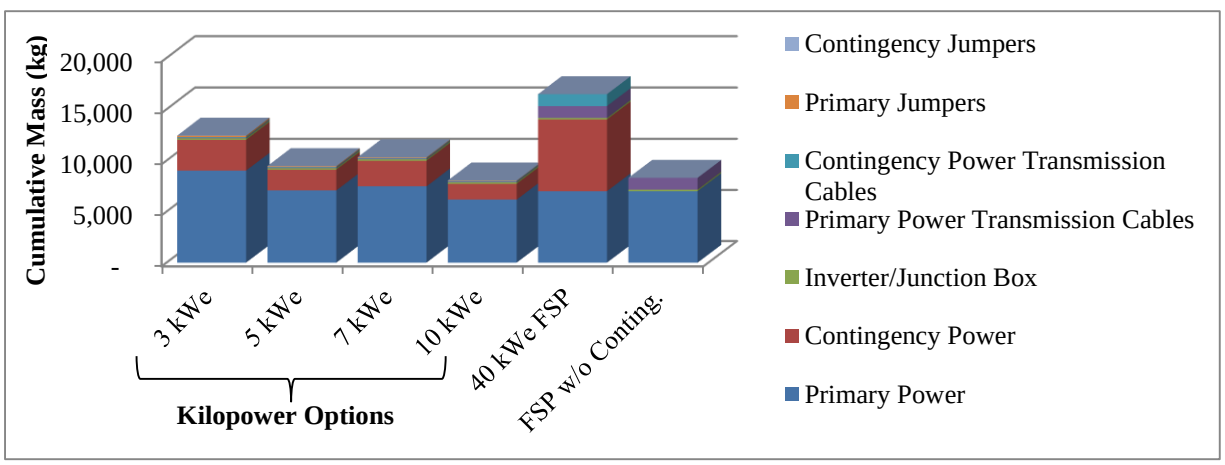

FIGURE 4. Mass Comparison of Fission System Options for 34 kWe Minimum Cumulative Power.

Optimizing Lander Power Mass

In the original scheme, the Cargo Lander must be self-sufficient for power for up to 40 sols while the single FSP is being relocated one kilometer, deployed, and activated. During that time, the Lander must provide keep-alive power to the MAV. Accelerating power system activation could dramatically reduce the Lander's internal power burden (which in turn could reduce Lander thermal and structural system mass, with flow-down impacts to descent propellant mass). Employing multiple, smaller units would allow an important operational change: one unit could be activated immediately near the Lander to sustain Lander functions while the remaining units were off-loaded and relocated. Once the rest of the systems were on-line, the first unit could then be turned off, repositioned, and reactivated. Because initial power system activation occurs on the cargo mission (before crew arrive), crew safety issues are minimized, though obviously Lander and other cargo electronics would have to be properly shielded.

Optimizing Surface Transportation Mass

At seven meters tall, the 40 kWe FSP is bigger than current pressurized rover concepts, making relocation a challenge. Either the FSP needs a dedicated mobility system, or the mobility systems used for other surface applications must accommodate the FSP, but both of these options are inefficient. By breaking the power system into smaller packages, these smaller units are more likely to fit onto existing mobility systems, eliminating the need for a dedicated mobility system.

Kilopower Concept Advantages

This study identified several additional advantages of the Kilopower concept over the baseline FSP.

Lower Startup Power

With fewer moving parts, a Kilopower requires the equivalent of two D-cell batteries for start-up. In comparison, the FSP requires an estimated 424 kg of solar arrays to supply the 5 kWe needed for startup.

Lower Cable Mass

Although both the FSP and Kilopower concepts require approximately one kilometer of 400 VAC power transmission cable, the FSP also requires a low voltage auxiliary power line due to parasitic power draw. At an estimated 60 kg per kilometer of high voltage cable versus more than 1,000 kg for the low voltage cable, the Kilopower option saves nearly a metric ton of landed mass for cabling alone. Even with the addition of a local inverter/junction box and cables to gang multiple units together, overall Kilopower cable mass is significantly lower than the baseline FSP cable, with additional mass savings for the spare FSP low voltage cable.

Precursor Mission Opportunities

At seven metric tons (eight with cabling), a full-scale 40 kWe FSP requires a relatively large Lander for Mars surface delivery. This precludes using smaller, one-ton class pre-cursor missions to demonstrate a full-scale fission surface power system. A sub-scale FSP unit could be developed for a smaller Lander, but the effort would dilute the flight design team from their primary task, and incur additional development cost. On the other hand, a single three or five kWe full-scale Kilopower unit could support pre-cursor missions with little additional development cost.

Increased Operational Flexibility

The ability to deploy small fission surface systems on precursor missions supports an "evolvable" Mars campaign by allowing a gradual buildup of assets over time. Conversely, a mission requiring a few kilowatts more than a baseline mission design would have to add at most a 1.5 metric ton Kilopower unit, rather than a seven metric ton FSP. Breaking the power system into smaller packages also opens up new opportunities: Kilopower units could be redeployed to support activities previously thought to be power-limited, such as deep drilling. Small, portable power systems could also be robotically transported over great distances, from one landing site to the next. One of the more intriguing aspects of the Kilopower concept is its potential to extend a surface crew's exploration radius around a particular landing site. Close proximity to the crew makes on-board radioisotope power problematic, so current Mars rover concepts favor solar power. However, Martian solar intensity, the possibility of dust storms, and the constraint that both recharging and driving can only be performed in daylight means that a solar-powered Mars rover will spend about 80% of its time standing still to recharge, limiting its range to only 14 km per day. The study team found that driving efficiency improved up to 46 km per day if two redundant Kilopower units were available as charging stations. Rover battery recharging could occur overnight while the crew sleeps, or battery packs could be swapped out at the charging station to minimize loiter time. For crew safety, a cable could be extended a safe

distance from the Kilopower station for charging. Four Kilopower units arrayed in pairs spaced 90 km apart could boost a pressurized rover's maximum range from the Habitat to 225 km—more than double the estimated performance of solar-powered pressurized rovers. Although these are relatively modest gains, excursion distance becomes an important factor if a campaign is limited to a single landing site. To illustrate the example, consider the distances between three areas of scientific interest and Jezero Crater, which was a Mars Science Laboratory mission candidate landing site: Nili Fossae Carbonate Plains (221 km), northeast Syrtis (81 km), and Nili Fossae Trough (246 km). Depending on the actual "terrain factor" (distance driven/range achieved), a pressurized rover with four deployable Kilopower units may be able to sweep all three sites plus Jezero Crater from a single landing point to the northwest of Jezero Crater.

Reduced Crew Separation Distance

Crew separation distance from a reactor is guided by the inverse square law for radiation dosage. A baseline 40 kWe FSP must be at least 1,000 m from the crew Habitat to keep radiation exposure below safe levels but a single 10 kWe Kilopower unit only has to be 500 m away for the same dose. Although four each 10 kWe Kilopower units ganged together require the same separation distance as the single baseline FSP, individual Kilopower units redeployed to special operations—such as deep drilling—would require smaller crew keep-out zones than the large baseline FSP. What's more, smaller units would be easier to bury or hide behind natural terrain features, which could further reduce crew separation distance.

Lower Cargo Handler/Surface Mobility Load

Autonomously handling each 751 to 1,545 kg Kilopower unit is likely to require smaller cargo handling and surface mobility equipment than what would be needed to unload/transport a seven metric ton baseline FSP, assuming the Kilopower units are unloaded individually. This mitigates the need for dedicated handling/transportation equipment.

Lower Cumulative Stowage Volume

Due to shroud packaging constraints, Mars landers are expected to be almost as volume-limited as they are mass-limited. The baseline FSP has a relatively large stowage footprint compared to the compact Kilopower units. As shown in Table 5, 40 kWe cumulative Kilopower systems require less stowage volume than the baseline FSP in all but one case. Concepts employing deployable radiators can save up to 60% stowed volume over the baseline FSP, but even the fixed radiator concepts stow as well or better than the baseline. What's more, a seven metric ton FSP must be carefully counter-balanced on a Lander to prevent landing instability problems, whereas multiple Kilopower systems are more easily distributed around the Lander cargo deck as needed for proper balance.

TABLE 5. Power System Stowed Volume Comparison

Power System Size	Concept Preliminary Dimensions	Per Unit	40 kWe Cumulative
40 kWe Baseline FSP	2.7 m Wide x 3.3 m Deep x 7 m Tall	62.4 m^3	62.4 m^3
10 kWe Kilopower	1.5 m Dia. x 3.3 m Tall (Deployable Radiators)	5.8 m^3	23.2 m^3
	1.5 m Dia. x 7.3 m Tall (Fixed Radiators)	12.9 m^3	51.6 m^3
7 kWe Kilopower	1.4 m Dia. x 3.0 m Tall (Deployable Radiators)	4.6 m^3	27.6 m^3
	1.4 m Dia. x 6.7 m Tall (Fixed Radiators)	10.3 m^3	61.8 m^3
5 kWe Kilopower	1.3 m Diameter x 2.7 m Tall (Deployable Radiators)	3.6 m^3	28.8 m^3
	1.3 m Dia. 5.9 m Tall (Fixed Radiators)	7.8 m^3	62.4 m^3
3 kWe Kilopower	1.2 m Diameter x 2.2 m Tall (Deployable Radiators)	2.5 m^3	35.0 m^3
	1.2 m Diameter x 2.7 m Tall (Fixed Radiators)	3.1 m^3	43.4 m^3

Kilopower Concept Disadvantages

Higher Cumulative HEU Mass

The smaller the reactor, the less Highly Enriched Uranium (HEU) is required but the correlation is not linear. Although each 10 kWe Kilopower unit only needs 50 kg HEU compared to the 110 kg required for a 40 KWe FSP, four Kilopowers would need 200 kg between them, or 250 kg if one spare unit is included. In the worst case (twelve each of the 3 kWe units), the Kilopower concept requires more than twice as much HEU as the baseline scheme.

Increased Security/Launch Safety Overhead

Breaking the power system into multiple packages could complicate ground handling and processing if it requires more oversight to follow and secure multiple units in different stages of production. Depending on how the power system is packaged on the launch vehicle, there may be increased safety overhead to analyze launch failure dispersion of reactor materials, or to design, test and certify packaging to ensure that all units stay together in the event of a launch failure. Note that for transportation architectures utilizing an aeroshell for Mars entry and descent, the aeroshell itself could help keep Kilopower materials together without additional mass penalty. One approach considered for minimizing security overhead was to switch from High to Low Enriched Uranium (LEU). A preliminary estimate of a 1 kWe LEU system found that the core fuel mass increased from 30 to approximately 300 kg, with the reactor mass increasing from 136 to approximately 700 kg. Overall system mass more than doubled, from 406 kg with HEU to over 1,000 kg with LEU. The mass increase for larger Kilopower systems can be extrapolated to more than 3 tons for a 10 kWe system, eliminating many of the advantages of the Kilopower concept. Aside from the complications of transporting a 300 kg reactor core, the mass eliminates an LEU Kilopower as a candidate for smaller in-space science payloads, or surface precursor missions.

Additional Surface Delivery Trips

A baseline FSP requires a single delivery trip to relocate it from the Lander to the installation site, though it is likely to be a slow trip with a seven metric ton payload. The number of trips required to deliver the entire complement of Kilopower units will depend on reactor size and how many units can be transported at one time. Current pressurized rover concepts could carry at least one 10 kWe unit, or at least two of the 3 or 5 kWe units. Once the rover has mapped a route on the first delivery, subsequent delivery trips should be relatively straightforward, with the main penalty being wear and tear on the rover.

Increased Operational Complexity

The baseline FSP requires two cables with a total of four connections (one at each end of each cable). A "Kilopower Farm" consisting of multiple small units only requires a single power transmission cable back to the Lander, but would need an inverter/junction box to gang together the individual power systems. The total number of connections will depend on the number of Kilopower units in the power farm; for example, four each of the 10 kWe units would require a total of 10 connections: two for power transmission (one at each end of the power transmission cable), and eight to gang together the four reactors (one at each end of the four jumpers between the reactors and the inverter/junction box). In the worst case of 12 each 3 kWe units, a total of 26 connectors would be required. Connector mass is not necessarily an issue, but so many field connections increases operational complexity, particularly when made robotically in a dusty environment. Risk can be reduced by making as many connections as possible in advance. For example, at least one end of each Kilopower-to-Inverter Box connection can be made on Earth, as can both ends of the power transmission cable (per the original FSP operations concept), reducing the number of field connections to no more than 12. Further reduction is possible if several Kilopower units can be deployed together with the junction box, already connected.

Potentially Lower Overall System Reliability

Due to its internally redundant design, the reliability of each Kilopower unit is expected to be quite high. The weak link from a system reliability standpoint then will be in the connections between the individual Kilopower units. As noted in a United States Air Force study[9] of electronic component failure rates, connectors are a leading cause of reliability problems for many avionics systems. As with the baseline FSP design, Kilopower connectors must resist Martian temperature cycling, launch/landing vibration, and corrosion. But as noted above, the risk of contaminant-induced failure is likely to be higher with the Kilopower systems due to the number of robotic field connections. Risk can be reduced by manifesting extra Kilopower-to-inverter box cables with connectors, or by adding redundant connectors to the Kilopower units themselves. Regardless, a robust connector design, capable of robotic operation and tolerant to surface dust contamination will be critical to the Kilopower concept for Mars surface applications.

10 kWe Scaling Limit

The Kilopower concept is expected to scale readily up to 10 kWe, but not beyond. Applications requiring very high power may be better served with an FSP design, unless multiple Kilopower systems can be ganged together.

Large Deployed System Footprint

The original scheme called for an FSP to be placed on a clear, level spot at least one kilometer from the Crew Habitat. Although the FSP's reactor core is a modest 0.8 m diameter at the base, the 34 m wide deployed radiators

require a relatively large area free of obstacles taller than about 3 meters. With their fixed or parasol-like deployed radiators, individual Kilopower units are considerably more compact, but ganging several of them together would require a large cumulative footprint. Separation distance between units will depend on final reactor and radiator designs, but will need to ensure radiators do not cross-communicate, and that failure of one unit cannot compromise nearby units.

Planetary Protection Considerations

Like all other crewed mission equipment, the power systems must comply with NPI 8020.7/NPD 8020.7G[10]. Planetary protection considerations are expected to be the same regardless of whether FSP or Kilopower units are used. As a general rule, neither the Crew Habitat nor the power system(s) will be located in a "special region" where water—and thus potential organic material—are likely to occur. The difficulty comes in preventing the power system itself from creating a localized special region by melting nearby ice. This may impact radiator design (to ensure heat radiates up, rather than down towards the regolith), or it may impact reactor baseplate design.

SURFACE POWER SYSTEM UNIQUE NEEDS

This study identified a number of power system features unique to a surface application that wouldn't necessarily be required for orbital or interplanetary systems, and are noted here for the purpose of commonality discussions.

Dust Tolerant Mechanisms. Because the surface power system will be exposed to dust storms--some lasting months-- power system mechanisms must be tolerant to surface dust contamination. For example, deployable radiators and connector covers must be robust to surface dust.

Robotic Handling. Because the surface power system is intended to support propellant production before the crew arrives, it must be robotically unloaded from the cargo lander, deployed a safe distance from the eventual crew habitation area, and activated. During crewed phases of the surface mission, individual power systems may need to be robotically re-deployed to remote areas to support exploration activities.

Surface Transport. The power system must be robust to surface transport, as it will be transported a safe distance from the eventual crew habitation area, and may be re-deployed to remote areas to support exploration activities. There are currently no plans to groom roadways on Mars.

Restart Ability. The ability to stop and start surface power systems allows mission planners the flexibility to relocate assets, add new assets, or allow crew to safely approach for inspections or repairs.

Surface Environment Compatibility. Unique design features must function in the Mars environment (gravity, atmosphere, temperature variations, etc.)

Planetary Protection. If the power system generates enough heat to melt surrounding ice it potentially creates a localized "special region" that would have implications for how close crew, crew rovers, or habitats be located. At best, this could complicate certification; at worst, it could drive cable mass.

System Connectivity. Surface power systems may be required to operate alone, or in combination with like systems. To minimize mass, it is desired to tailor power systems for a particular mission. This may involve ganging together multiple systems to support a large power load, or operating a single system to support a particular activity.

CONCLUSIONS

MAV propellant production is the single largest driver for surface mission power. Maximum surface power needs are estimated to be at least 34 kWe during the un-crewed cargo phase. Power needs drop only slightly to at least 33.6 kWe during the crewed portion of the surface mission; selective operations could reduce power needed near the Habitat to as low as 24 kWe. Estimates include 30% margin, but should be considered preliminary pending additional studies planned for 2015. Switching to multiple, small Kilopower systems are estimated to save 4 to 8 metric tons of landed mass, as compared to the baseline 40 kWe FSP concept, depending on sparing strategy. Breaking the power system up into smaller packages also helps minimize power system activation time, reduces

mobility system impacts, and allows Program Managers flexibility to absorb late mission changes, with less schedule or mass risk. All of the Kilopower concept options considered trade more favorably than the baseline FSP for landed mass and stowed volume. The baseline FSP offers lower complexity, but sacrifices operational flexibility. Of the Kilopower options, the 10 kWe solution trades best for landed mass, stowed volume, and operational complexity. Deploying four Kilopower units into the field allows a conceptual pressurized rover to explore up to 225 km from the Lander, more than doubling the 98 km range offered by solar-only pressurized rover concepts. This could be important for campaigns limited to a single landing site. Small Kilopower units offer additional operational advantages, including the possibility of supporting a 1-ton (Curiosity-class) precursor mission, or building up capability over time. On the other hand, there are several disadvantages to the Kilopower concept that must be carefully balanced against the mass and volume savings before selecting a system for the Mars surface application.

It must be emphasized that this exercise was not intended to recommend a particular Mars surface power system. The intent was to explore ways to minimize power system mass and volume. The results of this exercise will feed into a Mars Lander cargo packaging study and operations model, to compare different mission options. Final decisions regarding Mars surface power must weigh programmatic considerations such as funding availability, desired commonality with other missions, development schedules, life cycle costs and both ground and flight safety. Mars human system architectures may deviate from current concepts which could significantly alter power system needs for future crewed Mars surface missions.

ACKNOWLEDGMENTS

The author wishes to acknowledge contributions from the following study team participants and colleagues: Dr. Andrew Abercromby, Kevin Watts, Lee Mason, Don Palac, Dr. Steve Hoffman, Jason Poffenberger, Ryan Whitley, Alida Andrews, Jeff George, Dr. Joshua Kennedy, Steve Chappell, Dr. Mike Gernhardt, Pat Loyselle, Tony Colozza, Pat George, Jerry Sanders, Todd Peters, and Dr. John Warren.

REFERENCES

[1] NASA-SP-2009-566, *Human Exploration of Mars Design Reference Architecture (DRA) 5.0*, National Aeronautics and Space Administration, Washington, D.C. (2009).
[2] NASA/TM—2010-216772, *Fission Surface Power System Initial Concept Definition*, Fission Surface Power Team, National Aeronautics and Space Administration and Department of Energy, Washington, D.C. (2010)
[3] JSC 66738, *Design Considerations for a Crewed Mars Ascent Vehicle (MAV)*, National Aeronautics and Space Administration, Johnson Space Center, Houston (2014).
[4] Toups, L. et al, *Mars Surface Habitat System Sizing Report*, National Aeronautics and Space Administration, Johnson Space Center, Houston, Texas, 2007.
[5] Simon, M., *HAT Cycle C: Mars Transit Habitat and Mars Surface Habitat Modeling*, NASA Langley Research Center, Hampton, Virginia (2011).
[6] Provided by NASA/LARC/Matt Simon via electronic mail communication (December 8, 2013).
[7] Hanford, A.J., JETS-JE33-13-TAED-DOC-0046, *Martian Surface Habitat Lander Environmental Control and Life Support System Study for Fiscal Year 2013*, National Aeronautics and Space Administration, Johnson Space Center, Houston (updated February, 2013).
[8] Mason, Lee, et al, TM-2013-216541 *Kilowatt-Class Fission Power Systems for Science and Human Precursor Missions*, National Aeronautics and Space Administration, Cleveland (2013).
[9] Denson, William K, RL-TR-92-197, *Reliability Assessment of Critical Electronic Components*, I IT Research Institute, Rome Laboratory, Air Force Systems Command, Griffiss Air Force Base, NY (July, 1992).
[10] NPI 8020.7/NPD 8020.7G, *NASA Policy on Planetary Protection Requirements for Human Extraterrestrial Missions*, National Aeronautics and Space Administration, Washington DC (2014).

Engineering Space Nuclear Power Systems Using a System of Systems Perspective

Rebecca Onuschak[1], Carl E. Sandifer II[2]

[1]*Office of Space and Defense Power Systems, Office of Nuclear Energy, US Department of Energy, Germantown, MD 20874; 301-903-0023; rebecca.onuschak@nuclear.energy.gov*
[2]*Radioisotope Power Systems Program Office, Space Flight Systems Mission Directorate, NASA Glenn Research Center, Cleveland, OH 44135*

Abstract. The Department of Energy and its predecessor agencies have been developing, manufacturing and delivering nuclear power systems in support of space applications for more than fifty years. In addition to these deployed systems, there is a significant additional experience base available from the research and development of space nuclear technologies and systems that were not deployed for a variety of reasons. A review of decades of radioisotope power systems, fission power and nuclear propulsion programs reveals common themes in systems engineering (SE) approach that take into account the unique combination of factors that affect all types of nuclear development for space applications. This SE approach has been highly successful and there is significant documentation on a program-by-program basis, but no concise, recent reference tool is available to stakeholders to explain why the methods work and the basis by which SE application and tailoring decisions should be approached.

Common understandings within the space nuclear community of both the current SE approach and the system development environment are necessary to support informed discussion of the challenges inherent in developing these systems. While the authors acknowledge that some of the factors driving complexity and uncertainty may be inherently irresolvable, developers and stakeholders have always proposed means of mitigating them, but have not adopted any common approach to evaluating their effectiveness, before or after implementation. The authors propose adoption of a System of Systems (SoS) perspective as a first step in developing a decision-making tool set. An overview of the SoS thinking is provided along with rationale for its use. Highlights of historical and current SE approaches for space nuclear power systems (NPS) are presented and evaluated in an SoS context, as are several concepts that are emerging regarding how NPS development may proceed in the future. The paper does not conclude with a single recommended SE approach, but does identify the strengths and challenges of some options that have been considered and recommends best practices for analyzing their SoS effects prior to implementation.

Keywords: Systems Engineering, System of Systems, Radioisotope Power Systems, Fission Power Systems, policy

INTRODUCTION

A review of the research, development and deployment of space nuclear power and propulsion systems reveals common themes among systems used for flight missions and those that were not. Flight use is not the only indicator of project success. In fact, several projects never used for a mission were otherwise technically successful and contributed significantly to the space nuclear systems knowledge base. Nonetheless, most projects were initiated with an ultimate flight goal, and an understanding of factors associated with use or non-use in space is an important tool for continuous assessment of the decision methods and acquisition strategies for future systems. The authors reviewed elements of historical programs, identifying common themes. This paper reviews challenges associated with the development and use of space NPS and our interpretations of factors most likely related to "success," defined only from the limited criterion of whether or not the system was used in a space mission. An overview of System of Systems (SoS) thinking is presented with a rationale for applying such an approach to the development of space nuclear systems and their component technologies. Finally, we recommend steps for incorporating practices emerging in the SoS engineering community into space nuclear systems development, with specific emphasis on requirements management and acquisition strategy.

The historical literature survey revealed the following common, highly interdependent challenges to space nuclear systems development:

1. Cost. The use of space nuclear systems generally incurs significant cost. It could be assumed that this is related to safety, but the drivers are more complex than this. The steps required to protect nuclear workers and the public from radiological hazards do affect cost, but project costs are also driven by general factors such as requirements creep, overestimation of technical readiness and changes in mission need. While the necessarily rigorous approach may exacerbate these effects, no single factor drives the cost in isolation [1].

2. Technical Complexity. The various subsystems and components of nuclear systems, whether based on radioisotopes or fission, are highly interdependent. The required environments and reliability also pose challenges, which have manifested primarily as materials issues (basic properties, materials availability and/or compatibility) or as complex subsystem requirements and interfaces [1, 2, 3, 4, 5].

3. Project Duration. A variety of factors drive project durations to the point that system development often requires a longer life cycle than that of a mission [6, 3]. This has resulted in requirements creep, changes in the mission, and even obsolescence of the nuclear system prior to its mission.

4. Lack of Clearly Defined Mission. One strong factor correlating to flight use of a system is the identification of a specific space mission with a participatory role from system development through first use. An intuitive probable reason for this is that a compelling mission can drive political will and funding to complete the nuclear projects. However, other possible explanations include insufficient or inaccurate original identification of the mission need or deviation from user needs over the development life cycle.

5. Sustainment of Investments. The technical skill base and facility/equipment set used for nuclear systems are unique, and generally inapplicable to other purposes. This is true of capabilities at DOE National Laboratories, at NASA centers and in industry. Systems, once developed, require continued investment in order to remain available. This has led to difficult decisions when budgetary resources have not been sufficient to sustain system designs or the missions that would require them. The resulting loss of capabilities informs the need to consider sustainability early in any new project.

Common approaches for addressing these challenges have included concurrent engineering, skipped or streamlined testing and multi-purpose design. These approaches may mitigate the challenges described above, but their effects are not as intuitive as they may appear on the surface. We could locate no structured approach to evaluating the effectiveness of these strategies for space NPS, before or after use. We will not attempt a retroactive evaluation of this sort, but we will discuss the importance of including the usage context in selecting and evaluating these approaches. We also propose the use of SoS thinking as a framework for integrating the usage context into the entire life cycle of nuclear systems development.

SPACE NUCLEAR POWER AND PROPULSION AS "SYSTEMS OF SYSTEMS"

No single definition exists for a "system," or for a "system of systems." A comprehensive review of the various approaches and definitions is beyond the scope of this paper, so we have selected some key concepts to further the discussion. It is useful to define a system as "the combination of elements that function together to produce the capability required to meet a need [7]." There are clearly multiple levels of systems involved in any space mission, but this in itself does not imply the existence of an SoS. The term "system of systems" is widely used, but disagreement exists on how to differentiate complex systems from SoS, the latter implying differences in the approach to engineering and/or management. The US Department of Defense offers the following explanation:

> "An SoS is defined as a set or arrangement of systems that results when independent and useful systems are integrated into a larger system that delivers unique capabilities [8]."

Although helpful as a general definition, this does not assist in determining whether a system of interest should be approached as a system or as an SoS. Maier in 1998 offered two additional criteria:

"Operational Independence of the Components: If the system-of-systems is disassembled into its component systems, the component systems must be able to usefully operate independently. That is, the components fulfill customer-operator purposes on their own.

Managerial Independence of the Components: The component systems not only can operate independently, they do operate independently. The component systems are separately acquired and integrated but maintain a continuing operational existence independent of the system-of-systems [9]."

For space nuclear systems, it is helpful to think of "independence" not as a useful existence absent *any* SoS, but as usefulness independent of *which* SoS is selected. We will define the nuclear power or propulsion system as the systems of interest. The SoS of interest could be either a spacecraft or a mission architecture for various purposes, but we propose to select the mission architecture as the SoS for system-level decision-making purposes.

SYSTEM OF SYSTEMS COMPLEXITY

For a generalized nuclear power system used in a single mission, the N2 diagram in Figure 1 is a simplified means of representing the direct interdependencies among the various components and systems at different levels. Because it represents a generalized SoS and because we are not experts in all of the represented systems, the figure represents a few broad interfaces, only for the purpose of demonstrating the potential complexity. Even for the case of a nuclear system designed for a single mission, the SoS interactions are complex due to several factors. First, most of the systems involved are complex in their own right, with multifaceted requirements and rigorously designed subsystems. Second, the nature of space mission life cycles generally requires concurrent engineering with mismatched component system development timelines. Nuclear systems projects often begin while the associated mission is in a preliminary phase, with limited funding available to support system trade studies or to refine interface definitions. In some cases, a system being designed for a notional mission will develop requirements based on known information, but without a clear pathway for maintaining alignment to the mission architecture as it evolves over time.

E=Electrical/EMI/Grounding; M=Mechanical/Structural; T=Thermal; S=Nuclear Safety

A ⟹ B Interactions

Mission Comm. Systems	E	E		E			
E	Launch Vehicle	E,M,T,S	M,T,S	M,T	M,T	M	M,S
E	E,M,T	Spacecraft	E,M,T	E	M,T		
		E,M,T	Generator Housing/ Structure	E,M,T	M,T	M,T	M,T,S
		E	M	Control Electronics	T	E	
		M,T	M,T	T	Radiator	T	T,S
			M	E	T	Power Conversion	T,S,M
			T		T	M,T	Heat Source

Interactions A ⟸ B

FIGURE 1. System Interactions for a Generalized Mission Architecture Using Nuclear Power

In addition to the above types of interactions, an added layer of complexity arises from a common desire to leverage the greatest value from development efforts by designing components, subsystems, or whole systems to be usable in a multi-purpose or multi-mission context. The greater the number of application options that are desired for any given system element, the more complexity is introduced among systems. While this may predict development cost savings for the individual systems, there may be offsetting effects at the SoS level.

HISTORICAL MISSION SUCCESS FACTORS

In order to understand the issues that have challenged past nuclear development efforts, we conducted a brief literature review, focusing on potential lessons or good practices related to mission use of a system. In this survey, summarized in Table 1, we identified two common, but not universal, themes associated with flight: 1) relationship to a specific first mission, and 2) technical challenges in the system development.

The connection to clarity of mission requirements has also been cited in multiple published lessons learned documents [10, p. 100, 11, 12]. There are numerous possible explanations to this correlation, including the following:

- weak original mission need (technology "push" due to possible benefits, not a "technology gap");
- technology obsolescence, or perceived obsolescence, before mission launch;
- requirements creep as potential missions changed while progressing concurrently with system development; or
- accessibility of stakeholders with authority to clarify requirements and support decision-making.

It is not possible to determine conclusively the root causes behind specific past project outcomes, but there is the potential to mitigate the factors in the above list.

The second notable correlation to systems not used in flight is unexpected technical challenges [12, 2]. This may, in some cases, be related to the above relationship between mission need and project outcomes. Promising technologies may be incorporated into system development projects to drive progress, and those systems are in turn more viable when supporting missions. This is not to imply that technologies are deliberately selected before they are likely to succeed; rather, that long development cycles can drive programs to adopt a concurrent engineering approach at multiple simultaneous system levels. This approach has often been very successful, but incurs risk of losing promising technologies that may have thrived in a serial development model.

CURRENT SYSTEMS ENGINEERING APPROACH

Formal SE approaches have formed the basis of nuclear systems development since their origins in the SNAP program [18, 4, 6, 20, 16]. Mission needs are identified and converted into formal, traceable requirements, which in turn are developed into alternative system concepts and eventually realized in systems that undergo rigorous verification and validation processes. Figure 2 presents a generalized view of the SE process commonly applied to nuclear systems development, adapted with permission from an earlier representation of the DIPS technology program SE approach [20]. The details of the SE approach are beyond the scope of this paper, but incorporate common elements. Although these have been applied to varying degrees, the following reflect best practices:

- Nuclear systems generally support costly missions. Mission success probability is an important criterion in system selection and design [1, 21].
- Analysis and testing are used together at multiple levels – components and materials, subsystems, full system prototypes, and qualification systems. SoS levels above the system are also supported, as physical and software models and prototypes are provided to spacecraft designers for their use [21].
- Rigorous quality assurance practices evolved from both the nuclear and aerospace sectors are applied. This is particularly important when emergent properties cannot be understood using predictive specifications. Necessary system attributes are verified by testing, followed by process control to ensure consistency.
- For the most successful projects, users of the systems are highly involved in requirements development, and remain engaged throughout the system development life cycle.

TABLE 1. Historical Overview of Space Nuclear Systems Projects

Project or System	Requirements Basis	Outcome
Radioisotope Power Systems		
SNAP-1 (mercury Rankine), SNAP-1A (thermoelectric)	Air Force earth-orbiting satellite mission requiring 500 We and a 6-month design life (SNAP-1). Later changed to 125 We and 1 year (SNAP-1A) [13] (note – sources vary)	SNAP-1 replaced with SNAP-1A before mission was cancelled [14].
SNAP-3B	SNAP-3 demo design adapted for Navy Transit applications. Design was modified and additional tests conducted [14]	Launched on Transit 4A and Transit 4B satellites [14].
SNAP-9	Designed to purpose for Transit satellites.	Used for 3 Transit 5 satellites [10, p. 151].
SNAP-11 (thermoelectric) SNAP-13 (thermionic)	Both designed for fueling with Cm-242 and designed for Surveyor mission with 90-day mission life [13].	Mission decided to use solar power [15, p. 10].
SNAP-19	NASA Nimbus weather satellites. Design modified for Pioneer missions and modified further for Viking landers [10, pp. 163-164]. Original design life was 5 years [13].	Launched on Nimbus-B-1, Nimbus-III, Pioneer 10/ 11, Viking 1/2 [10, p. 151]
SNAP-27	Originally for Surveyor Roving Vehicle; later redirected to support Apollo program [10, p. 65]	Used on multiple Apollo missions.
Transit-RTG	Designed for Navy Transit; used updated thermoelectrics versus SNAP-9As [10, p. 75]	Used for Triad satellite [10, p. 73].
MHW RTG	Designed concurrently with known missions – NASA "grand tour" (later Voyager) and DoD Lincoln Laboratory Satellites [10, p. 73].	Used for Voyager 1/2, LES 8/9
GPHS-RTG	International Solar Polar (later, Ulysses) mission; Galileo mission updated baseline to add GPHS-RTG as it was being developed, instead of refurbished MHW-RTGs [16]	Used for Galileo, Ulysses, Cassini and Pluto New Horizons missions
MOD-RTG	Designed to use advanced thermocouples. No specific mission; environments based on shuttle launch [2].	Experienced technical challenges. Not flown.
DIPS	More than one program was known as DIPS. Multiple conversion technologies. No specific mission in the 1970s. 1980s program was for Air Force Boost Surveillance and Tracking System [17].	Mission cancelled. Not flown.
AMTEC	No specific mission, but envisioned for use on generic spacecraft concept known as X2000. [3].	Experienced technical challenges. Not flown.
MMRTG	Designed for general deep space and Mars missions, with Mars Science Laboratory (MSL) as first application. Late 1990's Europa concept was the basis for deep space requirements.	Currently in use on MSL.
SRG-110	Designed in parallel, with same requirements as MMRTG. When MSL down-selected to MMRTG, Mars emphasis was reduced.	Cancelled due to cost growth; used hardware to demo ASRG technology.
ASRG	Project initiated after successful testing of advanced Stirling engines in SRG-110 generator design. Initially adopted same requirements as SRG-110.	Cost growth and delays due to technical challenges. Flight development stopped.
Reactor Power and Propulsion Systems		
SNAP-2	First design in space reactor program, started in 1955. Mercury-Rankine conversion system, 3-5 kWe.	Two reactors ground tested. Flight demo plans cancelled due to funding [11].
SNAP-8	30-60 kWe mercury-Rankine reactor. No specific mission. Initially, AEC developed reactor system while NASA developed power conversion. Later, multiple power conversion systems were treated as interoperable with reactor system [11].	Two reactors built. Both had fuel issues during tests. Program eventually stopped due to funding [11].
SNAP-10A	Specific Air Force mission request. Initially to be 300 We. Redirected to use modified SNAP-2 core for 500 We [11].	Ground and flight tested; mission cancelled [11].
SNAP-50	Rankine-cycle nuclear electric power plant for electric propulsion and power needs. No specific mission [18].	Funding gradually reduced until project not viable [11].
SP-100	Designed for NASA and DoD applications during a time when high power needs were anticipated, but mission was not firmly defined at the start [6].	Envisioned missions did not occur. System not flown.
Prometheus	Designed specifically for Jupiter Icy Moons Orbiter (JIMO) Mission. 200kWe plant with 15-20 year life [5].	Cancelled when associated mission was cancelled.
Rover/NERVA/KIWI	Initially envisioned for missile applications, but over time multiple potential military and civilian applications considered [19].	Successful ground tests, but missions did not occur.

- Formal, independent reviews are conducted at critical steps of the development cycle. At a minimum, the areas reviewed include mission need; technology readiness before insertion into a system; requirements, analysis of alternatives and conceptual design; technical, cost and schedule baselines; preliminary and final designs; manufacturing readiness; test readiness; system acceptance; and turnover to the mission user.
- Hardware testing complements the review cycle. Subsystem testing precedes technology readiness reviews. Component testing culminates in fabrication of an engineering unit/prototype system (or significant system elements for some fission-based systems), built to the preliminary design. This step serves to 1) validate models, 2) confirm emergent behaviors of the system and 3) validate requirements prior to final design. Flight qualification, using flight-identical hardware to the extent feasible, precedes flight system fabrication and delivery. This sequence may require exceptions for long-lead work to support project objectives, but the associated risk is formally documented and accepted [20, 21, 18].

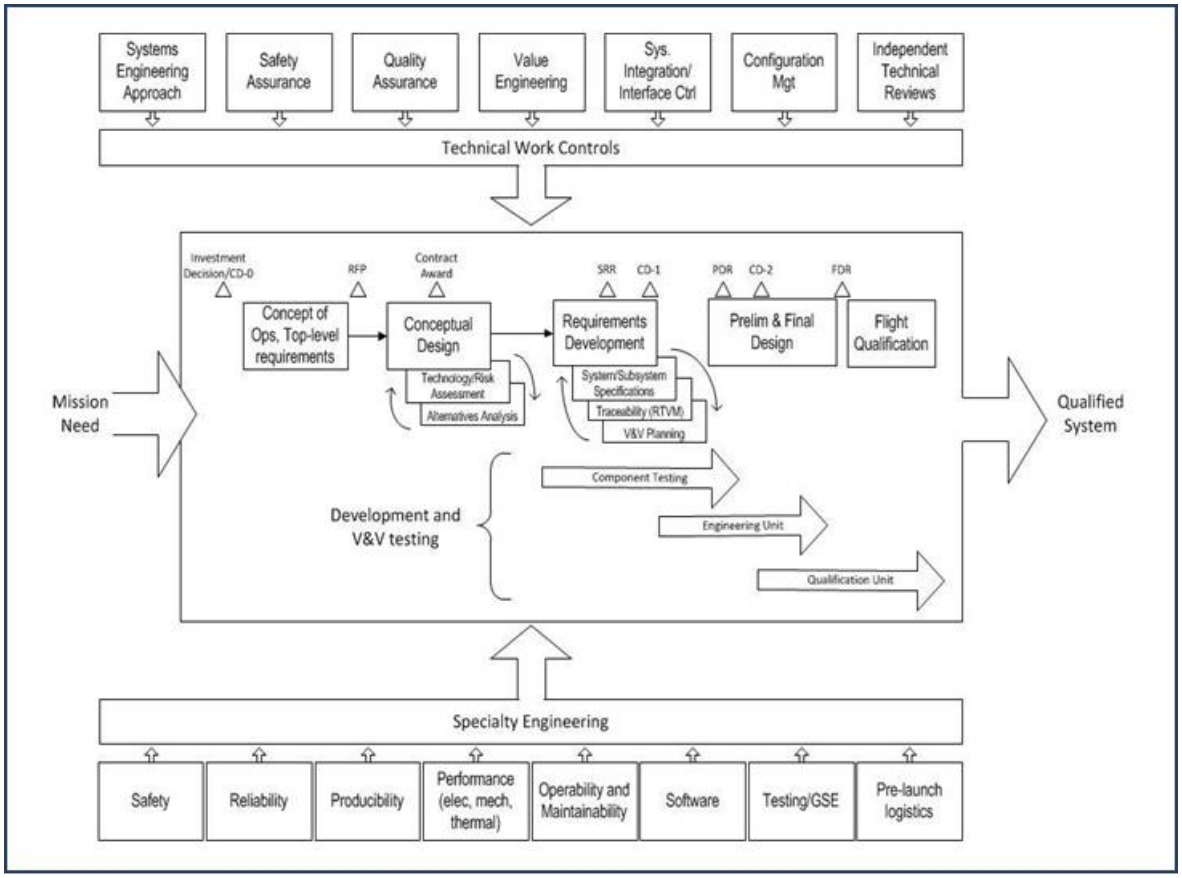

FIGURE 2. Generalized SE Approach for Space Nuclear Systems

ADAPTATIONS TO INCORPORATE A SYSTEM OF SYSTEMS PERSPECTIVE

SoS Engineering is evolving into a discipline unto itself, with distinct differences from the standard SE approach [8, 9]. This field can't be addressed comprehensively in a short paper. We recommend that DOE and NASA jointly perform a more rigorous assessment of the applicability of SoS emerging practices prior to their implementation, but from our initial review we believe that some key practices are particularly suited to the challenges of space NPS development. The most important elements for the purposes of this paper are those that support the design and development of individual systems within an unclear SoS context. We have chosen to focus on SoS engineering practices related to system-level decision-making and communication with multiple mission users. Inclusion of the following SE elements at the nuclear system development level may help to ensure that appropriate consideration is given to SoS influences on organizational processes, design approach, acquisition strategy, and the selection of SE processes and tools.

Element 1: Formal definition of the SoS context for a system or technology development effort
Perhaps the most important step in adopting an SoS framework at the system level is formally defining the overall SoS objectives and the role of the system in meeting them [22, 8]. It is important to define which missions, even notional ones, will form the SoS basis for system requirements, and how this basis may be changed. NASA has already taken steps in standardizing this process when it established its RPS Program. The RPS Program engages the science mission community, coordinating needs of multiple missions and serving as the requirements authority for new nuclear system development projects. However, additional steps could be taken for future systems, to require a formal approach to defining and controlling the configuration of the basis SoS. Missions that may use a nuclear system should participate in initial requirements development and in ongoing system design decisions. This occurs to varying degrees already, but no standard process exists to ensure continued alignment of the nuclear system to the evolving mission. Potential missions should be encouraged to define high level concept of operations (ConOps) documents at the SoS level [23] as early as possible, which may be used to generate a nuclear system ConOps with clearly defined interfaces. The ConOps should be maintained by the mission and made available to system developers, with the potential interfaces to nuclear systems maintained under configuration control and revisited periodically as the mission architecture evolves. If multiple potential applications are being considered, it is also important to define how system trades will balance competing objectives and to establish overall measures of effectiveness that span the needs of multiple missions. Formal value studies, conducted early in the mission need definition process and with the full participation of mission representatives, may be a helpful tool in this process [24]. Once established, the documented ConOps, value studies and any measures of effectiveness and requirements derived from them should be used as an evaluation basis for system and technology reviews.

Element 2: Understanding of non-technical factors affecting SE trades and decisions [8]
It is important to understand not only the technical objectives of each potential mission, but the other factors that affect its trades and decisions. This will include things such as political influences, available budgets, launch date constraints, and the status of other systems being developed to support the mission. These factors may require a mission to design an architecture incorporating elements that may not appear to be the most technically favorable absent such influences. Similar factors of course also affect standard SE approaches at all levels, but the key difference here is identifying a means of monitoring these at the SoS level, where not all factors may be obvious at the individual system level. Means of including these factors should be considered in formulating the SE approach.

Element 3: Adoption of an SE process acting at the SoS level
An important principle in SoS engineering is understanding SE functions for both the SE and SoS life cycles [8, 23]. SE plans for technology and system development projects should consider not only the known or assumed mission needs and requirements, but also should account for the span of control available to different participants [9]. Particularly important is the role of multiple SoS missions or programs in setting requirements, establishing measures of effectiveness, and making decisions. In absence of a clearly identified mission, projects often work to internally-generated assumptions about the SoS, or may consult with a mission for initial assumptions and then disengage. There is no incentive in this context to make SoS assumptions that add cost or difficulty to the system-level implementation, but if these issues are transferred to the mission, the nuclear system may become impractical. One potential solution would be to establish an SE proxy organization to perform the SoS roles. The RPS Program demonstrated such a process by acting in the role of “surrogate mission” for the ASRG project in the context of a specific Discovery Program Announcement of Opportunity. This was a critical first step, but further refinement is underway to formalize the links between surrogate missions and real missions, and to define the transition process. Efforts have been made to include real mission users as early as possible, but this can be challenging while missions are notional and resources are limited. It will be important to ensure that such participation does not convey financial responsibility or other commitments related to the nuclear system development or preclude participation in any competitive processes.

At a minimum, functions that should be assigned to an SoS engineering team should be 1) ensuring that SoS-level cost effects, benefits and risks are included in system trades; 2) exercising configuration control over decisions that support multiple SoS architectures; and 3) aligning nuclear systems projects with the SoS life cycle (e.g. other SoS element development cycles, key SoS downselect processes, reviews, and decisions).

Element 4: Prioritization of design attributes supporting multi-mission use

Assuming that nuclear systems and their components will continue to be developed for use in a multi-mission context, design goals should be selected to promote success in such a context. Historically, systems have been designed with emphasis on features valued by missions, such as mass, power, reliability and cost. Additional features suggested in the literature for addressing uncertainty include the use of open systems and loose coupling (interoperability) [8, 23], designs that facilitate changes to functionality, interfaces or environments (robustness) [22, 25], short development cycles to allow change [22], pursuit of stable intermediate forms (of the architecture, system designs or builds) [9] and stability of interfaces [9, 24]. There is no commonly adopted metric for establishing "interoperability" [23], and even if it existed, such a measure may not account for all of the aspects important to multi-mission nuclear systems development. The space nuclear development and user community should consider developing its own design parameters and measures for interoperability and sustainability.

Element 5: SoS perspective incorporated into system acquisition life cycle.
A structured SE approach becomes increasingly important as the systems and their applications increase in complexity, making their emergent SoS properties more difficult to predict [26]. Fortunately, the "standard" space NPS SE approach can be easily adapted to incorporate an SoS perspective. The technical approach to design and testing already incorporates an end-use context, but more could be done to formally treat SoS factors during reviews. The report of an international working group known as The Technical Cooperation Program describes a process for adding SoS perspectives to review criteria [27] at standard points in the development cycle. The approach is readily adaptable to the review cycle for nuclear systems. Similar guidance exists in the literature for considering SoS influences in acquisition strategies, with particular attention to the span of control of participants, changes resulting from concurrent design and emergent properties arising at integration [28, 29].

Element 6: Use of advanced SE tools to manage nuclear systems complexity.
The SE tool set is continuously evolving, and it is important to consider new available techniques periodically. Two specific tools not widely used on nuclear projects that could have value in managing across multiple SoS applications are SE Information Management Systems [23] and Model-Based Systems Engineering [24]. Per the International Council on Systems Engineering (INCOSE) Vision for 2020, "MBSE is the formalized application of modeling to support system requirements, design, analysis, verification, and validation activities beginning in the conceptual design phase and continuing throughout development and later life cycle phases [32]." The RPS Program is in the process of initiating model-based systems engineering (MBSE) practices, with the intent for incorporation within all of its SE activities. Elements of the approach that could be useful in the near future include standardizing SE models and data repositories for nuclear systems and the missions that may use them. If properly configuration controlled, these tools could facilitate ongoing alignment among system element design processes and provide up-to-date modeling tools to support design decisions at multiple SoS levels. The RPS Program seeks to maintain awareness of developments in NASA adoption of standardized tools and considers when and how to include nuclear systems information for use in mission trades and for communicating with potential system users.

CONCLUSIONS

A brief paper can only scratch the surface of the potential applicability of SoS engineering to nuclear systems development, and has not begun to explore related research in managing complexity. We have identified evidence to suggest that practices emerging in the SoS community may be valuable in space NPS development and have identified some potential practices to be explored further. We recommend a more thorough review of this material by a broader DOE and NASA team, with ongoing SE process engagement, prior to the initiation of any new nuclear systems projects, so that the SoS perspective can be formally included in the approaches to acquisition and systems engineering.

ACKNOWLEDGMENTS

We would like to express our appreciation to all of those who contributed to the compilation, interpretation and review of this material, with particular thanks to Dr. Gary Bennett for his assistance in locating and interpreting historical program information.

REFERENCES

[1] J. P. Kuspa, E. J. Wahlquist and D. A. Bitz, “Important Technology Considerations for Space Nuclear Power Systems,” U.S. Department of Energy, Washington, DC, 1988.

[2] GE Astro-Space Division, “Modular Radioisotope Thermoelectric Generator (RTG) Program Final Technical Report,” General Electric Company, Philadephia, PA, 1992.

[3] J. Mondt, “Space Radioisotope Power Source Requirements Update and Technology Status,” in *33d Intersociety Engineering Conference on Energy Conversion*, COlorado Springs, CO, 1998.

[4] W. W. Madsen, J. E. Neuman and D. H. VanHaaften, "Nuclear Propulsion Systems Engineering," in *Nuclear Technologies for Space Exploration*, Jackson, WY, 1992.

[5] J. Ashcroft and C. Eshelman, “Summary of NR Program Prometheus Efforts,” in *Space Technology and Applications International Forum*, Albuquerque, NM, 2007.

[6] R. V. Anderson, D. Bost, W. R. Determan, R. B. Harty, B. Katz, V. Keshishian, D. Kramer, A. F. Lillie, E. Matlin, M. P. Moriarty, D. K. Nelson and W. B. Thomson, “Space-Reactor Electric Systems Subsystem Technology Assessment,” Rockwell International, Canoga Park, CA, 1983.

[7] National Aeronautics and Space Administration, *NPR 7123.1B, NASA Systems Engineering Processes and Requirements*, 2013.

[8] US Department of Defense, "Systems Engineering Guide for Systems of Systems," v1.0, 2008.

[9] M. W. Maier, "Architecting Principles for Systems-of-Systems," *Systems Engineering*, vol. 1, no. 4, pp. 267-284, 1998.

[10] US Department of Energy, Atomic Power in Space: A History, Washington, DC, 1987.

[11] G. P. Dix and S. S. Voss, “The Pied Piper - A Historical Overview of the U.S. Space Power Reactor Program,” in *Proceedings of the First Symposium on Space Nuclear Power Systems*, Albuquerque, NM, 1984.

[12] R. O. Ballard, "REIMR - A Process for Utilizing Liquid Rocket Propulsion-Oriented ‘Lessons Learned’ to Mitigate Development Risk in Nuclear Thermal Propulsion," Marshall Space Flight Center, Huntsville, AL, 2006.

[13] US Atomic Energy Commission, "An Evaluation of Systems for Nuclear Auxiliary Power," 1964.

[14] J. L. Bloom, "Power Applications of Radionuclides," in *Research Applications of Radioisotopes to the Physical Sciences and Engineering*, Gatlinburg, TN, 1963.

[15] W. R. Corliss and R. L. Mead, Power from Radioisotopes: An Understanding the Atom Series Booklet, US Atomic Energy Commission, 1971.

[16] G. Bennett, R. J. Hemler, G. Silverman, C. W. Whitmore, W. R. Amos, E. W. Johnson, A. Schock, R. W. Zocher, T. K. Keenan, J. C. Hagan and R. W. Englehart, “Misison of Daring: The General-Purpose Heat Source Radioisotope Thermoelectric Generator,” in *4th International Energy Conversion Engineering Conference and Exhibit (IECEC)*, San Diego, CA, 2006.

[17] G. Bennett, "Dynamic Power Systems for Defense and Exploration: A Look at the Department of Energy's Nuclear Power Sources Assessment Team Report," in *7th International Energy Conversion Engineering Conference*, Denver, CO, 2009.

[18] Pratt & Whitney Aircraft, “Preliminary Development Plan for SNAP-50 Powerplant,” Middletown, CT, 1962.

[19] G. L. Bennett, H. B. Finger, T. J. Miller, W. H. Robbins and M. Klein, "Prelude to the Future: A Brief History of Nuclear Thermal Propulsion in th United States," in *A Critical Review of Space Nuclear Power and Propulsion 1984-1993*, M. S. El-Genk, Ed., New York, American Institute of Physics, 1994, pp. 221-267.

[20] G. L. Bennett, J. A. Janzen, J. J. Lombardo and A. S. Mehner, "The Dynamic Isotope Power System Technology Program," in *Procedings of the 23rd Intersociety Energy Conversion Engineering Conference*, Denver, CO, 1988.

[21] G. Bennett, “The Past as Prologue: A Look at Historical Flight Qualifications for Space Nuclear Systems,” in *Interesociety Energy Conversion Engineering Conference*, San Diego, CA, 1992.

[22] J. Dahmann and K. Baldwin, "Implications of Systems of Systems on System Design and Engineering," in *Proc. of the 2011 6th International Conference on System of Systems Engineering*, Albuquerque, NM, 2011.

[23] P. Chen and J. Clothier, "Advancing Systems Engineering for Systems-of-Systems Challenges," *Systems Engineering*, vol. 6, no. 3, pp. 170-182, 2003.

[24] INCOSE, "Systems Engineering Handbook: A Guide for System Life Cycle Processes and Activities, version 3.2.2," International Council on Systems Engineering (INCOSE), San Diego, CA, USA, 2011.

[25] R. de Neufville and S. Scholtes, Flexibility in Engineering Design, Cambridge, MA: The MIT press, 2011.

[26] C. Bloebaum and A.-M. R. McGowan, "The Design of Large-Scale Complex Engineered Systems: Present Challenges and Future Promise," in *12th AIAA Aviation Techonlogy, Integration and Operations (ATIO) Conference*, Indianapolis, IN, 2012.

[27] The Technical Cooperation Program, "Recommended Practices: System of Systems Considerations in the Engineering of Systems," *TCCP Technical Report TR-JSA/TP4-1-2014*, 2014.

[28] R. Creel and R. J. Ellison, "System-of-Systems Influences on Acquisition Strategy Development," Carnegie Mellon University, Pittsburgh, PA, 2008.

[29] R. G. Rendon, T. V. Huynh and J. S. Osmundson, "Contracting Processes and Stuctures for Systems-of-Systems Acquisition," *Systems Engineering*, vol. 15, no. 4, pp. 471-482, 2012.

[30] US Atomic Energy Commission, "Systems for Nuclear Auxiliary Power. A Report by the Commission.," 1964.

[31] D. Reed and J. Mandelbaum, "Value Engineering Throughout a Defense System's Life Cycle," *Defense AT&L*, Vols. May-June, pp. 52-59, 2009.

[32] INCOSE, " INCOSE Systems Engineering Vision 2020," INCOSE Technical Operations, Vol. September, p. 15, 2007.

Thermodynamic Analysis and Radiator Design of a Pulsed Bi-modal Radioisotope Propulsion System

Juha Nieminen[1,2], Justin Weatherford[1,3], Adarsh Rajguru[1,2]

[1]*Center for Space Nuclear Research, Idaho National Laboratory, Idaho Falls, ID 83401*
[2]*Department of Astronautical Engineering, University of Southern California, Los Angeles, CA 90089*
[3]*Department of Mechanical Engineering, George Fox University, Newberg, OR 97132, USA*

Abstract. Previous work done at CSNR, under Nathan Jerred's NIAC Phase 1 research on Dual-mode Propulsion System, proposed a bi-modal plutonium radioisotope thermal rocket. The power conversion cycle for this system would employ a closed loop Brayton cycle and operate in pulses to deliver up to 25 kW of electrical power that can be used for communications and electric propulsion. During this pulsed power generation, the waste heat will be accumulated in a lithium block, and then radiated to space over a long period of time while the system is in a "warm up" phase. Anticipated advantage was significant reduction in the size of the radiator compared to a continuous system, such as fission reactor, but no quantitative analysis was performed. In this paper we present our models of the power conversion cycle. Cycle parameters (temperatures and pressures) and radiator geometry were determined in a time-dependent flow and heat transfer simulation. Compressors and turbines were modeled using isentropic flow equations with efficiency corrections. Convective heat transfer in the radioisotope core and lithium radiator flow channels were analysed using one dimensional pipe flow mechanics. Requirements were to produce 25 kW_e for six minutes every 15 hours without exceeding 1100 K at turbine inlet. The paper will present the theoretical studies carried out in using helium and hydrogen as working fluids. In both cases cylindrical blocks of lithium with total mass of 200 kg was determined to be sufficient to sink waste heat during operation and radiate it to space between cycles. In the propulsion mode, propellant (H_2) is blown through the hot core and expelled through a nozzle, providing 20 N of thrust with specific impulse of 700s. Conducted study confirmed that pulsed Brayton cycles can operate on much smaller radiators than continuous systems, while bi-modal configuration provides moderate thrust needed for impulsive orbital maneuvers.

Keywords: Radioisotope, Propulsion, Power, Brayton Cycle and Bi-Modal.

INTRODUCTION

Previous work done at CSNR, under Nathan Jerred's NIAC Phase 1 research on Dual-mode Propulsion System, proposed a bi-modal plutonium radioisotope thermal rocket [1]. The power conversion cycle for this system would employ a closed loop Brayton cycle and operate in pulsed fashion to deliver up to 25 kW of electrical power that can be used for communications and electric propulsion. During this pulsed power generation, the waste heat will be accumulated in a lithium block, and then radiated to space over a long period of time while the system is in a "warm up" phase, i.e. when the heat from decaying plutonium is stored in the surrounding silicon. Anticipated advantage was significant reduction of the size of the radiator compared to a continuous system, such as fission reactor, but no quantitative analysis was performed.

In this paper we present our model of the power conversion cycle. Equations for turbomachinery are coupled with numerical analysis of heat transfer in the plutonium core and the lithium absorber. Complete model of the system allowed iterative design of the core and the absorber. Helium and hydrogen were the two studied working fluids, and lead to two slightly different core sizes.

The same system can also propel the spacecraft by blowing hydrogen through the hot Pu core and expelling it through a nozzle. Propulsion performance was analysed using a model similar to power generation.

POWER GENERATION

System Description

Figure 1 shows the power generation system (a Brayton cycle). Requirements were to provide 25 kW of electrical power for six minutes every 15 hours. Turbine inlet temperature was not to exceed 1100 K to limit thermal deterioration of the blades over time.

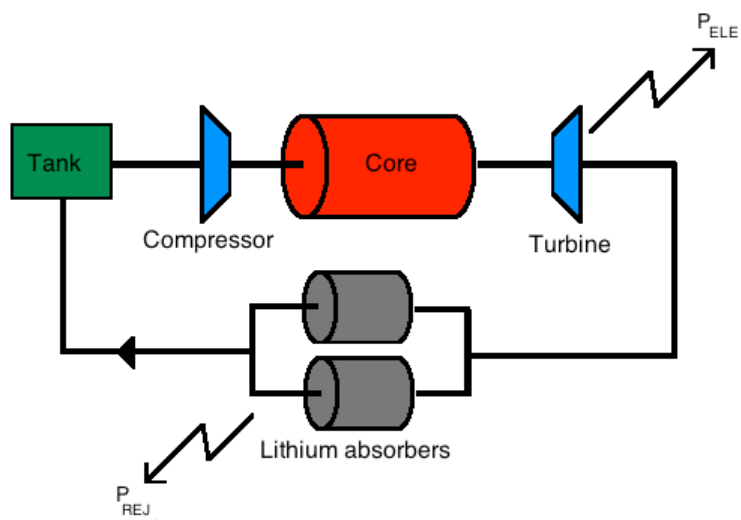

FIGURE 1. Brayton cycle for power generation.

Absorber and working fluid temperatures increase during the six minute power generation period (=blowdown), because heat is stored in the absorber to be radiated to space later. This makes the whole cycle time-dependent. Core temperature is constant 1686 K (melting point of silicon), so increasing fluid temperature reduces heat transfer at the core, and thus power extracted at the turbine. Therefore absorber needs to have a sufficient thermal mass to prevent power output from dropping too much (< 1 kW) towards the end of the blowdown.

Compressor And Turbine Models

Compressor and turbine were modeled using isentropic flow equations with efficiency corrections. Outlet temperatures are given by

$$T_{\mathrm{OUT\_COMP}} = T_{\mathrm{IN}}\, r_{\mathrm{p}}^{\frac{\gamma-1}{\gamma}} \tag{1}$$

$$T_{\mathrm{OUT\_TURB}} = T_{\mathrm{IN}}\, r_{\mathrm{p}}^{\frac{1-\gamma}{\gamma}} \tag{2}$$

and shaft powers by

$$\dot{W}_{TURB} = \dot{m} C_p T_{IN} \left(1 - \beta r_p\right)^{\frac{1-\gamma}{\gamma}} \eta_T \tag{3}$$

$$\dot{W}_{COMP} = \frac{\dot{m} C_p T_{IN} \left(r_p^{\frac{\gamma-1}{\gamma}} - 1\right)}{\eta_C} \tag{4}$$

Pressure ratio of compressor and turbine was chosen to be $r_p = 4$, which is typical for Brayton cycles. Compressor, turbine and generator were all assumed to have efficiencies of $\eta_T = \eta_C = \eta_G = 0.9$. A typical power plant pressure loss parameter $\beta = 1.05$ was assumed.

Core Heat Transfer

Core cross section is shown in Figure 2. Plutonium fuel rods are embedded in silicon, which is allowed to melt during the warm-up phase. Core geometry was changed from the original [1] to allow more even melting characteristics. Number of flow channels is 280, and their diameter is $d = 5$mm.

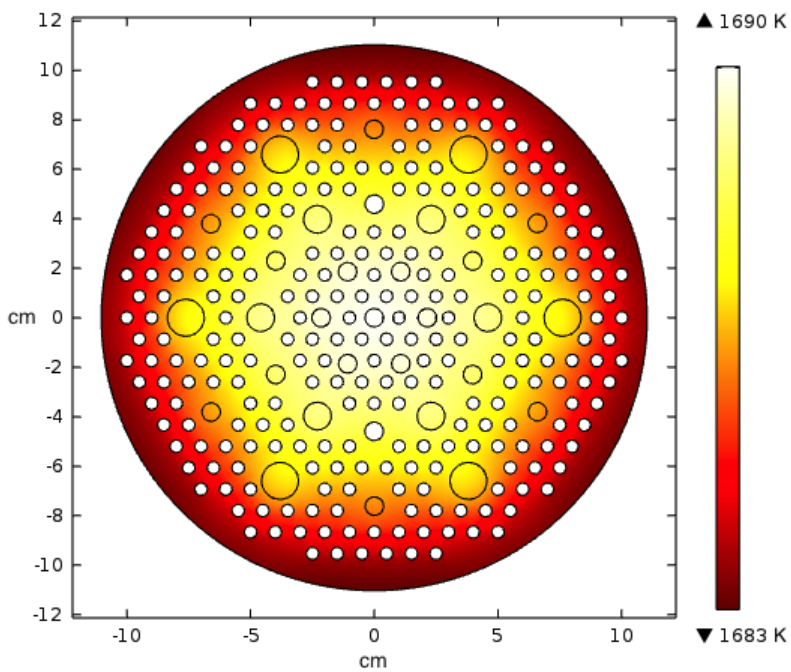

FIGURE 2. Core cross section and temperature distribution after 15 hours of heating.

1D heat transfer analysis was conducted by discretizing along the length of a single flow channel and assuming constant surface temperature (T_S=1686 K, melting point of Si), as shown in Figure 3.

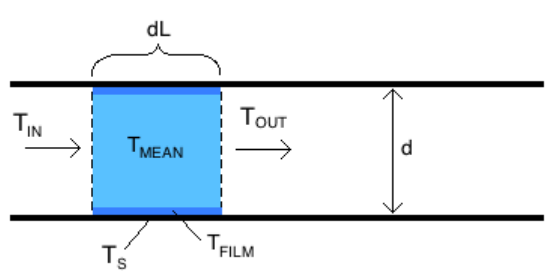

FIGURE 3. Flow channel heat transfer model.

$$T_{\mathrm{MEAN}}=(T_{\mathrm{IN}}+T_{\mathrm{OUT}})/2 \tag{5}$$

$$T_{\mathrm{FILM}}=(T_S+T_{\mathrm{MEAN}})/2 \tag{6}$$

Thermal power transferred from core to fluid is

$$\dot{Q}_{\mathrm{IN}}=hA_s(T_S-T_{\mathrm{FILM}}) \tag{7}$$

Fluid carries away

$$\dot{Q}_{\mathrm{OUT}}=\dot{m}C_p(T_{\mathrm{OUT}}-T_{\mathrm{IN}}) \tag{8}$$

Equating (7) and (8) gives

$$T_{\mathrm{OUT}}=\frac{K(T_S/2-T_{\mathrm{IN}}/4)+T_{\mathrm{IN}}}{1+K/4} \tag{9}$$

where

$$K=\frac{h\pi d\,dL}{\dot{m}C_p} \tag{10}$$

Heat transfer coefficient h is a function of fluid's thermal conductivity k, and Nusselt number:

$$h=\frac{Nu\,k}{d} \tag{11}$$

Gdielinski correlation of Nusselt number was used for turbulent flow. For laminar flow $Nu=3.66$.

Flow in the core is firmly laminar. Reducing the number and/or diameter of flow channels would allow turbulent flow, which would improve heat transfer to fluid. However, forcing turbulent flow isn't necessary for the given power requirement, and tinkering with core geometry would change its melting characteristics.

Absorber Design and Heat Transfer

Similar 1D heat transfer approach was used to evaluate fluid temperature profile as it flows through the lithium absorber. In this case surface temperature of the flow channel is not constant, as the temperature of the absorber increases with time. This translates to fluid exit temperature increasing with time.

Number of flow channels and their diameter can be determined by studying their effect on thermal conductance of the absorber. Parameter of interest here is absolute thermal conductance per unit length,

$$c=\frac{C}{L}=\frac{hA_s}{L}=\frac{h\pi NLd}{L}=h\pi Nd \qquad [\frac{W}{mK}] \tag{12}$$

where N is the number of channels.

It describes how many Watts of thermal power is transferred (per unit length) from fluid to absorber with given temperature difference between the two. Fixing mass flow rate makes h dependent on viscosity (which is known) and channel diameter d only, so c can be plotted as N vs. d, as in Figure 4.

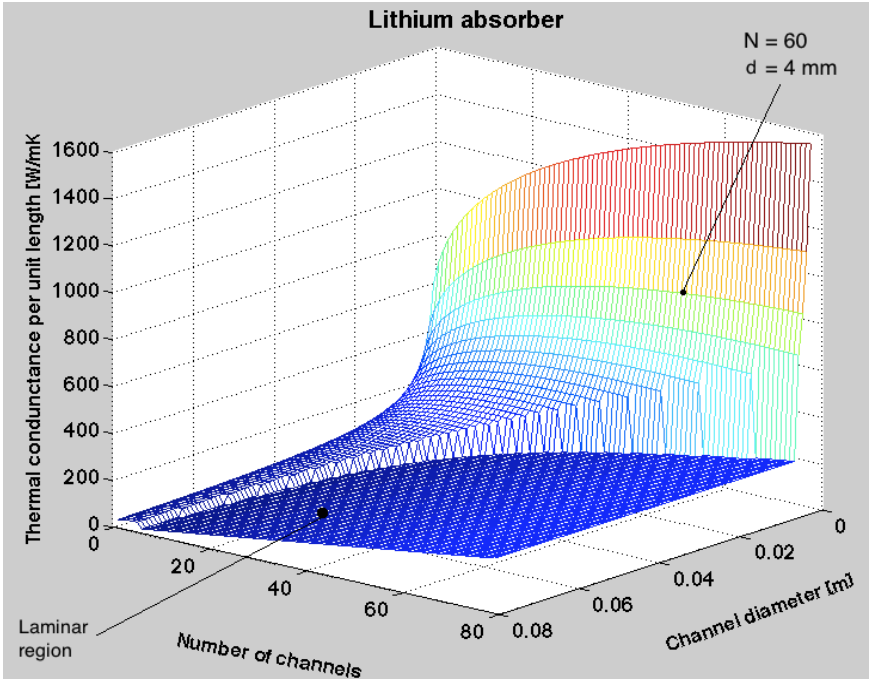

FIGURE 4. Effect of number and diameter of flow channels on absorber thermal conductance.

Decreasing the channel diameter is an effective way to increase heat transfer, but there is a practical limit how narrow channels can be manufactured. Increasing the number of channels is effective only to a certain point, and going beyond that, flow eventually enters the laminar region, where heat transfer reduces drastically (flatlands in the above figure). Selected parameters were $d = 4$mm and $N = 60$. This puts the design safely to turbulent flow region.

Once N and d are fixed, length of the flowpath can be studied. Figure 5 shows fluid temperature as it flows through the absorber.

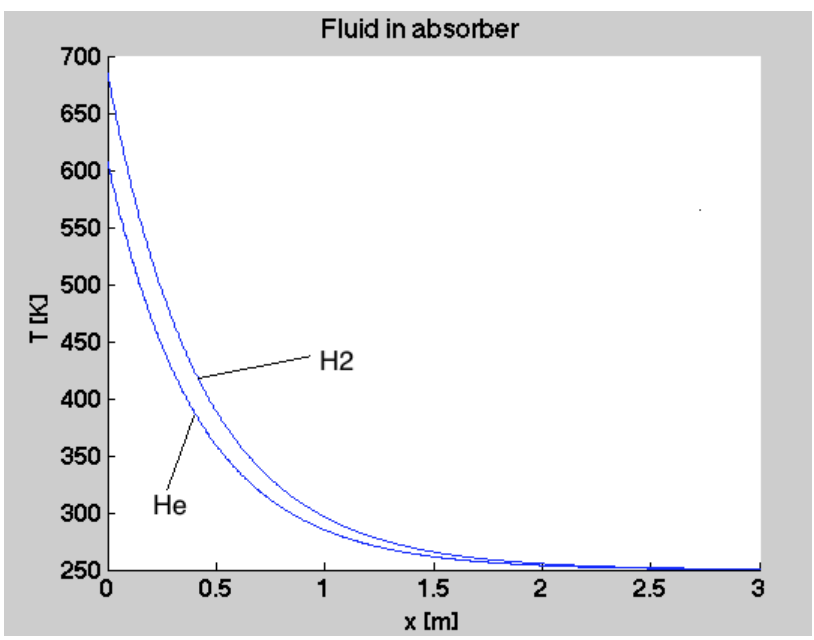

FIGURE 5. Absorber temperature 250 K.

After 2 meters fluid temperature is already close to absorber temperature, and at 3 m the minimum achievable temperature is reached. For storing all waste heat accumulated during the six minute blowdown, required lithium absorber mass was determined to be 200 kg. Dividing it into six cylinders gives L = 1m and diameter D_{ABS} = 0.28 m. 3 meter flowpath is then achieved by passing the fluid through three cylinders linked together. Figure 6 illustrates one of the cylinders.

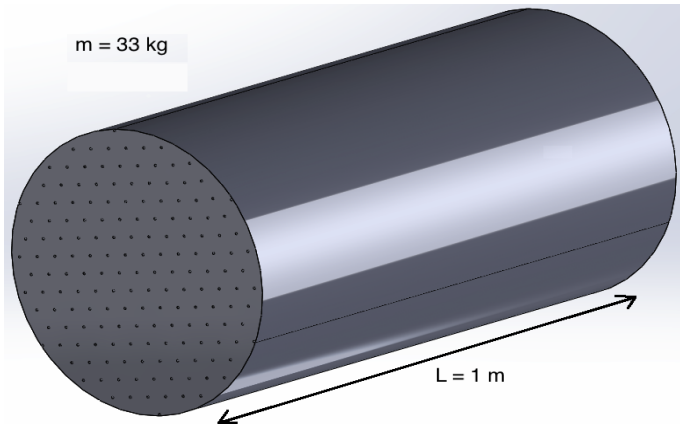

FIGURE 6. One of the six lithium cylinders comprising the absorber.

Described heat transfer model assumes even temperature distribution throughout the absorber, which in reality is not the case. *Biot number* is defined as

$$Biot = \frac{convection\ to\ solid}{conductance\ in\ solid} = \frac{hL}{k} \tag{13}$$

If Biot number is less than 0.1, heat transfer inside the solid is much faster than heat transfer into the solid. This is not the case (Biot number is 1.23 and 0.96 for hydrogen and helium, respectively), so in reality there are both axial and radial thermal gradients inside the absorber material. Flow channel surface temperature would be higher than predicted by the current 1D model, which would reduce the heat transfer rate. A 3D finite element analysis would be necessary to obtain a more accurate answer. It should be noted, however, that the selected 3 m flow path length provides more heat transfer area than necessary.

Once the six minute cycle is over, the absorber must return to its initial temperature (250 K) by radiating heat to space. Assuming emissivity ε = 0.8 and that 75% of the absorber area sees cold space, this is achieved in 12 hours, which is less than time needed to recharge the core.

Comparison of Power Cycles

Table 1 presents the studied power cycles and necessary core and absorber masses. It turned out in all cases that nominal amount (3.3 kg) of plutonium [1] was not enough to provide energy for a six minute blowdown while producing 25kW$_e$. Only length of the core was adjusted to add mass. Mass of the rest of the core (insulation and structures) was scaled up linearly with increasing Pu mass.

TABLE 1.

Fluid	m_{pu} [kg]	m_{CORE} [kg]	L_{CORE} [m]	$m_{ABSORBER}$ [kg]	Power conversion efficiency
He	4.0	159	0.24	200	24%
H_2	5.5	219	0.32	200	18%

Helium cycle is significantly more efficient in converting heat to electrical power, and therefore comes with a smaller core. Mass of the absorber, however, turned out to be the same for both fluids.

Figures 7 illustrates cycle parameters for both working fluids during the blowdown.

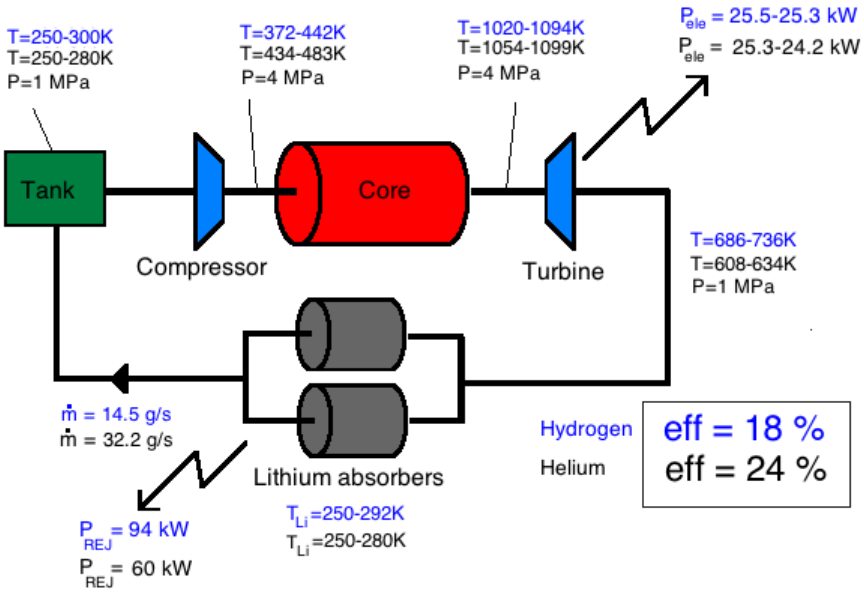

FIGURE 7. Helium as working fluid.

PROPULSION

Propulsion configuration is depicted in Figure 8. Propellant (hydrogen) is pumped from tank to the core, heated and then expelled through the nozzle. Nozzle was assumed to have typical space nozzle thrust coefficient C_F=1.78.

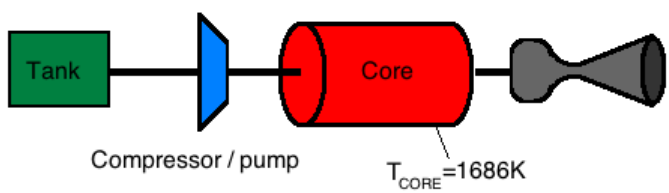

FIGURE 8. Thermal propulsion mode.

Performance parameters given in Table 2 maximize specific impulse, which is usually desirable. Compressor is driven by an electric motor that draws it power from spacecraft batteries, and as long as they can provide sufficient power, I_{SP} can be traded for higher thrust by increasing mass flow, if needed.

TABLE 2. Propulsion performance.

Cycle	$\dot{m}$ [g/s]	P_{COMP} [kW]	T_{CORE_OUT} [K]	I_{SP} [s]	F_{TH} [N]	T_{BURN} [s]
H_2	4	9	1664	697	27	641
He	3	6.8	1664	697	21	621

CONCLUSION

Suggested pulsed power generation concept was confirmed to offer significant savings in radiator mass and size. 200 kg of lithium in simple cylindrical blocks was deemed to be enough to sink waste heat for a six minute power generation period. Continuous systems running at 25 kW_e require more than $100m^2$ of radiator area to perform the same task.

Both hydrogen and helium are viable options for working fluid, while helium offers more efficient power conversion cycle and therefore runs on a smaller core.

Bi-modal configuration was confirmed to provide moderate thrust (>20N), which can be used for impulsive orbital maneuvers.

REFERENCES

[1] Jerred, N., "Dual-mode Propulsion System Enabling Cubesat Exploration of the Solar System ", *NASA Innovative Advanced Concepts Phase 1: Final Report,* 2014

Feasibility Study of Solid Matrix Fuels for Space Power Reactors

Christopher G. Morrison, Wei Ji, and Paul Blejwas

Department of Mechanical Aerospace and Nuclear Engineering, Rensselaer Polytechnic Institute, Troy, NY 12180
928-925-3842; morric7@rpi.edu

Abstract. Recent advances in nuclear fuel fabrication allow for new types of fuels with superior power density, safety, fabrication cost, and other traits. Spark plasma sintering (SPS) is one such technology that is currently being explored. The University of Florida and the Center for Space Nuclear Research have successfully demonstrated the technology for nuclear applications. SPS is unique in its ability to sinter disparate materials together allow for new types of cermets, heterogeneous metal alloys, and ceramic-ceramic composite fuels. SPS has been successfully demonstrated with fuels such as UO_2-W cermet matrix fuels and UO_2 with high thermal conductivity additives.

One of the fundamental requirements for space nuclear fuels is a high temperature capability. UO_2 is a high temperature fuel. However, its thermal conductivity is very low. SPS opens the door to creating composite materials with high thermal conductivity allowing the fuels to reach much higher power densities and lower temperature peaking factors. In addition, safety can be improved by utilizing small fuel pellets sintered to a fuel matrix which can retain fission products, possibly eliminating the need for fuel cladding.

This research focuses on exploring the design options for matrix composite fuels. Matrix material such as W, SiC, Be, BeO, and graphite are explored with UO_2, UN, and UC fuels. This analysis investigates neutronic properties, thermal conductivity of the composite matrix fuels.

Keywords: Spark Plasma Sintering, Space, Composite Fuels, Material Properties

INTRODUCTION

High temperature capability and high thermal conductivity are key attributes for high performance nuclear fuels. In space high temperatures are especially important as minimize the mass of space power systems; first by increasing the thermodynamic efficiency but more predominately by decreasing the size of the heat rejection system. A high thermal conductivity is necessary to reduce the temperature peaking in the fuel and protect the nuclear fuel from melt and creep.

Safety is a primary concern for nuclear fuels. In this research, analysis is directed toward encapsulated fissile fuel forms where fission products are kept within the fuel by a non-fissionable matrix material, adding a highly engineered barrier to fission product release. This research can also be applied to safety tolerant nuclear fuels for terrestrial reactors as high temperature capability and high thermal conductivity provide resistance to reactor accidents.

High temperatures place increasing demands on the materials for nuclear fuels and cause many traditional reactor components such as water to be incompatible. In this paper several materials were identified which hold promise to be used as high performance space nuclear fuels. Table 1 lists the fissile fuel and matrix materials that were analyzed in this study and Figure 1 lists some of their properties.

TABLE 1: Materials Analyzed [1-4].

Material	Type	Melting Point [K]	More Information
Graphite	Moderator Matrix	4000	Well Known, Moderating Properties
W	Structural Matrix	3695	Radiation Resistance, Strength, Thermal Conductivity, High Neutron Absorption
W-184	Structural Matrix	3695	Lower neutron absorption cross section, Must be enriched
Be	Moderator Matrix	1560	Well Known, Moderating Properties
BeO	Moderator Matrix	2780	Well Known, Moderating Properties
SiC	Structural Matrix	3000	Strength
$(B\text{-}11)C_4$	Moderator Matrix	2718	Moderating Properties
Nb	Structural Matrix	2741	Strength, Thermal Conductivity, Low Neutron Absorption
Mo	Structural Matrix	2893	Radiation Resistance, Strength, Thermal Conductivity, Low Neutron Absorption
Mo-92	Structural Matrix	2893	Corrosion Resistance, Radiation Resistance, Strength, Thermal Conductivity, Extremely Low Neutron Absorption
UO_2	Fissile	3140	Standard Fuel Form, Low Thermal Conductivity
UN	Fissile	3000	High Thermal Conductivity
UC	Fissile	2638	High Thermal Conductivity, High Uranium Density

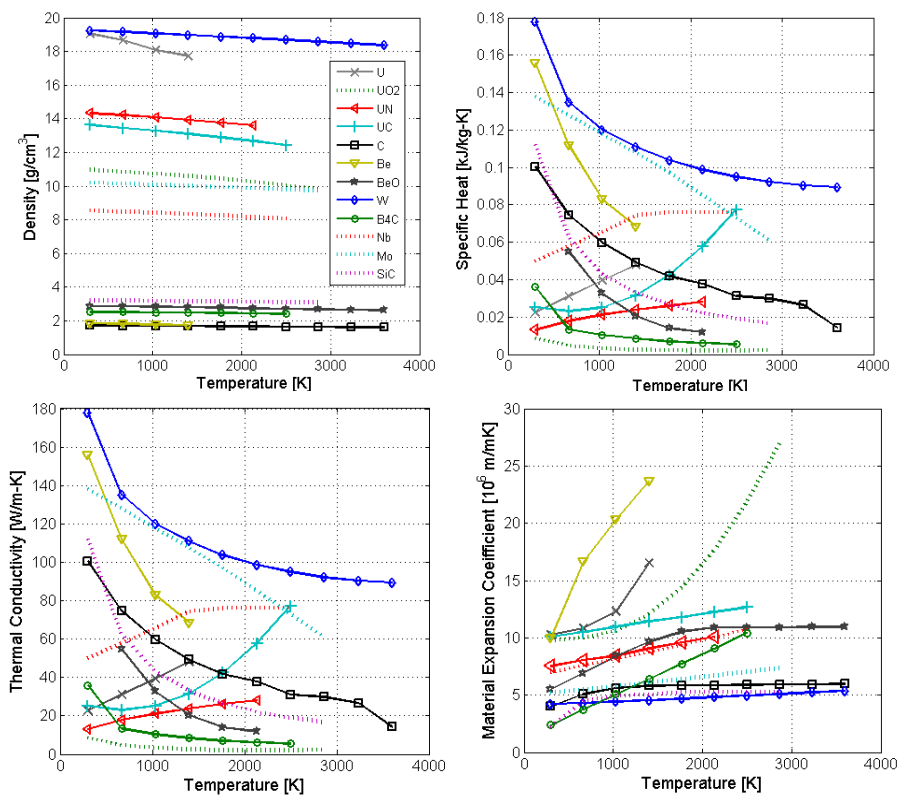

FIGURE 1: Material Properties

COMPOSITE MATRIX INFORMATION

Composite matrix solid nuclear fuels are composed of two distinct heterogeneously mixed materials. The matrix of the composite surrounds the nuclear fuel. Figure 2 below depicts a hypothetical cross section of the composite fuel. The nuclear fuel is represented as discrete spherical yellow dots in surrounded by the blue continuous matrix material.

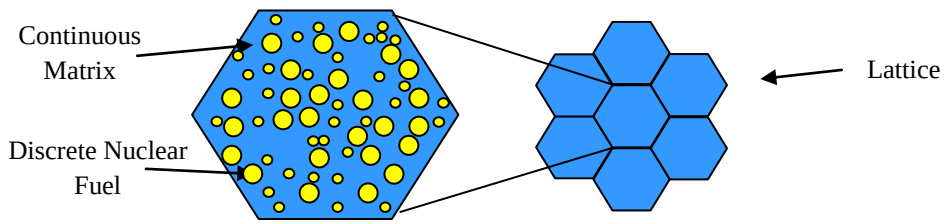

FIGURE 2. Hypothetical Composite Material Fuel Block

The discrete fissile fuel material is encapsulated by the continuous material. The matrix will keep the fission product waste contained inside the composite fuel block and the matrix material can be used to complement the shortcomings of the discrete nuclear fuel material providing superior composite fuel block properties.

$$_{f} = \frac{V_f}{V_f + V_m} \tag{1}$$

The fissile fuel volume fraction, ϕ_f describes the relationship of the matrix material to the fuel material. The packing of the discrete phase within the matrix sets an upper bound for matrix-type compose materials. For ordered spherical fuel particles, the maximum fuel volume fraction is 74 percent. For random spherical packing, the maximum fuel volume fraction is approximately 63 percent.

Matrix Composite Material Properties

Thermal conductivity is a key in determining the fuel centerline temperature and the power density achievable. The temperature increase of a hot spot in a fuel element is roughly inversely proportional to the thermal conductivity. The thermal conductivity of a composite material can be approximated by the Maxwell theoretical model for composite thermal conductivity show in Equation 2 [5].

$$k_{composite} \simeq k_{matrix}\left[\frac{k_{fuel} + 2k_{matrix} + 2\phi_{fuel}\left(k_{fuel} - k_{matrix}\right)}{k_{fuel} + 2k_{matrix} - {}_{fuel}\left(k_{fuel} - k_{matrix}\right)}\right] \tag{2}$$

The multiplication of the density and specific heat determine the thermal inertia of the reactor. A larger thermal capacity is advantageous for reactor control and balancing out transients. The density of composite materials can be determined by a volume weighted average. The composite specific heat can be calculated by a mass weighted average.

$$\rho_{composite} = {}_{fuel}\rho_{fuel} + \left(1 - {}_{fuel}\right)\rho_{matrix} \tag{3}$$

$$C_{p_{composite}} = \frac{{}_{fuel}\rho_{fuel}C_{p_{fuel}} + \left(1 - \phi_{fuel}\right)\rho_{matrix}C_{p_{matrix}}}{\rho_{composite}} \tag{4}$$

The linear coefficient of expansion is an important factor to match between the matrix and fuel. A large mismatch will cause internal stresses in the composite matrix during temperature swings. The net composite in a matrix-type arrangement can be expressed in the relationship in Equation 6 [2].

$$\alpha_{composite} = {}_{fuel}\left(\alpha_{fuel} - \alpha_{matrix}\right) + \left(1 - {}_{fuel}\right)\alpha_{matrix} \tag{6}$$

Neutronic Properties of Reactor Core with Matrix Composite Fuel

Due to the heterogeneous configuration of a typical reactor core design, core neutronic properties are dependent upon the neighboring geometries and materials. Those neighboring geometries may be comprised of composite fuel elements, moderating elements, coolants, reflectors, and other parts.

The disparate geometry and materials are simplified by looking at reactor systems composed of an infinite number of fuel elements, moderator elements, and coolant in an infinitely repeated grouping called a lattice. An infinite lattice is useful for approximating a finite reactor core's neutronic properties and can determine if a fuel is capable of going critical.

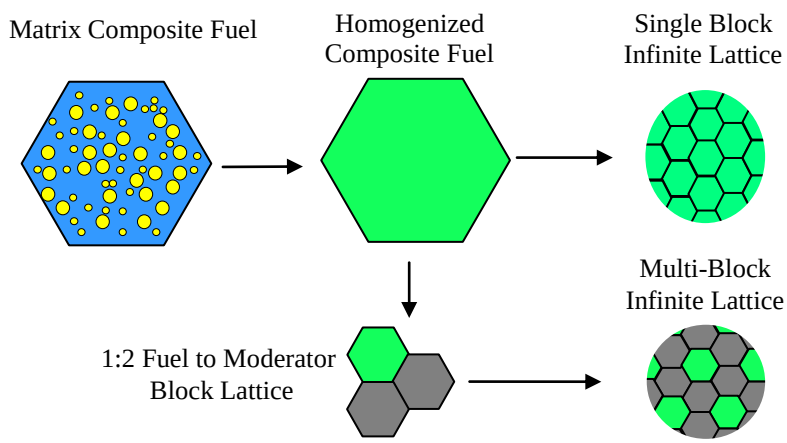

FIGURE 3: Infinite Lattice

Figure 3 depicts the process of infinite lattice creation. In many cases it is desirable to make a lattice with two block types. This applies directly to W, Nb, and Mo matrix fuel blocks which do not contain a moderating material. To effectively form a critical lattice these fuel forms typically require a moderator block and forms a multi-block lattice

Infinite lattice analysis misses one crucial aspect of reactor core design, the critical size of the reactor. A finite radius search explores the physical size of the reactor. A radius search with a defined reflector is also a useful gauge, as modern reactors typically have a reflector. Figure 4 depicts a criticality search.

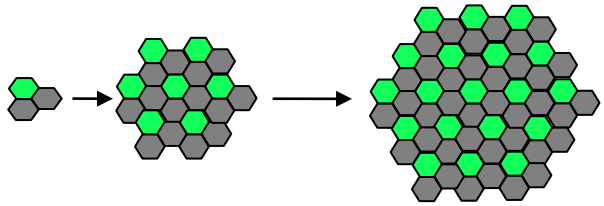

FIGURE 4: Finite Ring Criticality Search.

Reactor Core Design

Nuclear reactor design is an optimization process involving with three major analyses: neutronic, thermal-hydraulic, and material analyses. The neutronic analysis determines the minimum size of the reactor. The thermal-hydraulic analysis determines the maximum temperature and power of the reactor. The material analysis determines the ability of the reactor to resist damage. These three performance areas are coupled by each other. An unsatisfactory performance in one area requires a core redesign which is often achieved by changing the repeating lattice. Changes core geometry will affect the other areas performance areas. Figure 5 illustrates this process.

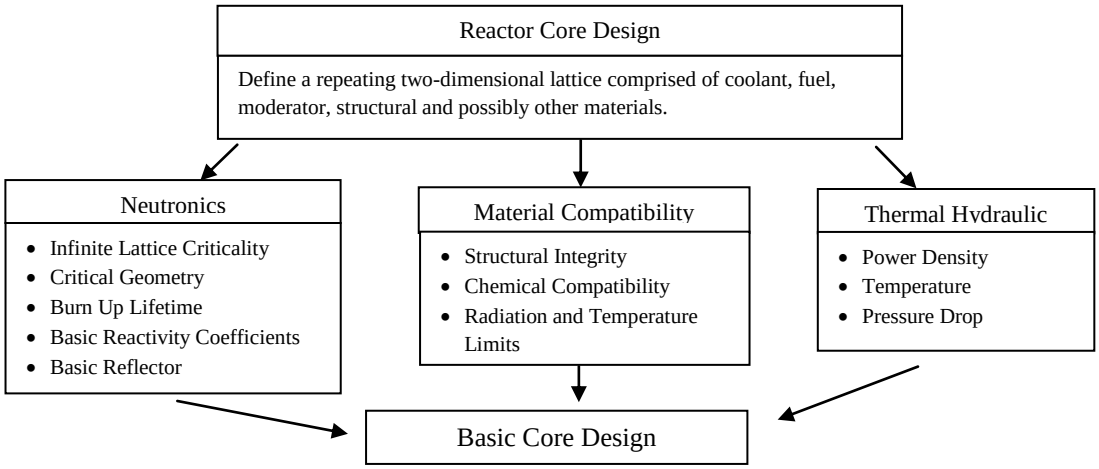

FIGURE 5: Basic Reactor Design Process

ANALYSIS AND DISCUSSION

Nuclear Properties

Figure 7 below depicts the results of the k-infinite analysis for homogenous mixtures of UO_2 combined with various matrix materials. On the x-axis the UO_2 fuel volume fraction is listed, and on y-axis the k-infinite value is given. On the left side, the fuel volume fraction is logarithmic going from 0.01 percent to 100 percent. Fast reactors exist in fuel volume fractions above 10 percent and thermal reactors in regions below 2 percent fuel volume fraction. The thermal region begins to taper around 0.1 percent as the fuel density becomes too small. A linear graph of the fast reactor domain is shown on the right.

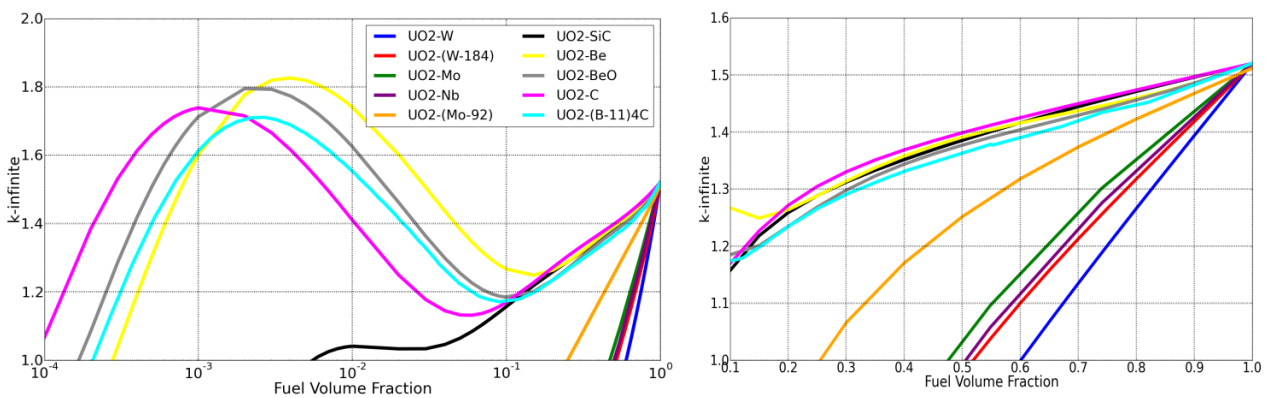

FIGURE 6: UO_2 Fuel Volume Fraction vs. k-infinite for a 300 K Temperature and 20 Percent Enrichment

Other fissile fuels such as UN and UC follow the same trend as UO_2 with slightly higher k-infinite values in the fast reactor range because of the higher Uranium density. In the thermal reactor, k-infinite is slightly shifted based on the absorption cross section of the nitrogen for UN and carbon for UC. Higher enrichments raise the value of k-infinite. Higher temperatures tend to decrease the k-infinite because of increased resonance absorption from Doppler broadening.

Figure 7 gives the critical radius of a reactor. On the x-axis the fuel volume fraction of UO_2 is given, and on the y-axis the critical radius in cm is given. The critical radius in this context is a cylinder's radius with a height of twice the radius size. On the left hand side a bare unreflected critical core radius is given. On the right side the critical radius has been reduced by surrounding the cylindrical reactor with a 30 cm axial and radial reflector.

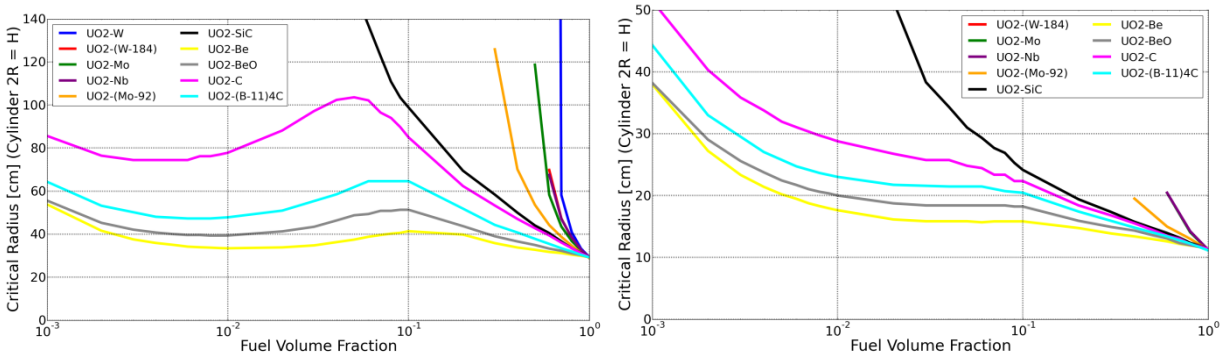

FIGURE 7: UO_2 Fuel Volume Fraction vs. Critical Radius for a 300 K Temperature and 20 Percent Enrichment Left: Bare Core Right: 30 cm Be Axial and Radial Reflector

The reflected core differs significantly from the bare core. The reflected core has a smaller critical radius. In addition the hump associated with the epithermal resonance region shown for the bare core was smoothed by the thermalization effect of the reflector in the reflected core.

Several matrix materials including Mo, Nb and W are non-moderating and become subcritical below 50 percent volume fraction and above. These matrix materials cannot effectively make fast reactors because of their large fast neutron absorption cross section. These fuels require a multi-block infinite lattice containing moderating blocks to form effective critical geometries. The non-moderating matrix material's primary purpose is to provide a structural material to encapsulate the fuel. A multi-block lattice structure could be developed to improve their criticality by adding a moderator block to shift the neutron spectrum into the thermal range.

A multi-block lattice cell was defined for Figure 8. The fuel block was given a one-to-one matrix to fuel ratio. The moderator fuel block is composed of BeO moderator. Figure 8 depicts the k-infinite and bare reflected core nuclear properties of the multi-block lattice with 20 percent enrichment at 300 K. The x-axis lists the fuel block volume fraction. One minus the fuel block volume fraction yields the moderator block fraction.

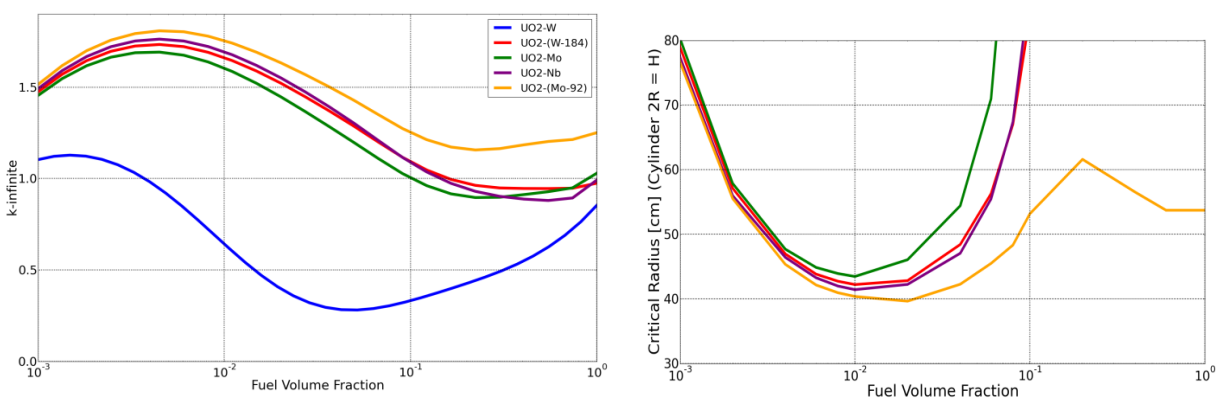

FIGURE 8: Multi-block lattice 1:1 UO_2 to Matrix for the Fuel Block and BeO for the Moderating Block. Left: k-infinite calculation. Right: Unreflected core critical radius.

The structural matrix materials shown in Figure 8 with the exception of Mo-92 can only exist as thermal reactors. The natural W lattice is almost incapable of being utilized as a thermal reactor because of its relatively large thermal neutron absorption cross section.

The trends for neutronic properties of composite fuels are dominated by the matrix material. The fissile fuel forms shift k-infinite and the critical radius but only to a small degree. Table 2 below summarizes matrix components and their respective neutronic traits.

TABLE 2: Neutronic Conclusions

Material	Type	Thermal Spectrum	Fast Spectrum	Other Notes
Graphite	Moderator Matrix	Strong	Strong	Larger Thermal Critical Radius
W	Structural Matrix	Very Weak	No	Challenging Criticality Requirements
W-184	Structural Matrix	Fair	No	
Be	Moderator Matrix	Strong	Strong	Small Thermal Critical Radius
BeO	Moderator Matrix	Strong	Strong	Small Thermal Critical Radius
SiC	Structural Matrix	No	Strong	
$(B\text{-}11)C_4$	Moderator Matrix	Strong	Strong	
Nb	Structural Matrix	Fair	No	
Mo	Structural Matrix	Fair	No	
Mo-92	Structural Matrix	Strong	Very Weak	Best Performing Refractory Metal

Thermal Conductivity

Thermal conductivity of composite material is given in Figure 9 for UO_2 and UC composites. The composite fuels contain a 50 percent fuel volume 50 percent matrix volume.

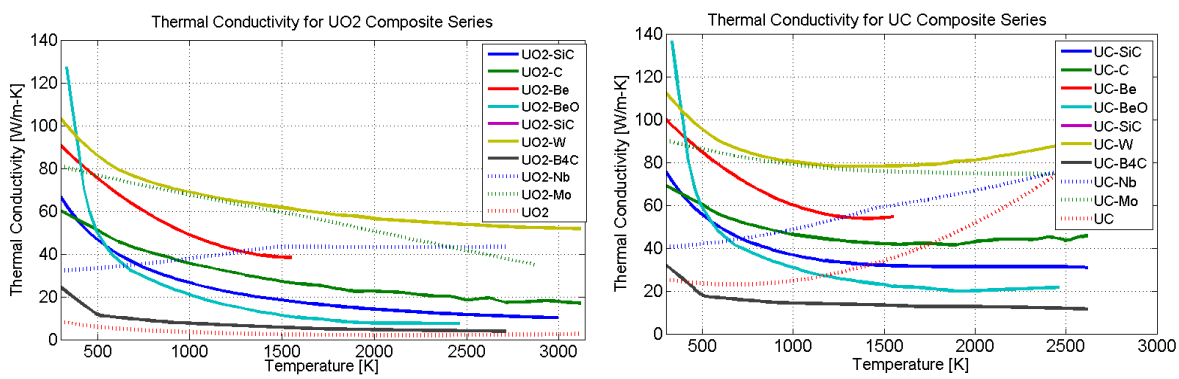

FIGURE 9: Composite Matrix Thermal Conductivity with a 50 Percent Fissile Fuel Volume Fraction Left: UO_2 Right: UC

For thermal conductivity both the matrix and fissile fuel components have a large impact upon the composite thermal conductivity. UO_2 has an extremely low thermal conductivity and its thermal conductivity greatly augmented with any of the matrix material analyzed. UC and to a lesser degree UN have significant thermal conductivity and form superior thermal conductivity composites mainly with the metal matrix materials.

CONCLUSION

In designing a nuclear fuel there are a series of key design questions. How much heat can be effectively removed, what temperature range can the fuel operate over, what are the critical configurations, and how much burn up can be achieved?

Composite materials allow nuclear fuel designers to combine positive traits of the constituent components to meet design and safety requirements. An intrinsic benefit of composite matrix fuels is that the matrix serves as a barrier to fission product release for improved safety. In this paper analysis was completed to explore the neutronic and thermal conductivity of various promising composite fuels. The data in this paper are not conclusive. There are many options for fuel design and the options can be explored by viewing the graphics in this paper.

This paper has focused (though not exclusively) on 20 percent enrichment, UO_2 fissile fuel, solid fuel forms, and high temperatures. This focus could be rescoped easily to accommodate, for example, liquid core reactors or high enrichments.

In future work, burn up analysis is planned to explore the question of fuel lifetime. A higher fidelity material compatibility analysis is planned. The eventual goal is to build upon this data a systematic process to complete full core reactor design.

ACKNOWLEDGMENTS

Thanks to the Nuclear Energy University Program which help fund this research.

REFERENCES

[1] Kirillov, P. L., "Thermophysical Properties of Materials For Nuclear Engineering," Institute for Heat and Mass Transfer in Nuclear Power Plants State Science Center of the Russian Federation, (2006)

[2] White, G., White "Heat Capacity of Reference Materials: Cu and W" NIST. (1984)

[3] Powell, R. W., "Thermal Conductivity of Selected Materials" National Bureau of Standards US Department of Commerce, (1966)

[4] Snead, L. L., "Handbook of SiC Properties For Fuel Performance Modeling.," *Journal of Nuclear Materials,* **371**, pp 329-377, (2007)

[5] Progelhof, R., "Methods for Predicting the Thermal Conductivity of Composite Systems: A Review" *Polymer Engineering & Science,* **16**, 615-625, (2004)

Storing Water Propellant Mined from Asteroids

Adarsh Rajguru[1], Juha Nieminen[1], Justin Weatherford[2], Nalini Nadupalli[3], Joseph Santora[4]

[1]*Department of Astronautical Engineering, University of Southern California, Los Angeles, CA 90089*
[2]*Department of Engineering, George Fox University, Newberg, OR 97132*
[3]*Department of Electrical Engineering, University of Michigan, Ann Arbor, MI 48109*
[4]*Department of Chemical Engineering, University of Utah, Salt Lake City, UT 84112*
Phone: 208-412-4430; email: Jweatherford10@georgefox.edu

Abstract. It has been proposed by planetary scientists that water is more abundant at the hydrated C-Class asteroids in the main asteroid belt than was originally thought. The information presented in this paper is part of a mission architecture study, conducted by a team at the Center for Space Nuclear Research (CSNR). The primary objective was to design the power and propulsion system of a spacecraft that can visit multiple such asteroids. The designed spacecraft will gather information about the asteroid composition using Ground Penetrating Radars. It would then attempt to land at suitable water extraction sites, place a beacon or "Pinger", and then harvest water from the surface. The craft would then blast off to the next target C-Class asteroid. The mined water on each asteroid will be electrolyzed and the hydrogen would be used as a propellant through a bi-modal Low Enriched Uranium Nuclear Thermal Rocket (LEUNTR) with LOX Augmentation. The operational conditions of the LEUNTR requires liquid hydrogen as input. During thermal thrust mode, the liquid hydrogen would flow through the LEUNTR core's tie tubes and undergo a phase change. The vapor would then propel the craft. If additional thrust is needed on larger asteroids, the hydrogen vapor will be combusted with the liquid oxygen in order to augment the chamber temperature like an afterburner. The thrust would increase, but the specific impulse (Isp) would reduce. This paper presents the detailed design of the cryocooling system that will be used to refrigerate the hydrogen and oxygen for future burns during the transits flight between asteroids. A radiator design was conducted as the primary means to expel the excess heat. During the design process it was found that liquefying hydrogen at the asteroid surface would be too difficult and expensive for the mission architecture. Hence, a potential alternative to liquefying hydrogen was also studied by looking at the fabrication of hydrocarbons on-board. Hydrocarbons are easier to liquefy than hydrogen. The carbonaceous composition of the C-Class Asteroids was identified as a potential carbon source to react the hydrogen for creating hydrocarbons. In this chemical process, one of the key and abundant product would be methane (CH4). Hence the cryocooling refrigeration process of Methane was also evaluated. In addition to a chemical process to store hydrogen, an alternate physical process to store the hydrogen was proposed. Certain carbon lattices have the ability to absorb hydrogen molecules like a sponge. This type of fuel cell allows the hydrogen to be stored at a temperature higher than if it were liquefied thus reducing the size of the radiator needed.

Keywords: Radiator Design, LEUNTR with LOX Augmentation, Cryocooling System, Methane production, Hydrogen & Oxygen.

ROCKET LAYOUT

A rocket design capable of harvesting water from asteroids has recently been proposed at the CSNR. The rocket will hydrolyze the water and use the byproducts for propellant. The rocket will primarily use hydrogen for its propellant. While the propellants are not being used, they will need to be stored. The propellants are too volatile to be stored in a gaseous state, so they must be altered after they have been separated.

The ideal way to store oxygen and hydrogen is when they are in their liquid state. Both elements have very low condensing points. There are only 2 available means of heat transfer in the mission specifications. One method is to conduct the heat to the asteroids when the craft is on them, and the other is to radiate the heat to space through radiator. The asteroids will be cooler than the water after it has been extracted from the regolith contents through heating. A heat sink could be used to conduct the heat to the asteroid. The heat sink would add mass to the craft. An

increase in mass is often disadvantageous to spacecraft design. Also, the asteroid's temperature is not low enough to liquefy hydrogen and oxygen. Radiation to space is the only way to get the elements cold enough to liquefy. The rocket will not have heat sinks designed to release heat.

The rocket is has a trefoil shape. It has one large circle with three ¾ circles connected to the full circle at 0, 120, and 240 degrees. The rocket has sometimes been called the "Mickey Mouse" rocket, because of this shape. At the crest of each smaller circle, there will be one to two vertical radiator perpendicular to the crest. This arrangement will increase the view factor of the radiators. The normal operating condition is one of these radiators will liquefy hydrogen while another will liquefy oxygen, however, if it is desired 2 radiators could liquefy hydrogen simultaneously and 2 others could liquefy oxygen simultaneously. If it becomes necessary, a single hydrogen radiator will be able to liquefy enough hydrogen for the craft to continue the mission while a single oxygen radiator would be able to liquefy enough oxygen. The radiators will be lined with capillary tubes to pull the liquids they produce to their respective tanks.

The hydrogen radiators will be identical to each other, and the oxygen radiators will be identical to each other. The oxygen radiators will be significantly smaller than the hydrogen radiators. They will also require larger compressors than the hydrogen radiators, because they will operate at a higher pressure. This helps balance the rocket's mass. The identical parts also allow the radiators to serve as a spares if one of them fails during the mission's estimated 20 year span.

RADIATOR DESIGN

Hydrogen is the most difficult to liquefy by molar weight and temperature. The original strategy was to use identical radiators and conditions, however this arrangements was too extreme for oxygen. Some of the oxygen would begin to freeze in the radiator, so a separate radiator system was designed for the oxygen.

Hydrogen

A steady state energy balance equation was used to size the hydrogen radiators. The amount of hydrogen going in would be equivalent to the amount going out, and the energy of entering hydrogen would be equivalent to the amount of energy leaving with the liquid hydrogen and the radiated heat. This set up can be seen in Equation (1).

$$0 = \dot{m}_\iota * h_i - \dot{Q} - \dot{m}_e * h_e \tag{1}$$

The equation for radiative heat transfer can be seen in Equation (2).

$$\dot{Q} = \varepsilon * \sigma * F * A * (T_s^4 - T_a^4) \tag{2}$$

The equation for the area of the radiators can be seen in Equation (3).

$$A = \frac{\dot{m}_\iota * h_i - \dot{m}_e * h_e}{2 * \varepsilon * \sigma * \mathrm{F} * (\mathrm{T}_s^4 - \mathrm{T}_a^4)} \tag{3}$$

Several assumptions have been made for this equation. It has been assumed that the water is being electrolyzed at 0.1 grams/second (g/s) at 10 amperes (amps) like it is at the International Space Station, the mass flow rate is constant, the mass flow rate is 0.0125 g/s (6.17* 10^{-7} moles/s (mol/s)) if water is being electrolyzed at 0.1 g/s, the temperature of the entering hydrogen is 300 Kelvin (K), pressure has negligible effects on the enthalpy of hydrogen in vapor form, hydrogen liquefies at 32 K at 1.1 MegaPascals (MPa) to 10 MPa, the enthalpy of the entering hydrogen is 8074.1 Joules/mol (J/mol) and the enthalpy of the exiting hydrogen is 453.18 J/mol based on the National Institute of Standards and Technology (NIST) values for hydrogen in those conditions[1], the entrance of the vapor hydrogen does not significantly affect the temperature of the hydrogen being cooled, the hydrogen will not begin to liquefy until the radiator has reached 1.1 MPa, the temperature of the radiator's surface is 32 K throughout, the temperature of space is 4 K, the emissivity is 0.9, and the view factor is 1. When these values are plugged into Equation (4), the area of one side of the radiator is found to be:

$$A = \frac{5.56 * 10^{-6}\frac{\text{mol}}{\text{s}} * (8074.1\frac{J}{mol} - 453.18\frac{J}{mol})}{2 * .9 * 5.67 * 10^{-8}\frac{W}{m^2 * K^4} * 1 * (32K^4 - 4\text{K}^4)} \approx 0.391m^2 \quad (4)$$

Considering that the limiting factor of the radiator is the height of the rocket which is 60 centimeters (cm), the radiator will be 60 cm by 65.2 cm. This is a reasonable size for the radiators for this rocket. The interior of the radiator will at most be 1 millimeter thick to hold 2 moles of hydrogen at 32K and 1.1 MPa. This ensures the hydrogen is in conditions that will allow it to liquefy. It is assumed that the hydrogen has a compressibility factor of 0.8 at this temperature and pressure based on Figure 1.

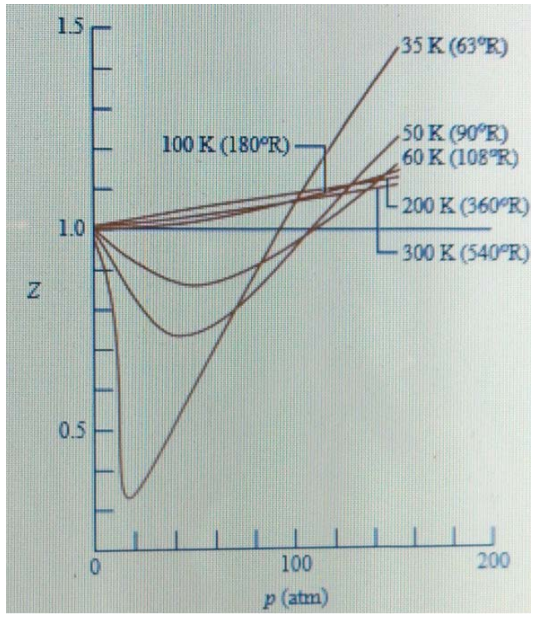

FIGURE 1. Variation of the Compressibility Factor of Hydrogen with Pressure at Constant Temperature.

The radiator can reach stable state temperature relatively quickly. Assuming the radiator begins empty, hydrogen brings 0.045 J/s to the radiator, and the radiator's initial temperature is 300 K, the radiator will radiate enough heat away to bring its temperature to 32 K in less than a second.

The limiting factor is how long it will take to produce enough hydrogen before liquefying begins. The radiator is designed to hold 2 moles of hydrogen at 32K and 1.1 MPa. The rocket will require 2 moles of hydrogen between refueling. It will take the hydrolysis unit just over 200 hours to produce 4 moles of hydrogen at a rate of 5.56 x 10^{-6} mol/s. Not all of the hydrogen that was used to pressurize the radiator will be liquefied. It can be stored in the radiators until the next refueling, so that the next time the rocket refuels it will not need to hydrolyze as much hydrogen.

There will be another radiator on the rocket used for hydrogen. It will be identical to the first radiator, and this one will be used if the first one is damaged beyond repair or is unable to produce enough hydrogen. Each radiator will be equipped with a means to measure pressure and temperature. These will be used to indicate if the radiator is leaking. If the radiator is leaking, it will attempt a self-repair. Water will be injected into the interior of the radiator. The water should find the leaks and move towards them. As the water approaches the leaks, it should cool and form ice in the gaps. Once the gaps have been filled, the water will be purged from the radiator through a combination of capillary tubes and low pressure. If the water is unable to fill the gaps the radiator will be isolated, and the hydrogen will be sent to the other radiator to be liquefied.

Oxygen

The oxygen radiators will be sized the same way as the hydrogen radiator with an energy balance equation. It is assumed that the oxygen will be entering at a rate of 0.0875 g/s and a temperature of 300 K, pressure has negligible effects on the enthalpy of oxygen in vapor form, oxygen liquefies at 154K at 5 MPa, the enthalpy of the entering oxygen will be 8348.0 J/mol and the enthalpy of the exiting oxygen is 666.02 J/mol based on the NIST values for oxygen in those conditions[1], the entrance of the vapor oxygen does not significantly affect the temperature of the oxygen being cooled, the oxygen will not begin to liquefy until the radiator has reached 5 MPa, the temperature of the radiator is 154 K. When these values are plugged into the equation, the area of one side of radiator is found to be:

$$A = \frac{2.78 * 10^{-6}\frac{\text{mol}}{\text{s}} * (8355.3\frac{J}{mol} - 666.02\frac{J}{mol})}{2 * .9 * 5.67 * 10^{-8}\frac{W}{m^2 * K^4} * 1 * (154K^4 - 4\text{K}^4)} \approx 0.000371m^2 \quad (5)$$

This radiator will be 2 cm by 2 cm. This is a reasonable size for the radiators for this rocket. The interior of the radiator will at most be 1 millimeter thick to hold 0.145 moles of oxygen at 154 K and 5 MPa. This ensures the oxygen is in conditions that will allow it to liquefy. There would be an identical radiator on the same side of the rocket that would be used for oxygen liquefaction if the original was damaged beyond repair. The oxygen radiators would undergo a self-repair attempt similar to the repair the hydrogen radiators would attempt.

The radiator can reach stable state temperature relatively quickly. Assuming the radiator is initially empty, oxygen brings 0.023 J/s to the radiator, and the radiator's initial temperature is 300 K, the radiator will radiate enough heat away to bring its temperature to 154 K in less than a second.

As mentioned above, it will take 200 hours for enough hydrogen to be collected. After 200 hours, 1.855 moles of oxygen will be collected. If more oxygen is desired, the rocket will need to stay longer or increase the hydrolysis rate.
When the rocket is ready to blast off, liquid hydrogen will flow through the core will undergo a phase change. After the hydrogen has passed through the core it will be combine with liquid oxygen past the nozzle of the thruster. The oxygen will be used to combust with the hydrogen. Normally, it is ideal to combust hydrogen and oxygen in an oxygen rich ratio. This can be set to any ratio, however, any molar ratio above 2:1.855 cannot be maintained for the entire flight between asteroids unless more oxygen is stored.

Methane

This entire study has been conducted under the pretense that the limiting factor for hydrogen refrigeration has been the rate at which hydrogen is produced. If hydrogen production wasn't the limiting factor, the factor would be the rate of heat removal. If something besides hydrogen which has a higher boiling point was being liquefied that would reduce the size of the radiators.

Hydrogen is the primary ingredient in several naturally occurring substances such as hydrocarbons and ammonia. Both of these compounds have higher boiling points than pure hydrogen. One theory to reduce the difficulty in liquefying the propellant is to change the fuel to a different compound with a higher boiling point.

Methane has a higher boiling point than hydrogen. It will condense at 190 K at 4.5 MPa. After assuming the methane enters the radiator at 300 K at 4.5 MPa and one mole of methane is produced for every two moles of hydrogen and the enthalpy values are determined, the energy balance equation used to determine the area of one side of the methane radiators can written as seen below:

$$A = \frac{2.78 * 10^{-6}\frac{\text{mol}}{\text{s}} * (13965\frac{J}{mol} - 6020.1\frac{J}{mol})}{2 * .9 * 5.67 * 10^{-8}\frac{W}{m^2 * K^4} * 1 * (190K^4 - 4\text{K}^4)} \approx 0.000166m^2 \quad (6)$$

This radiator will be 1.3 cm by 1.3 cm. This is a reasonable size for the radiators for this rocket. The interior of the radiator will at most be 1 millimeter thick to hold 0.00047 moles of methane at 190 K and 4.5 MPa. This ensures the methane is in conditions that will allow it to liquefy. There would be an identical radiator on the same side of the rocket that would be used for methane liquefaction if the original was damaged beyond repair. The methane radiators would undergo a self-repair attempt similar to the repair the other radiators would attempt.

The radiator can reach stable state temperature relatively quickly. Assuming the radiator is initially empty, methane brings 0.039 J/s to the radiator, and the radiator's initial temperature is 300 K, the radiator will radiate enough heat away to bring its temperature to 190 K in less than a second.

Methane is a possible material to convert hydrogen into to reduce radiator size, but its production must be considered. The asteroids could serve as a source of carbon for the methane. Enough carbon must be harvested and separated from the asteroid regolith in order to create methane. The carbon could be brought with the rocket, however, the methane would need to be dissociated into hydrogen and carbon to conserve the carbon for future burns if the rocket does not have a means to harvest and separate carbon from the asteroid regolith. Dissociating the methane and only burning the hydrogen would yield a better Isp than if methane was burned at the same temperature, however methane should burn at a higher temperature with oxygen then hydrogen alone would. Further research will need to be done to find ways to quickly create and dissociate methane in order for this idea to be usable for this mission.

Ammonia

The hydrogen fuel could also be converted to ammonia. Ammonia will liquefy at 300 K at 1.1 MPa, so no radiator is required to liquefy the fuel if ammonia is created. No nitrogen has been discovered at the destinations of the rocket. In order to produce ammonia, nitrogen must be brought with the craft. Ammonia must also be dissociated prior to burns in order to conserve the nitrogen for future uses. Nitrogen will need to be stored at cooler temperatures while not in use. Ammonia can undergo radiolysis. This is a 2 way process, so ammonia could be formed and dissociated. This could be one means to combine and separate the nitrogen and hydrogen, but more research will need to be done to find a fast enough way to create and separate ammonia so that it is readily available.

TABLE 1. This is a summary the radiators and their specifications.

Material	Area of one side (cm^2)	Temperature (K)	Pressure (MPa)	Moles (mol)
Hydrogen (H2)	3910	32	1.1	2.0
Oxygen (O2)	3.71	154	5.0	0.145
Methane (CH4)	1.66	190	4.5	0.00047
Ammonia (NH3)	0.0	300	1.1	N/A

CARBON BASED HYDROGEN STORAGE METHODS

There have been several studies done to attempt to store hydrogen on earth at room conditions. This is difficult because hydrogen is a highly reactive gas at room temperature. Even if it doesn't chemically bond with a compound it is small enough to lodge in the gaps in the crystalline structure of any nearby molecules as one might see in hydrogen embrittlement. These problematic traits may serve to be the solution to several hydrogen storage problems.

Hydrogen has the ability to be bonded with carbon through chemisorption and physisorption. Chemisorption is a phenomena in which hydrogen causes a carbon- carbon bond to break and forms a carbon hydrogen bond. In order for this to occur hydrogen cannot be bonded with another hydrogen atom. They must be single atoms of hydrogen. Physisorption is the phenomena in which hydrogen collects in the lattices of carbon molecules formations[2].

Single Walled Carbon Tubes

One way to store hydrogen is with single walled carbon tubes (SWCT). These carbon tubes are essentially one carbon atoms thick. A combination of these atoms form to create cylinders of varying diameter and length. Hydrogen will bind with these structures in both of the ways mentioned above, however, it seems to be more effective at bonding chemically bind with the carbon atoms at room temperature and pressure. Researchers at the National Renewable Energy Lab state, "Careful work at NREL indicates a maximum capacity for adsorption of hydrogen on SWNTs is ~8 wt%.[3]" Studies at Stanford have demonstrated the ability to saturate carbon with hydrogen to 65±5% or 5.1±1.2% weight percent through chemisorption at room temperature and pressure[2].

Based on these numbers and the assumption the rocket needs to store 4 kg of hydrogen. The rocket will need to bring 78.5 kilograms of nanotubes to store the hydrogen. The nanotubes could be stored where the radiators would be on the exterior of the rocket since the need for hydrogen tanks and capillary tubes in the radiators has been removed. Sigma-Aldrich sells carbon nanotubes that have a density of ~1.8 gm/cm^3[4]. Based on that number, the volume of the tubes would be about 43612 cm^3. To understand that size, one potential dimension for the 2 exterior carbon tube assemblies could be 60cm x 61cm x 6cm. The oxygen radiators would still be needed. Three carbon tube assemblies could be created, but one would have to be smaller than the others to allow for the oxygen radiators. In the rocket, the hydrogen should be able to be undergo chemisorption if the hydrogen is exposed to the SWCT soon after the water has been hydrolyzed. This will ensure the hydrogen atoms do not recombine to form hydrogen molecules.

Graphene

An additional way to store hydrogen is with graphene sheets. Graphene is essentially one carbon atom thick. Typically, these atoms are arranged into a plane, but they can be formed into other one atom thick shapes. Graphene seems to be able to store more hydrogen through physisorption. Researchers at the Istituto Nanoscienze – Cnr and Scuola Normale Superiore have been experimenting with hydrogen absorption in graphene sheets. They have been able to get 6% weight percent absorbed into graphene when the hydrogen was 77K and 0.1 MPa through physisorption[5]. This percentage was achieved by creating waves in the graphene and then arranging sheets of graphene, so that the cusps of the waves were close to each other as seen in Figure 2. The study suggests that graphene can hold more hydrogen at low temperatures and high pressures as seen in Figure 3. The figure also suggests several means to increase the density of hydrogen ranging from hydrocarbons to metal hydrides to liquid hydrogen.

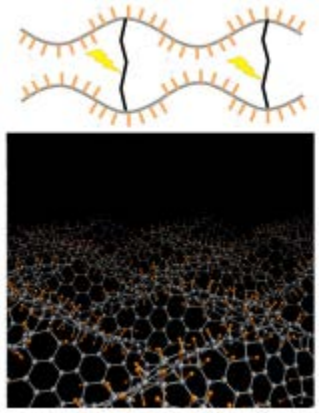

FIGURE 2. 2 Dimensional and 3 Dimensional Images of Graphene sheets with Wave like Arrangements[5].

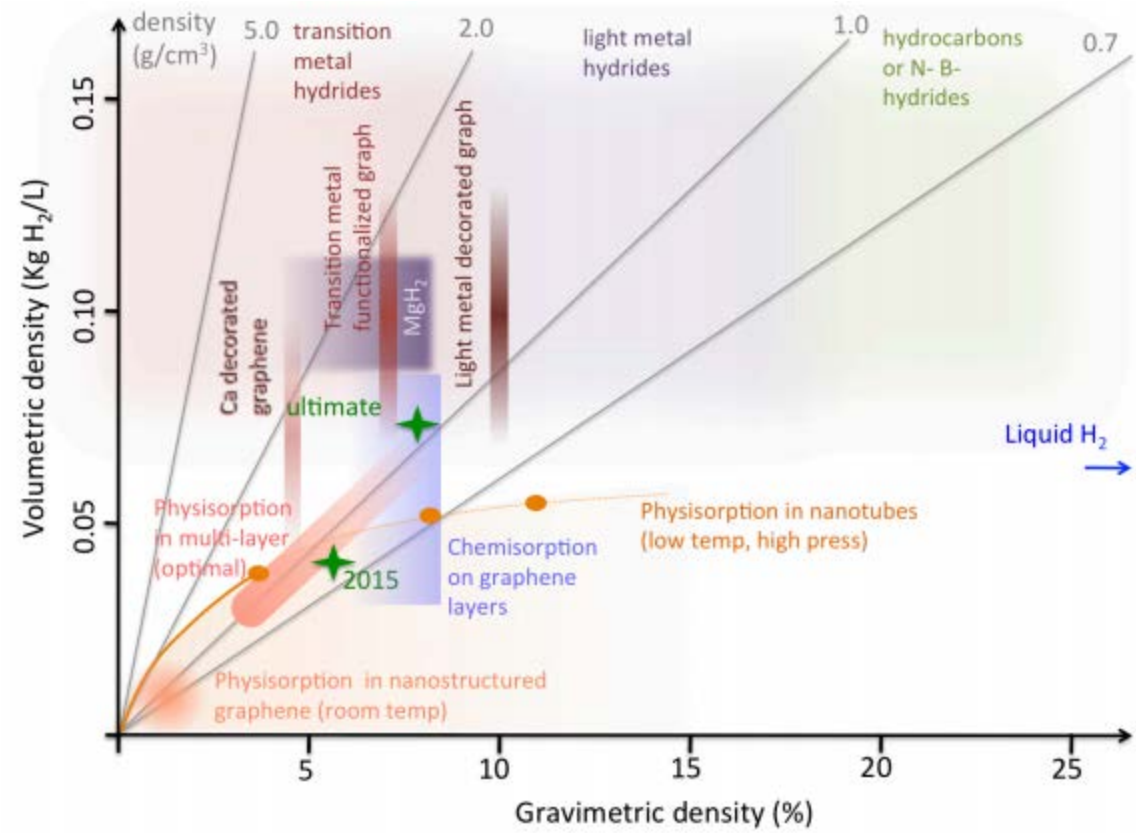

FIGURE 3. "Gravimetric vs. Volumetric Density Diagram for Several Hydrogen Storage Systems[5]."

As mentioned above, graphene could store 6% weight percent at 77K which is not easily achieved on earth, but the radiators on the rocket have shown to be able to get hydrogen to 32 K. At 6% weight percent, the rocket would require 67 kg of graphene. Applied Nanotech Inc. sells graphene that has a density of about 1.75 g/cm^3[6]. Based on that number, the volume of the graphene sheets would be about 37715 cm^3. To understand that size, one potential dimension for the 2 exterior graphene assemblies could be 60cm x 60cm x 5.25cm.

Other studies have arranged the carbon atoms in different alignments such as the pillared graphene arrangement seen in Figure 4. These other studies have also proposed doping carbon molecules with other atoms to improve its hydrogen capacity. There are several possibilities through geometrical and chemical means to improve the way hydrogen is stored.

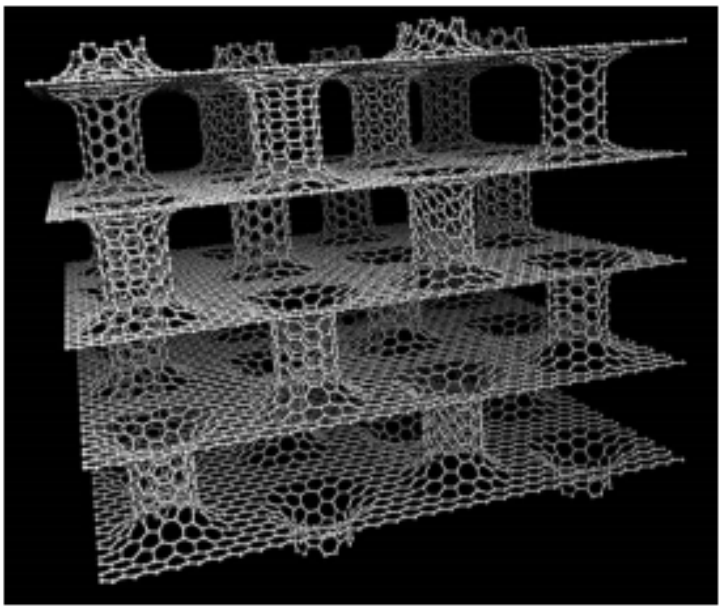

FIGURE 4. "Pillared graphene. A novel 3-D network nanostructure proposed for enhanced hydrogen storage. [Reproduced with permission from Ref. 42][7]."

Hydrogen storage now seems plausible within specifically arranged carbon atoms. In order for the mission to be performed, the hydrogen must be accessed easily and quickly and the means for storage must be reusable. The researchers at the Istituto Nanoscienze and Stanford both stated when the respective materials are annealed they would release their hydrogen stores. The Stanford researchers were able to cause the SWCT to release all of the hydrogen at 600 ºC. Both groups state that the respective materials are reusable and the hydrogen storage processes are reversible.
In order for the radiators to quickly release their contents, they must be able to reach a temperature of 600 ºC. It is proposed that the radiators are lined with electric wire heaters that can cause the graphene to reach the required temperature without damaging the graphene.

Graphene and SWCTs are carbon based materials. These materials when exposed to a hydrogen environment may form methane under the right conditions. If a mission requires methane to be used as a propellant, the craft could exhaust all of its carbon based hydrogen storage materials for a one time use of methane. This method would be performed in an emergency situation since the craft wouldn't be able to store hydrogen as effectively afterwards.

Graphene and SWCTs are stable under the conditions described in this paper. They should not break apart, however, if enough energy was put into these structures methane may form. When graphite is irradiated with particles, its carbon atoms can be dislocated from their original locations and dislodge other carbon atoms until the atoms fill vacancies in the carbon structure. These dislocations may eventually create new planes within the structure[8]. Until they do, it may be possible to get these dislocated carbon atoms to bond with hydrogen atoms if the carbon structure was in a hydrogen environment.

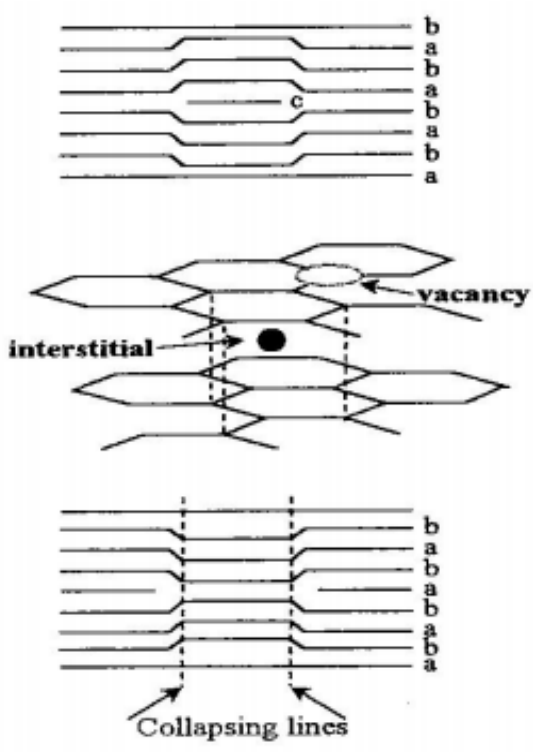

FIGURE 5. "Displacement damage mechanism in graphite[8]."

A study was performed in 2009 where carbon nanotubes were irradiated with a high energy proton beam of 10 MeV, an electron beam of 2 MeV, and Ultraviolet (UV) light in an ambient environment. The UV light caused oxygen molecules to dissociate into oxygen atoms. These atoms oxidized with the surface of the carbon nanotubes. This reaction was caused by the energy from the protons and electrons[9]. When enough radiation is present, it is feasible to hydrogenate carbon structures and create methane or other hydrocarbons.

Graphene and SWCT are fairly new materials. Several more studies will need to be conducted to fully understand their potential and qualities. How these materials function on a large scale will need to be known as well. Both of the studies mentioned above seem to have been performed on a small scale or tested by programs. One study performed at the Istituto Nanoscienze was performed with 180 carbon atoms[10], nevertheless, these materials have captured much attention in the short time of their discovery. Much research has and will continue to be put into them to better understand their potential and the optimal way to use them. Further research will be able to show how these materials function on a large scale basis too.

CONCLUSION

Several means to store hydrogen in a space environment have been proposed. It has been demonstrated that there is present technology that allows the rocket to store hydrogen if it was built and lifted off today. Radiators can be constructed to a reasonable size to create liquid hydrogen. A more efficient means to store hydrogen has also been proposed. This way has demonstrated the ability to store hydrogen on a small scale. It is believed that within a short amount of time this technology will improve to the point that hydrogen could be stored in some form of carbon molecule assembly and be used on a mission to space.

NOMENCLATURE

$\dot{m}$	=	Mass flow rate
$\dot{m}_i$	=	Mass flow rate at the inlet
$\dot{m}_o$	=	Mass flow rate at the outlet
h_i	=	Enthalpy at the inlet
h_o	=	Enthalpy at the outlet
$\dot{Q}$	=	Heat transfer rate
ε	=	emissivity
σ	=	Stephan Boltzmann constant, $5.67*10^{-8}\frac{W}{m^2*K^4}$
F	=	View factor
A	=	Area of the radiator
T_s	=	Absolute temperature of the radiator surface
T_a	=	Absolute temperature of the ambient
Z	=	Compressibility factor
P	=	Pressure
Atm	=	Atmosphere

ACKNOWLEDGMENTS

We want to thank the people at the CSNR for providing the inspiration and ground work and supporting us during our time there.

REFERENCES

[1] Thermophysical Properties of Fluid Systems. National Institute of Standards and Technology, 2011. Web. <webbook.nist.gov/chemistry/fluid/>.

[2] Nikitin, A., Ogasawara, H., Mann, D., Denecke, R., Zhang, Z., Dai, H., Cho, KJ, and Nilsson, A., *Hydrogenation of Single-Walled Carbon Nanotubes*,. http://arxiv.org/ftp/cond-mat/papers/0510/0510399.pdf

[3] Dillon, A.C., Gilbert, K.E.H., Parilla, P.A., Alleman, J.L., Hornyak, G.L., Jones, K.M., and Heben, M.J., *Hydrogen Storage in Carbon Single-Wall Nanotubes*, (2002). *http://www.nrel.gov/docs/fy02osti/32405b28.pdf*

[4] http://www.sigmaaldrich.com/catalog/product/aldrich/704121?lang=en&region=US

[5] Tozzini, V. and Pellegrini, V., *Prospects for Hydrogen Storage in Graphene*,(2013). http://arxiv.org/ftp/arxiv/papers/1207/1207.5703.pdf

[6] www.appliednanotech.net/tech/**graphene**_films.php.

[7] Spyrou, K., Gournis, D., and Rudolf, Petra., "Hydrogen Storage in Graphene-Based Materials: Efforts Towards Enhanced Hydrogen Absorption," *ECS Journal of Solid State Science and Technology*, (2013). http://jss.ecsdl.org/content/2/10/M3160.full.pdf+html

[8] Burchell, Tim. *Neutron Irradiation Damage in Graphite and Its Effects on Properties*. Oak Ridge, TN, 2008. http://web.ornl.gov/~webworks/cppr/y2001/pres/114924.pdf

[9] Celina, Mathias C. *Polymer Durability and Radiation Effects*. Washington, DC: American Chemical Society;, 2008. Print. http://pubs.acs.org/doi/pdf/10.1021/bk-2007-0978.ch020

[10]Goler, S., Coletti, C., Tozzini, V., Piazza, V., Mashoff, T., Beltram, F., Pelegrini, V., and Heun, S. *The Influence of Graphene Curvature on Hydrogen Adsoprtion: Towards Hydrogen Storage Devices.* (2014). http://www.researchgate.net/publication/252194761_Influence_of_Graphene_Curvature_on_Hydrogen_Adsorption_Toward_Hydrogen_Storage_Devices

Time Dependence of Fission Energy Deposition in Nuclear Thermal Rockets

Michael J. Eades[1] , Jarvis A. Caffrey[2]

[1]*Nuclear Engineering Program, The Ohio State University, Columbus, OH 43201*
[2]*Department of Nuclear Engineering & Radiation Health Physics, Oregon State University, Corvallis, OR 97301*
(740)375-5887; and eades.15@osu.edu

Abstract. Presented is a time dependent estimate of the effective energy absorbed in a reactor from a fission or $Q^f_{eff}(t)$ for a nuclear thermal rocket (NTR). An estimate of $Q^f_{eff}(t)$ is required for many aspects of reactor analyses as a value for $Q^f_{eff}(t)$ is needed to calculate fission rate in a reactor. Fission rate in a reactor has a direct impact on thermal, shielding, burn up, and decay heat analysis calculations and $Q^f_{eff}(t)$ serves as normalization constants to scale effects based upon reactor power. The $Q^f_{eff}(t)$ for a reactor is dependent on many factors such as faction of energy leaking out of the system, energy released from radiative capture of neutrons, energy released from the activated material in the core, and the decay of the current inventory of fission products. A NTR operates in a unique regime where decay emissions from fission products are not in equilibrium with fission product production. Decay of fission products account for ~7% of all energy produced in a nuclear reactor in steady state operation. Because the decay of fission products contribute a sizeable portion of the total energy deposited in the core and the inventory of fission products is not in equilibrium a static estimate of $Q^f_{eff}$is not well suited for NTR reactor analysis. Estimates of $Q^f_{eff}(t)$ in a representative NTR concept over a 30 minute burn were produced using a time-dependent MCNP6 model and an analytical model derived from information readily available in literature. The required fission rate to achieve the power profile of a representative 30 minute NTR burn was calculated with each model and compared against the default steady state assumption in MCNP6. The time-dependent MCNP6 and analytical models agreed very closely. It was found that over a representative 30 minute NTR burn the time-dependent MCNP6 model predicts a fission rate ranging from 0.99 to 1.07 times the value determined using the default steady state assumption for Q^f_{eff}in MCNP6 burnup calculations.

Keywords: Q-effective, time-dependent, NTP, MCNP6, CINDER90

INTRODUCTION

Many fundamental calculations in nuclear engineering require knowledge of the relationship between fission rate and reactor power, driven by the value of $Q^f_{eff}(t)$ that defines energy deposited per fission event. Fission rate has a directly proportional effect on heat deposition, flux, and dose calculations. Fission rate and flux in a reactor is important to burn up and ^{135}Xe related calculations as these calculations simulate a complex interconnected web of production, decay and transmutation of nuclides. Some behavior of burn up and ^{135}Xe system do not scale linearly to fission rate and flux. The fission rate and flux in a reactor also impacts estimates of decay heat produced after the reactor is shut down. As with burnup calculations, decay heat calculations capture a complex evolution of nuclides. An increase in fission rate is not only associated with a larger inventory of fission products but also with a higher flux that may produce more short lived nuclides

For analyses of traditional reactors, estimates of $Q^f_{eff}(t)$ generally assume steady state operation in which the energy deposited by decay emissions from fission products reaches equilibrium with fission product production. For this reason a static assumption of Q^f_{eff} can be used. For analyses of pulse reactors that operate on very short time scales, the decay emissions from fission products can be ignored for many calculations. Nuclear thermal rockets operate on the time scale of 30 minutes, and the time dependence of the build in of fission products cannot be ignored.

Effective Energy Released Per Fission

In order to relate power to fission-rate a value for effective energy absorbed in a reactor from a fission event is needed as a function of time; here deemed as $Q^f_{eff}(t)$. Several factors affect the effective energy absorbed in a reactor from a fission event. Equation (1), (2), and (3) with the subsequent explanation in Table 1 briefly discuss the various components of $Q^f_{eff}(t)$ and how they can vary. It should be noted that these explanations are in terms of energy absorbed in a reactor and not energy released from a fission or possibly recoverable energy from a fission.

$$Q^f_{eff}(t) = Q^f_p(t) + Q^f_d(t) \tag{1}$$

$$Q^f_p(t) = Q^f_{fe}(t) + Q^f_{pi}(t) \tag{2}$$

$$Q^f_d(t) = Q^f_{fpd}(t) + Q^f_{act}(t) + Q^f_{di}(t) \tag{3}$$

TABLE 1. Q-value Definitions

$Q^f_{eff}(t)$	Effective energy absorbed in the reactor after a fission event as of time t after the fission event.
$Q^f_p(t)$	Prompt energy absorbed in the reactor after a fission event at time t after the fission event. Here defined as less than 1 millisecond after fission.
$Q^f_d(t)$	Delayed energy absorbed in the reactor after a fission event at time t after the fission event. Here defined as greater than 1 millisecond after fission.
$Q^f_{fe}(t)$	Energy from fission fragments, prompt photons, prompt neutrons, and very short lived fission products that are absorbed in the reactor after a fission event at time t after the fission event.
$Q^f_{pi}(t)$	Energy from any reactions that are not neutron induced fission which occur as a consequence of the fission event that arises within 1 millisecond after a fission event. Primarily this terms accounts for radiative capture of neutrons and photofission.
$Q^f_{fpd}(t)$	Energy from the decay of fission products absorbed in the reactor after a fission event at time t after the fission event.
$Q^f_{act}(t)$	Energy from the decay of activated material in the core absorbed in the reactor after a fission event at time t after the fission event.
$Q^f_{di}(t)$	Energy from any reactions that are not neutron induced fission, which occur as a consequence of the fission event that arise more than 1 millisecond after a fission event. This is a minor term that accounts for phenomenon such as the radioactive capture delayed neutrons and photoneutrons created by the gamma ray emissions of fission products interacting with other parts of the core.

With an estimation of $Q^f_{eff}(t)$ it is possible to relate a fission rate profile in a reactor and the power of the reactor. This is outlined in Equations (4), (5) and the subsequent explanations. The relationship is not immediately straightforward and requires that separate time variables for time after a fission event and time along the operating timeline of the reactor be considered.

$$R(t) = \frac{d}{dt} Q^f_{eff}(t) \tag{4}$$

$$P(T) = \int_0^T R(T - t') * F(t')dt' \quad (5)$$

Where R(t) is the time derivative of the recoverable energy absorbed in the reactor after a single fission event as a function of time after the fission event, F(T) is total fission rate in the reactor as a function of time, T is a time along the operational timeline of the reactor, and P(T) is power of the reactor as a function of reactor operating time.

METHODS AND PROCEDURE

Representative Nuclear Thermal Rocket

The representative NTR concept used for this work is a LEU W-UO_2 cermet fuel, $ZrH_{1.8}$ moderated rocket using H_2 propellant. The $ZrH_{1.8}$ moderator is kept in tie tubes where the $ZrH_{1.8}$ actively cooled by cold H_2 that circulates though the tie tube. The concept is loosely based on the LEU NTR concepts recently produced by Center for Space Nuclear Research [1]. Figure 1 is an over view of the representative NTR concept's geometry. Table 2 lists key core dimensions and Table 3 gives details about the fuel. It should be noted that the core has a large leakage pathway at the bottom (nozzle end) of the fuel which has no reflector. A modified version of NTRgen [2] was used to generate the MCNP input decks.

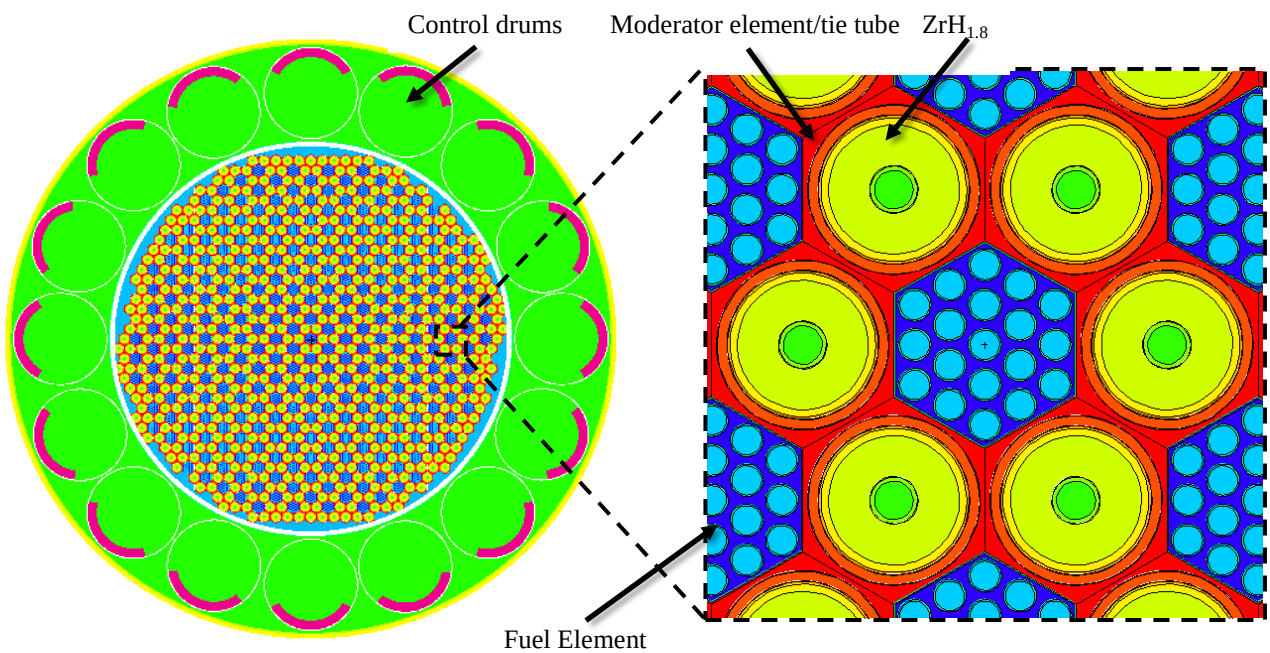

FIGURE 1. Cross section of the geometry of the representative NTR concept

TABLE 2. Key Dimensions

Active Core Length (cm)	84.0
Active core Diameter (cm)	64.0
Total Core Length (cm)	99.2
Total Core Diameter (cm)	99.7
Top axial BeO reflector (cm)	15.2
Radial Be Reflector thickness (cm)	16.0

TABLE 3. Fuel Properties

Composition (volume %)	UO_2-ThO_2-W (56-4-40)
Flat to Flat (cm)	1.900
^{235}U a%	19.75
% of Theoretical Density	95
Channel Diam. (cm)	0.345
Clad Material	^{184}W 95 a%
Clad Thickness (cm)	0.018

MCNP6 Model

MCNP6 features an implementation of the CINDER90 nuclide evolution code available through use of the Activation Control (ACT) and Depletion/Burnup (BURN) cards. In the present study, reaction rates for nuclide production through absorption were tracked by MCNP6 and fed to the CINDER90 algorithm to track the time-dependent emission of gamma radiation across 25 energy groups. Delayed neutron production is tracked by a separate library but is also controlled by the ACT card.

Absorption and heating tallies for all reactor components are binned in time increments such that average energy absorption in a time bin is determined from a single fission event. Integrating through time for a given fission rate demonstrates the time dependence of Q^f_{eff} as the delayed gamma source term builds into equilibrium. The $R(t)$ term used in this study was estimated by assuming that energy was deposited at a constant rate within each time bin interval. For the purposes of this work any energy deposited in the reactor in the first millisecond after a fission event is considered prompt energy. No individual time bin had a fractional standard deviation greater than 0.7 % due to Monte Carlo statistical uncertainty, and the vast majority of time bins had less than 0.1% relative error.

Analytical Model

A simple analytical model for $Q^f_{eff}(t)$ and $R(t)$ was derived using information readily available in literature. This analytical model is far simpler than the MCNP6 model but was intended to offer a comparison to demonstrate similar time dependent trends.

An estimation of $Q^f_p(t)$ was taken from a reference for the Advanced Test Reactor (ATR) [3]. This estimation uses MCNP5 and ENDF data files to calculate $Q^f_p(t)$ of the ATR. The ATR core design and operating characteristics are very different from the representative nuclear thermal rocket used in the MCNP6 model, but the results are considered applicable as the majority of fissions in both reactors occur in ^{235}U at thermal energies. Furthermore, the estimation of $Q^f_p(t)$ in the ATR reference is well suited for this work because it includes a $Q^f_{pi}(t)$ term that is often excluded from estimations of prompt fission energy. In the ATR reference, $Q^f_{pi}(t)$ term accounts for 8.20 MeV or about 4% of the total energy of a fission.

A time cutoff between prompt and delayed energy is not specified in the ATR reference [3]. The same convention presented in the MCNP6 model is followed where the prompt energy is assumed to be all the energy released evenly within the first millisecond of a fission event. This approach is sufficient when reactor power or fission profile does not change rapidly on the scale of milliseconds

The estimation of $Q^f_d(t)$ found in [3] was calculated with MCNP5 and values of delayed energy found in ENDF data files. The values of delayed energy found in ENDF data files do not have a time dependence. An estimation of $Q^f_d(t)$ with a time dependence was taken from the decay heat relation derivation for a general reactor presented in [4]. This relation is valid from 10 s < t < 100 days and has a quoted accuracy of "within a factor of 2" [4]. The period between the end of the prompt and the start of the decay heat correlation is treated as period of zero energy

production because of lack available models. The combined analytical model considering the prompt and delayed contributions is presented in Equation (6).

$$R(t) = \begin{cases} 1.889364 \times 10^5 \ \frac{MeV}{s} \ if \ t < 0.001 \ s \\ 0 \ \frac{MeV}{s} \ if \ 0.001 \leq \ t \leq 10 \ s \\ 2.66t^{-1.2} \frac{MeV}{s} \ if \ 10 \ s < \ t < 100 \ days \\ 0 \ \frac{MeV}{s} \ if \ 100 \ days \leq \ t \end{cases} \quad (6)$$

.

RESULTS

Figure 2 and 3 shows $R(t)$ and $Q^f_{eff}(t)$ produced from the time-dependent MCNP6 model for the representative NTR concept, the analytical model, and the default assumption in MCNP6 burn up calculations. Table 4 and Table 5 compare estimates from the models presented in this work with values found in literature of the prompt and total energy absorbed from fission.

It can be seen in Figure 3 and Table 5 that the time dependent MCNP6 solution and the analytical solution of $Q^f_{eff}(t)$ in time periods relevant to an NTR (~ 30 minutes) is notably less than the static estimates for Q^f_{eff} found in literature. The difference between the static estimates of Q^f_{eff} and the time dependent estimates of $Q^f_{eff}(t)$ in the NTR time scale can be primarily attributed to the inventory of fission products not fully decaying. In Figure 3 the time dependent MCNP6 solution can be seen trending towards the static value after approximately 100 days. A contributing factor as to why the $Q^f_{eff}(t)$ predicted by the time dependent MCNP solutions is lower than even after 100 days is that the representative NTR concept is a small high leakage reactor that is unreflected on one axial side. The time dependent MCNP6 solution for the representative NTR calculated that 0.67 MeV of fission energy leaks out of the reactor in the form of gammas, neutrons, and electrons liberated by ionizing radiation.

The $Q^f_{eff}(t)$ predicted by the MCNP6 produced model and analytical model agree closely in the time period from 10 seconds to 30 minute range (~2×10^3 seconds) relevant to NTR operation. After 30 minutes the analytical model predicts a $Q^f_{eff}(t)$ lower than the MCNP6 produced model.

At first glance close agreement would not be expected between the MCNP6 produced model and analytical model as the analytical model neglects the energy generated in the time period between 1 millisecond and 10 seconds after a fission. The time-dependent MCNP6 model demonstrates that 3.84 MeV of energy is absorbed in this period, however this absence is largely offset the analytical model's estimation of $Q^f_p(t)$ being 3.37 MeV larger than the MCNP6 model. The $Q^f_p(t)$ in the analytical model comes from ATR which generates a large amount of heat from neutron absorption in its hafnium control elements.

TABLE 4. Comparison of Prompt Energy Absorbed from a Fission

Prompt recoverable energy from a fission (MeV)	Notes	Source
180.88	MCNP6 assumption for prompt energy released directly from a fission of ^{235}U	[5]
180.75	ATR model without radiative capture gammas	[3]
188.95	ATR model with radiative capture gammas also assumed prompt Q_p^f for the analytical model	[3]
185.58	MCNP6 solution (all energy released within 1 millisecond of a fission)	Present work

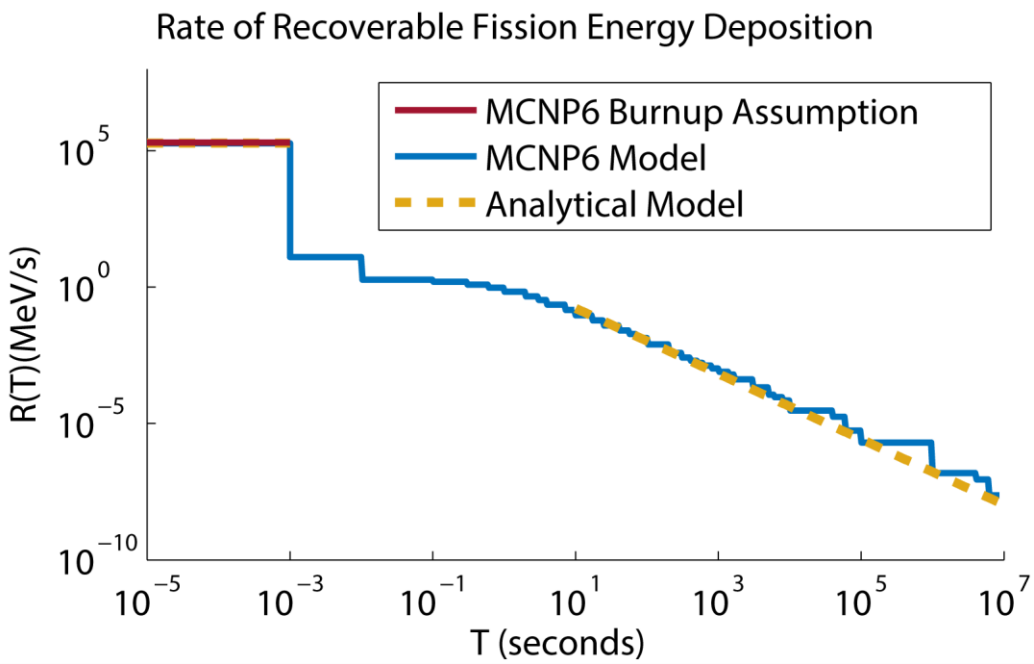

FIGURE 2: $R(t)$ for the models presented in this work.

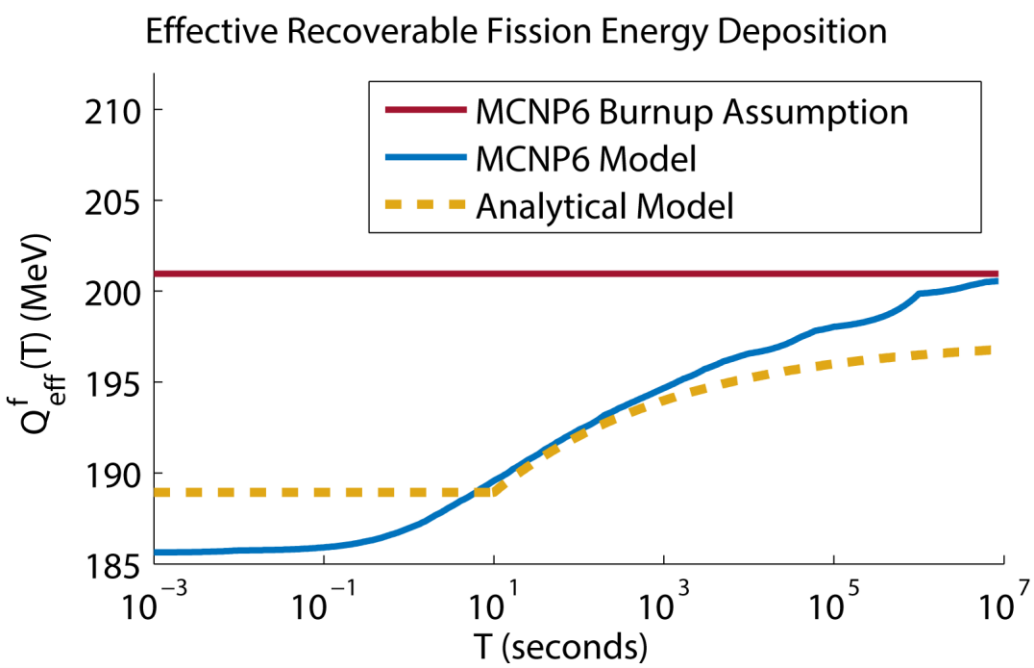

FIGURE 3: The $Q^f_{eff}(t)$ produced by integrating the models shown in Figure 2.

TABLE 5. Comparison of Total Energy Absorbed From a Fission

Total recoverable energy from a fission (MeV)	Notes	Source
198-204	General range	[6]
200.45	The assumption of 1.05 g of ^{235}U equates to MWD of energy	[7]
201.70	ORIGIN2 estimate ^{235}U	[8]
200.00	Assumption for all fissions in ORIGIN, suggested default for MONTEBURNS version 1.00, value used in many preliminary calculations	[8][9][7]
201.78	ATR model	[3]
200.96	MCNP 6.1 assumption for a fission in ^{235}U in burn up calculations	[5]
191.46	Analytical model after 1 minute	Present work
194.74	Analytical model after 1 hour	Present work
196.78	Analytical model after 100 days	Present work
191.78	MCNP6 model for representative NTR after 1 minute	Present work
195.84	MCNP6 model for representative NTR after 1 hour	Present work
200.56	MCNP6 model for representative NTR after 100 days	Present work

A required fission rate over a power profile for a representative 30 minute NTR burn was calculated for the MCNP6 produced model, the analytical model, and the default assumption in MCNP6 burn up calculations by solving Equation (5) iteratively with a node placed at every 5 seconds. The results of this calculation are shown in Figures 4 through 7. By maintaining a desired flux power profile and changing the fission rate, this represents the physical scenario where a NTR control system somehow senses the total power being produced by means other than neutron or gamma flux monitoring and the control system adjusts the fission rate or flux in the core accordingly.

The simple representative power profile increases linearly from 0 to 550 MW over 3 minutes, holds power at 550 MW for 30 min and then ramps down power at the same rate as that used in startup. Due to the possibility of there being no physical solution for fission profile as the power ramps down because of decay heat, only the first 2 minutes of the ramp down part of the power profile are solved.

Figure 7 shows that the time-dependent MCNP6 model predicts a fission rate ranging from 0.99 to 1.07 times the value determined using the default steady state assumption for Q^f_{eff} in MCNP6 burnup calculations. In addition it is seen that the time-dependent MCNP6 model fission rate varies by ~2% over the full power plateau of the NTR burn.

It is difficult to state precisely what the effect would be on the NTR system design if the information in Figures 4 through 7 was ignored and a static Q^f_{eff} was used that under predicted the required fission rate and assumed that fission rate was constant though the full power plateau. It is fair to say that such effects should certainly be considered in the design of instrumentation and control systems, and must be accounted for in the development reactor power and thrust profiles in mission planning.

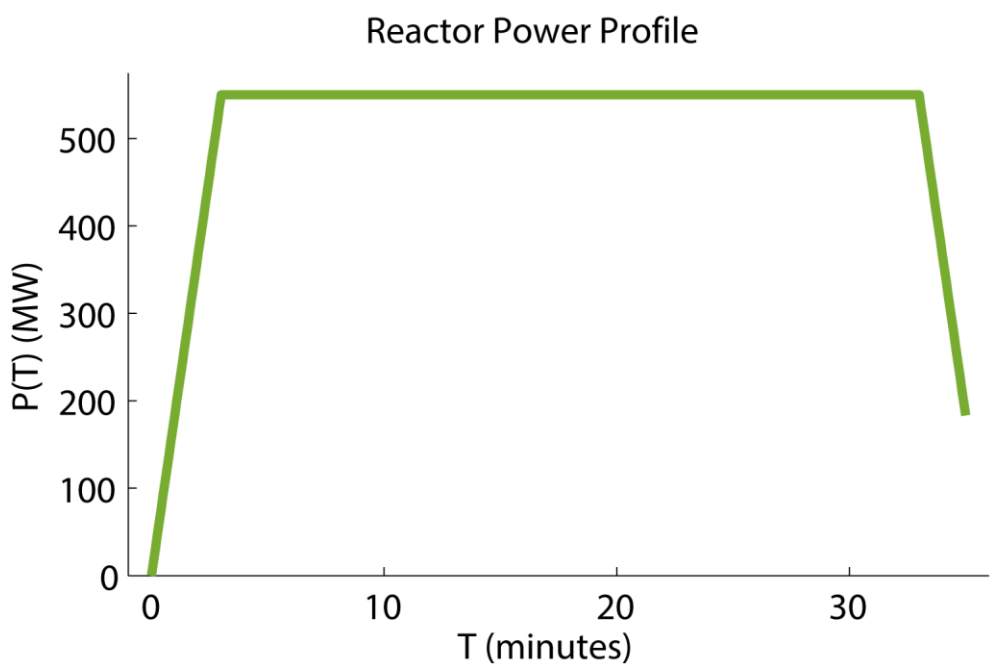

FIGURE 4: The representative power profile for an NTR burn.

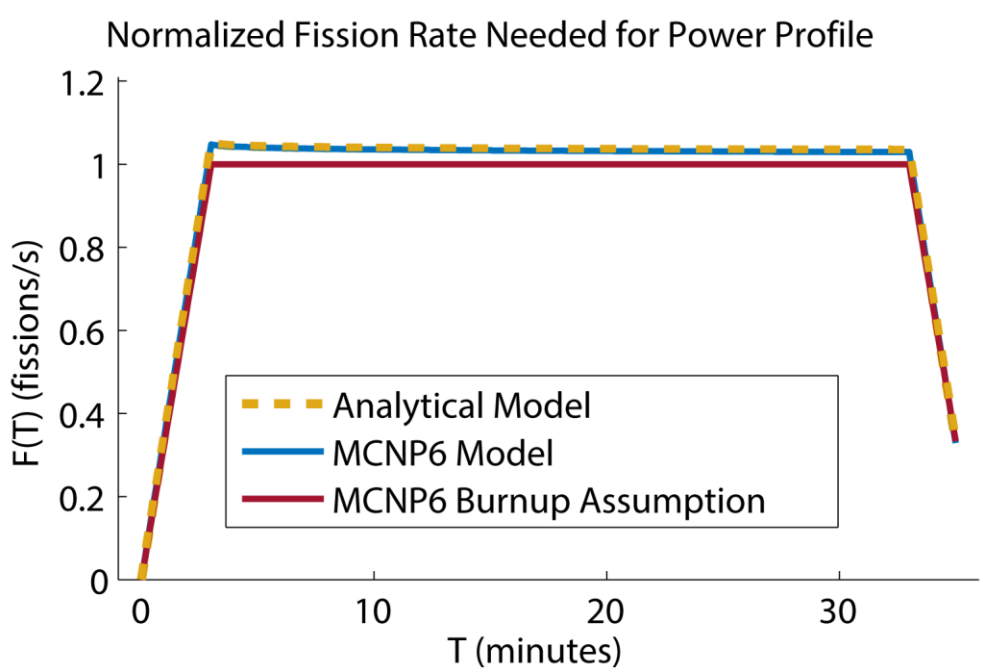

FIGURE 5: The fission profile required to achieve the power profile in figure 4.

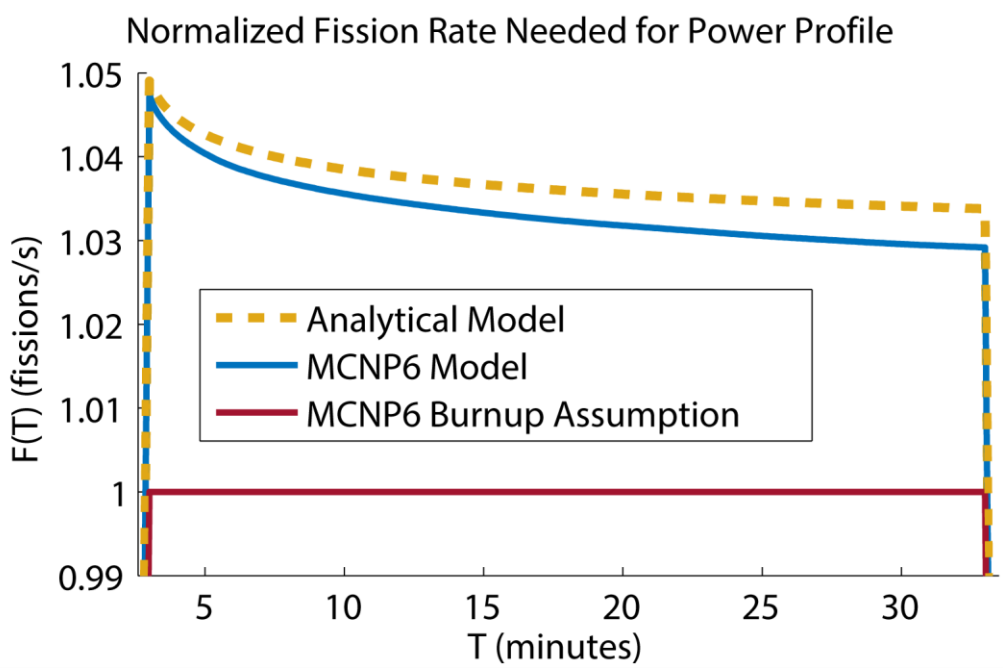

FIGURE 6: The fission profile required to achieve the power profile, an enlarged section of the fission profile.

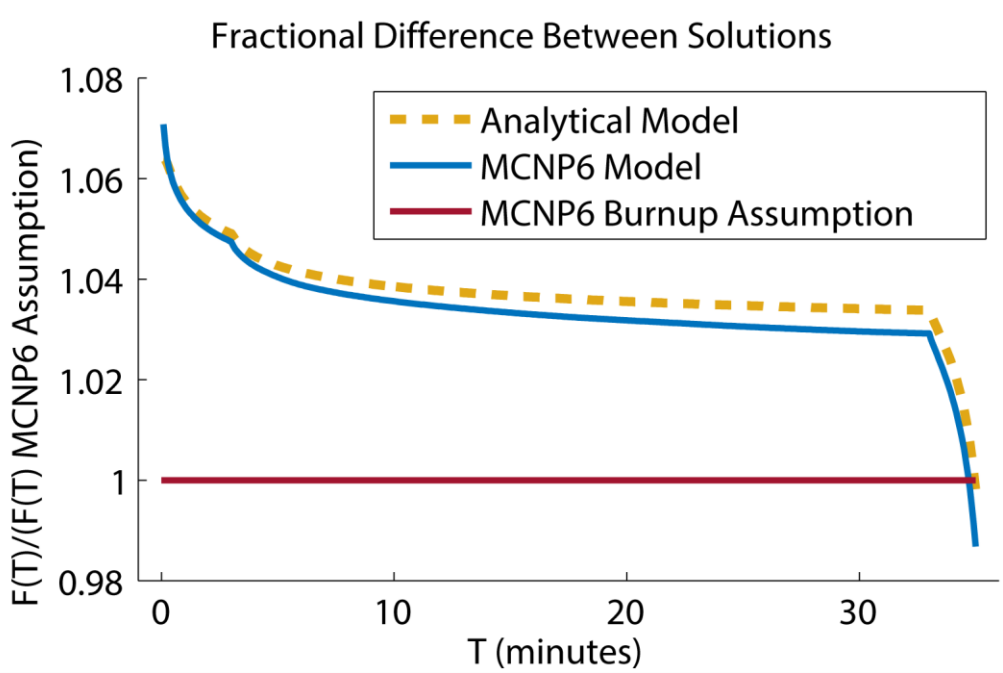

FIGURE 7: The fractional error of the solutions presented in the present work and the MCNP6 burn up assumption.

Additional consequences for ignoring time dependence of $Q^{f}_{eff}(t)$ in an NTR include lower fidelity estimations of key values such as ^{135}Xe worth, decay heat production, and dose calculations. It is also possible that if the change in

required fission rate to maintain a desired power with a time dependent $Q_{eff}^{f}(t)$ is not considered then the total power of the reactor could change in unexpected ways and violate temperature limits in fuel.

CONCLUSION

Estimations of $Q_{eff}^{f}(t)$ for a NTR were produced using MCNP6 and an analytical model derived from information readily available in literature. It was found that both models predicted a lower $Q_{eff}^{f}(t)$ than the static estimates for Q_{eff}^{f} found in literature over the time scales relevant to NTRs. When the time-dependent MCNP6 model was used to back calculate the required fission rate profile for a representative NTR power profile it was found that the time-dependent model for $Q_{eff}^{f}(t)$ predicts a fission rate that is at minimum 0.99 and at maximum 1.07 times the default MCNP6 assumption.

Explicitly calculating the fission rate in a reactor is essential for many aspects of thermal, shielding, burn up, and decay heat analysis calculations. Using methods such as those presented in this work to more thoroughly understand $Q_{eff}^{f}(t)$ will assist in high fidelity modeling and simulations of NTRs.

Future work includes refining estimates of $Q_{eff}^{f}(t)$ by ensuring that the MCNP6 model includes all relevant reactions and comparing estimates to established decay heat standards such as the American Nuclear Society's decay heat standard. In addition, the effect and sensitivity of $Q_{eff}^{f}(t)$ on burnup and ^{135}Xe calculations will be examined. Finally, issues related to the ability of radiometric probes to predict the thermal power of the reactor when a variable fission rate is needed to maintain constant power will be investigated.

NOMENCLATURE

MeV	=	Megaelectron-volts	MW	=	Megawatt
MWD	=	Mega-Watt-Day			

ACKNOWLEDGMENTS

This work was supported by the NASA Nuclear Cryogenic Propulsion Stage (NCPS) program and the NASA Office of the Chief Technologist's Space Technology Research Fellowship. The authors would like to thank David Dixon for supplying this work with NTRgen and the many people at NASA who have supported the NCPS and made this work possible.

REFERENCES

[1] P. F. Venneri, W. Deason, P. J. A. Husemeyer, G. C. Rosaire, R. O'Brien, S. Howe and Y. Kim, "Design of a Low-Enriched Uranium Tungsten CERMET Fueled Nuclear Thermal Rocket," Center for Space Nuclear Report 2014.

[2] B. W.AMIRI, "Iterative procedure for enrichment zoning of nuclear thermal rockets" Masters Thieses University of Florida, 2006

[3] Sterbentz J. W., *Q-value (MeV/fission) Determination for the Advanced Test Reactor,* Idaho National Laboratory Report INL/EXT-13-29256 (2013)

[4] Todreas N.E and Kazimi M.S., *Nuclear Systems Volume I: Thermal Hydraulic Fundamentals, Second Edition,* CRC Press, Boca Raton, page 104 (2011)

[5] Pelowitz, D.B. (et al), 2013. M*CNP6 User's Manual, Ver. 1*, LosAlamos National Laboratory, LA-CP-13-00634 (2013)

[6] Lamarsh J.R. and Baratta, *A.J., Introduction to Nuclear Engineering (3rd Edition)* Prentice Hal, Upper Saddle River, page 88 (2001)

[7] Lamarsh J.R. and Baratta, *A.J., Introduction to Nuclear Engineering (3rd Edition)* Prentice Hal, Upper Saddle River, page 89 (2001)

[8] Croff, A.G., *ORIGEN2: a revised and updated version of the Oak Ridge isotope generation and depletion code*, Oak Ridge National Laboratory Report ORNL-5621

[9] Poston, D.I. and Trellue, H.R., *User`s manual, version 1.00 for Monteburns, version 3.01*, Los Alamos National Laboratory Report, LA-UR-98-2718 (1998)

Reflector and Control Drum Design for a Nuclear Thermal Rocket

Tyler Goode[1], Jeffrey Clemens[2], Michael Eades[3,4], J. Boise Pearson

[1]*Department of Mechanical Engineering, The University of Alabama, Tuscaloosa, AL 35487*
[2]*Department of Nuclear Engineering, Texas A&M University, College Station, TX, 77843*
[3]*Nuclear Engineering Program, The Ohio State University, Columbus, OH 43201*
[4]*Center for Space Nuclear Research, Idaho National Lab, Idaho Falls, ID 83401*

Abstract. Solid-core nuclear thermal rocket engines will play a vital role in near-term manned deep space missions. Supporting the Space-Capable Cryogenic Thermal Engine (SCCTE) project, different ideas for the radial neutron reflector and control drums are explored. The design under consideration is a radial reflector made of beryllium with dispersed cooling channels for flowing cryogenic hydrogen. Embedded in the reflector, sixteen control drums made from beryllium with boron carbide poison elements control reactivity. The control drums have dispersed cooling channels for cryogenic hydrogen flow. Autodesk Simulation is used to study thermal and flow behavior of the components, and Monte Carlo N-Particle Transport code (MCNP) is used to investigate nuclear aspects. An iterative design approach using Autodesk Simulation and MCNP was undertaken to optimize the integral and differential reactivity worth of the control drums to ensure smooth power transitions during rotation and an adequate Shutdown Margin (SDM) of the reactor, while considering mechanical and thermal aspects of the materials. This was done by varying the size, number, and positioning of cooling channels within the reflector and control drum regions, as well as the geometry of the of the poison elements within the control drums. One potential design for the radial neutron reflector that meets the criteria of the SCCTE project is presented.

Keywords: Nuclear Thermal Rocket, Neutron Reflector, NTR Components

INTRODUCTION

Solid-core nuclear thermal rocket (NTR) engines are poised to play a vital role in future manned deep space missions. Capable of double the specific impulse of chemical engines, tolerant of almost any propellant, and having high technology readiness levels from experience gained in the Rover and NERVA programs begun in the 1960's, solid core NTR's are the ideal choice to drive near-term space exploration missions[1]. Marshall Space Flight Center, in cooperation with other entities, is developing a point design for an NTR to propel current Mars Transit Vehicle concepts. This design is termed the Space-Capable Cryogenic Thermal Engine (SCCTE). Due to its higher specific impulse, the use of NTP instead of chemical engines on the Copernicus Mars Transit Vehicle is expected to reduce the required launch mass by over 400 metric tons[1]. A key part of the SCCTE design is the decision to utilize low-enriched uranium fuel to power the reactor, allowing the engine to be developed without the enormous costs of working with high enriched fissile material. This decision represents a sizeable departure from the legacy designs of the NERVA program; several reactor components need significant and fundamental redesign. In this process, modern analysis techniques can be leveraged to provide a substantial performance increase over legacy NERVA designs. In support of this project, different ideas for the radial neutron reflector and control drums were explored and compiled into a first iteration design. This paper will follow the solution path taken to arrive at this design. First a coolant channel pattern was laid out based upon power deposition numbers provided by the SCCTE reactor design

team. Next, this layout was tested using Simulation CFD for thermal and fluid-flow performance, and using MCNP to analyze the effect on reactivity of the modified reflector. Lastly, mechanical design concepts for the reflector are discussed.

BACKGROUND

Nuclear reactors produce power in the form of heat by sustaining a fission chain reaction. The reaction is sustained when the amount of neutrons generated by fissions is in balance with the amount lost to absorptions and leakage, and the reactor is said to be critical. The parameter used to quantify this condition is the neutron multiplication factor, k_{eff}. A critical reactor has $k_{eff} = 1$, meaning that the neutron population is neither increasing nor decreasing. Another way to quantify this condition is reactivity, ρ, which is defined as:

$$\rho = \frac{k_{eff} - 1}{k_{eff}} \tag{1}$$

Reactivity describes how far away from criticality the reactor is. To more conveniently describe a reactivity insertion, units of percent mil (pcm) can be obtained by multiplying the reactivity difference by 10,000. To obtain a critical reactor configuration, there must be enough fissile material to sustain the chain reaction. In an NTR, it is desirable to minimize mass, therefore a neutron reflector is incorporated to reduce leakage and allow a lower mass of fissile material to be used. The material choice for an NTR reflector is beryllium, for its low density and superior neutronic properties. For controlling the reactor, beryllium drums containing neutron-absorbing material, are placed in the reflector such that when they are turned, the absorber is rotated closer or farther from the reactor core. This serves to control the neutron population and vary k_{eff} to obtain various operating conditions. The material of choice for the absorber in this NTR reactor is boron carbide for its high neutron absorption cross-section and high temperature limits. However, beryllium used in a reflector must be kept below a limit of around 325°C or helium bubbles will begin to form and cause swelling due to the high neutron flux [2]. This necessitates removal of heat from the reflector to keep it within this temperature limit. This is accomplished by flowing a portion of the cold propellant through the reflector, before it is heated in the core.

In an NTR, the power generated by the reactor will be used to heat a propellant that will then be expanded and accelerated in a nozzle to produce thrust. The propellant that maximizes the specific impulse of a rocket engine is hydrogen for its low molecular mass. Since it must be stored cryogenically, the reactor must be able to withstand a wide range of temperatures. In certain environments, hydrogen can be corrosive, and material degradation can occur if adequate measures are not taken. Since beryllium is particularly susceptible to hydrogen degradation, it would typically be coated or clad with a protective material wherever it would be in contact with hydrogen.

COOLING CHANNEL DESIGN

Determination of Heat-Deposition Boundary Conditions

The first step in obtaining a cooling channel geometry was to quantify the power deposition into the reflector. It is convenient using Monte Carlo N-Particle diffusion code to obtain fractions of power deposition into various regions of the reactor. These fractions can then be multiplied by the total reactor power to determine the power deposited into different regions of the reflector. Obtaining fractions to quantify the power deposition in an accurate way was accomplished in two steps. First, meshes were added to an MCNP model of the reactor (geometry depicted in Figure 1) across the absorber and reflector material to obtain the power deposition split between the two regions. In Figure 1, the reflector material is depicted in dark green and the absorber in light green. This was done for two operating conditions, with the absorber rotated fully in and with it rotated fully out. These results are presented in Table 1.

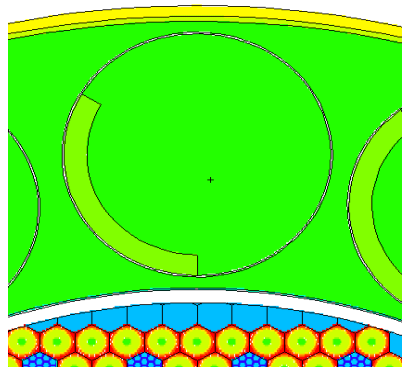

FIGURE 1. Reflector and control drum geometry from MCNP model.

Second, the reflector material was divided into 11 annuli and power deposition fractions determined for each of these annuli. This fixes the radial variation in power deposition to a reasonable resolution. These results are presented in Table 2 as well as Figure 2 showing the volumetric heat distribution as a function of distance from the core. One other thermal boundary condition that could be of interest is the conventional heat flux from the core. For this analysis, this value is assumed to be zero. This assumption is made because the reflector will be insulated from the core by a cooled support structure. Analysis of this component is left as future work.

TABLE 1. Power deposition into the three main reflector regions.

Total Reactor Power: 558,200 kW				
	Drums In		**Drums Out**	
Region	**Fraction**	**Power Deposition (kW)**	**Fraction**	**Power Deposition (kW)**
Reflector Material	0.000971	541.8	0.001188	663.4
Drum Material	0.001691	944.1	0.002660	1485.0
Absorber	0.006520	3639.4	0.002967	1656.4

TABLE 2. Annular power deposition in the reflector.

Annulus	**Radial Distance from Core Center (cm)**	**Fraction**	**Drum-In Deposition (kW)**	**Drum-Out Deposition (kW)**
1	32.94	0.1647	244.7	353.8
2	33.25	0.1567	232.8	336.6
3	33.75	0.1442	214.3	309.9
4	34.50	0.1281	190.4	275.3
5	35.50	0.1099	163.3	236.1
6	37.00	0.0882	131.1	189.5
7	39.00	0.0666	98.9	143.0
8	41.00	0.0509	75.6	109.3
9	43.00	0.0391	58.1	84.0
10	45.00	0.0301	44.7	64.6
11	47.44	0.0216	32.1	46.4

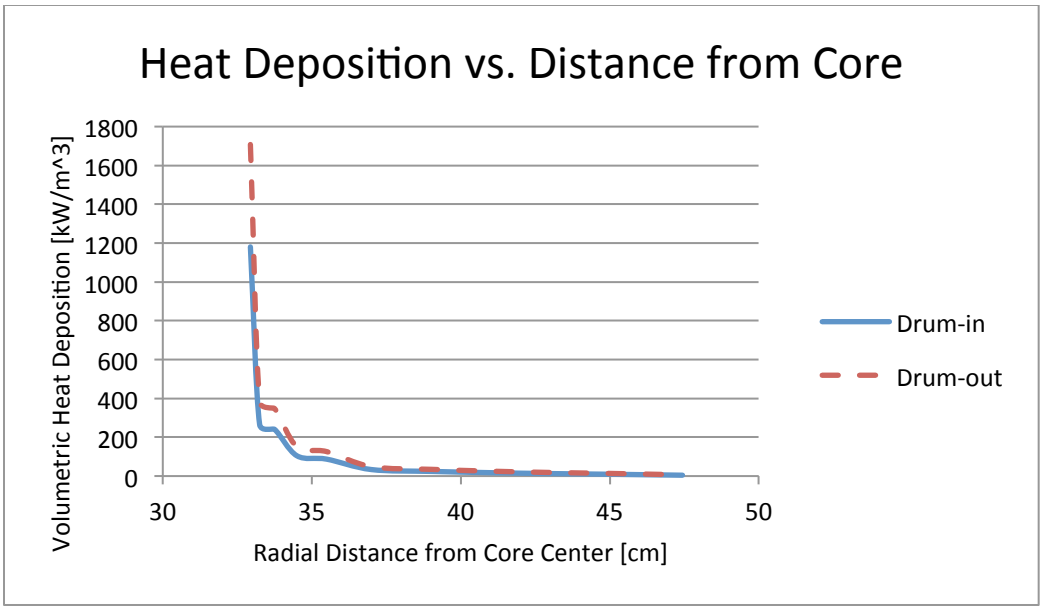

FIGURE 2. Volumetric heat deposition as a function of distance from the core.

It can be seen from the Figure 2 that the majority of the power is deposited almost at the surface of the reflector. This is consistent with predictions based on neutron diffusion theory.

Coolant Channel Layout

As a starting point, the coolant channel size was chosen to be 0.375 inches to match the size of legacy designs [3]. Using the initial constraints set by the SCCTE power balance team, the number of coolant channels was optimized to handle the proposed hydrogen flow of 6.577 kg/sec with a 0.414 MPa (60 psi) pressure drop. Next the distribution of cooling channels was determined using the power deposition figures presented in the previous section. This distribution is presented in Table 3. The distribution presented in Table 3 was then loosely used to lay out a cooling channel pattern that fit within geometric constraints of the reflector. This pattern is presented in Figure 3.

TABLE 3. Coolant channels needed in each annulus.

Annulus	Radial Distance from Core Center (cm)	Number of Coolant Channels
1	32.94	100
2	33.25	95
3	33.75	88
4	34.50	78
5	35.50	67
6	37.00	54
7	39.00	40
8	41.00	31
9	43.00	24
10	45.00	18
11	47.44	13

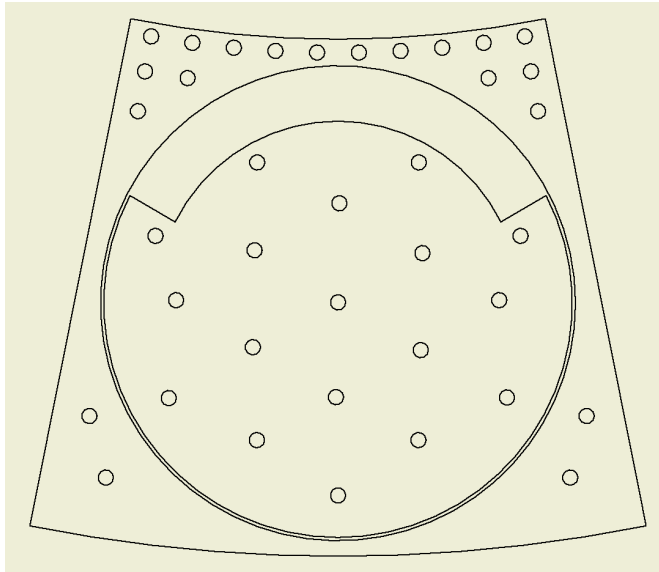

FIGURE 3. Coolant channel profile for 1/16th sector.

CFD Analysis

To test the thermal properties of the reflector design, the geometry was evaluated in Autodesk Simulation CFD. For both the drum-in and drum-out conditions, a 1/32nd sector, half-length model was tested at full power to determine which would be the limiting case. The drum-in condition was found to be the limiting case so analysis of a full-length sector drum-in is presented below.

Materials

The reflector material was modeled with the properties of pure beryllium to accurately model the high-purity beryllium proposed in the reflector design. The absorber rods are modeled with the properties of commercially produced boron carbide. The fluid is modeled as parahydrogen with isobaric properties from NIST at 4.21 MPa (610 psia), with the exception of density, which was modeled with the standard ideal gas law. These materials are shown in Figure 4.

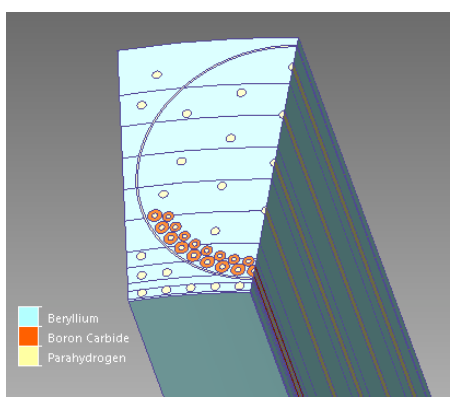

FIGURE 4. Reflector materials.

Boundary Conditions

Five different types of boundary conditions were needed to evaluate the simulation. Volumetric heat generation was assigned to the sectors by volume weighting the results from Table 2. A pressure of 4.41 MPa (640 psia) was assigned to fluid inlets and 4.00 MPa (580 psia) to fluid outlets (this determined the pressure drop to drive the flow). A temperature of 131 K (236 R) was assigned to fluid at the inlet. Surfaces along the cuts were defined as symmetry

planes. Defining pressure driven flow in lieu of the flow rate was done to determine flow splits between channels, and to increase the stability of the results.

Results

The total mass flow rate through this portion of the whole reflector would be 2.35 kg/sec with this pressure drop. Since the temperature limit of 325°C is exceeded, according to this analysis, either more cooling area should be added around the absorber or a higher pressure-drop budgeted in the power balance. The predicted mass flow rate is roughly 1/3 the 6.577 kg/sec total, which is desirable because significant flow will be needed to cool the support structure that is nearer the core. The temperature profiles are presented in Figure 5.

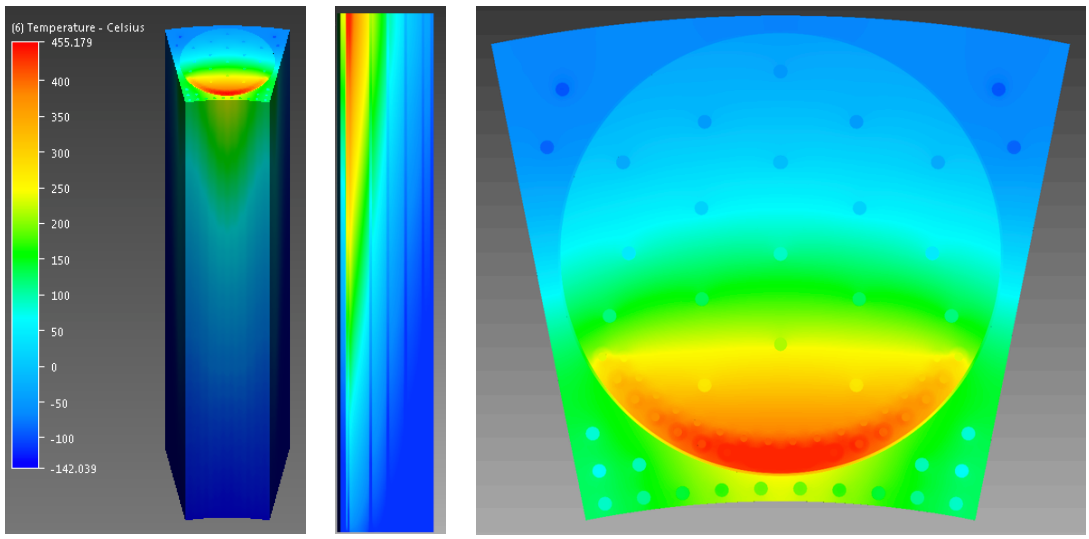

FIGURE 5. Isometric view (left), vertical midplane (middle), top horizontal plane (right) thermal profiles

MCNP Analysis

After finding a suitable cooling channel design, it was necessary to determine what effect this modification had on the reactivity. This was accomplished by running simulations using MCNP 6.1 [4]. The cooling channels were added to the model and a reactivity curve based on drum rotation was obtained for the modified geometry. The original geometry and the geometry with cooling added are depicted in Figure 6. The reactivity curves for these two cases are presented in Figure 7. Uncertainties in k_{eff} for all MCNP analyses fluctuated between 0.0005 and 0.0007. Error bars are included on all plots of MCNP data (Figure 7 and Figure 10).

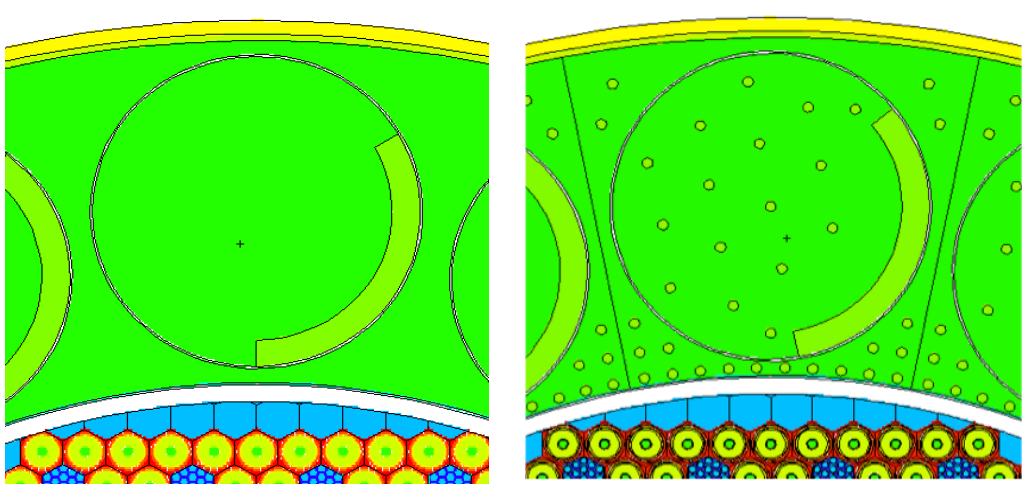

FIGURE 6. MCNP reflector geometry, original (left) and with cooling added (right).

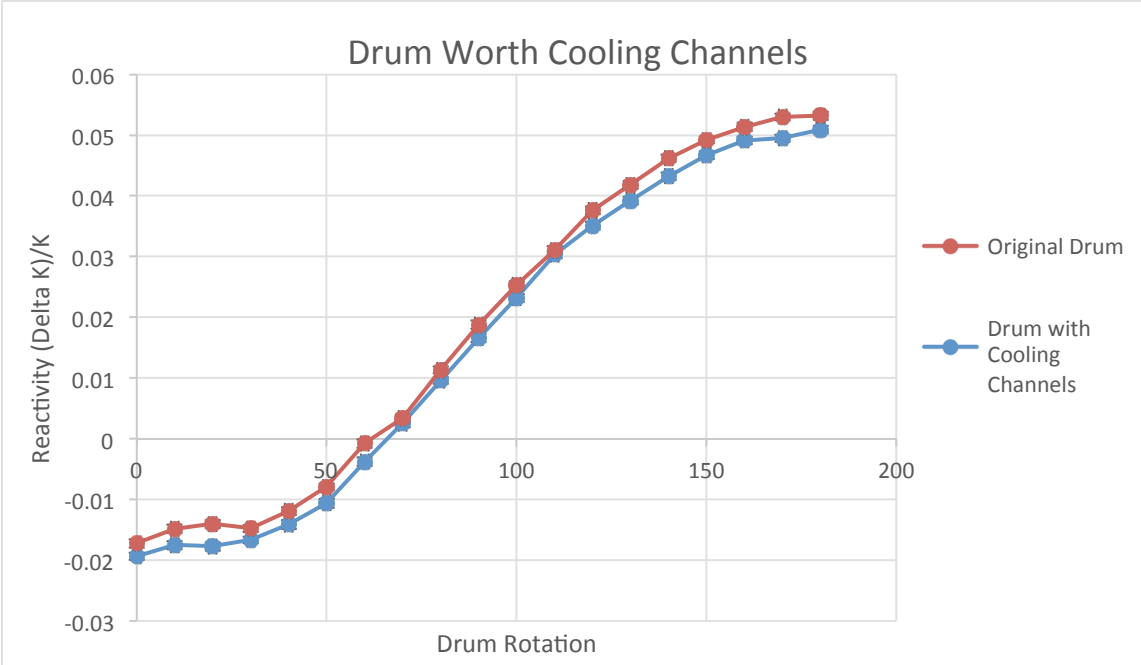

FIGURE 7. Reactivity curves for original and modified reflector.

These results provide a good indication of the reactivity hit that is to be expected from adding the cooling geometry to the design. The reactivity is reduced by 240 pcm on average.

STRUCTURAL DESIGN

Absorber Geometry

One serious challenge in designing the control drums is obtaining an absorber configuration that can be built, will meet the reactivity performance requirements, and will survive in the reactor environment. To this end, it was proposed to separate the absorber from one thick, uncooled plate into either several thin plates or several cooled rods (possible configurations shown in Figure 8), with the rods being the more desirable for ease of manufacture.

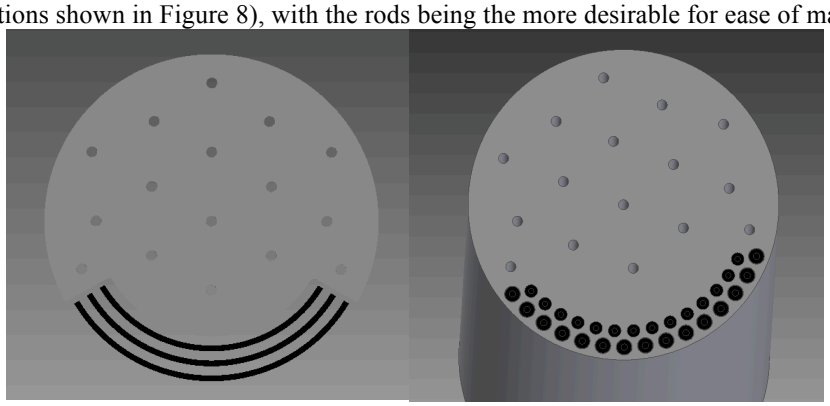

FIGURE 8. Plate-style absorber (left) and rod-style absorber (right).

To test the viability of using the rod style absorber, the geometry was added to the MCNP model of the reactor and a reactivity curve based on drum rotation was obtained. This curve is compared with the original thick plate design in Figure 10. The geometries tested are shown in Figure 9.

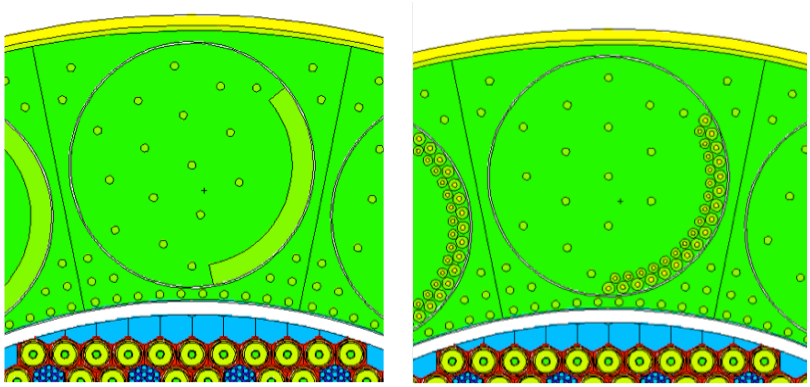

FIGURE 9. Original MCNP geometry with cooling (left) and rod-style absorber geometry (right).

This rod-absorber geometry reduces the shutdown margin by 395 pcm. While the reduction in shutdown margin is likely acceptable, the erratic reactivity insertion behavior shown in these analyses would prohibit its use in a reactor. Perhaps further refinement could even out the curve leading to a usable design.

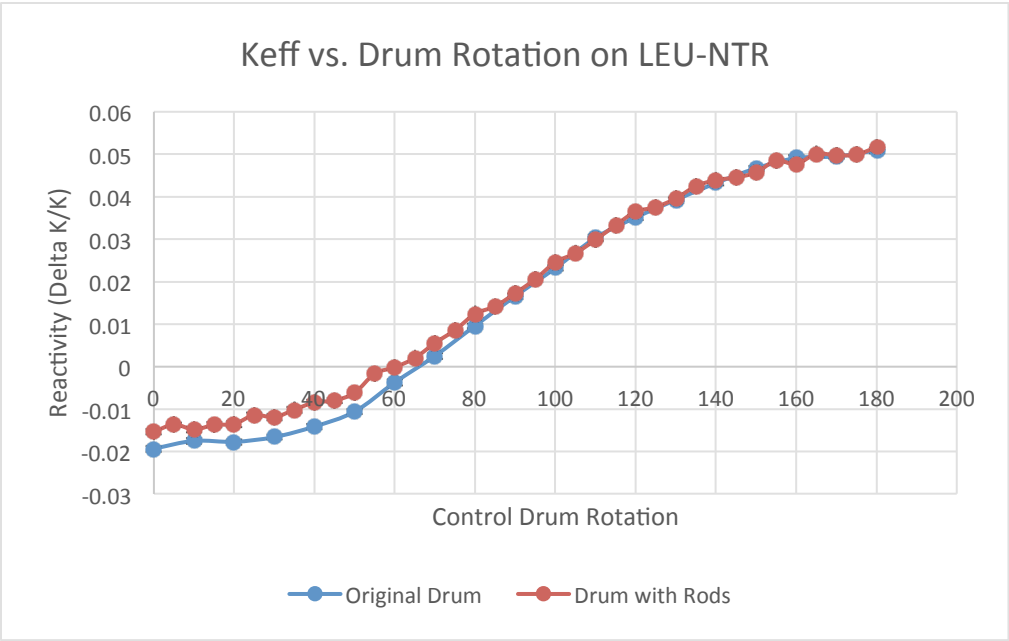

FIGURE 10. Reactivity curves showing effect of experimental rod geometry.

Structural Concept

Based on the structural design on the NERVA reactors, low fidelity models of a possible structure for the SCCTE reflector are presented. The design is centered around an aluminum support structure that holds blocks of beryllium reflector. Compression bands around the outside of the reflector secure the blocks. The blocks will be in contact with each other axially and secured using full-length tie bolts. Bearings to hold the control drums are incorporated into the support structure on the bottom, and for the top, individual support plates house bearings and the spring return fail-safe system. The control drums are connected to actuators via a spline drive. The control drums shown in the model incorporate the rod-style absorber. The design is depicted in Figure 11 and Figure 12.

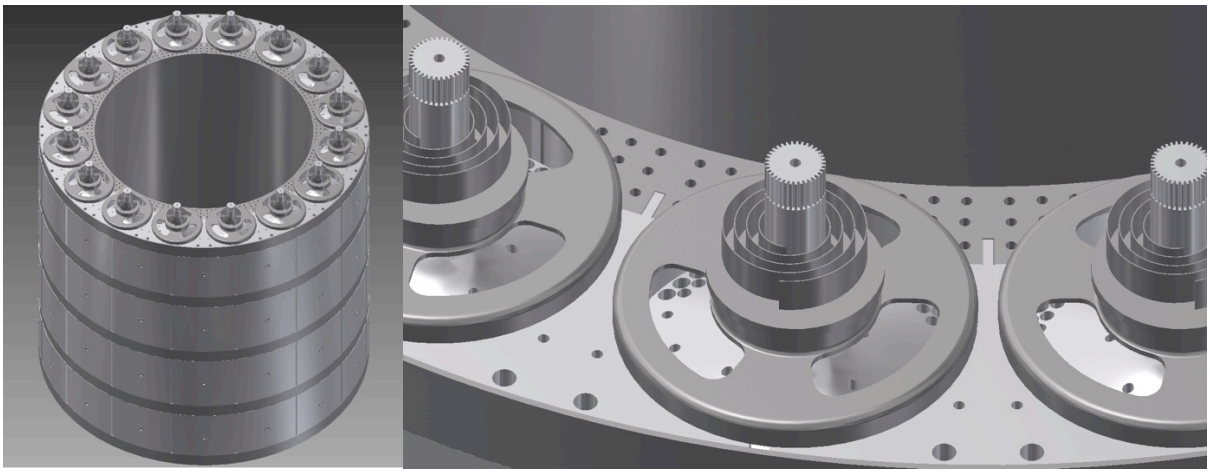

FIGURE 11. Assembled reflector (left) and close up of top support plates (right).

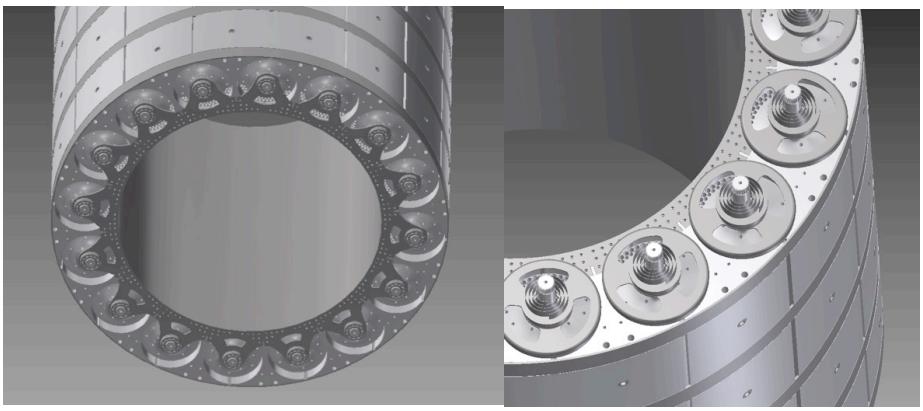

FIGURE 12. Bottom of reflector (left) and top view (right).

CONCLUSION

Several different aspects of NTR reflector design have been considered for the SCCTE reactor. After determination of operating conditions, a suitable coolant channel layout was obtained and tested with CFD and MCNP. CFD analysis suggests that more cooling is needed around the absorber for the rod-style design. Because of the poor thermal and nuclear performance of the rod-style design, further work on a multi-plate absorber design is recommended. These analyses presented show a viable design that further iterations can optimize. A design has been proposed and modeled that is able to be manufactured and could meet performance specifications.

It is recommended to continue this work in several areas. The first is optimization of the cooling channel pattern and the drum geometry using coupled mechanical, thermal, and neutronic parameters. Next, mechanical simulation is needed to explore stresses and thermal expansion. These can be anchored by testing of a prototype in a non-nuclear environment. Lastly, use of protective coatings, possibly BeO, on surfaces exposed to the coolant flow should be explored to reduce unwanted chemical interactions.

NOMENCLATURE

NTP	=	nuclear thermal propulsion
NTR	=	nuclear thermal rocket
SCCTE	=	Space Capable Cryogenic Thermal Engine
k_{eff}	=	neutron multiplication factor

ρ	=	reactivity
MCNP	=	Monte Carlo N-particle code, used for reactivity analysis
NERVA	=	Nuclear Engine for Rocket Vehicle Application

ACKNOWLEDGMENTS

The authors would like to thank Omar Mireles and Daniel Cavender of Marshall Space Flight Center for their help in interfacing with the SCCTE team. The authors would also like to thank Wes Deason from the Center for Space Nuclear Research for providing initial design constraints for the reactor, as well as Lewie Bates and Jon McDonald for providing power balance information for the engine. Lastly, the authors would like to thank David Konyndyk, NASA intern, for sharing his ideas and expertise.

REFERENCES

[1] Stanley K. Borowski, David R. McCurdy, and Thomas W. Packard, "Nuclear Thermal Rocket (NTR) Propulsion: A Proven Game-Changing Technology for Future Human Exploration Missions," in Global Space Exploration Conference, Washington D.C., 2012.

[2] L. L. Snead and S. J. Zinkle. "Use of Beryllium and Beryllium Oxide in Space Reactors". Proceedings of the American Institute of Physics. STAIF-2005, Space Technology and Applications International Forum. Feb 13-17, 2005.

[3] Pierce, B.L., & Woods, M.D. (1962). *B-1 and B-2 reactor design summary*. doi:10.2172/4174543

[4] MCNP6 Users Manual - Code Version 6.1.1beta, LA-CP-14-00745 (June 2014).

Temperature Profile in Fuel and Tie-Tubes for Nuclear Thermal Propulsion Systems

Vishal Patel[1,2]
[1]*Department of Nuclear Engineering, Texas A&M University, College Station, TX 77843*
[2]*Center for Space Nuclear Research, Idaho National Lab, Idaho Falls, ID 83401*

832-334-9762; vkp93@tamu.edu

Abstract. A finite element method to calculate temperature profiles in heterogeneous geometries of tie-tube moderated LEU nuclear thermal propulsion systems and HEU designs with tie-tubes is developed and implemented in MATLAB. This new method is compared to previous methods to demonstrate shortcomings in those methods. Typical methods to analyze peak fuel centerline temperature in hexagonal geometries rely on spatial homogenization to derive an analytical expression. These methods are not applicable to cores with tie-tube elements because conduction to tie-tubes cannot be accurately modeled with the homogenized models. The fuel centerline temperature directly impacts safety and performance so it must be predicted carefully. The temperature profile in tie-tubes is also important when high temperatures are expected in the fuel because conduction to the tie-tubes may cause melting in tie-tubes, which may set maximum allowable performance. Estimations of maximum tie-tube temperature can be found from equivalent tube methods, however this method tends to be approximate and overly conservative. A finite element model of heat conduction on a unit cell can model spatial dependence and non-linear conductivity for fuel and tie-tube systems allowing for higher design fidelity of Nuclear Thermal Propulsion.

Keywords: Nuclear Thermal Propulsion & Tie-Tubes & Heat Transfer & LEU

INTRODUCTION

Interest in Nuclear Thermal Propulsion (NTP) has been renewed with NASA [1] suggesting NTP as a good choice for a Mars mission. There is also an effort to make NTP compatible with NNSA's Global Threat Reduction Initiative by using low enriched uranium (LEU) rather than highly enriched uranium (HEU). It has been shown [2] that with design modification, LEU NTP designs are feasible. This has created a need to redesign the NTP since heritage designs to branch from are not available. These designs are completely new reactors, similar to reactors proposed in the Generation IV International Forum [3]. Even HEU designs will have similar ``new design'' characteristics because all NTP designs will need to be licensed by the US Nuclear Regulatory Commission. Predictive computer codes that agree with experimental results are needed to design and license reactors

Experiments requiring nuclear materials tend to be very expensive and difficult to create due to many regulatory and safety concerns. This has led to the creation of predictive computer codes that are validated by experiments whenever possible. Many of the tools used to create historical NTP designs are either outdated or unavailable. Modern, sophisticated CAD tools require highly skilled software users and a large amount of computer time to produced very detailed results. These tools are very useful when a point design is available to study, however they should not be used for quick parametric design scoping studies.

An initial design of any nuclear reactor begins with a hot channel analysis where the hottest section of the core is analyzed. This analysis is well studied in a single-pass core typical in terrestrial Light Water Reactors (LWRs), however a ``hot channel'' in an NTP core consists of a fuel element and a tie-tube (or moderator) element. There is a downward supply H_2 channel and an upward return H_2 channel within a tie-tube, and there are several coolant channels within the fuel element. This makes for a difficult geometry to solve flow and heat equations over. This

paper presents a method to determine the temperature profile in an NTP that contains fuel and tie-tube elements. This tool can be applied to any fuel choice such as composite or cermet with any fuel enrichment as long as material properties are available.

BACKGROUND

Thermal analysis of NTP has been the subject of many studies in the past. One of the most important aspects of NTP performance and safety is to maintain temperature under prescribed values. It's very easy to design a small neutronically critical NTP core, and very easy to design an NTP core that can be easily cooled. However obtaining both a small and coolable core is difficult. To have the best performance in an NTP, high thrust to weight with high specific impulse is required. This forces NTP designers to optimize performance and safety to multiple constraints. In order to accurately analyze cores the temperature profile in the fuel element and tie-tube (if applicable) must be known, and there are many methods to estimate these values.

A typical method as done in [2] used to capture maximum fuel temperature in a hexagonal geometry is to transform the geometry into an equivalent tube that conserves volume of fuel and the inner surface area of the coolant channel. A 1D heat equation with an appropriate thermal temperature dependent conductivity can analytically be solved on this geometry for fast determination of maximum fuel temperatures. The circularization method can under calculate the fuel centerline in some cases where surface area to fuel volume ratio is high.

Another method [4] is to use an analytical expression that takes into account geometry variations but neglects non-linear thermal conductivities. The analytical expression neglects temperature dependent conductivity, which is important when there is a large difference between the fuel centerline and wall temperatures.

A shortcoming of both methods is that the fuel region is only cooled through the coolant surface and thus heat conduction into tie-tubes is not present and so higher fuel centerline temperatures can be found which limits performance. Both methods also do not capture geometry where fuel is adjacent to fuel so the potential increased fission rate that would cause peak temperatures at the interface between fuel is not captured.

A third method [5] was to assume a portion of heat is transferred to the tie-tubes from fuel and use that known source in a 1D cylindrical heat equation model of the tie-tube. This assumes radial symmetry of the tie-tube, which is always not present, and works only when the heat into the tie-tube is known well, which is not the case unless experimental data is available for the geometry or more complex computer methods are used.

The Small Nuclear Rocket Engine (SNRE) final report [6] overviews an axially integrated finite element analysis used to predict temperature distributions in the fuel of SNRE core. The implementation details are not very clear and references cited in the report are not easily available. However, from what is known, a quarter-symmetry fuel element was modeled with thermal insulation at the fuel edges. The insulation had a presumed flux and sink temperature boundary condition. The analysis shows peaking near the insulation; however the real impact of tie-tubes with hydrogen flow and change of fuel/TT geometry cannot be found with the report's methods.

Computational fluid dynamics (CFD) has been performed in a few studies that focus on NTPs. A full core analysis [7] and hot channel analysis [8,5] both present results for a few point designs that use HEU W-Cermet fuel. Neither of these studies model tie-tubes so although they are much more complex than previous studies, the results are not useful for NTP systems with tie-tubes.

METHODOLOGY

A 1D compressible flow model using real hydrogen (H_2) gas properties [9] was implemented in MATLAB [10]. A 2D heat equation was implemented in MATLAB's PDE Toolbox [10]. These two implementations were coupled together to determine the maximum fuel temperature and H_2 outlet temperature of a hot channel in an NTP. This section details the models used and the solution implementation.

Flow Model

A 1D compressible flow modeled using real H_2 gas properties were implemented using a friction factor correlation to take into account pressure drop due to fluid-wall interactions. The governing equations and closer relations are

$$\rho v = G, \tag{1}$$

$$\frac{dP}{dx} - \left(\frac{G}{\rho}\right)^2 \frac{d\rho}{dx} = -\frac{G^2}{2\rho_{avg}} \frac{f}{D_H}, \tag{2}$$

$$\frac{dh}{dx} - \frac{G^2}{\rho^3}\frac{d\rho}{dx} = \frac{q}{\dot{m}}, \tag{3}$$

$$f = f_{Haaland} = \left(-1.8 * \log_{10}\left(\frac{6.9}{Re} + \left(\frac{\epsilon_{rel}}{3.7}\right)^{1.11}\right)\right)^{-2}, \tag{4}$$

$$P(0) = specified, \tag{5}$$

$$h\big(T(0), P(0)\big) = specified, \tag{6}$$

$$\rho = F(P, h), \tag{7}$$

where ρ is the fluid density, v is fluid velocity, G is the mass flux, P is the pressure, x, is the dimension, f is the friction factor, D_H is the hydraulic diameter, h is the enthalpy, q is the total heat added to the fluid, $\dot{m}$ is the mass flow rate, Re is the fluid Reynolds number, ϵ_{rel} is the relative pipe roughness, and $F(P, h)$ is a table lookup function to find the fluid density. Boundary conditions are supplied at the pipe inlet.

The flow equations are calculated on N nodes that create N-1 cells where heat transfer occurs for the fuel temperature solutions. These nodes can cells can be seen in Fig. 1.

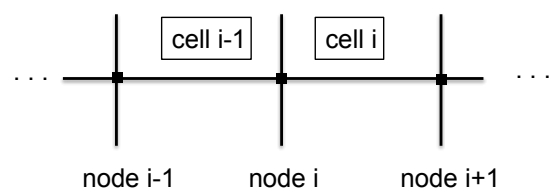

FIGURE 1. Node and Cell Stencil for Computations.

Average quantities are evaluated at the center point between nodes (i.e., the cell centers). The derivatives are discretized using first order forward differences as

$$\Delta x \frac{dp}{dx} = P_n - P_{n-1} = -\frac{G}{2\rho_{avg}}\frac{f\Delta x}{D_H} + \left(\frac{G}{\rho}\right)^2 (\rho_n - \rho_{n-1}) = b_n^P,\ n \in [1, N]\ , \tag{8}$$

$$\Delta x \frac{dh}{dx} = h_n - h_{n-1} = \frac{q\Delta x}{\dot{m}} + \frac{G^2}{\rho^3}(\rho_n - \rho_{n-1}) = b_n^h,\ n \in [1, N]\ , \tag{9}$$

where Δx is the width of a cell, n is the node number, N is the total number of nodes with the first nodes containing boundary conditions, and b_n^P & b_n^h as labels to make notation simple. The heat flux used is the one from the previous cell that the nth node defines. These equations are assembled into a non-linear matrix equation,

$$Ax = b(x), \tag{10}$$

$$\begin{bmatrix} 1 & & & & & & & & & & \\ -1 & 1 & & & & & & & & & \\ & -1 & 1 & & & & & & & & \\ & & \ddots & \ddots & & & & & & & \\ & & & -1 & 1 & & & & & & \\ & & & & & 1 & & & & & \\ & & & & & -1 & 1 & & & & \\ & & & & & & -1 & 1 & & & \\ & & & & & & & \ddots & \ddots & & \\ & & & & & & & & -1 & 1 & \end{bmatrix} \begin{bmatrix} P_1 \\ P_2 \\ P_3 \\ \vdots \\ P_N \\ h_1 \\ h_2 \\ h_3 \\ \vdots \\ h_N \end{bmatrix} = \begin{bmatrix} b_1^P \\ b_2^P \\ b_3^P \\ \vdots \\ b_N^P \\ b_1^h \\ b_2^h \\ b_3^h \\ \vdots \\ b_N^h \end{bmatrix}, \tag{11}$$

where blank spaces in the A matrix are zeroes. A fixed-point iteration scheme is used to solve the non-linear system with the matrix inversion handled by the ``backslash'' MATLAB operator so that an efficient inversion algorithm is used by default. The iteration scheme is

$$g(x_{i+1}) = A^{-1}b(x_i), \tag{12}$$

where the function $g(x_{i+1})$ is evaluated repeatedly until a convergence criteria of the L_2 norm of the error is met. The error is defined as

$$||err||_2 = \frac{||x_{i+1} - x_i||_2}{||x_i||_2}, \tag{13}$$

using $||\cdot||_2$ as the typical L2 norm operator.

Heat Conduction Model

A 2D heat equation was implemented into MATLAB using the PDE Toolbox. Typically with the PDE Toolbox, the frontend GUI interface is used to solve PDEs whereas in this implementation the backend was used directly by calling various toolbox functions. This allows for changing the mesh quickly for many different NTP cases.

Heat Equation

The heat equation is solved on a 2D mesh that is discretized using finite elements. The heat equation,

$$-\nabla \cdot (k\nabla T) = q''', \qquad x \in \Omega \tag{14}$$

$$q''(x) = h(T(x) - T_{bulk}), \; x \in \partial\Omega, \tag{15}$$

where k is the conductivity, T is the temperature, q''' is the volumetric heat generation rate, q'' is the areal heat generation rate, h is the heat transfer coefficient, x is the position on the domain Ω, and T_{bulk} is the bulk fluid temperature that is adjacent to the domain. The heat equation is cast into weak form and the solution is expanded using linear Lagrange elements, numerical integrals are solved using mid-point rule, and further solution implementation details are found in the toolbox manual [10]. The volumetric heat rate is taken to have no spatial dependence and is only present in the fuel meat.

Mesh

The PDE Toolbox can model 2D geometry using an unstructured mesh with triangular mesh elements. The geometry is meshed automatically at the beginning of a calculation automatically from various properties inputted into the code. The fuel channel radii, webbing thickness, and number of holes (up to 169) can be varied for 4 different combinations of fuel and tie-tube pairings ranging from 3 to 1, 2 to 1, 1 to 2, and 1 to 3 fuel to moderator ratio respectively. The smallest symmetry that arises from each of the fuel and tie-tube pairs is also implemented. Figure 2 shows a typical fuel element and moderating tie-tube. The fuel can be modeled as any fuel as long as material properties are available and the tie-tube dimensions and materials can be changed. Figure 3 shows the full lattice and the implemented symmetry. Cladding is not considered currently but will likely be added to the tool later. This study focuses on the 2 to 1 symmetries, as proof of concept. The other configurations have been considered and will be utilized to study different fuel and tie-tube element patterns.

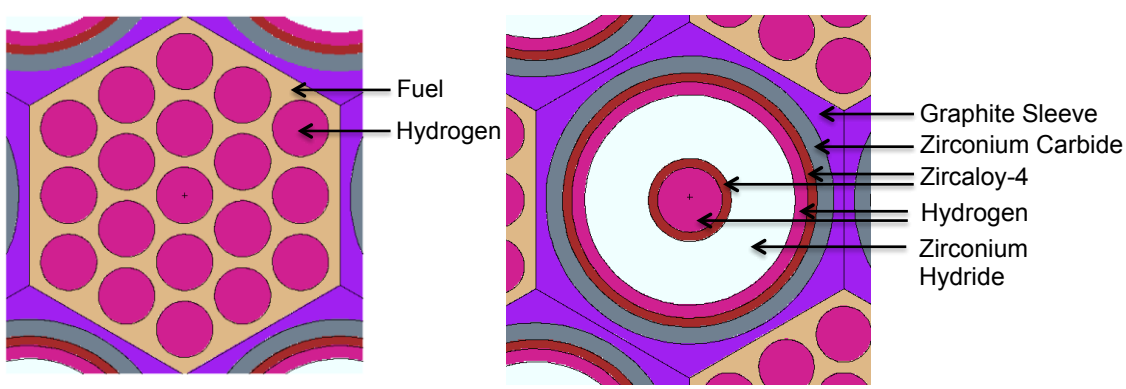

FIGURE 2. Fuel and Moderating Tie-Tube Geometry.

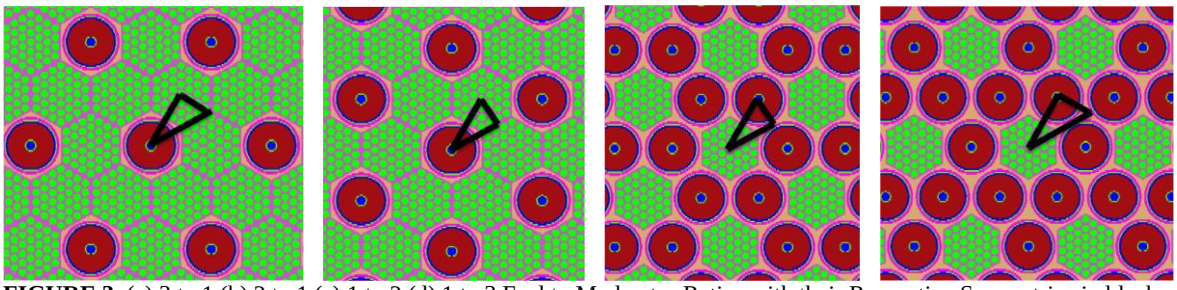

FIGURE 3. (a) 3 to 1 (b) 2 to 1 (c) 1 to 2 (d) 1 to 3 Fuel to Moderator Ratios with their Respective Symmetries in black.

The heat equation needs material properties for each material in the mesh. The heat equation can be solved as a linear or non-linear equation. The non-linear equation takes much more time to solve so the linear equation is solved with a few checks against the non-linear solution for the same case to determine how much error is introduced into the calculations. Both forms of the heat equation are initially solved using an adaptive mesh algorithm built into the PDE toolbox such that a good mesh can be created that is based on the solution.

Solution Implementation

The flow and temperature distribution implementations are coupled by heat transfer coefficient, fluid temperature, and heat profile into the fluid. The flow solution needs a heat profile input, and the fuel and tie-tube temperature distribution needs a heat transfer coefficient and a bulk fluid temperature input. The solution method is a staggered operator splitting with convergence criteria based on the information being passed between the two operators (flow and temperature) to not change by a given tolerance after some iteration. This section overviews the algorithm.

Algorithm Overview

All required parameters are initialized and then an initial guess of the heat into the fluid for the supply H, return H, and each coolant channel is made. The fluid temperature is then calculated using the assumed heat input with the 1D flow solver. This fluid temperature along with the assumed heat flux into the fluid is used to solve for the heat transfer coefficient and wall temperature. The heat transfer coefficient and the bulk fluid temperature found are used as the boundary conditions on all boundaries for the heat equation solver. A known (input) heat source is used as the heat source in the fuel region. A mesh is generated for the given geometry automatically and each cell is looped over until all cells have been calculated. The first cell on the first iteration of a calculation uses an adaptive mesh algorithm [10] to refine the mesh. This mesh is used in all further calculations because the adaptive mesh routine is time consuming and the same approximate mesh would be generated at each cell. Once the temperature distribution in each cell is found, the heat flux out of the edges is approximated using the mesh solution. Due to the mesh not being able to capture the true curvature of the circular coolant regions, the heat flux calculated is not equal to the known heat flux. Therefor, the total heat flux found is normalized to the known heat flux out. This heat flux out is used as the input to the 1D flow solver and the algorithm is looped. Before the loop a tolerance condition is evaluated such that the L_2 norm of the heat transfer coefficient for the central fuel coolant channel and heat flux profile does not change by a specified tolerance between iterations.

Boundary conditions are imposed onto the tie-tube coolant entrance and the fuel coolant entrance. A pressure drop from the tie-tube exit to the fuel inlet should be used; however the pressure is assumed so that the systems causing this pressure drop do not have to be modeled.

Pressure Drop Approximation

The flow solution is solved for each coolant channel. The proper boundary conditions should be the same inlet temperature and pressure with and outlet pressure for each coolant channel. The mass flow rate in the channel should be adjusted until the exit boundary condition can be met. Currently the outlet boundary condition is not enforced. By evaluating the difference between the maximum and minimum pressure drops out of the coolant channels, there is about a 15% difference in the pressure found so it is likely the mass flow rates would differ by a

non-negligible amount once the proper boundary conditions are met. However, in a real NTP, each coolant channel has a special orifice that introduces a pressure drop so the desired coolant mass flow rate can be achieved. Without these special orifices, it is likely proper cooling could not be established.

The physical impact of this approximation will likely be little as orificing can be introduced to match flow rates in channels. A real NTP design would likely need to cool hotter areas of fuel more than cooler areas so the orificing would take that into account too.

A numerical impact of this approximation is that pressure drops for different meshes are not all the same. This is due to heat flux into the fluid found from a coarse mesh will be slightly different than a fine mesh so a higher or lower heat input will result in a higher or lower pressure drop in the channel. This also means that convergence plots of the error introduced by the mesh do not follow the mathematical convergence rates predicted by theory. It is still valuable to create convergence plots, as they should still show similar trends.

Implementation Checks

Several checks were created to determine if the code written was correctly implemented. First, the flow solution was decoupled from the heat equation by inputting a known heat flux and increasing the mesh size. Since the derivatives in the flow equations are discretized by first order finite-difference, first order accuracy should be demonstrable. Figure 4 shows first order accuracy in the solution implementation. The ``known'' solution is a very fine mesh solution and the error is defined by an L2 norm between the found solution and the ``known'' solution.

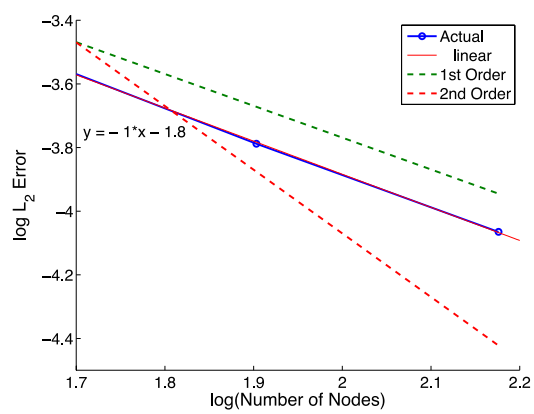

FIGURE 4. Convergence Plot for Flow Solution.

Next the PDE solution coupled with the flow solution was checked for dependence on the mesh. A 3 to 1 fuel to moderator ratio NTP was used with power densities and flow rates that seemed reasonable. The results should not be used as a performance merit. This was compared to a non-linear heat equation solver to demonstrate the inaccuracy of using a linear heat equation. Figure 5a shows that about 2.5E4 mesh elements are needed until the mesh does not have much effect on the maximum fuel temperature. Due to the approximation of not setting the pressure drop for each fuel channel and adjusting mass flow rate; there is some dependence on mesh for this implementation. A finer mesh is able to capture the heat flux into the fluid better than a coarser mesh. Small changes in the heat flux into the fluid cause changes in the pressure drop of the fluid and thus lead to changes in the temperature found in the fluid for different mesh sizes. This is believed to be the reason why the maximum temperature decreases with finer mesh up to a point then increases between 2.5E4 and 6E4 mesh elements. Similar behavior is seen in the non-linear solve. The difference between the linear and the non-linear equations is about 20 degrees at maximum and in general agree fairly well.

The total number of nodes used in the nodalization also has an effect on the solution. A 2 to 1 fuel to moderator ratio NTP was used with power densities and flow rates that seemed reasonable. The results should not be used as a performance merit. Not using enough nodes can lead to non-convergence and poor accuracy. Too many nodes can

lead to very long solution times or difficulties in the solver when root finding algorithms are needed and there is too small of a change between solutions to accurately find roots. Figure 5b shows the maximum fuel temperature does not vary more than about 2 degrees after 50 axial nodes are used. Sixty nodes are used in the studies show in this paper unless otherwise noted. Similar reasoning as the mesh dependence can be applied to the node dependence to explain why a solution is not converged upon refining the nodes.

One of the important figures of merit from each of the calculations is the maximum fuel temperature found. To verify that the convergence tolerance for the full calculation was set to a proper value, the change of maximum fuel temperature with the solution tolerance is shown in Fig. 5c—a tolerance of 10^{-4} is used for all results in this paper.

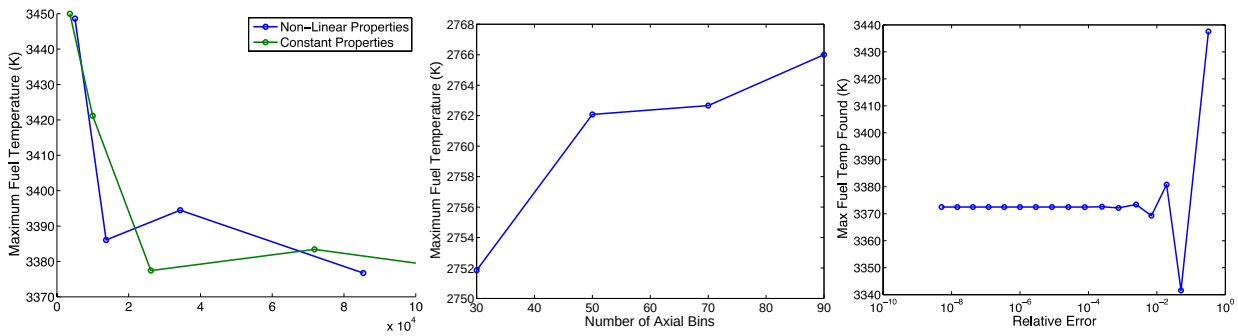

FIGURE 5. (a) Maximum fuel temperature dependence on mesh. (b) Maximum fuel temperature dependence on axial nodalization. (c) Effects of Solution Tolerance on Fuel Temperature.

Simple Performance Estimation Method

Simple methods to determine flow profiles and fuel temperatures involve neglecting the presence of tie-tubes. This was implemented by using the flow solutions described here and a maximum fuel temperature was found by using methods in [4]. This method is essentially a table lookup with a geometry correlation to take into accounts of 2D fuel geometry but does not take into account non-linear conductivities or tie-tubes.

INITIAL RESULTS

The tool developed takes about 30 minutes to run for a single case using about 120,000 mesh elements and solving the linear heat equation on a relatively old processor (2.66 GHz Intel Core i7) on one core. The MATLAB PDE Toolbox is not designed for multicore acceleration but multiple tasks may be spawned using the MATLAB Parallel Computing Toolbox.

The flow rate and power density to get approximately 2850 K maximum fuel temperature for a 2 to 1 fuel to moderator ratio core was found. This flow rate and power density was used in the simple performance estimation method to determine flow profiles and fuel temperatures. The power density shape was approximately cosine in shape with a slight bias for the peak of the cosine to be closer to the top of the core. The simple, linear-PDE and non-linear-PDE results are shown in Fig. 6.

Figure 6a compares the mean coolant temperature found from the PDE solution to the simple solution. The maximum and minimum coolant channels are also shown to show the relatively large difference between coolant channel temperatures. The mean coolant temperature is well predicted by the simple solution, however the simple solution cannot show the difference between maximum and minimum flow channels.

Figure 6b compares the maximum fuel temperature found from the PDE solution to the simple solution. There is a very large difference between temperatures predicted. All cases have the same inlet temperature and pressure. This shows that the simple method is not a good method to determine maximum fuel temperature in the fuel.

To further investigate the temperature profile in the fuel, the temperature solution along the cell where the maximum fuel temperature occurs is plotted in Fig. 7a. It can be seen that the maximum temperature occurs along the bottom fuel edge where the fuel meets another fuel element. This makes sense since more fuel would be present at the peripheries. In Fig. 7b a line segment of the fuel is plotted to better visualize the temperature distribution. It can be seen that about a third of the fuel element is hotter than the remaining two thirds.

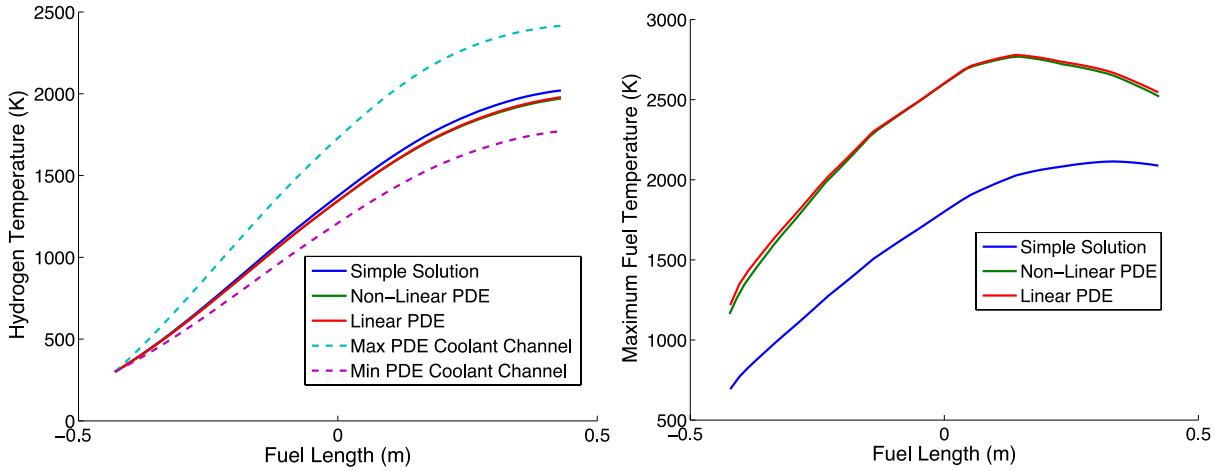

FIGURE 6. Comparing Simple Solution and PDE Solutions: (a) Coolant Temperature (b) Fuel Temperature

The simple method agrees much better to the minimum temperature found in Fig. 7b. This is reasonable since in the simple method, the fuel temperature is predicted by assuming there are no tie-tubes, which is approximately the case near the second two thirds of the fuel element plotted. Even if the maximum temperature in the two-thirds part of the fuel element was compared to the simple method, the simple method would be over predicting the temperature.

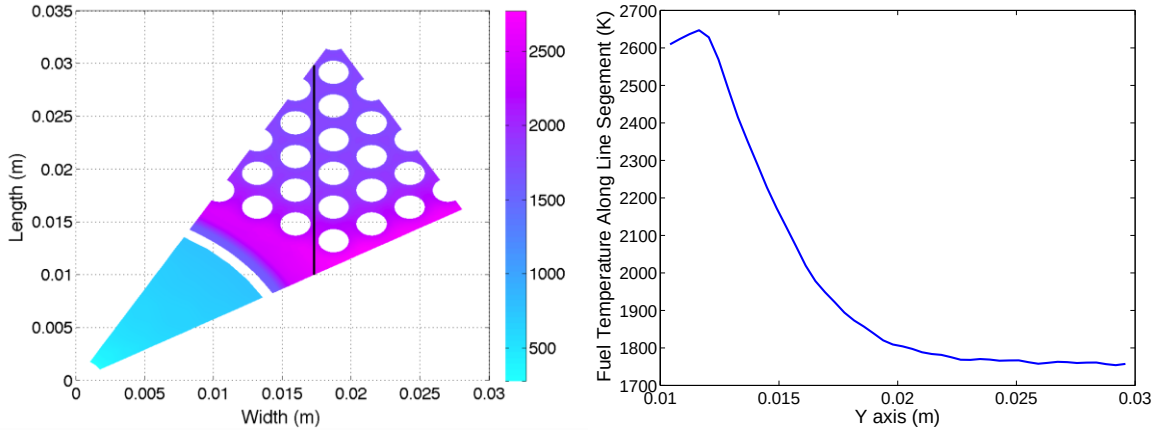

FIGURE 7. (a) Temperature Distribution in a Fuel Cell, (b) Temperature Profile Along Line Segment Shown in (a).

Future Works

The code may now be used for many different purposes. First methods to mitigate the large temperature peak in the fuel element should be evaluated. One simple method to do this would be to increase the mass flow rate in the channels near the peaked temperature in order to cool those areas more. This can also be easily physically accomplished by orificing each coolant channel to control flow rates. Another method would be to reduce the distance between the outer fuel wall and the outer fuel channels. This would reduce the amount of fuel meat between coolant channels when two fuel elements meet. This adjustment would be dependent on fuel manufacturing abilities. Another method could be to increase the distance between coolant channels in the central portion of the fuel in order to increase the heat generation in the central portion to increase the temperature there.

In order to decreasing the overall neutronic power peaking factor, several arrangements of fuel to moderator ratio may be used. This generally breaks symmetry in the core which makes it much more difficult to analyze temperature and flow profiles. It is likely CFD must be used in these cases though this tool might be useful for initial approximations of performance by estimating boundary conditions that would allow to partially model the non-symmetry of these cases.

Currently a constant power generation rate is used in the fuel. This approximation should be relaxed by using detailed power distributions based on neutron heating profiles. Portions of the fuel touching moderator tie-tubes will see a larger fission rate than portions of fuel touching other fuel. This might be enough to mitigate the large temperature peaks currently seen in the fuel. Furthermore neutron and gamma heating should be added as heat sources in the tie-tube in order to get the best estimate of the true temperature profile.

CONCLUSION

A tool to determine the temperature profile in an NTP that include fuel and tie-tubes has been developed and its implementation was detailed and demonstrated. Temperature profiles in the fuel and tie-tubes were coupled to a 1D flow channel solution in a staggered operator split in order to account for cooling by hydrogen coolant and to find NTP performance parameters. A 2 to 1 fuel to moderator ratio representative problem was examined to compare a simple solution scheme and the newly developed solution scheme. Flow profiles were found to be similar on the average between the two schemes but fuel temperatures were very poorly predicted by the simple scheme. The temperature profile in the fuel element was shown in detail and ideas to mitigate the large temperature peaks found were suggested. Improvements to the code were also discussed.

ACKNOWLEDGMENTS

Funding for this work is provided by NASA-MSFC. The author would like to thank Jon Mcdonald (NASA) for his help in selecting heat transfer coefficients. He would also like to thank Michael Eades (OSU) and Wesley Deason (CSNR) for encouragement and their help in discussing the solution algorithm.

REFERENCES

[1] NASA Johnson Space Center, "Human Exploration of Mars: Design Reference Architecture 5.0," Houston, (2009).

[2] Venneri et al., "Nuclear Thermal Rocket Design Using LEU Tungsten Fuel," in *Transactions of the Korean Nuclear Society Fall Meeting*, Gyeongju, (2013).

[3] OECD Nuclear Energy Agency, "Gen IV International Forum Annual Report," (2008).

[4] Sparrow, E.M. "Temperature Distribution and Heat_Transfer Results for an internally cooled, Heat-Generating Solid," *J. Heat Transfer*, vol. **82**, no. 4, pp. 389-392, (Nov 1960).

[5] Clough, J.A., Starkey, R.P., Lewis, M.J., and Lavelle, T.M., "Tie Tube Heat Transfer Modeling for Bimodal Nuclear Thermal Rockets," in *AIP Conference Proceedings*, vol. **880**, (2007), p. 281, doi: 10.1063/1.2437466.

[6] Los Alamos, "Nuclear Engine Definition Study Preliminary Report - Volume II," Los Alamos, NV, LA-5044-MS, (1972).

[7] Webb, J.A. and Gross, B. and Taitano, W.T., "A Combined Neutronic-Thermal Hydraulic Model of a CERMET NTR Reactor," *Nuclear and Emerging Technologies for Space*, (Feb. 2011).

[8] Cheng, G, and Ito, Y, and Rossi, D., "Numerical Simulations of Single Flow Element in a Nuclear Thermal Thrust Chamber," in *American Institute of Aeronautics and Astronautics*, Miami, FL, (2007).

[9] Walton, J, "Computer Program for Thermal and Transport Properties of Parahydrogen from 20 to 10 000 K," Nasa Technical Paper, NASA-TP-3378, (1993).

[10] The MathWorks, "MATLAB and Partial Differential Toolbox Release 2014a," (2014).

Advanced Stirling Radioisotope Generator Engineering Unit 2 (ASRG EU2) Final Assembly

Salvatore M. Oriti[1]

[1]*Thermal Energy Conversion Branch, NASA Glenn Research Center, 21000 Brookpark Rd., Cleveland, OH 44135*

Abstract. NASA Glenn Research Center (GRC) has recently completed the assembly of a unique Stirling generator test article for laboratory experimentation. Under the Advanced Stirling Radioisotope Generator (ASRG) flight development contract, NASA GRC initiated a task to design and fabricate a flight-like generator for in-house testing. This test article was given the name ASRG Engineering Unit 2 (EU2) as it was effectively the second engineering unit to be built within the ASRG project. The intent of the test article was to duplicate Lockheed Martin's qualification unit ASRG design as much as possible to enable system-level tests not previously possible at GRC. After the cancellation of the ASRG flight development project, the decision was made to continue the EU2 build, and make use of a portion of the hardware from the flight development project. GRC and Lockheed Martin engineers collaborated to develop assembly procedures, leveraging the valuable knowledge gathered by Lockheed Martin during the ASRG development contract. The ASRG EU2 was then assembled per these procedures at GRC with Lockheed Martin engineers on site. The assembly was completed in August 2014. This paper details the components that were used for the assembly, and the assembly process itself.

Keywords: ASRG, Stirling, Radioisotope

BACKGROUND

During the Advanced Stirling Radioisotope Generator (ASRG) flight development project, the team decided to pursue development of a flight-like test article for ground testing in the Stirling Research Laboratory (SRL) at NASA Glenn Research Center (GRC). The goal of this test article was to achieve a system-like assembly of a Stirling convertor generator, rather than the more research-style test articles that had previously been implemented in the SRL, and achieve a test article that would enable system-level tests [1]. The most notable differences were: assembly of the convertors into a dual-opposed pair inside a flight-like housing that acted as the heat rejection device, a flight-like insulation package, and a flight-like controller. The previous method for implementing support hardware on Advanced Stirling Convertor (ASCs) was tailored for research and measurements of performance at the convertor level. As such, the support hardware did not resemble a flight configuration, as it was designed to facilitate installation, enable specialty temperature measurements of the insulation, and enable precise temperature control on the various convertor interfaces. A flight-like assembly permits measurement of performance at the system level. During the development of this flight-like configuration, it was given the name ASRG Engineering Unit 2 (EU2), since it effectively became the second engineering unit produced by the project. Engineering Unit 1 was built by Lockheed Martin, subsequently tested, and delivered to GRC in 2008. EU1 operated for 33,000 hours before a fault in convertor operation required its shutdown and disassembly [2].

The support hardware for ASC-E3 performance mapping is illustrated in FIGURE 1. Notice that it does not resemble the geometry of the flight Generator Housing Assembly (GHA). The performance mapping hardware utilizes a round housing, a cooling loop attached directly to the convertor's Cold-side Adapter Flange (CSAF), and a method for controlling the alternator housing surface temperature. The heat source was also made small and compact, and does not resemble the General Purpose Heat Source (GPHS) module. These design decisions were made to enable accurate modelling and instrumentation, such that the convertor performance could be accurately measured.

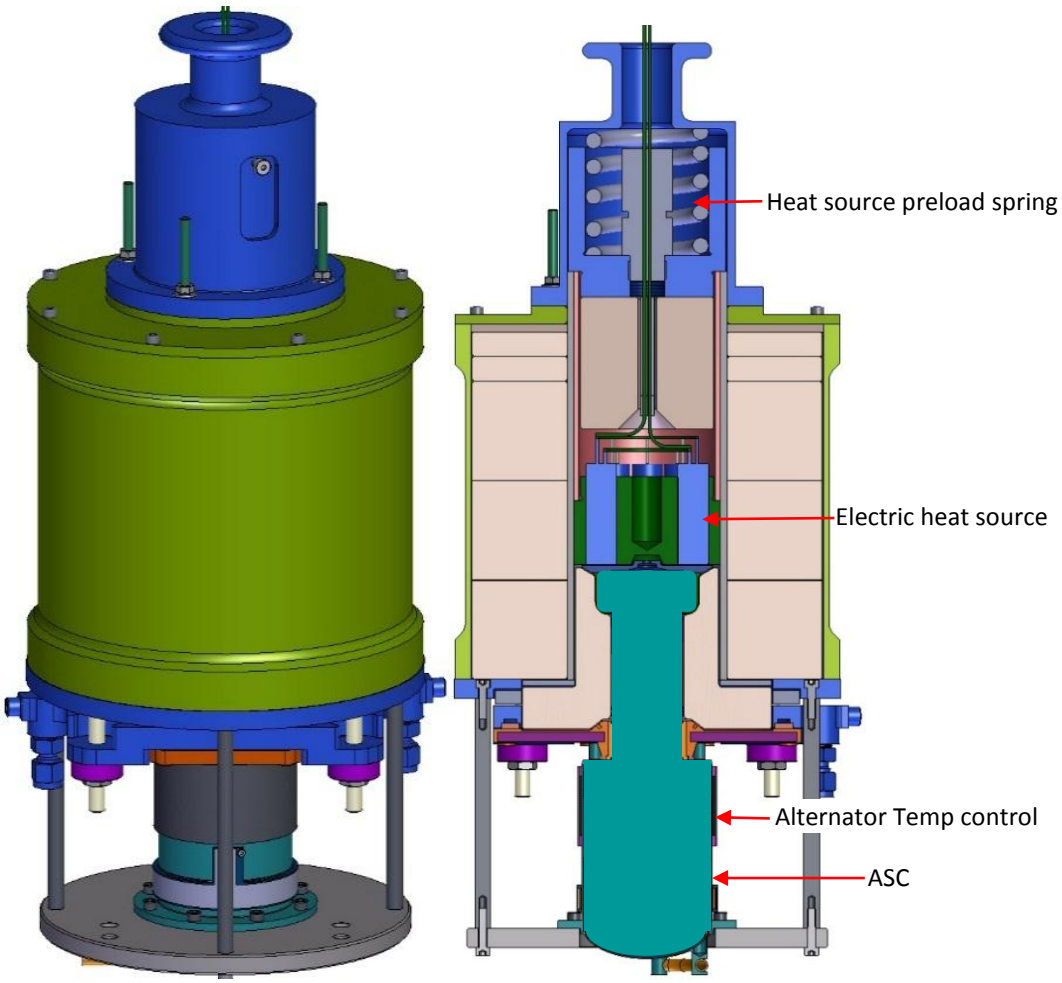

FIGURE 1. ASC-E3 Performance Mapping Support Hardware

The flight-like support hardware design is illustrated in FIGURE 2. Notice how it resembles the flight ASRG GHA. Deviations from the Lockheed Martin (LM) flight design were made to save cost, or adopt practices to improve extended operation. The differences from LM's flight design are highlighted in blue. Most notable is the use of aluminum for the housing material rather than beryllium. It was known from the initiation of the design effort that beryllium was not practical due to cost, lead time, and additional safety requirements. By way of quantification, the aluminum housing was fabricated for approximately $50,000 with a lead time of 6 weeks, while a beryllium housing required approximately 1 year of fabrication time. The aluminum housing segments (inboard and outboard) were fabricated from a solid billet of 6061 aluminum. With this, the bulkhead to which the convertors attach could be machined integral to the rest of the housing. This eliminated the need to braze the bulkhead piece into the housing, and the complexities associated with such an operation. This also made the critical heat rejection thermal pathway more reliable, as there is one less joint in the heat rejection path with an integral bulkhead feature. The thickness of all conduction pathways in the housing were increased to give the aluminum housing the same thermal resistance as the beryllium design. This was done by displacing only the outer surface of a thickness, so that the internal geometry and convertor interfaces remained the same as the LM design. The electric heat source also diverged from the LM flight design. GRC opted to make use of heritage heat source design knowledge. The EU2 electric heat source is comprised of a block of molybdenum with cartridge heaters inserted in a circular array. This is in contrast to LM's electric heat source, which utilizes flat-disc Boralectric heaters in a graphite shell. Empirical data suggest the GRC design will have a life greater than 10,000 hours, as an effort was made to reduce the cartridge heater heat flux as much as possible. The EU2 design makes use a GRC-style heat source load stud. This machinable ceramic (Cotronics Rescor 902) has been used in the past for the heat source preload path, as it has good temperature capability, low thermal conductivity, and good strength at temperature. This load stud was designed to have the same thermal resistance as the LM load stud assembly.

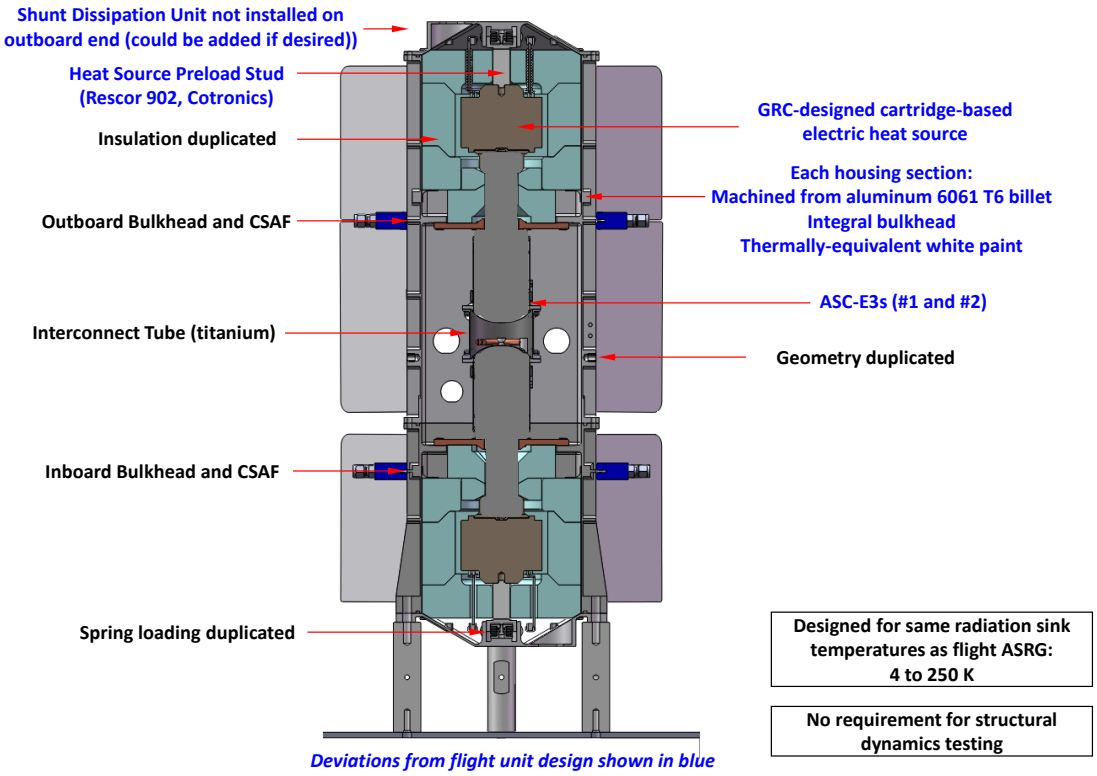

FIGURE 2. ASC Flight-like Support Hardware

ASC-E3 #1 and #2 were chosen for installation into the EU2. These convertors are the first pair of the ASC-E3 generation, which were being fabricated in parallel with the flight convertors (ASC-F). The ASC-E3s are the build closest to the flight design, and were the preferred choice for this effort. These convertors underwent the standard GRC set of tests including performance mapping [3], during which their performance was steady with no deviations from Sunpower's measurements prior to delivery. They were then reconfigured in a dual-opposed horizontal configuration for LM controller testing in Louisville, CO. The controller testing took place in February of 2014 [4]. The convertors were then returned to GRC in March 2014. A checkout test was performed upon their return to verify baseline performance. Following this, they were removed from their support hardware and the process of assembly into the EU2 began.

HARDWARE FROM LOCKHEED MARTIN

After the cancellation of the DOE flight development contract in October 2013, the decision was made to make use of some of the now-available LM hardware for assembly of EU2. At this point in time, the following items had already been procured and received by GRC:

- Inboard housing, Outboard housing, Housing end caps, Interconnect tube, Heat source spring load components, Heat source load stud, Insulation compression plate, Heat source components Electrical feedthroughs (Glenair)

The following items were transferred from LM to GRC for use on EU2:

- Convertor pair alignment fixture, GHA assembly fixture with Flotron, Convertor instrumentation and harnessing fixture, Hot-end thermal insulation (Microtherm), Insulation support brackets, Resistance Temperature Detector (RTD) mounting hardware (including specialty fasteners), RTD sensors, Accelerometers (internal), Accelerometer mounting brackets, Quartz yarn (unbaked), Various fasteners, for assembly

The availability of the LM's insulation and assembly fixtures greatly expedited the completion of EU2. GRC had previously designed fixtures to perform the convertor alignment and assembly into the housing, but these items were not fabricated.

ASSEMBLY SEQUENCE

Convertor alignment and pairing

The convertors (ASC-E3 #1 and #2) were first removed from their performance mapping support hardware. Only the affixed alternator and ASC Piston Sensor (APS) wires remained on the convertors. A joint GRC-LM procedure was developed to guide the convertor pairing process. The first step was to measure the housing geometry. Two housings have been built to date. Housing parts S/N 1 were used for EU2. The housing geometry was measured on May 13, 2014. The inboard and outboard housings were measured individually and a bulkhead-to-bulkhead distance was calculated by summing the distances between each housing's bulkhead and interface flange. The flatness of the bulkhead CSAF interface, the flatness of the interface flanges, and the parallelism between bulkhead and interface flange were also measured. Two trials of these measurements were made. The two trials agreed well, showing variances of only .0003 inches. The parallelism between the bulkhead and interface flanges was well within that required by the design.

The convertors were assembled into the convertor pair alignment fixture. The fixture was designed by LM to create two hole patterns in space that matched the CSAF mounting fastener patterns. This was achieved by using high-precision plates, guide rods, and linear bearings, similar to the techniques employed by the stamping industry (where alignment of dies is critical during up and down motion). Alignment pins were installed into the CSAF fastener holes to locate them in the patterns created by the plates. After the alignment plates were in place and properly engaging the CSAF alignment pins, the interconnect tube fasteners were then tightened, creating a dual-opposed pair assembly in which the CSAF mounting patterns were aligned in space. The upper alignment plate was then removed so that the CSAF flatness, parallelism, and distance could be measured using the Zeiss CMM (FIGURE 3). The convertors were installed such that the A convertor (inboard, ASC-E3 #1) was on the top, and the B convertor (outboard, ASC-E3 #2), was on the bottom.

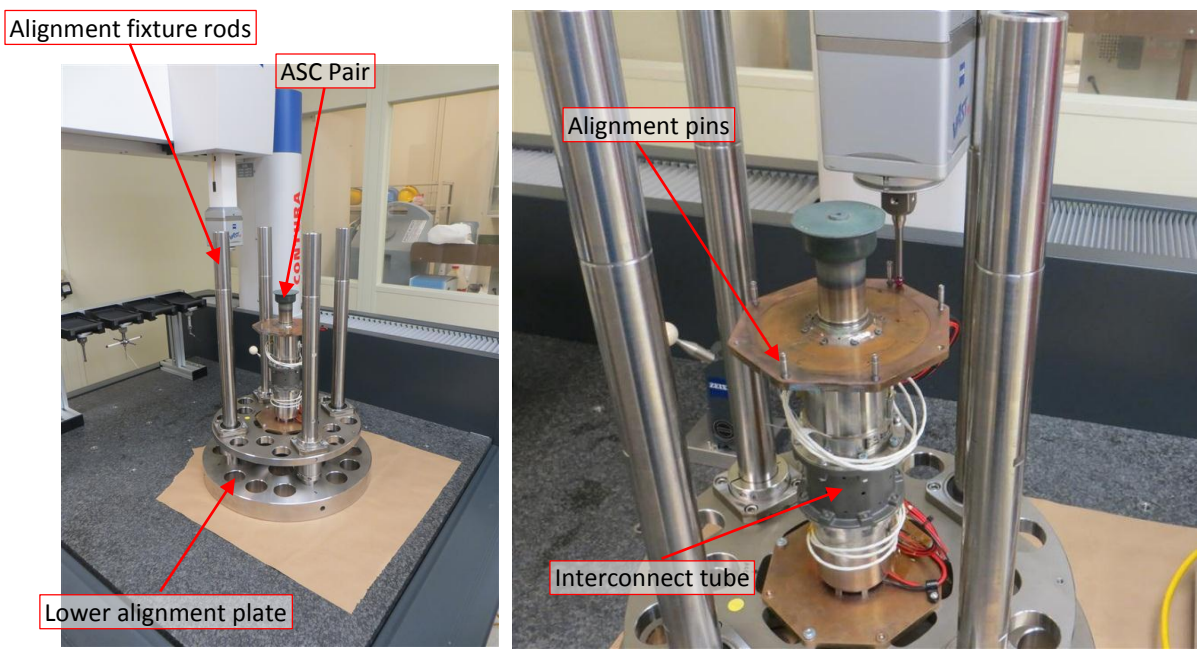

FIGURE 3. Measuring CSAF flatness, parallelism, and distance on CMM, with the convertors installed in the alignment fixture.

The CSAF-to-CSAF distance and parallelism were measured. The measurement data show that there was good parallelism between the CSAFs already, suggesting that a slanted trim cut of the interconnect tube would not be required. With these measurements, the required final geometry of the interconnect tube was calculated and represented in a dimensional drawing. The interconnect tube was cut such that the convertor pair CSAF-to-CSAF distance was .008 inches less than the bulkhead-to-bulkhead distance. The reason for the .008 gap is to make room for the thermal interface material (T-gon 805). The sheets of T-gon are .005-inches thick, so a zero-stress assembly would have the gap set at .010 inches. However, it was previously calculated that increasing the interconnect tube

length by .002 inches from the zero-stress state would most closely match thermal expansion forces to the LM flight design. Thus the CSAF-bulkhead assembly gap target was set at .010-.002 = .008 inches. This required removing .084 inches from the machinable face of the interconnect tube.

The convertors and trimmed interconnect tube were then reinstalled into the alignment fixture in the same manner as the first iteration. The clocking of the convertors in the fixture, the clocking of the convertors relative to each other, and the clocking of the interconnect tube relative to the convertors was duplicated. The CSAF-to-CSAF distance, flatness, and parallelism was again measured, to observe if the target geometry had been achieved. The measurements showed that both the target CSAF-to-CSAF distance and parallelism had indeed been achieved. The interconnect tube thread inserts were then installed, and the interconnect tube was reinstalled into the stackup. The target geometry had been achieved, so the interconnect tube fasteners were tightened to their final installation torque. This marked the completion of the alignment and assembly of the two convertors. At this point the convertors were in their final paired attachment configuration.

Convertor Instrumentation

Another procedure was jointly developed by LM and GRC engineers for this stage of assembly. The convertor pair was removed from the alignment fixture and installed into LM's instrumentation and harnessing fixture. The purpose of this fixture is to provide a mounting for the convertors convenient for installation of the instrumentation, the first layer of hot-end insulation, and to position the electrical feedthroughs. The feedthroughs are located by the fixture's base plate, which has cutouts of the same shape and locations as those in the GHA, relative to the convertors. This allows the installer to route and trim instrumentation and power wires to the proper lengths before attaching to the feedthroughs.

The RTD hardware was installed to check its fit on the heater head (FIGURE 4). The circular band that goes around the heater head required a custom-fabricated spreader to fit it over the heater head diameter. The RTDs were then formed (using mandrels of appropriate diameter) so that their sheaths followed the desired path. The hot-end and CSAF thermocouples were then formed in a similar manner. Accelerometers were then installed onto their mounting brackets, one per convertor. After the temperature instrumentation leads were pre-formed in the vicinity of the heater head, the items were removed to make way for wrapping of the quartz yarn around the heater head. To accomplish this, the convertors were removed from the fixture and attached to an inboard housing section, which was set on a rotating base. This allowed us to rotate the convertors while the yarn was held taut. The resulting layer of quartz yarn was uniform and without compromise. When the wrap reached the collector, the loose end was staked down using high-temperature ceramic adhesive.

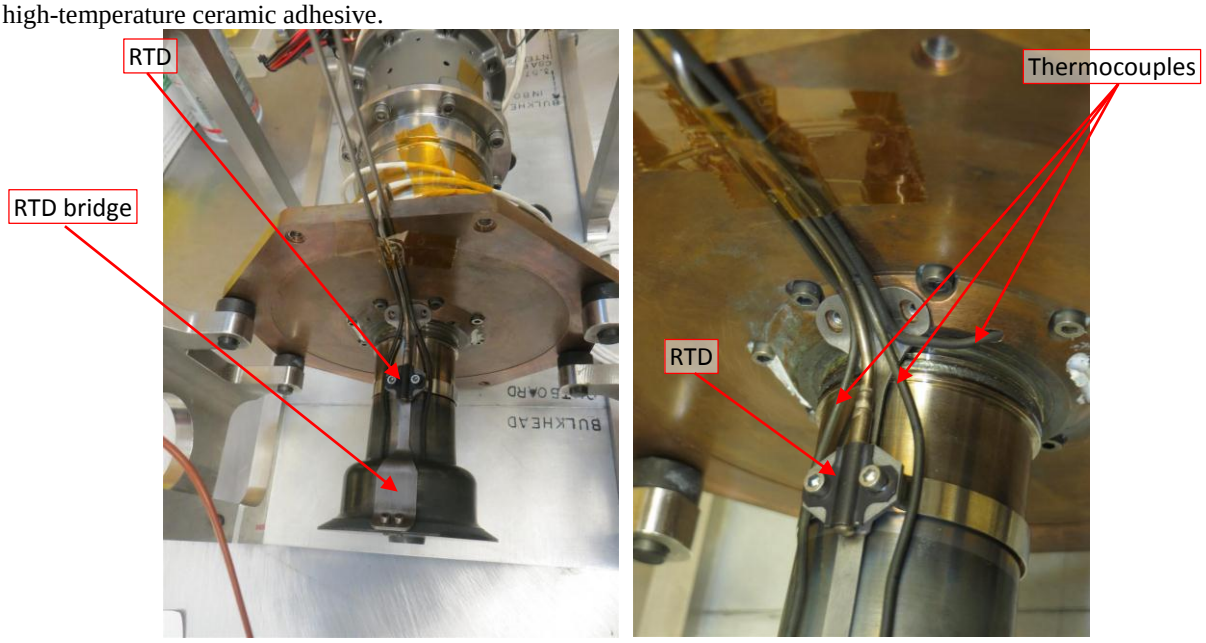

FIGURE 4. Fit check of RTD mounting hardware and forming of RTDs and thermocouples (TCs)

The RTD mounting hardware was then installed over the quartz yarn wrap. The convertors were returned to the horizontal instrumentation fixture. The hot-end thermocouples (TCs) were installed into the collector with nickel adhesive putty. The TC and RTD sheaths were staked to the face of the CSAF using a urethane potting compound. The transition of the RTD on the back side of the CSAF was also staked using urethane. Thermistors were installed into the CSAFs in an area near the CSAF TCs. The CSAF TCs and thermistors (TMs) were embedded in the CSAF features with the urethane potting compound. Thermistors were attached to the alternator housing with urethane and a layer of nickel foil over top of them. The completed instrumentation is shown in FIGURE 5.

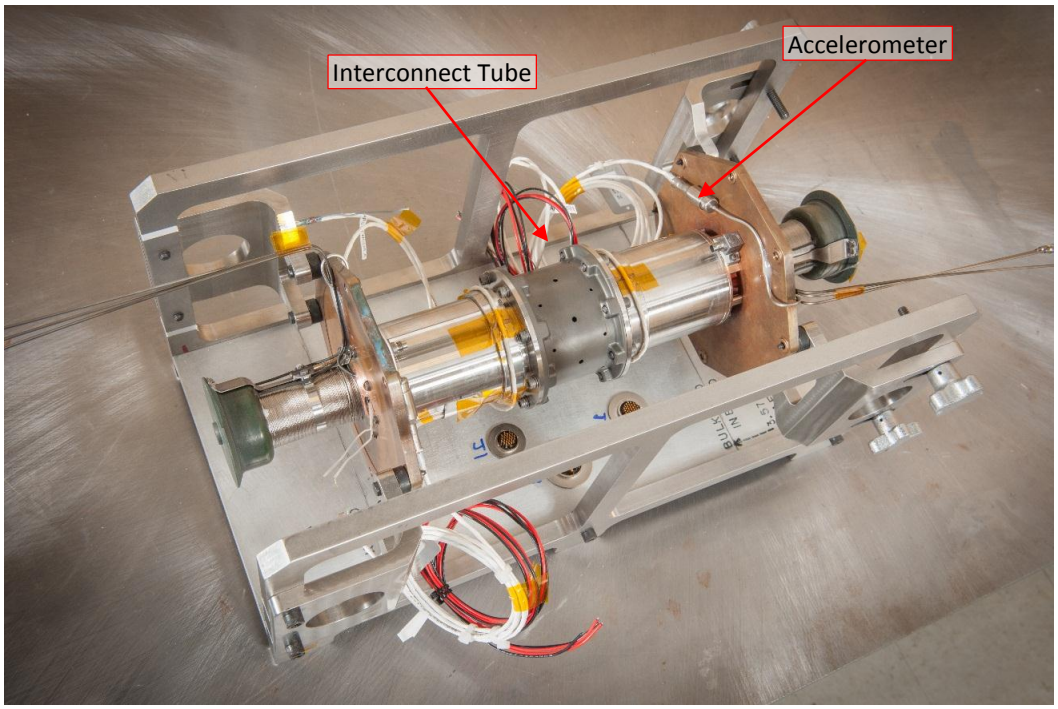

FIGURE 5. Instrumentation installation completed.

The convertor pair was then transported to a flight-qualified technician for completion of the wiring to the connectors. The wiring was completed on July 22, 2014 per LM drawings. This included routing and trimming of the wires, installation of sleeves over the wire bundles, and attachment of the lead wires to the appropriate connectors. A visual inspection of the wiring was completed, then the convertors were transported back to the SRL. A safe-to-mate procedure was completed on the connectors that had been attached at this point, and this check verified that all wires were attached properly. A layer of silica fiber blanket insulation was then fitted over the quartz yarn wrap around the heater head. The heater head microporous (Microtherm brand) insulation pieces were then modified to fit. The original design did not have sufficient clearance for the RTD attachment hardware. The channel in which the RTD and hot-end TCs reside was filled with silica fiber blanket insulation.

GHA Assembly

Once the instrumentation lead wires and heater head insulation were situated, the convertor pair was then placed onto the housing assembly fixture. The assembly fixture was the same used by LM during the ASRG flight development contract for the ASRG EU assembly. It consists of a rotatable holding fixture with a mounting plate designed to hold the GHA sections (FIGURE 6 left).

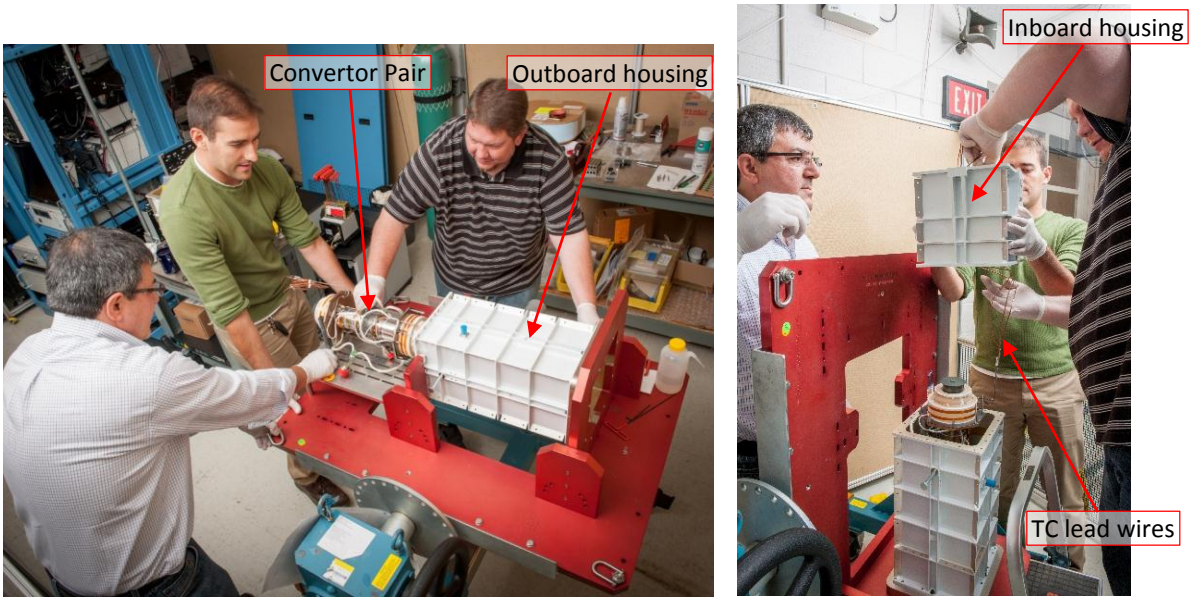

FIGURE 6. Convertor pair situated for installation into the aluminum housing (left) and installation of inboard housing section (right).

Alignment pins were installed into the top two outboard CSAF thread inserts to position the convertor pair when it would make contact with the housing's bulkhead. The alignment pins were also used to hold the layer of graphite thermal interface material while the convertor pair were slid into the outboard housing. As the convertors were then slid into the outboard housing, one person was responsible for guiding the outboard convertors' heater head insulation through the bulkhead cutout as the convertors moved into their final position. The CSAF attachment fasteners were then installed in the unoccupied threaded inserts to hold the CSAF against the bulkhead. The connectors were then pulled into their respective ports in the housing from the outside.

The assembly fixture was then rotated to place the convertor pair vertically, with the inboard end facing upwards (FIGURE 6 right). Alignment pins were installed into the inboard convertors' CSAF thread inserts, and a layer of graphite thermal interface material was placed onto the CSAF. The inboard housing section was then lowered onto the inboard CSAF, with an o-ring placed between the housing sections. As the housing section was moved into position, the thermocouple leads of the inboard convertor were pulled through the housing. The inboard CSAF fasteners were then installed after removing the alignment pins. The housing interface flange fasteners were then installed to fasten the two sections together (inboard to outboard).

The electric heat source, insulation pieces, and load stud were then installed into the inboard side of the GHA (FIGURE 7). This insulation came from the LM flight contract inventory. They are the same parts that were intended for use on LM's qualification unit ASRG. A thin disc of alumina was placed between the heat collector of the convertor and the molybdenum electric heat source. It was later discovered that this interface did not perform well under vacuum, and the disc will be replaced with a piece of graphite later. The molybdenum heater blocks had undergone an oxidation step so that their surface emissivity would closely match that of a GPHS module. It was discovered during heater build checkout testing that the oxide layer sublimates quickly at the temperature of use, which would introduce a contaminant inside the GHA. The oxide layer was thus removed from the majority of the surfaces via a sand-blasting operation. Thus the EU2 heat source emissivity is lower than that of a GPHS. Estimates of the effect on heat transfer were made, and these suggested the overall heat loss from the heat source would only change by 1 watt. The heat source was designed to have only two thin wires for electrical power protruding through the insulation. They can be seen in the right image of the figure.

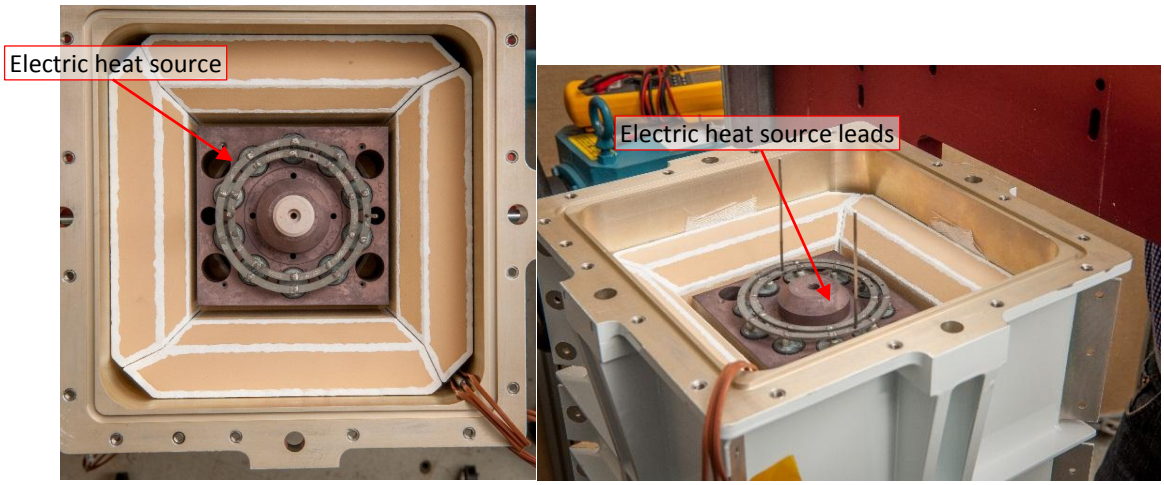

FIGURE 7. Installation of inboard housing section.

The cap piece of insulation was then placed over the heat source (FIGURE 8 left). The insulation compression plate was then placed onto the cap piece of insulation. A layer of quartz cloth was placed under the plate such that the housing end cap would compress the insulation stack the desired amount and hold it in place. This is of particular importance for launch vibration, but there are no plans to expose EU2 to a vibration environment test. After the compression plate was in place, heat source thermocouples were inserted through holes in the insulation cap piece and into blind wells in the heat source block. The thermocouple sheaths and lead wires were then formed to the desired path, and tied down to the compression plate with lacing cord. Thermocouple lead wires were trimmed to the proper length and then soldered to the feedthrough. A short harness was made to connect the two heat source lead wires to the heater power feedthrough. The heat source preload spring stack was placed onto the preload stud. The spring stack consists of a set of Belleville washers sitting in a cup that rests on top of the load stud. Prior to this activity, each spring stack assembly characterized determine its overall stiffness. The preload force between the heat source and ASC heat collector must be set to a particular value. The design of the ASRG permits adjustment of the spring stack compression via installation of shims of various thickness under the spring stack within the cup. With the knowledge of the spring stack stiffness and a measurement of the as-assembled geometry, the required shim thickness was calculated. The inboard housing end cap was then installed. The fasteners were then tightened down in an alternating side-to-side fashion, while alignment pins were in place to position the end cap relative to the inboard housing (FIGURE 8 right). The action of tightening down the end cap fasteners is what compresses the heat source spring stack.

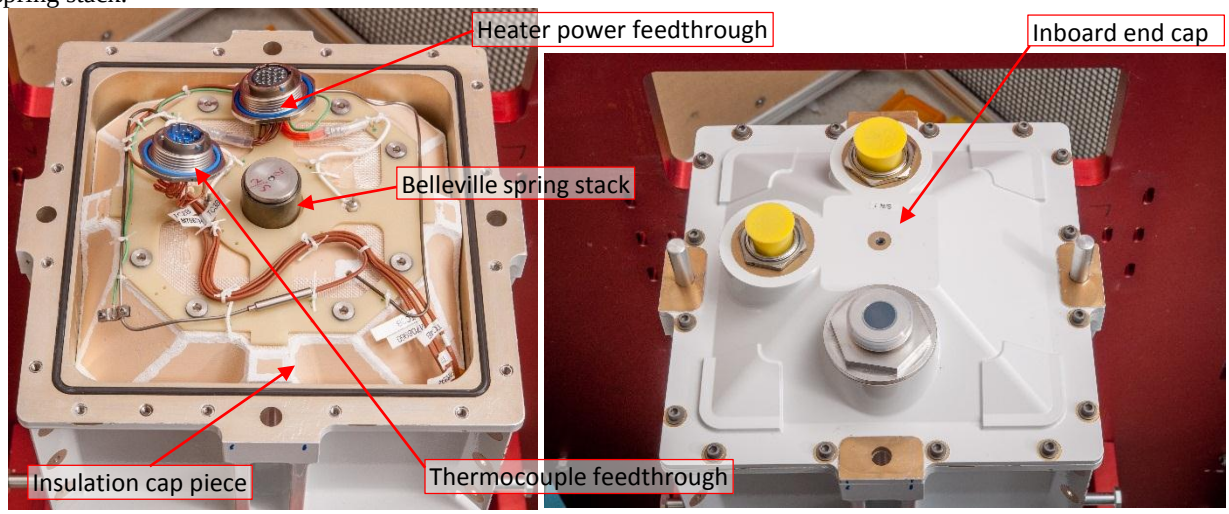

FIGURE 8. Installation of insulation end cap piece, and routing of TC wires.

The fixture was then rotated to place the outboard convertor upwards. The same steps for heat source, insulation, and feedthrough installation were repeated for the outboard convertor. The GHA was then removed from the rotating

assembly fixture and installed on the test stand (FIGURE 9). The GHA was installed on four standoffs. Load cells were previously installed between the standoffs and the table. These permit measurement of the mounting interface transmitted force. With this, tests can be conducted to evaluate methods to minimize residual vibration of the convertors. An argon supply system was implemented at the test station and connected to the gas port on the front of the GHA. A port was integrated into the end cap designs, onto which a vacuum valve is installed. These ports can be used to evacuate the gas volume from within the GHA. The microporous insulation operates more efficiently when gas is removed. Cooling blocks were attached to the ribs of the housing that coincide with the bulkhead locations. These can be used to adjust the rejection temperature of the convertors. This permits a wide range of testable operating conditions for the GHA.

Lockheed Martin's controller ASC Controller Unit (ACU) Engineering Development Unit (EDU) 4.0 was delivered to GRC on August 27, 2014. The ACU was then installed into the test rack and connected to the subsystems of the test stand.

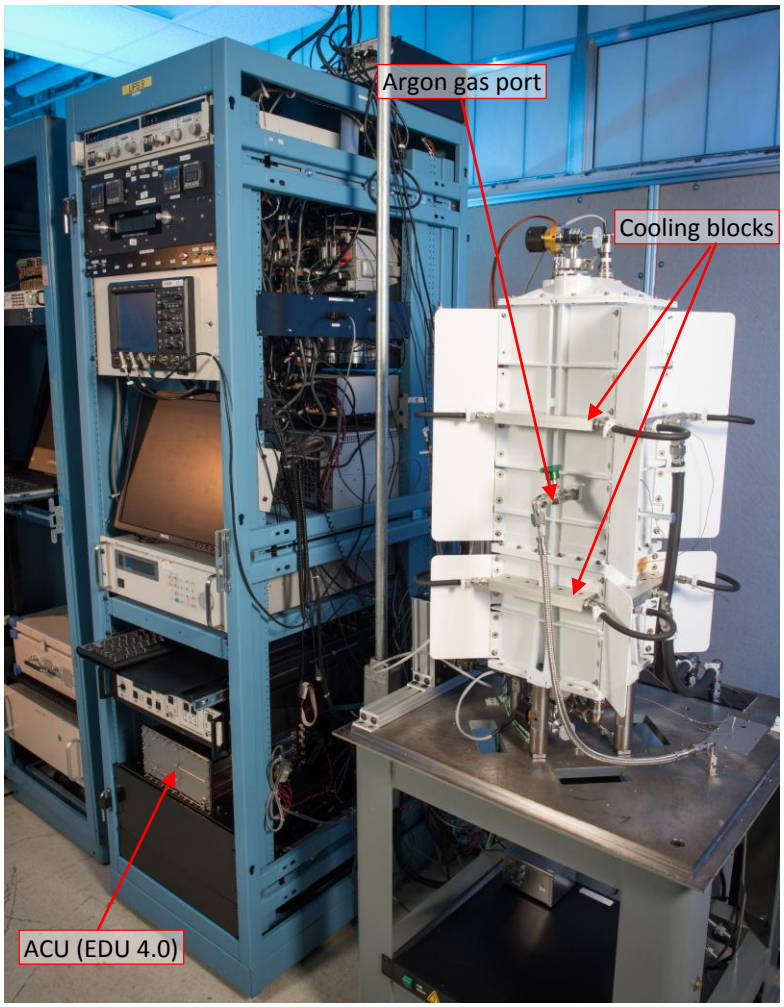

FIGURE 9. EU2 GHA installed on test stand.

CONCLUSION

A unique Stirling convertor test article has been assembled at NASA GRC. The test article is a flight-like configuration that thermally behaves in the same way as the flight ASRG design. The build process made use of Lockheed Martin hardware that became available after cancellation of the ASRG flight development project. NASA GRC and Lockheed Martin Valley Forge engineers collaborated to develop procedures for the assembly process. The assembly process consisted of steps to align the two convertors, install instrumentation, and align/install the convertors into the housing. The assembly task was fully successful and the test article was ready for operation in August 2014.

NOMENCLATURE

APS = ASC Piston Sensor
ACU = ASC Controller Unit
ASC = Advanced Stirling Convertor
ASC-E3 = Advanced Stirling Convertor model E3
ASRG = Advanced Stirling Radioisotope Generator
CMM = Coordinate Measuring Machine
CSAF = Cold-Side Adapter Flange
EDU = Engineering Development Unit
EU2 = Engineering Unit 2
GHA = Generator Housing Assembly
GRC = Glenn Research Center
GPHS = General Purpose Heat Source
LM = Lockheed Martin
RTD = Resistance Temperature Detector
TC = Thermocouple
TM = Thermistor

REFERENCES

[1] Lewandowski, E.J., Bolotin, G.S., and Oriti, S.M., "Test Program for Stirling Radioisotope Generator Hardware at NASA Glenn Research Center," in proceedings of *12th International Energy Conversion Engineering Conference (IECEC-2014)*, AIAA 2014-3964.
[2] Lewandowski, E.J., "Testing of the Advanced Stirling Radioisotope Generator Engineering Unit at NASA Glenn Research Center," in proceedings of *10th International Energy Conversion Engineering Conference (IECEC-2012)*, AIAA 2012-4253
[3] Oriti, S.M., "Performance Measurement of Advanced Stirling Convertors (ASC-E3)," in proceedings of *11th International Energy Conversion Engineering Conference (IECEC-2013)*, AIAA 2013-3813
[4] Chan, T., "System-level Testing of the Advanced Stirling Radioisotope Generator Engineering Hardware," in proceedings of *12th International Energy Conversion Engineering Conference (IECEC-2014)*, AIAA 2014-3966.

Full Submersion Criticality Accident Mitigation in the Carbide LEU-NTR

Paolo F. Venneri, Yonghee Kim

Deparrment of Nuclear and Quantum Engineering, Korea Advanced Institute of Science and Technology, Daejeon, South Korea, 305-701
+82 (042) 350-3810; yongheekim@kaist.ac.kr

Abstract. The present study seeks to characterize how to implement neutron poisons in the active core in order to mitigate the full submersion criticality accident in the Carbide Low Enriched Uranium Nuclear Thermal Rocket (Carbide LEU-NTR). In previous work, it was found that the increase in reactivity in the case of the full submersion is largely due to two factors: increased self-shielding by the core and an infinite reflector on the outside of the core. The increased core self-shielding is addressed by exploring the possibility of implementing a neutron spectrum shift absorber, despite the significant difficulties involved in successfully implementing a thermal neutron absorber in a thermal spectrum reactor. This is studied by looking at the implementation of Gd-157 in the fuel matrix and characterizing different parameters which make its implementation possible such as the degree to which and how the spectrum is hardened and the amount of poison included in the fuel.

Keywords: Full submersion criticality, LEU-NTR, carbide composite, neutron spectrum tailoring, spectral shift absorber

INTRODCUTION

The full submersion-criticality accident is one of the few design reference accidents given for space nuclear systems. The accident given varies from case to case, but is fundamentally the case where a reactor returns to the Earth's surface and lands in the ocean. This accident, given the rate of mission aborts on launch and the fraction of the Earth's surface covered by water, is not a standard design reference accident. It is not based on worst case scenarios that are highly unlikely to occur (such as a LOCA or SBO), but is instead a very real possibility that is more than likely going to occur given past experience and the hazards of entering low Earth orbit. Consequently, this accident has to be properly addressed in such a way that the nuclear system remains subcritical in the event of a full water submersion.

When this accident occurs, two things are happening to the core in terms of the neutronics. First of all, it is filled with water, one of the best moderators per unit volume in the world thanks to the elevated hydrogen density in it. This results in the significant thermalization of the neutron spectrum inside of the core, which in turn reduces the neutron leakage. The neutrons which are unable to leave the core are then able to cause further fission, resulting in a significant positive reactivity insertion into the core. The second factor is the surrounding of the core by an infinite and moderating reflector. This means that what neutron are able to leave the core despite the reduced leakage are reflected back into the core at lower energies, consequently further adding to the positive reactivity insertion due to the accident. This

Due its probable nature, space reactors have to be designed in addition to being compact, light, have a high power density, sufficient excess reactivity to operate for the required life time, and controllable, they also have to remain

subcritical in the event of being surrounded by an infinite reflector and filled with water. In past, a variety of methods have been implemented in reactor designs to ensure their safety. These can be roughly divided into two categories: external and internal. In the external methods, the focus is on ensuring that those neutrons which are able to leave the active core are unable to return to it. This can be done through having control drum with a large negative reactivity worth or the implementation of a reflector with enough worth that the addition of an infinite reflector has a largely negligible effect on the reactivity of the core. In terms of the internal methods, these have concentrated on making sure that the increased neutron population residing in the core is absorbed by non-fissile material rather than going on to begin new fission chain reaction. This last has typically been done by implementing thermal spectrum absorbers inside of the active core.

While this accident has been largely characterized for the instance of HEU and fast spectrum reactors, it has thus far been relatively unresolved in the case of the Low Enriched Uranium (LEU) and heavily thermalized spectrum reactors. In contrast with the HEU fast spectrum systems, LEU thermal spectrum cores face a series of unique challenges which makes the implementation of traditional mitigation design choices difficult and somewhat problematic. The reason for this stems from the fact that the core is already heavily thermalized. This means that first of all, the leakage from the core is already minimal, resulting in a low reflector worth and minimizing the effect of the external methods without increasing the size and mass of the system to unacceptable levels. Second, in order to operate in the thermal spectrum while maximizing the usage if the LEU fuel, all removable thermal neutron absorbers have been by necessity been removed from the active core. The result is that almost all additional moderation of the neutron spectrum results directly in the in the increase of the fission rate in the core and the consequent increase in reactivity. When the core is submerged, both of these effects are enhanced, resulting in an increasingly small reflector region worth and an increased fission rate inside of the core [1].

However, despite these difficulties, the advantages of previously verified and implement techniques for fast spectrum HEU reactors are undeniable in their passive nature and effectiveness. Here the implementation of a spectral shift absorber in the active core is explored and characterized in terms of neutronic feasibility. Once the effectiveness of this method is established, a path for future implementation is then proposed.

ANALYSIS METHOD

The analysis presented in this paper was done purely from a neutronics perspective. It was done by taking a reference Carbide LEU-NTR core design updated from previous work [2] and subjected to different parameter changes in order to verify their effect on the core neutronics. Core criticality calculations were all done using MCNP5-1.6 [3] on a lab cluster at the Korea Advanced Institute of Science and Technology (KAIST). All cross-sections were taken to be a room temperature, using the ENDF/B-VII library and 3 instances of natural composition cross-sections available in the ENDF/B-VI library distributed with the MCNP package [4]. All calculations were done using 50000 particles over 450 active cycles with 50 inactive cycles in order to achieve a typical standard deviation of .00015, more than suitable for the purpose of this study both in terms of accuracy as well as calculation speed. In the analysis of the neutron poison, three parameters were varies: poison content, moderator sleeve thickness, and the location of the modified moderator elements.

Reference Core Design

The reference core design is largely based off of a current design being developed at KAIST in order to flatten the radial power profile. The core measures 75 cm tall with an active core radius of 35 cm and 20 cm axial and radial reflectors. The core has been further modified for the purpose of this study to have a 1:1 moderator element to fuel element ratio and have an increased baseline moderator sleeve thickness in order to better observe the effects of varying the moderator sleeve thickness over a larger range. The is configured in a bulls-eye configuration with concentric rings alternating between fuel and moderator elements, allowing the relatively easy process of zoning modified moderator elements in terms of radial location. The baseline moderator geometry is given in Table 1 and the radial core geometry is shown in Figure 1.

TABLE 1. Moderator element detailed geometry

Component	Material	Inner Radius (cm)	Outer Radius (cm)
Inner Hydrogen	Hydrogen		.203
Inner tie tube	Zircaloy	.203	.254
Moderator	$ZrH_{1.8}$	.254	.684
Outer Hydrogen	Hydrogen	.684	.7605
Outer tie tube	Zircaloy	.7605	.786
Insulator tube	ZrC (50%TD)	.786	.9
Hexagonal element body	Graphite	1.905 cm face to face	

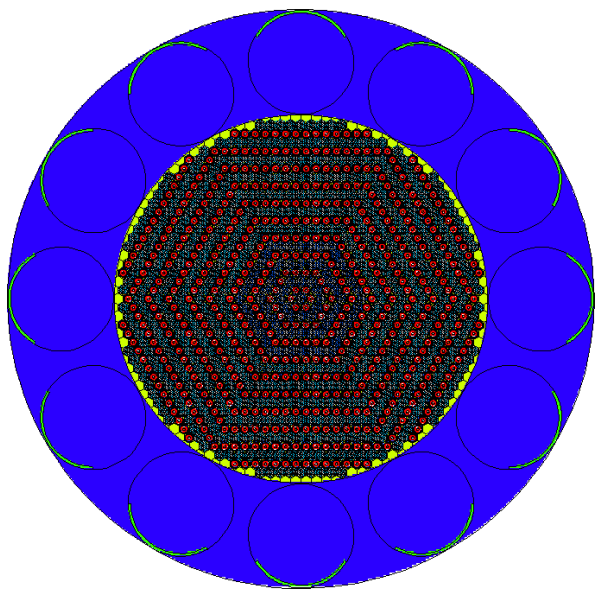

FIGURE 1. Reference core radial geometry.

The default configuration for the core for the purpose of this analysis is with the control drum in the "out" position, providing the maximum reactivity. In this configuration, the core's k-effective 1.21085 when dry, and 1.3576 when fully submerged and flooded. This results in a total positive reactivity insertion of .14675, roughly equivalent to 23$ assuming a delayed neutron fraction .0065.

In the prevision of inserting neutron poisons and hardening the neutron spectrum, the baseline core has been designed such that it is actually not a usable reactor without this modifications. In its baseline state, the control drums do not have the required negative reactivity worth to bring it subcritical, neither when fully submerged nor when in a dry state. This was done in order to achieve a functional design by the end of the study to provide a better idea as to what a carbide LEU-NTR core resistant to the full submersion criticality accident would look like. The k-effective of the baseline core in the shut down configuration when dry is 1.03476 and 1.28119 when fully submerged, with a worth of 27.5$ and 11.9$ respectively. This change in worth reflects the decrease in reflector zone worth and the decrease leakage from the core.

NEUTRON POISON

The neutron poison selected for the purpose of this study was Gd-157. Based on previous work [5], it is readily apparent that Gd-157 is particularly well suited for being used to prevent an increase in reactivity in the case of a full submersion. The principal neutronic reason for this is the presence of a steep increase in the absorption cross-section of Gd-157 in the heavily thermalized region of the neutron spectrum. This steep "edge" means that with even small amounts of Gd-157 in the core, a significant increase in the absorption of heavily thermalized neutrons is guaranteed. Furthermore, due to the significant presence of U0238 in the core, the strong negative temperature coefficient should

be able to with stand the negative effects to the temperature coefficient due the presence of the Gd-157 in core (R.B. Harty, 1985). The absorption cross-section of Gd-157 and Gd-155 are shown in Figure 2 along with the fission cross-section of U-235 and the neutron spectrum of the baseline core in this study.

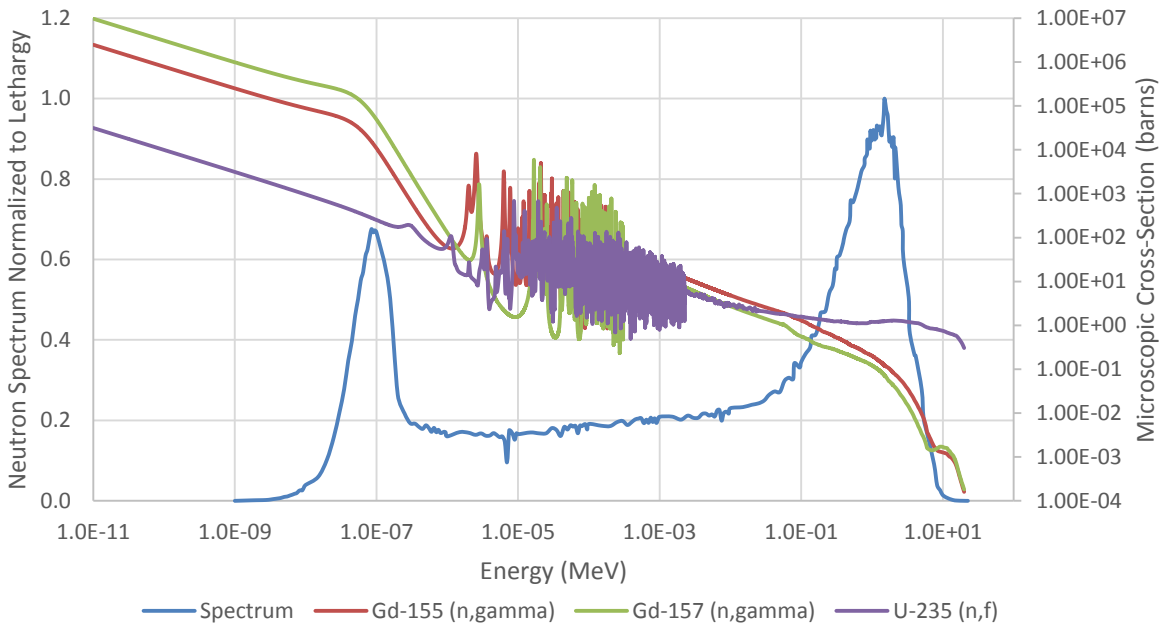

FIGURE 2. Neutron absorption cross-sections for Gd-157 and Gd-155 compared with the fission cross-section of U-235 and the neutron spectrum of the baseline core.

In addition to strong increase in the absorption cross-section of both Gd isotopes, there are two more aspects that follow from the graph in Figure 2. First of all is that the absorption cross-section of Gd-157 and Gd-155 is magnitude higher than that of the fission cross-section of U-235, making the reactivity of the core highly dependent to the on the Gd content in the core. Even minute amounts of Gd will result in noticeable negative reactivity insertions. The second factor is the strength and location of the thermal peak for the baseline reactor neutron spectrum. The thermal peak is placed right at the top of the absorption edge. This means that in order to take advantage of the, edge, the thermal peak needs to be shifted to higher energies. If the neutron spectrum can be hardened and the thermal peak shifted into the thermal region, than the resulting effect of the additional moderation from the flooding of the coolant channels will result directly in the a drastic increase of the absorption of neutrons by the Gd isotope, and a therefore produce a significant negative reactivity insertion.

The poison was implement in the core by mixing Gd-157 into the fuel matrix. This was done with different weight fractions of Gd-157 while ensuring that the fissile content remained constant by adjusting the density of the fuel to compensate accordingly. Depending on the study, the poison was either located only in the central region in the four center most rings, or varied to be present in different rings in order to see the effect of having the poison in different fraction of the core volume. This successive variation of the poison placement is shown in Figure 3.

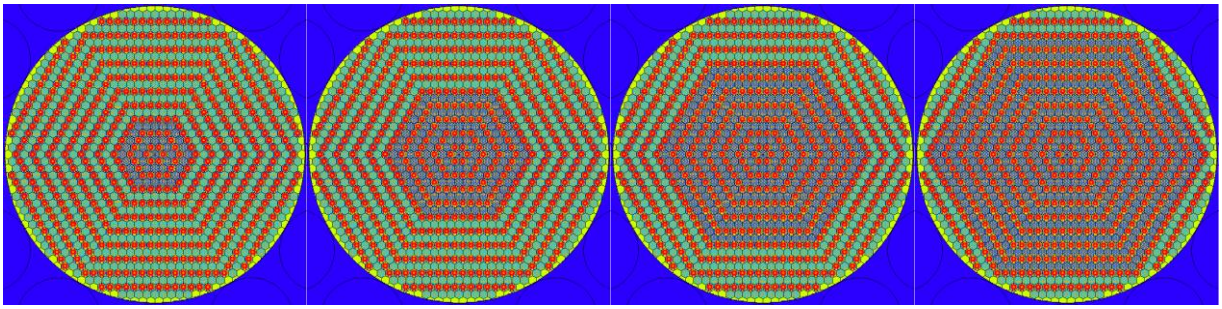

FIGURE 3. Neutron poison location in the blue fuel elements while the non-poisoned elements are green

NEUTRON SPECTRUM HARDENING

In order to implement the neutron poison in the active core, the spectrum has to be hardened significantly. As was shown in Figure 2, the spectrum of the reference core has its thermal peak squarely at the end of the cross-section edge of Gd-157. In such a position, further thermalization of the spectrum will have a relatively small effect on the absorption cross-section, and the implementation of the poison will have a much larger initial negative reactivity insertion than it would otherwise. This would result in a situation where the drawbacks of implementing a neutron poison are maximize while the benefits are minimized. Consequently to reverse the situation the spectrum in the region housing the poisoned fuel elements has to be hardened. This is done by reducing the amount of moderator in the active core during dry conditions. Here, the moderator was reduced by reducing the outer radius of the moderator sleeve in the moderator element in different sections of the core. The core sections were divided in the same way as the fuel elements were in the case of selecting where to place the poisoned fuel elements. The resulting effect on the neutron spectrum can be seen in Figure 4. Here, the neutron spectrum is shown for when the moderator sleeve of the 6 innermost rings of moderator elements are varied from the baseline radius of .684 cm down to .4125 cm. The effect on the neutron is quite pronounced, largely removing the thermal peak and causing the spectrum to closely resemble the spectrum of a Tungsten LEU-NTR. More importantly, the new spectrums are much more amenable to the implementation of Gd-157 without having a significant impact on the core's reactivity.

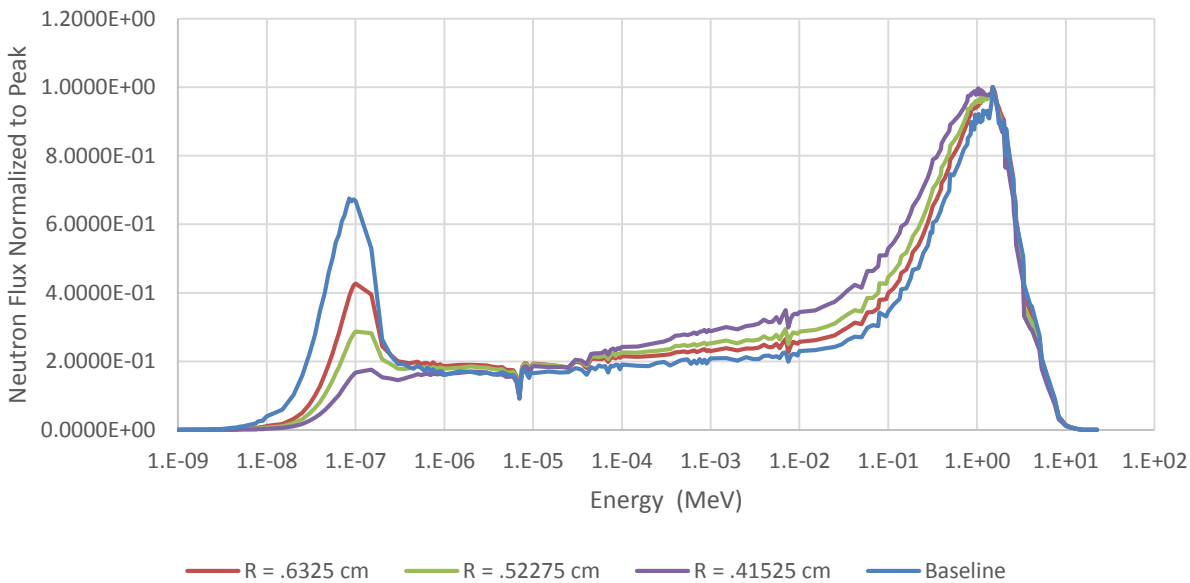

FIGURE 4. Neutron spectrum for different moderator sleeve radii are applied to the 6 innermost rings of the core compared with the neutron spectrum of the baseline core.

However, in hardening the spectrum, particular care has to be given to the effect of the moderator change to the reactivity of the core itself. In previous studies, it has been shown that one of the key enabling factors to having a small, compact LEU core is the implementation of a thermal spectrum. By hardening the spectrum, not only is the negative reactivity insertion from introducing the neutron poison reduced, but there is a simultaneous negative reactivity insertion due to the decrease in the fission cross-section at the same time. The result is two competing effects which need to be balanced in order to prevent an excessive loss in reactivity.

RESULTS

In applying the spectral shift absorber, two things become readily apparent. First of all is that what is important is to minimize the change in reactivity in the case of a full submersion. The second is that reactivity loss due the insertion of Gd-157 affects both the dry and the fully submerged cases while the negative reactivity insertion due to the

hardening of the spectrum applies only to the dry conditions. The result is that with each reduction in volume of the moderator only the dry condition is actually affected as the space previously occupied by the moderator is simply replaced by a nearly equivalent moderator during the full submersion accident. Consequently, the reactivity change during submersion is actually increased rather than decreased. This can be seen in Figure 5 where the change in k-effective with submersion is shown as a function of moderator sleeve thickness for three different configurations of modified moderator elements: 3 innermost rings, 6 innermost rings, and 9 inner most rings in comparison with the baseline configuration where no poison or changes the moderator sleeve radius have been applied. This particular case has a .0001 w/o Gd-157 applied to the fuel in the 3 innermost rings of the core.

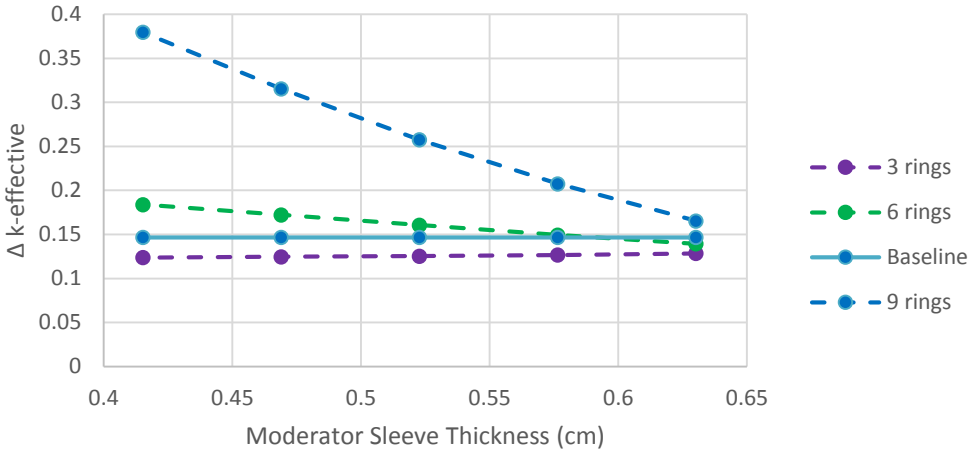

FIGURE 5. Change in k-effective with submersion for different moderator sleeve radii applied to the 3 innermost, 6 innermost, and 9 innermost moderator element rings in the compared with the baseline configuration.

Here, it becomes clear that in the case where there is relatively little Gd-157 present in the core, the effect of reducing the amount of moderator in the core is quite significant. This is further illustrated when one looks at the reactivity penalty for each configuration, again applied to the case where poison is applied only to the 3 centermost fuel element ring in Figure 6. Here, the negative reactivity insertion due to Gd-157 is plotted against changes in the moderator thickness. Here we can see that an optimum spectrum can be achieved when the 6 innermost rings of moderator elements are modified in order to minimize the negative reactivity insertion due to Gd-157 in the 3 innermost rings of fuel elements.

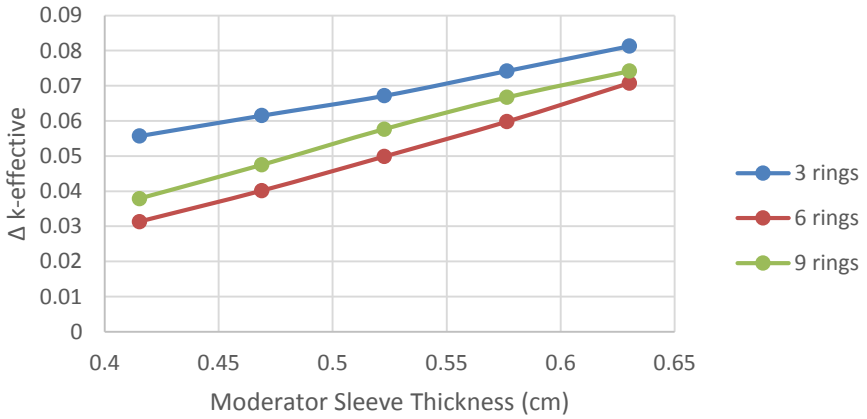

FIGURE 6. Penalty to k-effective due to Gd-157 in the fuel for different configurations assuming the same poison distribution in the 3 innermost fuel element rings.

However, when we look at the total reactivity loss due each configuration in relation to the baseline configuration, we find a very different picture as shown in Figure 7. Here, it becomes apparent that even though an optimum spectrum

is achieved in the case of the 6 innermost rings, the effect of having reduced moderation in the core is stronger than the reduction in the worth of the poison. The result is that by modifying the 3 innermost moderator element rings we are able to achieve the smallest reactivity penalty. This configuration also corresponds to the point where the benefits and disadvantages of hardening the spectrum match each other, resulting in a behavior that is relatively insensitive to the spectrum in the core.

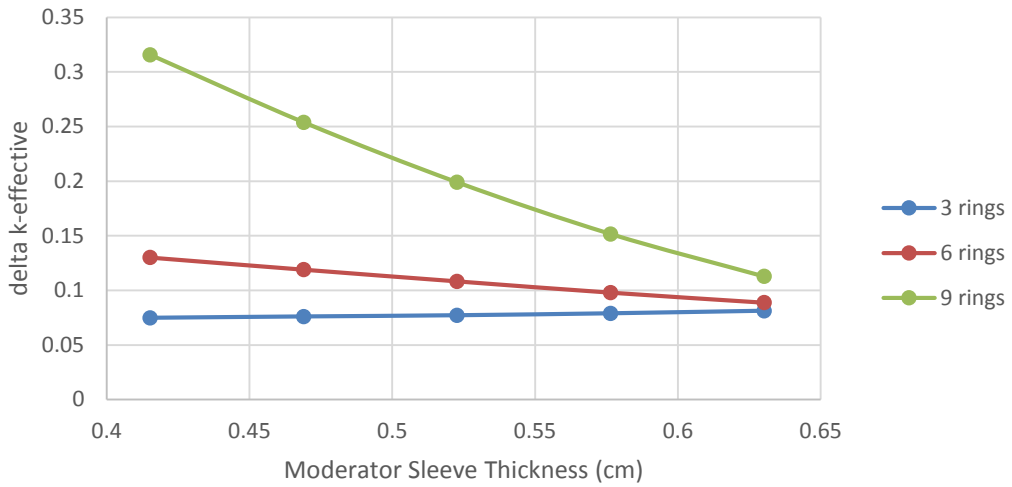

FIGURE 7. Total penalty to k-effective for different configurations assuming the same poison distribution in the 3 innermost fuel element rings.

When the poison is applied to more elements throughout the core we find that as the amount of poison is increased, the positive effects of introduction Gd-157 into the core become more pronounced. The penalty due to the poison insertion becomes dominated by the presence of the poison rather than the hardening of the spectrum. This can be seen in Figure 8 showing the decrease in penalty for each configuration as the size of the moderator sleeve is reduced. In this case, each line corresponds to a case where the number of rings where the moderator elements are modified as well as the fuel elements contain Gd-157. Of interest are the cases where poison is distributed and the spectrum hardened throughout the core. Here, for the configurations using the 8 and 10 innermost rings, the enhanced leakage becomes a dominant factor, resulting in an increased reactivity loss as the spectrum is hardened.

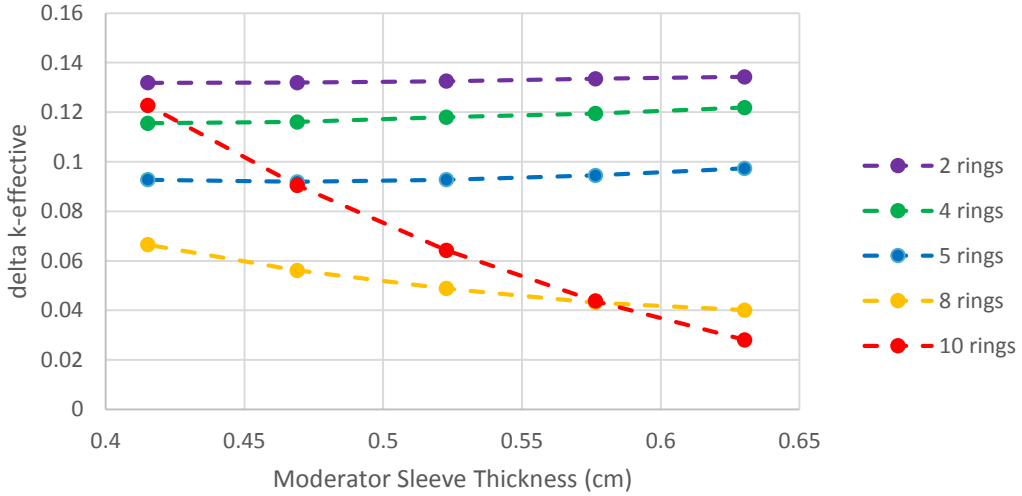

FIGURE 8. Total penalty to k-effective for different configurations assuming the same number of rings both for the poison distribution in the fuel elements and modified moderator elements.

CONCLUSION

In this paper the implementation of a spectral shift absorber in a Carbide LEU-NTR has been explored and characterized in terms of the poison content in the fuel and the moderation of the core. We have found that while an optimum spectrum for minimizing the effect of the poison when the core is not submerged is possible, achieving this spectrum without significant drawback is quite difficult. This is due to the heavy dependence of the Carbide LEU-NTR core on the thermalized spectrum. With hardening of the spectrum, a significant decrease in the reactivity is produced only in the dry condition, increasing the reactivity difference between dry and fully submerged conditions.

However, this paper has shown that an equilibrium between the advantages and disadvantages of hardening the spectrum in combination with a spectral shift absorber can be achieved. What remains is developing a method by which the disadvantages are minimized, maximizing the negative reactivity insertion in the case of a full submersion accident scenario.

REFERENCES

[1] Venneri P., Kim Y, Husemeyer P, Howe S., "Full Submersion Criticality Accident for Low Enriched Uranium Nuclear Thermal Rockets," Proc. *ANS Winter Meeting*, Anaheim, CA, (2014).

[2] Venneri P., Kim Y, Husemeyer P, Howe S., "Development of the 900 Second Specific Impulse Carbide Low Enriched Uranium Nuclear Thermal Rocket," *PHYSOR 2014*, Kyoto, Japan, (2014).

[3] X-3 Monte Carlo Codes, "MCNP5 - A General Monte Carlo N-Particle Transport Code," LA-UR-03-1987, LANL, (1987).

[4] Chadwick et al. "ENDF/B-VII.1 Nuclear Data for Science and Technology," LA-UR-11-05121, LANL (2011).

[5] King J.C. and El-Genk M.S., "Submersion Criticality Safety of Fast Spectrum Space Reactors: Potential Spectral Shift Absorbers," *Nuclear Engineering and Design*, vol 236 (2006).

A Guide to Nuclear Technologies for Space Applications: Past, Present, and Future

Laura K. Sudderth[1]

[1]*Department of Nuclear Engineering, Texas A&M University, College Station, TX 77843*
512-799-1292; LKSudderth@gmail.com

Abstract. Nuclear concepts have been investigated for space applications for nearly 60 years. Such concepts include radioisotope power systems, fission power systems, nuclear electric propulsion, nuclear thermal propulsion, and other advanced concepts. These technologies have enabled a variety of missions to explore the solar system and continue to make deep space exploration and manned mission architectures possible. This paper describes these technologies as they have been developed and implemented throughout history.

Keywords: Radioisotope, Fission, Power, Propulsion, History

INTRODUCTION

Nuclear concepts have been investigated for space applications for nearly 60 years. Systems can be divided into two major categories based on the intended purpose – electrical power production and spacecraft propulsion. Power systems include those that utilize either radioactive decay or fission as a heat source. Nuclear propulsion concepts include nuclear electric propulsion (NEP), nuclear thermal propulsion (NTP), and other advanced concepts.

Nuclear technologies have enabled a variety of unmanned missions to explore the solar system. Many other concepts have been designed for advanced missions. These technologies provide a foundation for current and future research to make deep space exploration and manned missions possible.

POWER SYSTEMS

Electrical power production systems convert heat from either the decay of radioisotopes or fission. These systems consists of three main components: the nuclear heat source, power conversion system, and excess heat radiators. The heat source and conversion systems are determined primarily based on the amount of power necessary for the mission. These systems span different stages of development and use, including deployment, prototypic development, and conceptual design.

Radioisotope Power Systems

Radioisotope power systems (RPS) uses the decay of plutonium-238 to produce heat and electricity for spacecrafts. Many systems have been launched that utilize both radioisotope heater units (RHU) and radioisotope thermoelectric generators (RTG) with lifetimes lasting up to 3 decades. Other technologies in development utilize alternative power conversion methods, such as a Stirling engine and thermophotovoltaic cells to improve conversion efficiencies.

Radioisotope Thermoelectric Generators

Radioisotope Heater Units utilize this heat to keep spacecraft components warm. These allow the systems to continue operating under harsh conditions when solar and other technologies are ineffective. Radioisotope Thermoelectric Generators convert the heat from decay into electricity using solid-state thermocouples. The United States has used RTGs in 26 missions over the last 50 years. RTGs are a highly reliable power source as no system has failed in their 50 year history. During this time, RTG technology has evolved and allowed spacecraft to explore farther regions of the solar system with lifetimes reaching over 30 years [1]. Figure 1 describes the mission history of system using RHUs and RTGs with the planets observed noted.

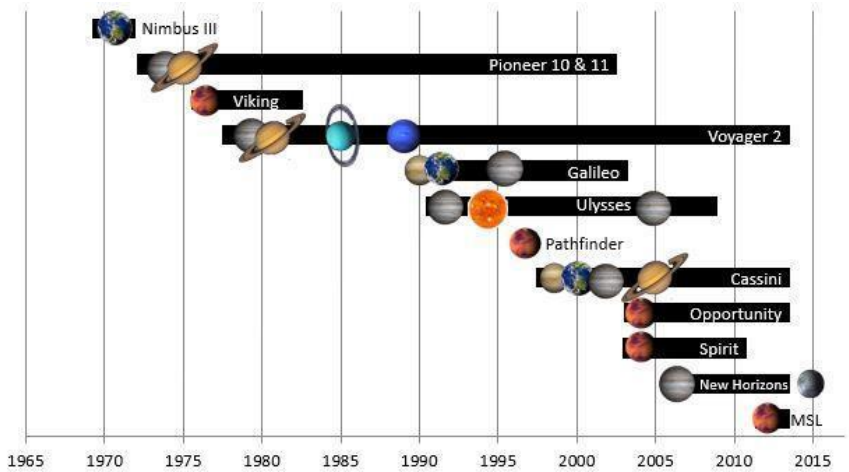

FIGURE 1. RPS Mission History.

A variety of RTG systems have been developed and flown since their beginning. Table 1 summarizes these systems and how many units were used in each mission [1]. A cutaway of the general purpose heat source (GPHS) is shown in Figure 2.

TABLE 1. RTG Technologies

	SNAP 19	**Multi-Hundred Watt RTG (MHW)**	**Multi-Missions RTG (MMRTG)**	**General Purpose Heat Source (GPHS)**
Electrical Power (W_e)	40	158	120	292
Missions	Viking (2) Pioneer (4)	Voyager (3)	Mars Science Lab	Galileo (2) Ulysses (1) Cassini (3) New Horizons (1)
Mass (kg)	< 35	37.7	45	57

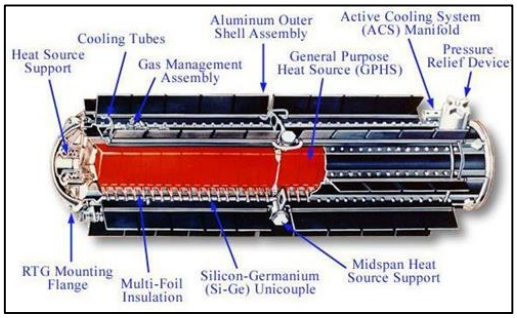

FIGURE 2. General Purpose Heat Source Cutaway [1].

Stirling Radioisotope Generators

Stirling Radioisotope Generators (SRGs) utilize~~s~~ a GPHS unit with a Stirling Engine to convert the heat from Pu-238 decay into electricity. Compared to the thermocouple converters, SRGs can achieve about 4 times the thermal efficiency, thus achieving much higher electrical output from the GPHS units. Although none of these units have been flown, they have been extensively tested [2]. NASA Glenn Research Center (GRC) continues development on Stirling technology for future deep space exploration [1].

FIGURE 3. SRG Test Unit [1].

Radioisotope Thermophotovoltaic Systems

Radioisotope thermophotovoltaic (RTPV) is an RPS system that directly converts heat from a GPHS unit to electrical power. This is done through a radiative emitter that converts the heat into radiative energy for a photovoltaic cell using components shown in Figure 4. An RTPV system is in development at NASA GRC to produce 100 We with ~15% conversion efficiency. Other studies involving tungsten encapsulation of the radioactive material may allow for a 3-5x reduction in the specific mass of the system [3]. Such systems enable lower power missions to explore the outer planets.

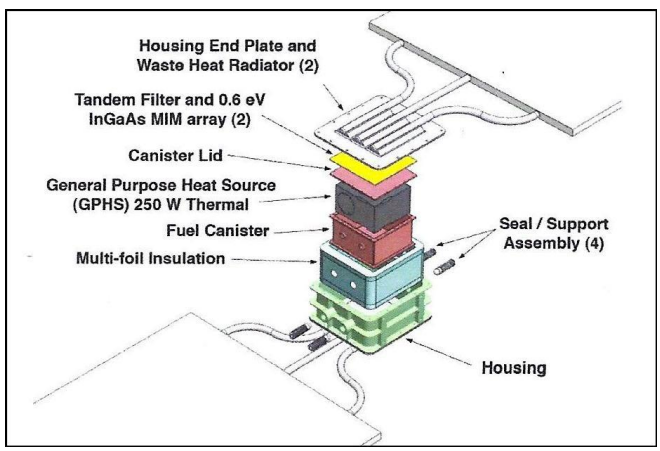

FIGURE 4. RTPV Component Schematic [3].

Fission Power Systems

Fission power systems are used to generate heat, which is then converted to electricity. Applications such as orbiting missions and surface power have higher electrical output requirements. At these higher powers, fission systems have cost advantages over RTGs. Table 2 describes Fission power system programs. The United States has only launched one fission reactor in space. The SNAP-10A, shown in Figure 5, flew for 43 days before shut down due to a non-reactor malfunction. Other US fission power initiatives were terminated prior to launch. The Soviet Union has launched 31 fission reactors as a part of Cosmos missions, including the Romashka and Bouk reactors. The Topaz 1 followed these reactors and was designed to operate 3-5 years. Two Topaz 2 reactors were sold to the US, but the launches were cancelled due to budget restrictions [2].

TABLE 2. Fission Power Systems [2].

	Snap-10A	**SP-100**	**Romashka**	**Topaz 1**	**Topaz 2**
Date	1965	1992	1987	1987	1992
Country	US	US	Russia	Russia	US-Russia
Electrical Power (kW_e)	0.65	100	0.8	5-10	6
Power Conversion	TE	TE	TE	TI	TI
Fuel Type	U-ZrHx	UN	UC_2	UO_2	UO_2
Mass (kg)	435	5422	455	320	1061
Neutron Spectrum	Thermal	Fast	Fast	Thermal	Epithermal
Coolant	NaK	Li	Graphite	NaK	NaK

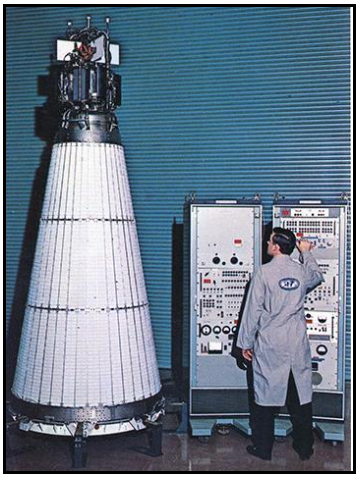

FIGURE 5. SNAP 10A Reactor

In 2008, NASA announced a plan to develop a fission surface power (FSP) system for the moon and Mars. The goal is to produce a 40 kWe system utilizing a liquid metal (NaK) cooled reactor and two Stirling Engines. Although the reactor has not yet been developed, NASA successfully tested the power conversion and radiator components in 2012 [2]. A shielding concept, shown in Figure 6, has been studied to minimize shield mass. This is accomplished by dividing the shield into sections and moving the fill water based on astronaut location.

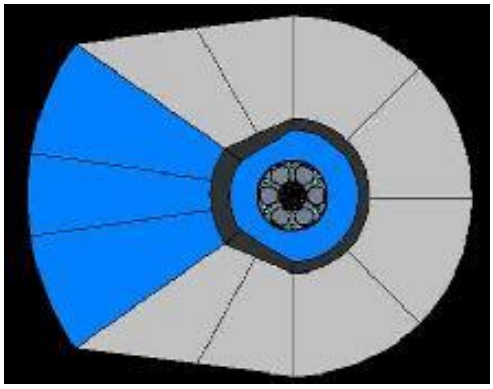

FIGURE 6. Shielding Concept for FSP [4].

PROPULSION SYSTEMS

Nuclear propulsion systems allow shorter mission times with large payload capabilities compared to traditional chemical rockets. Table 3 shows a comparison of NTP, NEP, and chemical rocket capabilities. Advanced concepts utilizing technologies such as fusion and fission fragment engines may exceed these capabilities once fully developed.

TABLE 3. Propulsion System Comparisons

	Chemical	**Nuclear Thermal**	**Nuclear Electric**
Energy Source	Reacting propellants	Fission reactions	Electricity
Propellant	Hydrogen and Oxygen	Hydrogen	Xenon
Isp Range (s)	200-450	500-1000	1000-5000
Thrust	Up to 6.6 MN	Up to 980 kN	Up to 1 N

Nuclear Electric Propulsion

Reactors for nuclear electric propulsion operate similarly as those for fission power systems, i.e. they use fission to produce heat and convert it to electricity. The main difference is that NEP reactors are designed to be paired with electric propulsion systems, such as ion drives, VASIMR, or MHD, thus requiring higher electrical outputs. Due to the high specific impulse and low thrust capabilities of electric propulsion, NEP is generally considered for unmanned, deep space missions.

Jupiter Icy Moons Orbiter

The Jupiter Icy Moons Orbiter (JIMO), shown in Figure 7, was a mission to explore the large moons of Jupiter (Callisto, Ganymede, Europa) to examine the possible existence of oceans underneath the icy surfaces. Although the system design was never determined, feasibility studies were performed on a 20-200 kWe systems. Concepts included a 100 kWe lithium-cooled reactor with a Stirling or Brayton power conversion system propelled by an ion propulsion system [5, 6]. The project lost funding in 2005.

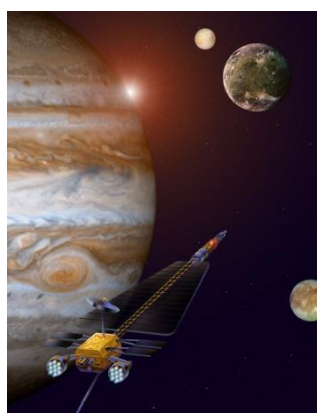

FIGURE 7. Artist Rendering of JIMO [7].

Heatpipe Power Systems

Heatpipe Power Systems are small fast fission reactors that produce up to 100 kWe. They utilize heatpipes filled with sodium paper to transfer heat from the core to the He-Xe loop of the power conversion system – either Brayton or Stirling. HPSs generally use UN fuel and Be-B4C control drums. Specific examples include the SAFE-400 (400 kWt, 100 kWe) and the smaller HOMER-15 (15 kWt) [2]. The SAFE-400 core consists of modules with a molybdenum-sodium heatpipe surrounded by 3 Mo tubes containing UN fuel pins, as shown in Figure 8 [8]. Another core design consists of a solid U-Mo fuel with heatpipes radial dispersed throughout the core, as shown in Figure 9 [9].

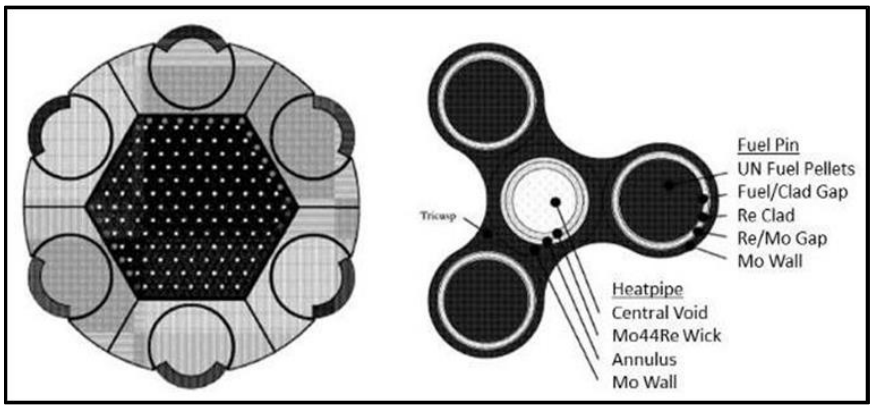

FIGURE 8. SAFE-400 Core Layout [8].

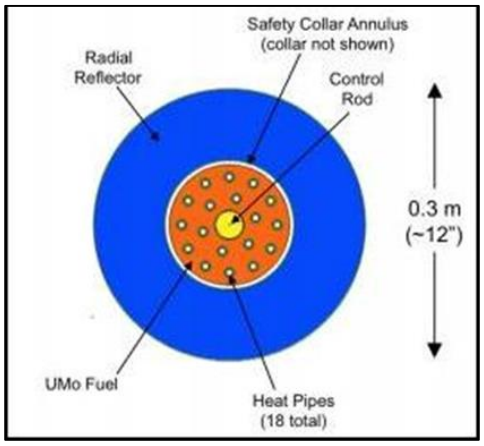

FIGURE 9. Solid Metal Core Radial Cross-Section [9].

Kilopower

Kilowatt-class fission power systems (i.e. Kilopower) are being investigated at NASA and DOE to address the gap that exists between the 100W-class RPSs and large-scale fission power systems (>100 kWe). System configurations ranging from 0.5 to 10 kWe have been developed using U-Mo heat-pipe cooled reactors with various power conversion systems, including thermoelectric (1 kWe) and Stirling (3kWe) converters, as shown in Figure 10. As the Kilopower concept has progressed, reactor concepts that replace the U-Mo core with a smaller monolithic uranium block with heat pipes outside the perimeter of the core have been incorporated to simplify fabrication and testing, significantly reducing development costs. These low power systems enable NEP for future planetary science missions or human precursors while being mass and cost competitive with RPSs.

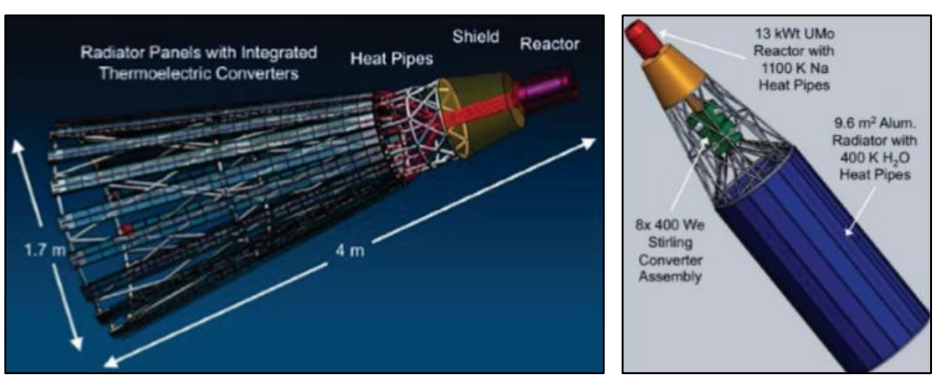

FIGURE 10. Kilopower Thermoelectric (Left) and Stirling (Right) System Designs [10].

Nuclear Thermal Propulsion

Nuclear thermal propulsion utilizes a HEU or LEU reactor, usually cooled by hydrogen. The reactor superheats the hydrogen, which is then passed through the nozzle as the propellant. Since NTRs do not utilize a reactor coolant loop or power conversion, the system mass can be minimized by eliminating many unnecessary components. The moderate thrust and specific impulse capabilities, compared to chemical and electric propulsion, makes NTP the preferred propulsion method for manned mission to Mars and deep space.

NERVA-Rover Program

Project Rover was initiated in 1955 at Los Alamos Scientific Laboratory (now LANL) to build and test nuclear reactors for an NTR. The program was split into 3 phases: Kiwi, Phoebus, and Pewee reactors, shown in Figure 11 [11]. All reactors were hydrogen-cooled and consisted of UC fuel particles in a graphite matrix. Eight Kiwi reactors were successfully built and tested, but were replaced with the larger Phoebus reactor, more favorable for manned missions. Three Phoebus reactors were built and tested. The smaller Pewee 1 and 2 were tested for unmanned missions. The Phoebus 1A fuel element cluster is shown in Figure 12 [12].

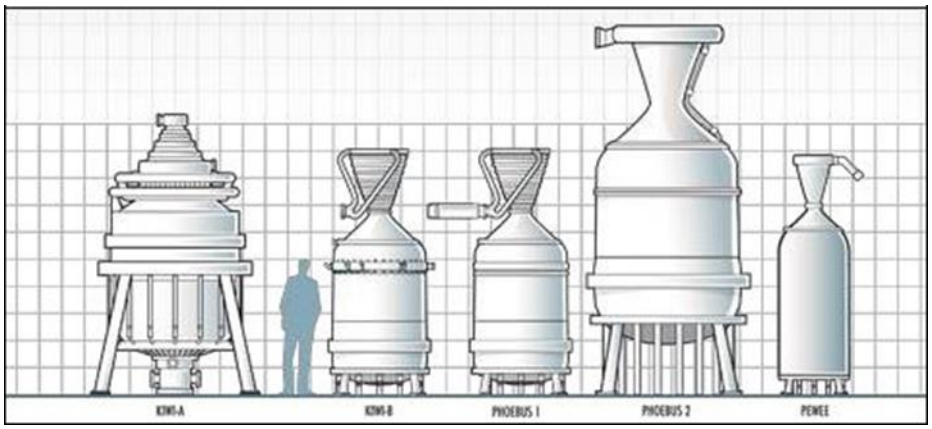

FIGURE 11. Rover Reactors [11].

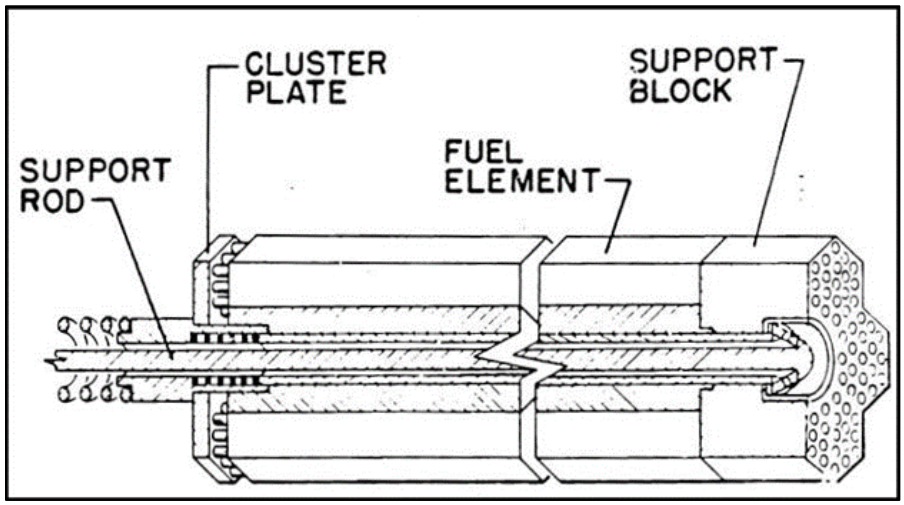

FIGURE 12. Phoebus 1A Fuel Element Cluster [12].

The Nuclear Engine for Rocket Vehicle Application (NERVA) program began in 1960 at NASA to create a rocket engine with a minimum of 75,000 lb_f thrust using the graphite-based reactor from the Rover program. The system configuration is shown in Figure 13. It was intended to be used for a manned mission to Mars, once scheduled for launch in 1981, but the program was cancelled in 1972. The NERVA/Rover program was proof that NTRs were a feasible and reliable option for space travel [2].

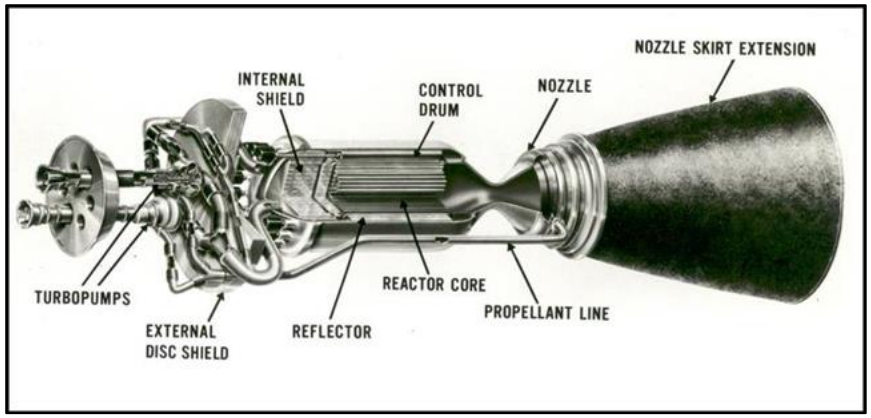

FIGURE 13. NERVA Rocket Engine.

Bimodal NTRs

The NERVA/Rover program has been used as the design basis for most modern NTR concepts. One such concept is the bimodal NTR, shown in Figure 14. The NERVA-derived bimodal NTR incorporates tie tubes dispersed throughout the core with NERVA-type hexagonal fuel elements, as shown in Figure 15. These tie tubes allow for double-pass heating of the working fluid for a power conversion system, in this case a He/Xe Brayton cycle, while the flow channels in the fuel elements heat the hydrogen propellant [13]. This allows the reactor to be used to generate electrical power as a secondary purpose.

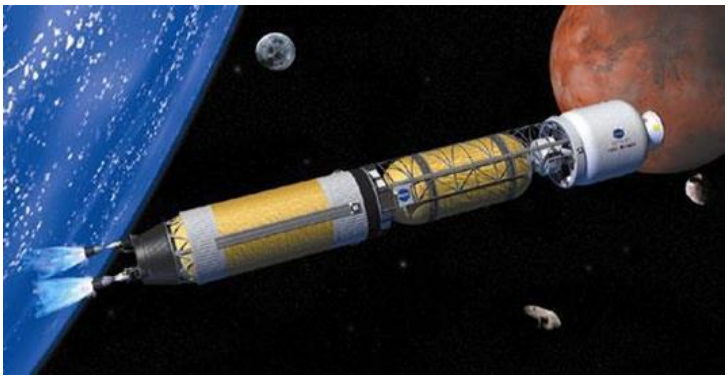

FIGURE 14. Artist rendering of a Bimodal NTR [14].

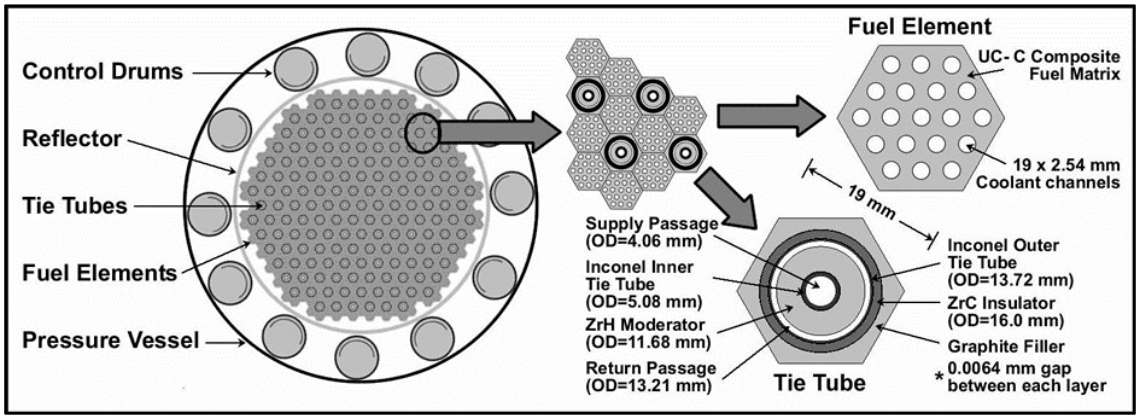

FIGURE 15. Bimodal NTR Core Elements [15].

Many modern NTR concepts now involve a ceramic-metallic (cermet) fuel composed of ceramic fuel (UO_2 or UN) in a tungsten alloy matrix. This fuel, currently in development, allows for higher operation temperatures due to its high melting point and provides other improved material properties [4]. These, and other modern NTR concepts, have become a primary focus of NASA's vision for a manned mission to Mars in the 2030s.

Advanced Concepts

Alternative propulsion concepts are being studied with advanced technologies to further improve system performance. Such concepts include fission fragment and fusion propulsion, as well surface exploration systems. Although these technologies are not fully developed, they provide capabilities for more advanced missions.

Mars Hopper

The Mars Hopper, shown in Figure 16, is in development for Mars Sample Return missions that involves collecting samples from all over the planet. The Hopper utilizes a radioisotopic thermal rocket that enables it explore a larger area and rougher terrain than the rovers can reach. As CO_2 is collected from the atmosphere, compressed by a Stirling engine, and frozen, a beryllium core stores the heat from radioactive decay. Once the tank is full of CO_2, it is injected into the core, heated, and expanded through a nozzle to produce thrust. This allows for multiple ascent/descents onto the surface [16].

FIGURE 16. Hopper for Mars Sample Return Missions [4].

Fission Fragment Engines

Fission fragment (FF) rocket designs operate by utilizing the hot fission fragments produced during operation. By using a dusty plasma of micron-sized fuel grains, the fission fragments can be separated with electrical and magnetic fields. Instead of heating the fuel, a major issue for NEP and NTP, the hot fission fragments can then be used to produce electricity at up to 90% efficiency for NEP, heat hydrogen for NTP, or directly produce thrust with a very high specific impulse [17]. The dusty plasma fission fragment rocket engine is shown in Figure 17.

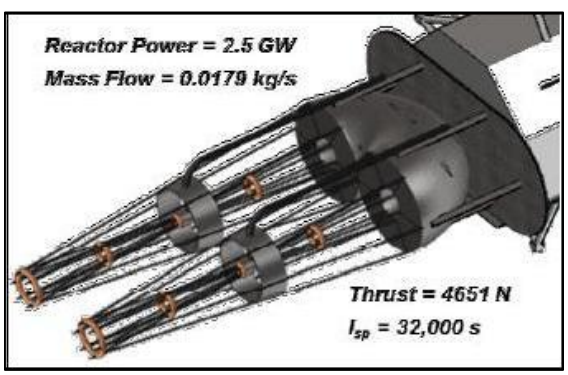

FIGURE 17. Torus-shaped reactor vessel with dual FF exhaust into hydrogen filled magnetic nozzles [17].

Fusion Propulsion

There are many concepts that have been investigated for fusion propulsion. One such concept directly converts fusion energy into a solid lithium propellant [18]. Other concepts, such as magnetic confined fusion (MCF) and inertial electrostatic confinement fusion (IEC), involve accelerating D-T fusion fragments to propel spacecraft. Inertial confined fusion (ICF) induces small thermonuclear explosions, whose force propels the craft forward.

Pulsed Fission-Fusion

The Pulsed Fission-Fusion (PuFF) system utilizes energy from both fission and fusion to produce thrust. Concentric columns of a gaseous UF_6 and D-T mixture are arranged in a z-pinch configuration. The pinch compresses the UF_6, creating a critical system. The energy released from fission triggers the D-T fusion reaction [19]. The system is currently being designed for a manned mission to Mars with minimal trip times, but also carries the potential to visit other stars.

CONCLUSION

Radioisotope power systems have successfully explored much of the solar system and have exceeded mission expectations. However, as interest in manned and deep space missions grows, focus turns to fission systems to meet higher performance requirements. Nuclear power systems enable missions deeper into space, while nuclear propulsion techniques allow shorter mission times compared to traditional chemical rockets while maintaining large payload capabilities. These rapidly advancing technologies determine the future of manned and unmanned space exploration.

REFERENCES

[1] "RPS Technology," *Radioisotope Power Systems*, NASA, (2014), <http://solarsystem.nasa.gov/rps/types.cfm>.

[2] "Nuclear Reactors and Radioisotopes for Space," World Nuclear Association, <http://www.world-nuclear.org/info/Non-Power-Nuclear-Applications/Transport/Nuclear-Reactors-for-Space/>.

[3] Howe, T., et. al., "Development of a Small-Scale Radioisotope Thermo-Photovoltaic Power Source," *Proceedings of Nuclear and Emerging Technologies for Space*, (2012).

[4] Howe, S. D., "Activities at the CSNR for the NTR, Mars Hopper and a Mars Sample Return," Center for Space Nuclear Research, Idaho National Laboratory, (2011).

[5] Mason, L. S., "A Power Conversion Concept for the Jupiter Icy Moons Orbiter." *Journal of Propulsion and Power*, **20** (5), 902-910, (2004).

[6] Schmitz, P.C, J. G. Schreiber, L.B. Penswick, "Feasibility Study of a Nuclear-Stirling Power Plant for the Jupiter Icy Moons Orbiter," *AIP Conference Proceedings*, **746**, 738-749 (2005).

[7] Mission. http://www2.jpl.nasa.gov/jimo/mission.cfm.

[8] Poston, D.I., R.J. Kapernick, R.M. Guffee, "Design and Analysis of the SAFE-400 Space Fission Reactor," *AIP Conference Proceedings*, **608**, 578 (2002).

[9] Mason, L.S., "Small Fission Power System Feasibility Study Final Report," NASA, (2010).

[10] Mason, L.S., M. Gibson, "Kilowatt-Class Fission Power Systems for Science and Human Precursor Missions," NASA, (2013).

[11] "Project Rover: Main Series of Nuclear-Rocket Engines," *National Security Science*, Los Alamos National Laboratory, (2014), <http://www.lanl.gov/science/NSS/issue1_2011/story4a.shtml>.

[12] Finseth, J.L., "Overview of Rover Engine Tests Final Report," NASA Marshall Space Flight Center, (1991).

[13] Fusselman, S.P., S.K. Borowski, et al, "NERVA-Derived Concept for a Bimodal Nuclear Thermal Rocket," *AIP Conference Proceedings*, **746**, 512-519, (2005).

[14] Bimodal Nuclear Thermal Rocket. http://www.nasa.gov/centers/glenn/multimedia/artgallery/art_feature_002_BNTR.html.

[15] Clough, J.A, et. al., "Tie Tube Heat Transfer Modeling for Bimodal Nuclear Thermal Rockets," *Space Technology and Applications International Forum - STAIF 2007*, **880**, 281-288 (2007).

[16] Howe, S.D., et. al., "The Mars Hopper: A Radioisotope Powered, Impulse Driven, Long-Range, Long-Lived Mobile Platform for Exploration of Mars", *Proceedings of Nuclear and Emerging Technologies for Space*, (2011).

[17] Sheldon, R.B. and R.L. Clark, "The Dusty Plasma Fission Fragment Rocket Engine: Design Constraints and Performance," *Proceedings of Nuclear and Emerging Technologies for Space*, (2014).

[18] Slough, J., A. Pancotti, D. Kirtley, and G. Votroubek. "The Fusion Driven Rocket: Nuclear Propulsion Through Direct Conversion of Fusion Energy," *Proceedings of Nuclear and Emerging Technologies for Space*, (2014).

[19] R. B. Adams, et. al. "Progress on the Pulsed Fission Fusion (PuFF) Propulsion Concept," *Proceedings of Nuclear and Emerging Technologies for Space*, (2014).

Preliminary Design of an Ultra-high Temperature Reactor Using MHD Power Conversion for Mars Exploration

Weijian An, Jian Song, Jiachun Xie, Gu Hu, Shouzhi Zhao, Zheng Sun, Yuanyuan Wu

Department of Reactor Engineering, China Institute of Atomic Energy, P.O.Box 275-33, Beijing 102413
+861069357336; awj1900@163.com

Abstract. The very high conversion efficiency of MHD (magnetohydrodynamics) reactor power source makes it a highly potential space power source in the future. Research work about ultra-high temperature reactor suitable for MHD power conversion is performed in this paper. Cermet is chosen as the reactor fuel after a comparison with the (U,Zr)C graphite-based fuel. A reactor scheme is presented as well as the calculation results of the reactor physics and thermal-hydraulics. Besides, preliminary calculation of nuclear criticality safety during launch crash accident is also carried out.

Keywords: MHD power conversion; ultra-high temperature reactor; cermet fuel.

INTRODUCTION

Nuclear propulsion system, including nuclear electric propulsion (NEP) and nuclear thermal propulsion (NTP), is indispensible for manned deep space exploration. NTP can provide high specific impulse which is more than 2 times as the best chemical propulsion system, while NEP can give even much larger specific impulse than NTP. Thus maximum payload capability and lowest launch cost can be achieved with NEP system. However, due to the low thrust capability of current electric propulsion system, large electric power is needed to maximize the thrust and minimize the trip time which is critical to the crew.

Power conversion efficiency is essential to NEP system. Among various power conversion systems, e.g., thermoelectric, thermionic, Stirling, Brayton, Rankine and MHD (magnetohydrodynamics), MHD possesses the best efficiency. Minimum thermal power, radiator area and shielding mass can be realized with MHD power conversion system. However, ultra-high temperature requirement (>2000 K) is a significant drawback to MHD system.
A concept of crewed Mars exploration mission with NEP using MHD power conversion is proposed recently in China. The main performances of the overall system are listed in Table 1. This paper focuses on the reactor design. A preliminary reactor concept using cermet fuel is studied.

TABLE 1. Main Performances of the Overall System

Parameters	Values
Thermal Power(MW_{th})	25.0
Electric Power(MW_e)	10.0
Coolant	helium
Coolant Inlet Temperature(K)	800.0
Coolant Outlet Temperature(K)	2200.0
Propellant	xenon
Thrust(N)	1000.0
Specific Impulse(s)	5000.0
Operating Lifetime(yr)	1.5

FUEL CONSIDERATION

Apparently, the critical performances of the reactor lie in the ultra-high temperature and long term duration. Two kinds of ultra-high temperature fuel derived from mainstream NTP programs are considered, i.e., (U,Zr)C graphite-based fuel and cermet fuel.

Extensive research work was conducted of (U,Zr)C graphite-based fuel during the Rover/NERVA program back in 1955-1973. Up to 22 high power rocket reactor tests were completed[1]. However, there was still some issue, i.e., cracking of ZrC coating on the coolant channels, remained unresolved till the end of the program. It is a significant limiting factor to the reactor lifetime because it may lead to a catastrophic loss of graphite and fuel[2,3]. Since the lifetime of the reactor required by NEP is much longer than NTP, (U,Zr)C graphite-based fuel, which has the maximum testing operation time no more than about 100 minutes, is considered not suitable for the present MHD reactor design.

Cermet, another option of NTP fuel, is mainly pursued during GE-710 and ANL nuclear rocket programs in 60s. Current research about cermet is being conducted as part of the Nuclear Cryogenic Propulsion Stage (NCPS) Advance Exploration System (AES) technology project at NASA's Marshall Space Flight Center (MSFC)[4]. Cermet fuel forms are composed of a tungsten or molybdenum fuel element matrix material[3]. Fuel tests show cermet is much more robust than that for either NERVA or PBR fuel[5]. It is considered that this fuel may provide a significant design advantage over graphite-based fuel. In particular, researches show that deformation but not cracking of the cermet fuel and cladding may occur under high stresses[2]. Besides, cermet has been proven to possess the capability of withstanding many thermal cycles. This offers an important potential of ability to restart which is indispensable for MHD reactor. In general, cermet fuel has its significant potential for long operating life, ability to restart, handling of temperature cycling at high temperature, and greater compatibility between the fuel and coolant (resulting from high fuel integrity and retention of fission products) [5].
Based on the comparison and analysis above, cermet is chosen as the fuel for the MHD reactor design.

REACTOR DESCRIPTION

The chosen hexagonal prismatic cermet fuel element, developed under the GE-710 program, is shown in Figure 1. It is 2.361 cm across the flats. The total active fuel element length is 60.96 cm. There're 91 coolant channels with diameter of 0.914 mm in each fuel element. The fuel has a composition of W-60vol.% UO_2-6vol.% Gd_2O_3 with W-25wt.%Re as the cladding material both on the coolant walls and exterior[6].

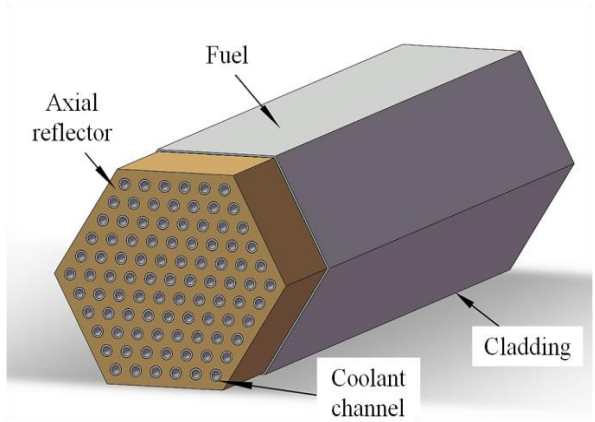

FIGURE 1. Fuel Configuration

The reactor configuration is illustrated in Figure 2-3. The radius of active zone is 21 cm. There're 246 fuel elements and 66 filler elements in the core. The filler elements are made of tungsten with the same geometric configuration as fuel elements. The ^{235}U enrichment of central 30 fuel elements is 70%, while the outer ones possess 93% ^{235}U enrichment. The axial reflector is made of BeO with the thickness of 10.24 cm. The radial reflector is also made of 10 cm thick BeO due to its much higher peak temperature than Be. There're 16 drums in the radial reflector. The thickness of B_4C absorber is 2 cm with the B-10 enrichment of 80%. The main design parameters of the reactor are listed in Table 2.

TABLE 2. Main Design Parameters of the Reactor

Parameters	Values
Active Fuel length(cm)	60.96
Effective Core Radius(cm)	21.0
Core Height(cm)	71.2
Core Radius(cm)	31.5
Safety Rod Channel Radius(cm)	1.05
Fuel Element Number	246
Filler Element Number	66
Drum Number	16
^{235}U Mass(kg)	254.0
Reactor Mass(kg)	1617.0

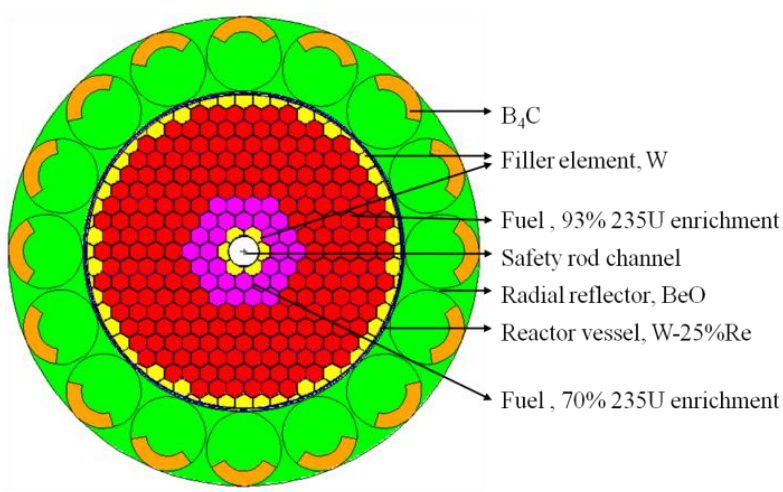

FIGURE 2. Radial Cross Section View of the Reactor Core (without Coolant Channels)

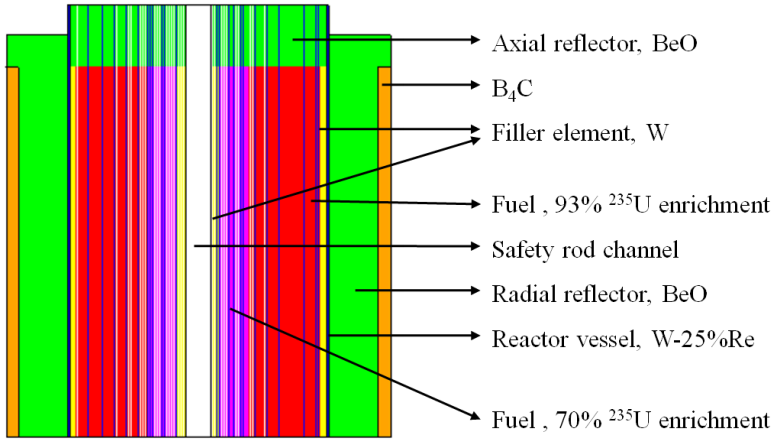

FIGURE 3. Axial Cross Section View of the Reactor Core

CALCULATION RESULTS

Critical calculation shows that the k_{eff} is 1.0417 and 0.9835 when the drums are rotated outward and inward, respectively. Normalized thermal power distribution of the reactor core is shown in figure 4. It has a normalized peak-to-average thermal power ratio of 1.253. The corresponding maximum thermal power of the fuel elements (hot channel) is 0.1136 MW_{th}. And the average thermal power per fuel element (average channel) is 0.0916 MW_{th}. Figure 5 shows the axial power distribution of the hot channel as well as the average channel.
Depletion calculation indicates that the operating lifetime of reactor is about 1.5 yr which has 50% margin as the real operating time is about 1 yr. The k_{eff} results in shown in Figure 6.

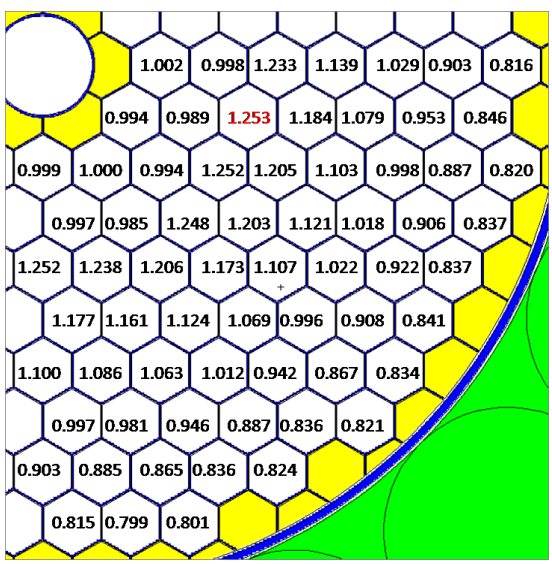

FIGURE 4. Normalized Thermal Power Distribution of 1/4 Core

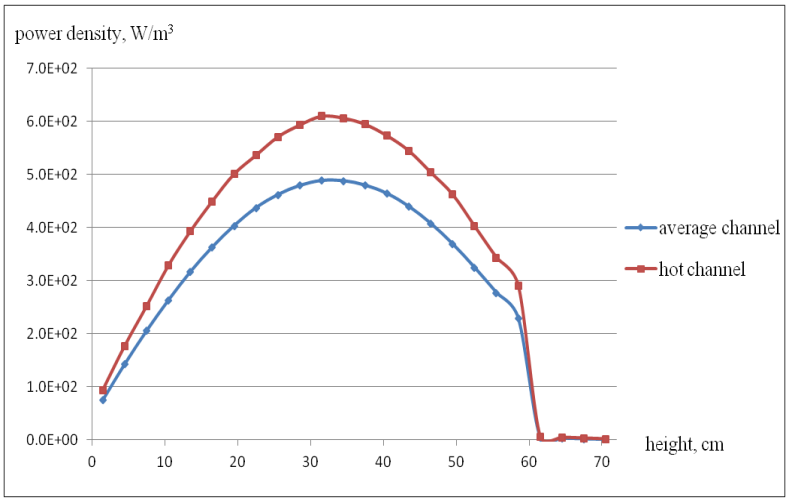

FIGURE 5. Axial Power Density Distribution of Hot Channel and Average Channel

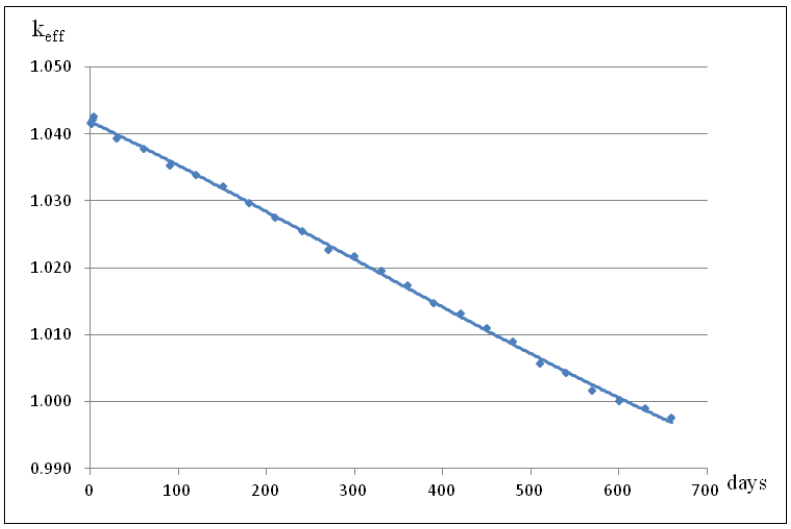

FIGURE 6. Depletion Calculation Result of the Reactor

Thermal-hydraulic analysis of hot channel and average channel is performed. The helium flow rate of the reactor is 3.0996 kg/s. The calculation results of average channel show that the mean inlet temperature of helium is 800 K, while the corresponding mean outlet temperature can reach 2217 K which meets the requirements very well. And the hot channel analysis indicates that the maximum temperature of the fuel is 2648 K which is far below the limiting temperature of cermet fuel. Radial temperature distributions of average channel and hot channel are presented in Figure 7-8. And Figure 9-10 give the axial temperature distributions of average channel and hot channel, respectively.

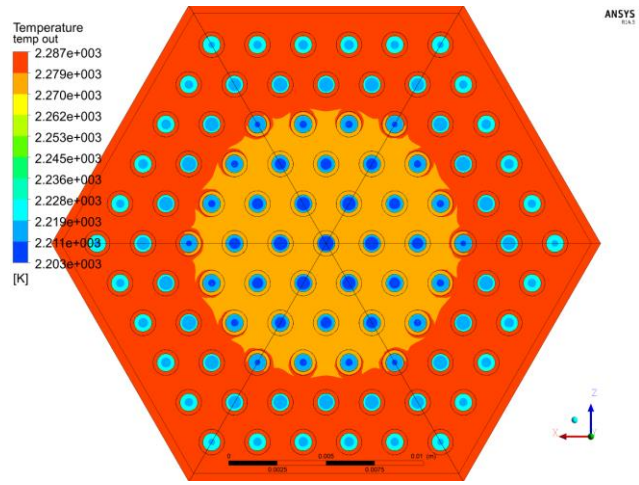

FIGURE 7. Radial Temperature Distribution at the Outlet of the Average Channel

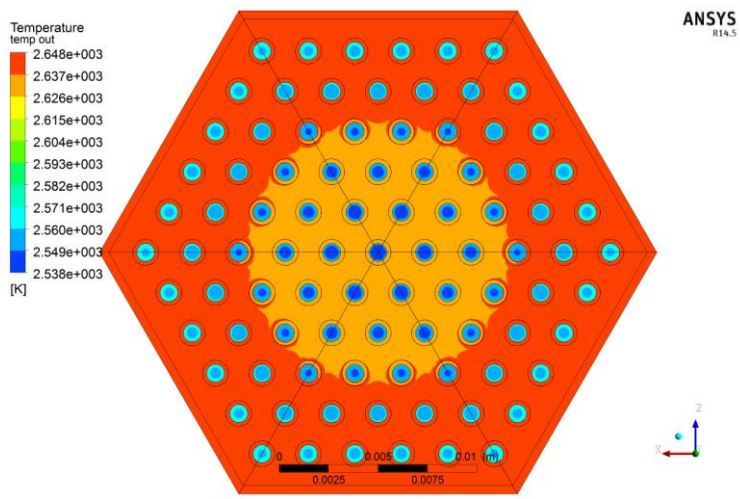

FIGURE 8. Radial Temperature Distribution at the Outlet of the Hot Channel

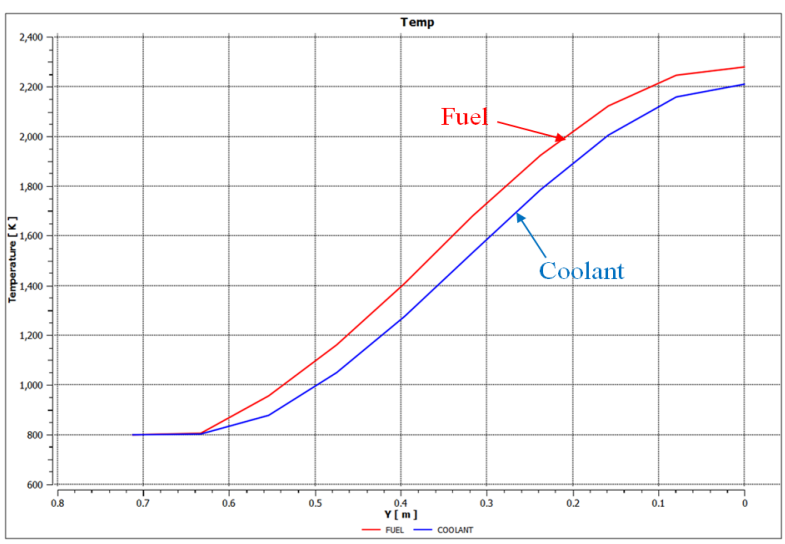

FIGURE 9. Axial Temperature Distribution of the Average Channel

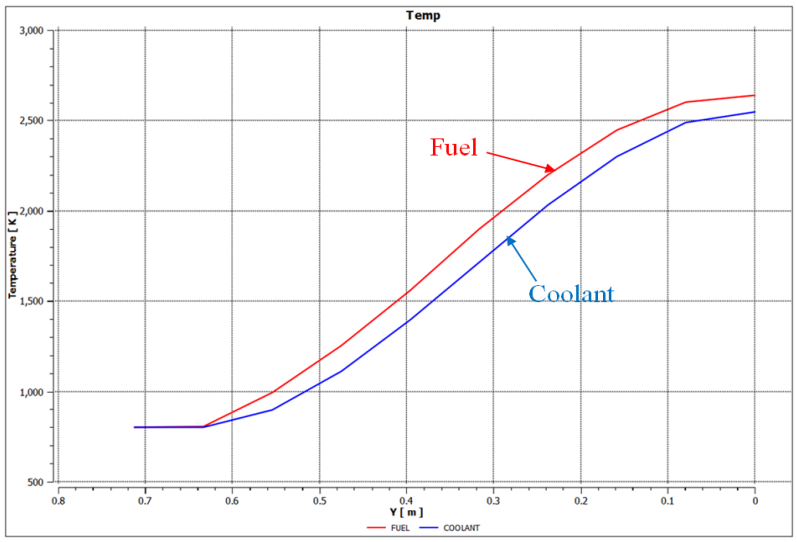

FIGURE 10. Axial Temperature Distribution of the Hot Channel

Apart from reactor physics and thermal-hydraulic analysis, preliminary critical safety analysis is also carried out. Two severe conditions during launch failure accident are considered. And the results show very inspiring safety performance. When the reactor is submerged in water and the coolant channels are all flooded with water, the relevant k_{eff} is 0.9652. And when the reactor is immersed in wet sand and the coolant channels become full of water, the k_{eff} is 0.9664. Both conditions have the drums rotated inward and the safety rod inserted inside the core. Figure 11 illustrates the reactor submerged in 50 cm thick (both in radial and axial direction around the reactor) wet sand which can be equivalent to an infinite-thickness reflector.

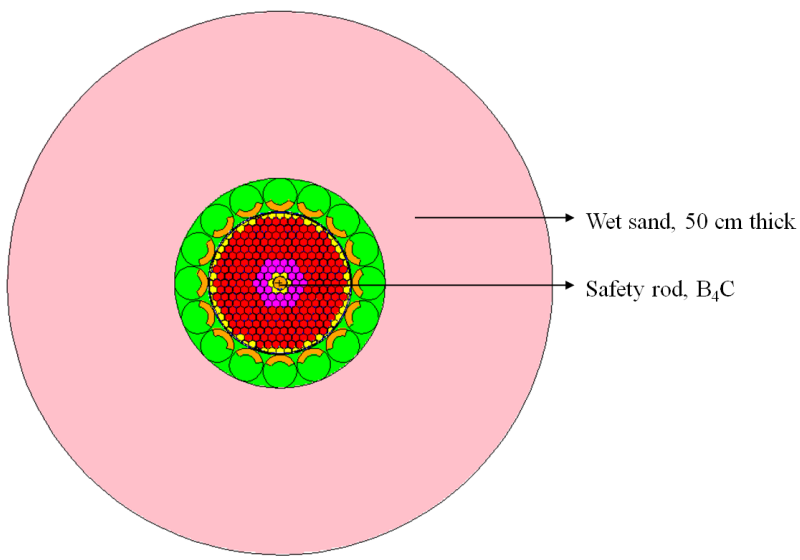

FIGURE 11. Reactor Submerged in Wet Sand

CONCLUSION

An ultra-high temperature reactor using MHD power conversion for crewed Mars exploration is researched in this paper. Cermet is chosen as the reactor fuel after a comparison with graphite-based fuel. A specific reactor core concept is presented as well as the corresponding calculation of its reactor physics, thermal-hydraulic and safety performances. Calculation show positive results which can meet the system requirements very well.

However, cermet fuel, which is still being under development at MSFC, holds the key to the whole reactor concept. Many issues, especially degradation of mechanical integrity and loss of fuel, remain to be resolved[7].

ACKONWLEDGMENTS

This work is carried out with lots of assistance from many colleagues and friends in the Department of Reactor Engineering, CIAE.

REFERENCES

[1] Michael G.Houts, Tony Kim, William J.Emrich, etc. "The Nuclear Cryogenic Propulsion Stage," *Proceedings of Nuclear and Emerging Technologies for Space*, (2014).

[2] M.E.M.Stewart, Bruce G.Schnitzler, "A Comparison of Materials Issues for Cermet and Graphite-Based NTP Fuels," *49th AIAA/ASME/SAE/ASEE Joint Propulsion Conference*, San Jose CA, (2013).

[3] Kelsa Benensky, "Summary of Historical Solid Core Nuclear Thermal Propulsion Fuels," *Thoshiba Westinghouse Undergraduate Fellows Program*, The Pennsylvania State University, (2013).

[4] C.F.Gomez, "Induction Heating Model of Cermet Fuel Element Environmental Test (CFEET)," *Proceedings of Nuclear and Emerging Technologies for Space*, (2014).

[5] Timothy J.Lawrence, "Nuclear Thermal Rocket Propulsion Systems," *IAA White Paper*, Paris, France, (2005).

[6] James E.Fittje, Bruce Schnitzler, "Analysis of NTR Utilizing Prismatic Fuel Elements Derived from the GE-710 Program," *49th AIAA/ASME/SAE/ASEE Joint Propulsion Conference*, San Jose CA, (2013).

[7] C.Haertling, R.J.Hanrahan Jr., "Literature review of thermal and radiation performance parameters for high-temperature, uranium dioxide fueled cermet materials," *Journal of Nuclear Materials*, **366**, 317-335, (2007).

Progress in Development of an LENR Power Cell for Space

George H. Miley[1,2], Kyu-Jung Kim[1], Erik Ziehm[1], Tapan Patel[1], Bert Stunkard[1]

[1]*Department of Nuclear, Plasma and Radiological Engineering, University of Illinois at Urbana-Champaign, USA, 61801*
[2]*Lenuco LLC, Champaign, IL 61821*

Abstract, Anomalous heat, attributed to Low Energy Nuclear Reactions (LENRs), is obtained by pressurizing metal alloy nanoparticles with deuterium gas. The reactions are enhanced by creation of ultra high-density deuterium clusters in the nanoparticles. Experiments comparing various nanoparticles and plans for a proof-of-principle power unit are presented. Potential applications to space power are briefly discussed.

Keywords: Low Energy Nuclear Reaction, Gas Loading System, and Nanoparticles.

INTRODUCTION

Our previous experimental results have demonstrated the formation of ultra high-density hydrogen/deuterium nanoclusters with 10^{24} atom/cm [3] in metal defects (Figure 1). [1-2, 5-6] Both experimental [7-11] and theoretical studies [12] have demonstrated that due to the close distance (ca. 2.3pm) [7] between ions in the cluster, they can easily be induced to undergo intense nuclear reactions among themselves and some neighboring lattice atoms. In view of their multi-body nature, such reactions are termed Low Energy Nuclear Reactions (LENRs) – a terminology generally accepted by workers in the cold fusion field. Because the interacting ions have little momentum, the compound nucleus formed in these reactions is near the ground state, thus no energetic particles (Gammas, neutrons, etc.) are emitted from its decay. There are, however, some low energy betas and transmutation products expected. We have observed some of these products and continue to study this aspect in more detail. Triggering excess heat generation, i.e., heat generation from nuclear reactions, in LENR experiments have been accomplished in various ways, all involving the loading of protons or deuterons into a solid metal or alloy material.

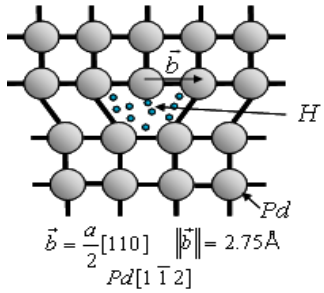

FIGURE 1. Scheme of edge dislocation loops in Pd containing condensed H/D.

Electrochemical loading was the initial approach of the experiment, and remains the most practiced approach. Gas loading is also widely used. [13-23] This method is currently gaining more attention, as it enables smaller heat capacity and thereby higher temperature change as compared with an electrolysis system. In addition, a gas can be easily heated to temperatures greater than 100 ^{o}C without excess pressure production. So, the excess energy production from a gas-loading system can be observed more efficiently and in a relatively higher temperature range, making the technology compatible with existing energy conversion methods. Although the nuclear physics of LENRs is independent of the loading method, advantages of the gas-loading system described above using Ultra-High Density Deuterium (UHD-D) clusters can be taken advantage of to move the field towards a practical power unit. In this study, we report the anomalous heat generated from metal alloy nanoparticles loaded with deuterium through pressurizing the sample chamber containing the nanoparticles.

Our gas-loading system is based on the design we first developed for thin film studies in 2010. Figure 2 shows the setup. Inside the large outer chamber (8-inch diameter) shown in Figure 2A is a much smaller cylindrical pressure chamber (1-inch diameter), shown in Figure 2B. This arrangement uses a vacuum between the two cylinders to minimize heat losses and also provided a basis for measurement of heat flow for the calorimeter measurement. The nanoparticles are placed in the smaller chamber and loaded with deuterium (D_2) or hydrogen (H_2) gas. Three thermocouples are attached to the small cylinder – two at the sides and one at the bottom – to record the temperature during the loading and unloading process. The experiments describe here used D_2 gas and Pd rich nanoparticles. Other work with H_2 uses Ni rich nanoparticles. A cold trap is connected between the smaller cylindrical chamber and the D_2 gas cylinder in order to provide extra purification for the flowing D_2 gas. [24] During the D_2 gas loading and unloading process, the large chamber remains under a vacuum to reduce heat losses. The remaining heat loss is predominantly by radiative heat transfer, which can be calculated for calorimetric purposes from the thermocouple data. Figure 3 shows the actual setup. The large vacuum chamber is not pictured because it was removed for the adiabatic experiments (discussed later) to reduce experiment setup times.

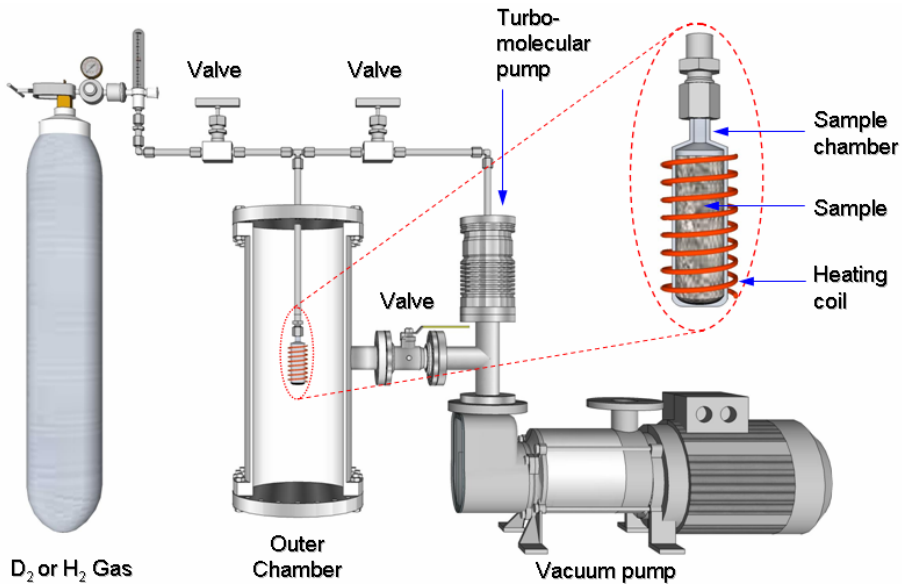

(A)

Diameter = 1 inch
Length = 3.69 inch,
Volume = 25 cm^3

(B)

FIGURE 2. (A) Schematic of gas loading system; (B) Sample cylinder chamber that contains nanoparticles

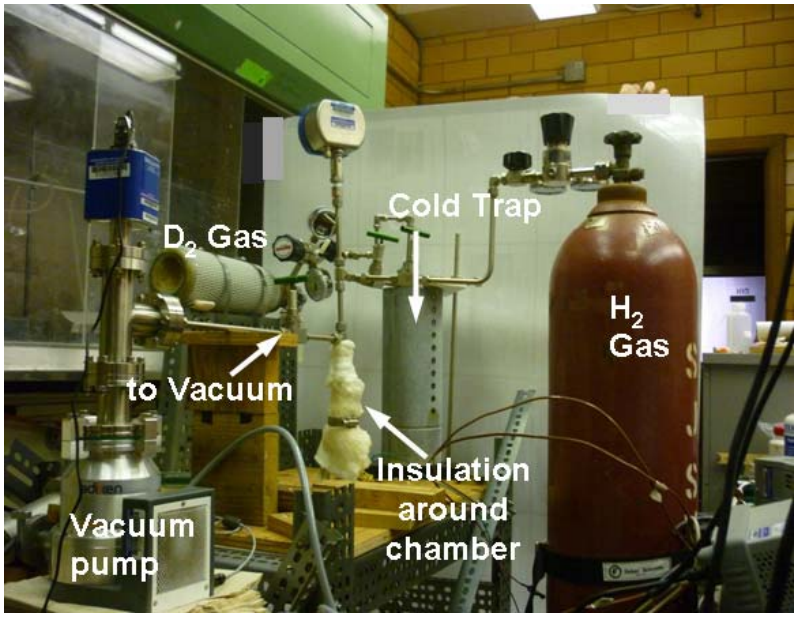

FIGURE 3. Gas-loading system. The 25 cc pressure vessel of Fig. 2 is covered by insulation to minimize heat loses.

Initial experiments with this system employed a "dynamic" loading where the system is first rapidly pressurized and after about 500 seconds depressurized. This was intended to study the adsorption and desorption cycle effects. The results shown in Fig. 4 are for experiments using high purity D_2 gas at 60 psi into 20 grams of Pd-rich nanoparticle powder (termed #1 nanoparticles). Fig. 4 shows some typical raw data of this type of dynamic experiment – the temperature profiles shown recorded by three thermocouples attached to different locations on the sample cylinder. The slower increase of the temperature in two of the three thermocouples was later attributed to a poor connection to the cylinder surface. The initial rapid D_2 gas pressurization caused the temperature increase from ca. 20 ^oC to ca. 50 ^oC that produced ca. 1480 J energy release. This is well above the exothermal energy 690 J that is calculated as the maximum possible from chemical reactions involving hydrating. (Note that the total heating energy was calculated by considering the heat capacity of both the sample cylinder and the nanoparticle powder, and the chemical exothermal energy was calculated using ΔH = ~35,100 J per mole of D_2 for the formation of PdD_x for $x < 0.6$. The volumetric loadings were well below this value in these experiments where the major loading involved the clusters) The temperature rose further from ca. 50 ^oC to ca. 140 ^oC during unloading D_2 gas. This is important because it is opposite from what would occur normally as deloading is an endothermic process. Thus, the heating is thought to be due to LENRs that are enhanced because of the increased deuterium flux inside the nanoparticles. Once clusters are formed, the flux is needed to cause momentum transfer to cluster particles, initiating the desired reactions. However, more experiments are needed to eliminate the contribution of all possible side reactions such as oxygen and deuterium reactions. Our current evaluation is that such reactions could reduce the gain calculated, but not eliminate the conclusion that excess energy is produced. In this experiment, the input power, including power consumed by gas compression process and vacuum pumping process, is negligible compared to the output power. For example, considering the pumping process, the whole system can reach ca. 10^{-2} Torr within one minute. The volume of the sample chamber is less than one percent of the whole system, thus the power needed for vacuum pumping is negligible. The exact power used for gas compression is difficult to determine exactly, but calculation of the energy required is approximated by the power required to compress deuterium. Although many more studies are needed to unveil the source of the excess heat during the first step rise in temperature shown in Fig. 4, this result has provides evidence of significant excess energy gain (Total energy out - energy in/energy in). In this short run the gain is already greater than 1.0. Since the input energy is mainly due to exothermal heating during adsorption of the gas into the nanoparticles at the beginning of the run, the gain can be significantly increased by longer run times. Some data from such runs is shown next.

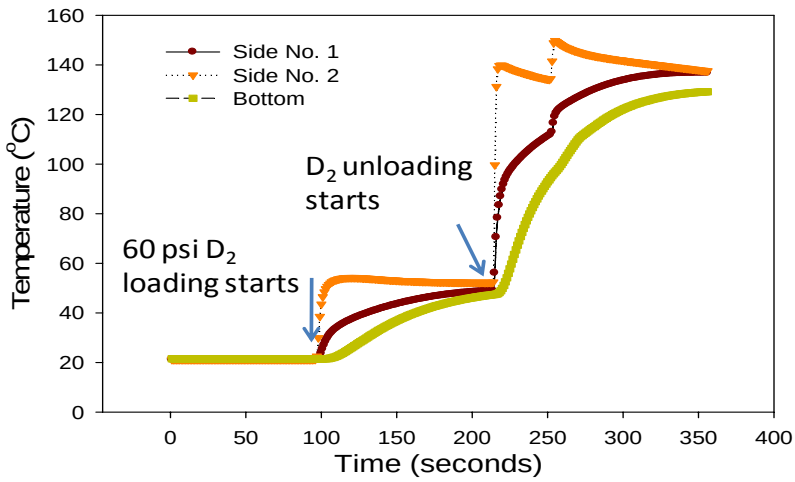

FIGURE 4. Raw data (temperature profile) from a dynamic experiment using gas-loading The purpose of this very short dynamic run was to demonstrate the rapid temperature rise following a sharp pressure rise and the same upon sudden depressurization. Note that the different in the temperature traces stem from the different locations of the thermocouples. The discontinuities in #2 are attributed to a poor connection to the vessel.

PARAMETRIC GAS-LOADING NANOPARTICLE EXPERIMENTS

We have performed various experiments to study the effect of changing some key parameters and to study longer run times. Each run involves loading and deloading deuterium gas into nanoparticles by pressurizing and vacuuming the sample cylinder. Two sets of different particles were used. The temperature profile for 23 g of nanoparticle #1 (same as in the dynamic run of Fig. 4) during the 60-psi deuterium loading is shown in Figure 5. We can see that the temperature increases right after gas loading starts. The increasing rate is low at the start, but then exponentiates until reaching ca. 115 °C. The initial slow rise is attributed to exothermal heating during the loading process, while

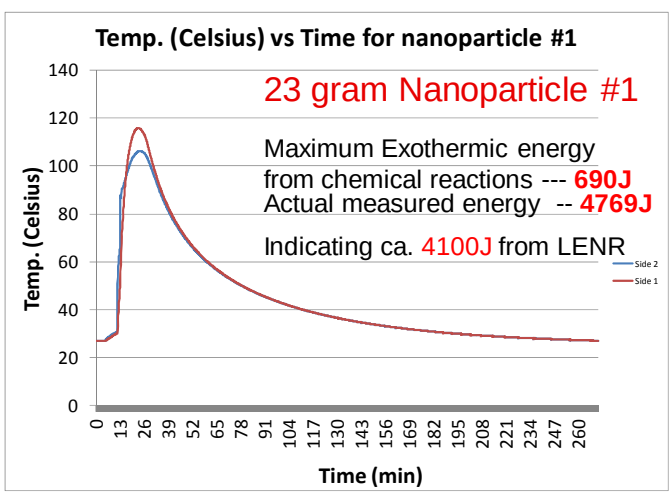

FIGURE 5. Temperature profile during the 60-psi deuterium loading of the #1 nanoparticle. Two different curves were recorded by two thermocouples attached to the sample cylinder at different sites. In this case, 99.99% deuterium gas was used.

the fast rise is attributed to LENRs. This is consistent with the theory that the LENRs are imitated once a certain threshold temperature is reached. The temperature rising phase lasts about half an hour and then begins to decrease. The total energy produced in this 4.2 hour run was ca. 4770 J. The maximum exothermic energy from chemical reactions is calculated to be 690 J, suggesting the LENRs dominated with a gain (LENR energy out/Chemical energy in) of ~ 6. This is viewed to be conservative. For example, if the calculation was based on the observed

desorption energy, the value will be roughly twice of the above value (the value is quoted later in Table I using the latter technique). In this run, the averaged power density about 15 W/gram.

Three runs using the same set of #1 nanoparticles followed the run in Fig. 5. Figure 6 shows the peak temperature versus pressure for these runs. Pressure is not expected to have a strong effect since one the clusters are formed; their volumetric density rather than the external pressure sets the reaction rate. Pressures has more affect on the flux, hence indirectly on the reaction rate. These three runs all have relative low temperature rises compared with the first run, but the three rises follow a linear relationship. The decreased temperature rise in the latter runs suggests the nanoparticles may be deteriorating, or sintering due to repeated use. Due to these complex variables, this pressure plot is difficult to interpret.

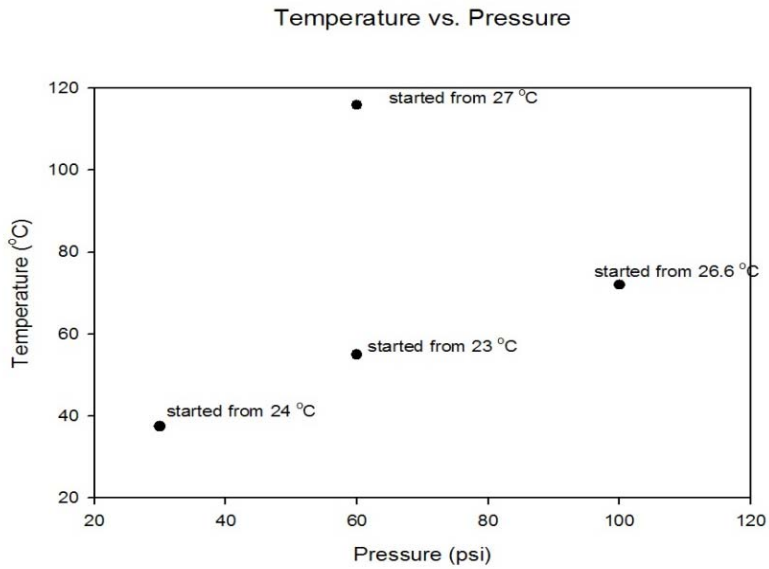

FIGURE 6. Temperature versus pressure for #1 nanoparticles. The one data point at the highest temperature is from fresh nanoparticles, whereas the other data are from the same particles used in the first run.

Figure 7 shows a SEM image of #1 nanoparticles before (Figure 7A) and after (Figure 7B) deuterium loading experiments. We can see that after deuterium loading, some nanoparticles, especially at the top layer, stick together compared with their loose-packed state before deuterium loading. The sintering of the layer may be blocking the deuterium gas from effectively going further into nanoparticles below the top layer, causing a lower temperature rise

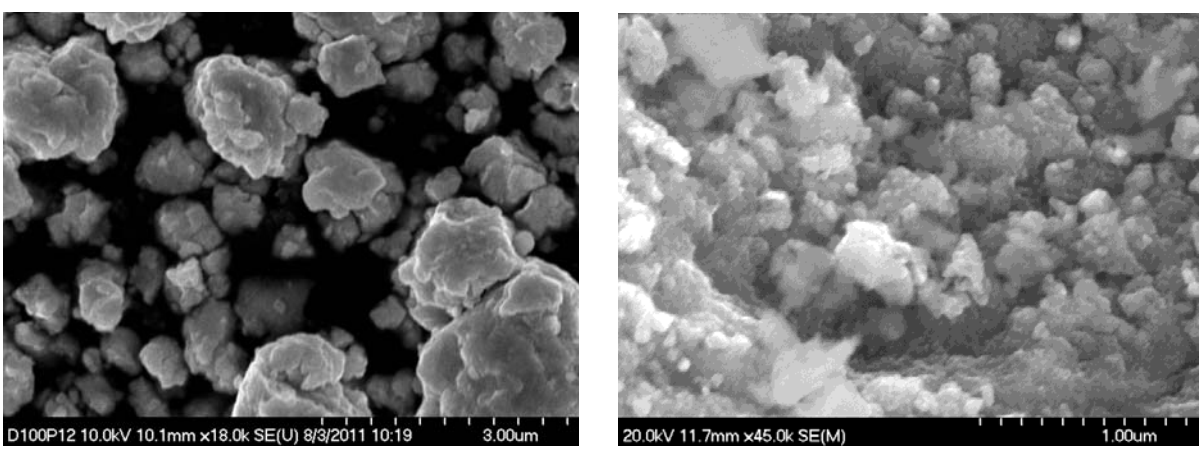

(A) (B)

FIGURE 7. SEM image of the #1 nanoparticles before (A) and after (B) the deuterium loading experiment. Note: The white color in B is because the distance of the nanoparticles to the electron gun is different. The closer, the brighter. Also note that the nanoparticles employed in the adiabatic experiments described here are considerably smaller than those shown here.

in the repeated experiment runs with the same packed nanoparticles. The sintering seems to occur at a lower temperature than expected, but hot spots may be caused by the localized loading cluster reactions. It is difficult to tell from the SEM image if there are any melted spots, but such local heating should not be neglected.

ADIABATIC EXPERIMENTS FOR NANOPARTICLE EVALUATION

Following the experiment summarized in Fig. 6, improvements were made in nanoparticle manufacturing to provide much smaller size. In this case, three different alloys were employed for the nanoparticles, type A is Pd rich similar to type #1 used earlier, type B and C contain both Pd and Ni, but with different percentages, along with small percentage of additional metals. As shown in following data, these new nanoparticles are much more reactive than that shown in Fig. 5. Table I lists a series of experiments performed to compare various types of nanoparticles. For these runs the outer vacuum chamber shown in Figure 2 was removed and smaller weight of nanoparticles was employed in order to save total experiment time. A set of runs for the Type A nanoparticle is shown in Figure 8. Only the initial run times up to 100 seconds from start of pressurization are analyzed for the comparisons. Note that with the decreased weight of nanoparticles used here and the faster heat loss due to the outer chamber removal, the temperature increase phase is much shorter than that in the runs of Fig. 5. As our main purpose for these experiments is to determine the best nanoparticles and to overcome sintering problems, the current adiabatic conditions with outer chamber removed are acceptable for such short times. Moreover, due to the fast heat loss, the analysis of the data is only done for the period of temperature increase as shown in Fig. 8. Three different types of nanoparticles (Type A, B, and C) were employed in the comparison. Some were reused, either with or without treatment, following initial use. This was done to study the effect of sintering and possible treatment of sintered particles. As seen in Table I, the highest gain achieved (LENR energy out/estimated maximum possible chemical energy in) was 15.1 using Type C nanoparticles. The gain in these new sets of experiments more than doubled compared with previous ones due to the improved procedure of making nanoparticles. Note that this gain was achieved in only 98 sec. of the run. Since the adsorption (chemical) energy release occurs at the beginning of the run and then ends, longer runs than employed for these comparisons can give gains of many thousands. The highest power density achieved was 42.7 W/gram using type A particles. This is largely due to the rapid heating achieved with these particles (about 10 sec. to the peak vs.70-100 sec. for other particles.) Runs 2 and 6 used the same nanoparticle employed in runs 1 and 5 respectively. Both suffered a significant reduction in performance, e.g. gains reduce roughly an order of magnitude. This is attributed to sintering effects caused in the initial run, even though it was fairly short. However, results from run three suggest that the sintering problem seems solvable. In this run, particles from run 2 were treated by reheating in the air for two hours. When these particles were run they were able to release energy of 426 J/gram, only 3% less than that achieved by the fresh particles in run #1. This is very encouraging, plus we are continuing studies of ways to treat (added coatings, etc.) the nanoparticles to achieve longer initial runs prior to their re-treatment. Initial results seem promising, but much more study and long run experiments are required to fully evaluate long run time issues.

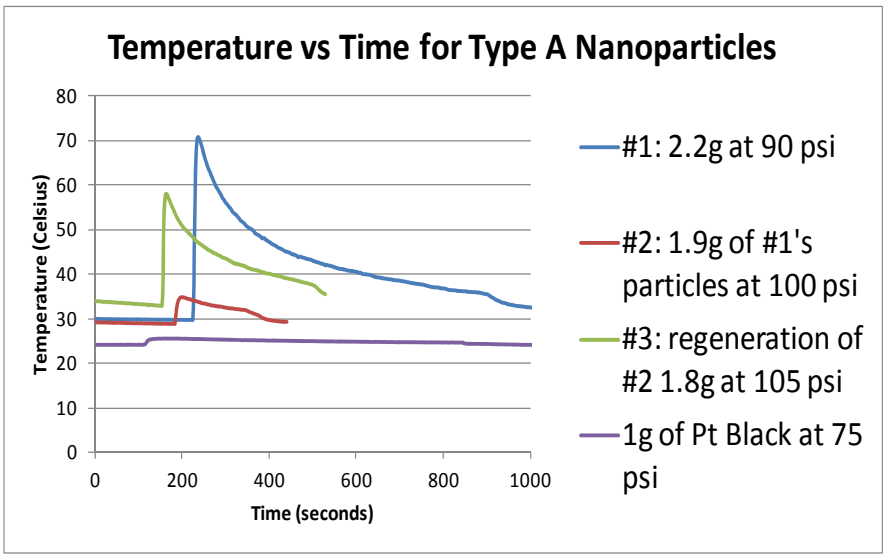

FIGURE 8. Typical Adiabatic Experiment with Type A nano-particles. Included is a Pt Black reference run Data from these runs as well as others for different nanoparticles is summarized in Table I.

TABLE I. Most recent adiabatic gas loading experiment results

Run #	Nano Particle Type	Gas	Pressure (psi)	Mass (grams)	Average Delta T (Celsius)	Joules (Peak)	Peak Energy /mass (J/gram)	Run Time - Initial Temp. to Peak Temp. (sec)	Watts/gram	Chemical Energy (J)	Measured Peak Energy (J) minus Chemical Energy (J)	Gain
1	Type **A**	D2	90	2.2	31.55	972.05	441.84	14.00	31.56	74.85	897.21	12.0
2	Type **A** (same particles from run 1)	D2	100	1.9	4.95	151.96	79.98	16.00	5.00	64.64	87.32	1.3
3	Type **A** (same particles as run 2, bur after heat treatment)	D2	105	1.8	25.05	768.01	426.67	10.00	42.67	61.24	706.77	11.5
4	Type **B**	D2	60	11.1	90.90	3588.88	323.32	95.00	3.40	271.29	3317.59	12.2
5	Type **C**	D2	100	6.4	84.90	2754.00	430.31	98.00	4.39	170.76	2583.24	15.1
6	Type **C** (same particles from run 5)	D2	100	6.4	6.80	220.58	34.47	76.00	0.45	170.76	49.82	0.3
7	Type **C**	D2	100	3.2	27.10	846.04	264.39	78.00	3.39	85.38	760.66	9.3

To investigate possible gas impurity effects, another deuterium loading and unloading run followed using the same nanoparticles but low purity (99.7%) deuterium gas at 60 psi. The temperature only raised to ca. 30 ^{o}C, suggesting excess heat production might be affected by the purity of deuterium gas. More study is needed, though, to confirm this and to identify the impurities involved that affect the reaction rate. This result also indicates that the heat from other reactions, such as a catalyzed deuterium oxidation reaction, is not a dominant reaction in the heat production process. However, a control experiment, such as using platinum black may be necessary to confirm this conclusion.

COMPARISON OF ENERGY OUTPUT TO OTHER POWER SOURCES

So far, our experiments suggest a remarkable proof-of-principle power unit at ca. 40 W/g, when using deuterium gas. This projection is based on the assumption that with an appropriate control system, the gas-loaded cell is able to

maintain a steady-state temperature profile once it reaches the peak temperature.
This also requires nanoparticles with coating permitting long runs before removal for re-treatment. As already noted, methods to achieve this are currently under study.

For perspective, it is useful to compare the LENR unit envisioned to a heat source such as Pu^{238} used for RTGs in NASA's deep space probes. Assuming a linear power/weight scaling, a 3 kW LENR unit (not including the gas tank) would use 0.5 kg or 0.3 liters of nanoparticles compared to a 3 kW Pu^{238} unit that would be 5.6 kg or 0.3 liters. For comparison, it is assumed that the power obtained in the short LENR runs can be extended using control strategy and improve nanoparticles has illustrated in Fig. 9. In that figure, the periodic oscillation pressure was employed to maintain the required flux in the nanoparticles giving a quasi-steady-state run. Note that the LENR data used is based on very preliminary experiments so improvements should be possible. Thus, it is foreseen that more stable, longer and continuous power release for LENR can be expected to increase with further research development.

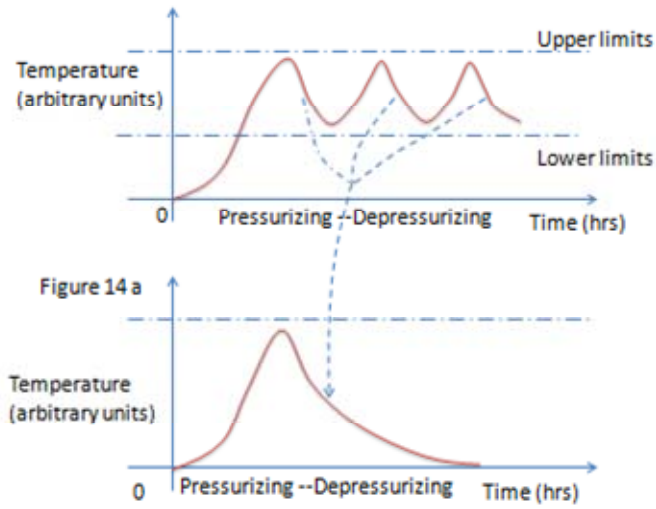

FIGURE 9. Illustration of pressure control to maintain flux of ions required for continuous long time operation. As seen once the temperature starts to decease, the pressure is reduced to initiate flow via desorption. These periodic pressure variations maintain a time-averaged temperature at the desired set point.

A new company, LENUCO, LLC has been set up in Champaign to commercialize this technology. The first goal is to develop modular units in the 1.5 kW (150 W_e) range for various uses. These would be stackable to form 30 kW (3 kW_e) units for small business applications. Thermoelectric energy conversion to electricity would be employed and the units would have cooling stream to allow use for co-generation operation. An earlier conceptual design for such a unit is shown in Fig. 10.

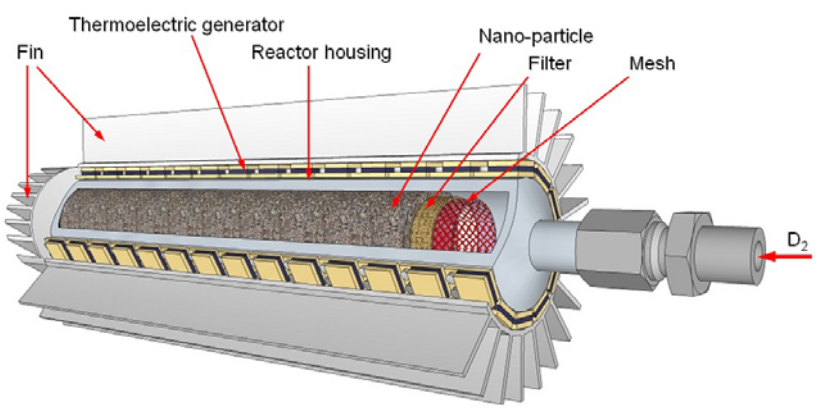

(A)

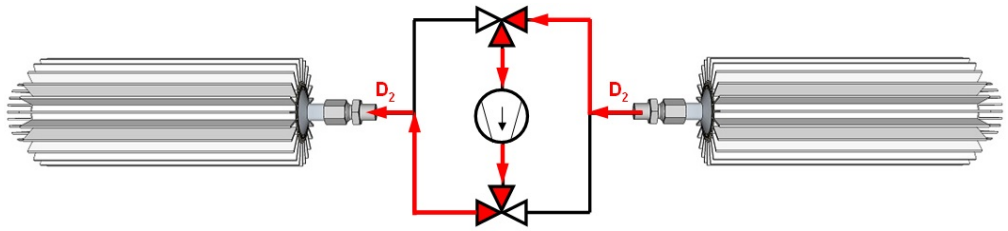

(B)

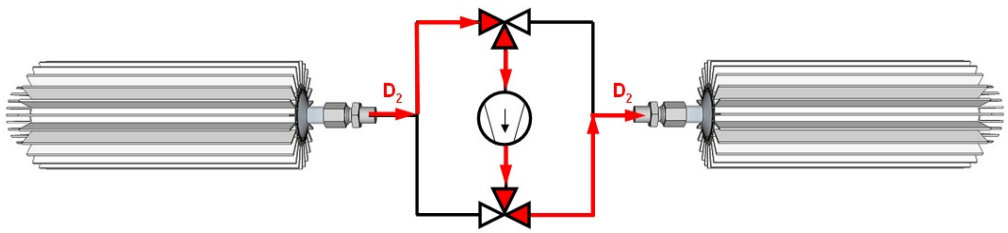

(C)

FIGURE 10. Conceptual design of a gas loaded cell using thermoelectric energy conversion. LENR reactor structure (A), a pair of reactors in cyclic absorption/desorption operation of D_2 gas using a compressor and 3 way valve system (B, C) This base 1.5 kW module can be stacked to provide sufficient power for use in space application similar to RTG.

Like other nuclear energy sources such as fusion and fission, a LENR cell offers a very high energy density. However LENR power sources offer other distinct advantages. Fission power faces limitations due to the need for long-term storage of its radioactive waste. Fusion has less radioactivity involvement but with the planned initial use of D-T fuel still faces tritium containment issues and induced radioactivity of plant materials due to the intense flux of 14.7-MeV neutrons. Also, scaling down to smaller power units is virtually impossible with these two nuclear sources. A LENR-based power source has reaction products that are mildly radioactive, mainly from low energy beta decay from transmutation reactions. But with the short range of the betas, this radioactivity can easily be shielded and quickly decays. The fuel it used, such as D_2, or H_2, is virtually inexhaustible. For LENR power sources, both scaling down and up in power are possible, and the huge energy released in the nuclear reactions (versus chemical reactions) makes this an extremely compact, long-lived energy source. As described earlier, the nuclear reactions occurring involve formation of a weakly excited compound nucleus. Thus the decay channels are quite different from hot fusion. If D_2 is used, D-D reactions resulting in He^4 and phonon heating of the lattice can occur. In addition, the D can react with neighboring host metal atoms, causing a transmutation into a large variety of products such as Cu. If H_2 is used, due to the very small H-H reaction cross-section, reactions are all of the transmutation type.

CONCLUSION

The primary result thus far is that the excess energies obtained in all experiments to date are all well above the maximum estimate of what could be attributed to chemical reactions. The external power/energy involved, such as deuterium gas compression and vacuum pumping, is minimal compared to the output, suggesting very large energy gain. This result then is extremely encouraging relative to this gas-loaded cell becoming a remarkable power unit.

The prime issue under study is to extend the run times using revised nanoparticle treatment combined with a pressure control to maintain a flux of ions in the nanoparticles following the initial loading. Finally optimization of the particle alloy and gas needs study involving the many system trade-offs. Along this line, our ongoing experiments are designed to compare Ni-rich-alloy-H2 with the present Pd-rich-alloy-D_2 system. Also, in order to understand the power scaling with pressure and weight of the nanoparticles, the earlier studies reported here need to be refined. In view of the many remaining issues at this point, it is premature to identify the best potential application. However, assuming the issues identified are resolved, numerous game-changing applications can be

envisioned, for both space and terrestrial power. There are also numerous commercial uses on land, e.g. use in small power units for residential use including hot water heaters, use in larger power units for local power sources in commercial plants, and even forward operating army bases. Space applications, ranging from station keeping on to propulsion would also be revolutionized with such power units.

ACKNOWLEDGMENT

The support from New York Community Trust, NPL Associates Inc., and Lenuco LLC is greatly appreciated. We also thank Materials Preparation Center, Ames Laboratory, US DOE Basic Energy Sciences, Ames, IA, USA for supplying precision alloy manufacturing.

REFERENCES

[1] Miley, G.H. and Patterson, J.A., Nuclear transmutations in thin-film nickel coatings undergoing electrolysis. J. New Energy, 1996. 1(3): p. 5.

[2] Miley, G. H., "Product Characteristics and Energetics in Thin-Film Electrolysis Experiments," *Proceedings of the International Conference on Cold Fusion*, Vancouver, Canada, 1998, pp. 241–246.

[3] Lipson, A., Heuser, B. J., Castano, C., Miley, G. H., Lyakhov, B., and Mitin, A., "Transport and Magnetic Anomalies below 70 °K in a Hydrogen-Cycled Pd Foil with a Thermally Grown Oxide," Physics Review B., Vol. 72, 2005, p. 212507.

[4] Lipson, A. G., Heuser, B. J., Castano, C. H., and Celik-Aktas, A., "Observation of a Low-Field Diamagnetic Contribution to the Magnetic Susceptibility of Deformed Single Crystal PdHx (x≃ 4.0×10−4)," Physics Letters A, Vol. 339, 2005, pp. 414–423.

[5] Miley, G.H., Yang, X and Hora, H, A Potentially Game Changing "Green" Power Source Based on Low Energy Nuclear Reactions (LENRs), Nuclear and Emerging Technologies for Space 2012, The Woodlands, TX March 19-23,

[6] Miley, G. H., and Yang, X., "Deuterium Cluster Target for Ultra-High Density," *18th Topical Meeting on the Technology of Fusion Energy*, San Francisco, CA, 2009.

[7] Holmlid, L., Hora, H., Miley, G., and Yang, X., "Ultra High-Density Deuterium of Rydberg Matter Clusters for Inertial Confinement Fusion Targets," *Laser and Particle Beams*, Vol. 27, 2009, pp. 529–532.

[8] Miley, G. H., Narne, G., Williams, M. J., Patterson, J. A., Nix, J., Cravens, D., and Hora, H., "Multilayer Thin-Film Microspheres after Electrolysis," *Proceedings of the International Conference on Cold Fusion,* Vol. 2, edited by New Energy and Industrial Tech. Dev. Org., Japan, 1996, p. 529.

[9] Lipson, A. G., Rusetskii, A. S., Karabut, A. B. and Miley, G. H., "D-D Reaction Enhancement and X-ray Generation in a High-Current Pulsed Glow Discharge in Deuterium with Titanium Cathode at 0.8–2.45 kV," *Journal of Experimental and Theoretical Physics,* Vol. 100, No. 6, pp. 1175–1187

[10] Karabut, A. B., Lipson, A. G., and Roussetsky, A. S., "Correct Measurement of D-D Reaction Yield and in High Current Pulse-Periodic Deuterium Glow Discharge Operating at 0.85–1.20keV Voltage Applied," *Proceedings of the 8th International Conference of Cold Fusion,* Italy, 2000, p. 335.

[11] Miley, G. H., Luo, N., Lipson, A. G., and Karabut, A. B., "A Unique Plasma Discharge Driven Solid-State X-ray Laser," *SPIE Ablation*, Taos, NM, 2004.

[12] Kim, Y. E., "Theory of Bose–Einstein Condensation Mechanism for Deuteron-Induced Nuclear Reactions in Micro/Nano-scale Metal Grains and Particles," *Naturwissenschaften*, 2009.

[13] Arata, Y., and Zhang, Y., "The Establishment of Solid Nuclear Fusion Reactor," *Journal of High Temp. Soc.,* Vol. 34, No. 2, 2008, p. 85.

[14] Arata, Y., Zhang, Y., and Wang, X., "Production of Helium and Energy in the 'Solid Fusion'," *15th International Conference on Condensed Matter Nuclear Science*, Rome, Italy, 2009.

[15] Sasaki, Y., et al., "Anomalous Heat Generation in Charging of Pd Powders with High Density Hydrogen Isotopes (I) Results of Absorption Experiments using Pd Powders," *15th International Conference on Condensed Matter Nuclear Science,* Rome, Italy, 2009.

[16] Sasaki, Y., et al., "Deuterium Gas Charging Experiments with Pd Powders for Excess Heat Evolution (I) Results of Absorption Experiments using Pd Powders," *9th Meeting of Japan CF-Research Society*, Shizuoka, Japan, 2009.

[17] Takahashi, A., et al., "Deuterium Gas Charging Experiments with Pd Powders for Excess Heat Evolution (II) Discussions on Experimental Results and Underlying Physics," *9th Meeting of Japan CF-Research Society*, Shizuoka, Japan, 2009.

[18] Kitamura, A., Nohmi, T., Sasaki, Y., Taniike, Y., Takahashi, A., Seto, R., and Fujita, Y., "Anomalous Effects in Charging of Pd Powders with High Density Hydrogen Isotopes," *Physics Letters A,* Vol. 373, No. 35, 2009, pp. 3109–3112.

[19] Kidwell, D. "Trace Analysis of Elements in a Palladium Matrix," *International Conference on Condensed Matter Nuclear Science*, Washington, DC, 2008.

[20] Kidwell, D., et al., "Does Gas Loading Produce Anomalous Heat?" *15th International Conference on Condensed Matter Nuclear Science*, Rome, Italy, 2009.
[21] Celani, F., et al., "Deuteron Electromigration in Thin Pd Wires Coated With Nano-Particles: Evidence for Ultra-Fast Deuterium Loading and Anomalous, Large Thermal Effects," *International Conference on Condensed Matter Nuclear Science,* Washington, DC, 2008.
[22] Celani, F., et al., "Towards a High Temperature CMNS Reactor: Nano-coated Pd Wires with D_2 at High Pressures," *15th International Conference on Condensed Matter Nuclear Science*, Rome, Italy, 2009.
[23] Li, X., et al., "Progress in Gas-Loading D/Pd System—The Feasibility of a Self-sustaining Heat Generator," *10th International Conference on* Cold Fusion, 2003.
[24] Errington, R. M. (1997). Advanced practical inorganic and metalorganic chemistry. London: Blackie Academic & Professional. p. 51.

Active Short Circuit - Chassis Short Characterization and Potential Mitigation Technique for the Multi-Mission Radioisotope Thermoelectric Generator

Gary Bolotin[1], Nicholas Keyawa[1]

[1]*Jet Propulsion Laboratory, California Institute of Technology, Pasadena CA 91109*
818-354-4355, nrkeyawa@jpl.nasa.gov
818-354-4126, gsbolotin@jpl.nasa.gov

Abstract. A flight-proven capable source of power is the Radioisotope Thermoelectric Generator (RTG)–essentially a nuclear battery that reliably converts heat into electricity. NASA and the Department of Energy (DOE) have developed a new generation of such power systems that could be used for a variety of space missions. The newest RTG, called a Multi-Mission Radioisotope Thermoelectric Generator (MMRTG), has been designed to operate on Mars and in the vacuum of space[1]. The MMRTG has been working on Mars for the Mars Science Laboratory mission successfully for about 2.5 years. However, shorts between the internal electrical power circuit and chassis frame of the MMRTG have been observed in the Engineering Unit, Qualification Unit, and flight unit[3,4,5]. The internal shorts seem to appear relatively frequently and clear spontaneously. A root cause has not been determined for these internal shorts. In addition, the resistance, power rating, and energy rating are largely unknown. Since these internal shorts are likely to occur, there is potential risk of MMRTG power loss or damaging of subsystems within a spacecraft in the case of multiple shorts forming. In order to quantify and potentially mitigate this risk, an internal MMRTG chassis short characterization technique was developed. The leading hypothesis suggests that the foreign object debris (FOD) which is causing the internal shorts are extremely small pieces of material that could potentially melt and or sublimate away given a sufficient amount of current. The engineering unit and qualification unit are planned to be electrically heated for performance testing in preparation for the next proposed mission to Mars in the year 2020. This period of performance testing will provide an opportunity to test this measurement technique that could characterize these shorts occurring inside the MMRTG. In the event that a short has formed inside the MMRTG, this technique would consist of applying another short (an active short) between the internal electrical power circuit and chassis frame of the MMRTG. This measurement technique will attempt to: (1) measure and characterize the MMRTG internal short to chassis, (2) safely determine if the MMRTG internal short can be cleared in the presence of another controlled short and (3) quantify the amount of energy required to clear the MMRTG internal short. The active short technique presented in this paper is a low risk, simple addition to an already existing performance test setup that will potentially characterize and mitigate the internal shorts forming inside the MMRTG. Data from the characterization test can potentially be incorporated into a mitigation technique for future missions of the MMRTG.

Keywords: MMRTG, MMRTG chassis short, active short

INTRODUCTION

The MMRTG is a state-of-the-art Radioisotope Power Source (RPS) that directly converts heat energy into electrical energy (Figure 1)[2]. The MMRTG utilizes a combination of PbTe, PbSnTe, and TAGS thermoelectric couples to produce electric current from the heat generated by the radioactive decay of plutonium dioxide. Eight General Purpose Heat Source (GPHS) modules, which house plutonium dioxide, are contained within the center of the MMRTG. Through the Heat Distribution Block, the heat from the GPHS modules is distributed to the sixteen thermoelectric modules where a portion of the heat energy is converted to electrical energy via the Seebeck effect.

Waste heat from the thermoelectric couples is transported to the housing and heat rejection system, which functions to transfer the waste heat to the environment via radiation in space or combined radiation and convection in planetary atmospheres. In addition, cooling loop(s) are available to reject waste heat to a liquid thermal control loop. The MMRTG is designed to operate on planetary atmospheres as well as in vacuum. Currently, the MMRTG is powering the Mars Science Laboratory (MSL) rover on Mars, and is planned to be used in the NASA' mission to Mars in 2020.

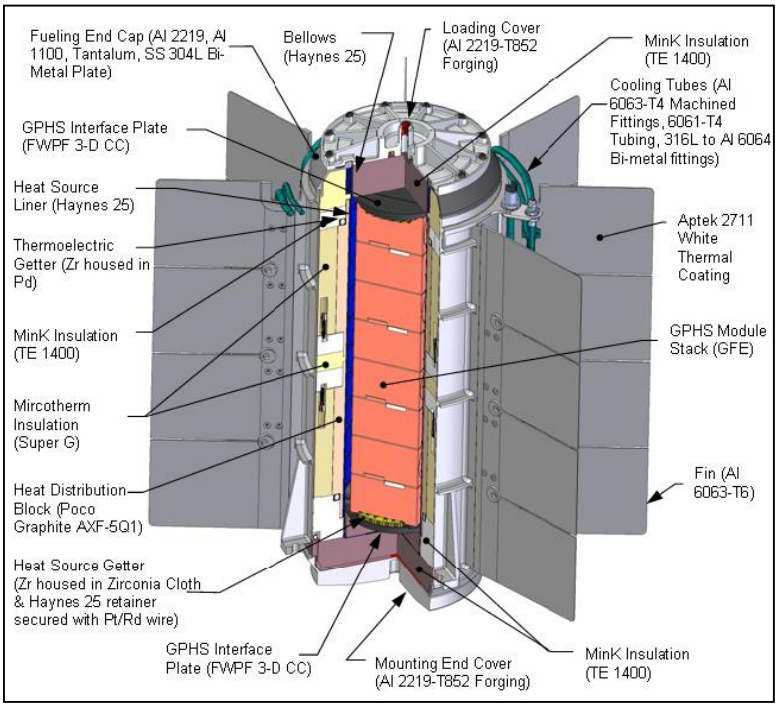

FIGURE 1. Configuration of the MMRTG

The thermoelectric modules of the MMRTG consist of forty-eight thermoelectric couples that are arranged in a series-parallel arrangement and surrounded with microtherm insulation (Figure 2). Each thermoelectric couple consists of PbTe, PbSnTe, and TAGS legs which are bonded to nickel electrodes and copper straps. Each leg of the thermoelectric couples are placed under a spring load using springs and pistons housed in the module bar (Figure 3). An anodized aluminum plate is placed in between the module bar and thermoelectric module in order to help mitigate FOD causing a short between the copper straps of the thermoelectric couple and modular bar. These anodized aluminum plates are unique to the flight units of the MMRTG, and are not present in the Engineering Unit (EU) or Qualification Unit (QU). Sixteen thermoelectric modules are wrapped around the core of the MMRTG and are encased inside an aluminum chassis frame (Figure 4).

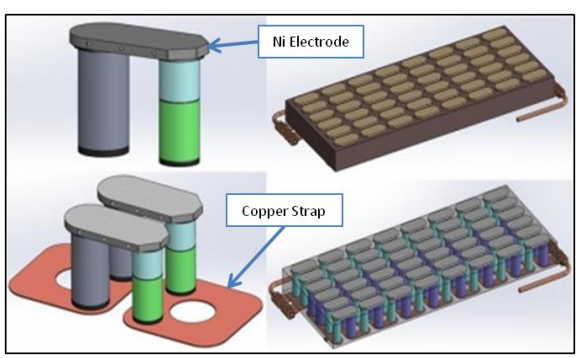

FIGURE 2. The MMRTG Thermoelectric Couples (Upper Left) are Arranged in a Series-parallel Configuration (Lower Left) Inside the Thermoelectric Modules (Upper and Lower Right).

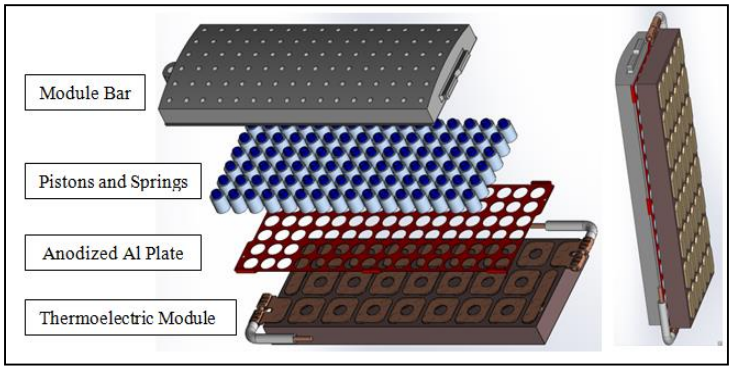

FIGURE 3. Assembly of the Thermoelectric Module with the Module Bar.

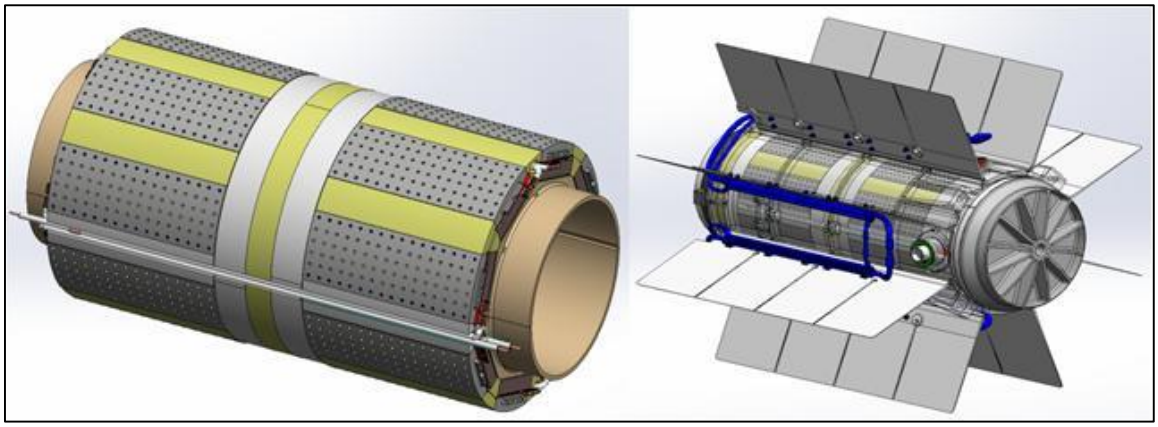

FIGURE 4. Sixteen Thermoelectric Module and Modular Bars are Placed Around the Core of the MMRTG (Left) and are Held in Inside an Aluminum Chassis with Fins (Right).

The Problem – Internal MMRTG Chassis Shorts

A change in the isolation resistance between the MMRTG's internal electrical power circuit and chassis frame of the MMRTG have been observed in the Engineering Unit (EU), Qualification Unit (QU), and flight unit[3,4,5]. These potential shorts were first detected in the QU and EU during vibe testing and electrical isolation checks. The measured resistance of the shorts varied from a few ohms to a couple hundred ohms, and the shorts seemed to appear and clear spontaneously. In response to the observance of these internal shorts, corrective actions were implemented on the flight units to mitigate the worst case scenario causes: stray copper wires and/or large conductive foreign object debris (FOD). Deeper wire channels were made in the insulation around the thermoelectric modules to ensure potential stray copper wires could not poke through the insulation and make contact with the chassis. In addition, anodized aluminum plates were added between the thermoelectric module and module bar to prevent FOD electrically connecting the copper straps of the thermoelectric couples to the module bar that contacts the MMRTG chassis (Figure 5). However, even with these corrective actions, an internal short appeared on the flight unit MSL MMRTG on Mars.

FIGURE 5. After Observing Shorts Inside the EU and QU, the MMRTG Flight Units Were Equipped with Additional Anodized Aluminum Plates (Left) and Deeper Wire Channels (Right).

Problem Risk

At the system level, the MSL rover is tolerant to one short to chassis. This is due to the fact that the rover uses a floating ground bus balance scheme, which enables the rover to be fault tolerant to a single short. However, due to the likely nature of the internal MMRTG shorts appearing, there is a risk of two internal MMRTG shorts forming. In the presence of two internal shorts that do not clear, the system can potentially experience MMRTG power loss. In addition, there is a risk of two shorts forming as follows: one from the MMRTG and a second from another subsystem. In this case the shorted subsystem can be damaged.

MMRTG CHASSIS SHORT CHARACTERIZATION AND POTENTIAL MITIGATION TECHNIQUE: THE ACTIVE SHORT

In order to quantify and potentially mitigate the potential risk of the internal MMRTG chassis shorts, an internal MMRTG chassis short characterization technique was developed. The technique, presented in this paper, involves introducing a controlled second short onto the MMRTG electrical system to chassis in order to characterize the internal MMRTG chassis short. The leading hypothesis suggests that the FOD which is causing the internal shorts are extremely small pieces of material that could potentially melt and/or sublimate away given a sufficient amount of current. The engineering unit and qualification unit are planned to be electrically heated for performance testing in preparation for the next proposed mission to Mars in the year 2020. This period of performance testing will provide an opportunity to test this measurement technique that could characterize these shorts occurring inside the MMRTG. By inducing a controlled second short, a significant amount of current flow can be generated to achieve three main design goals: (1) Measure and characterize the MMRTG internal short to chassis, (2) safely determine if the MMRTG internal short can be cleared in the presence of another controlled short and (3) quantify the amount of energy required to clear the MMRTG internal short. This controlled short is implemented in conjunction with a combination of relays and switches, which allows the short to be activated or de-activated accordingly. Thus, this controlled short to characterize the internal MMRTG chassis shorts is referred to as an active short.

Active Short Theory

Upon inducing the active short, the resulting surge of current may result in clearing away the FOD that is causing the MMRTG internal short. Under this testing scenario, the apparatus will be set up to measure the amount of time that was required to clear away the MMRTG internal short. This will allow one to calculate the I^2t rating of the MMRTG internal short. The I^2t rating is a gauge of the current surge capability of the short at various pulse widths. In addition, the I^2t rating is proportional to the amount of energy dissipated during the surge current pulse. One can calculate the amount of energy required to clear the short using Equation (1).

$$J = R_{short} {I_s}^2 t \tag{1}$$

Where R_{short} is the resistance of the MMRTG internal short, I_s is the amount of surge current through the MMRTG internal short, and t is the pulse width of the surge of current.

In order to determine the resistance of R_{short}, the differential voltages between the high of the MMRTG to chassis and chassis to the low of the MMRTG need to be measured. These measurements will indicate the location of the R_{short} in the electrical power circuit, and allow one to determine the voltage and resistance above and below the short. After determining the location of R_{short}, one can add in bus balance resistors in order to determine the short's resistance. The bus balance resistors introduce a small flow of current through the MMRTG internal short, which allows one to calculate the resistance of R_{short} using Kirchhoff's Voltage Law (KVL). When the active short is applied in the presence of an internal MMRTG short, the resulting current flow which travels through the active short (I_s) is approximately equal to the flow of current through the internal MMRTG short. Thus, the current through the MMRTG internal short can be calculated by measuring the voltage across the precision shunt resistor of the active short. If the FOD inside the MMRTG cannot tolerate the surge in current generated from the active short, the small piece of debris causing the internal short will burn or sublimate away as a result of joule heating. By monitoring the current surge using an oscilloscope, one will view a current pulse waveform. This will allow one to determine the pulse width of the surge current t. After calculating and measuring R_{short}, I_s, and t, the energy rating of the short can be calculated using Equation (1). However, as mentioned above, one; of the goals in this experiment is to determine if the MMRTG

internal short can be cleared in the presence of another controlled short. There is a possibility that when the active short is applied, the resulting surge in current will not be sufficient to clear the MMRTG internal short. This finding will indicate that the MMRTG internal shorts can be robust with sufficient energy ratings to handle current in the event that multiple shorts form on the spacecraft. This experiment will then work to measure and characterize the resistance of the MMRTG internal short, and quantify the risk associated with a high energy rated short.

Active Short Circuit Design and Component Layout

The active short circuit was designed as shown in Figure 6. The active short circuit components are all housed inside of a 9”x7”x2” aluminum box. As one can see from the photo, the inputs to the active short circuit are located at the top left corner. These inputs include the MMRTG chassis, MMRTG low voltage, MMRTG high voltage, earth ground, and a 5V input. The outputs of the active short circuit are located along the bottom edge. These outputs include the MMRTG voltage, bus balance voltage, shunt resistor voltage, and the on/off trigger signal. Towards the center of the box are the four toggle switches. Two of the toggle switches connect and disconnect the bus balance resistors. One toggle switch sets the position of the active short (shunt position), and one toggle switch sets power to the circuit. Inside the box, one can see the large gold bar current limiting resistor and limiting fuse to the left. On the right resides the circuit board for the solid state resistors, shunt resistor, instrumentation amplifier, DC/DC converter, and debounce circuit.

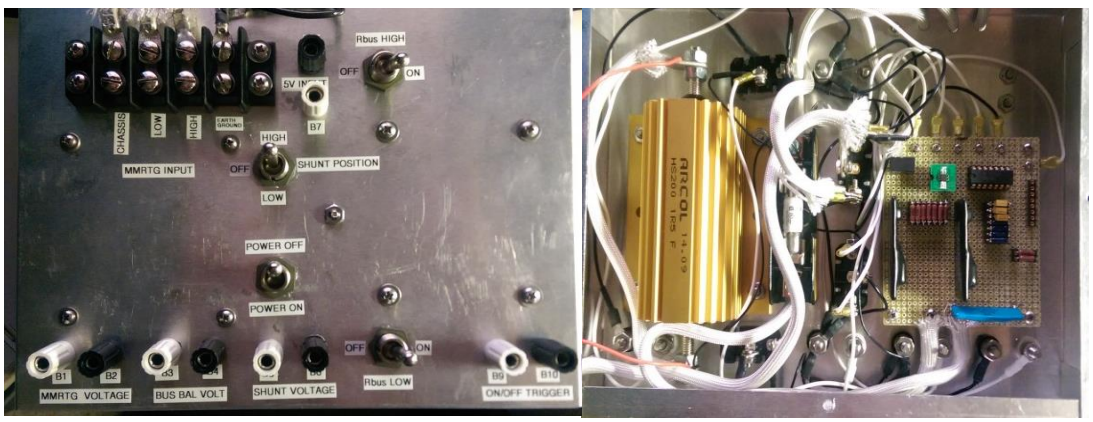

FIGURE 6. The Aluminum Box Interface which is used to House and Connect with the Active Short Circuit.

Future Work

Before the active short can be implemented and integrated onto the MMRTG performance test setup, additional analysis and testing is required. The choice of instruments (including the oscilloscope and DC power supply) needs to be finalized. The choice of the oscilloscope is key in order to accurately capture the surge current pulse waveform, and may require additional testing to validate a written and agreed upon procedure. Furthermore, analysis of the I^2t rating for the expected type of FOD inside the MMRTG needs to be carried out in order to predict the behavior of the unit when the active short is applied. This analysis will also be utilized to simulate the MMRTG FOD in a test experiment to further validate the functionality and performance of the active short circuit. Since the actual experiment is dependent on the formation of an MMRTG internal short, there is a possibility that a significant amount of time may pass before the experiment can be conducted. Discussions will be required to potentially make the active short a more permanent component to the performance test setup, and will require training individuals on the usage of the device.

CONCLUSION

In conclusion, the MMRTG is a flight-proven capable source of power that is currently in use by the Mars rover Curiosity. The MMRTG directly converts heat energy into electrical energy through the Seebeck effect of a series of thermoelectric couples. However, shorts between the internal electrical power circuit and chassis frame of the MMRTG have been observed in the engineering unit, qualification unit, and flight unit. The leading hypothesis suggests that these shorts are the result of product from sublimation or cracking at the hot junction of the thermoelectric couples bridging the gap between the thermoelectric module and module bar. The engineering unit and qualification

unit are planned to be electrically heated for performance testing in preparation for the next proposed mission to Mars in the year 2020. This period of performance testing provides an opportunity to test a measurement technique known as the active short, which could characterize the shorts occurring inside the MMRTG. In the event that a short has formed inside the MMRTG, this technique would consist of applying another short (active short) between the internal electrical power circuit and chassis frame of the MMRTG. By inducing a controlled second short, a significant amount of current flow can be generated to achieve three main design goals: (1) measure and characterize the MMRTG internal short to chassis, (2) safely determine if the MMRTG internal short can be cleared in the presence of another controlled short and (3) quantify the amount of energy required to clear the MMRTG internal short. Currently, if an internal short forms within the engineering unit or qualification unit, the action is to do nothing other than to record the time a chassis short has occurred. Once the experiment is conducted, the collected and analyzed data will be used to ultimately quantify the risk of these shorts, and potentially lead to using this instrument as a mitigation technique on future MMRTG missions.

The research described in this paper was carried out at the Jet Propulsion Laboratory, California Institute of Technology, under a contract with the National Aeronautics and Space Administration.

REFERENCES

[1] Bechtel, Ryan. "Multi-Mission Radioisotope Thermoelectric Generator (MMRTG)." *Jet Propulsion Laboratory - Mars Exploration Program*. JPL, 2 Oct. 2013. Web. 25 Nov. 2014.

[2] Department of Energy, DOE. "Radioisotope Missions." (n.d.): n. pag. *Jet Propulsion Laboratory*. Web. 17 Feb. 2015. <http://www.jpl.nasa.gov/msl/pdf/MMRTG_RyanBechtel_DOE.pdf>.

[3] Stabb, Jonathan. "MMRTG Qual Unit Intermittent Short to Case." *Problem Reporting System*. JPL, 7 Nov. 2008. Web. 25 Nov. 2014. <https://prs.jpl.nasa.gov/NET/PFRReadOnly.aspx?smode=pop&iAnomalyID=14145>.

[4] Webster, Guy. "Curiosity Resumes Science After Analysis of Voltage Issue." *Jet Propulsion Laboratory - Mars Exploration Program*. JPL, 25 Nov. 2013. Web. 25 Nov. 2014.

[5] Woerner, David. "EU Cold Electrical Check Finds Heater and Generator Circuits out of Isolation Specification." *Problem Reporting System*. JPL, 3 Dec. 2010. Web. 25 Nov. 2014. <https://prs.jpl.nasa.gov/NET/PFRReadOnly.aspx?smode=pop&iAnomalyID=47162>.

CSNR Space Propulsion Optimization Code: SPOC

Peter J. A. Husemeyer[1,2], Vishal Patel[1,3], Paolo F. Venneri[1,4], Wesley R. Deason[1], Michael J. Eades[1,5], Steven D. Howe[1]

[1]*Center for Space Nuclear Research, Idaho Falls, ID, USA*
[2]*University of Cambridge, Cambridgeshire, United Kingdom - pjah4@cam.ac.uk*
[3]*Department of Nuclear Engineering, Texas A&M University, College Station, TX 77843*
[4]*Department of Nuclear & Quantum Engineering, KAIST, Daejeon, Republic of Korea*
[5]*Nuclear Engineering Program, The Ohio State University, Columbus, OH 43201"*

Abstract.
The Low Enriched Uranium (LEU) Nuclear Thermal Rocket (NTR) represents a significant optimization opportunity because of the numerous design parameters that can be adjusted to improve system performance. Performing these optimization studies requires an automated analysis tool that allows for thousands of NTR design iterations to be considered. A code developed by the Center for Space Nuclear Research (CSNR), known as SPOC, brings MCNP, SERPENT and a range of analysis tools together, which makes performing these trade studies substantially faster than was previously possible. In addition to performing rapid analysis, SPOC has unique capabilities which facilitate the optimization of the neutron energy spectrum in a manner that has not previously been discussed in the literature.

Keywords: CSNR SPOC NTR LEU Cermet

INTRODUCTION

There has recently been renewed interest in the field of NTR design. One contributing factor for this trend are the numerous Human Mars Mission Architecture studies which call the NTR the "preferred approach" for a 2035 mission to Mars[1]. A second contributing factor is the intriguing possibility of an LEU fueled NTR[2].

In response to these developments, NASA Marshall Space Flight Center (MSFC) tasked the CSNR to investigate the feasibility of designing an NTR using LEU tungsten cermet fuel[3]. From the initial study, and those that followed, it became apparent that an LEU NTR was indeed feasible and that there was significant opportunity for system optimization[4,5,6,7]. To aid the investigation of the LEU NTR design space, the CSNR developed an analysis code known as the Space Propulsion Optimization Code (SPOC).

SPOC is a tool which brings together the capabilities of MCNP and SERPENT. SPOC's analysis begins with its own input file, which is written using MATLAB syntax. Using its input file, SPOC automates the creation of the MCNP and SERPENT input files. These input files can also be generated parametrically to run on clusters. With the input files created, SPOC coordinates the execution of MCNP and SERPENT, retrieves and parses the data contained in the output files and then makes the data available for a thermal-hydraulic analysis and full system power balance. Finally the data are summarized using SPOC's own output file, figures and graphs.

By combining the capabilities of MCNP and SERPENT SPOC enables the NTR designer to investigate important reactor design topics such as: criticality, neutron spectrum, neutron and gamma heating, core power profiles, fuel burn-up, cross sections, pressure drops, temperature profiles, propellant velocities, specific impulse, thrust-to-weight ratio and overall system power balance.

A full discussion of the capabilities of SPOC and the various validation techniques is beyond the scope of this paper. This paper will therefore present the high-level functioning of the code, which will be described under the headings, *Input File Generation* and *Thermal-Hydraulic Model*.

INPUT FILE GENERATION

MCNP and SERPENT input files have a similar structure: they both begin with cell definitions, then the geometry is defined and finally the materials are defined. SPOC creates an NTR input file for both codes based on settings in its own SPOC input. In this section, the basic SPOC generated NTR geometry is introduced followed by a description of some of the customization options.

The SPOC Generated NTR

The basic SPOC generated NTR geometry is shown in Figure 1. The configuration uses the major components that were used in the NERVA and SNRE designs; control drums, a radial neutron reflector, inner and outer pressure vessels, hexagonal fuel elements, structural elements, an internal neutron and gamma shield, as well as other components such as an axial neutron reflector[8,9].

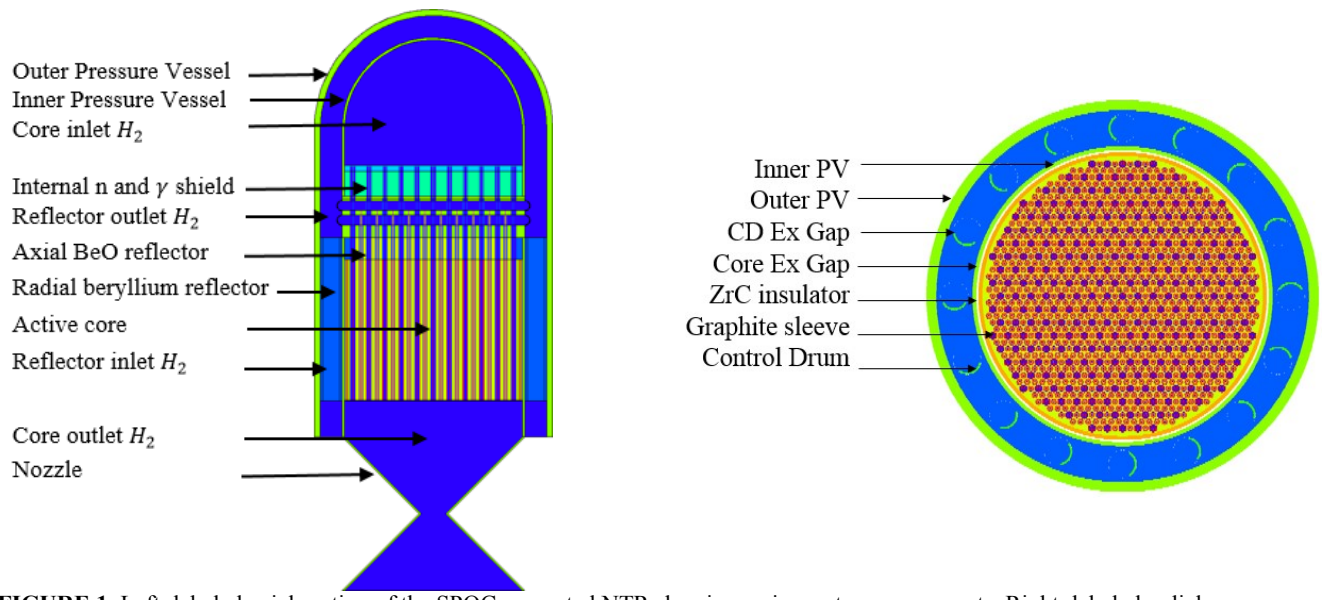

FIGURE 1. Left: labeled axial section of the SPOC generated NTR showing major system components. Right: labeled radial section through NTR core.

Control of the neutron flux and neutron energy spectrum in the core is achieved primarily through the use of control drums within the radial reflector and moderating material within the support elements[10]. To ensure adequate controllability, SPOC inserts as many control drums into the radial reflector as possible; however over-ride settings within its own input file can be used to adjust the number. Expansion gaps are automatically inserted around the core and control drums based on the thermal expansion coefficients of the core materials and their geometry.

The neutron energy spectrum is controlled within the core through the mass of moderator contained within the support elements. During the NERVA program, the primary role of the support elements was to hold the graphite fuel in compression and thus to support the core. For the LEU system, the primary role of the support elements is to provide moderation and, therefore, they are known as *Moderator Elements* in the present text.

The moderator elements, Figure 2, are cooled by LH_2 (liquid hydrogen) supplied by the inlet plenum at the top of the core, Figure 3. The LH_2 travels down the central moderator element supply passage towards the reactor exit where the flow turns 180 degrees before travelling back towards the reactor inlet via the peripheral return passage. The return passage then dumps the heated LH_2 into the outlet plenum at the top of the core, and the LH_2 then goes on to drive the turbine of the turbopump.

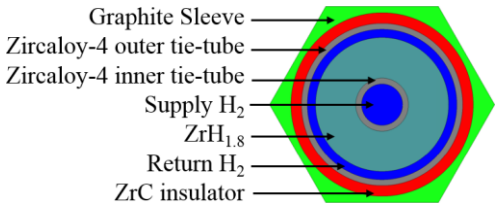

FIGURE 2. Labeled cross section of a moderator element. These elements form part of the core lattice along with the fuel elements.

SPOC Customization Options

An NTR can be defined by its geometry, the materials from which it is constructed and its operating conditions. Within the SPOC input file these definitions can be made by choosing from a list of existing options, or by entering the desired parameter values. This section will briefly discuss a selection of the options available.

Material, Geometry and NTR Operating Condition Options

SPOC was created to explore the possibility of an LEU fueled NTR. The materials that make up the components in Figure 2 and Figure 3 illustrate this point, for example, Inconel 718 which was used for the tie-tubes during the ROVER and NERVA programs has been replaced by Zircaloy-4 to reduce parasitic neutron absorption[11,12]. For some reactor configurations, possibly operating at higher pressures, Zircaloy-4 may be unsuitable. Settings within the SPOC input file allow the designer to easily change the inner and outer tie-tube materials to TZM or Inconel 718.

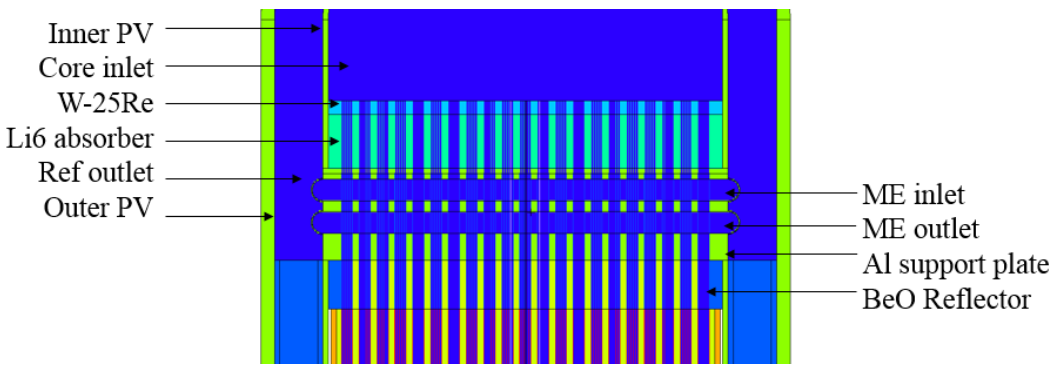

FIGURE 3. Labeled axial section of the internal shield, moderator element inlet and outlet plena and structural components.

Likewise, the compositions of other components can be easily altered using existing options within the SPOC input file. Other components, such as the radial and axial neutron reflector materials, the inner and outer pressure vessels, the internal neutron and gamma shields, the moderator element inlet and outlet plena as well as the moderator elements and fuel elements themselves all have alternate materials predefined.

SPOC includes many settings to control the composition of the fuel, fuel stabilizers and the coatings and claddings. The fuel can be changed between a tungsten cermet or carbide fuel, the enrichment of the uranium can be adjusted as can the tungsten-184 in the cermet case. Another setting allows the fissile component to be changed from uranium-235 to uranium-233 while another setting controls residual fuel porosity.

Fuel stabilizers are important materials that are added to the fuel kernels to prevent uranium migration[13]. Settings within SPOC allow the stabilizer to be changed between gadolinia, thoria, yttria and ceria and a further control parameter sets the stabilizer mole fraction. Fuel coatings and claddings can also be set using the input file. SPOC uses a tungsten coating on the fuel's exterior surface and a tungsten cladding on the wall of the coolant channels.

In addition to the materials settings, SPOC has geometry settings which allow the NTR to be easily customized. The user first sets the fuel and moderator element geometry which may include the choice of fuel flat-to-flat distance, the number of coolant channels, Figure 4, or the fuel cladding thickness. The user can specify the core length and core radius as well as the thickness of the radial and axial neutron reflectors, the inner and outer pressure vessels, the neutron and gamma shields and the core insulator. Other settings control the length of the nozzle, the plena clearances and more.

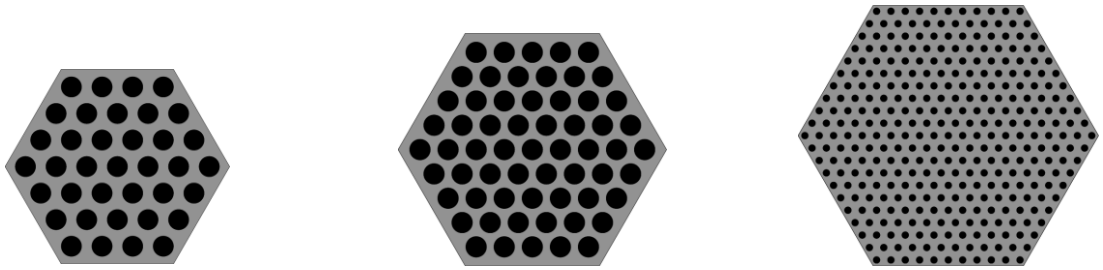

FIGURE 4. The number of coolant channels and the fuel element flat-to-flat can be changed within the SPOC input file. This figure shows three fuel elements of different flat-to-flat distances and with 37, 61 and 331 coolant channels respectively.

Moderator Element Lattices

The ratio of moderator to fuel is an important NTR core parameter. Due to structural concerns, the volume of moderator contained within the moderator element may not be easily adjusted. To allow the designer greater control over this ratio, SPOC has a setting which controls the structure of the moderator and fuel element lattice.

During the NERVA program, Pewee used a lattice with one moderator element for every three fuel elements, while SNRE used a lattice with one moderator element for every two fuel elements. By interchanging the positions of the moderator elements with the fuel elements one obtains two additional lattices which have not been discussed previously in the literature. These lattices have ratios of two tie-tubes per fuel element and three tie-tubes per fuel element respectively and are known as the *Inverted SNRE* and the *Inverted Pewee* lattices.

TABLE 1. Different lattice configurations and their moderator-to-fuel element ratios showing the effect on the normalized k-eff of a representative core.

Pewee	SNRE	Bullseye	Inverted SNRE	Inverted Pewee
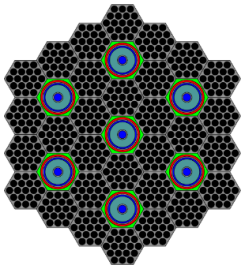	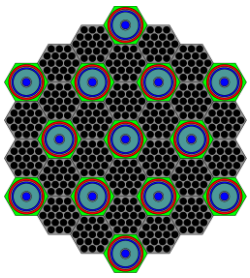	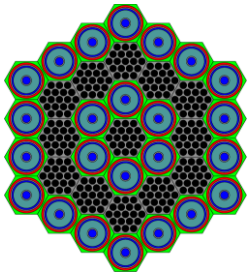	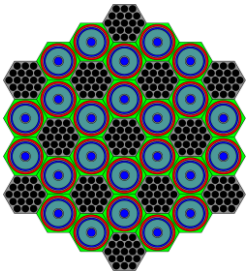	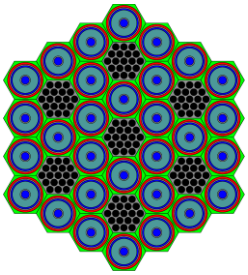
$Ratio = 1:3$	$Ratio = 1:2$	$Ratio = 1:1$	$Ratio = 2:1$	$Ratio = 3:1$
$k_{eff} = 0.745$	$k_{eff} = 0.763$	$k_{eff} = 0.843$	$k_{eff} = 0.940$	$k_{eff} = 1.000$

The different moderator-to-fuel element ratios afforded by these lattices are shown in Table 1. Despite the displacement of fuel, the higher moderator-to-fuel element ratios typically increase core reactivity. Indeed, the ability to use different core lattices is particularly important for the LEU NTR since a higher moderator-to-fuel element ratio helps to mitigate the loss of reactivity caused by using LEU. However, a lower moderator-to-fuel element ratio allows for a lower power density, so a balance must be found.

The use of only one particular lattice might in some circumstances prove to be insufficient. For example, the effect of the radial power profile on NTR performance has been discussed in the literature[6,14,15]. In the past, the radial power profile was flattened using radial enrichment zones. In the case of the LEU NTR radial enrichment zoning can be overly burdensome on the core's reactivity due to the already low enrichment of the fuel. In this case a unique capability of SPOC allows multiple lattices to be combined as shown in Figure 5.

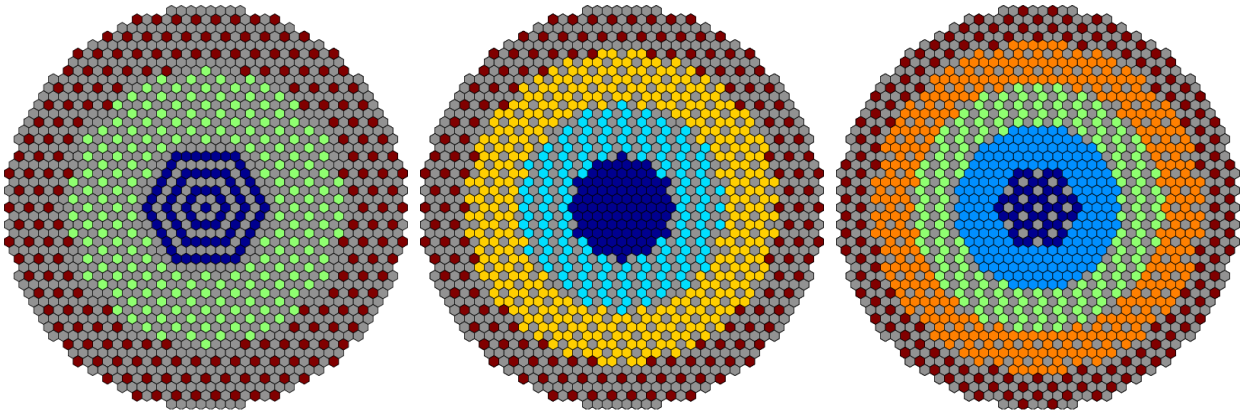

FIGURE 5. Examples of combined lattices where the gray elements represent moderator elements and the fuel elements are colored by zone. These configurations (a), (b) and (c), combine 3, 4 and 5 different lattices together respectively. Lattice (a) on the far left uses a 3:1 ratio in the outer zone (inverted Pewee), a 2:1 ratio in the middle zone (inverted SNRE) and a 1:1 ratio in the central zone (Bullseye).

The combined lattice can be used to place a higher density of moderating material on the periphery of the core and less in the center. To illustrate the effect that a combined lattice can have, the image on the left of Figure 6 shows the typical Bessel-like form of the relative power deposition in an NTR core using an inverted SNRE lattice with a 2:1 moderator-to-fuel element ratio. This core has a power peaking factor of 1.40. The image on the right of Figure 6 shows the same core using the combined lattice, on the far left of Figure 5, which has reduced the power peaking factor to 1.14. This corresponds to a 65% reduction in the maximum fuel element power versus the mean fuel element power.

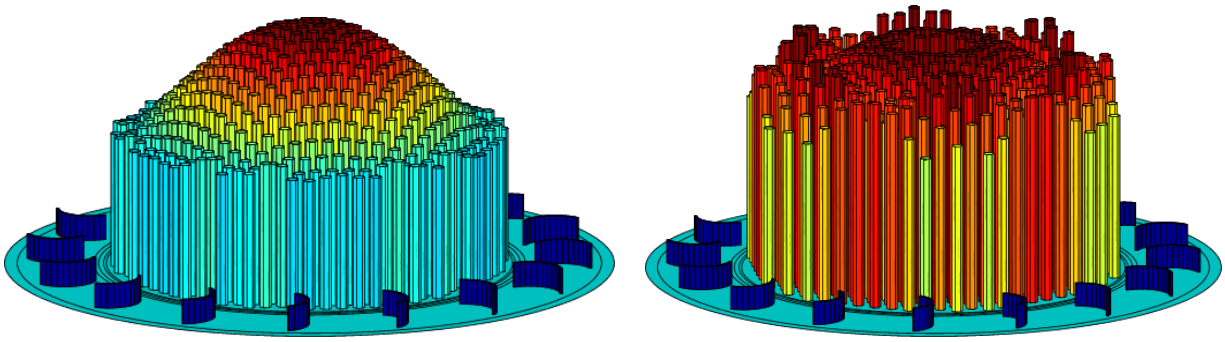

FIGURE 6. An example of the effect that lattice type has on the relative power deposition within an NTR core. The core in figure (a) uses an inverted SNRE lattice with a 2:1 moderator-to-fuel element ratio, while the core in figure (b) uses the lattice depicted on the far left of Figure 5

Radial and Axial Fuel Loading Zones

The ability to create combined lattices with SPOC gives the designer a new method to tailor the radial power peaking factor. Additional control over the power peaking factor can be exerted by using radial and axial fuel loading zones. Radial fuel loading zones can be used to further smooth the radial power peaking factor while the use of axial loading zones allows the axial power profile to be optimized[7].

SPOC can automatically generate an NTR core with any number of radial or axial fuel loading zones. Each zone is given its own material card and the fuel loading in each zone can be set independently. Furthermore, the temperatures of the fuel and moderator materials in these zones can also be independently set. These capabilities allow the designer to capture the most salient details of an NTR core, which is especially important for criticality and burn studies as well as power profile optimization.

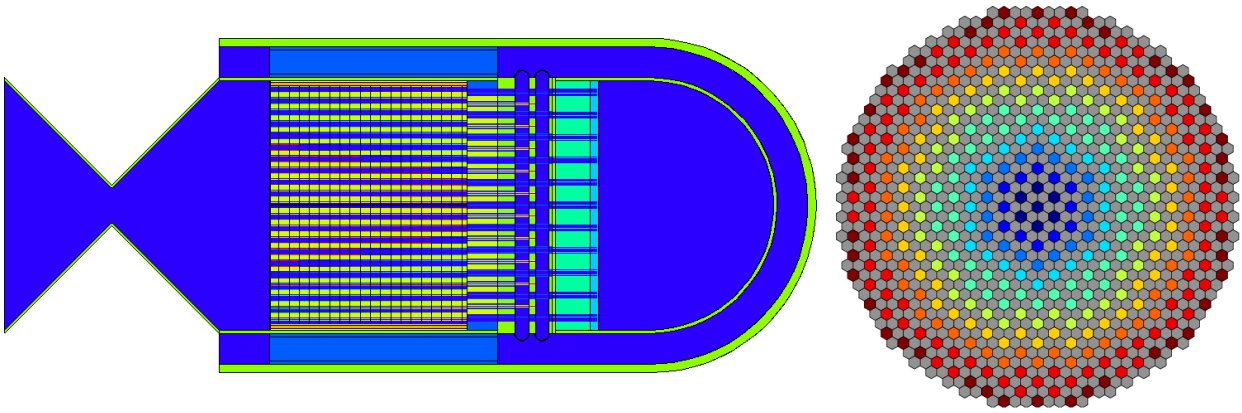

FIGURE 7. SPOC generated core using 20 axial fuel loading zones and 10 radial fuel loading zones. The image on the right shows an inverted SNRE lattice (moderator-to-fuel element ratio 2:1) where the fuel elements have been colored by zone.

THERMAL-HYDRAULIC MODEL

SPOC's thermal-hydraulic code was designed to converge quickly and to give conservative results. The code initially performs a hot-channel analysis to ensure that the core materials are within their safe operating limits. Pressure-drops within the fuel and moderator elements are then used as inputs fon Kerry r the full system power balance. Upon convergence of the power balance the reactor inlet temperature and pressure are returned to the hot-channel analysis. The code iterates in this manner until a convergence criterion has been satisfied.

Heat Transfer Model

SPOC's thermal-hydraulic code performs a hot-channel analysis on the fuel element with the highest power peaking factor. For SPOC to perform quick, conservative analyses it was necessary to simplify the complex geometry of the fuel and moderator elements and to ensure that the calculated temperatures in critical components were over-estimated.

For the fuel element this was done by creating an equivalent tube around a coolant channel and applying an adiabatic boundary condition to the outer surface, as shown in Figure 8. The fuel elements are in a lattice with actively cooled moderator elements which have a slight cooling effect. The application of this boundary condition, therefore, over-estimates the fuel centerline temperature since it does not account for power lost to the moderator element.

The heat transfer model, likewise, circularizes the moderator element and sets its outer surface temperature equal to the fuel centerline temperature. This analysis is also conservative because the boundary condition essentially represents a moderator-to-fuel element ratio of 1:6, which delivers more power to the element than would occur in a Pewee type lattice. These assumptions render the equivalent tube and the moderator element axisymmetric, which simplifies the governing equations and significantly increases the code's speed.

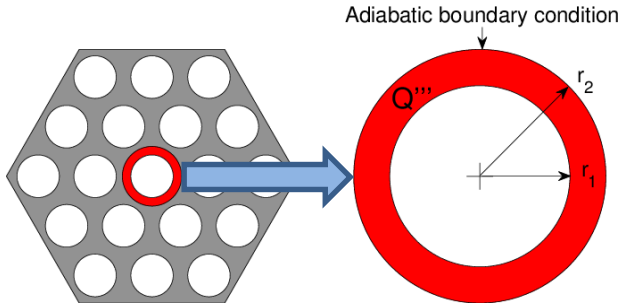

FIGURE 8. Creating an equivalent tube around the central coolant channel.

In the meat of the fuel and moderator elements the conduction equation is solved using temperature dependent thermal conductivities for the various materials. The effective thermal conductivity for the fuel, which is a porous composite, is calculated using whichever is the most conservative of the models due to Maxwell, Bruggeman and Meredith and Tobias[16]. In the hydrogen channels the steady 1D compressible duct flow equations are solved with friction, heat

transfer and temperature dependent LH_2 transport properties. Equations (1), (2) and (3) express the conservation of mass, momentum and energy in differential form[17].

$$\frac{d\rho}{\rho} + \frac{du}{u} = 0 \tag{1}$$

$$\rho u A du + A dP + dF_{shear} = 0 \tag{2}$$

$$dQ = \dot{m} dh + \dot{m} u du \tag{3}$$

The left hand side of Equation (3) requires a convective heat transfer coefficient and friction factor correlations. The heat transfer coefficient is obtained from the Nusselt Number using Taylor's correction to the McCarthy-Wolf correlation, and the friction factors for internal flow in smooth and rough pipes are given by Equation (5) and (6) [18,19].

$$Nu_b = 0.23 Re_b^{0.8} Pr_b^{0.4} \times \left(\frac{T_s}{T_b}\right)^{-\left(0.57 - \frac{1.59}{x/D}\right)} \times \left(\frac{f_{rough}}{f_{smooth}}\right)^{0.68 Pr_b^{0.215}} \tag{4}$$

$$f_{rough} = \left[-1.8 \times \log_{10}\left(\frac{6.9}{Re_D} + \left(\frac{\varepsilon/D}{3.70}\right)^{1.11}\right)\right]^{-2} \tag{5}$$

$$f_{smooth} = 4\left[1.5635 \times ln\left(\frac{Re_D}{7}\right)\right]^{-2} \tag{6}$$

SPOC uses these equations and correlations to determine the temperature field within the fuel element with the highest power peaking factor. The code can then produce a number of graphics to visualize the temperature field, one of which is shown in Figure 9. Likewise, the temperature field within the hottest moderator element is also visualized as shown in Figure 10.

SPOC also graphs the variation of the propellant transport properties within the fuel and moderator elements. It can create graphs showing the Nusselt, Prandtl, Reynolds or Mach number variation within the channels, and it can create graphs to show the variation of the pressure, velocity or propellant density. SPOC can also create a graphic to show the relative power distribution within the fuel elements, as in Figure 6, or visualize the reactor core lattice.

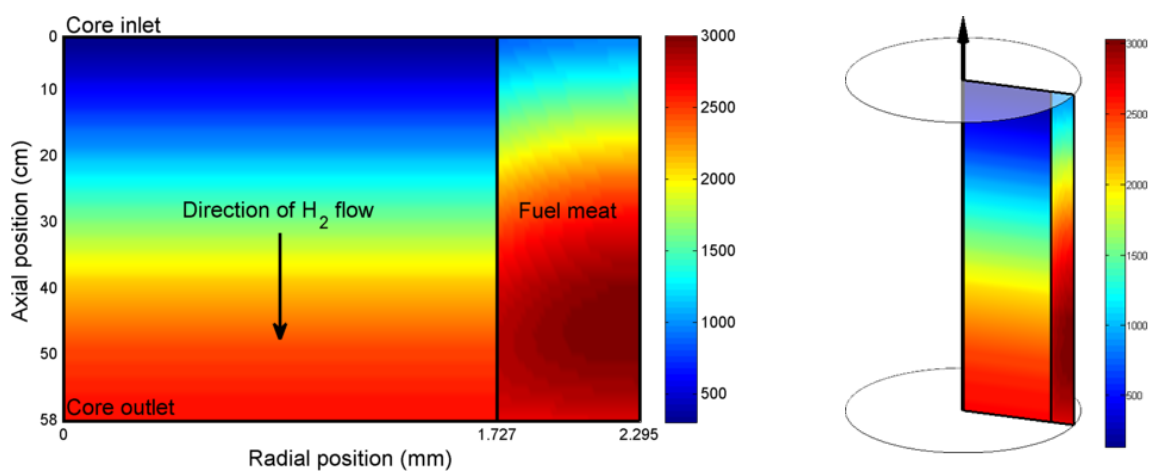

FIGURE 9. An example of the temperature field within the equivalent tube surrounding the central coolant channel of the fuel element with the highest power peaking factor. The image on the right is a reminder that the solution is axisymmetric.

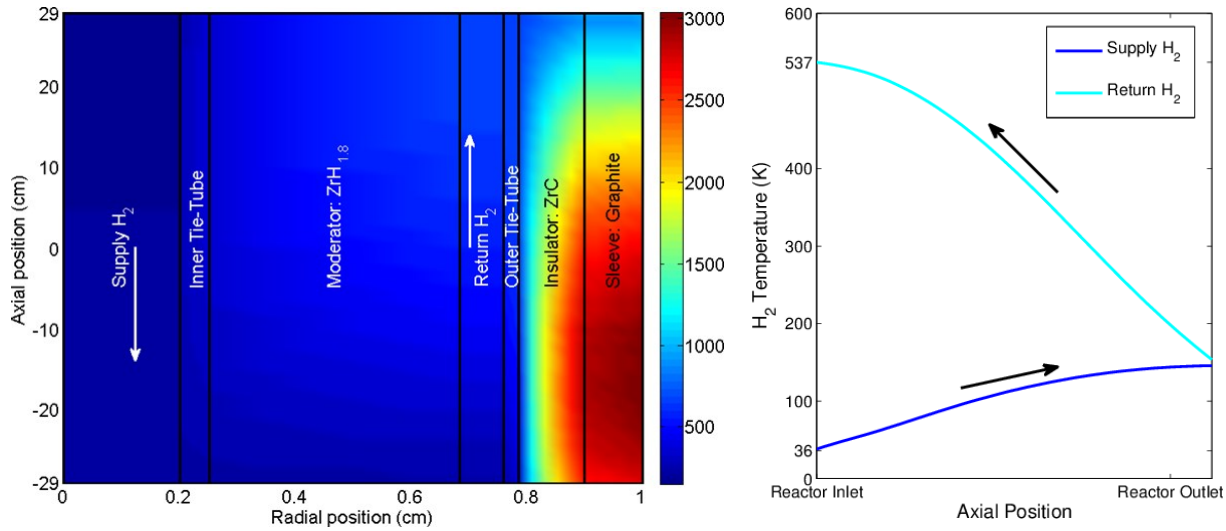

FIGURE 10. An example of the temperature field within a moderator element neighboring the fuel element with the highest power peaking factor. The image on the right shows the variation of the LH_2 temperature in the supply and return channels.

Full System Power Balance

The power balance is performed over 25 state points for an expander cycle NTR, shown in Figure 11[20]. The analysis begins with a set tank pressure, set chamber pressure, set turbine and pump efficiencies and initial estimates of the pump work and the pump outlet pressure. The code uses a set flow split ratio between the moderator element leg and the regenerative cooling leg at state point 4.

The code incrementally calculates the pressures and the temperatures starting at the pump outlet (state point 3), to the reactor core outlet (state point 22). The turbine leg shield inlet (state point 14), and the reflector cooling outlet (state point 19) are, in fact, collocated and should therefore be isobaric. To enforce this condition the code adds a valve pressure drop at the moderator element leg valve outlet (state points 5) or the nozzle leg valve outlet (state point 15).

The code iteratively adjusts the valve pressure drop at state points 5 or 15 until the isobaric pressure condition is achieved. This process essentially solves for the required valve pressure drop, at state point 5 or 15, to achieve the set flow split ratio. Within each iteration the code also updates the pump outlet pressure (state point 3) until the set chamber pressure condition has been satisfied.

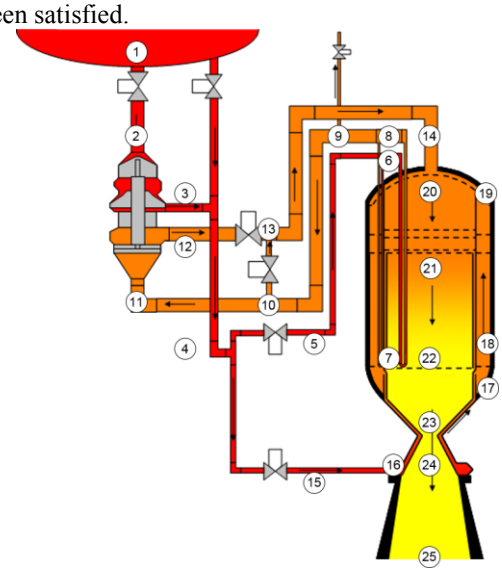

FIGURE 11. Schematic of an expander cycle NTR showing the 25 state points[20].

CONCLUSION

The CSNR's code SPOC significantly accelerates the NTR design process by automating the creation of MCNP and SERPENT input files and by coordinating the execution of those input files, parsing the output data and performing thermal-hydraulic analyses and a system power balance. SPOC was designed to perform rapid parametric investigations of the NTR design space and it is ideally suited to aid in full system optimization. SPOC's combination of traditional and novel capabilities, furthermore, make it possible to minimize the LEU NTR's radial power peaking factor with a degree of control that was previously not possible. Additionally, the ability to control the fuel loading in the axial direction enables power profile optimization. SPOC is unsuitable at present to replace analyses such as CFD, rather, SPOC is intended to complement these analyses and to function as an aid to the design process. By bringing together as many capabilities as possible under one framework, while new capabilities are continually being added, SPOC aims to enable the NTR designer to push the envelope of NTR performance.

NOMENCLATURE

A	=	Cross sectional area
C_p	=	Specific heat capacity
D_H	=	Hydraulic diameter
dh	=	Differential change in enthalpy
f_D	=	Darcy friction factor
M	=	Mach number
$\dot{m}$	=	Mass flow rate
Nu	=	Nusselt number
P	=	Pressure
Pr	=	Prandtl number
dQ	=	Differential change in energy transferred as heat
Re_D	=	Reynolds number by hydraulic diameter
T	=	Thermodynamic temperature
T_b	=	Bulk thermodynamic temperature
T_s	=	Wall thermodynamic temperature
u	=	H_2 velocity
γ	=	Ratio of the specific heats
ε	=	Tube roughness
ρ	=	Mean density between successive nodes

ACKNOWLEDGMENTS

The authors would like to thank Dr. Michael Houts of NASA Marshall Space Flight Center, for funding the LEU NTR research project and for generously providing his guidance and support. The authors would also like to acknowledge the significant contribution to this project made by Dr. Steve Howe, the director of the CSNR, whose passion for the NTR has inspired a new generation of space-minded nuclear engineers. Lastly Dr. Robert O'Brien, also of the CSNR and Jon McDonald of NASA Marshall Space Flight Center have provided invaluable guidance in improving SPOC to its current state.

REFERENCES

[1] NASA Johnson Space Center, "Human Exploration of Mars: Design Reference Architecture 5.0," Houston , 2009.

[2] P. J. A. Husemeyer and W. R. Deason, "Thermal Hydraulic Design and Optimization of a Low Enriched Uranium Nuclear Thermal Rocket," in *Nuclear Emerging Technologies for Space*, New Orleans, 2014.

[3] P. F. Venneri, W. Deason, P. J. A. Husemeyer, G. C. Rosaire, R. O'Brien, S. Howe and Y. Kim, "Design of a Low-Enriched Uranium Tungsten CERMET Fueled Nuclear Thermal Rocket," 2014.

[4] P. F. Venneri, Y. Kim, P. J. A. Husemeyer and S. Howe, "Development of the 900s Specific Impulse Carbide Low Enriched Uranium Nuclear Thermal Rocket," in *PHYSOR*, Kyoto, 2014.

[5] P. Venneri, P. J. A. Husemeyer, W. Deason, G. C. Rosaire, S. Howe and Y. Kim, "Nuclear Thermal Rocket Design Using LEU Tungsten Fuel," in *Transactions of the Korean Nuclear Society Fall Meeting*, Gyeongju, 2013.

[6] P. J. A. Husemeyer, "Thermal-Hydraulically Optimal Power Profile for a Nuclear Thermal Rocket Engine," in *American Nuclear Society*, Anaheim, 2014.

[7] Aerojet-General Corporation, "Volume II - NERVA Engine System Appendix - Specifications," Azusa, 1961.

[8] Los Alamos Scientific Laboratories, "Nuclear Engine Definition Study Preliminary Report Volume 1 - Engine Description," Los Alamos, 1972.

[9] S. K. Borowski, D. R. McCurdy and T. W. Packard, "Nuclear Thermal Propulsion (NTP): A Proven Growth Technology for Human NEO / Mars Exploration Missions," in *IEEE Aerospace Conference*, 2012.

[10] J. L. Finseth, "Overview of Rover Engine Tests Final Report," Huntsville, 1991.

[11] Los Alamost Scientific Laboratories, "Nuclear Engine Definition Study Preliminary Report Volume II - Supporting Studies," Los Alamos, 1972.

[12] D. E. Burkes, D. M. Wachs, J. E. Werner and S. D. Howe, "An Overview of Current and Past W-UO2 Cermet Fuel Fabrication Technology," in *Proceedings of Space Nuclear Conference* , Boston, 2007.

[13] T. M. Schriener and M. S. El-Ghenk, "Reactivity Control Options of Space Nuclear Reactors," *Progress in Nuclear Energy,* vol. 51, pp. 526-542, 2009.

[14] B. G. Schnitzler, "Small Reactor Designs Suitable for Direct Nuclear Thermal Propulsion: Interim Report," Idaho National Laboratories, 2012.

[15] J. D. Anderson, Modern Compressible Flow, McGraw-Hill, 2002.

[16] J. M. Locke and D. B. Landrum, "Study of Heat Transfer Correlations for Supercritical Hydrogen in Regenerative Cooling Channels," *Journal of Propulsion and Power,* vol. 24, 2008.

[17] A. Ghanbari, F. F. Farshad and H. H. Rieke, "Newly Developed Friction Factor Correlation for Pipe Flow and Flow Assurance," *Journal of Chemical Engineering and Materials Science ,* vol. 2, no. 6, pp. 83-86, 2011.

[18] M. Kandala, "On the Effective Thermal Conductivity of Porous Packed Beds with Uniform Spherical Particles," NASA Kennedy Space Center.

[19] R. C. O'Brien and N. D. Jerred, "Spark Plasma Sintering of W-UO2 Cermets," *Journal of Nuclear Materials,* vol. 433, pp. 50-54, 2011.

[20] K. W. Nelson and S. P. Simpson, "Engine System Model Development for Nuclear Thermal Propulsion," in *AIAA Joint Propulsion Conference* , Huntsville, 2006.

[21] E. Gutierrez-Miravete, "Conduction Heat Transfer," 2006. [Online]. Available: http://www.ewp.rpi.edu/hartford/~ernesto/S2006/CHT/Notes/ch03.pdf. [Accessed 6 2014].

Dilatometry Characterization of CeO_2 Ceramic Discs as a Function of Temperature and Atmosphere

Daniel P. Kramer, Steve M. Goodrich, Chadwick D. Barklay, and Christofer E. Whiting

University of Dayton Research Institute, 300 College Park, Dayton, Ohio, 45469
937-229-1038; daniel.kramer@udri.udayton.edu

Abstract. PuO_2 fuel pellets are currently employed in space radioisotope power systems (RPS). PuO_2 under various conditions can release oxygen atoms resulting in a change in its stoichiometry. CeO_2 exhibits many similar properties compared to PuO_2 and has the added advantage that it is not radioactive allowing it to be used as a surrogate for PuO_2. In this study a Linseis L75 duel push rod vertical research dilatometer system was used to measure dimensional changes of cold pressed + furnace sintered CeO_2 discs which were next heated to soak temperatures of 1000°C and 1400°C while under various oxidizing (air) and reducing atmospheres (95% argon/5% hydrogen). The dilatometer system employed in these experiments is capable of measuring very small (sub-micron) dimensional changes during a time-temperature-atmosphere dilatometer experiment. The observed dimensional changes occurring in the ceramic discs can be related to changes in the stoichiometry of the CeO_2 which provides insight into how various sintering parameters may affect the mechanical characteristics of a ceramic component such as the manufacturing of a PuO_2 fuel pellet for space nuclear power applications.

Keywords: CeO_2, Thermal expansion, Dilatometry, Sintering, PuO_2, RTG

INTRODUCTION

Over the last several decades over twenty-five Radioisotope Power Systems (RPS) have been successfully employed on a number of deep space missions including Galileo (launched 1989 to Jupiter), Ulysses (launched 1990 as a Solar orbital), Cassini (launched 1997 to Saturn), New Horizons (launched 2006 - scheduled fly-by Pluto the summer of 2015) spacecraft, and Mars Science Laboratory's rover Curiosity (landed on Mars in 2011). RPSs utilize the heat released from the decay of the radioisotope plutonium-238 via thermoelectrics to provide all of the electrical power needed for the spacecraft. Plutonium-238 is used since it is a strong alpha emitter with a half-life of ~87.7 years.

The employed fuel is an oxide, $^{238}PuO_2$, in the form of a ceramic pellet which is fabricated using classical ceramic processing operations. $^{238}PuO_2$ is highly radioactive making it difficult to use in various experiments related to the development and the understanding of how various physical/chemical properties (such as particle size, particle size distribution, etc.) impact its ceramic processing characteristics. Therefore, the application of a non-radioactive surrogate material for performing various endeavors in support of space nuclear power efforts would result in reduced personnel exposure, and additionally in reduced associated costs.

One surrogate material under investigation is cerium dioxide (CeO_2). Cerium dioxide has a number of chemical and physical characteristics which makes it an attractive cold surrogate. One interesting chemical characteristic of PuO_2 is that it will readily release oxygen atoms under various reducing atmospheres which results in sub-stoichiometric oxides which can be designated as $^{238}PuO_{2-x}$. Similar to $^{238}PuO_2$, CeO_2 also tends to release oxygen atoms under reducing conditions forming sub-oxides. CeO_2 exhibits a cubic crystal structure which is maintained as it is reduced down to Ce_4O_7[1.2]. However, if the material is reduced even further to Ce_2O_3 it will undergo a crystalline structural transformation since Ce_2O_3 is hexagonal[3]. The reduction of CeO_2 to Ce_2O_3 with hydrogen has been shown to

consist of a number of intermediate compositions which exhibit a range of colors[4]. This study lists over thirty intermediate compositions between CeO_2 and Ce_2O_3 whose color palette ranges from pale yellow, grey-blue, dark blue, blue-black, black, to olive green.

In terms of ceramic processing, it is very important to understand a materials thermal expansion characteristic as a function of processing parameters. A material which has a relatively high coefficient of thermal expansion will be more susceptible to thermal cracking/shock during cooling from the sintering temperature compared to a material which has a lower coefficient of thermal expansion. Therefore, it is preferable to have a surrogate material for PuO_2 which also exhibits similar thermal expansion characteristics.

Figure 1 is a plot of the percent linear thermal expansions (dL/L) of PuO_2 and some of its sub-oxides, and CeO_2 as a function of temperature which was developed employing data obtained in the literature[5,6]. Comparison of the expansion data shown in the figure shows that CeO_2 has a thermal expansion ~10-15% greater compared to the thermal expansion of PuO_2 between room temperature and ~1700 K which is within the general temperature range for sintering these oxides. In general, it would be more desirable if the thermal expansion difference between the two sets of materials was smaller, but the difference should be satisfactory for performing experiments with CeO_2 as a surrogate for PuO_2. The thermal expansions of two of the sub-oxides of PuO_2 also presented in Figure 1 demonstrate that various sub-oxides of PuO_2 have even higher thermal expansions within the temperature range shown.

As a reference the thermal expansion of a common ceramic alumina (Al_2O_3) as a function of temperature is also shown in the figure[7]. Because of alumina's relatively high thermal expansion the processing of alumina based ceramic components typically require a slow cooling ramp to minimize crack formation. As presented in Figure 1 alumina's thermal expansion is ~20 to ~30% lower compared to PuO_2 and CeO_2 suggesting that the cooling profile of sintered ceramic compacts fabricated with these two materials should be carefully selected and controlled.

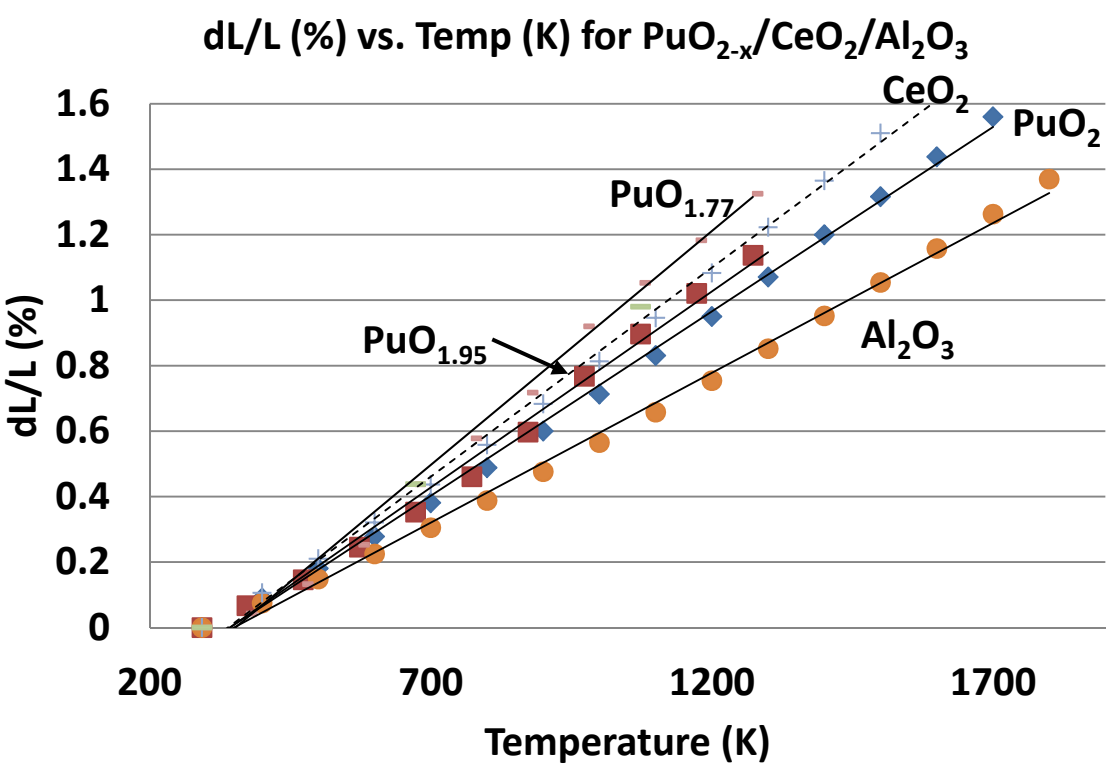

FIGURE 1. Comparison of the Percent Linear Thermal Expansion of PuO_2, $PuO_{1.95}$, $PuO_{1.77}$, CeO_2, and Al_2O_3 as a Function of Temperature.

DILATOMETER EXPANSION EXPERIMENTS AS A FUNCTION OF TIME, TEMPERATURE, AND ATMOSPHERE

CeO_2 Dilatometer Specimen Preparation

Since $^{238}PuO_2$ and CeO_2 have many similar properties a set of thermal expansion experiments were performed employing CeO_2 as a surrogate for $^{238}PuO_2$. For these experiments CeO_2 (99.9% trace metals basis) powder was obtained from Sigma-Aldrich (St. Louis, MO) with a reported particle size of <5µm. In fabricating the test specimens the CeO_2 powder was first loaded into a ~2.54 cm (~1") diameter steel die and it was cold pressed using a hydraulic press. After the green disc was removed from the steel die it was next sintered in air typically between 1400 - 1600°C for up to several hours. The theoretical densities of the sintered discs were in the 75% to 90% range which was easily controlled by the selection of the sintering temperature and soak time. Figure 2 (left) shows an example of a CeO_2 ceramic specimen disc which was cold pressed + air sintered.

The dilatometer employed in the experiments requires specimens less than ~6 mm (0.24") in diameter so they are able to fit into the unit. In order to fabricate sintered specimens of the require diameter a diamond core drill was used to cut-out smaller diameter specimens from the large diameter discs. The core drill was mounted on a drill press and the operation was performed while using water as a coolant. After some practice it was possible to obtain up to 4 or 5 small diameter sintered CeO_2 dilatometer specimens from a large diameter disc as shown in Figure 2 (right). An advantage of obtaining a number of individual dilatometer specimens from a single large diameter sintered disc is that all of the smaller specimens will have very similar densities. A potential disadvantage is that the core drilling operation itself could induce microcracks into the test specimens.

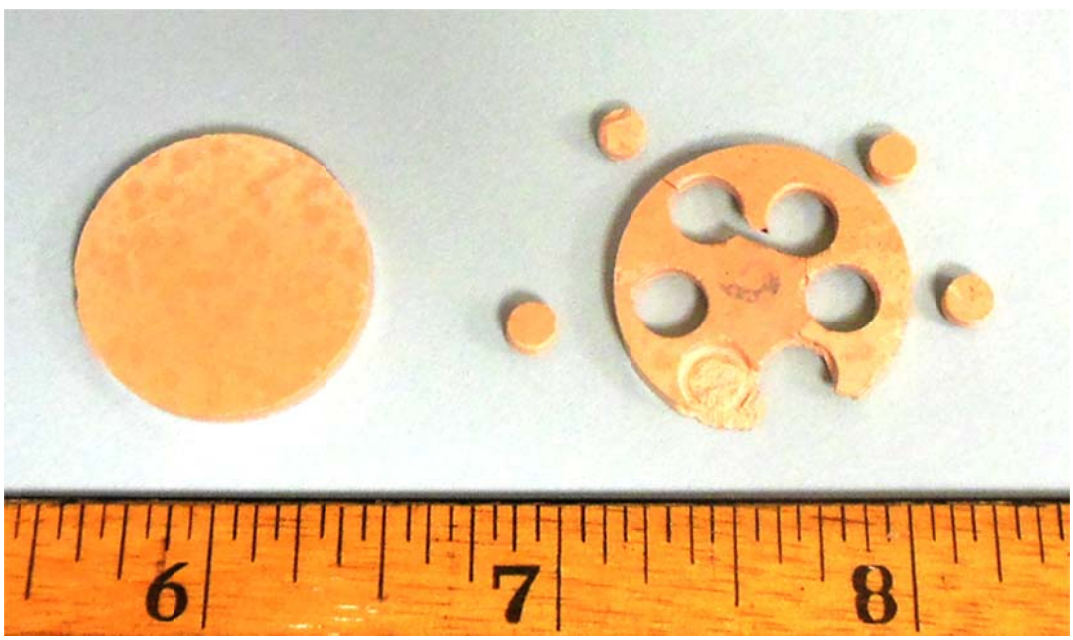

FIGURE 2. (Left) Example of a Sintered CeO_2 Ceramic Disc and (Right) Four Core Drilled Small Diameter CeO_2 Dilatometer Specimens.

Dilatometer Experimental Set-up

A Linseis Messgeraete GmbH (Selb, Germany) L75 duel push rod vertical research dilatometer system was used to measure dimensional changes of CeO_2 sintered specimens as a function of time, temperature, and atmosphere. Two LVDTs (Linear Variable Displacement Transducers) are used to accurately measure the expansion or contraction of the specimens during an experiment. Figure 3 shows the dilatometer used in the experiments which consists of a high temperature furnace (right-top), expansion measuring module (right-bottom), a gas management manifold (center), and a computer data acquisition system. The furnace has the capability of heating test specimens to above

1500°C while measuring very small changes in linear dimension. The gas management manifold is capable of providing a constant flow of a selected gas and automatically switching to another type of gas during an active experimental run.

FIGURE 3. Linseis Messgeraete GmbH L75 Duel Push Rod Vertical Research Dilatometer System Showing the Location of the Various Major Components.

A series of dilatometer experiments were performed using cored drilled small diameter CeO_2 pre-sintered discs as shown in Figure 2. Figure 4 (left) shows the high temperature furnace in the up position allowing the loading or unloading of test specimens. Figure 4 (right) shows the location of a CeO_2 test specimen after the completion of an experimental run. Since the dilatometer is a duel push rod system, two samples can be evaluated during each experiment. Typically, one CeO_2 specimen with a standard or two CeO_2 specimens would be run during a single experiment. Figure 4 (right) shows a single sample and an alumina standard each positioned on top of an alumina push rod after the completion of an experimental run.

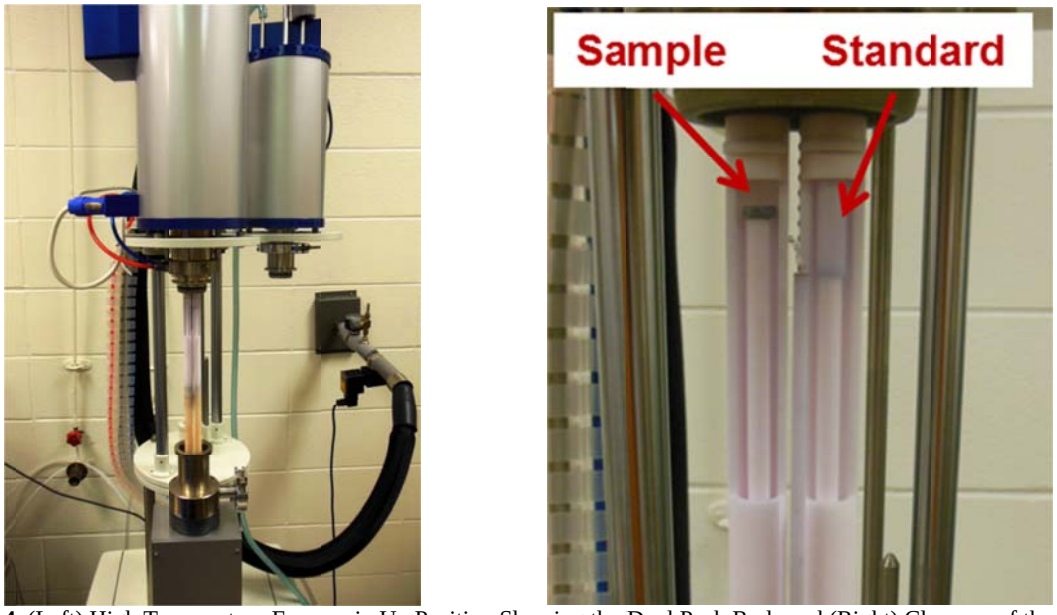

FIGURE 4. (Left) High Temperature Furnace in Up Position Showing the Duel Push Rods and (Right) Close-up of the Two Push Rods Showing the Position of a CeO_2 Disc Sample and an Alumina Standard after the Completion of an Experiment.

Prior to an experiment the dimensions of one or two pre-sintered core drilled CeO_2 discs are placed on the top of the push rod(s) of the dilatometer and the system readied to measure very small changes in linear dimension. The time-temperature profile is entered into the computer along with the selected cover gas(es) which is automatically switched during the run by the gas management manifold. Expansion/contraction is collected as a function of time, temperature, and atmosphere and after the completion of an experiment the data is analysed.

Dilatometer Experimental Results Obtained on Pre-Sintered Core-Drilled CeO_2 Specimens

Figure 5 shows two expansion vs. time plots obtained on two pre-sintered CeO_2 specimens "A" and "B" which were heated at 5°C/min from room temperature to 1000°C and then isothermally soaked for ~4 hours. Both CeO_2 test specimens were initially pre-sintered to ~77% theoretical density assuming a 100% theoretical density for CeO_2 of 7.1g/cm^3. The dilatometer system is capable of measuring very small changes in expansion as the y-axis scale in Figure 5 is in microns (µm).

During this experimental run the furnace gas atmosphere during the initial ramp up and during the first segment of the isothermal soak was air. After ~90 minutes the furnace gas atmosphere was changed from air (an oxidizing atmosphere) to 95% argon/5% hydrogen (a reducing atmosphere). At that point the plot demonstrates a rapid increase in the expansion of the two specimens. (Since the hydrogen to air explosive mixture ratio is between 5% to ~75%, the application of 95% argon/5% hydrogen is a safe experimental technique for obtaining a reducing atmosphere with a very minimal chance of unexpected consequences). The increase in measured expansion began to slow as a function of time and started to level off after ~two hours at a magnitude ~2x the initial expansion due to thermal expansion as the furnace temperature initially increased from room temperature to 1000°C. At that point the flow of the 95% argon/5% hydrogen cover gas was switched off and was replaced again with flowing air. The expansion vs. time plot shows an instantaneous and very rapid decrease in the expansion of the two specimens. After a very short time the expansion of "B" returns to basically its original expansion of ~40 µm. However, specimen "A" only contracts to ~50 µm and not to its original expansion of ~40 µm. A 5°C/min ramp was used during the cooling of the furnace and the test specimens back down to room temperature which is not shown in Figure 5.

The rapid change in expansion at the soak temperature when the furnace atmosphere was changed from air to 95% argon/5% hydrogen was likely due to the rapid reduction of the CeO_2 to CeO_{2-x}. After the furnace atmosphere was switched from 95% argon/5% hydrogen back to air, the specimen contracted sharply since it very rapidly re-oxidized from CeO_{2-x} back to CeO_2. The oxygen reduction of the specimen was anticipated but the exact value for "x" is unknown. This is mainly due to the inability of "quenching" and maintaining the sub-stoichiometric form of CeO_{2-x} produced during the experiments when re-exposed to air. Once reduced sub-stoichiometric specimens are re-introduced to an air atmosphere even at room temperature, re-oxidation initiates making X-ray diffraction, which could be used to determine stoichiometry, very difficult to be performed on the sub-stoichiometric specimens.

After the dilatometer system cooled down to room temperature the furnace was raised and the two specimens "A" and "B" were removed. It was determined that during the furnace cycle that specimen "A" had cracked into two pieces while specimen "B" was still integral and in one piece. The small separation between the two pieces of specimen "A" was determined to be the likely reason that its plot in Figure 5 did not return back to the original expansion of ~40 µm when air was reintroduce after ~400 minutes.

Figure 6 is an expansion vs. temperature plot obtained on a CeO_2 specimen heated to 1400°C at 5°C/min under an air atmosphere. The specimen was pre-sintered at 1500°C for only a short time so the contraction occurring in the figure during the ~90 minute isothermal soak is likely additional sintering of the specimen. The apparent contraction just before the start of the isothermal soak is unknown. After the initial ~90 minute isothermal soak under air, the gas atmosphere was changed to 95% argon/5% hydrogen. This initiated a rapid increase in expansion suggesting the reduction of CeO_2 to CeO_{2-x} was completed after only ~10 minutes. This compares to the time shown in Figure 5 which suggests that even after ~120 minutes at 1000°C the reduction of CeO_2 to CeO_{2-x} is not complete. Performing similar dilatometer experiments at different temperatures under different atmospheres it is possible to obtain some information on the kinetics of the reduction reaction.

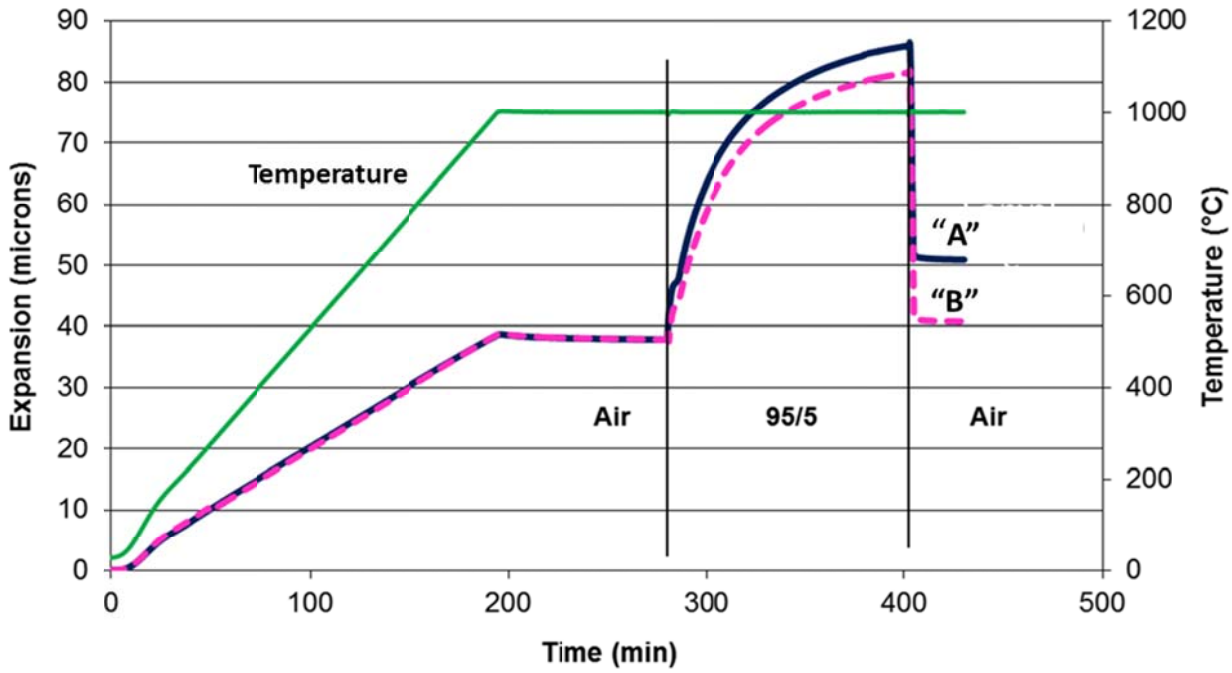

FIGURE 5. Expansion vs. Time Plots Obtained on Two Pre-sintered CeO_2 Specimens Heated to 1000°C while the Furnace Gas Atmosphere was Changed During the Experiment from Air, to 95%Argon/5%Hydrogen, and Back to Air.

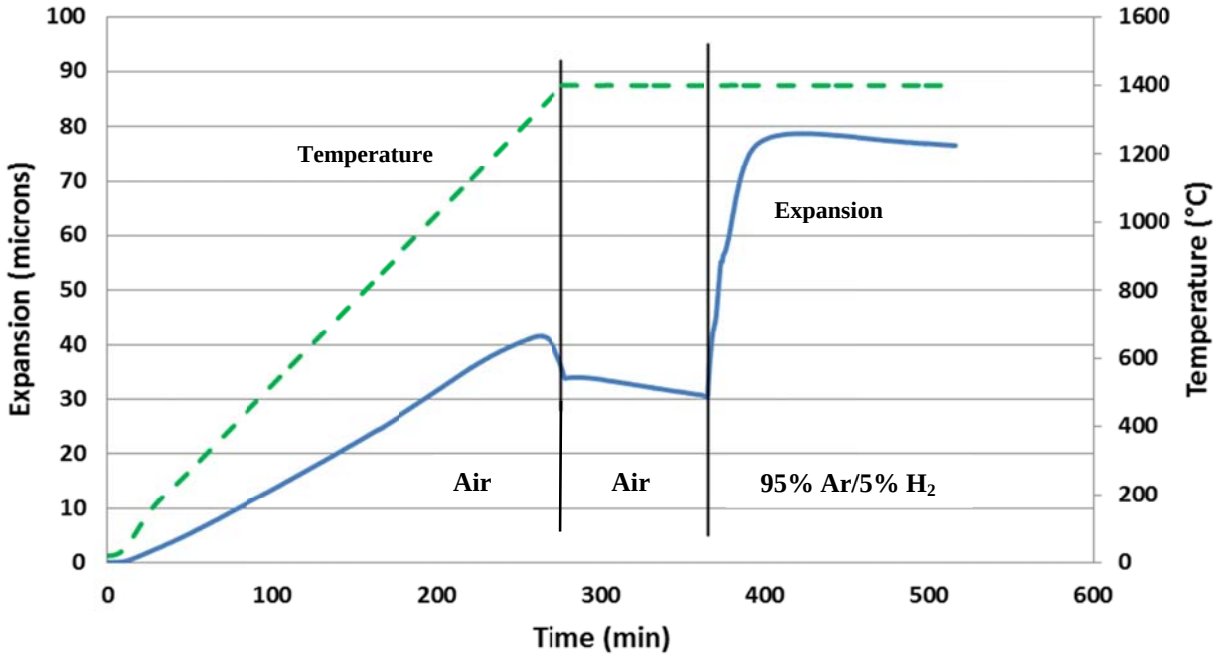

FIGURE 6. Expansion vs. Time Plot Obtained on a Pre-sintered CeO_2 Specimen Heated to 1400°C While the Furnace Gas Atmosphere was Changed During the Experiment from Air to 95% Argon/5% Hydrogen.

SUMMARY

Dilatometry has been demonstrated to be a useful technique for determining some of the expansion/contraction characteristics of CeO_2 as a function of time, temperature, and furnace atmosphere. CeO_2 has been shown to be susceptible to reduction and/or oxidation as a function of the experimental conditions. When CeO_2 specimens were heated to and isothermally soaked at 1000°C in an air atmosphere, specimen expansion was mainly due to thermal expansion. When the furnace atmosphere was changed to 95% argon/5% hydrogen, the specimen exhibited significant expansion likely from its reduction from CeO_2 to CeO_{2-x}. When the furnace cover gas was changed back to air, the contraction of the two specimens was rapid indicating re-oxidation back to CeO_2. A similar set of experiments were performed at 1400°C which showed the same general results when the furnace atmosphere was switched from air to 95% argon/5% hydrogen at temperature. However, at the higher temperature the reduction from CeO_2 to CeO_{2-x} was again very rapid but it apparently was completed in only one-tenth of the time it took for the reduction reaction to occur in the lower temperature experiment. The observed time for the reduction to occur at the two temperatures can be used to provide information on the kinetics of the reaction.

ACKNOWLEDGMENTS

This research was conducted under U.S. Department of Energy contract DE-NE0000422 and the technical support of Mr. Dirk Cairns-Gallimore (U.S. DOE) is greatly appreciated by the authors.

REFERENCES

[1] Pattern: 03-065-5923 (CeO_2), Inorganic Crystal Structure Database (ICSD), National Institute of Standards and Technology (NIST), Gaithersburg MD.
[2] Pattern: 03-065-7999 (Ce_4O_7), Inorganic Crystal Structure Database (ICSD), National Institute of Standards and Technology (NIST), Gaithersburg MD.
[3] Pattern: 00-023-1048 (Ce_2O_3), Inorganic Crystal Structure Database (ICSD), National Institute of Standards and Technology (NIST), Gaithersburg MD.
[4] Bevan, D.J.M., "Ordered Intermediate Phases in the System CeO2-Ce2O3," J. Inorganic and Nuclear Chemistry, v. 1, Pergamon Press Ltd., London, UK, page 49-page59, 1955.
[5] Touloukian, Y.S., *Thermophysical Properties of Matter*, v.13, IFI/Plenum, New York, page 331-page 335, 1977.
[6] Touloukian, Y.S., *Thermophysical Properties of Matter*, v.13, IFI/Plenum, New York, page 212-page 216, 1977.
[7] Touloukian, Y.S., *Thermophysical Properties of Matter*, v.13, IFI/Plenum, New York, page 176-page 193, 1977.

High-Rate Strain Testing on High-Strength Graphite as a Simulant for Fine Weave Pierced Fabric (FWPF) Aeroshell Material

Daniel P. Kramer, Susan I. Hill, John Chumack, Steve M. Goodrich, Chadwick D. Barklay, and Christofer E. Whiting

University of Dayton Research Institute, 300 College Park, Dayton, Ohio, 45469
937-229-1038; daniel.kramer@udri.udayton.edu

Abstract. Exploratory spacecraft to Pluto (New Horizons) and the surface of Mars (rover Curiosity) are powered by space nuclear power systems which convert the heat generated from the decay of the radioisotope plutonium-238 fuel into electricity. The $^{238}PuO_2$ fuel pellets are contained within several protective layers including an outer aeroshell which is fabricated using a ~3-D carbon/carbon composite (Fine Weave Pierced Fabric - FWPF). During an inadvertent launch incident the aeroshell is designed to tumble, and to help protect the integrity of the fuel pellets upon impact. Initial high-strain rate experiments have been performed on test specimens fabricated out of a high-strength graphite, as a low-cost simulant for FWPF, in order to enhance understanding of an aeroshell's response under high-rate strain impact scenarios.

Keywords: Fine Weave Pierced Fabric, FWPF, RTG, MMRTG, PuO_2

INTRODUCTION

Over the last several decades, Radioisotope Power Systems (RPS) have been successfully employed on a number of deep space missions. GPHS-RTGs (General Purpose Heat Source - Radioisotope Thermoelectric Generators) provided all of the electrical power for the Galileo (launched 1989 to Jupiter), Ulysses (launched 1990 as a Solar orbiter), Cassini (launched 1997 to Saturn), and New Horizons (launched 2006 scheduled to fly-by Pluto during the summer of 2015) spacecraft. Mars Science Laboratory's rover Curiosity (landed on Mars in 2011) is powered by another very similar type of RPS called a Multi-Mission Radioisotope Thermoelectric Generator (MMRTG). Both GPHS-RTGs and MMRTGs produce electrical power through the conversion of the decay heat released principally from the radioisotope plutonium-238. Plutonium-238 is employed as it is a strong alpha emitter with a half-life of ~87.7 years. Currently, thermoelectric materials (SiGe unicouples in GPHS-RTGs and TAGS-85 in MMRTGs) are utilized to convert the released heat into electrical energy with a typical thermal-to-electrical conversion efficiency of ~5 to 7%. Future planetary space missions that will require an RPS will most likely employ the MMRTG, shown as a schematic cutaway in Figure 1 (left).

RPSs, such as the MMRTG, are very carefully designed to protect and contain the radioactive ^{238}Pu material during normal use conditions and in case of launch accident or inadvertent re-entry scenarios. Several of the safety aspects designed into an MMRTG are presented in Table 1. The employed fuel is an oxide, $^{238}PuO_2$, in the form of a ceramic pellet which is fabricated using classical ceramic processing operations. After fabrication, the pellets are welded inside an iridium alloy cladding. Iridium does not interact detrimentally with the fuel pellet and remains ductile at the high operating temperatures of an MMRTG. The iridium alloy is designed to help protect the fuel pellet during any inadvertent impact scenario. After welding, two cladded fuel pellets are loaded into a Graphite Impact Shell (GIS) which also is designed to protect the fuel under an inadvertent impact scenario. Two loaded

Graphite Impact Shells are then installed into a General Purpose Heat Source (GPHS) aeroshell which is designed to withstand re-entry environments. The MMRTG metal alloy housing is designed to release the 8 modules in the GPHS stack during an inadvertent event.

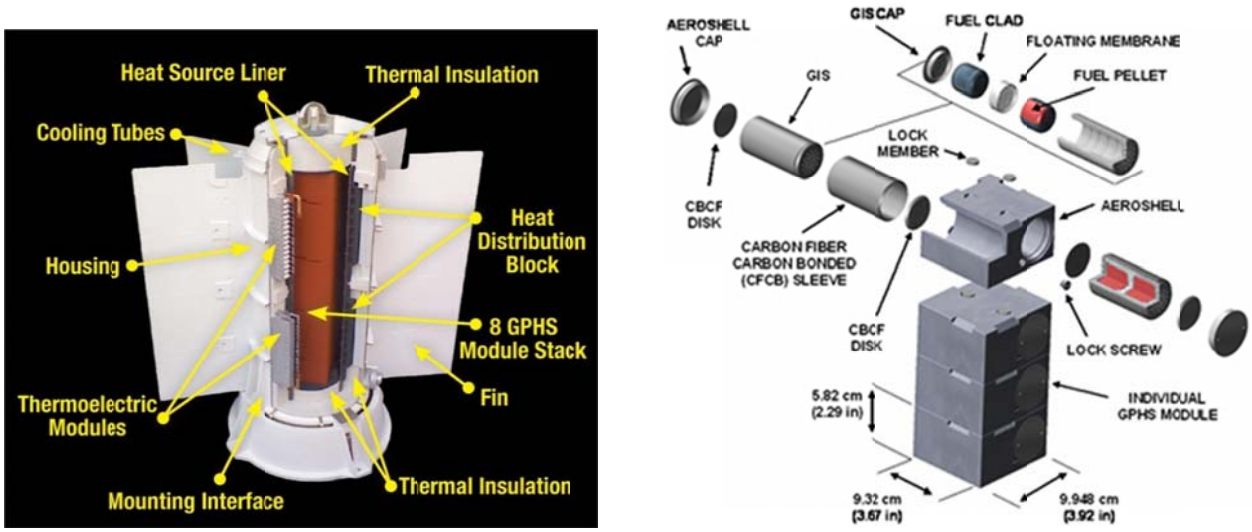

FIGURE 1. (Left) Schematic of a Multi-Mission Radioisotope Thermoelectric Generator Showing Several Internal Components and (Right) Schematic of a Four GPHS Stack Showing How Various Components are Arranged and Assembled.

TABLE 1. RPSs Contain Various Design Attributes Employed to Enhance Safety.

Design Attribute	Safety
Oxide Fuel	Chemically stable
Ceramic Pellet	Minimizes particle fines
Iridium Cladding	High temperature ductility
Graphite Impact Shell	Adds impact strength
Low Melting Housing	Aids separation of individual GPHSs
GPHS Modules	Aeroshell material
GPHS Stack Release	Separation of individual GPHSs

The GPHS modules employed in Galileo, Ulysses, Cassini, Curiosity, and New Horizons RPSs were all fabricated out of Fine Weave Pierced Fabric (FWPF) which is a ~3-D carbon-carbon material. GPHS modules have been carefully designed to protect the nuclear fuel in case of inadvertent conditions that could occur during the life of the RPS including terrestrial transport, inadvertent launch events, or re-entry scenarios. Many of the chemical and physical properties of FWPF play an important role in the utilization and protection of the $^{238}PuO_2$ fuel. Recent research has been performed on FWPF specimens employing high power lasers to simulate the extremely rapid thermal ramp that is expected to result from atmospheric re-entry and cause oxidation of the carbon-based aeroshell material [1,2]. Obtaining these ablation characteristics helps us understand the behavior of a GPHS module during a hypothetical re-entry scenario, and improves our ability to properly assess the safety analysis during the launch of a GPHS based RPS. Understanding the impact characteristics of FWPF is another property that will help improve our ability to perform safety analysis on the GPHS design. In an attempt to simulate the forces experienced during a theoretical impact scenario, the research presented here will test the performance of initial high-rate strain experiments on test specimens fabricated out of a high-strength graphite, as a low-cost simulant for FWPF.

HIGH-RATE STRAIN TESTING EXPERIMENTS

Specimen Preparation

FWPF is a specialized re-entry aeroshell material which has very limited availability and is expensive. So a simulant material was employed in these initial high-rate strain experiments. Test specimens were machined out of EDM-3 which is an isotropic fine grained graphite with excellent surface finish machining characteristics. EDM-3 is manufactured by POCOGRAPHITE (Decatur, TX). Some of EDM-3's physical and mechanical properties are presented in Table 2. Several of the chemical and physical properties of EDM-3 reasonably mimic those of FWPF making it a realistic simulant for the current set of experiments.

TABLE 2. Some Typical Property Data on EDM-3[3].

Property	Typical Value
Average Particle Size	<5μm
Flexural Strength	935 kg/cm^2 (13,300 psi)
Compressive Strength	1,273 kg/cm^2 (18,100 psi)
Hardness	73 Shore
Electrical Resistivity	15.6 μΩm (615 μΩin)

Tensile test bars were fabricated out of EDM-3 0.38 cm thick x 10.16 cm x 15.24 cm (0.15" x 4" x 6") sheet stock. The bottom and top surfaces of the sheet stock were ground flat prior to the fabrication of the tensile bars. The tensile bars were machined out of the EDM-3 sheet stock to ISO 8256 Type 3 dimensions as presented in Figure 2[4]. This specimen type ensured a large surface area for loading the bars within the grips of the servo-hydraulic test station. The gage length and gage width were both machined to be 10 mm. After machining was completed, all of the gage area surfaces of the machined tensile bars were carefully checked to ensure that they were smooth with no irregularities which could affect the mechanical test results.

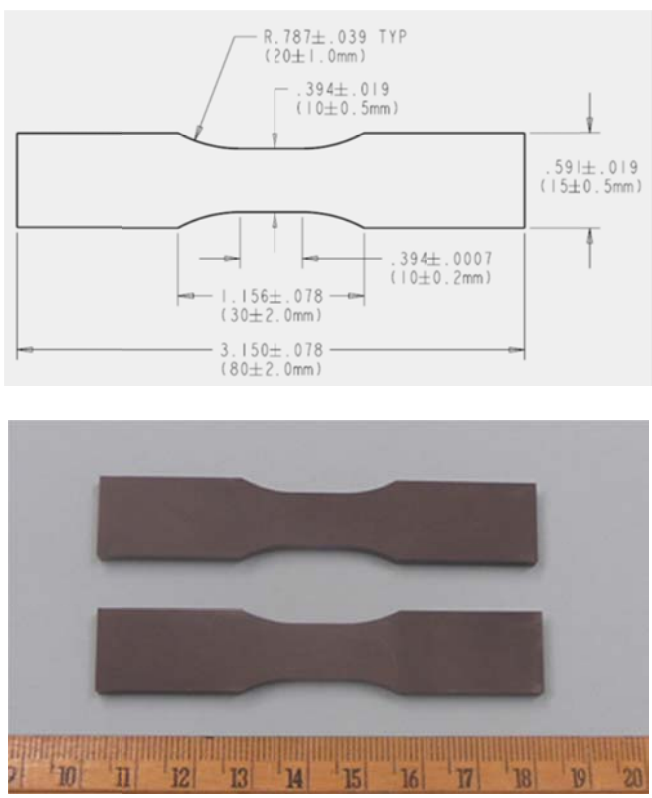

FIGURE 2. (Top) Dimensions of ISO 8256 Type 3 Tensile Specimens and (Bottom) Examples of Tensile Bars Machined out of EDM-3 Graphite. The Scale is in Centimeters.

High-Rate Strain Testing of EDM-3 Test Specimens

The specimens were tested at 9.906 meters/s (390 in/sec) in a MTS Systems Corporation (Eden Prairie, MN) servo-hydraulic test station equipped with a 14,680 N (3300 lb_f) actuator. Figure 3 (top) shows the servo-hydraulic test station. Load was measured with a piezoelectric washer and the full-scale load was 4,448 N (1,000 lb_f). Strain gages were located on both faces of the test specimens at the center of the straight gage section and each gage was wired as a quarter bridge. Data were collected separately for each gage and averaged to compensate for any potential bending moment which could have occurred during the high-rate strain experiments. The strain gages were Vishay Micro-Measurements (Raleigh, NC) CEA-06-125-UW120. CEA strain gages use a constantan foil with a high-elongation polyimide backing and are a general purpose strain gage with a gage length of ~0.32 cm (0.125”). The strain gages were bonded to the test specimens with Vishay Micro-Measurements M-Bond AE-10. Figure 3 (bottom) is a test specimen prior to testing showing one of the bonded strain gages as the second one is positioned on the other side of the gage length out of view. Prior to applying the adhesive, the gage bonding areas of each specimen were very lightly sanded to improve the adhesion of the strain gages. The full-scale test setting for all of the high-rate strain experiments was 5% strain. Figure 4 (left) shows a test specimen after the completion of a test while still in the servo-hydraulic test station, and Figure 4 (right) shows a test specimen after removal from the test station. In all of the high-rate strain experiments failure occurred within the gage length of the specimen. Some of the experimental test results are summarized in Table 3 and the stress-strain curves are presented in Figure 5.

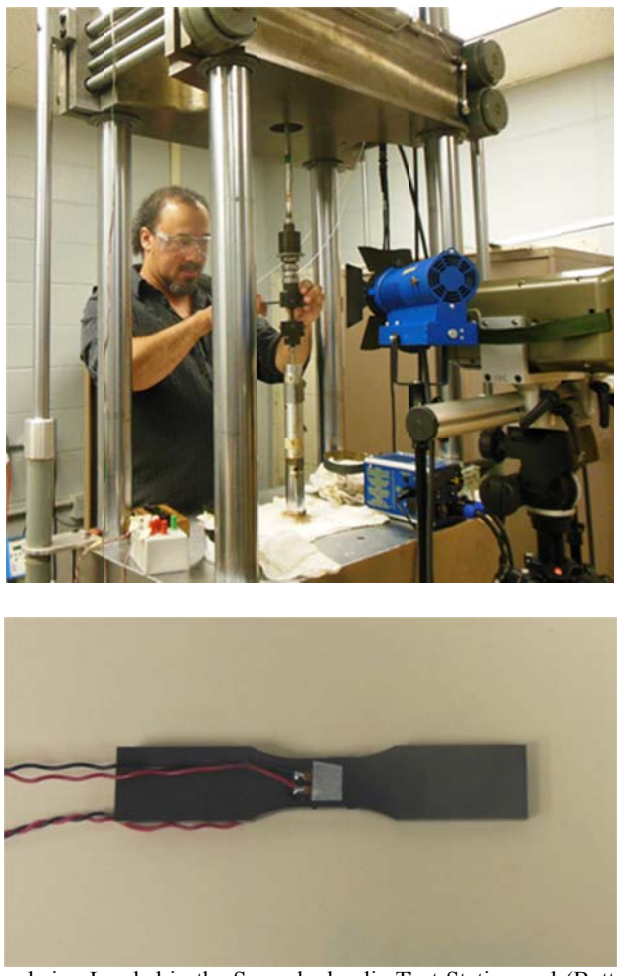

FIGURE 3. (Top) Test Specimen being Loaded in the Servo-hydraulic Test Station and (Bottom) Test Specimen Showing the Location of One of the Two Strain Gages Mounted in the Gage Area of the Test Specimen.

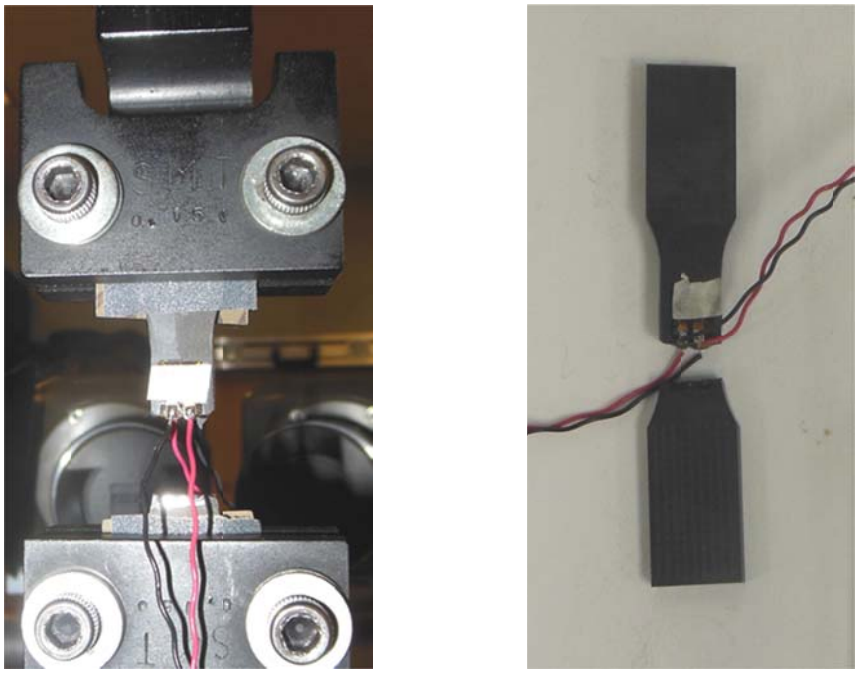

FIGURE 4. (Left) Test Specimen After a High-Strain Rate Experiment and (Right) After Removal from the Test Station with Both Strain Gages Still Attached to the Specimen.

STL #3 was used as a test set-up specimen, so it was not strain gaged and only load and displacement data were captured when it was tested. Strain gages were positioned on both sides of specimen STL #1 and STL #2. The measured strain rates before failure 59.4/s and 50.6/s for STL#1 and STL#2, respectively. The measured strain rates before failure were much lower than the nominal rate of 990/s.

The stress-strain curve for specimen STL #1 in Figure 5 is based on a single gage since one of the strain gages on this specimen did not function properly during the experiment due to a data acquisition error. Some initial bending was present upon load introduction. The lower apparent modulus and higher failure strain of STL #1 probably reflects the lack of compensation for bending.

TABLE 3. Summary of Data Collected During Three of the High-Rate Strain Experiments Performed on EDM-3 ISO 8256 Type 3 Tensile Bar Specimens.

Specimen	Ultimate Failure Stress	Strain at Failure	Modulus	Machine Rate	Nominal Plastic Strain Rate	Measured Strain Rate	Comments
STL #1	57.2 MPa (8,300 psi)	1.02%	9997 MPa (1.45 Msi)	9.804 m/s (386 in/s)	983/s	59.4/s	Single strain gage as one failed
STL #2	58.2 MPa (8,440 psi)	0.79%	13,100 MPa (1.90 Msi)	9.931 m/s (391 in/s)	996/s	50.6/s	Back-to-back strain gages averaged to compensate for potential bending during test
STL #3	51.4 MPa (7,460 psi)			8.661 m/s (341 in/s)	869/s		Set-up specimen not strain gaged

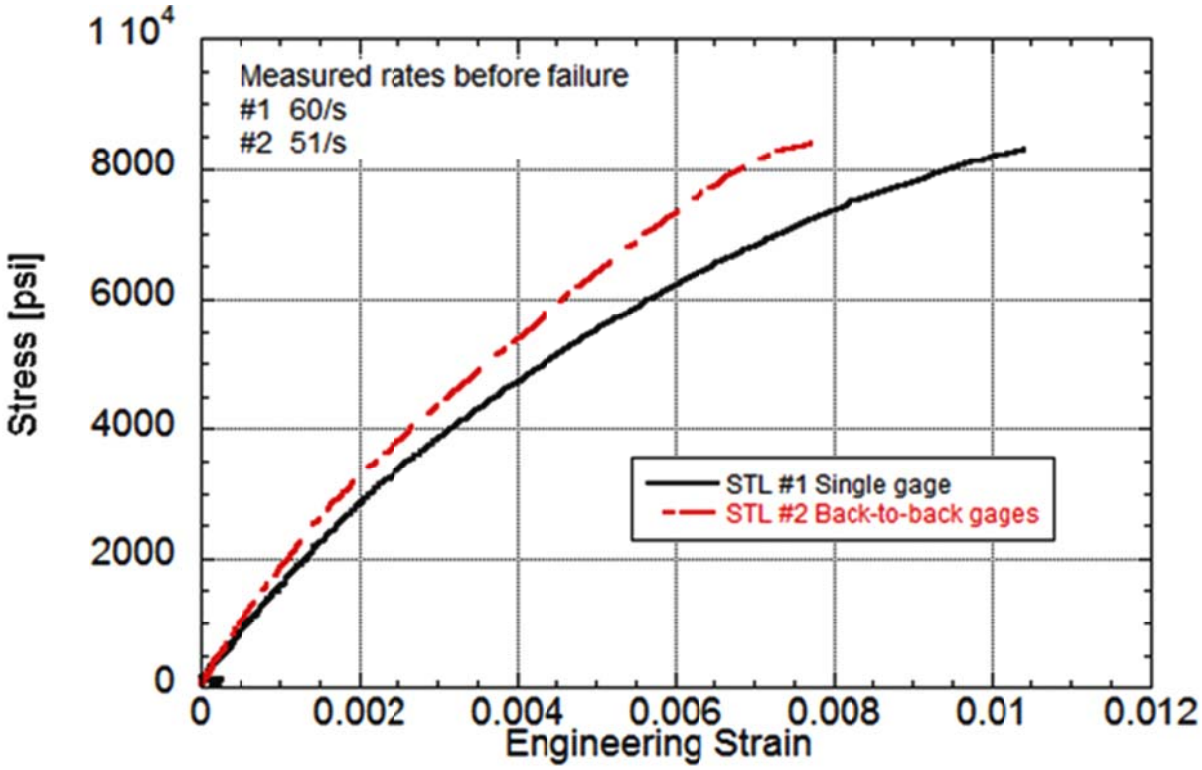

FIGURE 5. Stress vs. Strain Curves Obtained on EDM-3 Tensile Specimens STL #1 and STL #2.

SUMMARY

Initial high-rate strain tests on tensile bars machined out of EDM-3 graphite were completed. Due to the limited availability and cost of FWPF, EDM-3 was used instead of FWPF for the fabrication of the test specimens for this set of experiments. Strain gages were mounted on test specimen's gage length prior to testing. The high-rate strain experiments were performed in a servo-hydraulic test station capable of machine speeds of up to 22 m/s. Strain rates on the specimens were measured to be in the 50 to 60/s range at a test rate of 9.85 m/s. The failure strain was ~1%. The ultimate tensile strength was 57.7 MPa and the measured modulus ranged from 10 to 13 GPa. The test results demonstrate that the servo-hydraulic test equipment and the developed testing procedures can be employed to obtain high-rate strain data on graphitic materials such as EDM-3 and ultimately on FWPF. Performing future high-rate strain experiments employing FWPF test specimens would enhance understanding of MMRTGs aeroshell's response to inadvertent conditions that could occur during the life of the RPS including during terrestrial transport, inadvertent launch events, and/or unexpected re-entry scenarios.

ACKNOWLEDGMENTS

This research was conducted under U.S. Department of Energy contract DE-NE0000422 and the technical support of Mr. Dirk Cairns-Gallimore (U.S. DOE) and Mr. Ryan Bechtel (U.S. DOE) is greatly appreciated by the authors.

REFERENCES

[1] Kramer, D.P, Barklay, C.D., Goodrich, S.M., and Cairns-Gillimore, D., "Laser Simulated Re-Entry Oxidation Experiments on Possible Replacement Materials for FWPF in $^{238}PuO_2$ Fueled Space Power Systems," Proceedings of NETS 2011 - Nuclear and Emerging Technologies for Space Conference, paper #3259, ANS Order #700365, Albuquerque, NM, February, 2011.

[2] Kramer, D.P., Barklay, C.D., Goodrich, S.M., Whiting, C.E., and Cairns-Gallimore, D., "High-Power Laser Experiments on Rotating Small-Scale GPHS Modules," Proceeding of NETS 2014 - Nuclear and Emerging Technologies for Space Conference, NASA/Stennis, MS, February 2014.

[3] Sheppard, R.G., Morgan, D., D.M. Mathes, and Bray, D.J., "Properties and Characteristics of Graphite," POCO Graphite, Inc., Decatur, TX, page 3, 2002.

[4] ISO 8256, "Plastics – Determination of Tensile-Impact Strength," International Organization for Standardization, Geneva, Switzerland, 1990.

Radioisotope Fueled Thermophotovoltaic Power Systems for Space Applications

Jason Strauch[1], Andre Klein[1], Patrick Charles[1], Chris Murray[2], Miting Du[3]

[1]*Special Projects Office, General Atomics, San Diego, CA 92121*
[2]*Power Paragon, L-3 Communications, Anaheim, CA 92806*
[3]*Oak Ridge National Laboratory, Oakridge, TN 37831*

Abstract. Thermo-photovoltaic (TPV) based power systems are of particular interest to any system requiring solid state long life power, such as deep space missions. General Atomics has done extensive testing and development in small-scale TPV power systems in the milli-Watt to 10s of Watts scale. The most significant contributions have been in the electrical testing of a watt-scale TPV system and in studying neutron degradation in a mW-scale, fueled TPV power source. When comparing competing technologies for use with a radioisotope heat source, a critical criteria is that the power generating technology is not subject to excessive degradation due to exposure to the heat source radiation or space based radiation. This paper describes the analysis, modeling and testing of 0.6 eV Indium Gallium Arsenide (InGaAs) fueled TPV devices with special consideration paid to neutron degradation. The purpose of the paper is to present the research showing the relative device degradation as observed in actual radioisotope fueled power systems, as well as the design space and considerations of an electrically heated TPV power system. As part of General Atomics Internal Research and Development (IRAD) program the microscale mW power level MIPS was scaled up to designs at the single Watt and multi Watt level. Neutron degradation of 0.6% per year of the InGaAs TPV devices has been predicted and measured for Plutonium 238 radioisotope heat sources. Leading from the small scale TPV power system work, larger scale systems were designed and an electrically heated 1-2 Watt scale of TPV power system has been tested to assess system efficiency and power output relative to thermal input. In addition, designs for high power systems to many 10s of Watts have been developed based on standard NASA GPHS heat sources.

Keywords: Thermophotovoltaics, Spacepower, Energy Conversion, Radioisotope Power Sources, Solid State Power Conversion, GPHS

FUELED MILLIWATT-SCALE TESTING AND DEVICE DEGREDATION

A millWatt scale radioisotope thermophotovoltaic (RTPV) power system was develop for the Micro-Isotope Power System (MIPS) program funded by DARPA. This work led to the first radioisotope fueled TPV power system being tested at Oak Ridge National Laboratory. This work led to further understanding of small and larger scale RTPV power, and long term performance data on the fueled RTPV system.

Methodology

There are a variety of methods that may be employed to accurately predict the amount of degradation a semiconductor will experience, with a primary driver being the need to get a long term prediction in an accelerated time frame. Methods include neutron irradiation by an electron beam source, allowing precise control of the neutron fluence, as well as exposure to radioisotopes with a higher level of neutron emissions than the fuel of interest, which is Plutonium 238. As part of the DARPA funded MIPS (Micro-Isotope Power Source) program, both of these methods were employed and the fueled power system degradation data is presented here.

Degradation Physics

Testing has been performed at Oak Ridge National Laboratories (ORNL) with the MIPS TPV power system using both Curium 244 and Plutonium 238. Curium 244 was used due to its high energy density and ability to duplicate many years of neutron damage with testing in a shorter several month time frame. The degradation acceleration factor between Curium 244 and Plutonium 238 is over a factor of 400, with the physics described in Figure 1 below.

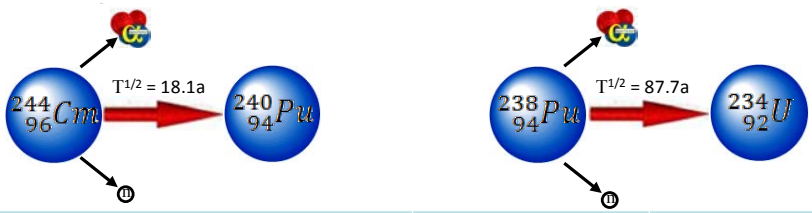

	^{244}Cm	^{238}Pu
Neutrons per spontaneous fission	2.72	2.22
Spontaneous fission branching ratio	1.37×10^{-4} %	1.85×10^{-7} %
Activity per gram of isotope	2.99×10^{12} dis/s-g	5.94×10^{11} dis/s-g
Neutrons emitted per sec per gram	1.12×10^{7} n/s-g	3.81×10^{3} n/s-g (1)
Fuel loading	0.2 g	1.4 g
Neutrons per sec	2.23×10^{6} n/s	5.55×10^{3} n/s
Acceleration factor at beginning of life	420	1

(1) Includes neutrons due to <a,n> reactions with oxygen assuming 90% ^{16}O enrichment (1,400 n/s-g)

FIGURE 1. Neutron degradation factors of Cm244 and Pu238

Based on this acceleration factor, the MIPS experiment was run using a Curium 244 heat source for over 120 days, which provides over 100 years of effective neutron degradation to the semiconductor InGaAs TPV devices. The plot below shows graphically the time relation between the two different neutron sources of degradation, and it can be seen that testing was performed beyond the asymptote of the relative life graph shown in Figure 2. The half life equivalents of Plutonium 238 to Curium 244 are shown with the dotted lines in the chart, and show that Curium 244 testing was performed beyond the 4th half life equivalent of Plutonium 238, and thus beyond the vertical asymptote where the Plutonium 238 pellet will have cooled beyond the point of useful heat generation.

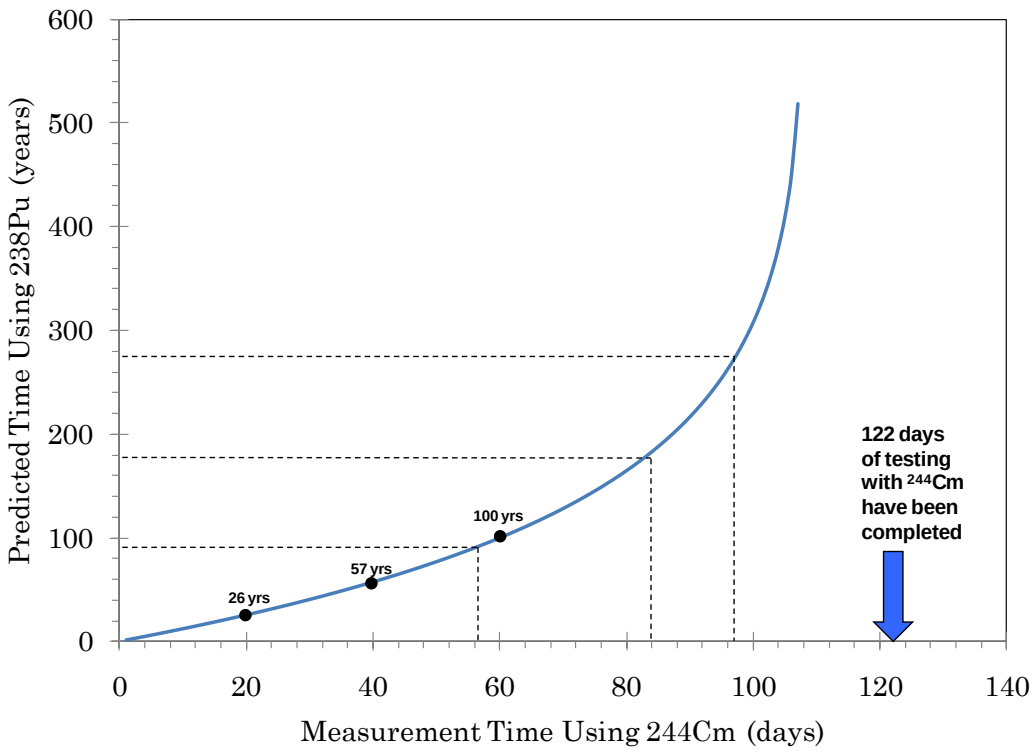

FIGURE 2. Neutron degradation damage time correlation between Cm244 and Pu238

In addition to the testing performed with the Curium 244 heat source, a thermally equivalent heat source of enriched Pu238 was produced at ORNL and used for testing the MIPS system, equipped with different undamaged TPV cells. This testing was performed for a total of over 500 days and the results for the first year are shown in Figure 3. The degradation of the system power output tracks almost exactly along the prediction based on the nuclear physics and shows a total power degradation level of about 1% per year, which is a combination of the radioisotope decay (temperature of heat source decreasing) and cell degradation (neutron induced damage and dislocations to the semiconductor). This Plutonium 238 heat source was not oxygen enriched, so still has the degradation mechanisms due to the alpha-N reaction of the of the other isotopes of oxygen present in the fuel source. During the DARPA Radioisotope Micropower Source (RIMS) program 0.6 eV InGaAs TPV devices were bombarded with an electron beam to perform accelerated life testing, and Monte Carlo analysis was performed to develop the degradation model that is used to generate the predicted power output shown in Figure 3. The more recent Plutonium 238 test data shows very good correlation to those 10 year old models, and the experimental results indicate the 0.6 eV InGaAs devices have less than 1% degradation per year due to neutron damage.

Results

In addition to the testing performed with the Curium 244 heat source, a thermally equivalent heat source of enriched Pu238 was produced at ORNL and used for testing the MIPS system, equipped with different undamaged TPV cells. This testing was performed for a total of over 500 days and the results for the first year are shown in Figure 3. The degradation of the system power output tracks almost exactly along the prediction based on the nuclear physics and shows a total power degradation level of about 1% per year, which is a combination of the radioisotope decay (temperature of heat source decreasing) and cell degradation (neutron induced damage and dislocations to the semiconductor). This Plutonium 238 heat source was not oxygen enriched, so still has the degradation mechanisms due to the alpha-N reaction of the of the other isotopes of oxygen present in the fuel source. During the DARPA Radioisotope Micropower Source (RIMS) program 0.6 eV InGaAs TPV devices were bombarded with an electron

beam to perform accelerated life testing, and Monte Carlo analysis was performed to develop the degradation model that is used to generate the predicted power output shown in Figure 3. The more recent Plutonium 238 test data shows very good correlation to those 10 year old models, and the experimental results indicate the 0.6 eV InGaAs devices have less than 1% degradation per year due to neutron damage.

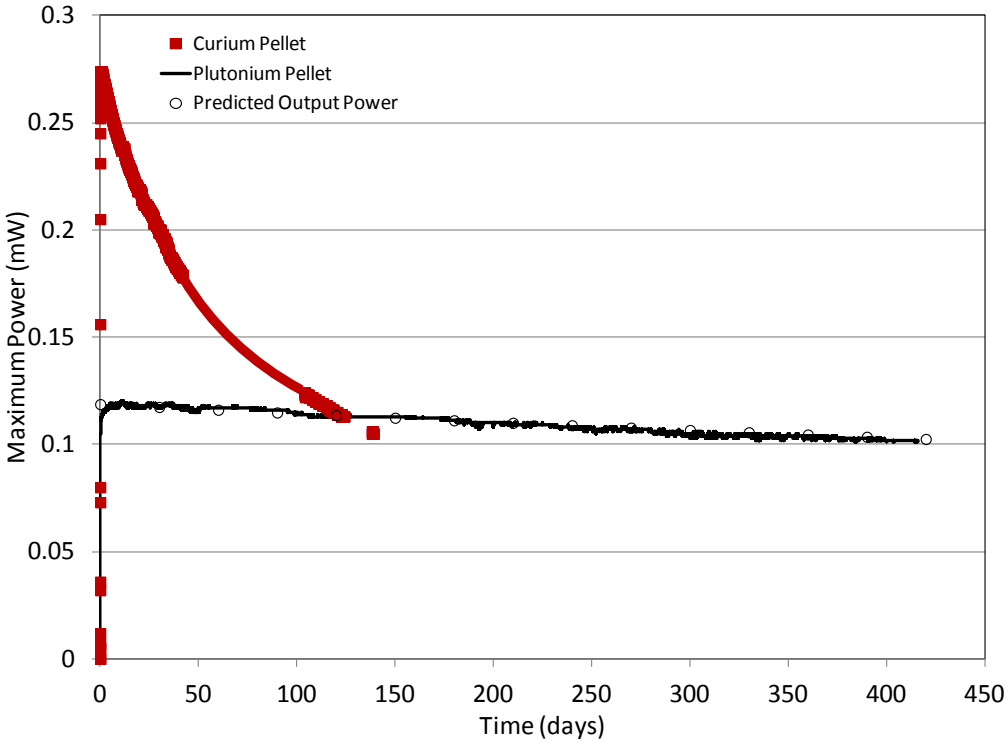

FIGURE 3. TPV Power System Radioisotope testing results compared to model

WATT SCALE POWER SYSTEM TESTING

Following the work funded by DARPA on the MIPS (Micro-Isotope Power Source) program, General Atomics continued to research scaled up versions of a thermo-photovoltaic (TPV) power system fueled by a radioisotope heat source. The 1-10 Watt scale of power system developed and tested by General Atomics has applications to aerospace power systems such as the new generations of smaller and more capable spacecraft and satellites being developed by NASA and others. Beyond being simply an electrically heated test of the TPV power system, this development and testing is of a complete hermetically sealed system and demonstrates true system efficiency testing as the ratio of the input electrical power (thermal power) and the electric power produced by the TPV power system.

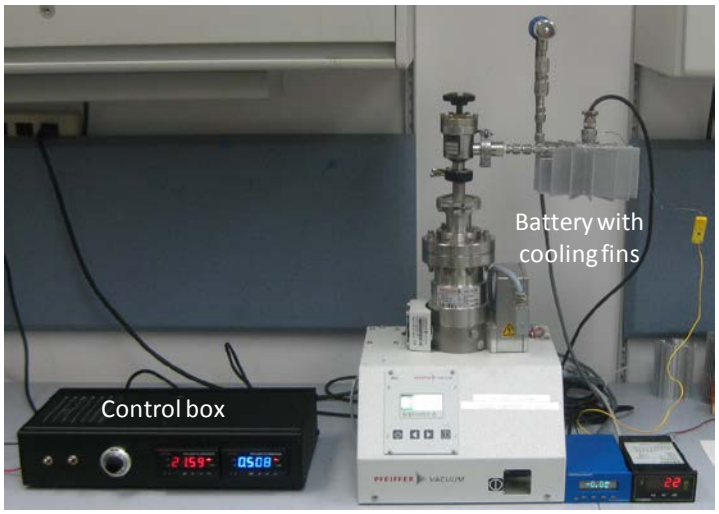

FIGURE 4: TPV Power System Testing Set Up

Methodology

The TPV power system was assembled and tested within a large vacuum system during development. Once system design parameters had been optimized and power levels were at expected levels, the system was moved to external testing, initially while under externally driven vacuum and then finally as a standalone power system which is hermetically sealed and maintains vacuum during testing out in atmospheric conditions without active vacuum pumping. The system also employed passive convective cooling for the earth atmosphere testing (cooling fins shown in Figure 4), though is designed to be integrated as a power supply (battery) into a full space power system. Figure 5 shows the power systems configurations that have been tested: one including an in-situ vacuum sensor to determine vacuum levels during testing, and a second as the standalone power system.

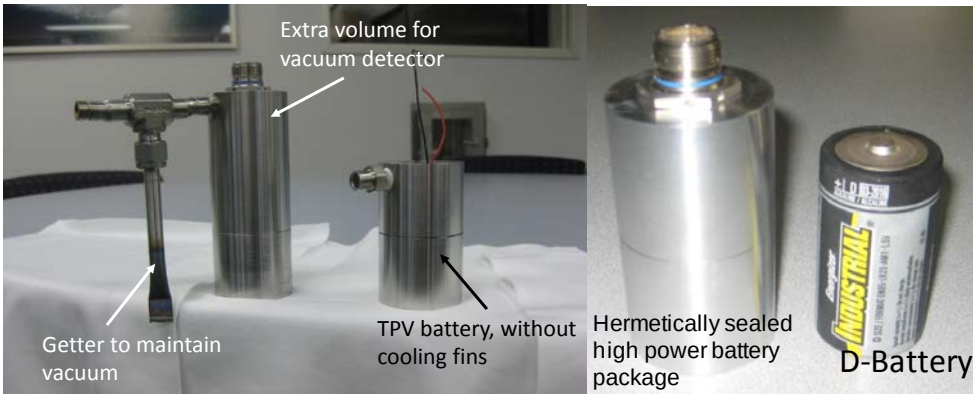

FIGURE 5. Tested power systems showing vacuum connection and comparison to a standard D cell

Results

Testing has provided results of interest at different power levels and scales. While the mW scale MIPS TPV power system was on the order of (much) less than 1% system efficiency, this larger scale system has efficiency of 5% or greater, depending on input power. The input power can be equated to isotope loading for a radioisotope heated TPV power system.

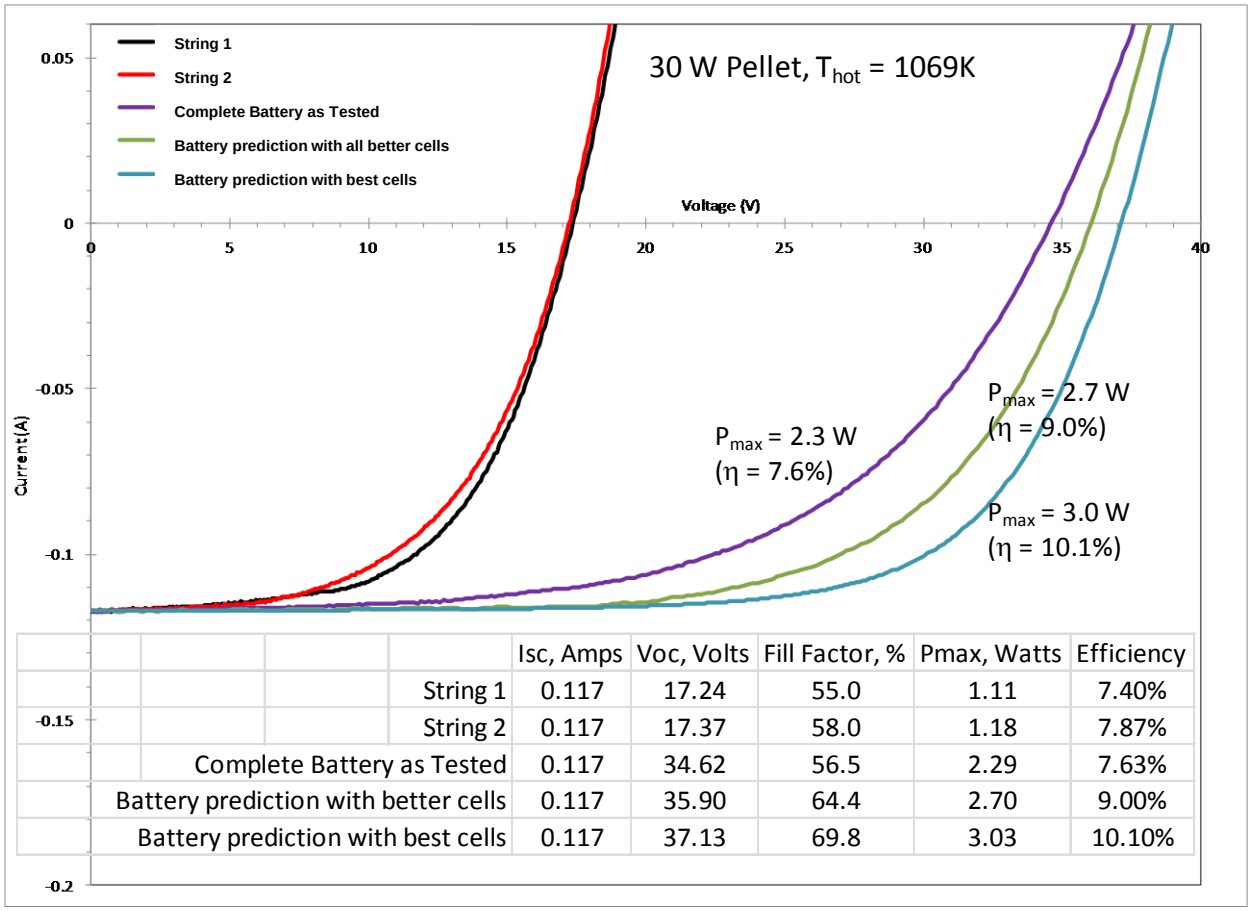

	Isc, Amps	Voc, Volts	Fill Factor, %	Pmax, Watts	Efficiency
String 1	0.117	17.24	55.0	1.11	7.40%
String 2	0.117	17.37	58.0	1.18	7.87%
Complete Battery as Tested	0.117	34.62	56.5	2.29	7.63%
Battery prediction with better cells	0.117	35.90	64.4	2.70	9.00%
Battery prediction with best cells	0.117	37.13	69.8	3.03	10.10%

FIGURE 6. Measured results of 2.29 W (7.6% efficiency) at 30 W pellet conditions

The black and red lines are actual measured data from our system, with the purple line being the sum of those individual strings. Testing was performed using the best available cells at the time, with one an 'A grade' and the balance not as high performing. The actual system testing resulted in a peak of 7.6% efficiency. The system efficiency using all cells equal to the best single cell was estimated at 9%, and if using all best quality cells, would produce over 3 Watts with 10% efficiency. This testing and modeling indicate that 10% system efficiency is attainable at this scale and that higher efficiencies are attainable with higher fuel loadings in larger systems. Thermo-photovoltaic power systems have a large dependency on heat source temperature, which is related to the surface area to volume ratio of the heat source. This results in about a temperature to the 8th power effect (T^8) [1], and the ability of the TPV power system to produce vastly more power with only slight increases in volume and mass (thus temperature). The scaling of power with system volume is shown in Figure 7, and includes data from both the recent larger single Watt power level system and the prior DARPA microscale TPV power system, MIPS.

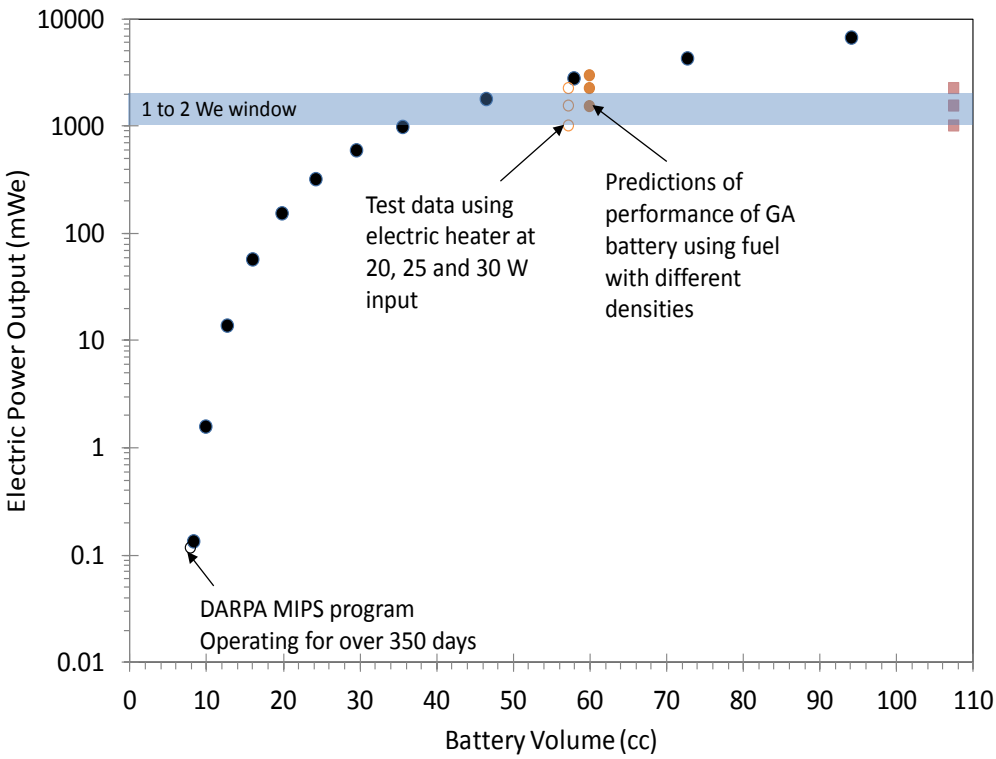

FIGURE 7. TPV Power System Scaling

RECENT TPV POWER SYSTEM WORK

Most recently GA has developed a TPV power system specifically using a NASA General Purpose Heat Source (GPHS) pellet and cladding design with the same graphite impact shell, carbon fiber sleeve and aeroshell thickness as previous launch approved systems have used. This system design is 7 cm tall by 6 cm diameter (a bit larger than a D cell battery at 6.1 cm tall by 3.3 cm diameter), but modeling indicates that it will put out 7 W of electric power at beginning of life at near 12% efficiency. The reason for the increased power in almost the same form factor is that the GPHS heated system is NOT designed to contain the 20 year buildup of helium pressure, thus has more fuel at over 60 W of thermal power compared to the data herein, which is based on a 20-30 W thermal fuel pellet (thermal power depends of fuel density and purification level). The NASA specific design is based on NASA's standard GPHS module and will be developed into a hardware test demonstration when funding becomes available. Figure 8 shows a comparison of a TPV power system's specific power vs mission duration to that of the Voyager's RTG system.

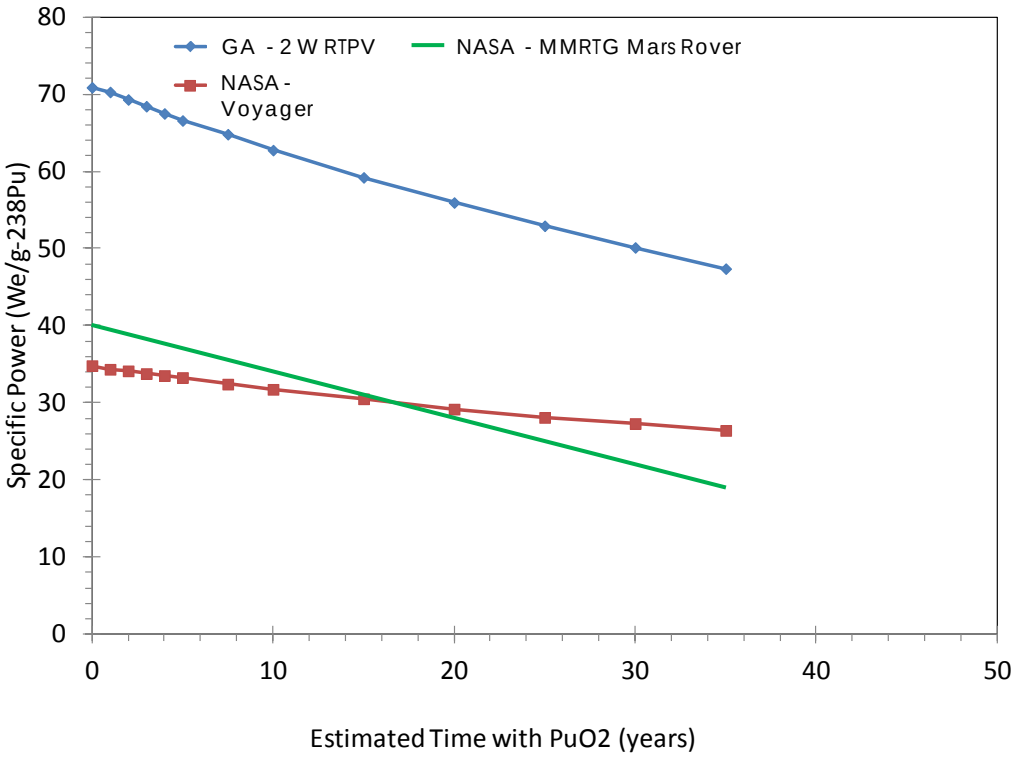

FIGURE 8: TPV Power System Specific Power vs Time compared to NASA Voyager RTG Power System

TPV power systems have been successfully developed demonstrated in a variety of form factors (see Figure 9), and it has been verified that the technology is highly flexible in terms of mission power needs and duration. The same design principles apply

FIGURE 9. Watt and mW scale TPV System Hardware that has been developed, modeled and tested, D and AA size batteries for scale

CONCLUSION

System testing with Curium 244 and Plutonium 238 radioisotope heat sources has shown that the high performing 0.6 eV InGaAs TPV cells display less than 1% of degradation in power performance degradation per year due to all effects, primarily that of the decay in source heat and neutron damage to the TPV semiconductor devices. This result shows that these TPV devices are suitable for long life power sources fueled by radioisotopes such as those needed for aerospace power systems which cannot make use of solar. This work represents a resource for the space power community aspiring to develop TPV based power systems. General Atomics has developed a higher power version of a TPV power system that has demonstrated over 3 Watts of output power and a system efficiency near 8% in a hermetic package suitable for applications to aerospace power for long life missions. This system is ready for testing using a Plutonium 238 heat source at Los Alamos National Lab in FY2015-2016. The scaling laws of TPV power systems have been demonstrated and the technologies needed to deploy a 1-100 Watt TPV based power system have all been developed. TPV power systems use solid state indirect conversion technology to generate power with no moving parts and minimal power degradation over time.

ACKNOWLEDGMENTS

Initial MIPS scale RTPV work funded by DARPA Micortechnologies Office (MTO). Testing of fueled RTPV systems performed at Oak Ridge National Laboratory.

REFERENCES

[1] J. S. Ward, A. Duda, M. W. Wanlass, J. J. Carapella, X. Wu, R. J. Matson, T. J. Coutts, T. Moriarty, C. S. Murray, D. R. Riley, Thermophotovoltaic Generation of Electricity 1997, 227
[2] J. G. Cederberg, M. J. Hafich, R. M. Biefeld, M. Palmisiano, *J. Cryst. Growth* **2003**, *248*, 289.
[3] J. G. Cederberg, S. R. Lee, Sandia Report *SAND2007-0108* **2007**
[4] S. L. Murray, F. D. Newman, C. S. Murray, D. M. Wilt, M. W. Wanlass, P. Ahrenkiel, R. Messham, R. R. Siergiej, *Semicond. Sci. Technol.* **2003**, *18*, S202.
[5] F. D. Newman, M. A. Stan, S. L. Murray, C. S. Murray, *J. Cryst. Growth* **2004**, *272*, 650.
[6] D. Wilt, R. Wehrer, M. Palmisiano, M. Wanlass, C. Murray, *Semicond. Sci. Technol.* **2003**, *18*, S209.
[7] D. M. Wilt, N. S. Fatemi, P. P. Jenkins, V. G. Weizer, J. R. W. Hoffman, R. K. Jain, C. S. Murray, D. R. Riley, "Electrical and optical performance characteristics of 0.74 eV p/n InGaAs monolithic interconnected modules", presented at *Third NREL Conference on thermophotovoltaic generation of electricity*, Colorado Springs, Colorado (USA), **1997**.
[8] J. G. Cederberg, S. R. Lee, *Appl. Phys. Lett.* **2007**, *91*.
[9] J. S. Ward, A. Duda, M. W. Wanlass, J. J. Carapella, X. Wu, R. J. Matson, T. J. Coutts, T. Moriarty, C. S. Murray, D. R. Riley, *Thermophotovoltaic Generation of Electricity* **1997**, 227.
[10] N. S. Fatemi, D. M. Wilt, P. P. Jenkins, V. G. Weizer, R. W. Hoffman, Jr., C. S. Murray, D. Scheiman, D. Brinker, D. Riley, "InGaAs monolithic interconnected modules (MIMs)", presented at *Photovoltaic Specialists Conference, 1997., Conference Record of the Twenty-Sixth IEEE*, **1997**.
[11] R. R. Siergiej, B. Wernsman, S. A. Derry, R. G. Mahorter, R. J. Wehrer, S. D. Link, M. N. Palmisiano, R. L. Messham, S. B. Murray, C. S. Murray, F. Newman, J. Hills, D. Taylor, *Thermophotovoltaic Generation of Electricity* **2003**, *653*, 414.
[12] S. L. Murray, F. D. Newman, C. S. Murray, D. M. Wilt, M. W. Wanlass, P. Ahrenkiel, R. Messham, R. R. Siergiej, *Semicond. Sci. Technol.* **2003**, S202.
[13] N. S. Fatemi, D. M. Wilt, P. P. Jenkins, R. W. Hoffman, V. G. Weizer, C. S. Murray, D. Riley, *Thermophotovoltaic Generation of Electricity* **1997**, 249.
[14] R. R. Siergiej, B. Wernsman, S. A. Derry, R. J. Wehrer, S. D. Link, M. N. Palmisiano, D. R. Riley, C. S. Murray, F. Newman, J. Hills, *Device Research Conference. Conference Digest (Cat. No.01TH8561)|Device Research Conference. Conference Digest (Cat. No.01TH8561)* **2001**, 159.
[15] C. J. Crowley, N. A. Elkouh, S. Murray, D. L. Chubb, *Space Technology and Applications International Forum-Staif 2005* **2005**, *746*, 601.
[16] M. B. Clevenger, C. S. Murray, S. A. Ringel, R. N. Sacks, L. Qin, G. W. Charache, D. M. Depoy, *Thermophotovoltaic Generation of Electricity* **1999**, *460*, 327.

[17] B. Wernsman, R. R. Siergiej, S. D. Link, R. G. Mahorter, M. N. Palmisiano, R. J. Wehrer, R. W. Schultz, G. P. Schmuck, R. L. Messham, S. Murray, C. S. Murray, F. Newman, D. Taylor, D. M. DePoy, T. Rahmlow, *IEEE Transactions On Electron Devices* **2004**, *51*, 512.
[18] S. Y. Lin, J. Moreno, J. G. Fleming, *Appl. Phys. Lett.* **2003**, *83*, 380.
[19] J. E. Strauch, Sandia National Lab Cooperative Research and Development Agreement CRADA #1573.55.
[20] F. O'Sullivan, I. Celanovic, N. Jovanovic, J. Kassakian, S. Akiyama, K. Wada, *J. Appl. Phys.* **2005**, *97*.

A History, the Development and Potential Mission Uses for a 40mW Radioisotope Power System

Frederick A Leavitt(1), Bill J Nesmith(2), John C Bass(1) and Carmen Brown(1)

(1) Hi-Z Technology, Inc., 7606 Miramar Road, San Diego, CA 92126-4210 USA
+1 858 695 6660; info@hi-z.com

(2) Jet Propulsion Laboratory, MS 277-207, 4800 Oak Grove Dr., Pasadena, CA, 91109 USA
bill.j.nesmith@jpl.nasa.gov

Abstract. This paper discusses the history of the design of the Radioisotope Power System (RPS) which dates back to the late 1960's. Several iterations of the original design have evolved over the years, as both the power system and missions have changed. It started as a potential power source for under water use by the Navy in the 1970's, and has recently evolved into a small power system that could be used by NASA on future space missions. The current RPS design uses a circuit of 676 small Bi_2Te_3 elements arranged in a multiple redundant circuit. It is designed to be powered by a single 1 watt thermal radioisotope heater unit (RHU) which is currently used by NASA for thermal control on-board various deep space missions. The RHU is powered by the heat released by the decay of ^{238}Pu, which has a half-life of 87.7 years.

The original NASA mission intending to use the RPS needed to provide power to 24 weather stations to be placed on the surface of Mars. These stations would provide data to an orbital satellite for relay to Earth.

Other potential missions are anticipated and these include Mars 2020 "drop-and-forget" science/instrumentation packages operating for several years on the Martian surface (beacons, seismometers, weather stations, etc…), a high G-impact mission for penetrators to be launched to investigate the interior temperature and chemistry of various celestial/small bodies. A description of these potential missions is discussed.

Keywords: RPS, RTG, ^{238}Pu

BACKGROUND ON RPS WORK

The genesis of today's RPS began in the 1970's when the Department of Defense (DoD) requested that General Atomic Corporation, now General Atomics (GA), build several milliwatt sized generators for the Navy. The generator shown in Figure 1 used a four Watt ^{238}Pu heat source and a 75mW thermoelectric module (TEM) made of P type and N type bismuth telluride alloys. The module elements had to be small to produce the required 5 volts and relatively long to maintain the desired 230°C hot side temperature. The RPS's were transferred to the customer after they were fueled by the Los Alamos National Laboratory. Several of these fueled RPS's were monitored for more than ten years and were found to perform as predicted. Figure 2 is a chart showing the performance of four of these RPS's as a function of time.

Since Hi-Z's founders all came from GA's thermoelectric program they continued this work at Hi-Z Technology[1]. Between 1998 and 2007, Hi-Z participated in the development of the 40mW RPS. This program was funded by the Department of Energy (DOE) and the 40mW RPS was intended to be used by NASA as the power source for a series of weather stations to be placed on Mars.

This program was cancelled along with NASA's PASCAL mission. Figure 3 depicts the proposed landing of the PASCAL weather station.

FIGURE 1. 75mW RTG without housing and insulation

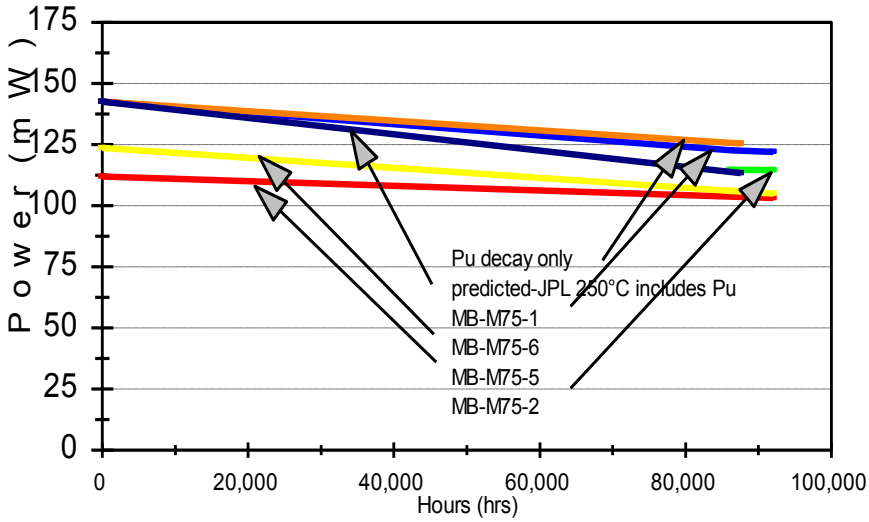

FIGURE 2. 11-year life test data for 4 fueled General Atomics 75 mW generators. The 4 units shown here represent typical data of the twenty seven RPSs fabricated. The generators were used by the Navy from the 1970s through the 1990s.

The 40 mW RPS was designed to use the 1 Wt Radioisotope Heater Unit (RHU) which is fueled by $^{238}PuO_2$ as exhibited in Figure 4. A photograph of the fuel pellet at the core of the RHU is shown in Figure 5. The construction of the 40mW RPS is similar to the RPS designed at General Atomics using four titanium wires to securely hold the fuel capsule holder (FCH) containing the RHU against one end of the module. An electrically heated 40mW RPS is shown in Figure 6 without its housing and the multi-foil insulation that surrounds the FCH and TEM.

The original RPS designed at General Atomics included a TEM with single electrical circuit of 324 individual thermoelectric legs. This large number of legs was required to deliver the power at a matched load of five volts. NASA added the additional requirement of redundancy.
To accommodate this new requirement a new module was designed and fabricated that included 676 legs arranged in a series / parallel circuit. The series parallel circuit is illustrated in Figure 7 alongside a more conventional series circuit. Figure 8 is a photograph of the original 75 milliwatt module alongside the new 40mW module with the redundant circuit.

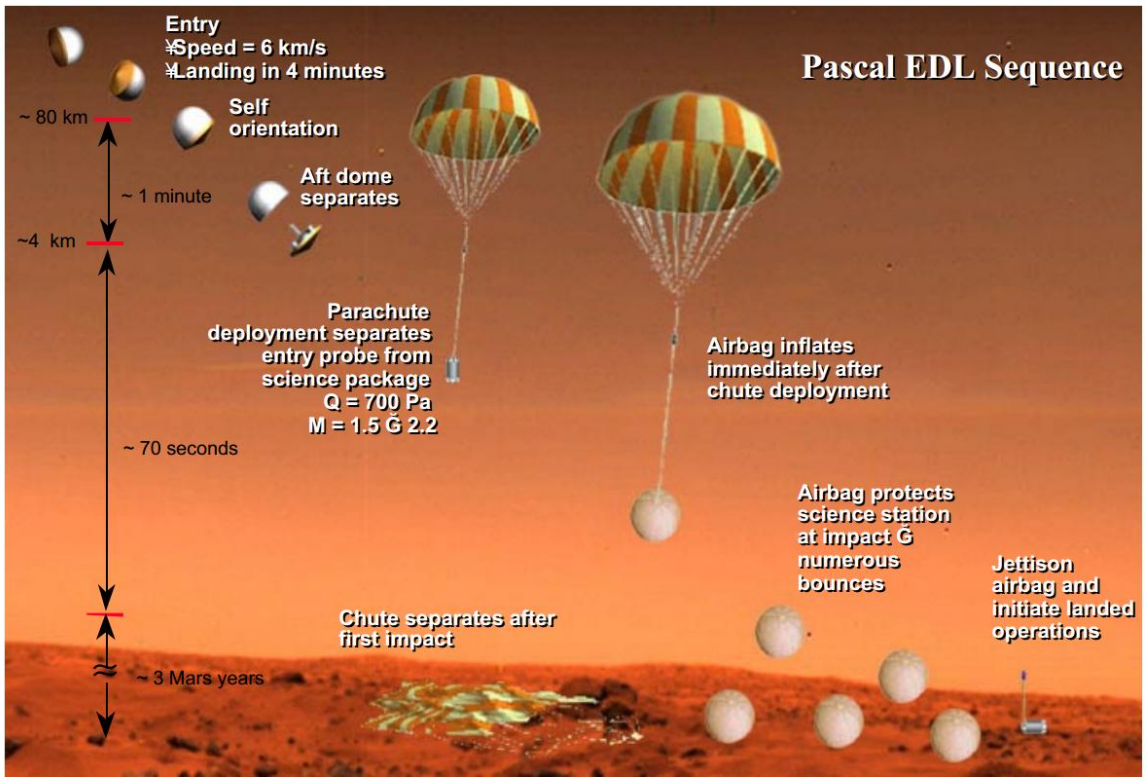

FIGURE 3. The Proposed Landing Sequence of the PASCAL Weather Station

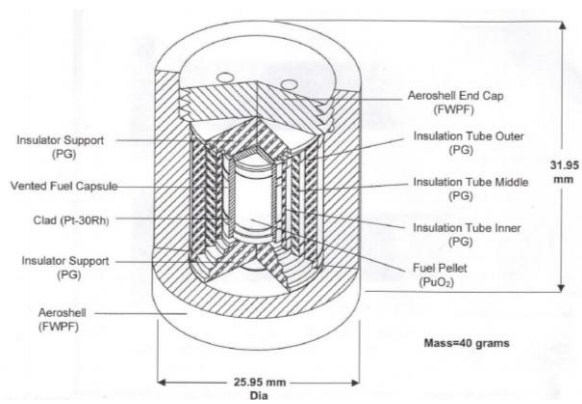

FIGURE 4. 1 Watt radioisotope heating unit (RHU)

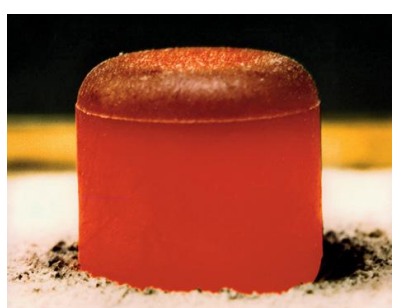

FIGURE 5. Fuel pellet glowing under its own heat

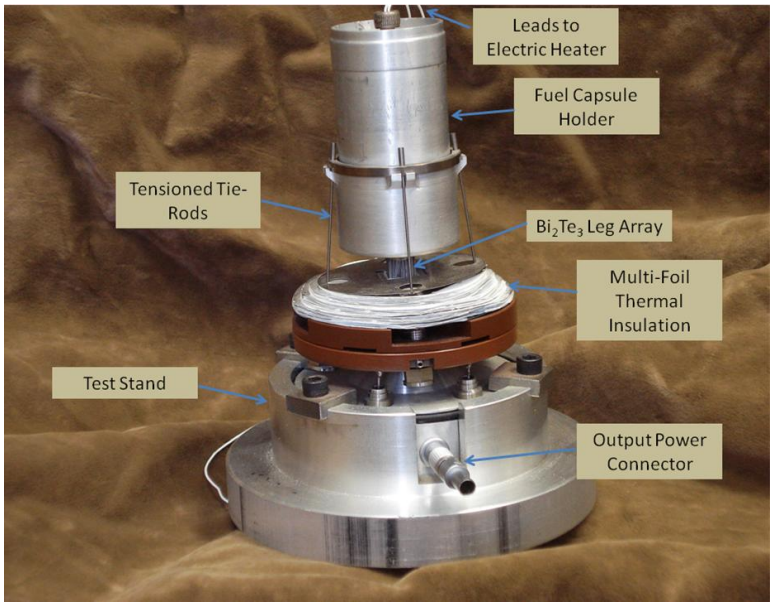

FIGURE 6. Electrically-heated version of the 40 milliwatt RPS used for test purposes. Shown with outer housing removed and mounted on a test fixture.

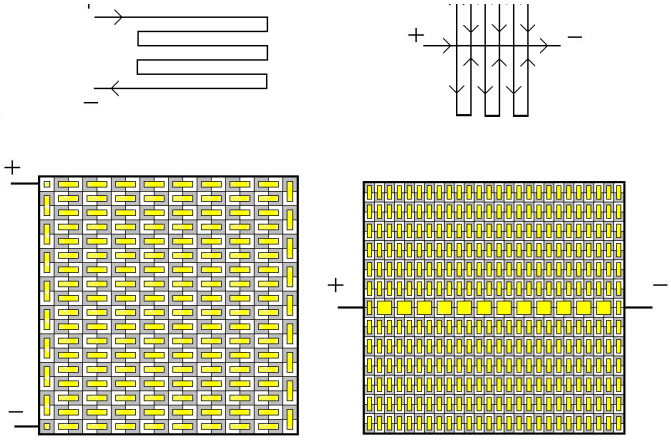

FIGURE 7. A single series circuit on the left compared to a cross linked parallel circuit on the right.

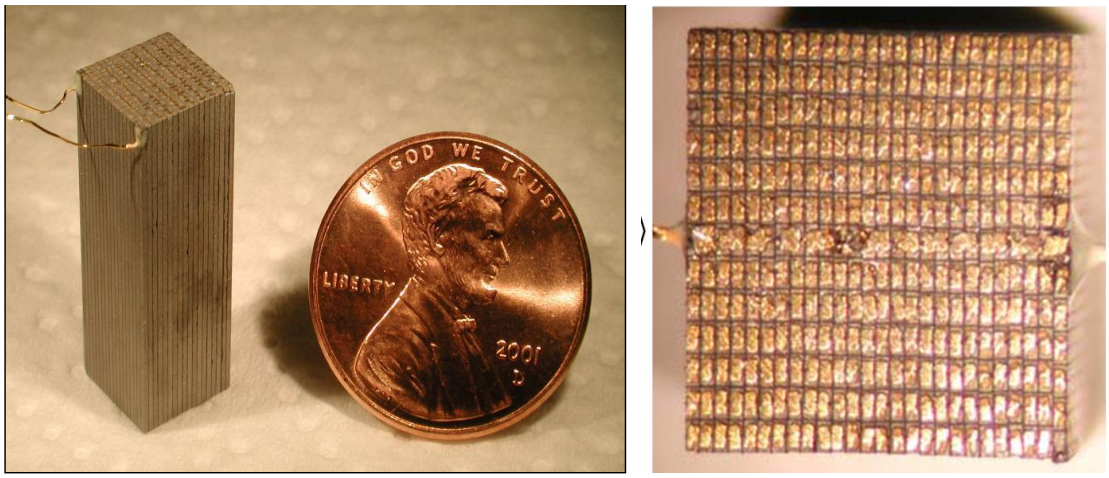

FIGURE 8. A single series circuit on the left compared to a cross linked parallel circuit on the right.

Current RPS work

In 2014 Hi-Z was awarded a Phase I SBIR to design an RPS fueled by a single 1 watt RHU similar to the RPS already built and tested by Hi-Z but this RPS was required to survive a 10,000 G shock.
NASA had already shock tested Hi-Z's 40mW RPS design and found it to be quite shock resistant along the vertical axis of generator. However, due to the ability of the FCH to rock on top of the TEM it had little shock resistance once the direction of impact deviated from vertical as shown in Figure 9.

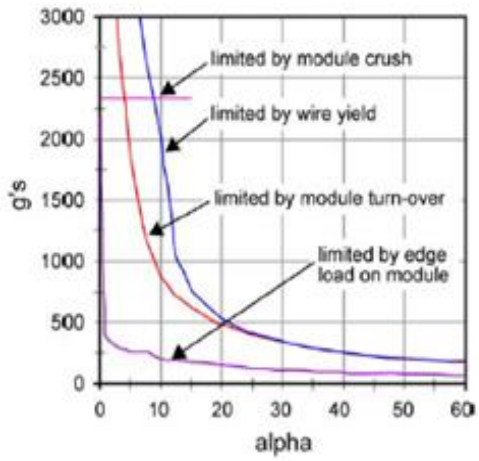

FIGURE 9. 40 mW Generator tested for G load at NASA Ames. It sustained over 2,000 G's along its axis.

With the aid of ATA Engineering and their skills in computer modeling, Hi-Z developed a concept for a 40mW RPS that is expected to be able to survive a 10,000 G shock from any orientation.

The key points that came out of the modeling were that the FCH and the TEM cannot be allowed to touch each other. The rocking and impact between the two components will destroy the module. It was decided to suspend the module and the FCH independently and make thermal connections between the TEM and the FCH with flexible graphite heat straps.

It also quickly became obvious that the suspension fibers could not be metal. Wires that are strong enough to survive the shock will carry far too much heat away from the FCH.

It was decided to suspend the FCH and the TEM from glass fibers. Glass fibers have the added advantage of having a low thermal conductivity compared to metal wires. Even when several hundred fibers are used to survive the 10,000 G shock, the heat lost through the fibers is similar to what is lost in the original design using four titanium wires. The final concept that was proposed in the phase II effort is illustrated in Figure 10.

The one feature that does have a significant impact on the performance of the RPS is the choice of insulation. Thermal modeling performed at Hi-Z indicates that in a vacuum 75% of the heat from the 1 watt heat source can be driven through the module. If the cavity is filled with Xe gas then only 60% of the heat can be driven through the module. In practice this means that a Xenon filled RPS can produce about 33 mW BOL and a vacuum filled RPS can produce 41mW BOL. If the RPS is not required to sustain a 10,000G shock then fewer suspension fibers will be required and an RPS that produces 44mW BOL could be designed.

Figure 11 is a schematic drawing of the RPS showing the heat paths from the RHU to the housing when the cavity of the RPS is filled with Xe gas and when the cavity is under a vacuum. In addition to the multi-foil insulation that has been successfully used in previous RPS designs, an opacified aerogel was also studied. The performance of the two insulations is expected to be similar but the aerogel may be better able to survive high shock loads than the multi-foil insulation.

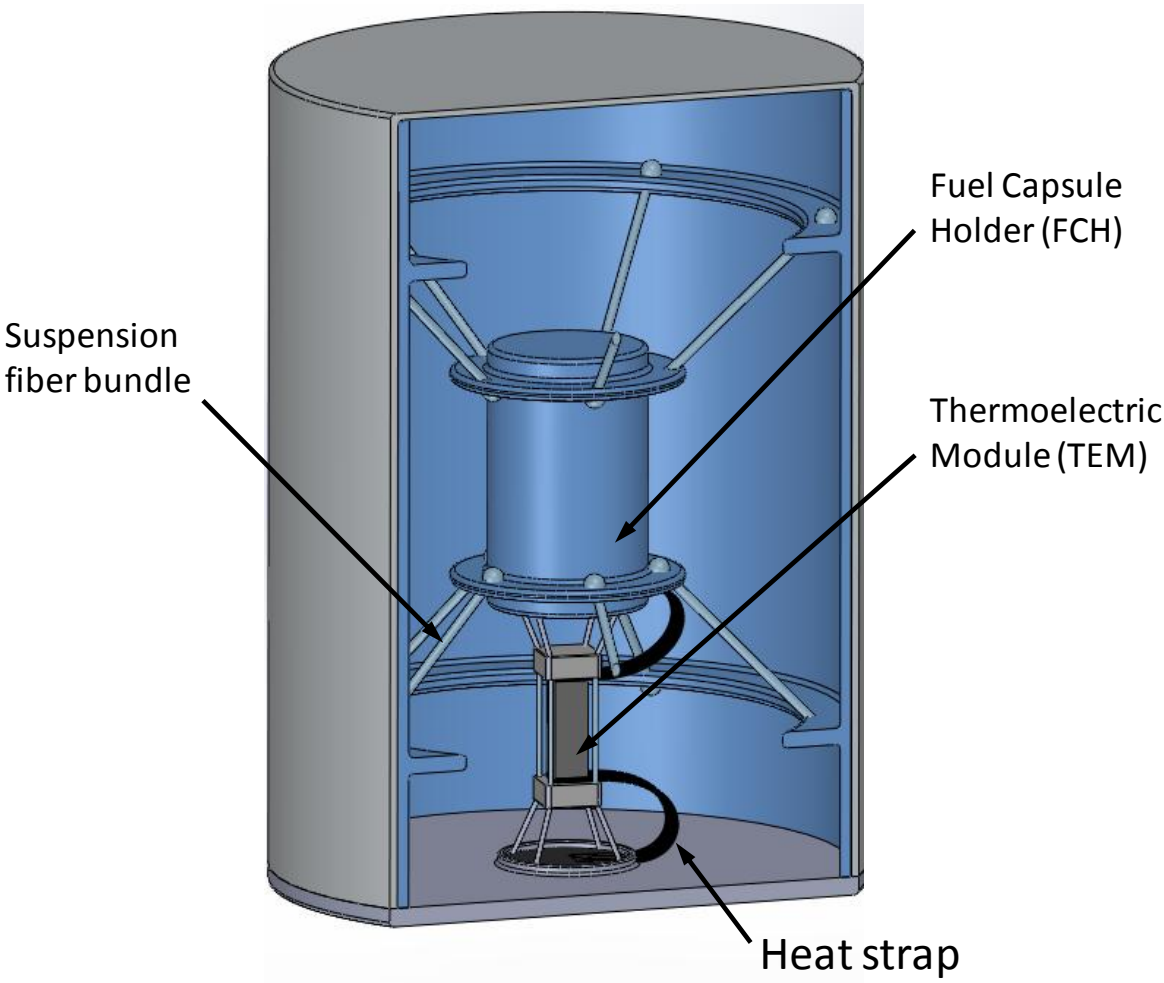

FIGURE 10. Conceptual drawing of the 10,000 G RPS with independently suspended FCH and TEM.

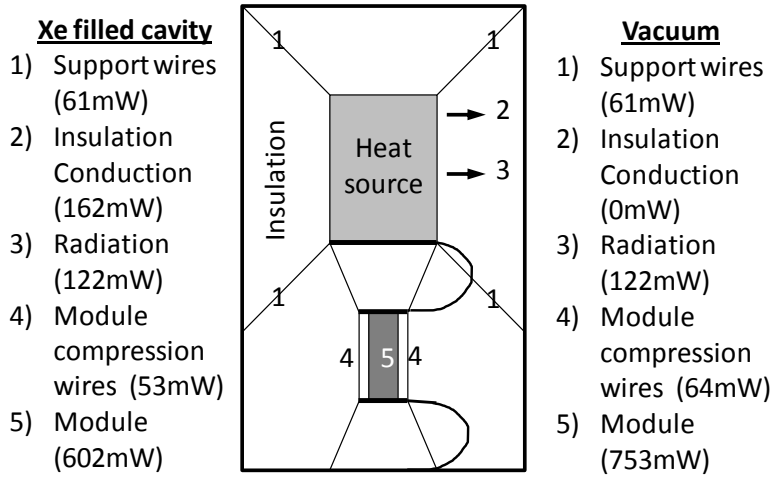

FIGURE 11. Thermal paths for heat flow in a 10,000 G RPS.

If the RPS is to be used in space then the obvious choice would be to vent the cavity of the RPS to space but when the RPS is to be used in an atmosphere it may be safer to fill the cavity with Xe gas. When the RPS is being fabricated a small pinhole leak can be easily detected and repaired but small leaks are notorious for forming after fabrication especially under conditions where high shock forces and vibration are present. With the cavity filled with a slightly positive pressure of Xe the Xe leaking out would prevent the influx of any gas. For small leaks the Xe gas could protect the RPS for years.

Potential Missions for the RPS

The availability of a 40mW RPS with a twenty year lifetime can potentially enhance or enable many future deep space science instrument packages and missions that could be otherwise limited or constrained by conventional solar arrays and/or energy storage systems. Solar energy limitations could result from large distances between the sun and the spacecraft (Low Intensity, Low Temperature (LILT) effects), high latitude positions on planetary bodies (seasonal effects), sun blocking surface features like craters or mountains, eclipses or day night cycles on moons/small bodies (orbital/rotational effects), or atmospheric blockage from particulates/vapors. Low temperature environments are a challenge for energy storage systems and this system could provide both electricity for charging and heat for temperature control. For long lived missions, the energy density of this 87.7 year half-life radioisotope system exceeds that of any chemical energy storage. Lunar missions must deal with 14 days of continuous darkness; Martian missions have limited sunlight during the Martian winter especially in locations near the poles and they are always at risk of being covered by dust.

Perhaps the nearest planned mission that could benefit from the 40mW RPS is the Mars 2020 mission. A rover similar to the Curiosity (see Figure 12) is planned for this mission and small experimental packages will be dropped

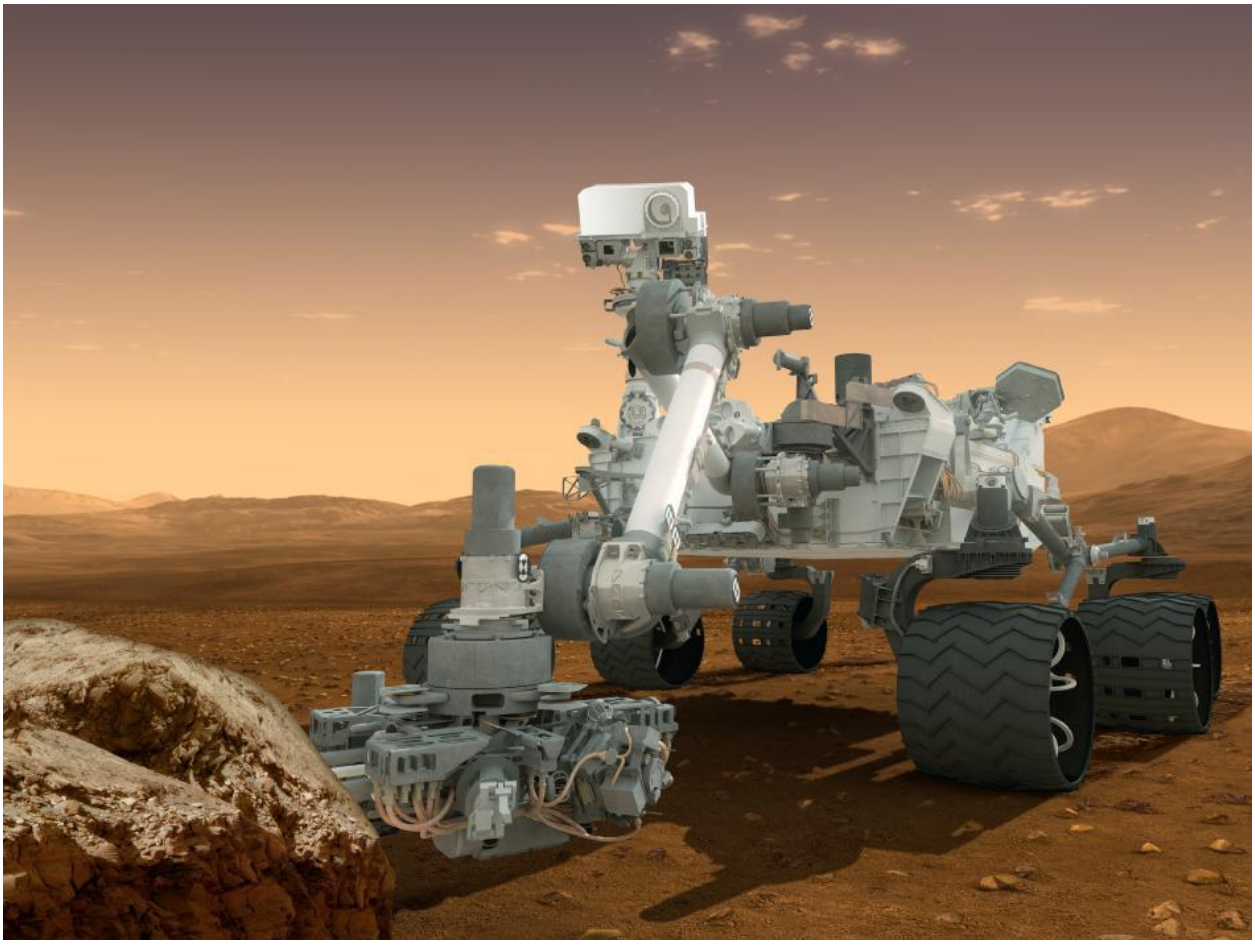

FIGURE 12. Curiosity Rover

off by the rover as it travels across the Martian landscape. Without the RPS these experimental packages must be powered by photovoltaics that are at risk of failing due to dust and low light levels. An RPS could power the package and keep the electronics warm.

Other potential missions where the 40mW RPS is needed are surface packages landed on comets and meteors. Using photovoltaic's adds complexity to the experimental package and runs the risk of the lander ending up in the shade as happened in the recent Philae lander (see Figure 13) that landed on the comet.

FIGURE 13. Philae lander on comet surface.

Further study of the moons of other planets is also of great interest, especially Europa. Large subsurface bodies of water are thought to be a potential habitat for extraterrestrial life. These potentially very radiation hard power systems could be placed on the surface with science packages or surface landers or just below the surface for future Europa missions providing communication links back to orbiters and then to earth. These small power systems could be used in the next generation Europa missions using cryobot and hydrobot with the communication links enabled through the ice with small transceivers that would be dropped off in the melted ice and refrozen in the ice behind the cryobot.

With its ability to survive impacts up to 10,000 g's, the new 40mW RPS could potentially power long lived high impact penetrators, probes and landed packages.

CONCLUSIONS

The availability of a 40mW RPS with a twenty year lifetime can potentially enhance or enable many future deep space science instrument packages and missions that could be otherwise limited or constrained by conventional solar arrays and/or energy storage systems. Solar energy limitations could result from large distances between the sun and the spacecraft (Low Intensity Low Temperature (LILT) effects), high latitude positions on planetary bodies (seasonal effects), sun blocking surface features like craters or mountains, eclipses or day night cycles on moons/small bodies (orbital/rotational effects), or atmospheric blockage from particulates/vapors. Low temperature environments are a challenge for energy storage systems and this systems could provide both electricity for charging and heat for temperature control. For long lived missions, the energy density of this 87.7 year half-life radioisotope system exceeds that of any chemical energy storage system.

The basic design of Hi-Z's RPS is proven with terrestrial based applications that have exceeded ten years. The modules have demonstrated good stability and high strength and with the proposed design the RPS is expected to be able to survive shocks up to 10,000 G's.

15-50002